BEILSTEIN JOURNAL OF NANOTECHNOLOGY

Organized films

Edited by Maurizio Canepa and Helmuth Möhwald

Imprint

Beilstein Journal of Nanotechnology
www.bjnano.org
ISSN 2190-4286
Email: journals-support@beilstein-institut.de

The *Beilstein Journal of Nanotechnology* is published by the Beilstein-Institut zur Förderung der Chemischen Wissenschaften.

Beilstein-Institut zur Förderung der Chemischen Wissenschaften
Trakehner Straße 7–9
60487 Frankfurt am Main
Germany
www.beilstein-institut.de

BEILSTEIN JOURNAL OF NANOTECHNOLOGY

Organized films

Maurizio Canepa*[1] and Helmuth Möhwald[2]

Editorial

Open Access

Address:
[1]Department of Physics, University of Genova, via Dodecaneso 33, 16146 Genova, Italy, and [2]Max Planck Institute of Colloids and Interfaces, Am Mühlenberg 1, 14476 Potsdam, Germany

Email:
Maurizio Canepa* - canepa@fisica.unige.it

* Corresponding author

Beilstein J. Nanotechnol. **2016,** *7,* 406–408.
doi:10.3762/bjnano.7.35

Received: 09 February 2016
Accepted: 24 February 2016
Published: 09 March 2016

This article is part of the Thematic Series "Organized films".

Editor-in-Chief: T. Schimmel

Langmuir–Blodgett (LB) films, prepared by transferring an amphiphilic molecular monolayer (Langmuir monolayer) from a water surface onto a solid substrate, represent both archetypal and prototypical “organized films” (OFs). Known since about 80 years, LB films can be considered from many points of view as one of the prominent predecessors of what we call nanoscience today [1]. Their impact on interface science over the last four decades was undoubtedly based on pioneering works such as the beautiful studies of Kuhn and Möbius on energy transfer between molecules arranged with angstrom precision [2], or the stimulating works of Roberts and Petty [3], which envisaged many applications. This was most notable in the fields of molecular electronics and biosensors, which were emerging in those times and are now undergoing flourishing development.

The interdisciplinary character of OFs, at the fortunately ill-defined borders between physical chemistry, chemical physics, biophysics and surface engineering, is a constant that marks the evolution of the field. In fact, one of us (H.M.) with his group entered the field many years ago, initially motivated by the biophysics of membranes and contributed to the development of new methods to characterize monolayers. Fluorescence microscopy and Brewster angle microscopy [4-7] were successfully employed to show that Langmuir monolayers exhibit an interesting domain structure on the micrometer scale with peculiar features due to the anisotropy of the interface. Surface X-ray diffraction revealed a multitude of ordered and disordered phases [8] that could be mapped on smectic liquid crystals.

These and other studies, while revealing the interesting two-dimensional physics of Langmuir monolayers, also brought to attention some important issues in obtaining films with high geometric order extending over micrometer length scales. On one hand, the domain structure causes grain boundaries, which are almost impossible to remove. Furthermore, the tight packing of alkane chains in classical LB films prohibits the incorporation of foreign molecules with high precision. This fact is a significant disadvantage if one aims to arrange a molecule in a controlled way for electronic and optoelectronic applications. In this respect, defined protein incorporation, for example, for designing a biosensor, seemed hopeless. Incidentally, these problems were largely shared by self-assembled monolayers (SAMs), as exemplified by the most popular examples of alkanethiols on Au or silanes and siloxanes on SiO_2. These are yet another very broad class of OFs whose investigation proceeded in parallel with that of Langmuir films [9,10].

Clearly, the whole research sector benefited from the evolution of new analysis tools and surface spectroscopy methods, which allowed for characterization at all length scales. One may first think of monolayer-sensitive optical methods [11] or of the wealth of techniques based on third and fourth generation synchrotron sources. However, the most striking example is by far represented by the invention and extensive development of scanning probe methods in the late 1980s. With these methods, one could learn much more about details of the molecular structure and the surface order [12,13], penetrating the nanoscale realm. Furthermore, AFM in particular enabled continuous developments in manipulating and modifying films, opening the way to patterning and even to nanolithography methods [14]. This was a crucial step in the development of nanosensors and biochips, especially in new and emerging fields such as nanomedicine.

Coming back to LB films, irrespective of other technical difficulties in fabrication and long term stability, the problems mentioned above made such films less appealing for applications, emphasizing the need for exploration and invention of new processes of film fabrication. The most successful of these processes evolved during the habilitation of Gero Decher. In this process, popularly known as the layer-by-layer (LbL) technique, one consecutively adsorbs polyelectrolytes of opposite charge to form multilayers of nanometer thickness [15,16].

The studies were quickly extended to explore other types of (i) interactions (towards bio-specific ones and hydrogen bonding), (ii) adsorbents (from polymers to particles, proteins, polyvalent molecules), and (iii) substrates (from planar to colloidal particles and porous membranes). The know-how accumulated on OFs reinforced well-established links with bio-oriented research, as in the case of lipid–protein interactions [17,18] or in the development of functional capsules, opening interesting application perspectives [19-21]. Another side of the field of OF met the explosion of research on nano-objects such as nanoparticles, carbon nanotubes or the latest, graphene [22]. These have been used to build hybrid structures endowed with specific functionalities for applications in strategic technology fields as varied as theranostics, energy production and storage, and photovoltaics.

Similar trajectories were observed for SAMs, with increasing attention on new combinations of functional molecules and substrates, new analysis tools and new preparation methods [23], which varied significantly from the more traditional deposition from solution [24]. This is the case for MBE-like deposition in vacuum or UHV conditions [25], which is of current interest in the area of organic photovoltaics [26]. This also applies for biological molecules such as small amino acids, which allow fundamental and still open issues to be addressed about the subtle interplay between molecule–molecule and molecule–substrate interactions in determining the molecular networking at surfaces [27-29].

These few notes introduce this Thematic Series, which aims to present a partial overview of the current research on OFs. The articles emphasize the strong interdisciplinary character, the evident connections with nanoscience and nanotechnology, and some directions of expansion of the field of OFs.

This Thematic Series was conceived while organizing ECOF-14, the European Conference on Organized Films, which took place in Genova in July 2015, chaired by one of us (M.C.) and Ornella Cavalleri. This conference has an established tradition that dates back to a discussion meeting organized in 1986 by Helmuth Möhwald and Wolfgang Knoll in Munich and a follow-up meeting organized as a NATO workshop in Paris by André Barraud in 1988. These meetings finally evolved into a Europe-based conference, ECOF-3 (Mainz, 1990), organized by the Möhwald group. The number following the conference name abbreviation was preserved to indicate successive conferences, and since then, the conference has traveled all over Europe, with the next conference announced for Dresden, 2017. It still encompasses lively and fruitful discussions of about 200 participants, again this time with high scientific quality and openness to nearest neighbor fields, as the readers of this series are invited to verify.

Maurizio Canepa and Helmuth Möhwald

Genova and Potsdam, February 2016

Acknowledgements

The authors warmly thank the editorial and production teams of the *Beilstein Journal of Nanotechnology* for their highly professional collaboration in the preparation of this Thematic Series. M.C. thanks Ornella Cavalleri, Annalisa Relini and Ranieri Rolandi for their help at ECOF-14 and with this article.

References

1. Kuhn, H.; Möbius, D. *Angew. Chem., Int. Ed. Engl.* **1971,** *10,* 620–637. doi:10.1002/anie.197106201
2. Nakahara, H.; Fukuda, K.; Möbius, D.; Kuhn, H. *J. Phys. Chem.* **1986,** *90,* 6144–6148. doi:10.1021/j100281a019
3. Roberts, G. G.; Petty, M. C.; Baker, S.; Fowler, M. T.; Thomas, N. J. *Thin Solid Films* **1985,** *132,* 113–123. doi:10.1016/0040-6090(85)90463-8
4. Lösche, M.; Sackmann, E.; Möhwald, H. *Ber. Bunsen-Ges. Phys. Chem.* **1983,** *87,* 848–852. doi:10.1002/bbpc.19830871004

5. Knobler, C. M. *Science* **1990,** *249,* 870–874. doi:10.1126/science.249.4971.870
6. Hénon, S.; Meunier, J. *Rev. Sci. Instrum.* **1991,** *62,* 936–939. doi:10.1063/1.1142032
7. Hönig, D.; Möbius, D. *J. Phys. Chem.* **1991,** *95,* 4590–4592. doi:10.1021/j100165a003
8. Kjaer, K.; Als-Nielsen, J.; Helm, C. A.; Laxhuber, L. A.; Möhwald, H. *Phys. Rev. Lett.* **1987,** *58,* 2224–2227. doi:10.1103/PhysRevLett.58.2224
9. Sabatani, E.; Rubinstein, I.; Maoz, R.; Sagiv, J. *J. Electroanal. Chem. Interfacial Electrochem.* **1987,** *219,* 365–371. doi:10.1016/0022-0728(87)85054-4
10. Laibinis, P. E.; Whitesides, G. M.; Allara, D. L.; Tao, Y. T.; Parikh, A. N.; Nuzzo, R. G. *J. Am. Chem. Soc.* **1991,** *113,* 7152–7167. doi:10.1021/ja00019a011
11. Canepa, M. A Surface Scientist's View on Spectroscopic Ellipsometry. In *Surface Science Techniques;* Bracco, G.; Holst, B., Eds.; Springer-Verlag: Berlin, Heidelberg, 2013; Vol. 51, pp 99–135. doi:10.1007/978-3-642-34243-1_4
12. Schwartz, D. K.; Garnaes, J.; Viswanathan, R.; Zasadzinski, J. A. N. *Science* **1992,** *257,* 508–511. doi:10.1126/science.257.5069.508
13. Poirier, G. E.; Tarlov, M. J. *Langmuir* **1994,** *10,* 2853–2856. doi:10.1021/la00021a001
14. Xu, S.; Liu, G.-y. *Langmuir* **1997,** *13,* 127–129. doi:10.1021/la962029f
15. Decher, G.; Hong, J.-D. *Makromol. Chem., Macromol. Symp.* **1991,** *46,* 321–327. doi:10.1002/masy.19910460145
16. Lvov, Y.; Decher, G.; Möhwald, H. *Langmuir* **1993,** *9,* 481–486. doi:10.1021/la00026a020
17. Maltseva, E.; Kerth, A.; Blume, A.; Möhwald, H.; Brezesinski, G. *ChemBioChem* **2005,** *6,* 1817–1824. doi:10.1002/cbic.200500116
18. Canale, C.; Torrassa, S.; Rispoli, P.; Relini, A.; Rolandi, R.; Bucciantini, M.; Stefani, M.; Gliozzi, A. *Biophys. J.* **2006,** *91,* 4575–4588. doi:10.1529/biophysj.106.089482
19. Caruso, F.; Caruso, R. A.; Möhwald, H. *Science* **1998,** *282,* 1111–1114. doi:10.1126/science.282.5391.1111
20. Diaspro, A.; Silvano, D.; Krol, S.; Cavalleri, O.; Gliozzi, A. *Langmuir* **2002,** *18,* 5047–5050. doi:10.1021/la025646e
21. Sukhorukov, G.; Fery, A.; Möhwald, H. *Prog. Polym. Sci.* **2005,** *30,* 885–897. doi:10.1016/j.progpolymsci.2005.06.008
22. Li, X.; Zhang, G.; Bai, X.; Sun, X.; Wang, X.; Wang, E.; Dai, H. *Nat. Nanotechnol.* **2008,** *3,* 538–542. doi:10.1038/nnano.2008.210
23. Love, J. C.; Estroff, L. A.; Kriebel, J. K.; Nuzzo, R. G.; Whitesides, G. M. *Chem. Rev.* **2005,** *105,* 1103–1170. doi:10.1021/cr0300789
24. Barth, J. V.; Costantini, G.; Kern, K. *Nature* **2005,** *437,* 671–679. doi:10.1038/nature04166
25. Schreiber, F.; Eberhardt, A.; Leung, T. Y. B.; Schwartz, P.; Wetterer, S. M.; Lavrich, D. J.; Berman, L.; Fenter, P.; Eisenberger, P.; Scoles, G. *Phys. Rev. B* **1998,** *57,* 12476–12481. doi:10.1103/PhysRevB.57.12476
26. Gottfried, J. M. *Surf. Sci. Rep.* **2015,** *70,* 259–379. doi:10.1016/j.surfrep.2015.04.001
27. Kühnle, A.; Molina, L. M.; Linderoth, T. R.; Hammer, B.; Besenbacher, F. *Phys. Rev. Lett.* **2004,** *93,* 086101. doi:10.1103/PhysRevLett.93.086101
28. Cavalleri, O.; Gonella, G.; Terreni, S.; Vignolo, M.; Floreano, L.; Morgante, A.; Canepa, M.; Rolandi, R. *Phys. Chem. Chem. Phys.* **2004,** *6,* 4042–4046. doi:10.1039/b405516k
29. Gonella, G.; Terreni, S.; Cvetko, D.; Cossaro, A.; Mattera, L.; Cavalleri, O.; Rolandi, R.; Morgante, A.; Floreano, L.; Canepa, M. *J. Phys. Chem. B* **2005,** *109,* 18003–18009. doi:10.1021/jp051549t

License and Terms

BEILSTEIN JOURNAL OF NANOTECHNOLOGY

Electrochemical behavior of polypyrrol/AuNP composites deposited by different electrochemical methods: sensing properties towards catechol

Celia García-Hernández[1], Cristina García-Cabezón[*2], Cristina Medina-Plaza[1], Fernando Martín-Pedrosa[2], Yolanda Blanco[2], José Antonio de Saja[3] and María Luz Rodríguez-Méndez[*1,§]

Full Research Paper

Open Access

Address:
[1]Department of Inorganic Chemistry, Engineers School, Universidad de Valladolid, 47011 Valladolid, Spain, [2]Department of Materials Science, Engineers School, Universidad de Valladolid, 47011 Valladolid, Spain and [3]Department of Condensed Matter Physics, Faculty of Sciences, Universidad de Valladolid, 47011 Valladolid, Spain

Email:
Cristina García-Cabezón[*] - anacrigar@gmail.com;
María Luz Rodríguez-Méndez[*] - mluz@eii.uva.es

* Corresponding author
§ Phone: +34 983 423540; Fax: +34 983 423310

Keywords:
catechol; conducting polymers; electropolymerization; gold nanoparticles (AuNPs); polypyrrole

Beilstein J. Nanotechnol. **2015,** *6,* 2052–2061.
doi:10.3762/bjnano.6.209

Received: 29 July 2015
Accepted: 02 October 2015
Published: 21 October 2015

This article is part of the Thematic Series "Organized films".

Guest Editor: M. Canepa

Abstract

Two different methods were used to obtain polypyrrole/AuNP (Ppy/AuNP) composites. One through the electrooxidation of the pyrrole monomer in the presence of colloidal gold nanoparticles, referred to as trapping method (T), and the second one by electrodeposition of both components from one solution containing the monomer and a gold salt, referred to as cogeneration method (C). In both cases, electrodeposition was carried out through galvanostatic and potentiostatic methods and using platinum (Pt) or stainless steel (SS) as substrates. Scanning electron microscopy (SEM) demonstrated that in all cases gold nanoparticles of similar size were uniformly dispersed in the Ppy matrix. The amount of AuNPs incorporated in the Ppy films was higher when electropolymerization was carried out by chronopotentiometry (CP). Besides, cogeneration method allowed for the incorporation of a higher number of AuNPs than trapping. Impedance experiments demonstrated that the insertion of AuNPs increased the conductivity. As an electrochemical sensor, the Ppy/AuNp deposited on platinum exhibited a strong electrocatalytic activity towards the oxidation of catechol. The effect was higher in films obtained by CP than in films obtained by chronoamperometry (CA). The influence of the method used to introduce the AuNPs (trapping or cogeneration) was not so important. The limits of detection (LOD) were in the range from 10^{-5} to 10^{-6} mol/L. LODs attained using films deposited on platinum were lower due to a synergy between AuNPs and platinum that facilitates the electron transfer, improving the electrocatalytic properties. Such synergistic effects are not so pronounced on stainless steel, but acceptable LOD are attained with lower price sensors.

Introduction

Polypyrrole (Ppy) is one of the most extensively studied, conducting polymers due to its good electrical conductivity and redox properties [1,2]. Ppy films can be easily generated by electropolymerization and used as a strong adherent layer using different electrochemical techniques [3]. Electrodes that are chemically modified with Ppy have good electrocatalytic activity. For this reason, they have been widely used as chemical sensors for the detection of a variety of substances. The structure and sensing properties of the Ppy films are considerably influenced by the electrochemical method used for the polymerization (potentiostatic, galvanostatic or potentiodynamic), by the electrochemical conditions (such as voltage, intensity, or scan rate), and by other experimental conditions such as the nature and concentration of the doping agent or the nature of the substrate [4]. This versatility can be used to better control the development of electrochemical sensors with the appropriate selectivity, reproducibility and sensibility towards a particular application.

Recently, composite nanomaterials based on conducting polymers and metal nanoparticles (NPs) of different metals have been developed. Gold nanoparticles (AuNPs) have attracted considerable interest because of their unique optical, electronic and catalytic properties [5-8]. Conducting polymer–gold nanoparticle composites exhibit improved physical and chemical properties over their single-component counterparts and are the focus of intensive research [9-12]. In the case of sensors, it has been reported that the insertion of NPs into the sensing layer provides remarkable properties compared to conventional polymeric matrices. Several examples have been reported in the literature. For instance, electrochemically deposited Ppy/AuNP films have demonstrated a great potential to detect DNA [13], ammonia gas at room temperature [14], caffeine [15] or hydroxylamine [16] among others.

Ppy/AuNP composites can be prepared by chemical and electrochemical polymerization. Electrochemical methods provide a better control of the structure and properties of the composite by controlling the electrochemical conditions during film generation [17]. The electrodeposition of the composite can be achieved using different strategies [18], mainly through the electrooxidation of the monomer in the presence of colloidal gold nanoparticles and the corresponding doping agent [19] but also by electrodeposition of polymer and metal from two separate solutions [20,21] or by electrodeposition of both components from one solution containing a monomer and a metal salt [17]. Finally, layers of electrodeposited polypyrrole and gold nanoparticle films can also been obtained from a single solution where PPy chains served as the reductant of tetrachloroauric acid [22].

Most of the works devoted to the electrosynthesis of Ppy/AuNPs films, are often limited to establish recipes to prepare the films and to tests their electrocatalytic or sensing properties. It could be expected that the electrocatalytic and the sensing properties of the Ppy/AuNPs films directly depend on the polymerization conditions. However, the influence of the polymerization conditions in the properties of Ppy/AuNPs electrodes has not been yet studied.

One of the fields where electrochemical sensors are having an important success is in the detection of phenolic compounds, which are strong antioxidant reagents present in foods, with beneficial effects on human health [23]. As phenols are electroactive compounds, they can be detected by amperometric or voltammetric techniques using graphite or platinum electrodes [24-26]. In addition, electrodes chemically modified with a variety of sensing materials (e.g., phthalocyanines or conducting polymers) have been successfully used as voltammetric sensors for the detection of antioxidants [27]. It has also been demonstrated that the combined use of electrocatalytic materials such as phthalocyanines and nanoparticles, can induce synergistic effects that increase the sensitivity of the sensors [28]. Following this idea, Ppy/AuNPs composites could be good candidates as electrocatalytic materials for the detection of phenols.

The objective of this work was to develop new voltammetric sensors based on electrodeposited Ppy/AuNps for the detection of catechol (an antioxidant of interest in the food industry) and to evaluate the influence of the electrodeposition method in their performance. For this purpose Ppy/AuNp films doped with 1-decanesulfonic acid (DSA) were deposited using different methods. The first approach consisted on the electrodeposition of the Ppy/AuNPs films from a solution containing the monomer and tetrachloroauric acid (denoted as “cogeneration”, C). The second approach consisted of the electrodeposition of the Ppy/AuNPs composited from a solution containing the monomer and gold nanoparticles previously formed (denoted as “trapping” method, T). In both methods, electrodeposition was carried out by chronoamperometry (CA) and by chronopotentiometry (CP). Particular attention was paid to the study of the influence of the substrate used for the electrodeposition that was carried out onto classical platinum electrodes and on stainless steel substrates. This aspect could play a crucial role not only in the structure, properties and performance of the sensor but also in the final price.

The structure and sensing properties of voltammetric sensors modified with Ppy/AuNPs films prepared under different conditions were evaluated and compared.

Results and Discussion

PPy/AuNPs films were prepared using two different approaches referred as “trapping method” and “cogeneration method”, which are described in the Experimental section. The electropolymerization of pyrrole was generated under potentiostatic and galvanostatic conditions on both platinum and stainless steel substrates, resulting in the formation of nanocomposites based on gold nanoparticles within the polypyrrole layer.

Electropolymerization of Ppy/AuNPs

Figure 1 shows the potential (E) vs time (t) curves registered during the electrodeposition PPy/AuNPs films using a galvanostatic process. The figure compares the results obtained by the trapping and the cogeneration methods. The CP registered for Ppy (in the absence of AuNPs) is also shown for comparison. As expected, as the current pulse was applied, a sharp decrease in the potential was observed. This was due to the charge of the double layer capacitance that produces a nucleation process at the electrode surface. Then, at the potential at which the monomer is oxidized, a stabilization and growth step was attained, which was characterized by a “plateau”, where the potential varied only slightly.

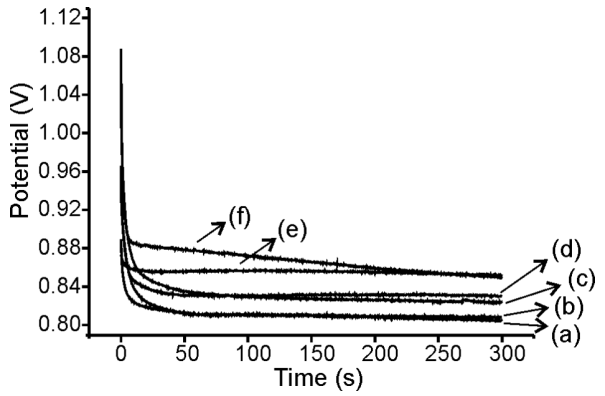

Figure 1: Chronopotentiometric curves obtained during the polymerization of (a) Ppy-CP_{Pt}, (b) Ppy-CP_{SS} (c) Ppy/AuNPs-T-CP_{SS} (d) Ppy/AuNPs-T-CP_{Pt}, (e) Ppy/AuNPs-C-CP_{Pt} and (f) Ppy/AuNPs-C-CP_{SS}.

The highest nucleation rate (faster electrode potential variation) was observed when Ppy was polymerized in the absence of gold nanoparticles or tetrachloroauric acid. At the same time, the final potential (at which the monomer is oxidized) was clearly lower for Ppy films. According to these results, it can be assumed that, the the presence of AuNPs affects the nucleation of Ppy, making impeding the oxidation of the monomers.

The final potential attained when polymerization was carried out in the presence of previously formed AuNPs (trapping), was lower than the potential obtained when AuNPs were generated in situ (cogeneration). This result seems to confirm that AuNPs affect the nucleation process. Only a small difference was found in the final potential attained by Ppy/AuNPs deposited on Pt or on SS.

Nanocomposites Ppy/AuNP were also prepared by trapping and cogeneration using CA. Curves show the characteristic stepped shape of the potentiostatic polymerization: After a short induction period where diffusion controls the monomer oxidation, the current increased rapidly with time, where polymer started nucleating and growing on the electrode surface. Finally, the current reached a plateau coinciding with a continuous and gradual polymer growth [29,30]. The calculated charges are shown in Table 1.

Table 1: Polymerization charges calculated for Ppy and Ppy/AuNPs composites prepared by chronoamperometry.

Sample	Q (C/cm^2)	
	SS	Pt
Ppy-CA	0.62	0.62
Ppy/AuNPs-T-CA	0.07	0.08
Ppy/AuNPs-C-CA	0.12	0.22

In good accordance with results shown in previous paragraphs, also when using CA, the polymerization charge was strongly dependent on the presence of AuNPs and the mass deposited in the absence of AuNPs was higher than the mass deposited in the presence of gold. The charge calculated for films obtained by cogeneration was higher than that of the films obtained by trapping. That is, the amount of polymer deposited followed the same trend regardless whether CP or CA was used (Ppy > Ppy/AuNP-C > Ppy/AuNP-T). This result also points to the role of AuNPs in the nucleation of Ppy, which impede the the oxidation of the monomers. The coefficients of variation (% CV) were always lower than 2% regardless of the electropolymerization method or the susbstrate used.

Structural characterization: SEM studies

The microscopic structure of the Ppy/AuNP films analyzed by scanning electron microscopy confirmed the incorporation of the AuNPs into the Ppy films (Figure 2). They were uniformly dispersed in the typical granular raspberry PPy matrix. The structures of films deposited onto SS or Pt were almost identical.

The average size of the AuNPs was between 30 and 40 nm (regardless of the method used), which is consistent with the absorbance at 540 nm observed by colloid that was used to obtain the nanocomposites by trapping. The number of AuNPs

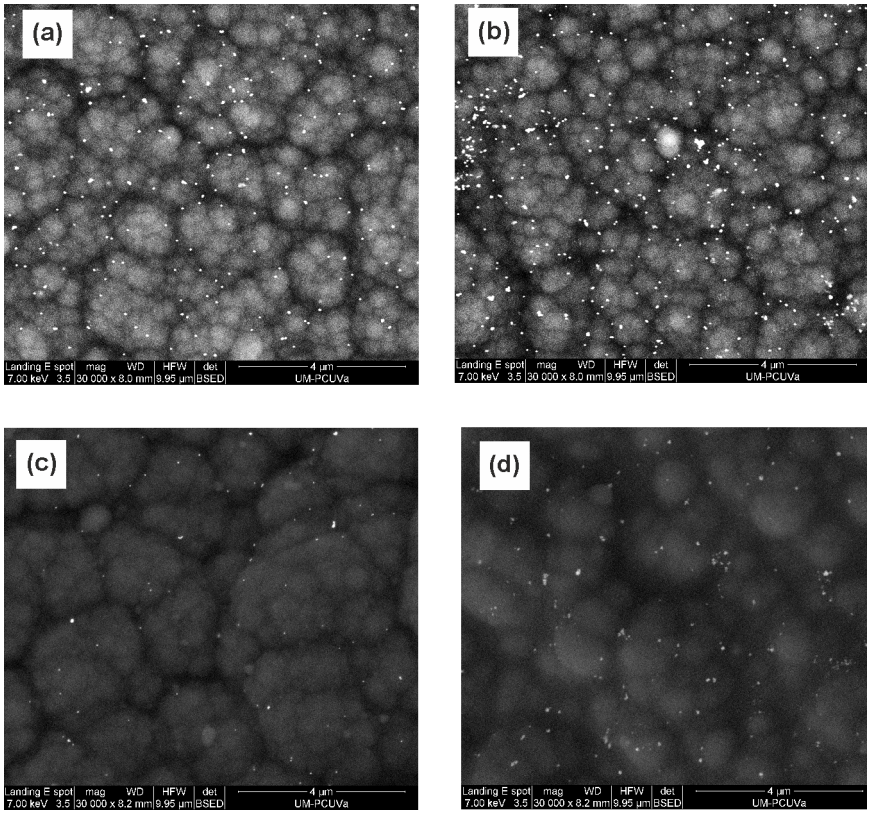

Figure 2: SEM images of Ppy/AuNP fims deposited on SS (a) Ppy/AuNP-T-CPss; (b) Ppy/AuNP-C-CPss; (c) Ppy/AuNP-T-CAss; (d) Ppy/AuNP-C-CAss.

incorporated in the Ppy films was higher when using CP than that when using CA. In turn, using cogeneration, the amount of nanoparticles incorporated was higher than using trapping.

Electrochemical impedance spectroscopy

Electrochemical impedance spectroscopy (EIS) can provide information about the conductivity changes resulting from the insertion of AuNPs in the Ppy films. The complex impedance can be plotted as the real (Z_{real}) vs imaginary ($Z_{imaginary}$) components (Nyquist plot), which are related to the resistance and capacitance of the cell, respectively. At high frequencies (left part of the diagram) the semicircular part is associated to electron-transfer limited processes. The diameter of the semicircle is equivalent to the electron-transfer resistance (R_{ct}). The linear part that appears at lower frequencies is related to diffusion limited processes. In the case of Ppy deposited by CA, the Nyquist plot (Figure 3a) was a semicircle (R_{ct}, 45.54 kΩ). The electrochemical process was thus, dominated by electron transfer.

The insertion of AuNPs in the Ppy films clearly modified the electrical behavior. In effect, the Nyquist plot of Ppy/AuNP-T-CA_{Pt} films obtained by trapping (Figure 3b) showed a semicircle with a smaller R_{ct} (13.52 kΩ) in the high frequencies region. At low frequencies a straight line with a slope of 45° was observed indicating a contribution of both electron transfer and diffusion processes. In Ppy/AuNPs-C-CA_{Pt} films obtained by cogeneration R_{ct} was practically zero and only the linear part corresponding to diffusion control was observed (Figure 3c).

These results confirm the ability of AuNPs to reduce the resistance by facilitating the electron transfer. In fact, as observed in SEM images the number of AuNPs inserted in the films was higher using cogeneration, explaining the drastic decrease in the resistance. This is in good agreement with previous published results that indicated that the presence of AuNPs in the polymer matrix resulted in an increase in conductivity [31].

EIS results of Ppy/AuNPs films deposited by CP showed similar trends, but resistance and impedance values were clearly smaller than those observed in films deposited by CA. For instance, the impedance values of Ppy/AuNP-C-CP_{Pt} were one third smaller than those obtained by CA (Figure 3d). Again, the high number of AuNPs inserted in the nanocomposite by CP, explains the improvement in the conductivity.

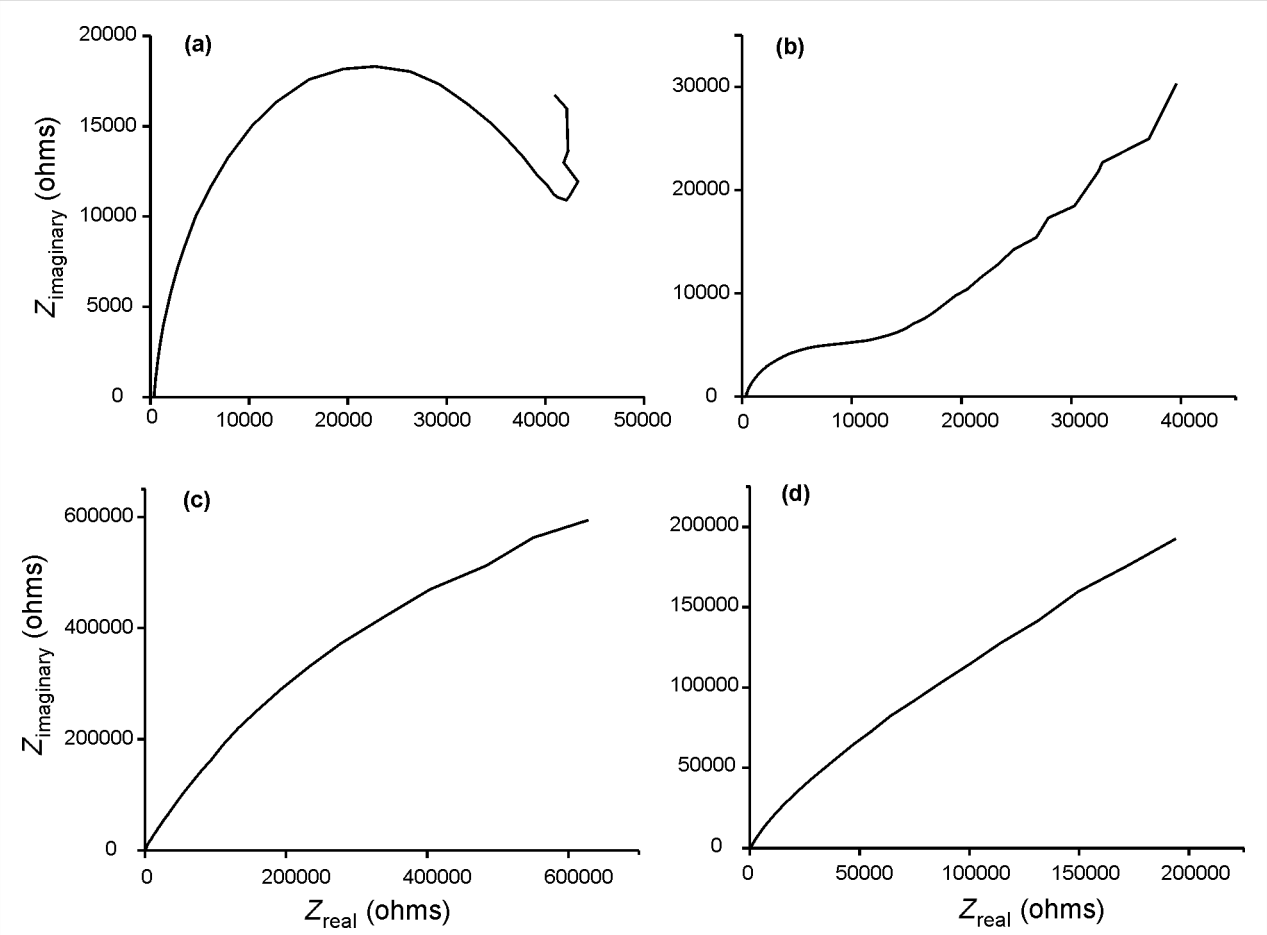

Figure 3: Nyquist plot of films deposited onto Pt registered in 0.1 mol/L KCl. Frequency swept from 105 to 0.1 Hz (a) Ppy-CA_{Pt}; (b) Ppy/AuNP-T-CA_{Pt}; (c) Ppy/AuNP-C-CA_{Pt}; (d) Ppy/AuNP-C-CP_{Pt}.

It is important to point out, that EIS measurements carried out in films deposited on SS by CA where irreproducible, indicating that the films obtained were unstable. Films deposited on SS by CP produced reproducible results but with higher R_{ct} and impedance values than those found on the platinum substrate. In fact, in the Nyquist plot for bare Ppy-CP_{SS} the R_{ct} was so high that the semicircle was not completed.

According to these results, and taking into account that lower R_{ct} values correspond to an increase of the voltammetric signal [32] the cogeneration combined with chronopotentiometry seems to be the most suitable electrodeposition technique to prepare voltammetric sensors.

Electrochemical behavior of Ppy/AuNPs prepared using different techniques

The electrochemical behavior of Ppy and Ppy/AuNP films was analyzed using cyclic voltammetry in 0.1 mol/L KCl solution. The responses are influenced by the polymerization method, the deposition technique and the type of substrate. Before going into the details, it is important to notice that, in good accordance with previously published results, the first scan was always different from the subsequent cycles. Subsequent cycles were highly reproducible [22]. For this reason, in the next figures, the fifth scan will be displayed.

For Ppy films deposited on platinum using CA or CP, the first cycle showed two redox processes corresponding to the polaron and bipolaron. In successive cycles one single process (anodic wave at −0.35 V and the corresponding cathodic peak at around −0.5 V) was found. When deposition was carried out on SS, voltammograms showed lower intensities and in the case of Ppy-CA_{SS}, a certain irreproducibility.

When AuNPs were introduced in the films (Ppy/AuNPs), the preparation method induced important differences. In films deposited on platinum, the insertion of AuNPs caused an increase in the intensity of the peaks. Simultaneously the separation between the anodic and the cathodic waves was reduced. This is illustrated in Figure 4 for films deposited on Pt by CP.

According to this, it can be concluded that the reversibility of the redox processes is improved in Ppy/AuNP composites. The increase was more pronounced in films deposited by CP than in films deposited by CA. As the number of AuNPs inserted in the films was higher in films deposited by CP (Figure 2), the electrocatalytic effect of the AuNPs is confirmed. This is also in agreement with EIS results that demonstrated that the insertion of AuNPs increased the conductivity.

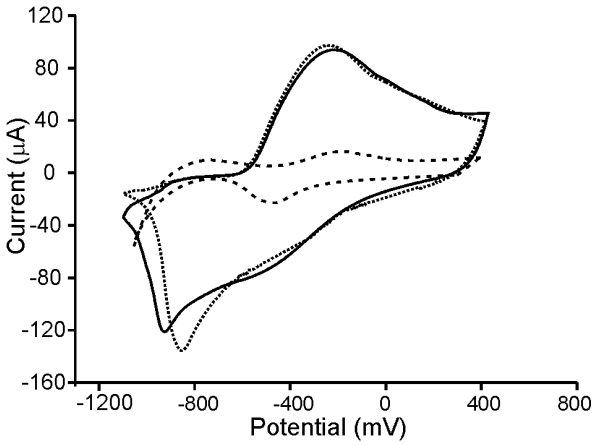

Figure 4: Cyclic voltammograms of Ppy-CP_{Pt} (dashed line), Ppy/AuNPs-T-CP_{Pt} (dotted line) and Ppy/AuNPs-C-CP_{Pt} (solid line) immersed in 0.1 mol/L KCl. Scan rate 0.1 V/s.

It is important to point out that, when the deposition was carried out on SS, a decrease in the intensity of the peaks accompanied by a separation between the anodic and cathodic waves was observed. This behavior pointed to the interference between SS and AuNPs. In addition, some irreproducibility was observed (as it also happened in EIS experiments).

In fact, a part from the differences already commented in the electrochemical behavior of Ppy/AuNps films deposited onto Pt and SS, the most remarkable difference was related to their stability and lifetime. We already mentioned that the first cycle was different from the subsequent ones, but the changes occurring in successive cycles were more pronounced in films deposited on stainless steel substrates. The variation coefficients calculated in films deposited on Pt by CP or CA were less than 2% and 5%, respectively. The %CV calculated from films deposited on SS were 8% for CP and 15–20% for CA. Moreover, when electrodes were withdrawn from the solution and reintroduced in the tested solution, electrodes deposited onto SS, changed completely their electrochemical response and could not be further used.

The above results established the important influence of the electropolymerization method (CA or CP) and of the nature of the substrate in the electrochemical properties of the films. The influence of the method used to introduce the AuNPs (trapping or cogeneration) was not so important. In fact, when films were deposited onto Pt, the differences in the voltammograms prepared by trapping or by cogeneration were minimal. In contrast, when SS was used as the substrate, the differences observed between trapping and cogeneration could be ascribed to the irreproducibility and therefore conclusions could not be deduced.

The irreproducibility observed in stainless steel can be clearly attributed to pitting processes produced by chloride ions. In consequence, reproducibility could be improved by changing the supporting electrolyte.

According to this idea, the influence of the supporting electrolyte was further investigated using phosphate buffer. As expected, the large size and high charge of the phosphate anions, made difficult the diffusion of anions inside the polymeric film producing a broadening of the peaks and the increase in the separation between the anodic and the cathodic waves that appeared at −0.15 and −0.8 V, respectively [33] . A part from the broadening of the peaks, the effects caused by AuNPs were similar to those observed in KCl (e.g., increase in the intensity of the peaks accompanied by a decrease in the separation between anodic and cathodic waves.

Using phosphate buffer, the pitting processes were avoided and the reproducibility of films deposited on SS was clearly improved and was similar to that calculated in films deposited on platinum (CV less than 5%).

Electrocatalytic and sensing behavior towards catechol

Once stable Ppy/AuNP electrodes were obtained, their electrocatalytic and sensing properties towards catechol (a phenolic compound of interest in the food industry), were analyzed in terms of signal amplification and peak shifts. Experiments were carried out in the range between −0.1 and 0.8 V at a scan rate of 0.1 V/s in phosphate buffer. Under these conditions, SS could be used as a substrate due to the absence of pitting processes. Notice also that the polaron–bipolaron response of pyrrole occurs out of this range at negative potentials.

Catechol produced the expected well-shaped redox pair generated by the two-electron oxidation/reduction of the *ortho*-dihydroquinone to benzoquinone [26]. The reversibility of the peaks was improved with the incorporation of the AuNPs. Simultaneously, the intensity of the peaks increased with the concentration of AuNPs. This is illustrated in Figure 5 for electrodes deposited on SS by CP. As observed in the Figure, the

separation between the anodic and cathodic waves was 300 mV in Ppy-CPss films and only 100 mV in Ppy/AuNP-T-CP_{SS}.

These effects were stronger in films deposited by CP than in films deposited by CA, due to the higher concentration of nanoparticles. In contrast, the method to insert the nanoparticles (trapping or cogeneration) only produced small changes in the intensities and positions of the peaks, probably due to the minimal differences in the AuNPs concentration.

The electrocatalytic effect was stronger in films deposited on platinum than in SS. This is in good accordance to previously published reports that have established that AuNPs exhibit a catalytic behavior when deposited onto platinum due to the synergy between both metals [34].

The effect of the concentration of catechol was studied by immersing the electrodes prepared by CP in $1{\cdot}10^{-5}$ to $1{\cdot}10^{-3}$ mol/L catechol solutions. A linear increase in the intensity of the peaks with the concentration was observed in the studied range. The limit of detection (LOD) was calculated from the calibration curves following the "3sd/m" criterion. As observed in Table 2, the LODs were in the range from 10^{-5} to 10^{-6} mol/L. The LOD obtained using Ppy/AuNP composite films was almost one order of magnitude lower than the one observed in Ppy films. The synergy between platinum and AuNPs increased the sensitivity, allowing a further decrease in the LODs. This synergy is not so important when using SS. Therefore, the use of SS as a substrate, provides stable sensors with good LODs while decreasing the price of the devices considerably.

Conclusion

Ppy/AuNP nanocomposites have been successfully prepared employing in situ polymerization of pyrrole using tetrachloroauric acid as an oxidant in the presence of gold ions and by trapping AuNPs in a Ppy matrix during the electropolymerization. SEM images confirmed the formation of uniform nanocomposites on smooth platinum and stainless steel substrates.

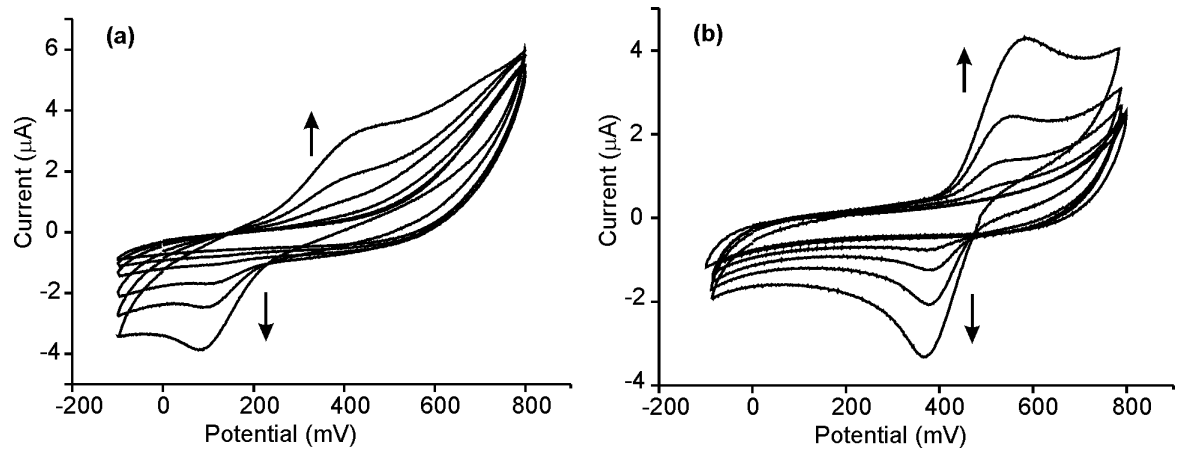

Figure 5: Voltammograms registered using electrodes deposited by CP on SS immersed in $1{\cdot}10^{-5}$ to $1{\cdot}10^{-3}$ mol/L solutions of catechol in 0.01 mol/L phosphate buffer (pH 7.0): (a) Ppy-CP_{SS} (b) Ppy/AuNP-T-CP_{SS}.

Table 2: LOD, sensitivity and regression coefficients calculated from the anodic and cathodic peaks of catechol.

Sensor	LOD (mol/L) (cathodic peak)	R^2	LOD (mol/L) (anodic peak)	R^2
Ppy-CP_{Pt}	$9.1{\cdot}10^{-5}$	0.977	$5.3{\cdot}10^{-5}$	0.989
Ppy/AuNP-C-CP_{Pt}	$2.4{\cdot}10^{-5}$	0.976	$8.8{\cdot}10^{-5}$	0.996
Ppy/AuNP-T-CP_{Pt}	$0.9{\cdot}10^{-5}$	0.984	$0.3{\cdot}10^{-5}$	0.981
Ppy-CP_{SS}	$8.9{\cdot}10^{-5}$	0.956	$7.2{\cdot}10^{-5}$	0.975
Ppy/AuNP-C-CP_{SS}	$4.3{\cdot}10^{-5}$	0.977	$3.1{\cdot}10^{-5}$	0.971
Ppy/AuNP-T-CP_{SS}	$3.2{\cdot}10^{-5}$	0.968	$1.1{\cdot}10^{-5}$	0.975

The presence of AuNPs in the polymer matrix resulted in an increase in the conductivity and in the intensity of the voltammetric signals. These variations in conductivity and intensity of voltammograms are directly related to the number of AuNPs inserted in the Ppy films.

Irreproducibility observed in the EIS and voltammetric measurements carried out in KCl using films deposited on stainless steel, caused by pitting process can be avoided by using phosphate buffer as supporting electrolyte.

As an electrochemical sensor, the Ppy/AuNP deposited on platinum exhibited important electrocatalytic activity towards the oxidation of catechol. The effect was higher in films obtained by CP than in films obtained by CA. The influence of the method used to introduce the AuNPs (trapping or cogeneration) was not so important. The detection limits were in the range of 10^{-5} to 10^{-6} mol/L, which is lower than the concentration usually found in foods and beverages such as wines and musts. The synergy between Pt and Au nanoparticles gave rise to lower LODs. In turn, stainless steel can be used as the substrate in the absence of KCl, with a LOD only slightly higher than those obtained in sensors deposited on Pt, but at a lower cost.

Experimental

Reagents and solutions

All experiments were carried out in deionized Milli-Q water (Millipore, Bedford, MA). Pyrrole, tetrachloroauric acid, 1-decanesulfonic acid (DSA), potassium chloride, sodium phosphate, potassium phosphate and catechol were purchased from Sigma-Aldrich. Commercially available reagents and solvents were used without further purification.10^{-3} mol/L stock solutions of catechol were prepared by solving the corresponding compound in KCl solution (0.1 mol/L) or phosphate buffer solution (pH 7.0; 0.1 mol/L). Solutions with lower concentration were prepared from the stock solutions by dilution.

Preparation of the Au colloidal suspension

The synthesis of AuNPs colloids was carried out according to the procedure proposed by Slot and Geuze [35]. Two solutions were prepared: (1) $HAuCl_4$ ($0.25 \cdot 10^{-3}$ mol/L) in deionized water and (2) sodium citrate dehydrate ($17 \cdot 10^{-3}$ mol/L) in deionized water. 20 mL of solution (1) was heated until boiling on a hot plate, then 1 mL of solution (2) was quickly added to the $HAuCl_4$ solution while stirring. The mixture was then boiled for 20 min. Using this procedure, a red colloid with a UV absorbance maximum at λ = 540 nm was obtained.

Instruments

Electropolymerizations and electrochemical studies were carried out at room temperature in an EG&G Parstat 2273 potentiostat/galvanostat using a three-electrode configuration. The same instrument was used for the EIS experiments. UV–vis spectra were recorded on a Shimadzu UV-2600 model spectrometer. A SEM-FEI (QUANTA 200F) was used to record the images of the electrode surfaces.

Electropolymerization methods

The auxiliary electrode was a conventional Pt electrode. The reference electrode was an Ag/AgCl electrode in a 3 mol/L KCl solution. Pt and stainless steel 316L (SS) disks (1 mm diameter) were used as working electrodes. The disks were polished with 0.3 μm alumina suspension using a microcloth polishing pad and rinsed with deionized water in an ultrasonic bath.

Electropolymerization of Ppy films

The Ppy films were obtained by electropolymerization from a solution containing 0.1 mol/L pyrrole and 0.05 mol/L 1-decanesulfonic acid (DSA) using two electrochemical techniques: chronopotentiometry (CP) using a constant potential at 0.8 V over a period of 300 s, and chronoamperometry (CA) using 0.02 mA over a period of 300 s (except otherwise indicated). Films were deposited onto Pt and SS.

Electropolymerization of Ppy/AuNPs films

Ppy/AuNPs films were obtained using two different approaches. On one hand, Ppy/AuNPs films were synthesized by the "trapping method" from a solution containing 0.2 mol/L pyrrole, 0.1 mol/L DSA. This solution was mixed (1:1) with a solution containing AuNPs previously formed (Au colloidal suspension). Films were polymerized by chronoamperometry using a constant potential at 0.8 V over a period of 300 s, and by chronopotentiometry using 0.02 mA over a period of 300 s. Sensors obtained by trapping were termed as Ppy/AuNP-T-CA (obtained by chronoamperometry) and Ppy/AuNP-T-CP (obtained by chronopotentiometry).

Ppy/AuNPs films were also synthesized using the "cogeneration method" by mixing a solution containing tetrachloroauric acid 10^{-3} mol/L and a solution containing pyrrole and DSA. In this method, and according to the oxidation potentials of pyrrole (0.7 V vs SCE) and the reduction potential of $AuCl_4^-$ (1 V), the AuNPs where generated in situ and inserted in the polymeric film during the electrochemical growth. Also in this case, electropolymerization was carried out by CA and CP under the same conditions used for trapping. Sensors obtained by cogeneration were termed as Ppy/AuNP-C-CA (obtained by chronoamperometry) and Ppy/AuNP-C-CP (obtained by chronopotentiometry).

In all cases, films were deposited onto Pt and SS disks. The type of substrate will be denoted using a subscript (i.e., Ppy/AuNPs-

C-CP_{Pt} or Ppy/AuNPs-T-CP_{SS}). Once prepared, the polymeric films were extracted from the generation solution and washed thoroughly with water.

Electrochemical impedance spectroscopy (EIS) characterization

EIS was performed in a 0.1 mol/L KCl solution with a frequency range from 105 to 0.1 Hz and a signal amplitude of 10 mV, at a working potential of 0.0 V.

Tests of the voltammetric sensors

The Ppy and Ppy/AuNPs films were used as working electrodes in electrochemical experiments. The reference electrode was Ag/AgCl/KCl 3 mol/L and the counter electrode was a platinum wire.

Cyclic voltammetry was carried out at room temperature with a scan rate of 0.1 V/s in the potential range between −1.0 V and 0.8 V (vs Ag/AgCl) except otherwise indicated.

Calibration curves were constructed from catechol solutions with concentrations ranging from $1\cdot10^{-5}$ to $1\cdot10^{-3}$ mol/L. The limits of detection (LODs) were calculated following the "3sd/m" criterion, where "m" is the slope of the calibration graph, and "sd" was estimated as the standard deviation ($n = 5$) of the voltammetric signals at the concentration level corresponding to the lowest concentration of the calibration plot [36,37].

Acknowledgements

Financial support by the MINECO and FEDER (grant CICYT-AGL2012-33535) and Junta de Castilla y León (VA-032U13) is gratefully acknowledged. CMP would also like to thank the University of Valladolid for the grant (PIF-UVa).

References

1. Ramanavičius, A.; Ramanavičienė, A.; Malinauskas, A. *Electrochim. Acta* **2006,** *51,* 6025–6037. doi:10.1016/j.electacta.2005.11.052
2. Ates, M. *Mater. Sci. Eng., C* **2013,** *33,* 1853–1859. doi:10.1016/j.msec.2013.01.035
3. Li, C. M.; Sun, C. Q.; Chen, W.; Pan, L. *Surf. Coat. Technol.* **2005,** *198,* 474–477. doi:10.1016/j.surfcoat.2004.10.065
4. Chillawar, R. R.; Tadi, K. K.; Motghare, R. V. *J. Anal. Chem.* **2015,** *70,* 399–418. doi:10.1134/S1061934815040152
5. Yoon, H. *Nanomaterials* **2013,** *3,* 524–549. doi:10.3390/nano3030524
6. Saha, K.; Agasti, S. S.; Kim, C.; Li, X.; Rotello, V. M. *Chem. Rev.* **2012,** *112,* 2739–2779. doi:10.1021/cr2001178
7. Lin, X.; Ni, Y.; Kokot, S. *Anal. Chim. Acta* **2013,** *765,* 54–62. doi:10.1016/j.aca.2012.12.036
8. Valcárcel, M.; López-Lorente, A. I. Gold Nanoparticles in Analytical Chemistry. In *Comprehensive Analytical Chemistry (Wilson and Wilson's);* Barcelo, D., Ed.; Elsevier: Amsterdam, NL, 2014; Vol. 66, pp 1–601.
9. Jiang, H.; Moon, K.-S.; Li, Y.; Wong, C. P. *Chem. Mater.* **2006,** *18,* 2969–2973. doi:10.1021/cm0527773
10. Pogulyaichenco, N. A.; Hui, S.; Malev, V. V.; Kondratiev, V. V. *Russ. J. Electrochem.* **2009,** *45,* 1176–1182. doi:10.1134/S1023193509100103
11. Zhang, Z.; Wang, F.; Chen, F.; Shi, G. *Mater. Lett.* **2006,** *60,* 1039–1042. doi:10.1016/j.matlet.2005.10.071
12. Zanardi, C.; Terzi, F.; Pigani, L.; Heras, A.; Colina, A.; Lopez-Palacios, J.; Seeber, R. *Electrochim. Acta* **2008,** *53,* 3916–3923. doi:10.1016/j.electacta.2007.07.057
13. Spain, E.; Keyes, T. E.; Forster, R. J. *Electrochim. Acta* **2013,** *109,* 102–109. doi:10.1016/j.electacta.2013.07.018
14. Zhang, J.; Liu, X.; Wu, S.; Xu, H.; Cao, B. *Sens. Actuators, B* **2013,** *186,* 695–700. doi:10.1016/j.snb.2013.06.063
15. Rezaei, B.; Boroujeni, M. K.; Ensafi, A. A. *Biosens. Bioelectron.* **2014,** *60,* 77–83. doi:10.1016/j.bios.2014.03.028
16. Li, J.; Xie, H.; Chen, L. *Sens. Actuators, B* **2011,** *153,* 239–245. doi:10.1016/j.snb.2010.10.040
17. Rapecki, T.; Donten, M.; Stojek, Z. *Electrochem. Commun.* **2010,** *12,* 624–627. doi:10.1016/j.elecom.2010.02.015
18. Malinauskas, A.; Malinauskiene, J.; Ramanavičius, A. *Nanotechnology* **2005,** *16,* 51–62. doi:10.1088/0957-4484/16/10/R01
19. Chen, W.; Li, C.-M.; Yu, L.; Lu, Z.; Zhou, Q. *Electrochem. Commun.* **2008,** *10,* 1340–1343. doi:10.1016/j.elecom.2008.07.001
20. Heinig, N. F.; Kharbanda, N.; Pynenburg, M. R.; Zhou, X. J.; Schultz, G. A.; Leung, K. T. *Mater. Lett.* **2008,** *62,* 2285–2288. doi:10.1016/j.matlet.2007.11.094
21. Razavipanah, I.; Rounaghi, G. H.; Zavvar, M. H. A. *Anal. Lett.* **2014,** *47,* 117–133. doi:10.1080/00032719.2013.832277
22. He, Y.; Yuan, J.; Shi, G.; Wu, P. *Mater. Chem. Phys.* **2006,** *99,* 253–257. doi:10.1016/j.matchemphys.2005.10.033
23. Hurtado-Fernández, E.; Gómez-Romero, M.; Carrasco-Pancorbo, A.; Fernández-Gutiérrez, A. *J. Pharm. Biomed. Anal.* **2010,** *53,* 1130–1160. doi:10.1016/j.jpba.2010.07.028
24. Makhotkina, O.; Kilmartin, P. A. *Anal. Chim. Acta* **2010,** *668,* 155–165. doi:10.1016/j.aca.2010.03.064
25. Brett, A. M. O.; Ghica, M.-E. *Electroanalysis* **2003,** *15,* 1745–1750. doi:10.1002/elan.200302800
26. Kilmartin, P. A.; Zou, H.; Waterhous, A. L. *Am. J. Enol. Vitic.* **2002,** *53,* 294–302.
27. Parra, V.; Hernando, T.; Rodríguez-Méndez, M. L.; de Saja, J. A. *Electrochim. Acta* **2004,** *49,* 5177–5185. doi:10.1016/j.electacta.2004.06.031
28. Medina-Plaza, C.; Furini, L. N.; Constantino, C. J. L.; de Saja, J. A.; Rodríguez-Mendez, M. L. *Anal. Chim. Acta* **2014,** *851,* 95–102. doi:10.1016/j.aca.2014.08.049
29. Arrieta Almario, A. A.; Vieira, R. L. *J. Chil. Chem. Soc.* **2006,** *51,* 971–974. doi:10.4067/S0717-97072006000300009
30. Arrieta Almario, A. A.; Tarazona Caceres, R. L. *J. Chil. Chem. Soc.* **2009,** *54,* 14–19. doi:10.4067/S0717-97072009000100004
31. Singh, S.; Jain, D. V. S.; Singla, M. L. *Anal. Methods* **2013,** *5,* 1024–1032. doi:10.1039/c2ay26201k
32. Di Carlo, G.; Curulli, A.; Trani, A.; Zane, D.; Ingo, G. M. *Sens. Actuators, B* **2014,** *191,* 703–710. doi:10.1016/j.snb.2013.10.063

33. Ratautaite, V.; Ramanaviciene, A.; Oztekin, Y.; Voronovic, J.; Balevicius, Z.; Mikoliunaite, L.; Ramanavicius, A. *Colloids Surf., A* **2013,** *418,* 16–21. doi:10.1016/j.colsurfa.2012.10.052
34. Xiao, F.; Zhao, F.; Zhang, Y.; Guo, G.; Zeng, B. *J. Phys. Chem. C* **2009,** *113,* 849–855. doi:10.1021/jp808162g
35. Slot, J. W.; Geuze, H. J. *Eur. J. Cell Biol.* **1985,** *38,* 87–93.
36. IUPAC Analytical Chemistry Division. *Pure Appl. Chem.* **1976,** *45,* 99–103. doi:10.1351/pac197645020099
37. Medina-Plaza, C.; García-Cabezón, C.; García-Hernández, C.; Bramorski, C.; Blanco-Val, Y.; Martín-Pedrosa, F.; Kawai, T.; de Saja, J. A.; Rodríguez-Méndez, M. L. *Anal. Chim. Acta* **2015,** *853,* 572–578. doi:10.1016/j.aca.2014.10.046

License and Terms

BEILSTEIN JOURNAL OF NANOTECHNOLOGY

Nanostructured superhydrophobic films synthesized by electrodeposition of fluorinated polyindoles

Gabriela Ramos Chagas, Thierry Darmanin and Frédéric Guittard*

Full Research Paper

Open Access

Address:
Univ. Nice Sophia Antipolis, CNRS, LPMC, UMR 7336, 06100 Nice, France; Fax: (+33)492076156; Tel: (+33)492076159

Email:
Frédéric Guittard* - guittard@unice.fr

* Corresponding author

Keywords:
bioinspiration; conducting polymers; electrochemistry; nanostructures; polyindoles; superhydrophobic

Beilstein J. Nanotechnol. **2015,** *6,* 2078–2087.
doi:10.3762/bjnano.6.212

Received: 01 August 2015
Accepted: 08 October 2015
Published: 28 October 2015

This article is part of the Thematic Series "Organized films".

Guest Editor: M. Canepa

Abstract

Materials with bioinspired superhydrophobic properties are highly desirable for many potential applications. Here, nine novel monomers derived from indole are synthesized to obtain these properties by electropolymerization. These monomers differ by the length (C_4F_9, C_6F_{13} and C_8F_{17}) and the position (4-, 5- and 6-position of indole) of the perfluorinated substituent. Polymeric films were obtained with C_4F_9 and C_6F_{13} chains and differences in the surface morphology depend especially on the substituent position. The polyindoles exhibited hydrophobic and superhydrophobic properties even with a very low roughness. The best results are obtained with **PIndole-6-F_6** for which superhydrophobic and highly oleophobic properties are obtained due to the presence of spherical nanoparticles and low surface energy compounds.

Introduction

The number of studies about materials with superhydrophobic properties, characterized by extremely high water contact angles (θ_w) and low water adhesion or hysteresis (also known as "Lotus effect"), grows exponentially because of the importance for both the scientific and industrial community [1-6]. Superhydrophobic properties are quite common in nature, in both animals and plants, and allow them surviving against predators or hostile environments such as extremely humid or dry regions, for example [7-12]. Bioinspiration has shown the importance of developing structured surfaces in the presence of low surface energy materials that allow one to obtain more easily superhydrophobic properties with higher robustness [13-15]. Controlling the surface energy and the roughness is hence fundamental to achieve the superhydrophobicity.

All kind of materials can be used to reach superhydrophobicity, but conducting polymers have many advantages such as an easiness to functionalize and opto-electronic properties [16] with the possibility to introduce various dopants (smart materials) [17,18]. Conducting polymers are also exceptional materials for

the control of surface nanostructures and wettability. First of all, nanostructures of extremely various shapes can be produced in solution by self-assembly [19-21] or directly formed on substrates by different strategies such as preferential growth [22], grafting [23], vapor phase polymerization [24], plasma polymerization [25] and electropolymerization [26-30]. The last method allows for a very quick and easy deposition of conducting polymer films while the formation of surface structures can be controlled by electrochemical parameters [26] and the used monomer [27]. In order to control the formation of surface nanostructures, the core responsible for the polymerization (such as thiophene, pyrrole or 3,4-ethylenedioxythiophene) [27-30] is probably the most important parameter. Then, the polymer can also be controlled by introducing hydrophobic/hydrophilic substituents or dopant agents [17,18,27-30]. In most of the cases, fluorocarbon or hydrocarbon chains were used to reach superhydrophobic properties.

Here, we report for the first time the formation of superhydrophobic properties from indole derivatives. Nine novel indole monomers substituted by fluorocarbon chains of different length (C_4F_9, C_6F_{13} and C_8F_{17}) and in different positions (4-, 5- and 6-position of indole) were synthesized and electropolymerized (Scheme 1). We report the influence of the fluorocarbon chain length and the substituent position on the surface morphology and hydrophobicity.

Results and Discussion

Electrodeposition

In order to develop structured polymeric films, the monomers were electropolymerized. First of all, it was necessary to determine the oxidation potential (E^{ox}) of all the monomers. These E^{ox} were determined by cyclic voltammetry and were found to be in the range of 0.9–1.3 V vs SCE for the functionalized monomers, as shown in Table 1. A cyclic voltammogram for **Indole-6-F_6** is shown in Figure 1, where it is possible to see the maximum peak of oxidation of the monomer. Then, the polymerization was followed from −0.7 V to a potential slightly lower than E^{ox} (working potential E^{w}) by the same electrochemical method. Examples of cyclic voltammograms for the polyindoles are presented in Figure 2.

Table 1: Oxidation potential (E^{ox}) and working potential (E^{w}) for each monomer by electrochemical process. Electropolymerization in 0.1 M of acetonitrile/Bu_4NClO_4.

monomer	oxidation potential E^{ox} (V)	working potential E^{w} (V)
Indole	1.64	1.56
Indole-4-F_4	1.30	1.23
Indole-5-F_4	1.31	1.26
Indole-6-F_4	1.13	1.08
Indole-4-F_6	1.19	1.13
Indole-5-F_6	1.15	1.10
Indole-6-F_6	1.07	1.03
Indole-4-F_8	1.14	1.08
Indole-5-F_8	1.06	1.01
Indole-6-F_8	0.99	0.96

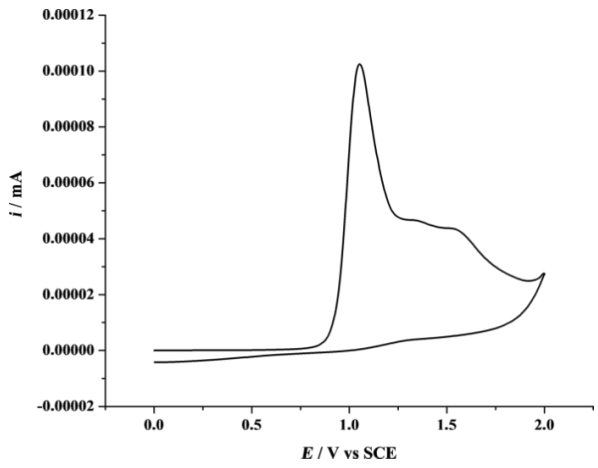

Figure 1: Cyclic voltammogram of the monomer **Indole-6-F_6** (1 scan at 20 mV·s^{-1}). Electropolymerization in 0.1 M of acetonitrile/Bu_4NClO_4.

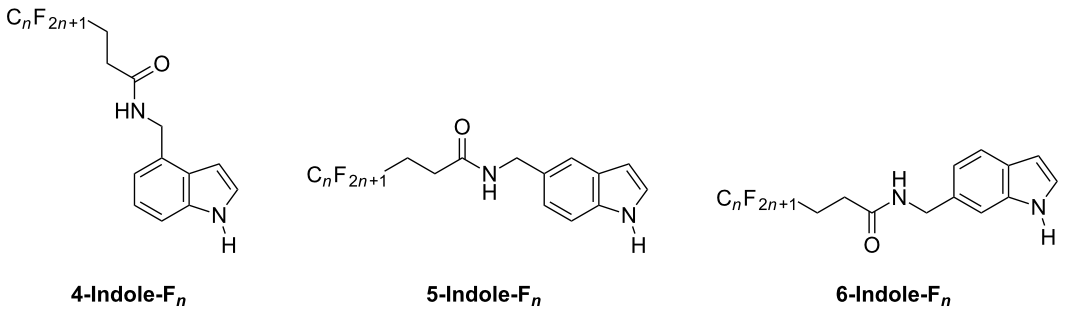

4-Indole-F_n **5-Indole-F_n** **6-Indole-F_n**

Scheme 1: Original indole monomers synthesized and used in this manuscript.

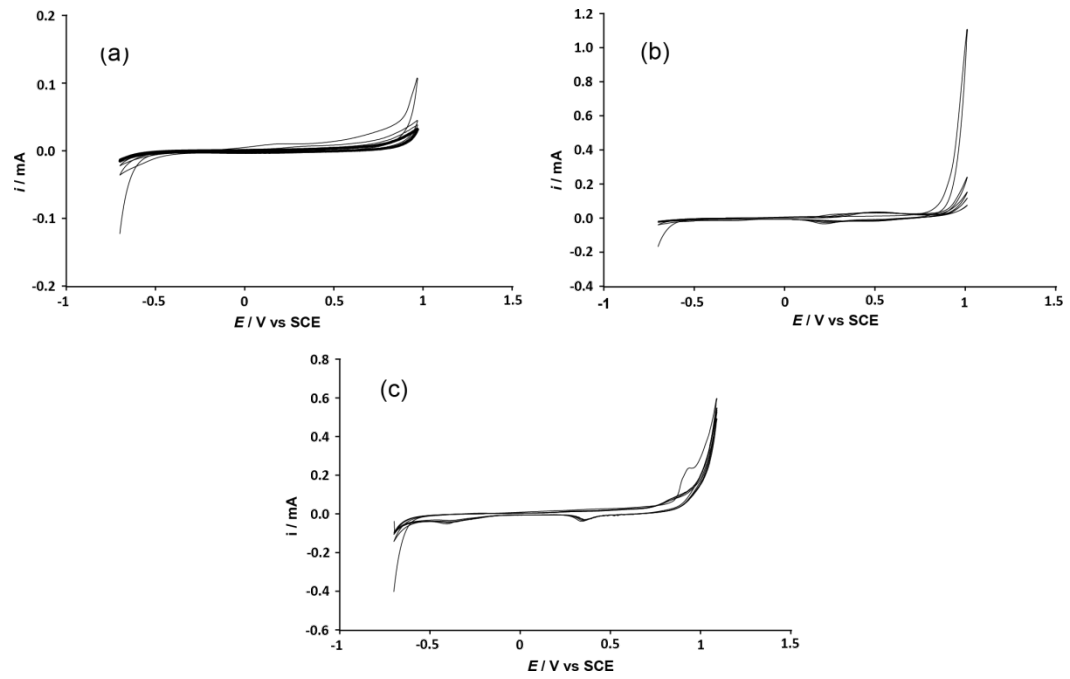

Figure 2: Cyclic voltammogram of polyindoles. (a) **Indole-6-F$_8$**, (b) **Indole-6-F$_6$** and (c) **Indole-6-F$_4$** (5 scans at 20 mV·s^{-1}). Electropolymerization in 0.1 M of acetonitrile/Bu_4NClO_4.

These cyclic voltammograms show only little variation in the polymer oxidation and reduction peaks due to the low conductivity of the polymers. Also, the short length of the new oligomers formed during the electropolymerization process increases their solubility resulting in polymeric films with a very low thickness. This may be explained by the reaction of amine groups of indole with the H^+ ions released during the electropolymerization process. For these reasons, the deposition method has been changed and the depositions have been then performed at constant potential and using different normalized deposition charges, *Qs*, (from 0 to 100 mC·cm^{-2}) in order to better control the amount of polymer electrodeposited. However, polymeric films were obtained with all the monomers except that with C_8F_{17} chains because their large size induced very huge steric hindrances during the reaction and the polymerization is not favorable.

Surface structures and wettability

The surface structures were characterized by scanning electron microscopy (SEM) and surface roughness measurements. The SEM images for *Qs* = 100 mC·cm^{-2} are given in Figure 3 and Figure 4 and the surface roughness measurements can be found in Table 2. First of all, the surfaces are not very rough, however differences were observed especially with the substituent positions. Even if some craters are observed on **PIndole-4-F$_6$**, the substitution in the 4-position gives the less structured surfaces. By contrast, nanofibers are observed with the substituents in the 5-position (**PIndole-5-F$_n$**) and spherical particles in the 6-position (**PIndole-6-F$_n$**). This confirms previous works in which authors showed that the polymerization is favorable in the indole positions 2, 3, 5 and 7 [31,32]. Indeed, if the polymerization of indole is more favorable in certain positions, the location of the substituent may influence the polymerization and the way in which the monomers are linked to one another forming different structures. This work is also in agreement with the literature where the authors showed that due to preferable polymerization positions on indole, fiber structures can be obtained by interfacial polymerization because the polymerization is directional, while spheres are obtained when the polymerization is equal in all directions [33]. In this case, the polymerization of the fluorinated indoles seems to be directional for **PIndole-5-F$_n$** and proceeds equally in all directions for **PIndole-6-F$_n$**. For **PIndole-4-F$_n$**, the polymerization should not be favorable to form any structure on the surface. Previous works showed that one of the main parameters governing the surface roughness is the solubility of the oligomers formed in the first instance [26,34]. Hence, higher roughness of **PIndole-6-F$_n$** can be explained by the formation of longer polymer chains. **PIndole-5-F$_4$** and **PIndole-6-F$_4$** also showed an increase in roughness for normalized charges of 50 and 100 mC·cm^{-2} without significant changes in the wettability comparing the others polyindoles. In contrast, **PIndole-4-F$_6$** showed the same tendency as the other polymers in terms of conserving the same wettability even if their roughness only

Table 2: Arithmetic roughness (R_a), quadratic roughness (R_q) and apparent contact angles (θ) for the four probe liquids (water, diiodomethane, sunflower oil and hexadecane) for the polymers as a function of the normalized deposition charge.

polymer	normalized deposition charge (mC·cm^{-2})	R_a (nm)	R_q (nm)	θ_{water}	$\theta_{diiodomethane}$	$\theta_{sunflower}$	$\theta_{hexadecane}$
PIndole	12.5	13.0	15.9	73.2	30.5	13.3	0
	25	10.8	13.2	71.5	25.3	12.0	0
	50	14.3	16.9	71.5	23.0	14.6	0
	100	21.9	31.0	69.8	27.2	10.9	0
PIndole-4-F$_6$	12.5	15.5	19.5	109.2	83.1	57.7	65.1
	25	12.9	15.8	110.0	89.3	65.7	69.3
	50	12.7	15.2	112.4	88.8	77.0	72.4
	100	45.2	65.4	109.9	82.3	68.1	72.0
PIndole-5-F$_6$	12.5	8.7	13.4	117.1	98.7	78.8	75.3
	25	9.5	19.0	116.3	100.7	92.5	73.8
	50	8.5	18.1	122.1	99.8	96.8	77.5
	100	17.7	31.2	124.8	103.3	87.0	74.8
PIndole-6-F$_6$	12.5	17.5	25.3	146.5	106.5	92.1	79.8
	25	11.6	18.3	149.3	111.3	86.9	87.7
	50	22.1	33.4	159.0	116.3	107.1	93.3
	100	26.3	38.9	158.9	117.6	107.3	92.6
PIndole-4-F$_4$	12.5	17.0	20.8	96.7	75.2	39.6	45.6
	25	16.5	20.2	99.5	83.3	59.4	52.3
	50	16.6	19.6	100.2	78.8	53.4	60.3
	100	15.4	18.9	98.7	78.1	59.6	43.4
PIndole-5-F$_4$	12.5	36.8	50.2	107.6	85.7	68.0	48.8
	25	50.2	67.0	106.4	86.9	84.6	74.4
	50	117.0	158.9	108.4	85.7	70.2	61.4
	100	150.6	194.2	106.0	92.6	75.0	71.1
PIndole-6-F$_4$	12.5	76.1	99.8	127.1	114.9	97.1	88.6
	25	71.5	98.8	142.9	122.7	106.7	97.7
	50	174.5	243.3	133.1	119.5	103.3	93.3
	100	153.3	202.9	131.2	120.2	100.8	93.4

exhibited a significant increase at a normalized charge of 100 mC·cm^{-2}.

The wettability properties (Table 2) are in agreement with the SEM images. The polymers **PIndole-4-F$_n$** are just slightly hydrophobic confirming the low effect of the surface structures for these polymers, independent of the fluorinated chain size. The polymers **PIndole-5-F$_n$** are more hydrophobic with apparent water contact angles (θ_{water}) of 124.8° for a normalized deposition charge of 100 mC·cm^{-2}. Here, the contact angles are not very high because the nanofibers are horizontally aligned on the substrate. By contrast, the polymers **PIndole-6-F$_n$** display extremely high θ_{water} and also superhydrophobic properties for **PIndole-6-F$_6$**, even with a low roughness. The differences between the θ_{water} for the C_6F_{13}-polyindoles can be seen in Figure 5. Indeed, not only θ_{water} of 159.0° were measured on this polymer, but also highly oleophobic properties with $\theta_{hexadecane}$ = 93.3°. Moreover, the polymer presents extremely low hysteresis and sliding angles for normalized charges of 50 and 100 mC·cm^{-2}, as shown in Table 3. For all polymers, the wettability changed with the position of the substituent on indole due to the differences in the structuration and with the increase of the length of the fluorinated chains. The different normalized charges did not result in large variations of wettability for any probe liquid, however, the highest normalized charge (100 mC·cm^{-2}) presented the best results for wettability and roughness in almost all polyindoles.

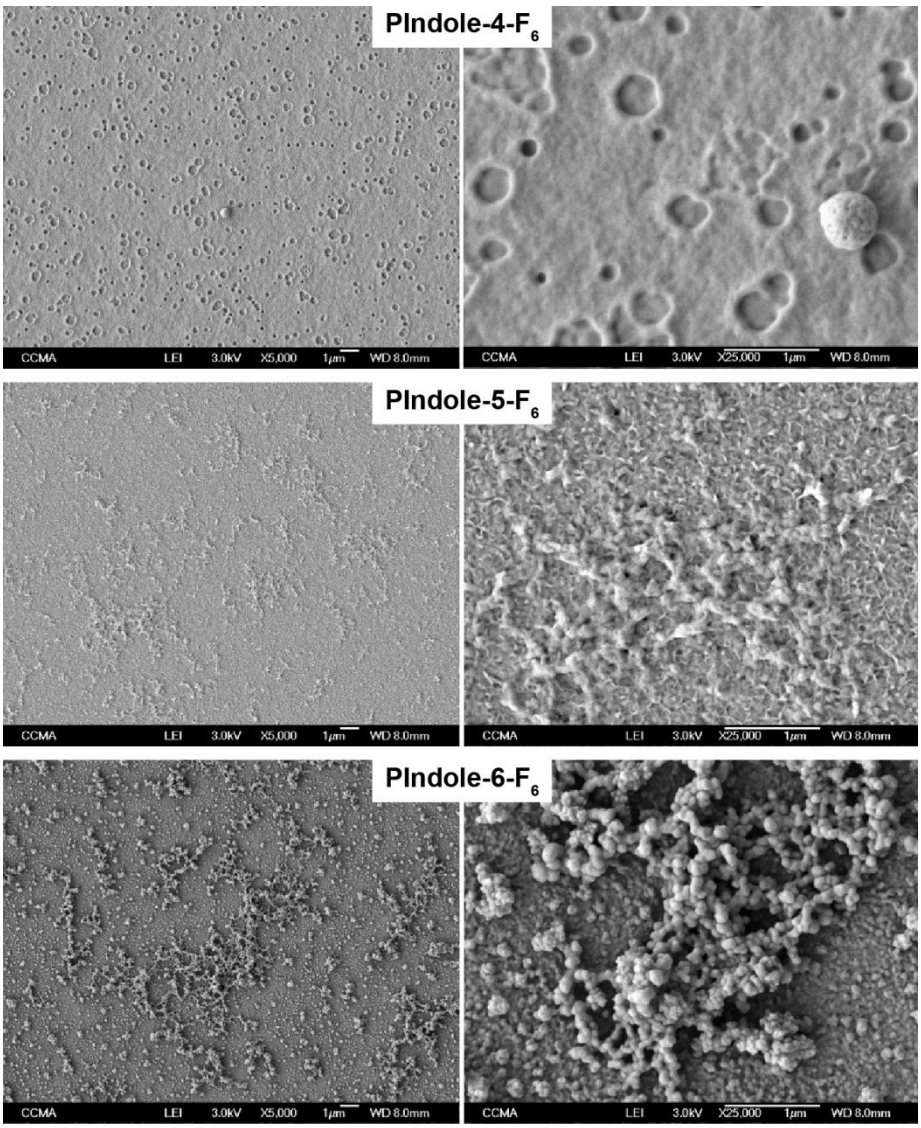

Figure 3: SEM images at two different magnifications (5000× and 25000×) of the polyindoles substituted with C_6F_{13} chains in the different positions.

Table 3: Dynamic water contact angles (hysteresis *H* and sliding angle α) for **PIndole-6-F$_6$** as a function of the normalized deposition charge.

normalized deposition charge (mC·cm^{-2})	*H* (°)	α (°)
12.5	sticky behavior	
25	sticky behavior	
50	2.1	20.6
100	0.8	9.5

In order to explain the effects of the surface structures on the wetting properties, it is first necessary to prepare smooth substrates with each polymer and determine the contact angles (θ^Y) for each probe liquid. These contact angles are dependent on the solid–vapor (γ_{SV}), solid–liquid (γ_{SL}) and liquid–vapor (γ_{LV}) surface tensions following the Young equation [35] ($\cos\theta^Y = (\gamma_{SV} - \gamma_{SL})/\gamma_{LV}$). The smooth substrates were obtained by reducing the normalized deposition charge (*Qs*) to 1 mC·cm^{-2} in order to cover all the substrate by a very thin polymer layer while avoiding the formation of surface structures. The roughness and the apparent contact angles of these smooth substrates are given in Table 4 confirming their ultra-low roughness and wettability. These results show that the polymers with C_6F_{13} fluorinated chains are intrinsically hydrophobic ($\theta^Y_{water} > 90°$) while the polymers with C_4F_9 fluorinated chains as well as the polyindoles without fluorinated chain are slightly hydrophilic ($\theta^Y_{water} < 90°$). As expected the polymers with C_6F_{13} fluorinated chains have also the highest oleophobicity even if the oil contact angles are relatively low.

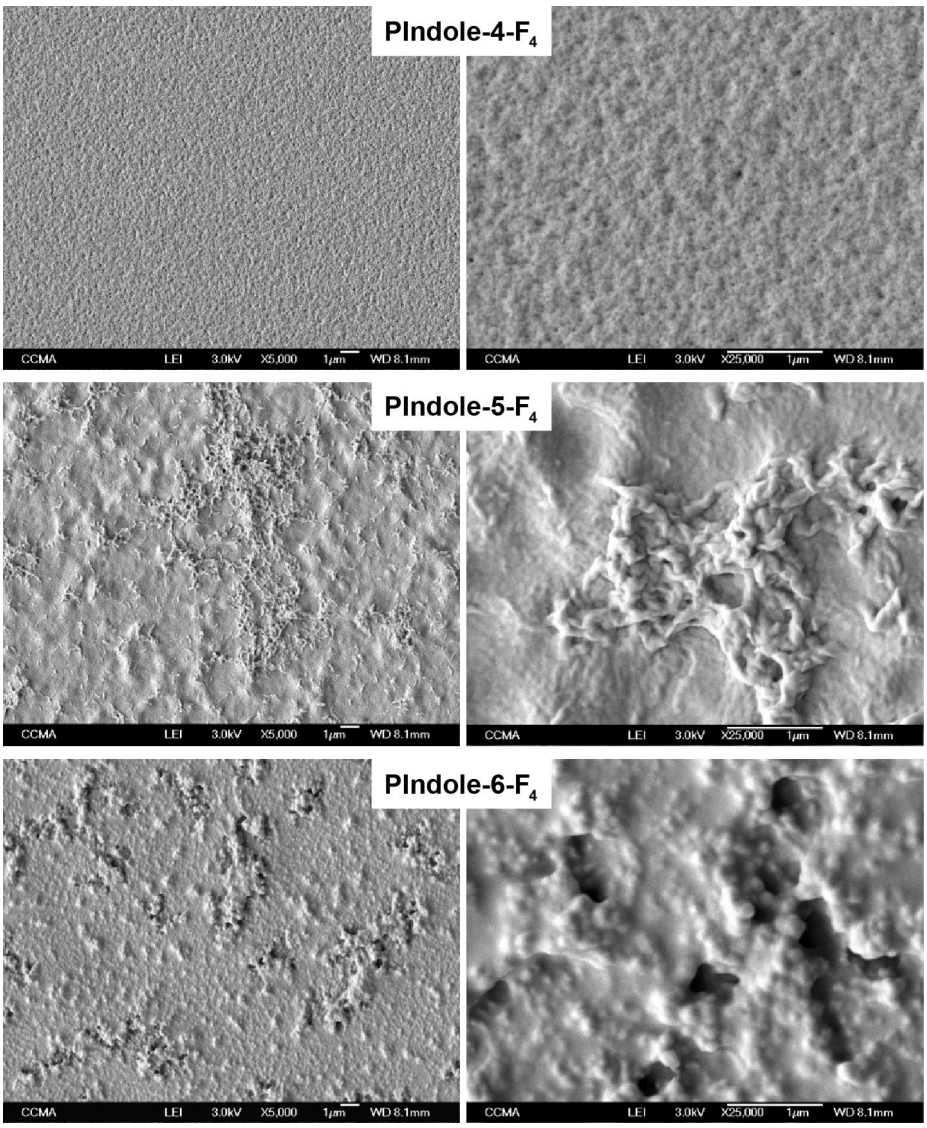

Figure 4: SEM images at two different magnifications (5000× and 25000×) of the polyindoles substituted with C_4F_9 chains in the different positions.

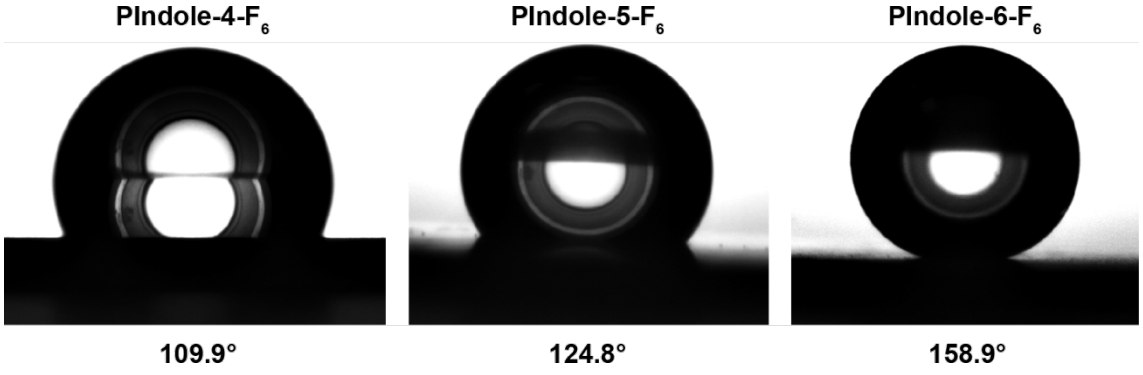

Figure 5: Image of a water droplet deposited on **PIndole-4-F$_6$**, **PIndole-5-F$_6$** and **PIndole-4-F$_6$**; *Qs* = 100 mC·cm^{-2}.

Table 4: Arithmetic roughness (R_a), quadratic roughness (R_q) and apparent contact angles (θ) for the four probe liquids (water, diiodomethane, sunflower oil and hexadecane) for the "smooth" polymers.

polymer	R_a (nm)	R_q (nm)	θ^Y_{water}	$\theta^Y_{diiodomethane}$	$\theta^Y_{sunflower}$	$\theta^Y_{hexadecane}$
PIndole	6.3	8.8	79.9	47.3	0	0
PIndole-4-F_6	6.6	9.5	97.5	51.3	41.5	25.6
PIndole-4-F_4	7.3	9.4	78.7	35.6	16.0	0
PIndole-5-F_6	6.4	9.8	96.8	60.4	47.3	37.9
PIndole-5-F_4	6.3	8.1	81.4	44.9	0	0
PIndole-6-F_6	6.8	9.5	99.4	66.8	50.7	44.1
PIndole-6-F_4	7.8	10.1	81.1	45.7	19.5	0

Indeed, two equations (the Wenzel and the Cassie–Baxter equation) [36,37] depending on θ^Y are very often used to explain the effect of the surface roughness on the wetting properties. In the Wenzel equation [36] ($\cos\theta = r\cdot\cos\theta^Y$, where r is a roughness parameter), the surface roughness can increase θ, but only if $\theta^Y > 90°$. Hence, it is possible to have an extremely high θ_{water}, but the contact angle hysteresis (H) is usually high because the surface roughness increases also the solid–liquid interface and thereby, increasing the adhesion between the water drop and the surface. Only the Cassie–Baxter equation [37] ($\cos\theta = r_f f\cdot\cos\theta^Y + f - 1$, where r_f is the roughness ratio of the substrate wetted by the liquid, f the solid fraction and $(1 - f)$ the air fraction) can predict the superhydrophobicity of **PIndole-6-F_6**, for example. Here, the presence of a high amount of air between the droplet and the substrate can lead to extremely high θ_{water} with a very low H. In the case of **PIndole-6-F_6**, the presence of the spherical nanoparticles formed on the surface during the polymerization allows to trap a high amount of air leading to superhydrophobic properties. These nanoparticles also induce a high increase of the surface oleophobicity, for example an increase of $\theta_{hexadecane}$ of 49.2°, from 44.1° on the smooth surface to 99.3° on the structured surface.

Conclusion

Here we report for the first time the possibility to obtain hydrophobic and superhydrophobic polymeric films with a very low roughness by electropolymerization of fluorinated indoles differing by the length (C_4F_9, C_6F_{13} and C_8F_{17}) and the position (4, 5 and 6-position on indole) of the perfluorinated substituent. Polymeric films were obtained for C_4F_9 and C_6F_{13} showing several differences mainly with the substituent position, affecting the surface morphology and the wetting properties. The best results were obtained with **PIndole-6-F_6** for which a superhydrophobic state with a self-cleaning condition and highly oleophobic properties were reached due to the presence of spherical nanoparticles and the fluorinated compounds on the surface. This work opens new ways in the formation of superhydrophobic polyindoles films by electrodeposition for future applications.

Experimental

Monomer synthesis and characterization

4-(aminomethyl)indole, 5-(aminomethyl)indole and 6-(aminomethyl)indole were purchased from Sigma-Aldrich. The monomers were synthesized by amidification between the corresponding (aminomethyl)indole and fluorinated acid (Scheme 2). More precisely, 0.26 g (1.4 mmol, 1 equiv) of *N*-(3-dimethylaminopropyl)-*N*′-ethylcarbodiimide hydrochloride (EDC) and 0.17 g of 4-dimethylaminopyridine (DMAP) (1.4 mmol, 1 equiv) were added to 20 mL of dichloromethane containing 1 equiv of the corresponding fluorinated acid. After stirring for 30 min, 0.2 g (1.4 mmol, 1 equiv) of the corresponding (aminomethyl)indole was added. The solution was stirred at room temperature for 24 h. The crude product was

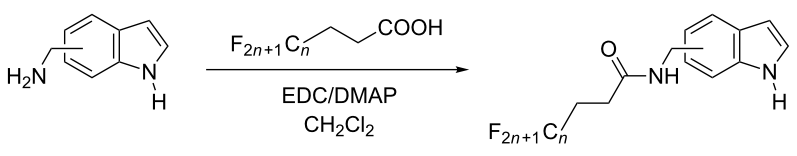

Scheme 2: Synthesis way to the indole derivatives.

purified by column chromatography (stationary phase: silica gel; eluent: chloroform/methanol 95:5).

***N*-((1*H*-Indol-4-yl)methyl)-4,4,5,5,6,6,7,7,8,8,9,9,10,10,11,11,11-heptadecafluoroundecanamide (Indole-4-F_8):** Yield 15%; yellow solid; mp 163.2 °C; ^{1}H NMR (200 MHz, CD_3OD) δ 7.32 (d, *J* = 8.0 Hz, 1H), 7.24 (d, *J* = 3.2 Hz, 1H), 7.06 (m, 1H), 6.93 (d, *J* = 6.8 Hz, 1H), 6.51 (dd, *J* = 3.2, 0.9 Hz, 1H), 4.65 (s, 2H), 2.55 (m, 4H); ^{19}F NMR (188 MHz, CD_3OD) δ −82.38 (m, 3F), −115.74 (m, 2F), −122.87 (m, 6F), −123.75 (m, 2F), −124.52 (m, 2F), −127.29 (m, 2F); ^{13}C NMR (50 MHz, CD_3OD) δ 172.45, 137.84, 130.34, 128.04, 125.64, 122.22, 119.39, 111.83, 100.41, 42.98, 28.1 (t, *J* = 23.1 Hz), 27.62 (t, *J* = 6.2 Hz); MS (70 eV) *m*/*z*: M^+ 620 (82), $C_9H_9N_2^{+\bullet}$ 145 (100), $C_9H_8N^{+\bullet}$ 130 (92), $C_8H_8N^+$ 118 (52).

***N*-((1*H*-Indol-4-yl)methyl)-4,4,5,5,6,6,7,7,8,8,9,9,9-tridecafluorononanamide (Indole-4-F_6):** Yield 25%; yellow solid; mp 150.2 °C; ^{1}H NMR (200 MHz, CD_3OD) δ 7.32 (d, *J* = 8.0 Hz, 1H), 7.24 (d, *J* = 3.2 Hz, 1H), 7.06 (m, 1H), 6.92 (d, *J* = 7.0 Hz, 1H), 6.50 (dd, *J* = 3.2, 0.9 Hz, 1H), 4.65 (s, 2H), 2.55 (m, 4H); ^{19}F NMR (188 MHz, CD_3OD) δ −82.43 (m, 3F), −115.74 (m, 2F), −122.93 (m, 2F), −123.91 (m, 2F), −124.60 (m, 2F), −127.36 (m, 2F); ^{13}C NMR (50 MHz, CD_3OD) δ 172.43, 137.81, 130.32, 128.04, 125.64, 122.22, 119.38, 111.82, 100.41, 42.98, 27.90 (t, *J* = 22.5 Hz), 27.47 (t, *J* = 2.8 Hz); MS (70 eV) *m*/*z*: M^+ 520 (25), $C_9H_9N_2^{+\bullet}$ 145 (100), $C_9H_8N^{+\bullet}$ 130 (87), $C_8H_8N^+$ 118 (59).

***N*-((1*H*-Indol-4-yl)methyl)-4,4,5,5,6,6,7,7,8,8,8-undecafluorooctanamide (Indole-4-F_4):** Yield 21%; yellow solid; mp 139.8 °C; ^{1}H NMR (200 MHz, CD_3OD) δ 7.32 (d, *J* = 8.1 Hz, 1H), 7.24 (d, *J* = 3.2 Hz, 1H), 7.06 (m, 1H), 6.93 (d, *J* = 7.6 Hz, 1H), 6.50 (dd, *J* = 3.2, 0.9 Hz, 1H), 4.65 (s, 2H), 2.55 (m, 4H); ^{19}F NMR (188 MHz, CD_3OD) δ −82.69 (m, 3F), −115.98 (m, 2F), −125.63 (m, 2F), −127.31 (m, 2F); ^{13}C NMR (50 MHz, CD_3OD) δ 172.37, 137.75, 130.26, 127.98, 125.58, 122.16, 119.32, 111.76, 100.35, 42.91, 27.82 (t, *J* = 22.1 Hz), 27.50 (t, *J* = 4.0 Hz); MS (70 eV) *m*/*z*: M^+ 420 (40), $C_9H_9N_2^{+\bullet}$ 145 (95), $C_9H_8N^{+\bullet}$ 130 (100), $C_8H_8N^+$ 118 (65).

***N*-((1*H*-Indol-5-yl)methyl)-4,4,5,5,6,6,7,7,8,8,9,9,10,10,11,11,11-heptadecafluoroundecanamide (Indole-5-F_8):** Yield 28%; yellow solid; mp 135.9 °C; ^{1}H NMR (200 MHz, CD_3OD) δ 7.47 (s, 1H), 7.33 (d, *J* = 8.4 Hz, 1H), 7.21 (d, *J* = 3.1 Hz, 1H), 7.04 (dd, *J* = 8.4, 1.6 Hz, 1H), 6.40 (dd, *J* = 3.1, 0.8 Hz, 1H), 4.49 (s, 2H), 2.53 (m, 4H); ^{19}F NMR (188 MHz, CD_3OD) δ −82.40 (m, 3F), −115.74 (m, 2F), −122.90 (m, 6F), −123.77 (m, 2F), −124.60 (m, 2F), −127.36 (m, 2F); ^{13}C NMR (50 MHz, CD_3OD) δ 172.32, 137.03, 129.90, 129.53, 126.06, 122.45, 120.51, 112.24, 102.24, 45.09, 27.82 (t, *J* = 21.4 Hz), 27.53 (t, *J* = 4.1 Hz); MS (70 eV) *m*/*z*: M^+ 620 (4), $C_9H_9N_2^{+\bullet}$ 145 (100), $C_9H_8N^{+\bullet}$ 130 (92), $C_8H_8N^+$ 118 (47).

***N*-((1*H*-Indol-5-yl)methyl)-4,4,5,5,6,6,7,7,8,8,9,9,9-tridecafluorononanamide (Indole-5-F_6):** Yield 51%; yellow solid; mp 85.5 °C; ^{1}H NMR (200 MHz, CD_3OD) δ 7.47 (s, 1H), 7.33 (d, *J* = 8.3 Hz, 1H), 7.21 (d, *J* = 3.1 Hz, 1H), 7.03 (dd, *J* = 8.3, 1.6 Hz, 1H), 6.40 (dd, *J* = 3.1 Hz, 0.8 Hz, 1H), 4.44 (s, 2H), 2.47 (m, 4H); ^{19}F NMR (188 MHz, CD_3OD) δ −82.45 (m, 3F), −115.74 (m, 2F), −122.95 (m, 2F), −123.93 (m, 2F), −124.60 (m, 2F), −127.36 (m, 2F); ^{13}C NMR (50 MHz, CD_3OD) δ 172.38, 137.10, 129.97, 129.61, 126.13, 122.52, 120.58, 112.31, 102.31, 45.16, 27.86 (t, *J* = 22.8 Hz), 27.60 (t, *J* = 3.0 Hz); MS (70 eV) *m*/*z*: M^+ 520 (35), $C_9H_9N_2^{+\bullet}$ 145 (100), $C_9H_8N^{+\bullet}$ 130 (90), $C_8H_8N^+$ 118 (54).

***N*-((1*H*-Indol-5-yl)methyl)-4,4,5,5,6,6,7,7,8,8,8-undecafluorooctanamide (Indole-5-F_4):** Yield 61%; yellow solid; mp 47.7 °C; ^{1}H NMR (200 MHz, CD_3OD) δ 7.47 (s, 1H), 7.33 (d, *J* = 8.4 Hz, 1H), 7.21 (d, *J* = 3.1 Hz, 1H), 7.04 (dd, *J* = 8.4, 1.6 Hz, 1H), 6.40 (dd, *J* = 3.1, 0.8 Hz, 1H), 4.44 (s, 2H), 2.47 (m, 4H); ^{19}F NMR (188 MHz, CD_3OD) δ −82.67 (m, 3F), −115.97 (m, 2F), −125.60 (m, 2F), −127.21 (m, 2F); ^{13}C NMR (50 MHz, CD_3OD) δ 172.32, 137.03, 129.91, 129.54, 126.07, 122.45, 120.52, 112.24, 102.25, 45.09, 27.78 (t, *J* = 22.5 Hz), 27.64 (t, *J* = 3.9 Hz); MS (70 eV) *m*/*z*: M^+ 420 (98), $C_9H_9N_2^{+\bullet}$ 145 (90), $C_9H_8N^{+\bullet}$ 130 (100), $C_8H_8N^+$ 118 (70).

***N*-((1*H*-Indol-6-yl)methyl)-4,4,5,5,6,6,7,7,8,8,9,9,10,10,11,11,11-heptadecafluoroundecanamide (Indole-6-F_8):** Yield 30%; yellow solid; mp 121.0 °C; ^{1}H NMR (200 MHz, CD_3OD) δ 7.49 (d, *J* = 8.1 Hz, 1H), 7.32 (s, 1H), 7.20 (d, *J* = 3.1 Hz, 1H), 6.95 (dd, *J* = 8.1, 1.4 Hz, 1H), 6.40 (dd, *J* = 3.1, 0.8 Hz, 1H), 4.45 (s, 2H), 2.56 (m, 4H); ^{19}F NMR (188 MHz, CD_3OD) δ −82.39 (m, 3F), −115.76 (m, 2F), −122.86 (m, 6F), −123.78 (m, 2F), −124.58 (m, 2F), −127.29 (m, 2F); ^{13}C NMR (50 MHz, CD_3OD) δ 172.36, 137.73, 132.46, 128.79, 125.87, 121.30, 120.22, 111.47, 102.17, 45.10, 27.79 (t, *J* = 21.0 Hz), 27.43 (t, *J* = 5.0 Hz); MS (70 eV) *m*/*z*: M^+ 620 (4), $C_9H_9N_2^{+\bullet}$ 145 (100), $C_9H_8N^{+\bullet}$ 130 (97), $C_8H_8N^+$ 118 (45).

***N*-((1*H*-Indol-6-yl)methyl)-4,4,5,5,6,6,7,7,8,8,9,9,9-tridecafluorononanamide (Indole-6-F_6):** Yield 19%; yellow solid; mp 120.7 °C; ^{1}H NMR (200 MHz, CD_3OD) δ 7.49 (d, *J* = 8.1 Hz, 1H), 7.31 (s, 1H), 7.20 (d, *J* = 3.1 Hz, 1H), 6.94 (dd, *J* = 8.1, 1.5 Hz, 1H), 6.40 (dd, *J* = 3.1, 0.8 Hz, 1H), 4.45 (s, 2H), 2.47 (m, 4H); ^{19}F NMR (188 MHz, CD_3OD) δ −82.45 (m, 3F), −115.77 (m, 2F), −122.95 (m, 2F), −123.93 (m, 2F), −124.60 (m, 2F), −127.36 (m, 2F); ^{13}C NMR (50 MHz, CD_3OD) δ 172.43, 137.80, 132.52, 128.86, 125.93, 121.36, 120.28, 111.54, 102.23, 45.15, 27.88 (t, *J* = 21.0 Hz), 27.58 (t, *J* = 3.5 Hz); MS

(70 eV) *m*/*z*: M^+ 520 (40), $C_9H_9N_2^{+\bullet}$ 145 (100), $C_9H_8N^{+\bullet}$ 130 (94), $C_8H_8N^+$ 118 (53).

***N*-((1*H*-Indol-6-yl)methyl)-4,4,5,5,6,6,7,7,8,8,8-undecafluorooctanamide (Indole-6-F_4):** Yield 33%; yellow solid; mp 105.7 °C; ^{1}H NMR (200 MHz, CD_3OD) δ 7.50 (d, *J* = 8.1 Hz, 1H), 7.31 (s, 1H), 7.20 (d, *J* = 3.2 Hz, 1H), 6.95 (dd, *J* = 8.1, 1.5 Hz, 1H), 6.40 (dd, *J* = 3.1, 0.8 Hz, 1H), 4.45 (s, 2H), 2.58 (m, 4H); ^{19}F NMR (188 MHz, CD_3OD) δ −82.66 (m, 3F), −115.91 (m, 2F), −125.60 (m, 2H), −127.27 (m, 2H); ^{13}C NMR (50 MHz, CD_3OD) δ 172.43, 137.72, 132.45, 128.78, 125.87, 121.29, 120.21, 111.47, 102.21, 45.08, 27.72 (t, *J* = 21.0 Hz), 27.56 (t, *J* = 4.0 Hz); MS (70 eV) *m*/*z*: M^+ 420 (85), $C_9H_9N_2^{+\bullet}$ 145 (85), $C_9H_8N^{+\bullet}$ 130 (100), $C_8H_8N^+$ 118 (70).

Electrodeposition parameters

The polyindole films were electrodeposited by using a potentiostat (Autolab). For this, 2 cm^2 gold plates were chosen as working electrode, a carbon rod as counter-electrode while saturated calomel (SCE) was taken as reference electrode. The electrolyte used was a 0.1 mol solution of tetrabutylammonium perchlorate (Bu_4NClO_4) in anhydrous acetonitrile. Before the electrodeposition, the solution was degassed under argon and 0.01 mol of monomer was introduced. After the electrodeposition, the coated substrates were washed three times in acetonitrile and slowly dried.

Polymer and surface characterization

The surface roughness (arithmetic R_a and quadratic R_q) were determined by using a Wyko NT 1100 optical microscope of Bruker. The data were obtained using the High Mag Phase Shift Interference (PSI) working mode, the objective 50× and the field of view (FOV) 0.5×.

The scanning electron microscopy images were obtained by using a 6700F microscope of JEOL.

The contact angles were determined by using a DSA30 goniometer of Krüss. Liquids of different surface tension were chosen to characterize the surface hydrophobicity and oleophobicity: water (γ_{LV} = 72.8 mN·m^{-1}), diiodomethane (γ_{LV} = 50.0 mN·m^{-1}), sunflower oil (γ_{LV} ≈ 31 mN·m^{-1}) and hexadecane (γ_{LV} = 27.6 mN·m^{-1}). The apparent contact angles (θ) were obtained by taken the angle at the triple point of a liquid droplet put on the substrate. The contact angle hysteresis (*H*) and sliding angle (α) were determined with the tilted-drop method. Here, a 6 µL liquid droplet was put on the substrate and the substrate was inclined until the droplet moving. The maximum inclination angle is α. The advanced (θ_{adv}) and receding (θ_{rec}) contact angles and by deduction the hysteresis $H = \theta_{adv} - \theta_{rec}$ were taken just before the moving of the droplet, the angle in the moving direction being θ_{adv} and that in the opposite direction θ_{rec}.

Acknowledgements

This work was supported by CNPq, Conselho Nacional de Desenvolvimento Científico e Tecnológico - Brazil (Process No. 202280/2014-4). We thank Jean-Pierre Laugier (CCMA, UNS) for the SEM images.

References

1. Liu, M.; Zheng, Y.; Zhai, J.; Jiang, L. *Acc. Chem. Res.* **2010,** *43,* 368–377. doi:10.1021/ar900205g
2. Simpson, J. T.; Hunter, S. R.; Aytug, T. *Rep. Prog. Phys.* **2015,** *78,* 086501. doi:10.1088/0034-4885/78/8/086501
3. Si, Y.; Guo, Z. *Nanoscale* **2015,** *7,* 5922–5946. doi:10.1039/C4NR07554D
4. Nishimoto, S.; Bhushan, B. *RSC Adv.* **2013,** *3,* 671–690. doi:10.1039/c2ra21260a
5. Rahmawan, Y.; Xu, L.; Yang, S. *J. Mater. Chem. A* **2013,** *1,* 2955–2969. doi:10.1039/C2TA00288D
6. Wang, J.-N.; Zhang, Y.-L.; Liu, Y.; Zheng, W.; Lee, L. P.; Sun, H.-B. *Nanoscale* **2015,** *7,* 7101–7114. doi:10.1039/C5NR00719D
7. Darmanin, T.; Guittard, F. *Mater. Today* **2015,** *18,* 273–285. doi:10.1016/j.mattod.2015.01.001
8. Koch, K.; Bhushan, B.; Barthlott, W. *Prog. Mater. Sci.* **2009,** *54,* 137–178. doi:10.1016/j.pmatsci.2008.07.003
9. Sun, M.; Watson, G. S.; Zheng, Y.; Watson, J. A.; Liang, A. *J. Exp. Biol.* **2009,** *212,* 3148–3155. doi:10.1242/jeb.033373
10. Bush, J. W. M.; Hu, D. L.; Prakash, M. *Adv. Insect Physiol.* **2007,** *34,* 117–192. doi:10.1016/S0065-2806(07)34003-4
11. Ju, J.; Bai, H.; Zheng, Y.; Zhao, T.; Fang, R.; Jiang, L. *Nat. Commun.* **2012,** *3,* 1247. doi:10.1038/ncomms2253
12. Andrews, H. G.; Eccles, E. A.; Schofield, W. C. E.; Badyal, J. P. S. *Langmuir* **2011,** *27,* 3798–3802. doi:10.1021/la2000014
13. Sarkar, A.; Kietzig, A.-M. *Soft Matter* **2015,** *11,* 1998–2007. doi:10.1039/C4SM02787F
14. Cha, T.-G.; Yi, J. W.; Moon, M.-W.; Lee, K.-R.; Kim, H.-Y. *Langmuir* **2010,** *26,* 8319–8326. doi:10.1021/la9047402
15. Huovinen, E.; Takkunen, L.; Korpela, T.; Suvanto, M.; Pakkanen, T. T.; Pakkanen, T. A. *Langmuir* **2014,** *30,* 1435–1443. doi:10.1021/la404248d
16. Beaujuge, P. M.; Reynolds, J. R. *Chem. Rev.* **2010,** *110,* 268–320. doi:10.1021/cr900129a
17. Xu, L.; Chen, Z.; Chen, W.; Mulchandani, A.; Yan, Y. *Macromol. Rapid Commun.* **2008,** *29,* 832–838. doi:10.1002/marc.200700891
18. Taleb, S.; Darmanin, T.; Guittard, F. *ACS Appl. Mater. Interfaces* **2014,** *6,* 7953–7960. doi:10.1021/am501279h
19. Santos, J. L.; Li, Y.; Culver, H. R.; Yu, M. S.; Herrera-Alonso, M. *Chem. Commun.* **2014,** *50,* 15045–15048. doi:10.1039/C4CC06056C
20. Pringle, J. M.; Ngamna, O.; Chen, J.; Wallace, G. G.; Forsyth, M.; MacFarlane, D. R. *Synth. Met.* **2006,** *156,* 979–983. doi:10.1016/j.synthmet.2006.06.009
21. D'Arcy, J. M.; Tran, H. D.; Tung, V. C.; Tucker-Schwartz, A. K.; Wong, R. P.; Yang, Y.; Kaner, R. B. *Proc. Natl. Acad. Sci. U. S. A.* **2010,** *107,* 19673–19678. doi:10.1073/pnas.1008595107
22. Chiou, N.-R.; Lu, C.; Guan, J.; Lee, L. J.; Epstein, A. J. *Nat. Nanotechnol.* **2007,** *2,* 354–357. doi:10.1038/nnano.2007.147

23. Im, S. G.; Yoo, P. J.; Hammond, P. T.; Gleason, K. K. *Adv. Mater.* **2007,** *19,* 2863–2867. doi:10.1002/adma.200701170
24. Vucaj, N.; Quinn, M. D. J.; Baechler, C.; Notley, S. M.; Cottis, P.; Hojati-Talemi, P.; Fabretto, M. V.; Wallace, G. G.; Murphy, P. J.; Evans, D. R. *Chem. Mater.* **2014,** *26,* 4207–4213. doi:10.1021/cm5014653
25. Tarrade, J.; Darmanin, T.; Taffin de Givenchy, E.; Guittard, F.; Debarnot, D.; Poncin-Epaillard, F. *Appl. Surf. Sci.* **2014,** *292,* 782–789. doi:10.1016/j.apsusc.2013.12.051
26. Poverenov, E.; Li, M.; Bitler, A.; Bendikov, M. *Chem. Mater.* **2010,** *22,* 4019–4025. doi:10.1021/cm100561d
27. Darmanin, T.; Guittard, F. *Adv. Mater. Interfaces* **2015,** *2,* 1500081/1–1500081/7. doi:10.1002/admi.201500081
28. Mortier, C.; Darmanin, T.; Guittard, F. *Macromolecules* **2015,** *48,* 5188–5195. doi:10.1021/acs.macromol.5b01054
29. Yan, H.; Kurogi, K.; Mayama, H.; Tsujii, K. *Angew. Chem., Int. Ed.* **2005,** *44,* 3453–3456. doi:10.1002/anie.200500266
30. Mortier, C.; Darmanin, T.; Guittard, F. *Adv. Eng. Mater.* **2014,** *16,* 1400–1405. doi:10.1002/adem.201400212
31. Singh, V.; Chauhan, D. S.; Pandey, P. C. A comparative study on electrochemical synthesis of carboxylic acid substituted indoles and their application in selective oxidation of dopamine.. IEEE Sensors 2009, Christchurch, New Zealand, Oct 25–28, 2009; pp 1140–1144. doi:10.1109/ICSENS.2009.5398578
32. Ma, X.; Zhou, W.; Mo, D.; Wang, Z.; Xu, J. *Synth. Met.* **2015,** *203,* 98–106. doi:10.1016/j.synthmet.2015.02.025
33. Yakhmi, J. V.; Saxena, V.; Aswal, D. K. Conducting Polymer Sensors, Actuators and Field-Effect Transistors. *Functional Materials: Preparation, Processing and Applications;* Elsevier, 2012; pp 61–110. doi:10.1016/B978-0-12-385142-0.00002-7
34. Mortier, C.; Darmanin, T.; Guittard, F. *ChemPlusChem* **2014,** *79,* 1434–1439. doi:10.1002/cplu.201402187
35. Young, T. *Philos. Trans. R. Soc. London* **1805,** *95,* 65–87. doi:10.1098/rstl.1805.0005
36. Wenzel, R. N. *Ind. Eng. Chem.* **1936,** *28,* 988–994. doi:10.1021/ie50320a024
37. Cassie, A. B. D.; Baxter, S. *Trans. Faraday Soc.* **1944,** *40,* 546–551. doi:10.1039/tf9444000546

License and Terms

BEILSTEIN JOURNAL OF NANOTECHNOLOGY

Selective porous gates made from colloidal silica nanoparticles

Roberto Nisticò*[1], Paola Avetta[1], Paola Calza[1,2], Debora Fabbri[1], Giuliana Magnacca[1,2] and Dominique Scalarone[1,2]

Full Research Paper

Open Access

Address:
[1]University of Torino, Department of Chemistry, Via P. Giuria 7, 10125 Torino, Italy and [2]NIS Research Centre, Via P. Giuria 7, 10125 Torino, Italy

Email:
Roberto Nisticò* - roberto.nistico@unito.it

* Corresponding author

Keywords:
block copolymers; coatings; colloidal nanoparticles; silica; sol–gel synthesis

Beilstein J. Nanotechnol. **2015,** *6,* 2105–2112.
doi:10.3762/bjnano.6.215

Received: 25 August 2015
Accepted: 21 October 2015
Published: 04 November 2015

This article is part of the Thematic Series "Organized films".

Guest Editor: M. Canepa

Abstract

Highly selective porous films were prepared by spin-coating deposition of colloidal silica nanoparticles on an appropriate macroporous substrate. Silica nanoparticles very homogenous in size were obtained by sol–gel reaction of a metal oxide silica precursor, tetraethyl orthosilicate (TEOS), and using polystyrene-*block*-poly(ethylene oxide) (PS-*b*-PEO) copolymers as soft-templating agents. Nanoparticles synthesis was carried out in a mixed solvent system. After spin-coating onto a macroporous silicon nitride support, silica nanoparticles were calcined under controlled conditions. An organized nanoporous layer was obtained characterized by a depth filter-like structure with internal porosity due to interparticle voids. Permeability and size-selectivity were studied by monitoring the diffusion of probe molecules under standard conditions and under the application of an external stimulus (i.e., electric field). Promising results were obtained, suggesting possible applications of these nanoporous films as selective gates for controlled transport of chemical species in solution.

Introduction

The development of smart nanoporous devices for the separation of chemical species, ions and biomolecules in solution is a field of increasing interest for researchers involved in microfiltration and separation science [1-7]. In this topic, it is important to remind that microfiltration is one of the oldest processes optimized since the dawn of membrane technology in the 1920s, mostly used for separation of bacteria from water [8]. In the following years, microfiltration devices have found application in several technological fields: water treatments, food industry, biotechnology, electronics and microfluidics [9-13]. Recently, it has been stated that microfiltration devices account for almost half of the whole membrane market [14].

Two different kinds of membranes for microfiltration have been developed over the years: namely screen-filters and depth-filters [8]. Screen-filters, characterized by having well-ordered straight

pores, realize the separation by a sieving mechanism based only on pore size: molecules and/or particles smaller than the pore diameter pass easily through the porous membrane, whereas species larger than the pore diameters are retained. They can be obtained by lithographic techniques or templating approaches [15,16]. Depth-filters are characterized by having a tortuous disordered porous network. Even if the real mechanism of separation is not clear yet, particles are generally supposed to be retrained within the filter bulk thorough adsorption and mechanical entrapments [8].

A step forward in the preparation of microfiltration devices was realized by the surface functionalization of macroporous supports or membranes by nanoporous functional coatings [17-20]: the macroporous, permeable supports, in fact, can provide mechanical strength to the thinner functional coatings on top, thus becoming resistant selective gates [4].

Microsieve membranes are very thin flat-sheet devices with a well-ordered porous organization. They can be made of different materials, either inorganic (such as silicon or silicon nitride) or organic (such as polysulfone or polyethersulfone). Silicon nitride (Si_3N_4) inorganic microsieves are mainly used in the semiconductor industry [21], even though recently they are finding application in the clarification of milk, beers and juices as well as in biotechnology for the separation of bacteria and/or blood cells [7,22].

Silicon nitride microsieves with hexagonally ordered pores were also employed as substrate for MCM-48 silica films, giving promising results [4,23,24]. The sol–gel polymerization process is a key procedure for the bottom-up synthesis of nano- and mesoporous silica films and in the literature there are several reviews focusing on this field [25,26]. Conventional procedures for the synthesis of mesoporous silica involve the use of amphiphilic templates [27-30]. Either low molecular weight surfactants or polymers have been used as structure-directing agents in the preparation of organic–inorganic hybrid solutions and they have proved to generate a variety of well-ordered materials by self-assembling processes [31-35].

Here, we describe the synthesis, deposition and physicochemical characterization of silica coatings, obtained by spin-coating deposition of soft-templated silica colloidal nanoparticles onto commercial Si_3N_4 microsieves for membrane applications. Moreover, permeability and size-selectivity were studied by monitoring the diffusion of different probe molecules under standard conditions and under the application of an electric field as external stimulus. Selected probe molecules were the cationic dye methylene blue (MB, molecular weight (M_W) = 320 Da) and the cationic protein ribonuclease A (RNAse, M_W = 13700 Da).

Results and Discussion

Synthesis, preparation and physicochemical characterization of the colloidal silica nanoparticles and mesoporous coatings

Amphiphilic block copolymers in solution are able to form various types of aggregates, such as micelles and vesicles that can be employed to build novel nanomaterials [36,37]. Figure 1 reports the possible supramolecular organizations of amphiphiles when dissolved in solution. In particular, by changing the ratio between the silica precursor (i.e., tetraethyl orthosilicate, TEOS) and the soft-templating agent (block copolymer), different architectures of the final oxidic material can be achieved [27]. The driving force for self-assembling is the thermodynamic incompatibility of the different blocks in the

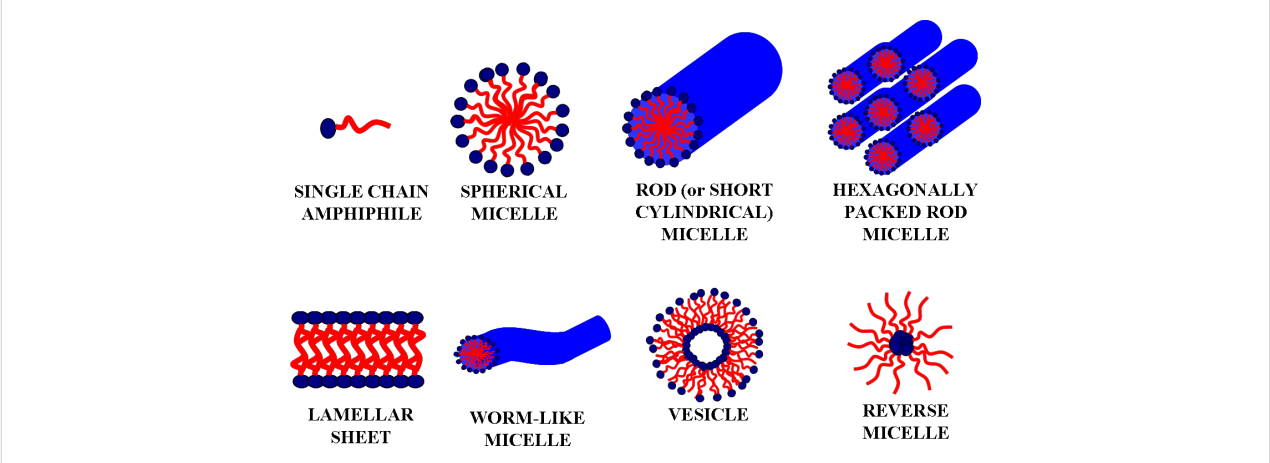

Figure 1: Schematic representation of different micellar architectures. Hydrophilic polar heads are indicated in blue, whereas hydrophobic non-polar tails are drawn in red.

polymeric chains, which brings them to spontaneously segregate in well-defined nanostructures. Therefore, when block copolymers are mixed to solvents which are selective for one of the blocks, polymer chains spontaneously aggregate into micelles having different architectures (i.e., spheres, rods, tubes, lamellae) and degree of order depending on the physicochemical properties of the block copolymer [38]. Next to the widespread spherical and short cylindrical (rod-like) micellar systems, also other types of supramolecular organizations were found, like lamellar sheets [39], worm-like systems [27] and vesicles [38]. When reverse micellization takes place, reverse micelles can work as nanoreactors [40] and used to produce nanoparticles.

Basing on our results, the reverse micellization regime definitively establishes with a TEOS/block copolymer weight ratio of 75/25 and the corresponding samples, obtained after calcination, appear as aggregates of individual silica nanoparticles with an average diameter of 25–30 nm (Figure 2A).

Once the colloidal solution is deposited via spin-coating onto the macroporous support and then calcined to remove organic moieties, colloidal silica nanoparticles aggregates, forming a layer covering the macroporous support. Figure 2B represents a schematic top-view of a single macropore (diameter of 5 μm) functionalized with nanoparticles in a depth-filter arrangement. The tortuous porosity is due to the tiny voids between the nanoparticles (interparticles voids) forming a disordered porous network. Figure 2C and 2D represent the Si_3N_4 microsieve surface before and after functionalization with the colloidal silica particles. The coating seems to be homogeneous, as confirmed by insets showing micrographs of the individual pores collected at higher magnification.

In order to evaluate the porosity of such depth-filter coatings, thicker samples of large weight were prepared by solvent-casting and N_2 adsorption/desorption gas-volumetric analyses were performed. TEM measurements confirmed that the casting procedure adopted for this preparation provided a morphology similar to spin-coated materials (see inset in Figure 3A). The N_2 gas-volumetric isotherm shown in Figure 3A is of the IV type, with a small hysteresis loop of H2 type (from IUPAC classification) in the relative pressure range 0.9–1, next to the condensation limit. The BET surface area is of ca. 260 m^2 g^{-1} and the DFT pore size distribution curve (Figure 3B) indicates a complex pore size distribution. In detail, pores present a bimodal distribution, with the presence of meso/macroporosity in the range 15–200 nm, probably due to interparticle voids (i.e., depth-filter porosity), together with a certain degree of microporosity in the range 1–2 nm, probably due to intraparticle voids

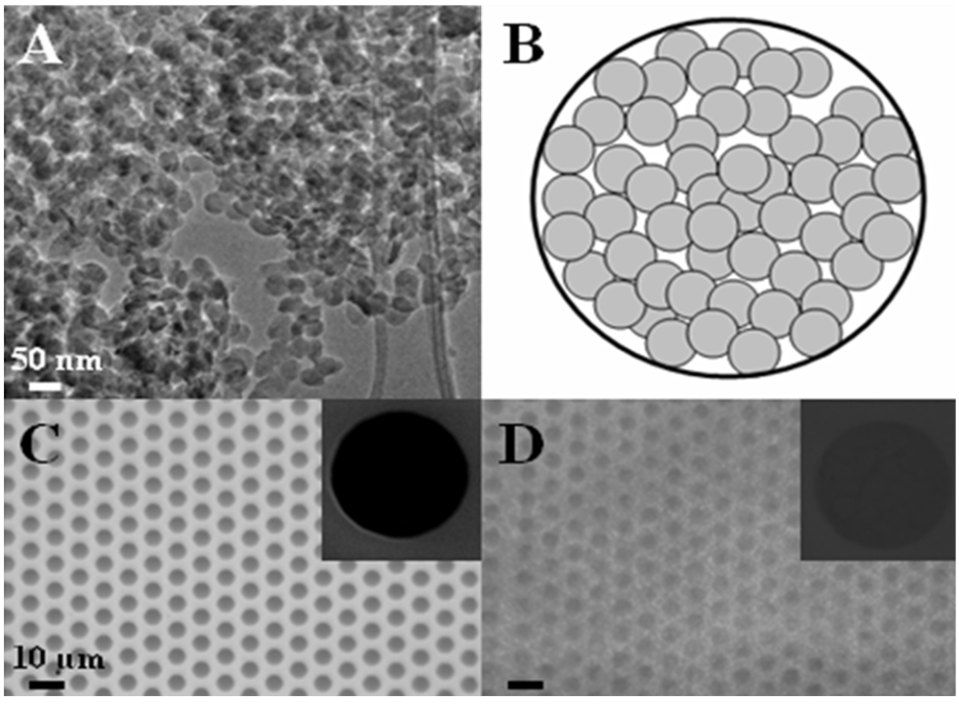

Figure 2: TEM micrograph of 75TEOS/25PS_{308}-*b*-PEO_{250} silica nanoparticles (A), schematic top-view of a depth-filter functionalized 5 μm pore (B), optical micrograph of a Si_3N_4 microsieve before (C) and after (D) fuctionalization with silica nanoparticles. Insets in pictures C and D show the SEM micrograph of a single microsieve pore collected at high magnification.

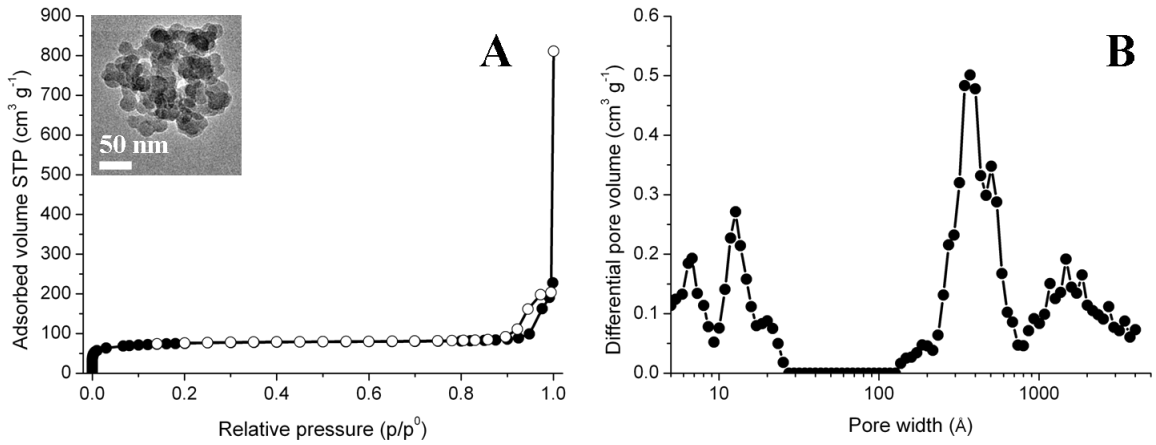

Figure 3: N_2 adsorption-desorption isotherm at 77 K (A) and DFT pore size distribution curve of 75TEOS/25PS_{308}-*b*-PEO_{250} silica powder (B). Dark symbols refer to the adsorption branch of the isotherm, empty symbols to the desorption branch. Inset shows the TEM micrograph of the powdery samples obtained by solvent-casting deposition.

generated from the elimination of poly(ethylene-oxide) moieties during the calcination step [41].

Transport testing of the functional coating

UV–vis spectroscopy was used to study the diffusion of two positively charged chemical probes (i.e., MB and RNAse) through the composite membrane. The hydrodynamic radius of MB is 0.5 nm [42], whereas the molar diameter of RNAse is approximately 3.8 nm [43]. According to these values, both probes should cross the depth-filter device whose porosity is in the range of 15–200 nm. In Figure 4A the values of percentage ratio between the effective concentration (C) of probe molecules passed through the membrane and the concentration at the equilibrium (C_e) is plotted as a function of time. The resulting diffusion curves demonstrate that dye molecules cross the membrane more easily than the protein which is partially blocked: at the time value of 167 h the diffusion of MB is ca. 10%, whereas for RNAse it is significantly lower, ca. 3%. These trends evidence a steric selectivity of the silica membrane. Interestingly, the functionalized membranes can be regenerated and reused by gently washing them with 2-propanol. Transport tests carried out using a regenerated membrane gave diffusion curves that are very similar to those reported in Figure 4A, thus proving that the proposed composite membranes are not damaged by the cleaning treatment and can be reused. This means that the interactions between the silica surface and probe molecules are weak

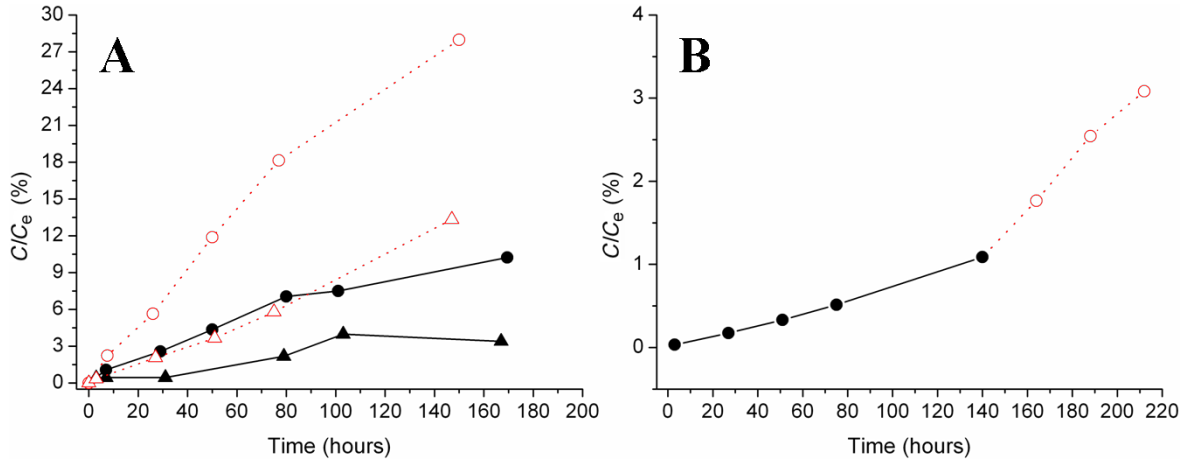

Figure 4: Concentration of probe molecules transported through the silica nanoparticle-functionalized microsieve. Section A: diffusion (black symbols, black solid lines) and migration (red symbols, red dotted lines) of MB (circle) and RNAse (triangle). Section B: diffusion (black circle, black solid line) followed by migration after 140 h (red circle, red dotted line) of MB in a mixed solution containing both MB and RNAse.

and labile interactions that can be broken by mild treatments. Also because of this, the membrane selectivity is here mainly attributed to steric effects, while specific interactions and adsorption phenomena have been ignored.

In addition, the migration properties of the membrane were tested by applying an electric field as external stimulus. It was found that it is possible to accelerate the passage of both probes trough the membrane without any loss in selectivity. In fact, at the time value of 147 h the migration of MB is ca. 28%, showing an increase of 18% with respect to the plain diffusion, whereas for RNAse migration is ca. 13%, corresponding to an increase of 10% with respect to the diffusion.

By making a comparison between diffusion and migration conditions, two main aspects deserve to be stressed. First, the application of an electric field increases the transport rate of the two species, which are both positively charged at the pH condition of the experiment, but it does not affect the membrane selectivity. This will result in a reduction of the time required for the separation. Second, the different increase in the transport rate of MB and RNAse under the migration regime proves that transport is affected by both the probe size and the effective charge. In fact, after 147 h MB transport passed from 10% to 28% with an increase of ca. 180%, whereas RNAse passed from 3% to 13% with an increase of ca. 333%.

Moreover, in order to clarify the effect of RNAse on the MB transport a further experiment was carried out. A mixed solution containing both MB and RNAse was prepared and the transport of MB through the membrane was evaluated examining the intensity of the signal at 664 nm. As reported in Figure 4B, the amount of MB diffused in the presence of RNAse at the time value of 140 h is ca. 1%, whereas for the neat MB solution it is ca. 9%. Furthermore, it can be observed that the application of an electric field causes a sharp increase of the amount of MB passing through the membrane. However, the amount of dye which migrates in the receiving cell is still lower if compared to the experiments carried out in the presence of MB alone. In general, these data suggest that the MB transport kinetics in the mixed solution were slowed down by the presence of RNAse.

Further studies are currently in progress in order to elucidate if this behavior has to be ascribed to specific interactions between MB and RNAse or to membrane fouling due to preferential interactions between RNAse and the Si_3N_4 surface.

Conclusion

Large-mesopore silica thin films were prepared via soft-templating by using PS-*b*-PEO block copolymer micelles and were characterized in order to assess their applicability as selective gates for controlled dosing and transport of chemical species in aqueous solution.

The development of mesoporous silica membranes with depth-filter porous organization opens new perspectives in the production of miniaturized devices for separation processes and dosing of chemicals. In this study, the surface functionalization of silicon nitride commercial microsieves by means of colloidal silica nanoparticles has been proposed as a novel strategy to fabricate composite membranes for microfluidic devices.

The permeability and size-selectivity of the functional microsieves we have prepared were studied by monitoring the diffusion of probe molecules with different molecular weight (i.e., methylene blue and ribonuclease A) under standard conditions and under the application of an external stimulus (i.e., electric field). Promising results have been obtained, suggesting possible applications of these mesoporous films as selective gates for controlled transport of chemical species in solution.

Experimental

Synthesis and preparation of coatings from colloidal silica nanoparticles

Colloidal silica nanoparticles were synthesized by sol–gel reaction of tetraethyl orthosilicate (TEOS, 99.0%, Aldrich) in ethanol (95.0%, Carlo Erba Reagents) under acidic conditions (HCl 37 wt %, Fluka Chemika), with a TEOS/HCl molar ratio of 3.5 and in the presence of PS_{308}-*b*-PEO_{250} (M_n = 32,000-*b*-11,000, Polymer Source Inc., Dorval, Canada) as structure directing agent. Benzene (≥99.7%, Riedel-de-Haën) was used as a solvent to solubilize the block copolymer. All chemicals were used without further purifications.

Copolymer benzene solutions (1 wt %) were prepared and let stirring until complete dissolution of the copolymer. Micellar solutions were obtained by adding the proper amount of sol–gel solution, as reported in previous studies [27]. In particular, the TEOS/PS_{308}-*b*-PEO_{250} weight ratio was fixed to 75/25.

The final solution was spin coated at 1000 rpm for 20 s, using a 8” Desk-top Precision Spin Coating System, model P-6708D vs. 2.0, both onto mica sheets and on commercial silicon microsieves purchased from Aquamarijn Micro Filtration BV (Zutphen, Netherlands). Silicon microsieves have on top a 5 mm × 5 mm × 0.6 mm Si_3N_4 membrane with macropores having a diameter of 5 μm and arranged in a hexagonal setting (Figure 5). After deposition, functionalized hybrid materials were dried in a hood at RT for at least 12 h in order to reach complete evaporation of solvents. Hybrid coatings were then transformed into colloidal silica nanoparticle layers by thermal

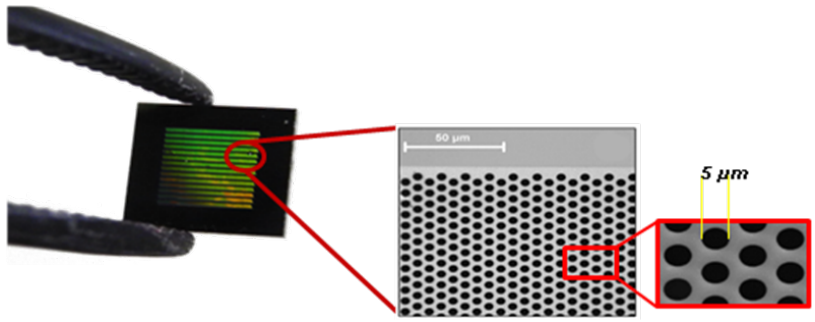

Figure 5: Macroporous commercial silicon nitride microsives purchased from Aquamarijn Micro Filtration BV (Zutphen, Netherlands), having on top a Si_3N_4 membrane (5 mm × 5 mm × 0.6 mm) with macropores arranged in a hexagonal setting and diameter of 5 µm.

treatments in a furnace under air atmosphere (400 °C for 2 h, ramp of 2 °C/min).

Synthesis and preparation of the colloidal silica powder

The same reactants described above were used to prepare silica powders for N_2 gas-volumetric adsorption at 77 K. In this case the sol–gel solutions were deposited onto glass Petri dishes, the solvent was evaporated, the hybrid films gently scratched and then calcined using the same conditions applied for the coating preparation (400 °C for 2 h, ramp of 2 °C/min). Silica powders thus obtained were analyzed by HRTEM to verify that their morphology was identical to that of thin spin-coated films obtained from the same micellar solution.

Physicochemical characterization

Transmission electron microscopy (HRTEM) was used to evaluate the morphology of colloidal silica nanoparticle coatings after the removal of the templates. Micrographs were obtained by using a JEOL JEM 2010 instrument (300 kV) equipped with a LaB_6 filament. For the specimen preparation a few drops of water were poured on the supported silica layer. After few seconds the surface was gently scratched and the functionalized layer separated from the support. Fragments were then transferred onto holed carbon coated copper grids by lifting the grids onto the water layer. Integrity and large-scale homogeneity of the membranes prepared on silicon microsieves were assessed by a Leica DM2005 optical microscope equipped with a digital camera for image acquisition and by scanning electron microscopy (SEM) [42].

SEM analyses were carried out using a ZEISS EVO 50 XVP with LaB_6 source, equipped with detectors for secondary electrons collection and EDS probe for elemental analyses.

N_2 adsorption-desorption experiments were carried out by means of ASAP 2020 instrument (Micromeritics) in order to determine specific surface area (BET model) [44] and porosity (DFT method) [27,45] of samples. The density functional theory (DFT) model for slit pores with low regularization was applied on the adsorption branch of the isotherm in order to examine simultaneously both micro- and mesoporosity of samples. The analyses were performed on powdery samples (ca. 100 mg) outgassed for several hours at 300 °C in vacuo (residual pressure 10^{-2} mbar) to ensure complete removal of atmospheric contaminants from surface and pores.

Transport tests

Transport tests were carried out following the same procedure already described elsewhere [42]. A homemade side-by-side diffusion cell was used, consisting of two half-cells in Pyrex physically separated by the porous membrane, fixed by two silicone seals covered with Teflon and held together with a metal clamp. The sealing of the system was evaluated with diffusion tests performed in the presence of a metallic diaphragm in place of the membrane. TOC analysis excluded the release of organic impurities from the device. TOC analysis were carried out with a Shimadzu TOC-VCSH Total Organic Carbon Analyzer, equipped with an ASI-V autosampler and fed with zero-grade air (Sapio, Italy).

Solutions of target molecules, i.e., methylene blue (MB in the following, Sigma Aldrich, 5.0×10^{-4} mol L^{-1}, water solution) and/or ribonuclease A from bovine pancreas (RNAse in the following, Sigma Aldrich, 1.0 wt %, water solution) [46], were put in the donor cell and the passage through the membrane was evaluated by means of UV–vis spectrophotometric analysis (UV–vis spectrometer Lambda 25 Perkin–Elmer) performed on the solution in the receptor cell (filled with water). Diffusion tests were carried out under continuous stirring in both cells at acid pH (thus both probes are positively charged). Spectrophotometric determination of target molecules was done at 664 nm for MB and at 277 nm for RNAse. Quantification was performed with external calibration curves ($R^2 \geq 0.9999$ for MB

and $R^2 \geq 0.9998$ for RNAse, see Figures S1 and S2 in Supporting Information File 1). Additionally, some tests were performed applying an external stimulus (i.e., electric field) by using a battery of 9 V connected with two graphite electrodes immersed in the two half-cells, with the positive electrode in the donor cell and the negative one in the receptor cell. Reported transport tests are averages of two replicas.

Supporting Information

Supporting Information File 1

External calibration curves performed by UV–vis spectroscopy.
[http://www.beilstein-journals.org/bjnano/content/supplementary/2190-4286-6-215-S1.pdf]

Acknowledgements

Compagnia di San Paolo and University of Torino are gratefully acknowledged for funding Project ORTO114XNH through "Bando per il finanziamento di progetti di ricerca di Ateneo – anno 2011". The Marie Sklodowska-Curie Research and Innovation Staff Exchange project funded by the European Commission H2020-MSCA-RISE-2014 within the framework of the research project Mat4treaT (Project number:645551) is acknowledged. The authors would like to thank Mrs. F. Franconieri for TEM technical assistance, Dr. Giorgio Volpi and Ms. Laura Campagnolo for the helpful availability.

References

1. Lee, M.; Wu, Z.; Wang, R.; Li, K. *J. Membr. Sci.* **2014,** *461,* 39–48. doi:10.1016/j.memsci.2014.02.044
2. Mecha, C. A.; Pillay, V. L. *J. Membr. Sci.* **2014,** *458,* 149–156. doi:10.1016/j.memsci.2014.02.001
3. Boffa, V.; ten Elshof, J. E.; Blank, D. H. A. *Microporous Mesoporous Mater.* **2007,** *100,* 173–182. doi:10.1016/j.micromeso.2006.10.035
4. Garcia-Juez, R.; Boffa, V.; Blank, D. H. A.; ten Elshof, J. E. *J. Membr. Sci.* **2008,** *323,* 347–351. doi:10.1016/j.memsci.2008.06.043
5. Young, S. Y.; Ryu, I.; Kim, H. Y.; Kim, J. K.; Jang, S. K.; Russell, T. P. *Adv. Mater.* **2006,** *18,* 709–712. doi:10.1002/adma.200501500
6. Svanborg, S.; Johansen, A.-G.; Abrahamsen, R. K.; Skeie, S. V. *Int. Dairy J.* **2014,** *37,* 26–30. doi:10.1016/j.idairyj.2014.02.004
7. Brans, G.; Schroën, C. G. P. H.; van der Sman, R. G. M.; Boom, R. M. *J. Membr. Sci.* **2004,** *243,* 263–272. doi:10.1016/j.memsci.2004.06.029
8. Huisman, I. H. Membrane separations – Microfiltration. In *Encyclopedia of Separation Science;* Wilson, I. D., Ed.; Academic Press: San Diego, CA, U.S.A., 2000; pp 1764–1777. doi:10.1016/B0-12-226770-2/05251-0
9. Jin, J.; Wakayama, Y.; Peng, X.; Ichinose, I. *Nat. Mater.* **2007,** *6,* 686–691. doi:10.1038/nmat1980
10. Martin, C. R.; Siwy, Z. S. *Science* **2007,** *317,* 331–332. doi:10.1126/science.1146126
11. Fa, K.; Tulock, J. J.; Sweedler, J. V.; Bohn, P. W. *J. Am. Chem. Soc.* **2005,** *127,* 13928–13933. doi:10.1021/ja052708p
12. Liu, S.; Pu, Q.; Gao, L.; Korzeniewski, C.; Matzke, C. *Nano Lett.* **2005,** *5,* 1389–1393. doi:10.1021/nl050712t
13. Kuiper, S.; van Rijn, C. J. M.; Nijdam, W.; Elwenspoek, M. C. *J. Membr. Sci.* **1998,** *150,* 1–8. doi:10.1016/S0376-7388(98)00197-5
14. Ripperger, S.; Altmann, J. *Sep. Purif. Technol.* **2002,** *26,* 19–31. doi:10.1016/S1383-5866(01)00113-7
15. Han, K.; Xu, W.; Ruiz, A.; Ruchhoeft, P.; Chellam, A. *J. Membr. Sci.* **2005,** *249,* 193–206. doi:10.1016/j.memsci.2004.09.044
16. Boissiere, C.; Prouzet, E.; Grosso, D.; Sanchez, C. Hierarchically structured porous coatings and membranes. In *Hierarchically Structured Porous Materials: From Nanoscience to Catalysis, Separation, Optics, Energy and Life Science;* Su, B.-L.; Sanchez, C.; Yang, X.-Y., Eds.; Wiley-VCH: Weinheim, Germany, 2012; pp 335–361.
17. Sung, I.-K.; Yoon, S.-B.; Yu, J.-S.; Kim, D.-P. *Chem. Commun.* **2002,** 1480–1481. doi:10.1039/b203629k
18. Chau, C. F.; Mervin, T. *J. Micromech. Microeng.* **2012,** *22,* 85028. doi:10.1088/0960-1317/22/8/085028
19. Jun, H.; Im, B.; Lee, K. H.; Yang, I. K.; Jeong, Y. H.; Lee, J. S. *Nanotechnology* **2012,** *23,* 135602. doi:10.1088/0957-4484/23/13/135602
20. Ali, N.; Duan, X.; Jiang, Z.-T.; Goh, B. M.; Lamb, R.; Tadich, A.; Poinern, G. E. J.; Fawcett, D.; Chapman, P.; Singh, P. *Appl. Surf. Sci.* **2014,** *289,* 560–563. doi:10.1016/j.apsusc.2013.11.042
21. van Rijn, C. J. M.; Nijdam, W.; Kuiper, S.; Veldhuis, G. J.; van Wolferen, H.; Elwenspoek, M. *J. Micromech. Microeng.* **1999,** *9,* 170–172. doi:10.1088/0960-1317/9/2/316
22. Daufin, G.; Escudier, J.-P.; Carrére, H.; Bérot, S.; Fillaudeau, L.; Decloux, M. *Food Bioprod. Process.* **2001,** *79,* 89–102. doi:10.1205/096030801750286131
23. Schmuhl, R.; Nijdam, W.; Sekulić, J.; Roy Chowdhury, S.; van Rijn, C. J. M.; van den Berg, A.; ten Elshof, J. E.; Blank, D. H. A. *Anal. Chem.* **2005,** *77,* 178–184. doi:10.1021/ac049219c
24. Schmuhl, R.; Sekulic, J.; Roy Chowdhury, S.; van Rijn, C. J. M.; Keizer, K.; van den Berg, A.; ten Elshof, J. E.; Blank, D. H. A. *Adv. Mater.* **2004,** *16,* 900–904. doi:10.1002/adma.200306660
25. de A. A. Soler-Ilia, G. J.; Sanchez, C.; Lebeau, B.; Patarin, J. *Chem. Rev.* **2002,** *102,* 4093–4138. doi:10.1021/cr0200062
26. Yang, P.; Rizvi, A. H.; Messer, B.; Chmelka, B. F.; Whitesides, G. M.; Stucky, G. D. *Adv. Mater.* **2001,** *13,* 427–431. doi:10.1002/1521-4095(200103)13:6<427::AID-ADMA427>3.0.CO;2-C
27. Nisticò, R.; Scalarone, D.; Magnacca, G. *Microporous Mesoporous Mater.* **2014,** *190,* 208–214. doi:10.1016/j.micromeso.2014.02.012
28. Wan, Y.; Zhao, D. *Chem. Rev.* **2007,** *107,* 2821–2860. doi:10.1021/cr068020s
29. de A. A. Soler-Illia, G. J.; Crepaldi, E. L.; Grosso, D.; Sanchez, C. *Curr. Opin. Colloid Interface Sci.* **2003,** *8,* 109–126. doi:10.1016/S1359-0294(03)00002-5
30. Reynhout, I. C.; Cornelissen, J. J. L. M.; Nolte, R. J. M. *Acc. Chem. Res.* **2009,** *42,* 681–692. doi:10.1021/ar800143a
31. Krämer, E.; Förster, S.; Götner, C.; Antonietti, M. *Langmuir* **1998,** *14,* 2027–2031. doi:10.1021/la9712505
32. Kresge, C. T.; Leonowitz, M. E.; Roth, W. J.; Vartuli, J. C.; Beck, J. S. *Nature* **1992,** *359,* 710–712. doi:10.1038/359710a0

33. Zhao, D.; Yang, P.; Melosh, N.; Feng, J.; Chmelka, B. F.; Stucky, G. D. *Adv. Mater.* **1998,** *10,* 1380–1385. doi:10.1002/(SICI)1521-4095(199811)10:16<1380::AID-ADMA1380>3.0.CO;2-8
34. Yu, K.; Smarsly, B.; Brinker, C. J. *Adv. Funct. Mater.* **2003,** *13,* 47–52. doi:10.1002/adfm.200390005
35. Templin, M.; Frank, A.; Du Chesne, A.; Leist, H.; Zhang, Y.; Ulrich, R.; Schädler, V.; Wiesner, U. *Science* **1997,** *278,* 1795–1798. doi:10.1126/science.278.5344.1795
36. Riess, G. *Prog. Polym. Sci.* **2003,** *28,* 1107–1170. doi:10.1016/S0079-6700(03)00015-7
37. Förster, S.; Antonietti, M. *Adv. Mater.* **1998,** *10,* 195–217. doi:10.1002/(SICI)1521-4095(199802)10:3<195::AID-ADMA195>3.0.CO;2-V
38. Discher, D. E.; Eisenberg, A. *Science* **2002,** *297,* 967–973. doi:10.1126/science.1074972
39. Lin, Y.-H.; Yager, K. G.; Stewart, B.; Verduzco, R. *Soft Matter* **2014,** *10,* 3817–3825. doi:10.1039/C3SM53090F
40. Qi, L. Synthesis of inorganic nanostructures in reverse micelles. In *Encyclopedia of Surface and Colloid Science;* Somasundaran, P., Ed.; Taylor & Francis Group: Boca Raton, FL, U.S.A., 2006; pp 6183–6207.
41. Impéror-Clerc, M.; Davidson, P.; Davidson, A. *J. Am. Chem. Soc.* **2000,** *122,* 11925–11933. doi:10.1021/ja002245h
42. Iannarrelli, L.; Nisticò, R.; Avetta, P.; Lazzari, M.; Magnacca, G.; Calza, P.; Fabbri, D.; Scalarone, D. *Eur. Polym. J.* **2015,** *62,* 108–115. doi:10.1016/j.eurpolymj.2014.11.019
43. Ramm, L. E.; Whitlow, M. B.; Mayer, M. M. *J. Immunol.* **1985,** *134,* 2594–2599.
44. Brunauer, S.; Emmett, P. H.; Teller, E. *J. Am. Chem. Soc.* **1938,** *60,* 309–319. doi:10.1021/ja01269a023
45. Ou, D. L.; Chevalier, P. D.; Mackinnon, I. A.; Eguchi, K.; Boisvert, R.; Su, K. *J. Sol-Gel Sci. Technol.* **2003,** *26,* 407–412. doi:10.1023/A:1020737618745
46. Townsend, M. W.; Deluca, P. P. *J. Pharm. Sci.* **1990,** *79,* 1083–1086. doi:10.1002/jps.2600791209

License and Terms

BEILSTEIN JOURNAL OF NANOTECHNOLOGY

Conformational switching of ethano-bridged Cu,H_2-bis-porphyrin induced by aromatic amines

Simona Bettini*[1], Emanuela Maglie[1], Rosanna Pagano[2], Victor Borovkov[3], Yoshihisa Inoue[4], Ludovico Valli[1] and Gabriele Giancane[5]

Full Research Paper

Open Access

Address:
[1]Department of Biological and Environmental Sciences and Technologies, DISTEBA, University of Salento, Via per Arnesano, Lecce, Italy, [2]Department of Engineering for Innovation, University of Salento, Via per Arnesano, Lecce, Italy, [3]Tallinn University of Technology, Faculty of Science, Department of Chemistry, Chair of Green Chemistry, Akadeemia tee 15, 12618 Tallinn, Estonia, [4]Department of Applied Chemistry, Osaka University, 2-1 Yamada-oka, Suita 565-0871, Japan and [5]Department of Cultural Heritage, University of Salento, Via per Arnesano, Lecce, Italy

Email:
Simona Bettini* - simona.bettini@unisalento.it

* Corresponding author

Keywords:
aromatic amines; bis-porphyrin; conformational switching; Langmuir film; surface plasmon resonance

Beilstein J. Nanotechnol. **2015,** *6,* 2154–2160.
doi:10.3762/bjnano.6.221

Received: 31 August 2015
Accepted: 29 October 2015
Published: 17 November 2015

This article is part of the Thematic Series "Organized films".

Guest Editor: M. Canepa

Abstract

Cu,H_2-bis-porphyrin (Cu,H_2-Por$_2$), in which copper porphyrin and free-base porphyrin are linked together by an ethano-bridge, was dissolved in chloroform and spread at the air/liquid subphase interface of a Langmuir trough. The bis-porphyrin derivative, floating film was characterized by reflection spectroscopy and the surface pressure of the floating film was studied as a function of the mean area per molecule. When aromatic amines are dissolved in the subphase, an evident interaction between the bis-porphyrin host and the aromatic amine guest is observed. A clear-cut variation of the profile of surface pressure vs area per molecule curve is observed. Reflection spectroscopy highlights that the aromatic amines dissolved in the subphase are able to induce the *syn*-to-*anti* conformational switching in the bis-porphyrin derivative. The Langmuir–Schaefer technique has been used to transfer the floating bis-porphyrin film (when using pure water as a subphase) to a surface plasmon resonance (SPR) substrate and the resulting device was able to detect the presence of aniline at concentrations as low as 1 nM in aqueous solution. The high selectivity of the SPR sensing device has been verified by checking the spectral response of the active layer towards other analytes dissolved in the aqueous solutions.

Introduction

Various porphyrin derivatives, both free-base and metal complexes, have been widely employed as active molecules for detecting analytes in vapor as well as in liquid phase [1-3]. Porphyrins are endowed with good host material properties and the ability to form films [4], allowing realization of thin film devices with variable physical and

chemical properties upon complexation with guest molecules [5-7].

One of the most appealing classes of porphyrins is the bis-porphyrins, which can switch their conformational form as a result of the interaction with specific guest molecules, such as analytes [8]. For example, in the case of ethano-bridged bis-porphyrins, the structural change between the closed form (*syn*-form, Figure 1a) and the open form (*anti*-form, Figure 1b) can be easily detected by various spectroscopic methods.

Previously it was shown that doubly metallated bis-porphyrins transferred onto solid substrates have been effectively used to detect the presence of amines in aqueous solution [9]. The organization and orientation of active molecules in corresponding host–guest interactions play the crucial role of quenching or enhancing the affinity of a host towards a specific guest. This is particularly relevant when a structural change can be influenced by environmental conditions [10]. For this reason, a horizontal variation of the Langmuir–Blodgett technique, the Langmuir–Schaefer (LS) method, is used to transfer the active layers onto solid supports [11].

In general, procedures to detect and remove amines in water and food matrices have been established [12,13]. Amines can be harmful to living organisms and can induce pseudo-poisoning effects, such as the scombroid syndrome [14], and in some cases, they may react with other compounds in the human body promoting the formation of cancer cells [15]. Aromatic amine sensors with different transduction methods have also been developed [16-19]. In the present work, a copper, free-base bis-porphyrin complex of ethano-bridged bis-porphyrin (shown in the Figure 2), herewith named Cu,H_2-Por_2, was characterized at the air/water interface and transferred by means of the LS method onto a gold SPR substrate for the detection of aromatic amines in water.

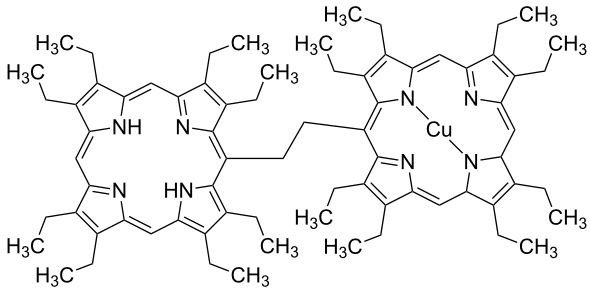

Figure 2: Chemical structure of the monometallated copper complex of the ethano-bridged bis-porphyrin derivative, Cu,H_2-Por_2.

Results and Discussion

Air/liquid interface characterization

Cu,H_2-Por_2 was dissolved in chloroform at a concentration of $1.3 \cdot 10^{-4}$ M and the UV–vis spectrum was recorded (blue line in Figure 3). The absorption spectrum is comprised of the absorptions of the individual porphyrin moieties (Cu complex and free-base) resulting in a broadened Soret band and three peaks in the Q band region. The maximum absorption peak is centered at 414 nm, suggesting that the bis-porphyrin derivative is mainly arranged as the *syn*-conformer, whilst a minor contribution from the *anti*-form cannot be ruled out due to the flexibility of the ethano bridge [20]. After spreading 100 µL of the chloroform solution onto the ultrapure water subphase, the isotherm curve was recorded (inset of Figure 3). The surface pressure vs area per molecule curve shows at least three bends, indicating the rearrangement of the molecules in the floating film. A conformational change of the Cu,H_2-Por_2 molecules can be excluded upon the motion of the barriers as evidenced by the invariant absorption properties. In fact, Figure 3 (black lines) demonstrates that the reflection spectra acquired at different values of surface pressure do not show any appreciable shift of the maximum reflection peak.

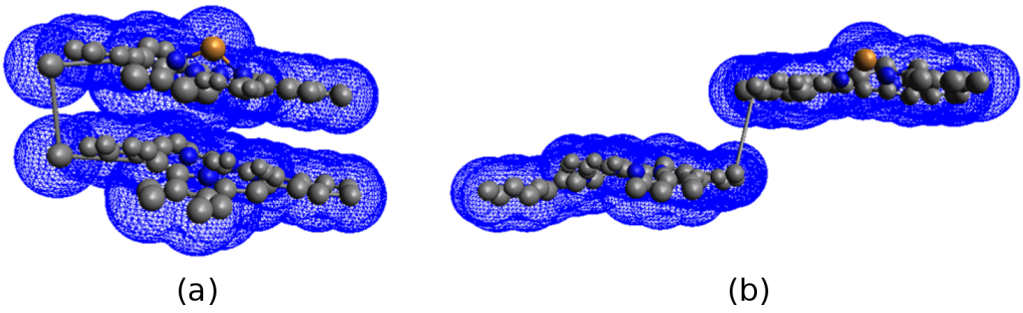

Figure 1: (a) *Syn*- and (b) *anti*-conformations of an ethano-bridged bis-porphyrin.

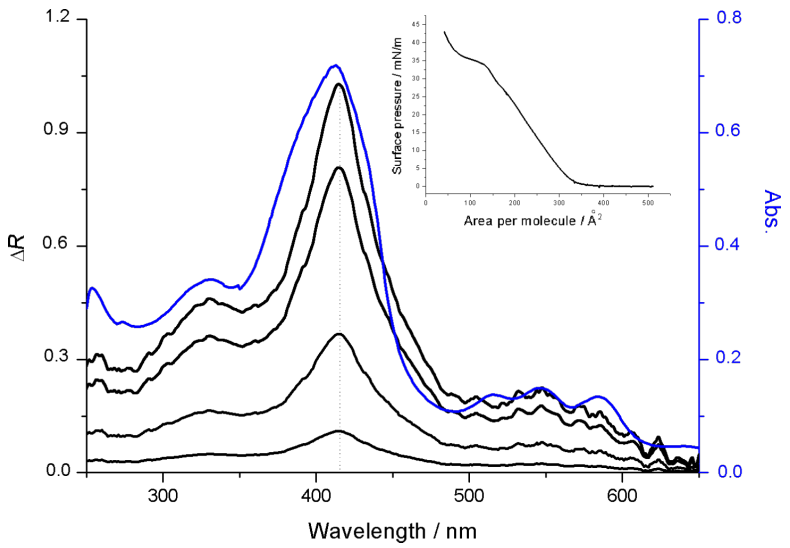

Figure 3: UV–vis solution spectrum (blue line) and reflection spectra of the Cu,H_2-Por_2 Langmuir film (black lines). The maximum reflection peak is centered at 414 nm for all the investigated surface pressures (2, 16, 35 and 40 mN/m), suggesting a closed form of the bis-porphyrin derivative as the major conformer. In the inset, the surface pressure vs area per molecule curve is reported.

The surface pressure vs area per molecule curves of Cu,H_2-Por_2 spread on ultrapure water and on the subphase containing aniline (10^{-5} M) have very different features (Figure 4a). Both curves show the first slope variation at a value of 200 Å^2. At least three changes of the curve slope are recorded for the Cu,H_2-Por_2 on water subphase, probably a consequence of the formation of a multilayer film. The floating film spread on the subphase containing the aromatic amine showed the first slope change at about 20 mN/m and another more drastic variation at 37 mN/m. Even though the limiting area per molecule, obtained by the extrapolation of the steep region of the isotherm to zero surface pressure, is in a good agreement with a conformational change from the *anti*- to *syn*- form, such a rationale can be excluded by the reflection spectroscopy carried out at the air/water interface (Figure 4b).

Such a behavior confirms the host–guest interaction between the molecules of the floating film and the analyte dissolved in the subphase, which is further confirmed by reflection spectroscopy at the air/subphase interface. In fact, a red shift of the

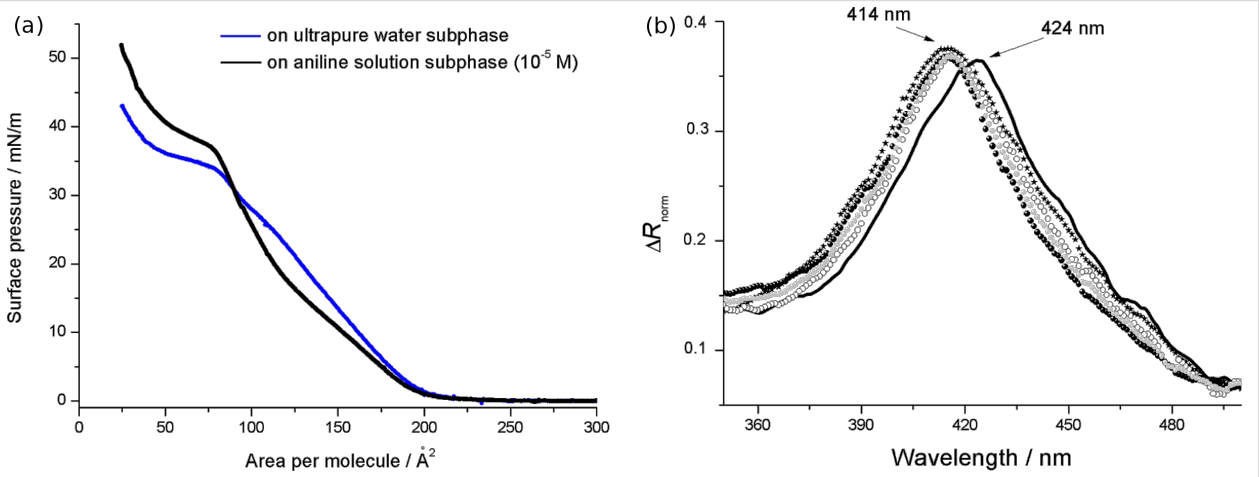

Figure 4: (a) The effect of aniline dissolved in the subphase (10^{-5} M) on the surface pressure vs area per molecule curve (black line) of a bis-porphyrin derivative, floating layer in comparison to the ultrapure water subphase (grey line). (b) Reflection spectra of the Cu,H_2-Por_2 floating film in the presence of aniline in the subphase (solid black line) in comparison with the reflection spectra of the bis-porphyrin Langmuir film spread on ultrapure water (filled black circles) and *tert*-butylamine (stars), putrescine (unfilled circles) and diaminocyclohexane (filled grey circles) aqueous solutions (all the analytes were dissolved in a concentration of 10^{-5} M). All the spectra were recorded at a surface pressure of 12 mN/m and appropriately multiplied or divided in order to have the same maximum value of Δ*R* of the Cu,H_2-Por_2 floating layer on the ultrapure water subphase.

Soret band by about 10 nm was induced by the aniline, thus suggesting the *syn*-to-*anti* conformational switching in the Cu,H_2-Por_2 molecules (Figure 4b). This effect is similar to that previously observed for bis(zinc porphyrin) [8]. The behavior of the bis-porphyrin floating film upon interaction with other aliphatic acyclic and cyclic amines (*tert*-butylamine, 1,4-diaminobutane and 1,2-diaminocyclohexane) dissolved into the subphase was also checked. It was found that there are no variations in the absorption spectra, suggesting that the aromatic group of the analyte is crucial for the conformational switching in the bis-porphyrin derivative. Therefore, these results prompted us to test a phenol solution as a subphase for the Cu,H_2-Por_2 floating film. As highlighted by the invariant reflection spectrum (Figure 4b), the phenol guest does not induce a conformational change. Therefore, it is reasonable to suggest that the simultaneous presence of an amino group and aromatic ring is necessary to induce the *syn*-to-*anti* conformational change in Cu,H_2-Por_2. As a further confirmation of such rationale, for the bis-porphyrin floating film obtained on a water subphase containing 10^{-5} M 2-methyl-2-propanethiol, the *syn*-conformer remains unchanged even at high surface pressure values.

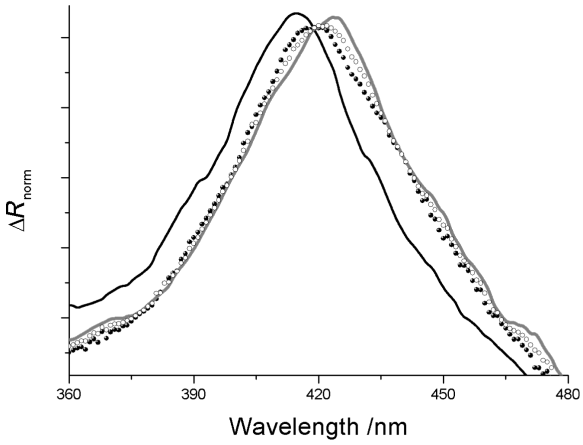

Figure 5: Normalized reflection spectra of the Cu,H_2-Por_2 floating films spread on a subphase containing *N*-methylphenethylamine (filled black circles), α-methylbenzylamine (unfilled circles) and aniline (grey solid line) (10^{-5} M) compared with the reflection spectrum of the bis-porphyrin derivative, floating film recorded on ultrapure water (black solid line). All the spectra were recorded at a surface pressure of 12 mN/m and appropriately multiplied or divided in order to have the same maximum value of Δ*R* of the Cu, H_2-Por_2 floating layer on the ultrapure water subphase.

In order to confirm this assumption, the effect of two additional aromatic amines on the bis-porphyrin derivative, floating film was investigated. α-Methylbenzylamine and *N*-methylphenethylamine were dissolved in the subphase at a concentration of 10^{-5} M. As was the case for aniline, α-methylbenzylamine and *N*-methylphenethylamine induced the corresponding red shift in the reflection maximum of the Cu,H_2-Por_2 floating film (Figure 5). It is likely that the effect of the aromatic amines is influenced by the steric hindrance of the guest molecule. A more detailed host–guest interaction mechanism will be the subject of future investigations.

Amine sensing experiments

In order to utilize the observed host–guest interaction between the bis-porphyrin derivative and aromatic amines, amine sensing experiments have been carried out. A Langmuir film of Cu,H_2-Por_2 was repeatedly transferred by the LS method onto quartz substrates and the UV–vis spectra were recorded with each additional LS run (Figure 6). For all the LS films, the maximum absorption peak was the same and centered at 414 nm suggesting that the molecular conformation was not changed with the deposition process retaining essentially the closed *syn*-form as in the case of the floating Cu,H_2-Por_2 Langmuir film.

The linear relationship between the number of Cu,H_2-Por_2 layers and the absorbance peak illustrated the good deposition rate and uniformity of the deposition procedure (Figure 6, inset). Furthermore, the absorption profile was not changed with increasing layer deposition, suggesting negligible interlayer interactions.

Five LS runs of Cu,H_2-Por_2 were deposited on the SPR slide, and the shift of the SPR angle induced by the injection of amine aqueous solutions at different concentrations was monitored. The effect of aniline on the plasmon resonance of the Cu,H_2-Por_2 film could be detected when only 1 nM of analyte was fluxed over the active layer (Figure 7a). A semi-logarithmic dependence of the SPR angle shift on the aniline concentration is evident at least up to 1 mM with a dynamic range of more than 6 orders of magnitude (Figure 7b). This behavior can be explained by the equation:

$$\theta = \theta_{max} \frac{KC}{KC+1}$$

where *K* is the binding constant and *C* is the analyte concentration [21]. If the product *KC* is relatively small (<<1), the SPR angle θ is linearly dependent on the analyte concentration. On the contrary, when *KC* is comparable to 1, the linearity is not preserved. This deviation from linearity was thoroughly studied and reported in the literature and a semi-logarithmic trend was proposed [22-24].

The recovery of the SPR device was investigated. The initial plasmon resonance angle was obtained when the Cu,H_2-Por_2 LS

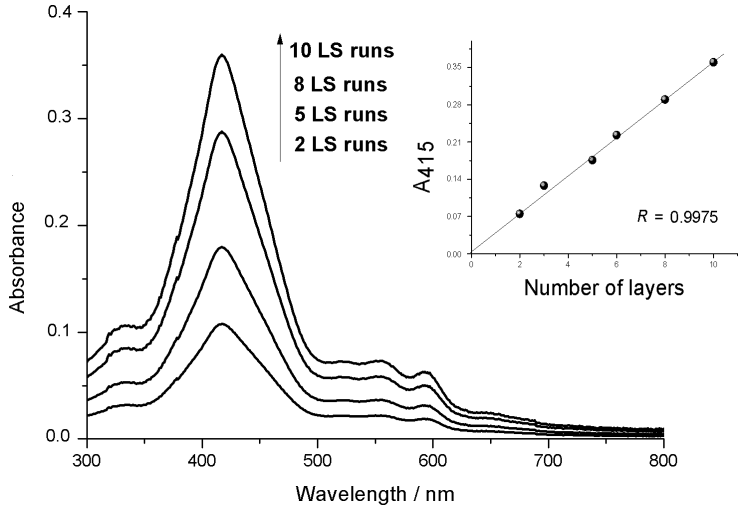

Figure 6: UV–vis spectra in the range of 300–800 nm of the Cu,H_2-Por_2 Langmuir–Schaefer films. The linear dependence of the absorbance on the LS layer number is highlighted in the inset.

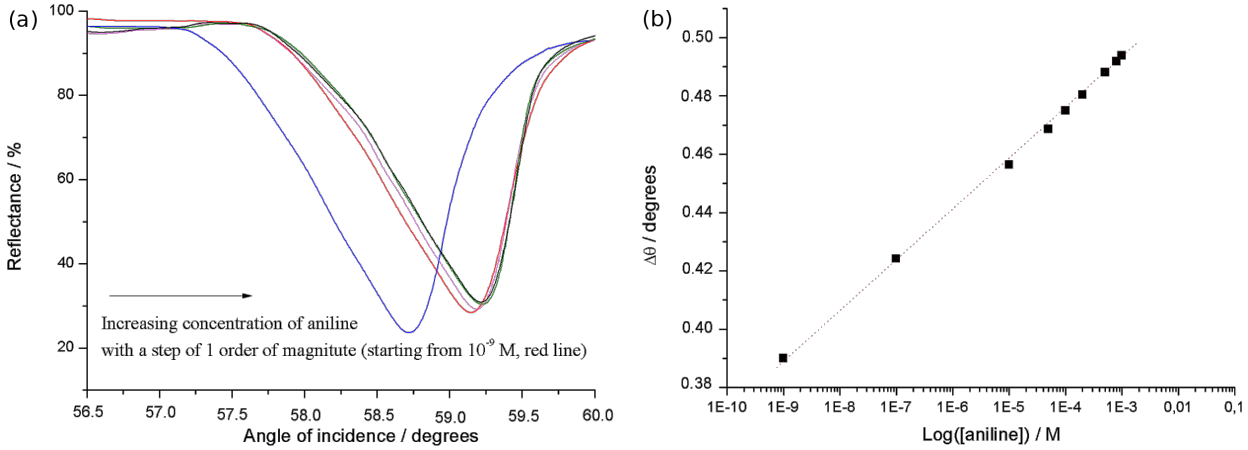

Figure 7: (a) Reflectance variation of Cu,H_2-Por_2 LS films and (b) SPR angle shift as a function of analyte concentration.

film, previously exposed to aniline, was treated for 15 min at 50 °C and then washed with a flow of ultrapure water for 5 min.

The response of the Cu,H_2-Por_2 device to α-methylbenzylamine and *N*-methylphenethylamine was also monitored and a reduced sensitivity of the active layer towards these molecules was observed (Figure 8). This behavior is in good agreement with the reflection spectra recorded on the Langmuir film. α-Methylbenzylamine and *N*-methylphenethylamine induced a less intense shift of the reflection peak of the Cu,H_2-Por_2 Langmuir film in comparison with aniline. Both the reflection spectroscopy and SPR measurements suggested that α-methylbenzylamine and *N*-methylphenethylamine weakly interact with Cu,H_2-Por_2 molecules. However, the injection of phenol solutions (up to 0.01 M) did not induce any detectable shift in the plasmon peak of the SPR sample.

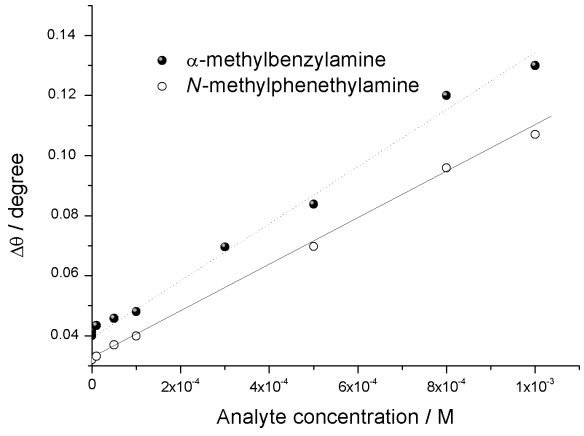

Figure 8: SPR angle shift as a function of α-methylbenzylamine (filled black circles) and *N*-methylphenethylamine (unfilled circles) concentration in aqueous solution.

Conclusion

In this study, an ethano-bridged bis-porphyrin with a free-base ring and a copper metallated ring was dissolved in a chloroform solution and spread at the air/liquid interface of a Langmuir trough. The floating film was characterized both on the ultrapure water subphase and on the subphase containing different amine solutions. The surface pressure vs area per molecule curve was influenced by the presence of aromatic amines, and in particular aniline, in the subphase. A confirmation of the host–guest interaction between the floating molecule and the analyte in the subphase was provided by the reflection spectroscopy measurements carried out directly at the air/subphase interface. This interaction induces the *syn*-to-*anti* conformation switching in the structure of the bis-porphyrin, hence producing an approximately 10 nm red shift of the absorption maximum. Neither aliphatic amines nor phenol induced the same variation in the reflection spectra of the Langmuir film, suggesting that a cooperative effect of the amine and aromatic groups is needed. The bis-porphyrin Langmuir film was transferred onto an SPR substrate and the host–guest interaction with amines in aqueous solution was investigated. Interestingly, the preliminary sensor tests evidenced that a significant angle shift of the surface plasmon resonance was recorded when only 1 nM of aniline was fluxed on the active layer. According to the reflection spectroscopy results, this interaction appeared to be highly selective towards aniline and more general towards aromatic amines, proposing the Cu,H_2-bis-porphyrin derivative as an effective active layer for aromatic, amine sensors in aqueous solution.

Experimental

Cu,H_2-Por_2 was synthesized by a previously reported method [20].

A NIMA trough equipped with two optical fibers was used for the reflection spectroscopy measurements and the same trough was employed for transferring the LS films. A chloroform solution of Cu,H_2-Por_2 was spread onto the aqueous subphase and the floating film formed was left to stand for 15 min before starting the Langmuir experiment. A barrier speed of 5 mm/min was used in all the experiments at the air/water interface. The reflection spectra were obtained as a difference between the reflectivities of the clean subphase and the Cu,H_2-Por_2 floating film.

Aqueous solutions of amines were fluxed over the LS, Cu,H_2-Por_2 films deposited on metal/glass substrates (Corning 7059, with a refractive index of 1.723 at 632.8 nm, gold thickness of 44 nm) by a peristaltic pump. The SPR measurements were carried out using a Nanofilm apparatus.

References

1. Giancane, G.; Valli, L. *Adv. Colloid Interface Sci.* **2012,** *171–172,* 17–35. doi:10.1016/j.cis.2012.01.001
2. Bussetti, G.; Violante, A.; Yivlialin, R.; Cirilli, S.; Bonanni, B.; Chiaradia, P.; Goletti, C.; Tortora, L.; Paolesse, R.; Martinelli, E.; D'Amico, A.; Di Natale, C.; Giancane, G.; Valli, L. *J. Phys. Chem. C* **2011,** *115,* 8189–8194. doi:10.1021/jp200303t
3. Arnold, D. P.; Manno, D.; Micocci, G.; Serra, A.; Tepore, A.; Valli, L. *Thin Solid Films* **1998,** *327–329,* 341–344. doi:10.1016/S0040-6090(98)00665-8
4. Hembury, G. A.; Borovkov, V. V.; Inoue, Y. *Chem. Rev.* **2008,** *108,* 1–73. doi:10.1021/Cr050005k
5. Ishihara, S.; Labuta, J.; Van Rossom, W.; Ishikawa, D.; Minami, K.; Hill, J. P.; Ariga, K. *Phys. Chem. Chem. Phys.* **2014,** *16,* 9713–9746. doi:10.1039/C3cp55431g
6. Webb, M. J.; Deroo, S.; Robinson, C. V.; Bampos, N. *Chem. Commun.* **2012,** *48,* 9358–9360. doi:10.1039/c2cc33668e
7. Tepore, A.; Serra, A.; Manno, D.; Valli, L.; Micocci, G.; Arnold, D. P. *J. Appl. Phys.* **1998,** *84,* 1416–1420. doi:10.1063/1.368252
8. Giancane, G.; Borovkov, V.; Inoue, Y.; Conoci, S.; Valli, L. *Soft Matter* **2013,** *9,* 2302–2307. doi:10.1039/C2sm27141a
9. Manera, M. G.; Ferreiro-Vila, E.; Cebollada, A.; García-Martín, J. M.; García-Martín, A.; Giancane, G.; Valli, L.; Rella, R. *J. Phys. Chem. C* **2012,** *116,* 10734–10742. doi:10.1021/jp3019843
10. Giancane, G.; Valli, L.; Sortino, S. *ChemPhysChem* **2009,** *10,* 3077–3082. doi:10.1002/cphc.200900451
11. Ulman, A. *Chem. Rev.* **1996,** *96,* 1533–1554. doi:10.1021/Cr9502357
12. Önal, A. *Food Chem.* **2007,** *103,* 1475–1486. doi:10.1016/j.foodchem.2006.08.028
13. Bettini, S.; Santino, A.; Valli, L.; Giancane, G. *RSC Adv.* **2015,** *5,* 18167–18171. doi:10.1039/c5ra01699a
14. Kanki, M.; Yoda, T.; Tsukamoto, T.; Baba, E. *Appl. Environ. Microbiol.* **2007,** *73,* 1467–1473. doi:10.1128/Aem.01907-06
15. Ahn, H. J.; Kim, J. H.; Jo, C.; Lee, C. H.; Byun, M. W. *J. Food Sci.* **2002,** *67,* 1370–1373. doi:10.1111/j.1365-2621.2002.tb10291.x
16. Azab, H. A.; El-Korashy, S. A.; Anwar, Z. M.; Khairy, G. M.; Duerkop, A. *J. Photochem. Photobiol., A* **2012,** *243,* 41–46. doi:10.1016/j.jphotochem.2012.05.029
17. Hu, S.-M.; Niu, H.-L.; Qiu, L.-G.; Yuan, Y.-P.; Jiang, X.; Xie, A.-J.; Shen, Y.-H.; Zhu, J.-F. *Inorg. Chem. Commun.* **2012,** *17,* 147–150. doi:10.1016/j.inoche.2011.12.037
18. Guo, K.; Chen, Y. *Anal. Methods* **2010,** *2,* 1156–1159. doi:10.1039/c0ay00316f
19. Jia, L.; Mane, G. P.; Anand, C.; Dhawale, D. S.; Ji, Q.; Ariga, K.; Vinu, A. *Chem. Commun.* **2012,** *48,* 9029–9031. doi:10.1039/c2cc33651k
20. Borovkov, V. V.; Lintuluoto, J. M.; Inoue, Y. *Helv. Chim. Acta* **1999,** *82,* 15.
21. Dong, H.; Cao, X.; Li, C. M.; Hu, W. *Biosens. Bioelectron.* **2008,** *23,* 1055–1062. doi:10.1016/j.bios.2007.10.026
22. Ensafi, A. A.; Fouladgar, M. *Sens. Actuators, B* **2006,** *113,* 88–93. doi:10.1016/j.snb.2005.02.027
23. Yusof, N. A.; Ahmad, M. *Talanta* **2002,** *58,* 459–466. doi:10.1016/S0039-9140(02)00308-9
24. Filik, H.; Giray, D.; Ceylan, B.; Apak, R. *Talanta* **2011,** *85,* 1818–1824. doi:10.1016/j.talanta.2011.07.052

BEILSTEIN JOURNAL OF NANOTECHNOLOGY

Electrochemical coating of dental implants with anodic porous titania for enhanced osteointegration

Amirreza Shayganpour[1], Alberto Rebaudi[2], Pierpaolo Cortella[3], Alberto Diaspro[1] and Marco Salerno*[1]

Full Research Paper

Open Access

Address:
[1]Nanophysics Department, Istituto Italiano di Tecnologia, via Morego 30, 16149 Genova, Italy, [2]Rebaudi Dental Office, piazza della Vittoria 8, 16121 Genova, Italy, and [3]Odontosalute, via Edmondo de Amicis 2, 16122 Genova, Italy

Email:
Marco Salerno* - marco.salerno@iit.it

* Corresponding author

Keywords:
anodization; dental implants; nanopores; surface treatment; titania

Beilstein J. Nanotechnol. **2015,** *6,* 2183–2192.
doi:10.3762/bjnano.6.224

Received: 08 September 2015
Accepted: 11 November 2015
Published: 20 November 2015

This article is part of the Thematic Series "Organized films".

Guest Editor: M. Canepa

Abstract

Clinical long-term osteointegration of titanium-based biomedical devices is the main goal for both dental and orthopedical implants. Both the surface morphology and the possible functionalization of the implant surface are important points. In the last decade, following the success of nanostructured anodic porous alumina, anodic porous titania has also attracted the interest of academic researchers. This material, investigated mainly for its photocatalytic properties and for applications in solar cells, is usually obtained from the anodization of ultrapure titanium. We anodized dental implants made of commercial grade titanium under different experimental conditions and characterized the resulting surface morphology with scanning electron microscopy equipped with an energy dispersive spectrometer. The appearance of nanopores on these implants confirm that anodic porous titania can be obtained not only on ultrapure and flat titanium but also as a conformal coating on curved surfaces of real objects made of industrial titanium alloys. Raman spectroscopy showed that the titania phase obtained is anatase. Furthermore, it was demonstrated that by carrying out the anodization in the presence of electrolyte additives such as magnesium, these can be incorporated into the porous coating. The proposed method for the surface nanostructuring of biomedical implants should allow for integration of conventional microscale treatments such as sandblasting with additive nanoscale patterning. Additional advantages are provided by this material when considering the possible loading of bioactive drugs in the porous cavities.

Introduction

Titanium (Ti) is the standard material used for dental and orthopedic implants, thanks to its very good strength, corrosion resistance and biocompatibility [1,2]. Despite the very high success rate of Ti dental implants (>90%), there is still room for optimization of osteointegration, particularly for diabetics, smokers and oncology patients [3]. As with most metals, Ti in wet or

even ambient air environment develops a thin layer of native oxide, namely TiO_2 (titania). While it is generally recognized that surface topography is a major factor for osteointegration of all implants [4], the lower surface energy of titania as compared to that of alumina and silica for example [5], makes micro-nanoscale patterning of this material of even more critical importance for implant success.

The surface micropatterning of Ti implants is usually achieved by mechanical (sandblasting) or purely chemical (etching) treatments [4]. However, Ti is also known as a valve metal, similar to the more common Al [6]. As such, electrochemical (EC) anodization of Ti, which is a combination of metal etching and oxide growth in the presence of applied voltage, results in the formation of porous titania nanotubes grown perpendicular to the metal – a material called anodic porous titania (APT).

APT is usually of interest for applications in catalysis or optoelectronics [7]. Here we present its use as a coating for nanopatterning the surfaces of dental implants. One advantage of APT for applications in biomedicine is with respect to its analogue obtained on Al, namely, anodic porous alumina (APA), which is mainly used in nanotechnology [8] because no particular pore order is required in this field. Here, a relatively uniform pore size and spacing is required and thus the preliminary electropolishing and two-step anodization used for APA to form hexagonal pore arrays are not necessary [9]. A single anodization is sufficient and from this perspective, may represent a simple and inexpensive nanopatterning procedure for biomedical Ti.

In fact, the application of nanoporous oxides as biological surfaces (where living cells should adhere and grow) has been already explored for APA also [10-12]. Generally speaking, oxide inertness provides biocompatibility, while controlled porous patterning allows for tuning the roughness for optimized stimulation of living-cell response. The role of nanotopography in guiding cell differentiation and tissue generation is not fully understood yet, but is a well-known phenomenon [13-15]. In extreme synthesis, a nanorough substrate with possible adhesion/growth factors mimics the extracellular matrix [16].

Since Ti is used for most permanent implants, interest in nanopatterning biomedical surfaces with anodization has recently shifted from Al (i.e., APA) to Ti (i.e., APT [17-19]). However, the anodization of Ti implants poses several challenges: the Ti used for implants is not ultrapure (as is used in basic research), but is rather an alloy, and the medical implants are not flat surfaces, but are 3D objects with curved surfaces. Therefore, even though positive results have been recently achieved [20-22], the transfer of the required processes from laboratory specimens to real implants is not trivial.

The fabrication of APT in itself forms an organized film where the pores grow in a columnar form with the oxide according to mutual interaction in a form of self-assembly. In addition, further opportunities for surface organization are provided by subsequent functionalization of the APT with functional overcoating layers of bioactive materials, eventually using the pores as a template. Here we report on APT fabrication for dental implants and give an example of pore loading with a bioactive element.

Results and Discussion

In Figure 1a,b pictures of the two types of implants investigated, Sweden & Martina (S&M, Figure 1a) and Stark (Figure 1b), are shown. They are both conical implants of similar geometry and same nominal Ti purity, namely grade 4 and both available in machined-only form (i.e., not finished

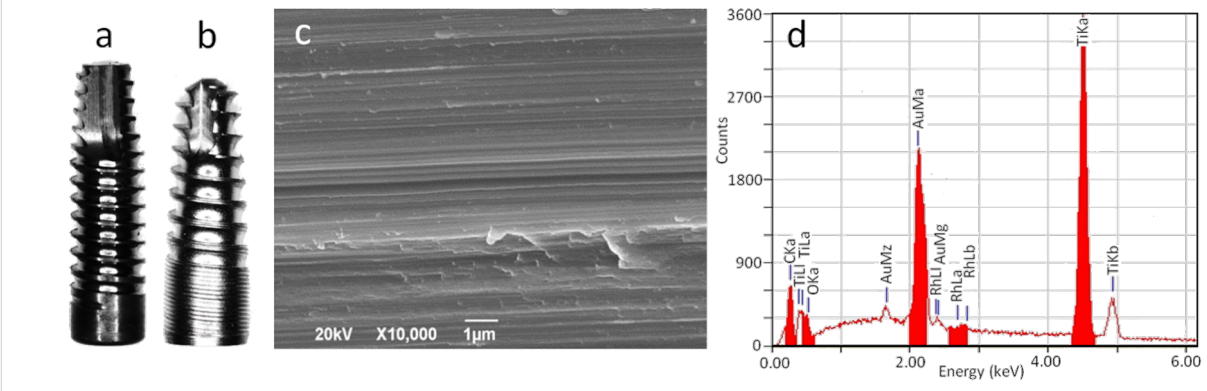

Figure 1: (a,b) Pictures of the implants used in this experiment, (a) Premium Straight from S&M and (b) Stark. (c) Typical SEM micrograph of the surface of the implants, as received. (d) Corresponding EDS spectrum of an S&M implant, as received.

with the final roughening treatment). Indeed, under scanning electron microscope (SEM) imaging at high (10,000×) magnification they looked the same with the typical lay of machined pieces (Figure 1c). Concurrently, the chemical composition, as assessed by energy dispersive spectroscopy (EDS), also looked quite similar. In Figure 1d the EDS spectrum of a typical S&M implant is shown. It appears that, in addition to Ti from the bulk implant core and gold (Au) from the coating deposited for SEM analysis, traces of additional chemical elements are present, such as carbon, ascribed to organic contamination during packaging, and, to a lower extent, oxygen, ascribed to native metal oxide on the surface. Contamination of rhodium also appears at very low levels (estimated ≈0.8 at %), which was the same for both types of implants. According to the producing companies, these contaminates may be associated with the machining tools and/or the final washing, or possibly due to cross-contamination among different manufacturing processes carried out with the same equipment. In the case of Stark implants, a minor difference in the spectrum is the occurrence of another minor peak assigned to Al (see Supporting Information File 1, Figure S1). While both Ti materials should be of commercial grade 4 (and not grade 5, also called Ti6Al4V, which contains 6 wt % Al), our interpretation is that the detected Al is yet another contaminant appearing during the bulk metal machining. Al cannot even be associated with sandblasting by means of alumina abrasive particles, since it appears on just-machined implants.

Both types of implants were subjected to two slightly different processes, both carried out at room temperature (RT) for 1 min: in one case only anodization was applied (Ti positive, voltage +150 V), while in the other case, this step was preceded by inverted polarization (voltage −150 V). The latter step, called cathodization, should protonate the surface and make anodization more effective according to some literature [23]. The typical chronopotentiometric and chronoamperometric profiles of these processes are shown in Figure 2a,b for the cathodization pretreatment (where applied) and the standard subsequent anodization, respectively.

It should be mentioned that the electrochemical settings involved both a target voltage, V_t, and a target current, i_t. When the power supply is switched on, both quantities are simultaneously raised and the one that first reaches the target value is clamped. Therefore, also partly due to the peculiar shape of the anodized element, it is not always possible to define the whole process as either potentiostatic or galvanostatic. During this process the conditions may change, making one target value easier to attain than the other at a given electrolyte conductivity and temperature.

Within intermediate ranges of the above quantities (e.g., 20–180 V and 0.1–1.5 A), thus avoiding the burning regime, the selected temperature is only of secondary importance with respect to the applied voltage (or current). Nevertheless, for proper interpretation of the results, it is important that the temperature be kept as constant as possible, regardless of its value. For this reason we chose a temperature close to typical RT.

From Figure 2a it appears that the cathodization pretreatment lasted for the whole duration period under conditions of constant current (i.e., a galvanostatic process) and almost constant voltage as well, and this was the same for both implant types. In particular, despite the selected V_t = 150 V applied to

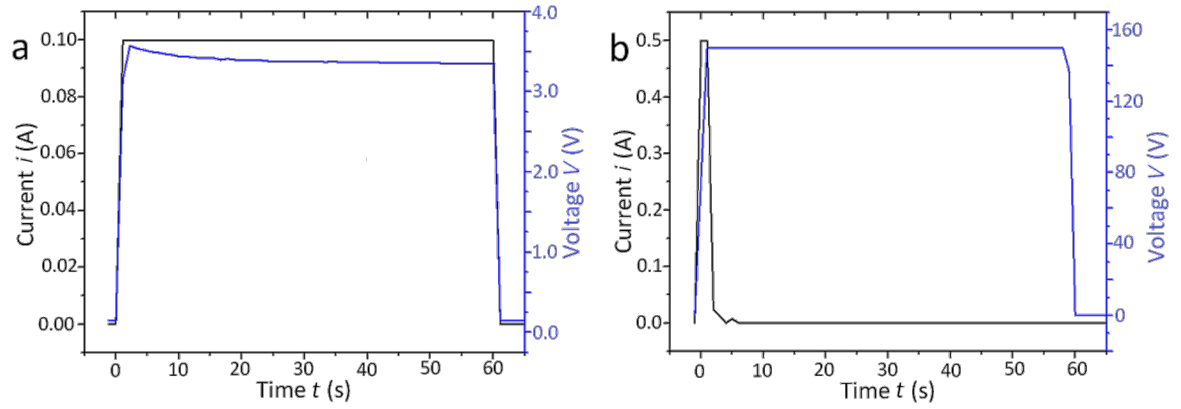

Figure 2: Plots of both current and voltage during the surface modification of the dental implants. (a) Preliminary, optional cathodization pretreatment, and (b) standard, subsequent anodization. The current, *i*, is plotted in black, the voltage, *V*, in blue. The curves were obtained from the anodization of Stark implants, but were very similar for S&M implants as well.

the cathode, a value of only ≈3.5 V was reached, given the low i_t = 0.1 A set as a protection limit against unwanted side effects.

The profiles for anodization were similarly equivalent for the different implants, yet different from the cathodization, as shown in Figure 2b. In all cases, anodization was self-terminated after a very short time of 2–4 s. When the total passed charge was calculated, it appeared to be always comparable (≈12 C), which sets a limit to the surface coating of the implants with the passivating anodic oxide of ≈0.1 C/mm^2.

The fact that a longer anodization time does not increase the APT thickness is different from what is known for APA [24], where the oxide continues to grow at the expense of the underlying metal. In fact, in previous extensive studies, the nature of the porosity resulting in Ti from anodization was also described to be of a different nature than for Al [25]. The APT pattern was ascribed to a pitting regime of anodization, occurring above the electrical breakdown threshold for the material, which would probably account for the more disordered appearance of the emerging pores with respect to those of APA.

In Figure 3 the typical results of anodization are shown with respect to both the surface morphology (SEM, Figure 3a) and its composition (EDS, Figure 3b). The reported data are from S&M implants, but equivalent results were obtained for Stark implants. In Figure 3a, the characteristic nanoporosity of APT appears. The pores, which are rather irregular, present a broad size distribution, with a diameter of 100–200 nm. The underlying lay of machining is still visible, although partly obscured by the nanopatterning. Similar pores were obtained in our group on ultrapure Ti (see Supporting Information File 1, Figure S2). In that case, the temperature was lower and sulphuric acid was used instead. As a result, the pore edges were sharper, while here we have rounded pore mouths, in agreement with literature results [26].

The comparatively large pore size, at the border between nano- and micro-scale, is associated with the high anodization voltage used here, which should be proportional to the pore size, similar to the case of APA [7]. This high voltage has been selected because, according to Choi [25], no pore formation occurs at a voltage below ≈100 V, even if formation of oxide is still observed. At the same time, it has also been observed in in-vitro experiments that too small nanopores can even be detrimental to living cell adhesion, as they may give rise to a kind of hydrophobic and thus antiwetting behavior [27].

In Figure 3b, the EDS analysis confirms the presence of Ti oxide on the surface. In fact, the O content significantly increased with respect to Figure 1d from ≈3 at % up to ≈14 at %. This is consistent with the presence of surface titania with a thickness significantly higher than native oxide. A stoichiometric ratio to Ti cannot be obtained from EDS (in fact Ti is still dominant, ≈73 at %), given the deep penetration (≥1 µm) of the energetic, primary electrons (10 kV) with respect to the APT thickness (≈100 nm), such that the probed volume is mainly in the bulk of the Ti implant under the surface.

In Figure 3b a new type of contamination, phosphorus, also appears at a concentration as high as ≈10 at %. In fact, from APA fabrication, it is also known that some amount of elec-

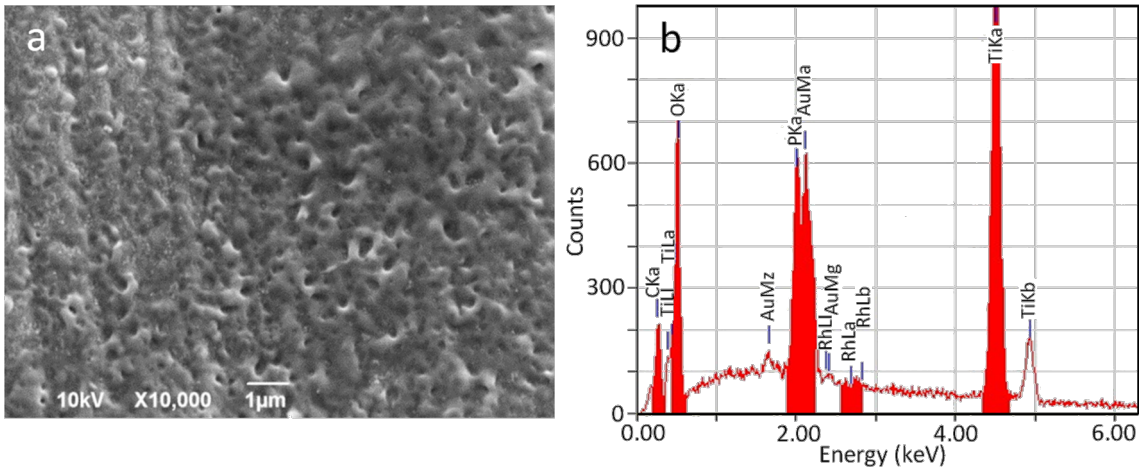

Figure 3: Typical results of anodization for both implant types, with or without cathodization pretreatment. (a) SEM micrograph of the surface showing the characteristic APT pores and (b) EDS spectrum, showing the increased O content and P contamination.

trolyte anions (typically 3–8 wt %) are incorporated into the porous oxide during anodization [6]. The same applies also for the anodization of Ti, and thus the observed P has to be ascribed to phosphate anions PO_4^{2-} entrapped within the porous oxide during its growth. Actually, this is the reason why we decided to use phosphoric acid as the anodizing electrolyte, since phosphate is likely to be biocompatible and even bioactive in the foreseen application of the coatings for osteointegration, due to its affinity to tri-calcium phosphates or hydroxylapatite.

Both the Stark and S&M implants were made using grade 4 Ti. Actually, grade 5 Ti is commonly used only for abutments and other parts, since it presents higher mechanical performance (e.g., yield stress of 860 MPa vs 550 MPa) but is less biocompatible [1].

The successful patterning of Ti by means of oxide nanopores, as shown in Figure 3a on machined implants, can be of greater importance when demonstrated on implants patterned on the microscale by the different and most common methods of either sandblasting and/or acid etching (simple wet etching in the absence of driving electrical field). In fact, it is possible that a combination of both roughening scales, the micro- and the nano-, may be the most effective procedure for osteointegration of the pristine Ti surface. Therefore, in a separate set of experiments, we also anodized implants of both types (S&M and Stark) that were already patterned according to the standard technique of the respective company. Anodization was confirmed to be successful in formation of nanopores on the micropatterned Ti implants also. In Figure 4 we report the case of Stark implants, but similar results were also obtained for the S&M implants.

Figure 4 shows the SEM micrographs of finished Stark implants after their standard process of sandblasting. We can see similar areas before (left) and after (right) anodization. Additionally, in both cases, the same area pictured at low magnification (top) has been taken at higher magnification (bottom). Interestingly, at lower magnification the same microscale roughness is observed before and after anodization (Figure 4a,b), meaning

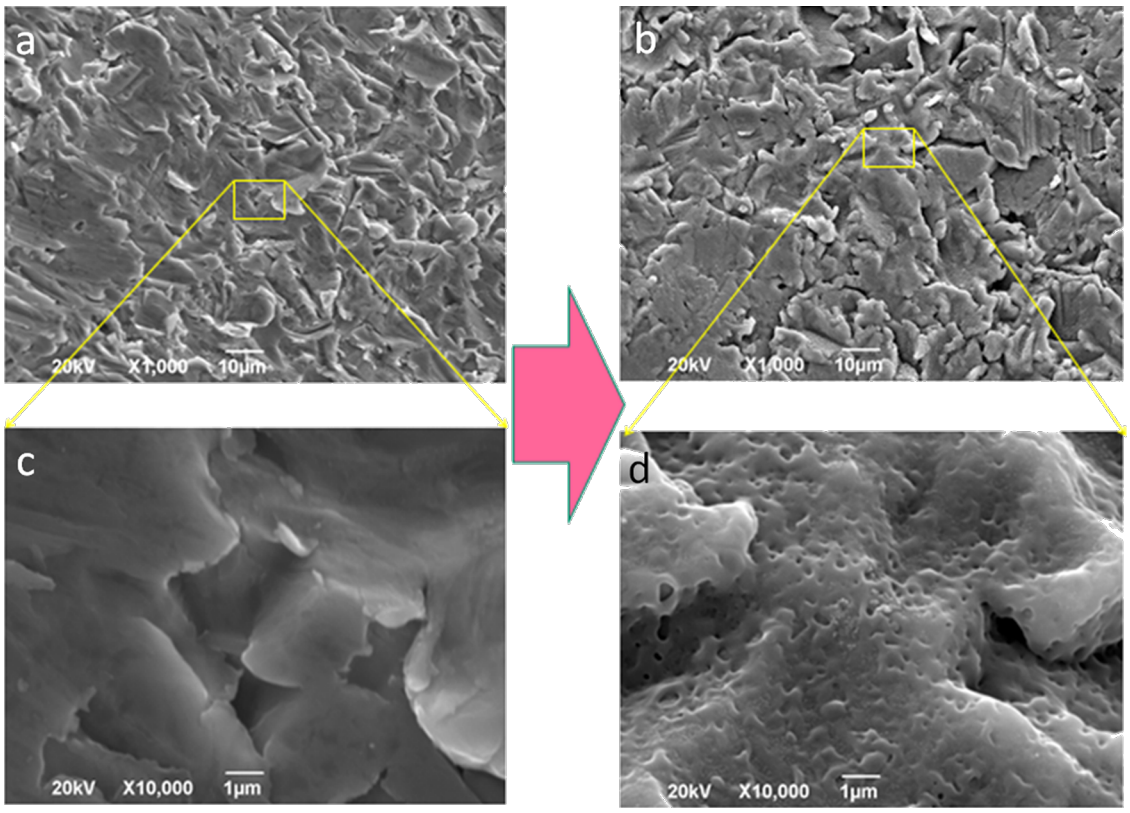

Figure 4: SEM micrographs of finished Stark implants, before (a,c) and after (b,d) anodization, at 1,000× (a,b) and 10,000× (c,d) magnification. The high magnification images are close-up views extracted from the corresponding regions (see yellow lines) of the same area. The large arrow represents the anodization process.

that the treatment did not destroy it. At the same time, at high magnification, the typical nanopores due to APT appear on the anodized implant (Figure 4d) and were not present before anodization (Figure 4c). In Figure 4d these nanopores are obviously overlaid onto the microscale roughness due to sandblasting. The effectiveness of the anodization treatment is thus confirmed, which is important in view of real manufacturing carried out in combination with the standard microscale patterning processes of sandblasting and wet etching.

According to both SEM morphology and EDS composition, no significant difference was observed on average after inspection of several different locations on different implants ($N \geq 6$), and between implants pretreated or not pretreated with cathodization. This pretreatment should result in loading the Ti with hydrogen, which would decrease the oxide breakdown voltage, and thus increase the pore density at constant potential. However, we observed no significant change in pore size with the pretreatment. The previous authors who used that [23] applied the same anodic potential as set here but a different electrolyte, namely 1 M sulphuric acid. However, the major difference, and the possible reason for the lack of this effect in our case, could be the low current limit of 0.1 A set here.

In any case, the pretreatment should not change either the crystalline phase of the formed APT or its thickness. With or without pretreatment, Tanaka et al. [23] observed a combination of anatase and rutile for APT by means of X-ray diffraction spectroscopy. On the other hand, Choi states in his extensive work that rutile is formed at an anodization voltage as high as 150 V, while amorphous titania is obtained at lower voltages [25]. The crystalline phase of APT is of some importance since it seems that, with respect to osteointegration, anatase is preferred over rutile [28]. Unfortunately, if rutile is formed upon anodization, no existing easy route is known to convert this more stable form of titania back to transient anatase. We performed Raman spectroscopy on both types of anodized implants, those with or without pretreatment. Again, we observed no major differences in the different cases. For all measurements, given the limited thickness of APT, we had to use collecting conditions of low magnification (objective of 10×), high laser power (≈100 mW) and long accumulation time (1 min) to obtain spectra with reasonable signal to noise ratio. A representative Raman spectrum is presented in Figure 5.

According to the triplet peaks appearing in Figure 5 at around 395, 519 and 639 cm^{-1} and upon comparison with former data available in the literature for Raman analysis of anatase titania [29,30], the APT formed in our case seems not to be rutile but rather anatase. This is in agreement with the results of anodization of Ti by a different group [31].

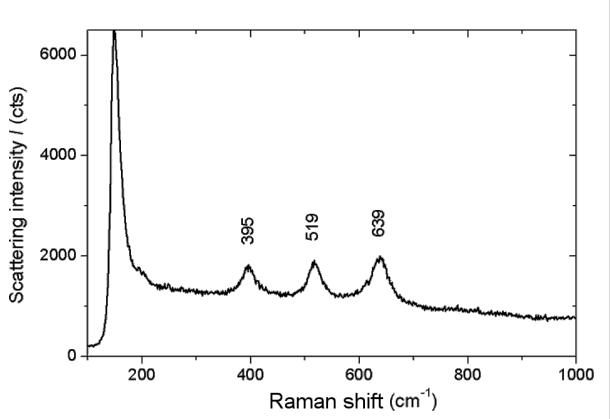

Figure 5: Typical uncorrected Raman scattering spectrum of an anodized implant, representative of all implant types with or without pretreatment.

The spontaneous phosphate incorporation occurring during anodization in H_3PO_4 is not the only form of doping that may be exploited in order to increase the possible bioactivity of the APT coating. In fact, one may explore the possibility to add different chemical species to the APT coating from those naturally resulting in the dissolved acid electrolyte. Interesting candidate elements are F, Ca and Mg and P, as demonstrated by recent loading carried out on implants coated with nanoporous titania by means of different techniques [22,32,33]. We selected Mg, which is essential to all living cells for its interaction with polyphosphate compounds such as ATP, DNA and RNA, required by many enzymes for their functioning, and present in many pharmaceutical products. In the research literature, Mg has also been added to hydroxylapatite to support to bone formation but with varying results (e.g., positive in [34] and missing in [35]).

With the goal of the incorporation of Mg in the APT coating, in a separate set of experiments, we added magnesium sulfate ($MgSO_4$) to the electrolyte. The salt was added in two different concentrations (0.5 and 1.5 M) and for two different processing times of the subsequent anodization (1 and 10 min). The presence of Mg was confirmed by means of SEM and EDS. In Figure 6 representative SEM micrographs of the implant surfaces after anodization with the Mg additive at an intermediate magnification (1,000×) are shown.

In Figure 6a, it appears that the lower Mg concentration (0.5 M) for the short anodization time (1 min) gave rise to surface aggregates covering only a minor portion of the surface, (20–30%, the image is representative). In Figure 6b, the effect of increasing the concentration to 1.5 M while keeping the anodization time at 1 min appears to result in an almost full coverage of an aggregated overlayer (80–90%). Concurrently,

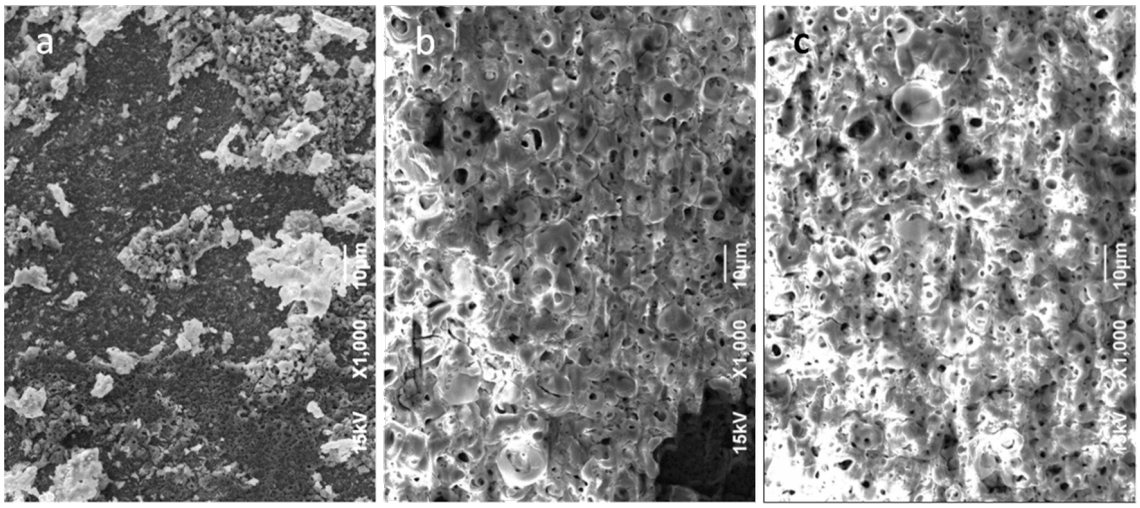

Figure 6: SEM micrographs of implants (S&M) anodized in the presence of a Mg additive. (a) 0.5 M Mg, 1 min anodization; (b) 1.5 M Mg, 1 min anodization; (c) 1.5 M Mg, 10 min anodization.

despite the standard overcoating with 10 nm Au (in order to avoid the static charging effect due to the electron beam), the enhanced contrast still appears to be an effect of the thick insulating coating on top of the anodized Ti. As shown in Figure 6c, the case of high concentration (1.5 M) and long anodization time (10 min) further increases the overlayer coverage, reaching ≈100% in all regions ($N \geq 3$).

EDS also confirmed the overlayer aggregates comprised of Mg. A quantitative EDS analysis pointed out that in the above three cases of Figure 6, the Mg content detected was ≈0.5, ≈1.0 and ≈1.3 at %, respectively. The entire amount of Mg found may not necessarily be incorporated in the APT or loaded in the APT pores. However, anodizing seems to enhance this functionalization. Indeed, when control implants were submerged after anodization in Mg solutions with same concentration and for the same soaking time, we observed a lower Mg content of ≈0.1, ≈0.3 and ≈0.6 at %, respectively. The reason why Mg is more effectively coated on the APT when added during anodization is not clear, since this is a cation, and in principle, should be preferentially driven to the cathode. However, we may suppose that at least electrically neutral species containing Mg are also formed in the electrolyte, such as $Mg_3(PO_4)_2$ or, more likely, $Mg(OH)_2$. These species with comparatively large size and low mobility could be trapped within the flow of the other anions.

An example of EDS chemical mapping is presented in Figure 7. It appears that all the elemental species of interest, namely Ti, P from the electrolyte phosphate and Mg additive, are evenly distributed over the surface (and the same is for O, not shown). Occasional defects appear, such as in the top right region of Figure 7 (circled in yellow). The depressed (dark) region on the morphological image (Figure 7a) probably corresponds to an area of missing or thinner Mg coating. Indeed, the Mg map (Figure 7d) shows a locally lower level in that spot. The Ti (Figure 7b) is apparently more concentrated there, due to the decreased screening effect of the Mg overlayer (a similar effect was observed for the map of O). However, the P content (Figure 7c) is also lower in that spot, meaning that not only the Mg was coated less efficiently but also the APT did not form in that site. This can be ascribed to the presence of different contaminants on the Ti (e.g., C, not mapped here). Therefore, where no APT forms, the decreased ionic flow lines also prevent formation of a good Mg overlayer. However, overall, a high coverage of Mg is obtained on the surface.

As shown in Figure 6a, the Mg overlayer results in apparent clogging of the APT pores. This may cause the implant to lose the desired nanostructure patterned by the anodization, at the cost of gaining the chemical functionalization of Mg. However, at a longer anodization time, the Mg overlayer itself seems to form a nanoporous structure. These pores are on average 5–10 times larger than those in the pristine APT (i.e., on the microscale). We make the hypothesis that the coating is porous due to local percolation of the ionic current through it, with the arrangement of such conduction channels favoring the merging into large pores. In any case, the underlying structure of APT nanopores, which is made in an inorganic inert material, is not lost, and will eventually be revealed after bio-utilization of the Mg overlayer at an implant site, providing interaction with the host tissue.

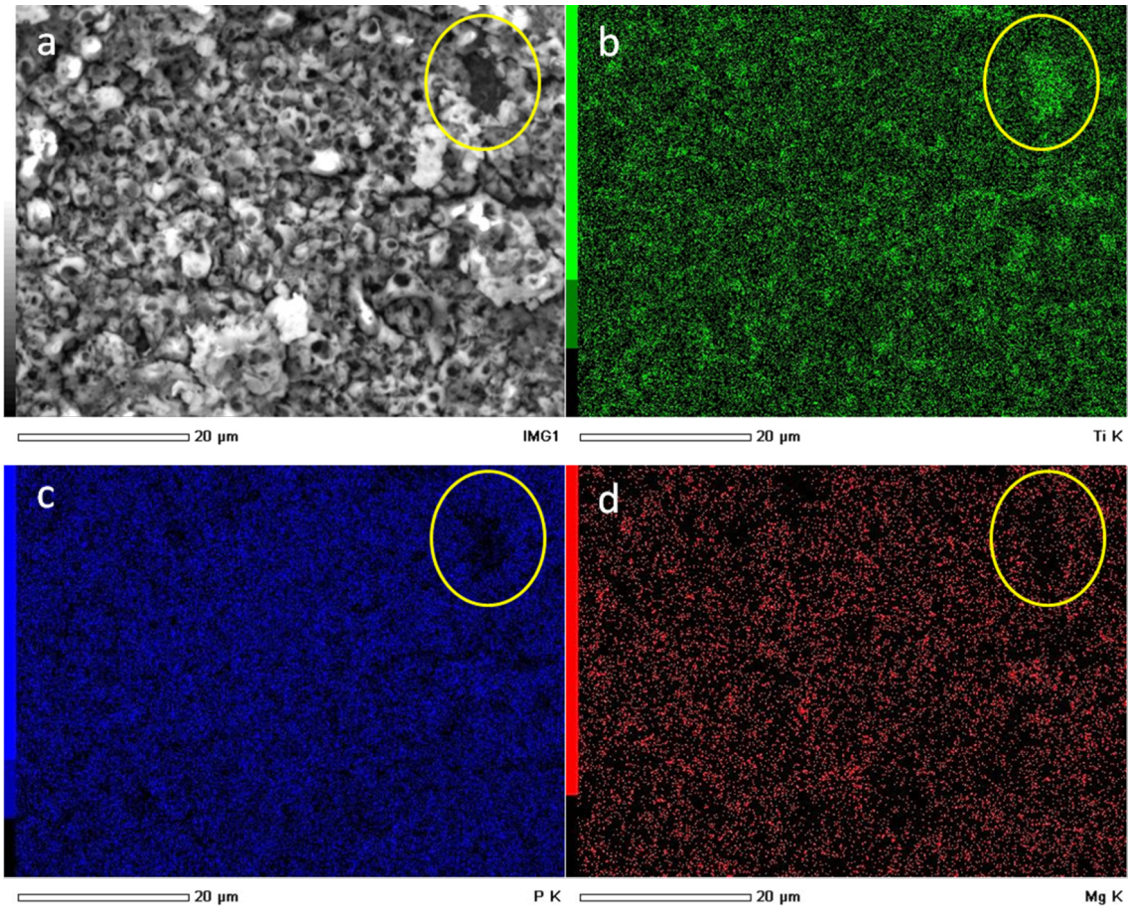

Figure 7: SEM and EDS mapping of the elemental species on the surface of implants (S&M) anodized in the presence of 1.5 M Mg for 1 min. (a) SEM (backscattered electron) morphology, (b) Ti map, (c) P map, and (d) Mg map.

Conclusion

Anodization in acid electrolyte provides a conformal coating with pores also formed on curved surfaces of commercial grade Ti, and is thus a feasible approach for the nanopatterning of dental implant surfaces.

The implants of the same Ti grade from the two different companies considered here did not present significant differences.

In our experience, the cathodic pretreatment did not provide different morphological, compositional or structural results for the subsequent anodization at the given electrolyte concentration, bath temperature, and applied voltage and current conditions.

The nanoporosity resulting from the anodization did not alter the underlying surface profile on the microscale. Therefore, when not sufficient to provide osteointegration by itself, anodization can be an additive treatment in addition to microscale sandblasting or wet etching.

By anodizing in phosphoric acid, a remarkable doping of the fabricated APT coating with phosphate ions occurs spontaneously, which can be already considered as a biofunctionalization of the nanoporous surface. Further in situ functionalization aiming at improved bioactivity of the nanoporous surfaces may be obtained by using additive species in the anodizing electrolyte, such as Mg as shown here. The amount of functionalization obtained with Mg additive is approximately a factor 10 less effective than for the phosphate anions of the electrolyte base acid, and optimization conditions should be sought for optimal Mg adsorption.

The as fabricated APT was found to be at least partly anatase, which is desirable for osteointegration. A higher crystallinity,

with removal of water and residual amorphous APT phase, may likely be obtained by post-fabrication annealing at moderate temperatures to avoid the transition to rutile.

The next step in our research will be the further functionalization of the organized porous film surface with bioactive molecules such as proteins and adhesion factor, and in vitro experiments with osteoblast-like cell cultures.

Experimental

Implants used

We used dental implants from two different manufacturers, Sweden & Martina (S&M) and Stark. From the range of available S&M implants, the type Premium Straight was selected. Both implant types were of grade 4 Ti and were provided in machined form only (i.e., without surface treatment for roughening and osteointegration). The implants were sterilized and sealed in plastic boxes, and were used as received, taking care to minimize contamination prior to anodization, by handling only with clean tweezers and gloves. For mounting in the anodization setup, we took advantage of the metallic screw available for connection of the abutment, which fit the inner base cavity of the implants.

Anodization

The implants were suspended vertically upside-down and submerged in a 1.5 M aqueous solution of phosphoric acid H_3PO_4 (Sigma Aldrich, Milan, Italy). The counter electrode (normally the cathode) was an inert Pt wire (1 mm thickness), curled in a spiral to form an almost compact circle of ≈3 cm in diameter in front of the implants at a distance of ≈2 cm. The anodization was carried out by means of a high power supply (N5751A, Agilent Technologies, USA), connected for both control and output to a laptop computer. A Visual Basic macro allowed for the collection of both current (i) and voltage (V) data from the circuit. The anodization was carried out in prevailing potentiostatic mode, by setting the target voltage and target current to 150 V and 0.5 A, in a double-walled beaker with circulating silicone oil, kept at an approximately constant temperature of 25 °C (RT) by means of a thermocryostat RP 3530 (Lauda, Germany). The cathodization treatment, when applied, was set 150 V and applied to the Pt counter electrode (with the implant set to ground) and 0.1 A target current.

Imaging and chemical analysis

Both types of implants were characterized before and after anodization by SEM. They were mounted on Al stubs by means of double-sided adhesive carbon tape and overcoated with a ≈10 nm thick layer of sputtered gold before inserting into the SEM chamber. We used a JSM-6490LA (JEOL, Japan) instrument equipped with energy dispersive spectroscopy (EDS) for the chemical identification of the coating composition. For imaging, the instrument was operated at a primary electron beam energy of 20 kV, aperture 2, and spot size 30, while for EDS we used 10 kV, aperture 3 and spot size 60, respectively.

Additionally, on implants not coated with gold, we used a micro-Raman Raman spectrometer (inVia, Renishaw, UK) equipped with the software program WiRE 3.4 to assess the surface resulting from the anodization. A 785 nm wavelength laser was used together with a 1200 grooves/mm grating, collecting spectra with a 10× objective in the 100–3200 cm^{-1} range. The incident power was ≈100 mW with an accumulation time of 1 min.

Supporting Information

Supporting Information File 1

Additional experimental information.
[http://www.beilstein-journals.org/bjnano/content/supplementary/2190-4286-6-224-S1.pdf]

Acknowledgements

Mr. Riccardo Moffa of Stark and Dr. Roberto M. Mangino of Odontosalute are kindly acknowledged for having provided the dental implants of the two companies, Stark and Sweden & Martina, respectively, on which the currently reported experiments were carried out.

References

1. Park, J. B.; Lakes, R. S. *Biomaterials: An Introduction,* 2nd ed.; Plenum Press: New York, 1992. doi:10.1007/978-1-4757-2156-0
2. Letic-Gravrilovic, A.; Scandurra, R.; Abe, K. *Dent. Mater. J.* **2000,** *19,* 99–132. doi:10.4012/dmj.19.99
3. Esposito, M.; Hirsch, J.-M.; Lekholm, U.; Thomsen, P. *Eur. J. Oral Sci.* **1998,** *106,* 721–764. doi:10.1046/j.0909-8836..t01-6-.x
4. Wennerberg, A.; Albrektsson, T. *Clin. Oral Implants Res.* **2009,** *20,* 172–184. doi:10.1111/j.1600-0501.2009.01775.x
5. Kim, H.-M.; Miyaji, F.; Kokubo, T.; Nakamura, T. *J. Biomed. Mater. Res.* **1996,** *32,* 409–417. doi:10.1002/(SICI)1097-4636(199611)32:3<409::AID-JBM14>3.0.CO;2-B
6. Diggle, J. W.; Downie, T. C.; Goulding, C. W. *Chem. Rev. (Washington, DC, U. S.)* **1969,** *69,* 365–405. doi:10.1021/cr60259a005
7. Mor, G. K.; Varghese, O. K.; Paulose, M.; Shankar, K.; Grimes, C. A. *Sol. Energy Mater. Sol. Cells* **2006,** *90,* 2011–2075. doi:10.1016/j.solmat.2006.04.007
8. Shingubara, S. *J. Nanopart. Res.* **2003,** *5,* 17–30. doi:10.1023/A:1024479827507
9. Toccafondi, C.; Dante, S.; Reverberi, A. P.; Salerno, M. *Curr. Nanosci.* **2015,** *11,* 572–580. doi:10.2174/1573413711666150415225541
10. Karlsson, M.; Pålsgård, E.; Wilshaw, P. R.; Di Silvio, L. *Biomaterials* **2003,** *24,* 3039–3046. doi:10.1016/S0142-9612(03)00146-7

11. Salerno, M.; Caneva-Soumetz, F.; Pastorino, L.; Patra, N.; Diaspro, A.; Ruggiero, C. *IEEE Trans. NanoBioscience* **2013,** *12,* 106–111. doi:10.1109/TNB.2013.2257835
12. Toccafondi, C.; Thorat, S.; La Rocca, R.; Scarpellini, A.; Salerno, M.; Dante, S.; Das, G. *J. Mater. Sci.: Mater. Med.* **2014,** *25,* 2411–2420. doi:10.1007/s10856-014-5178-4
13. Ross, A. M.; Jiang, Z.; Bastmeyer, M.; Lahann, J. *Small* **2012,** *8,* 336–355. doi:10.1002/smll.201100934
14. Bucci-Sabattini, V.; Cassinelli, C.; Coelho, P. G.; Minnici, A.; Trani, A.; Dohan Ehrenfest, D. M. *Oral Surg., Oral Med., Oral Pathol., Oral Radiol.* **2010,** *109,* 217–224. doi:10.1016/j.tripleo.2009.09.007
15. Luo, C.; Li, L.; Li, J.; Yang, G.; Ding, S.; Zhi, W.; Weng, J.; Zhou, S. *J. Mater. Chem.* **2012,** *22,* 15654–15664. doi:10.1039/c2jm32007j
16. Poinern, G. E.; Shackleton, R.; Mamun, S. I.; Fawcett, D. *Nanotechnol., Sci. Appl.* **2011,** *4,* 11–24. doi:10.2147/NSA.S13913
17. Brammer, K. S.; Frandsen, C. J.; Jin, S. *Trends Biotechnol.* **2012,** *30,* 315–322. doi:10.1016/j.tibtech.2012.02.005
18. Meirelles, L.; Melin, L.; Peltola, T.; Kjellin, P.; Kangasniemi, I.; Currie, F.; Andersson, M.; Albrektsson, T.; Wennerberg, A. *Clin. Implant Dent. Relat. Res.* **2008,** *10,* 245–254. doi:10.1111/j.1708-8208.2008.00089.x
19. Han, G.; Müller, W. E. G.; Wang, X.; Lilja, L.; Shen, Z. *Mater. Sci. Eng., C* **2015,** *47,* 376–383. doi:10.1016/j.msec.2014.11.021
20. Lee, J.-K.; Choi, D.-S.; Jang, I.; Choi, W.-Y. *Int. J. Nanomed.* **2015,** *10,* 1145–1154. doi:10.2147/IJN.S78138
21. Elias, C. N.; Fernandes, D. J.; Resende, C. R. S.; Roestel, J. *Dent. Mater.* **2015,** *31,* e1–e13. doi:10.1016/j.dental.2014.10.002
22. Park, K. H.; Heo, S. J.; Koak, J. Y.; Kim, S. K.; Lee, J. B.; Kim, S. H.; Lim, Y. J. *J. Oral Rehabil.* **2007,** *34,* 517–527. doi:10.1111/j.1365-2842.2006.01688.x
23. Tanaka, S.; Fukushima, Y.; Nakamura, I.; Tanaki, T.; Jerkiewicz, G. *ACS Appl. Mater. Interfaces* **2013,** *5,* 3340–3347. doi:10.1021/am400398d
24. Salerno, M.; Patra, N.; Cingolani, R. *Nanoscale Res. Lett.* **2009,** *4,* 865–872. doi:10.1007/s11671-009-9337-3
25. Choi, J. Fabrication of monodomain porous alumina using nanoimprint lithography and its applications. Ph.D. Thesis, Martin-Luther-Universität Halle-Wittenberg, Germany, 2004.
26. Uttiya, S.; Contarino, D.; Prandi, S.; Carnasciali, M. M.; Gemme, G.; Mattera, L.; Rolandi, R.; Canepa, M.; Cavalleri, O. *J. Mater. Sci. Nanotechnol.* **2014,** *1,* 106–114. doi:10.15744/2348-9812.1.S106
27. Boyan, B. D.; Lossdörfer, S.; Wang, L.; Zhao, G.; Lohmann, C. H.; Cochran, D. L.; Schwartz, Z. *Eur. Cells Mater.* **2003,** *6,* 22–27.
28. Yao, C.; Webster, T. J. *J. Biomed. Mater. Res., Part B* **2009,** *91B,* 587–595. doi:10.1002/jbm.b.31433
29. Hsien, Y.-H.; Chang, C.-F.; Chen, Y.-H.; Cheng, S. *Appl. Catal., B: Environ.* **2001,** *31,* 241–249. doi:10.1016/S0926-3373(00)00283-6
30. Frank, O.; Zukalova, M.; Laskova, B.; Kürti, J.; Koltai, J.; Kavan, L. *Phys. Chem. Chem. Phys.* **2012,** *14,* 14567–14572. doi:10.1039/c2cp42763j
31. Giordano, C.; Saino, E.; Rimondini, L.; Pedeferri, M. P.; Visai, L.; Cigada, A.; Chiesa, R. *Colloids Surf., B* **2011,** *88,* 648–655. doi:10.1016/j.colsurfb.2011.07.054
32. Alves, S. A.; Bayón, R.; de Viteri, V. S.; Garcia, M. P.; Igartua, A.; Fernandes, M. H.; Rocha, L. A. *J. Biocorros. Tribocorros.* **2015,** *1,* 23. doi:10.1007/s40735-015-0023-y
33. Oliveira, F. G.; Ribeiro, A. R.; Perez, G.; Archanjo, B. S.; Gouvea, C. P.; Araújo, J. R.; Campos, A. P. C.; Kuznetsov, A.; Almeida, C. M.; Maru, M. M.; Achete, C. A.; Ponthiaux, P.; Celis, J.-P.; Rocha, L. A. *Appl. Surf. Sci.* **2015,** *341,* 1–12. doi:10.1016/j.apsusc.2015.02.163
34. Canullo, L.; Heinemann, F.; Gedrange, T.; Biffar, R.; Kunert-Keil, C. *Clin. Oral Implants Res.* **2012,** *24,* 398–406. doi:10.1111/clr.12035
35. Caneva, M.; Botticelli, D.; Stellini, E.; Souza, S. L. S.; Salata, L. A.; Lang, N. P. *Clin. Oral Implants Res.* **2011,** *22,* 512–517. doi:10.1111/j.1600-0501.2010.02040.x

License and Terms

BEILSTEIN JOURNAL OF NANOTECHNOLOGY

Fabrication of hybrid nanocomposite scaffolds by incorporating ligand-free hydroxyapatite nanoparticles into biodegradable polymer scaffolds and release studies

Balazs Farkas, Marina Rodio, Ilaria Romano, Alberto Diaspro, Romuald Intartaglia and Szabolcs Beke*§

Full Research Paper

Open Access

Address:
Department of Nanophysics, Istituto Italiano di Tecnologia (IIT), Via Morego 30, 16163 Genova, Italy

Email:
Szabolcs Beke* - szabolcs.beke@iit.it

* Corresponding author
§ Phone: +39 010 71781982, Fax: +39 010 71781 236

Keywords:
biodegradable scaffolds; biodegradation; hydroxyapatite; laser ablation in liquid; stereolithography

Beilstein J. Nanotechnol. **2015,** *6,* 2217–2223.
doi:10.3762/bjnano.6.227

Received: 13 August 2015
Accepted: 03 November 2015
Published: 25 November 2015

This article is part of the Thematic Series "Organized films".

Guest Editor: M. Canepa

Abstract

We report on the optical fabrication approach of preparing free-standing composite thin films of hydroxyapatite (HA) and biodegradable polymers by combining pulsed laser ablation in liquid and mask-projection excimer laser stereolithography (MPExSL). Ligand-free HA nanoparticles were prepared by ultrafast laser ablation of a HA target in a solvent, and then the nanoparticles were dispersed into the liquid polymer resin prior to the photocuring process using MPExSL. The resin is poly(propylene fumarate) (PPF), a photo-polymerizable, biodegradable material. The polymer is blended with diethyl fumarate in 7:3 w/w to adjust the resin viscosity. The evaluation of the structural and mechanical properties of the fabricated hybrid thin film was performed by means of SEM and nanoindentation, respectively, while the chemical and degradation studies were conducted through thermogravimetric analysis, and FTIR. The photocuring efficiency was found to be dependent on the nanoparticle concentration. The MPExSL process yielded PPF thin films with a stable and homogenous dispersion of the embedded HA nanoparticles. Here, it was not possible to tune the stiffness and hardness of the scaffolds by varying the laser parameters, although this was observed for regular PPF scaffolds. Finally, the gradual release of the hydroxyapatite nanoparticles over thin film biodegradation is reported.

Introduction

Interfaces between osteochondral prosthetics and the surrounding bone tissue are of great importance with regard to the promotion and enhancement of biological fixation (firm bonding of the implant to the host bone by on-growth or ingrowth). Hydroxyapatite (HA) nanoparticles (NPs) are one of the most commonly used materials in osteochondral tissue engineering, since they bear chemical similarity to the mineral constituent of human bones, are bioactive and can be fairly easily bioconjugated [1]. HA NPs can enhance cell proliferation in bone tissue regeneration [2].

Tissue engineering is an interdisciplinary field that combines the principles of life sciences and engineering to improve tissue growth and functions. Whenever the need arises for a certain type of scaffold to be produced, all these fields have to be utilized together to get an appropriate solution.

HA is an essential ingredient of normal bone and teeth and is widely used for bone tissue regeneration. Given the high degree of chemical similarity between synthetic HA and the natural bone mineral, a large number of studies have introduced synthetic HA as bone replacement material for biomedical applications [3,4]. The benefits of synthetic HA, most notably its biocompatibility, slow biodegradability and good osteoconductive and osteoinductive capabilities [5,6], made it a platform for large-scale biomedical applications, such as controlled drug release and bone tissue engineering materials [7,8].

Lee et al. [9] reported on cellular responses to crosslinkable poly(propylene fumarate)/hydroxyapatite nanocomposites and showed that these nanocomposites are beneficial for hard tissue replacement due to the excellent mechanical strength and osteoconductivity. They used commercially available HA NPs, whereas we prepared HA NPs by PLAL and controlled the size by this method. They demonstrated also that the addition of HA enhanced hydrophilicity and serum protein adsorption, and as a result, this increased pre-osteoblast cell attachment, spreading, and proliferation after four days of culture.

Different technical routes have been explored for the synthesis of HA NPs, including mechanochemical synthesis [10], combustion preparation [11] and various wet chemistry techniques [12,13]. However, these routes have drawbacks regarding the synthesis attributed to the use of hazardous surfactants that are not suitable for biomedical applications [14].

Pulsed laser ablation of solid targets in liquids (PLAL) for the production of highly pure nanoparticles, has attracted research over the last decade mainly because of the simplicity of the method [15-18]. The main advantages of the technique include the green synthesis without chemical agents, a high production yield [17], the possibility to work under ambient conditions, and the versatility that allows for in situ manipulations [16].

Earlier, we had reported on the incorporation of Au NPs [19] and titanate nanotubes (TNTs) in and on the scaffolds [20] to develop poly(propylene fumarate)/diethyl fumarate (PPF:DEF) scaffolds for specific biomedical applications. We also proved that these scaffolds did not cause immune rejection [21]. A constant release of HA NPs during scaffold degradation may vastly improve the healing process. Also, certain tuning capabilities emerge with PPF:DEF resins when fabrication parameters are changed [22,23]: The stiffness/Young modulus of our rapid prototyping-fabricated scaffolds can be adjusted over a range of four orders of magnitude without any implied modifications concerning the chemical composition of the resin itself.

In this study, we present the combination of two laser methods (PLA and MPExSL) to incorporate HA NPs into biodegradable polymer resin. We also present HA NPs release studies.

Results and Discussion

Materials characterization

In order to evaluate the effects of nanoparticle incorporation, the cured resins have been characterized through nanoindentation, thermogravimetric analysis (TGA), profilometry, and FTIR measurements similar to a previous work performed on Au NPs embedded in the same polymer matrix [19]. Shortly, 2D samples were made to measure the changes of penetration depth (and thus, the layer thickness), while five layer, non-porous circular scaffolds with 2 mm diameter were prepared for nanoindentations. For TGA and FTIR, the same 20 layer, 5 mm diameter non-porous samples were used. For all 3D scaffolds, the layer thickness was adjusted to 100 μm. Most results were then compared to our previously acquired data.

Figure 1 shows a TEM image of hydroxyapatite colloidal solution (Figure 1a) prepared by UV laser ablation of a hydroxyapatite target in ethanol solution, and the corresponding size distribution histogram of the HA NPs (Figure 1b). The mean size of HA NPS was found to be around 17.2 nm.

Since the particles were already dispersed in ethanol, no surface modifications were needed to achieve direct compatibility between the particles and the PPF resin. As seen in Figure 2a, the added nanoparticles only barely affected the penetration depth of the light from the XeCl excimer laser (308 nm) even with the highest particle concentration. On the other hand, TGA (Figure 2a inset) and nanoindentation (Figure 2b) measurements show that the stiffness of the fabricated samples can be considered identical, independent of the concentration of the nanoparticles, as well as the laser parameters. Also, the samples (samples 1–6) fabricated with three different HA concentrations (50, 100 and 300 ppm) and two different fluences (10 and 30 mJ/cm^2) show the same behavior as the ones fabricated without nanoparticles at 10 mJ/cm^2 (which corresponds to the highest stiffness achieved before, sample 7), independently of the fluence. When the highest fluence (30 mJ/cm^2) is used on the non-NP sample, it leads to a sharp drop in the stiffness (sample 8), just as expected from our previous results [23].

FTIR (Figure 3a) shows no disparities in the chemical composition of the HA samples compared to the „high stiffness" pris-

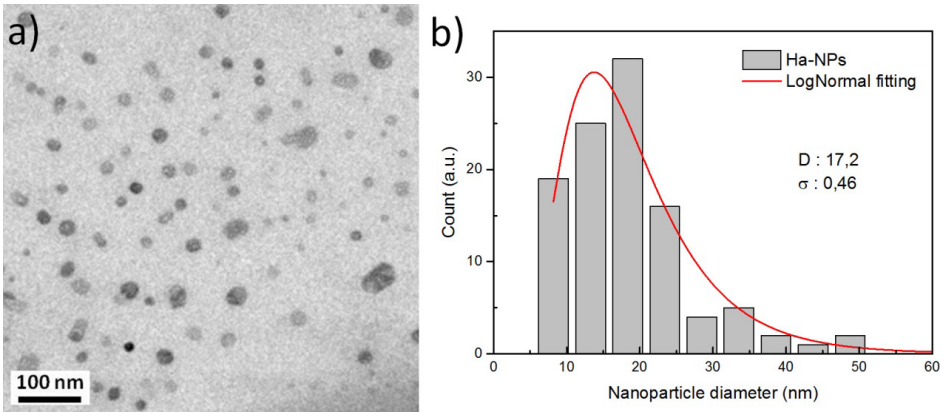

Figure 1: TEM image of hydroxyapatite colloidal solution prepared by UV laser ablation of hydroxyapatite target immersed in ethanol solution. b) Size distribution histogram of the colloidal solution revealing the mean size around 17 nm. The particle size distribution is obtained by using the ImageJ software. D and σ correspond to the mean size and the corresponding standard deviation obtained from a log-normal fitting, respectively.

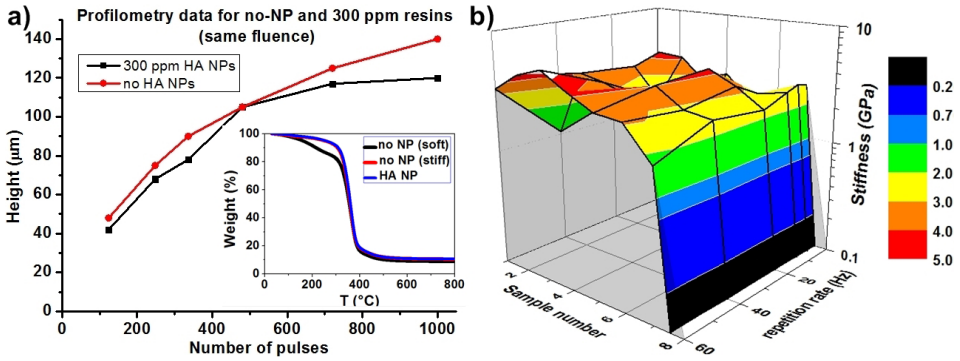

Figure 2: a) Profilometry data shows no disparity between the non-NP samples and the 300 ppm HA samples; inset presents TGA which shows that the HA samples exhibit the same behavior as the „high stiffness" no-NP samples; b) nanoindentation presents the lacking tuning capability of the HA samples.

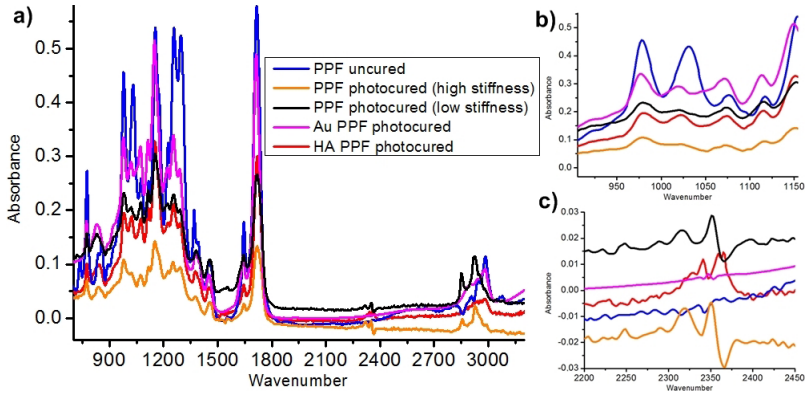

Figure 3: a) Comparison of the FTIR spectra received for HA samples and samples from previous studies [19,23]. All HA show the same FTIR, following closely the „high stiffness" samples fabricated without any nanoparticles. The sole differences that can be found is where the main peak of the pure HA NPs is and where the three carbonate peaks arise (HA reacting with environmental CO_2); b) close-up of peaks 1020 and 980 cm^{-1} and c) is a close up of peaks at 2340, 2360 and 2365 cm^{-1}.

tine samples, apart from a slight difference in the ratio of the peak height of the peaks 1020 and 980 (Figure 3b). Three new peaks also emerge at 2340, 2360 and 2365 cm^{-1} (Figure 3c). These latter three are obvious markers of the carbonates formed by the reaction between the Ha NPs and the CO_2 in the air during the laser processing. The slight change in the peak ratio at 1060 cm^{-1} is supposedly due to the HA NPs having a prominent peak there.

From these measurements, we can claim that HA NPs do not react chemically with the resin during the photocuring process. They do not absorb either, but act like scattering points for the incoming UV irradiation and therefore increase the photocuring efficiency. This scattering effect also reduces any kind of tuning capability that we observed before on non-NP and Au NP resins, resulting in samples with uniformly high stiffness. In other words, the previously presented possibility to tune the stiffness is not observed.

Nanoparticle resin

Figure 4 illustrates the degradation, the scaffold swelling, and HA NPs release during degradation in Dulbecco's Modified Eagle's Medium (DMEM). In order to test the release of HA NPs from the bulk scaffolds, 20 layer of 3 mm diameter porous (400 µm pore size) scaffolds were fabricated from HA NPs–PPF resins containing HA NPs with different concentrations of 50, 100 and 300 ppm (Figure 4, inset). The scaffolds were immersed in 100 µL of DMEM solution for 4 weeks. The degradation medium was extracted daily, then 3 times, 2 times and once a week. The release profile of Ha NPs during the PPF scaffold degradation as a function of time was estimated by inductively coupled plasma optical emission spectrometry measurements (ICP-OES, ICAP 6300 duo ThermoScientific). Every time a volume of 25 µL was taken for ICP-EOS analysis and replaced by the same volume of fresh DMEM solution buffer.

Results have shown a stable increase in the amount of particles in the DMEM for the first two weeks. When normalized (to percentage and considering the diluting effect of the replaced medium), all concentrations have shown the exact same release mechanism: a fast ramp up for the first two weeks, followed by saturation at 80–90% released HA NPs. This release mechanism fits well to our empirical observations concerning the degradation of high stiffness PPF scaffolds in DMEM: the material becomes a hydrogel during the first two weeks, then disperses into the medium in the next 4–6 weeks. Such degradation obviously leads to a ramp up in the release mechanism due to the hydrogel transition phase. Of note, the experiment had to be cancelled after 2 weeks due to contamination: the vials became infected by fungi, gradually digesting the nanoparticles (data not shown).

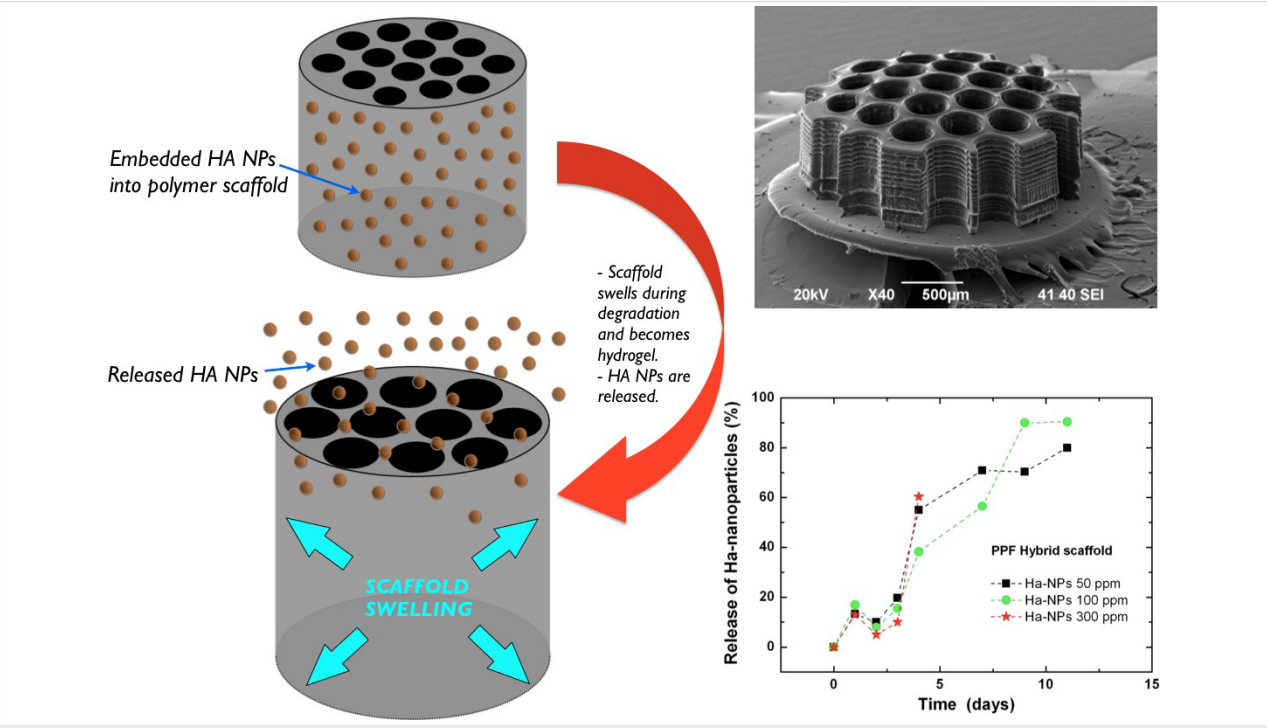

Figure 4: Release and degradation of HA NP-incorporated polymer scaffolds are presented during its degradation in DMEM. The scaffold becomes hydrogel, swells and releases the HA NPs. The plot shows the released fraction in percent as a function of the time, estimated by inductively coupled spectrometry (ICP-EOS).

Conclusion

We presented the combination of two laser processing methods (PLA and MPExSL) to incorporate hydroxyapatite nanoparticles (HA NPs) into a biodegradable polymer resin. Ligand-free production of NPs can be considered a green route of NP synthesis that is beneficial for biological applications. HA NP release test was performed and showed that a controlled release of HA NPs is feasible and highly favorable since the HA is widely utilized along with prosthetics these days and can only supply the particles for a few days before the pure, sprayed-up HA layer completely disperses into the surrounding tissue. With the PPF-HA NP resin, a stable dosing can be achieved for the most crucial first two weeks of the healing process.

Experimental

Poly(propylene fumarate)

Poly(propylene fumarate) (PPF) has been chosen as the carrier for the HA nanoparticles following our previous success with gold nanoparticles (Au NPs) [19]. PPF itself is a versatile synthetic biopolymer, a biodegradable and photocurable material. The photocrosslinking efficiency is usually adjusted by the added photoinitiator (PI) concentration („chemical tuning"), though we recently demonstrated that great stiffness tuning (over four orders of magnitude) could be achieved by changing various fabrication/laser parameters as well („physical tuning") [23] with pristine resins as well as the Au NP ones. The obvious advantage of the chemical tuning over physical tuning is reliability, while physical tuning can be conducted in situ, leading to a highly versatile, albeit hard to evaluate, fabrication procedure. With the physical tuning, it is also possible to achieve complex scaffold structures, for instance, mimicking composite materials.

The PPF used in this work is not commercially available. The synthesis is reported elsewhere [22]. The PI phenylbis(2,4,6-trimethylbenzoyl)phosphine oxide (BAPO) was dissolved in purified PPF and in the PPF:DEF (7:3 w/w) blend. Diethyl fumarate (DEF) is applied as diluent to reduce the resin viscosity as needed for the proper resin recast for MPExSL.

MPExSL

Mask-projected excimer laser stereolithography (MPExSL) is a rapid prototyping stereolithography method, relying on a layer-by-layer building-up process where one layer is fabricated by image projection using pulsed excimer laser radiation. The method is explained in detail in [22].

Briefly, the method goes as follows: the output beam of a XeCl excimer laser (at 308 nm wavelength) is coupled to a customized mask projection optical system with a telescope and a motorized variable attenuator. The system also includes a motorized mask holder (which can house five masks at the same time) that selects the image to be projected on the resin surface, adding great control for the scaffold internal architecture for each layer. The outer shape of the scaffold (e.g., the scaffold diameter in the horizontal plane) can be further adapted by means of an iris placed right in front of the mask holder [22]. Above the optical setup, a CCD camera is housed to on-line image the resin surface and in situ monitor the fabrication process.

During the stereolithography process, the photocurable resin is filled in a cup supported by a multi-axis motorized stage. The proper position of the resin surface to be exposed by the laser is achieved by moving the sample with an XYZ stage, while a fourth motorized stage (W) controls the vertical position of the scaffold-holding platform immersed in the resin container cup. After one layer is photocured the W stage moves downwards into the resin and allows the recast of a fresh liquid resin layer on top of the previously cured layer. The applied light dose determines the actual photocured depth, i.e., layer thickness, while the magnitude of the downward step of the W stage determines the overlap between two adjacent layers.

Hydroxyapatite nanocomposite synthesis by using two laser-processing methods

Figure 5 presents the experimental setups of the two laser-assisted methods applied for HA/PPF nanocomposite production.

HA NPs were prepared by UV laser ablation of a HA target placed in ethanol solution using a picosecond laser system (continuum leopard) delivering 60 ps laser pulses with a wavelength of 355 nm at a repetition rate of 20 Hz. The synthesis was performed following the previous work [15]. The laser pulse energy was controlled with a variable attenuator and fixed at 42 mJ. A lens with a focal length of 250 mm and a focal position of −10 cm with respect to the target surface was used. The target material (hydroxyapatite from CELLYARDTM pellet, PENTAX), in the form of a cylinder with a diameter of 5 mm and a thickness of 2 mm, was placed on the bottom of a quartz cuvette (dimension 10 × 10 × 30 mm^3) with 2 mL of ethanol solution. The target was placed on a motorized stage (T-cube DC Servo controller, Thor labs) that moved at a constant speed of 1 mm/s in a spiral with an outer radius of 1 mm. The irradiation time was fixed at 120 min. Particle size distribution was evaluated by TEM.

The HA NP/ethanol colloidal solution was added to the PPF:DEF during resin production: The colloidal solution was mixed with DEF, then added to the PPF in 7:3 w/w followed by 1% photoinitiator. In the end, the resin was stirred for 24 h

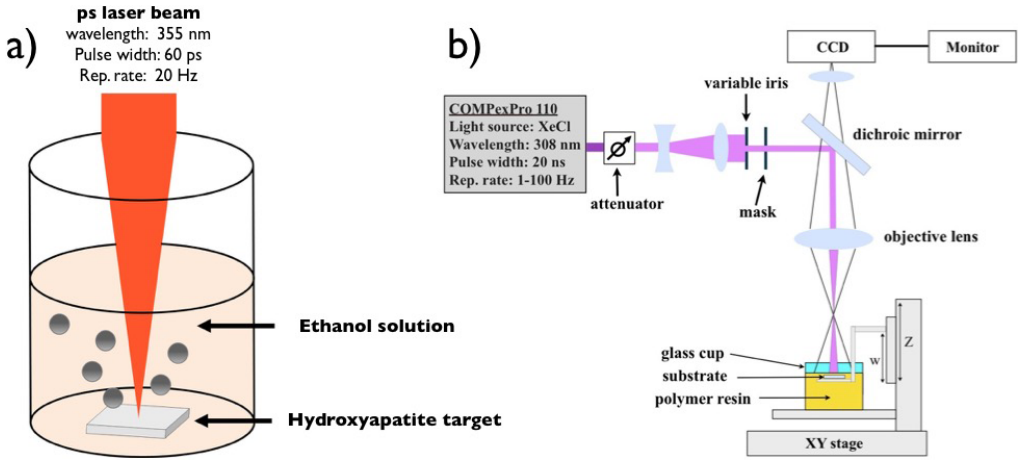

Figure 5: a) Illustration of the ultrafast laser-assisted method for the synthesis of HA colloidal solution and b) MPExSL setup for the scaffold production with incorporated HA NPs.

under a hood to evaporate all ethanol. Various concentrations of HA NP resins were made from colloidal with concentrations of 20, 50, 100 and 300 ppm. Each solution was 5 mL.

Characterizations

Inductively coupled plasma optical emission spectrometry measurement (ICP-OES, ICAP 6300 duo thermo scientific) was used to determine the quantity of Ha colloidal solution. For this measurement, 25 µL solution of NPs colloidal solution was introduced in aqua regia, and after overnight acid digestion the final volume was adjusted with Milli-Q water to 25 mL. The dilution factor is kept into consideration while determining the final concentration.

Height measurements were carried out by a Veeco Dektak 150 profiler with 2 mg of load on the tip.

Stiffness measurements were performed by using a Micro Materials Ltd. NanoTest. The tests were conducted by applying a Berkovich tip with a maximum load of 0.6 mN, a dwell time at maximum load of 30 s, loading and unloading periods of 30 and 15 s, respectively. Every sample has been measured at 16 different points (in a matrix of 4 × 4, the distance between measurement points was 50 µm). Young's modulus was calculated through the Oliver and Pharr method each time. The stiffness of the whole sample was acquired eventually by calculating the mean value of these aforementioned 16 points.

Thermogravimetric analysis (TGA) was conducted in a TGA Q500 from TA Instruments. The sample was placed in a platinum pan with an equilibrating step at 30 °C. The annealing went to 800 °C with a 10 °C/min rate. The nitrogen flow was 50 mL/min.

Transmission electron microscopy (TEM) was performed with a JEOL Jem1011 microscope working at an acceleration voltage of 100 kV. Samples were prepared by dropping the colloidal solution directly onto a carbon-coated 300 mesh copper grid and allowing the ethanol solution to evaporate under room temperature and pressure.

FTIR spectroscopy analysis was performed by using the Bruker Vertex 80V infrared spectrometer. HA-NPs scaffold samples were analyzed in transmission mode in the range of 600–4000 cm^{-1}.

References

1. Sadat-Shojai, M.; Khorasani, M.-T.; Dinpanah-Khoshdargi, E.; Jamshidi, A. *Acta Biomater.* **2013,** *9,* 7591. doi:10.1016/j.actbio.2013.04.012
2. Jaffe, W. L.; Scott, D. F. *J. Bone Jt. Surg., Am. Vol.* **1996,** *78,* 1918–1934.
3. Hutmacher, D. W.; Schantz, J. T.; Lam, C. X. F.; Tan, K. C.; Lim, T. C. *J. Tissue Eng. Regener. Med.* **2007,** *1,* 245–260. doi:10.1002/term.24
4. Habraken, W. J. E. M.; Wolke, J. G. C.; Jansen, J. A. *Adv. Drug Delivery Rev.* **2007,** *59,* 234–248. doi:10.1016/j.addr.2007.03.011
5. Poinern, G. E.; Brundavanam, R. K.; Mondinos, N.; Jiang, Z.-T. *Ultrason. Sonochem.* **2009,** *16,* 469–474. doi:10.1016/j.ultsonch.2009.01.007
6. LeGeros, R. Z. *Clin. Mater.* **1993,** *14,* 65–88. doi:10.1016/0267-6605(93)90049-D
7. Ginebra, M. P.; Traykova, T.; Planell, J. A. *J. Controlled Release* **2006,** *113,* 102–110. doi:10.1016/j.jconrel.2006.04.007
8. Ginebra, M.-P.; Traykova, T.; Planell, J. A. *Biomaterials* **2006,** *27,* 2171–2177. doi:10.1016/j.biomaterials.2005.11.023
9. Lee, K.-W.; Wang, S.; Yaszemski, M. J.; Lu, L. *Biomaterials* **2008,** *29,* 2839–2848. doi:10.1016/j.biomaterials.2008.03.030

10. Mochales, C.; Briak-BenAbdeslam, H. E.; Ginebra, M. P.; Terol, A.; Planell, J. A.; Boudeville, P. *Biomaterials* **2004,** *25,* 1151–1158. doi:10.1016/j.biomaterials.2003.08.002
11. Rivera, E. M.; Araiza, M.; Brostow, W.; Castano, V. M.; Díaz-Estrada, J. R.; Hernández, R.; Rogelio Rodríguez, J. *Mater. Lett.* **1999,** *41,* 128–134. doi:10.1016/S0167-577X(99)00118-4
12. Tung, M. S.; O'Farrell, T. J. *Colloids Surf., A* **1996,** *110,* 191–198. doi:10.1016/0927-7757(95)03450-1
13. Pang, Y. X.; Bao, X. *J. Eur. Ceram. Soc.* **2003,** *23,* 1697–1704. doi:10.1016/S0955-2219(02)00413-2
14. Zhou, H.; Lee, J. *Acta Biomater.* **2011,** *7,* 2769–2781. doi:10.1016/j.actbio.2011.03.019
15. Musaev, O. R.; Dusevich, V.; Wieliczka, D. M.; Wrobel, J. M.; Kruger, M. B. *J. Appl. Phys.* **2008,** *104,* 084316. doi:10.1063/1.3000666
16. Bagga, K.; Barchanski, A.; Intartaglia, R.; Dante, S.; Marotta, R.; Diaspro, A.; Sajti, C. L.; Brandi, F. *Laser Phys. Lett.* **2013,** *10,* 065603. doi:10.1088/1612-2011/10/6/065603
17. Intartaglia, R.; Bagga, K.; Brandi, F. *Opt. Express* **2014,** *22,* 3117–3127. doi:10.1364/OE.22.003117
18. Intartaglia, R.; Beke, S.; Moretti, M.; De Angelis, F.; Diaspro, A. *Lab Chip* **2015,** *15,* 1343–1349. doi:10.1039/C4LC01293C
19. Abdelrasoul, G. N.; Farkas, B.; Romano, I.; Diaspro, A.; Beke, S. *Mater. Sci. Eng., C* **2015,** *56,* 305–310. doi:10.1016/j.msec.2015.06.037
20. Beke, S.; Barenghi, R.; Farkas, B.; Romano, I.; Kőrösi, L.; Scaglione, S.; Brandi, F. *Mater. Sci. Eng., C* **2014,** *44,* 38–43. doi:10.1016/j.msec.2014.07.008
21. Farkas, B.; Zsedenyi, A.; Gyukity-Sebestyen, E.; Romano, I.; Nagy, K.; Diaspro, A.; Brandi, F.; Buzas, K.; Beke, S. *J. Laser Micro/Nanoeng.* **2015,** *10,* 11–14. doi:10.2961/jlmn.2015.01.0002
22. Beke, S.; Farkas, B.; Romano, I.; Brandi, F. *Opt. Mater. Express* **2014,** *4,* 2032–2041. doi:10.1364/OME.4.002032
23. Farkas, B.; Romano, I.; Ceseracciu, L.; Diaspro, A.; Brandi, F.; Beke, S. *Mater. Sci. Eng., C* **2015,** *55,* 14–21. doi:10.1016/j.msec.2015.05.054

License and Terms

BEILSTEIN JOURNAL OF NANOTECHNOLOGY

Core-level spectra and molecular deformation in adsorption: V-shaped pentacene on Al(001)

Anu Baby*[1], He Lin[1], Gian Paolo Brivio[1], Luca Floreano[2] and Guido Fratesi[1,3]

Full Research Paper

Open Access

Address:
[1]ETSF, CNISM, Dipartimento di Scienza dei Materiali, Università di Milano-Bicocca, Via Cozzi 55, I-20125 Milano, Italy, [2]CNR-IOM, Laboratorio TASC, Basovizza SS-14, Km 163.5, I-34149 Trieste, Italy and [3]Dipartimento di Fisica, Università degli Studi di Milano, Via Celoria 16, I-20133 Milano, Italy

Email:
Anu Baby* - a.baby@campus.unimib.it

* Corresponding author

Keywords:
aluminum; density functional theory (DFT); near-edge X-ray absorption fine structure (NEXAFS); pentacene; X-ray photoelectron spectroscopy (XPS)

Beilstein J. Nanotechnol. **2015,** *6,* 2242–2251.
doi:10.3762/bjnano.6.230

Received: 27 August 2015
Accepted: 11 November 2015
Published: 27 November 2015

This article is part of the Thematic Series "Organized films".

Guest Editor: M. Canepa

Abstract

By first-principle simulations we study the effects of molecular deformation on the electronic and spectroscopic properties as it occurs for pentacene adsorbed on the most stable site of Al(001). The rationale for the particular V-shaped deformed structure is discussed and understood. The molecule–surface bond is made evident by mapping the charge redistribution. Upon X-ray photoelectron spectroscopy (XPS) from the molecule, the bond with the surface is destabilized by the electron density rearrangement to screen the core hole. This destabilization depends on the ionized carbon atom, inducing a narrowing of the XPS spectrum with respect to the molecules adsorbed hypothetically undistorted, in full agreement to experiments. When looking instead at the near-edge X-ray absorption fine structure (NEXAFS) spectra, individual contributions from the non-equivalent C atoms provide evidence of the molecular orbital filling, hybridization, and interchange induced by distortion. The alteration of the C–C bond lengths due to the V-shaped bending decreases by a factor of two the azimuthal dichroism of NEXAFS spectra, i.e., the energy splitting of the sigma resonances measured along the two in-plane molecular axes.

Introduction

Pentacene has been studied extensively as it is a potential candidate in the field of organic electronic devices [1-5]. It acts as a p-type organic semiconductor in its intrinsic state with high hole mobility and exhibits a very high melting point [6]. The pentacene–Al junction is known to exhibit a Schottky barrier and, hence, finds numerous applications in the manufacturing of diodes, transistors and other devices [7-12]. Despite of these interesting applications, only very few basic studies have been done on this system. In particular the challenges in the preparation of a well-ordered Al surface might have hindered the experimental investigations, while the previous ab initio theoretical studies [13,14] on this system were missing long-range

van der Waals (vdW) corrections. Simeoni and Picozzi reported a numerical investigation of pentacene on Al(001) by density functional theory (DFT) with the local density approximation (LDA) and the generalized gradient approximation (GGA) [13]. They found that the interaction between pentacene and Al is rather weak and adsorption occurs at a height from the surface of about 5.71 Bohr (3.02 Å) in LDA and of 7.20 Bohr (3.81 Å) in GGA, with a molecular corrugation of 0.74 Å in LDA. The same system was later investigated with LDA and GGA by Saranya et al. [14] who also obtained a very weak adsorption energy with pentacene adsorbed at larger distances from the Al surface (3.4 Å) in LDA and comparable to the previous ones in GGA. Both papers also report Schottky barriers at the junction due to the interfacial electron transfer.

In our recent work [15], we studied experimentally and theoretically the adsorption of pentacene on the Al(001) substrate. We performed simulations including the long range vdW interactions and without them. In the latter case we observed that the bonding energy is clearly underestimated. In our calculations including vdW, the most stable adsorption site is found to be the bridge (B) site where the adsorbed pentacene is bent around the central C atoms, which are more strongly bound to the surface Al atoms, forming a V-shape with the long molecular axis aligned along the [110] direction [15]. A similar V-shaped deformation was also obtained in the configuration with the long molecular axis along the [010] direction but with 0.42 eV higher adsorption energy. On the contrary, other adsorption configurations would result in planar molecular geometries with higher adsorption energies (at least by 0.7 eV) and hence are considered unphysical. Scanning tunneling microscopy (STM) measurements showed that a large percentage of pentacene molecules adsorb with a V-shape on a reconstructed Al(001) surface with the longer axis along the [110] direction. The calculated results of XPS and NEXAFS assuming the V-shaped adsorption are in agreement with the experiments. For comparison only a minor bending of the molecule was reported in experimental and theoretical studies of pentacene on Au(111) [16], Cu(110) [17], and Cu(001) [18], while an asymmetric adsorption along the long edge was determined for Co islands on Cu(111) [19].

The peculiar V-shaped bending attained in our work [15] is a very interesting feature, which was never reported before and whose influence on the electronic and spectroscopic properties of the interface is investigated in this paper. We evaluate by DFT the screening charges of the adsorbed system and relate them to the deformation of pentacene. Comparison of the results with those obtained for the undistorted non-physical adsorption at top (T) site allows for a better understanding of the system properties. The contributions to XPS and NEXAFS of non-equivalent carbon atoms in which a 1s core hole is created are calculated. Together with the screening charges they allow for a detailed understanding of the spectral features as modified by the molecular V-shaped distortion.

Results and Discussion

Origin of the V-shape

In Baby et al. we showed that the most stable bonding configuration of pentacene on Al(001) is the B-site [15]. As depicted in Figure 1a,c this configuration is highly distorted around the central C atoms (1,1') so as to bind on top of the two surface Al atoms at the short C–Al distance of 2.20 Å. As a comparison, Figure 1b,d show the undistorted adsorption configuration as it is calculated at a T site. Bending at the central position is in agreement with the findings about the reactivity of pentacene and related molecules [20], as described in terms of the molecular aromaticity (defined as the ability of the π-electrons to delocalize above and below the plane of cyclic molecules resulting in their extra stabilization [21,22]). If we consider benzene the most aromatic molecule as an example, as more rings are added to it, the electron density within the molecule rearranges in such

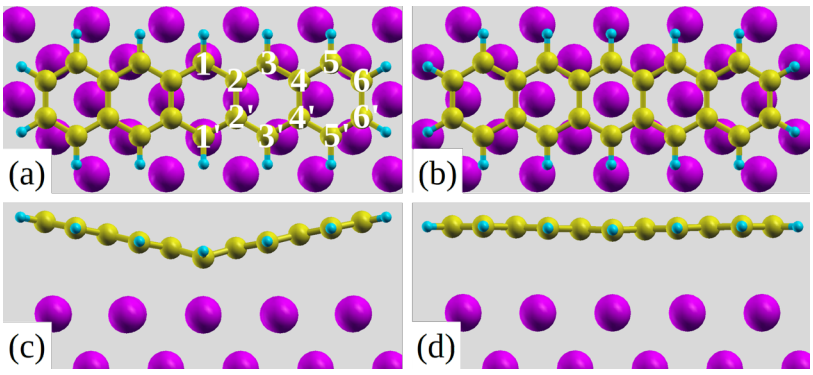

Figure 1: Top views (a), (b) and side views (c), (d) of bridge (B) and top (T) sites, respectively, where (a) also shows the numbering of the C atoms.

a manner that it is largest for the central ring (hence highly reactive even if more aromatic) and decreases towards the outer ones [23,24]. Taking part in reactions through the most aromatic central ring is convenient for the molecule as the activation energy barrier is lower [25]. Furthermore the HOMO coefficients are highest for the central carbon atoms in acenes and decrease towards the outer ring ones [25]. Other studies related reactivity to the ring current showing that this is highest for the central ring in the case of pentacene and also the highest proton chemical shift is found for the hydrogen atoms attached to the central carbon atoms in the case of acenes [26]. All these results support the reactive nature of the central carbon atoms in pentacene. In agreement with such properties we verified that V-shaped pentacene bonds to the Al atoms underneath through the two central carbon atoms of the innermost phenyl ring as the distance between them (C1–C1', see Figure 1a for numbering) becomes comparable to the Al–Al one.

Effects of V-shape on bond length

The V-shaped molecular deformation influences the carbon–carbon bond lengths of adsorbed pentacene. This is reported in Table 1, in which the bond lengths of the free molecule in the gas phase (g) are compared to those of the molecule adsorbed flat and bent at T and B sites, respectively. A common trend is found while moving from the free molecule to the flat and to the bent adsorbed molecule, as they keep either increasing or decreasing, conversely decreasing or increasing the π-character of those bonds [27]. Note that the bond lengths for g and T cases are very similar and different from those of the B configuration. Due to the strong coupling between C1 and the underlying Al atom at the B site the C1–C2 bond experiences the highest variation in length, which increases by 0.07 Å from g to B. Such an elongation occurs because the C1 orbital modifies from sp^2 to sp^3 hybridization, which results in a displacement of the valence electron density of C1 from the C1–C2 bond to the newly formed C1–Al bond, as recently discussed for self-assembled monolayers [28]. This further affects the delicate electron density balance within the molecule, i.e., while the C1–C2 bond length increases (decreasing π-character), the C2–C2' bond length decreases (increasing π-character) at the B site. This kind of rearrangement in the electron density reduces the aromaticity of the central carbon ring of pentacene but in a smaller way than that for bending through the outer rings [25], as discussed before. Furthermore we observe shorter C2–C2', C4–C4' and C6–C6' bond lengths (with an average of about 0.02 Å) moving from second to fourth column of Table 1 additionally indicating that the molecule shrinks along the short molecular axis. On the contrary an increase in the length of the molecule is observed along the long axis in the B configuration hinting a slight weakening in the coupling of outer atoms with respect to those of pentacene in gas phase. Summarizing, the differences between the bond lengths in the two directions reduces.

Table 1: Carbon–carbon bond lengths for free pentacene (g) and for pentacene adsorbed at the top (T) and the bridge (B) site.

C–C	g (Å)	T (Å)	B (Å)
C1–C2	1.400	1.408	1.466
C2–C3	1.411	1.409	1.396
C3–C4	1.390	1.400	1.420
C4–C5	1.429	1.423	1.414
C5–C6	1.368	1.375	1.383
average	1.400	1.403	1.416
C2–C2'	1.458	1.454	1.428
C4–C4'	1.453	1.448	1.428
C6–C6'	1.427	1.422	1.410
average	1.446	1.441	1.422

Ground-state electronic properties and charge transfer

We now quantify the interactions taking place between the molecule and the metal substrate in terms of charge transfer upon adsorption. The isodensity plots showing the three-dimensional charge rearrangements for pentacene at B and T sites are shown in Figure 2, which can be defined using the equation $\Delta\rho = \rho(\text{pentacene/Al}) - \rho(\text{pentacene}) - \rho(\text{Al})$, where ρ(pentacene/Al) is the total charge of the combined system, ρ(pentacene) is that of the non-interacting pentacene monolayer and ρ(Al) is that of the non-interacting Al substrate (all atoms are fixed at the same positions as in the combined system). Red colour indicates regions of higher electron density and blue ones of lower density. For B site adsorption, at an isovalue of $\Delta\rho = 0.005$ e/Bohr^3 we can clearly observe in Figure 2c accumulation of electron density between the two central carbon atoms (C1 and C1') and the two Al atoms underneath them confirming the bonding of the molecule at that specific site. At a lower isovalue (0.002 e/Bohr^3), as depicted in Figure 2a,b we can see that such charge originates from the electronic density depletion in the close proximity of the C–Al bond, with overall electron transfer from the surface to pentacene. An excess electronic charge of $\Delta Q = 0.56e$ is calculated on the adsorbed molecule, by means of Löwdin charge partitioning scheme [29,30]. One also observes (see the red regions in Figure 2a,b) electron accumulation between the atoms C3, C3' and the surface, while other C atoms at larger distances are clearly less interacting with the surface. Intramolecular charge displacements in Figure 2a show electronic charge accumulation between the atoms C3–C2–C2'–C3'. It has to be stressed that at the same

isovalue, no charge restructuring is visible for the flat molecule at the T site and hence a lower isovalue of 0.001 e/Bohr^3 is chosen in Figure 2d to plot a much less localized charge displacement amounting to $\Delta Q = 0.20e$.

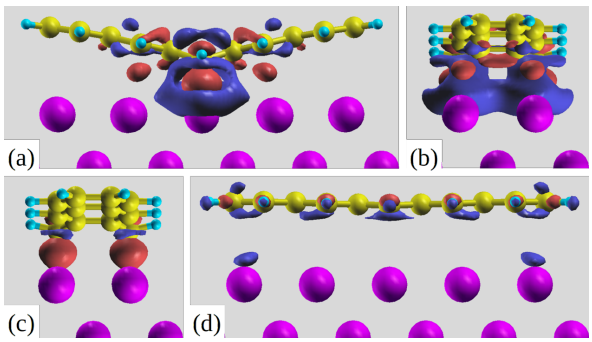

Figure 2: (a,b) Side views of the isodensity plot showing the bond charge of pentacene at the B-site for an isodensity = 0.002 e/Bohr^3 (red regions: high electron density and blue regions: low electron density), (c) pentacene at the B-site for an isodensity of 0.005 e/Bohr^3, (d) pentacene at the T-site for an isodensity of 0.001 e/Bohr^3.

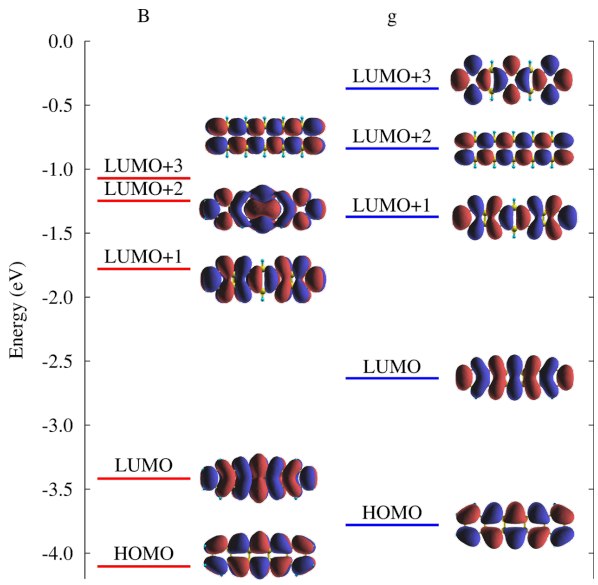

Figure 3: Comparison between the Kohn–Sham eigenvalues of the V-shaped gas phase pentacene with coordinates extracted from the bridge site adsorption (B) and the undistorted gas phase one (g). The corresponding orbital wave functions are also shown for each case.

The structural change in the V-shape of adsorbed pentacene induces alterations in the molecular orbitals, which are best perceived by looking first at the gas-phase molecule, but with the same geometry as that in the B site. In particular, the Kohn–Sham eigenvalues for bent and flat molecules are compared in Figure 3. One of the major features emerging is the reduction in the HOMO–LUMO gap of the free V-shaped molecule by 0.5 eV which decreases further for adsorption at the B site due to electron transfer. Upon adsorption, these states broaden and spread as a result of the substantial hybridization with the Al surface states. In particular for the LUMO an appreciable filling was observed as this state displays an energy range as large as 4 eV with its main peak below the Fermi energy level [15]. From the results in Figure 3 we add that the orbital corresponding to the LUMO+2 of the undistorted free molecule becomes the LUMO+3 of the V-shaped gas phase molecule (also compare with Table 2 below). This point is relevant in explaining the NEXAFS features in the following.

XPS

To understand the XPS features we connect the calculated core level shifts (CLS) to the screening charge of the system. The CLS are computed as the difference between the total energy of the system in the presence of a full core hole on the different non-equivalent C atoms and its weighted average taking into account their multiplicity. In Figure 4 we plot the core level C 1s photoemission spectra (XPS) obtained by experiment, and by simulations for free undistorted pentacene and pentacene adsorbed at T and B sites. Calculated initial state-binding energies are indicated as vertical bars with height proportional to the multiplicity of the non-equivalent carbon atoms (see Figure 1). These vertical bars when broadened (here with pseudo-Voigt profiles having 0.52 eV Lorentzian and 0.36 eV Gaussian full width at half maximum) determine the simulated XPS spectra reported in Figure 4. We remark that the use of a pseudopotential scheme does not allow us to access the absolute energy values and hence the simulated spectra are aligned to the experimental ones. The C 1s CLS spectrum computed in the gas phase [31], Figure 4a, is already able to capture the main features of the experimental result for adsorbed pentacene [15]. When we consider pentacene adsorbed on Al(001) at the T site, Figure 4b, the agreement actually worsens as the spectrum becomes too broad. Conversely, a good agreement is eventually observed for such V-shaped molecule on the B site, see Figure 4c, where the CLSs are smaller, further supporting the structural model.

The differences in the spectra reported in Figure 4 can be understood stepwise as follows. When the molecule is adsorbed almost undistorted at the T site, it may be affected by the surface coupling through several effects [32]. First, the full molecule is subjected to an effective potential due to the Al surface that influences similarly all atoms in the planar configuration and results in no net CLS. Second, the surface electrons screen the perturbation of the core hole, which is at the same distance in all cases determining, a net electron transfer, which may induce changes in the CLS. This effect can be estimated by performing additional simulations for the free undistorted molecule to calculate the shifts in binding energies as a function of a

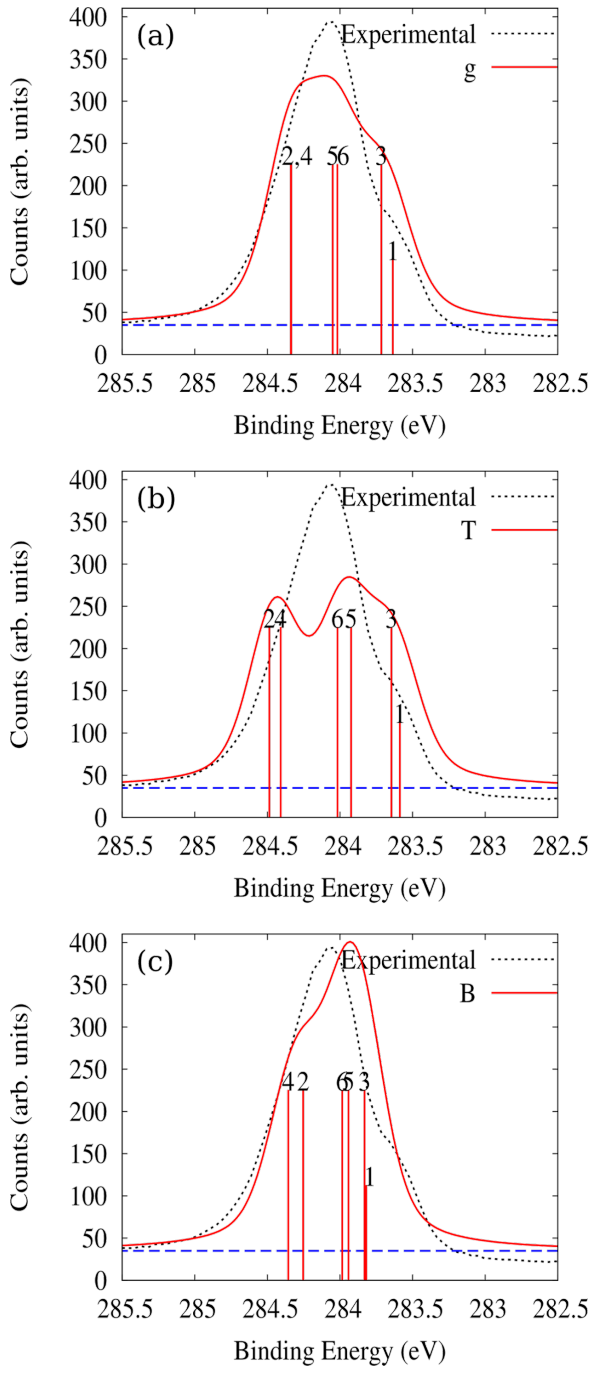

Figure 4: Experimental C 1s XPS spectrum for pentacene/Al(001) compared with the simulated spectra of (a) free pentacene, g, (b) pentacene at the T site and (c) pentacene at the B site. The individual contributions from the six non-equivalent carbon atoms are shown as vertical bars. These are convoluted with pseudo-Voigt profiles with 0.52 eV Lorentzian and 0.36 eV Gaussian full widths at half maximum and offset by a constant (see the dashed blue line) to obtain the simulated spectra (solid red line).

given excess electronic charge uniformly distributed. Such an excess charge results in a more negative shift of the binding energy for atoms C1, C3 and C5 and a more positive one for the C2, C4 and C6 energies, providing a broader spectrum in the charged molecule case (not shown in this paper) than in the gas phase neutral one. In particular, the C1–C2 binding energy difference amounts to 0.70 eV in the gas phase for neutral molecules and increases to 0.76 eV (0.84 eV) with 0.2 (0.5) additional electrons, in qualitative agreement to the value of 0.86 eV computed at the T site. Indeed, comparing Figure 4a and Figure 4b we point out that the excess charge is unevenly redistributed in the molecule, i.e., more electron density around C1, C3 and C5 and less around C2, C4 and C6, see also the LUMO amplitude in Figure 3. This reduces/increases the binding energy of 1s electrons in the first/second group of atoms, respectively [32].

This simple argument alone cannot explain the narrowing of the spectrum as we move from the T to the B site, where charge transfer upon adsorption is even higher but the C2–C1 binding energy difference amounts to 0.43 eV only (0.54 eV for C4–C1). Here the additional effect exists that the potential of the aluminum surface experienced by the various carbon atoms, is not a constant any more as the C atom heights differ by up to 1.35 Å. However, a non monotonic dependence on distance is observed, as a similar variation with respect to C2 is computed for C1 and C3 which are at smaller and larger heights respectively. Hence, the variations in screening offered by the system for the hole at the various sites must play an important role. To visualize such variations, we evaluated the screening charge following the C 1s level ionization, which we define as: $\Delta\rho^* = \rho(\text{pentacene}^{fch}/\text{Al}) - \rho(\text{pentacene/Al})$, where $\rho(\text{pentacene}^{fch}/\text{Al})$ is the total charge of the combined system with a full core hole on the selected C atom, and ρ(pentacene/Al) is that of the combined system in its ground state. The same is compared in Figure 5 for the T and B sites, in the presence of a full core hole on atoms C1 and C2. We observe that the screening charge at the T site is similar for the two atoms C1 and C2 (Figure 5a–f), when seen from the excited atom, and that the largest charge displacements are localized in its proximity. Conversely, $\Delta\rho^*$ for the molecule at the B site (Figure 5g–l) extends throughout the molecule as it also involves large contributions from the π system polarizing towards the surface, because the planar symmetry of pentacene is lost at the B site. Note in particular the region of electron depletion (blue coloured) that is observed in Figure 5h,i just above the Al atom located below the 1s-excited C1: such depletion corresponds to a reduction of the C–Al bond shown in Figure 2c, and is absent in Figure 5k,l for excitation on C2. Hence, a larger destabilization of adsorption is expected for the core hole in C1 than in C2. Therefore the presence of core hole reduces the binding energy of C2 and

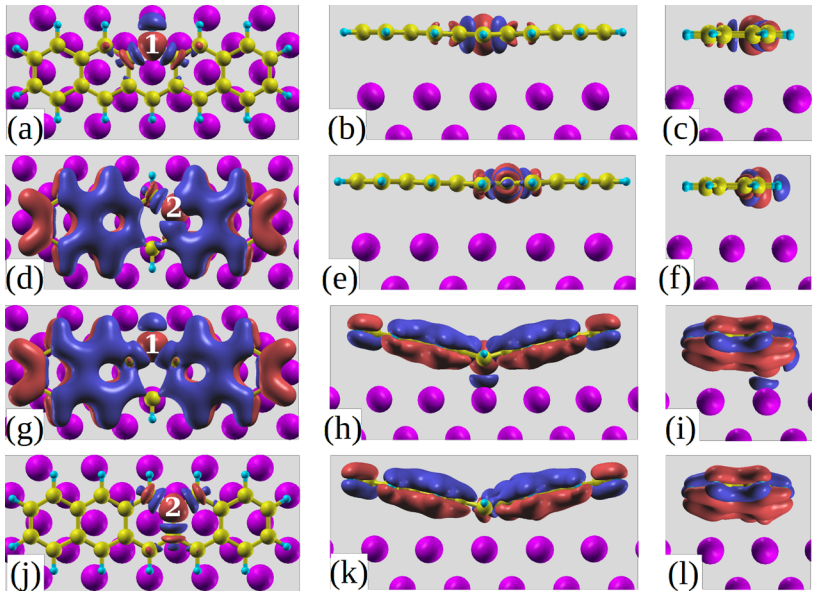

Figure 5: Top and side views of the screening charges in the presence of a full core hole on (a,b,c) C1 at the T site; (d,e,f) C2 at the T site; (g,h,i) C1 at the B site and (j,k,l) C2 at the B site for an isodensity value of 0.005 *e*/Bohr^3.

increases that of C1 in agreement with a reduction in the difference between their core level binding energies thereby determining a narrower spectrum for B site adsorption as seen in Figure 4c and compensating the effects of electron transfer.

NEXAFS

We wish now to relate the simulated NEXAFS spectrum of pentacene/Al(001) with the electronic properties of the system. The calculation of NEXAFS is performed with half a core hole in the carbon 1s orbital. It is convenient to consider first a molecule in the gas phase but retaining the V-shaped geometry as in Figure 3. In particular, let us focus on the transitions to the lowest lying LUMO states with π^* symmetry, which characterize the low-energy part of the spectrum for the different C atoms. This for photon electric field along the *z*-direction, i.e., perpendicular to the plane of the molecule is shown in Figure 6 as a solid line. Owing to the lack of absolute energy reference from the calculation, this spectrum is arbitrarily offset so as to align it with the most prominent features in the spectra measured for absorbed molecules (to be presented subsequently). The contributions by individual excitations (initial and final states) is also marked in Figure 6 by vertical bars displaying the projected amplitude of the final state on the p_z atomic states of the absorbing atoms, which produces a good qualitative description of the NEXAFS spectrum [31,33]. One can see two visibly separated broad features with multiple peaks. The first one (spanning the energy range between 282.5 eV and 284 eV) is completely due to the core–electron excitations to the LUMO of pentacene. The first peak of the second broad feature lying between 284.5 and 285.5 eV is mainly constituted by the LUMO+1 excitations and partly also by the LUMO+2 ones. The larger energy contributions to the second broad feature are from higher lying LUMO+*i* orbitals. One has to recall that the presence of a half core hole affects the molecular orbitals resulting into their intermixing and hybridization, as compared to the ground state. To show this, in Table 2 we report the overlap between the molecular orbitals of the excited V-shaped molecule in gas phase with those of the

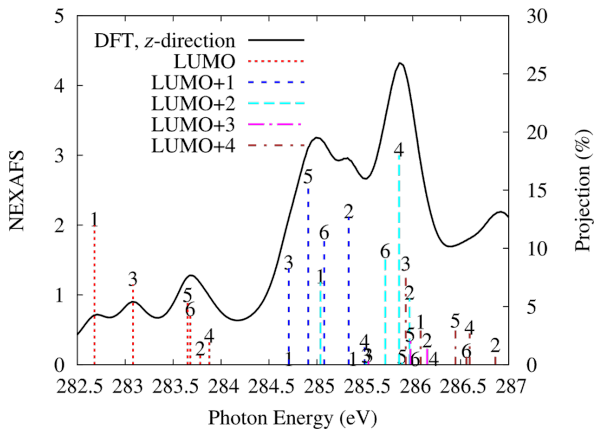

Figure 6: Simulated NEXAFS of the gas phase V-shaped pentacene from the B-site along the *z*-direction of the field, perpendicular to the molecular plane. For excitations from each C atom, the vertical bars numbered correspondingly show the projection of the various molecular orbitals, computed with a half core hole in that atom, on the $2p_z$ state of the same carbon atom, and are referred to the axis on the right (in %).

Table 2: Overlap of the molecular orbitals of the gas phase pentacene with a half core hole (hch) at C1 in the V-shaped geometry, with those of the free molecule in the ground state, g. Values below 0.5% are not reported here.

$C1^{hch}$	orbitals of the free molecule in the ground state (g)			
	LUMO	LUMO+1	LUMO+2	LUMO+3
LUMO	77.2%	—	—	5.6%
LUMO+1	—	89.2%	—	—
LUMO+2	11.0%	—	—	51.4%
LUMO+3	—	—	86.5%	—
LUMO+4	—	—	—	9.5%
LUMO+5	—	—	—	16.8%

ground state of the free molecule (g), which are referred as former LUMOs, selecting as a representative example that of excited C1.

We can observe that the presence of a half core hole has not affected the LUMO but has significantly altered the higher lying LUMOs as also found for perylene derivatives [33] (here, from the LUMO+2). It is noteworthy that a free pentacene molecule has a nodal plane for (former) LUMO+1 and LUMO+2 along the central carbon atoms C1 and C1' (see Figure 3) so no contribution to NEXAFS would be expected by transitions to these molecular orbitals from the 1s orbital of C1 at variance with the result in Figure 6 of a non-negligible contribution from the transition from the C1 1s to the LUMO+2. This is because we verified that the LUMO+2 and LUMO+3 orbitals get interchanged due to the V-shaped bending of pentacene already in the ground state, where its structural deformation causes the former LUMO+2 to shift to a higher energy than that of LUMO+3, which is retained also with the core hole. Indeed, now the LUMO+2 displays contributions by the former LUMO and LUMO+3 (see Table 2). Furthermore, we can see that LUMO+3 in Figure 6 has no weight on C1, as it originates mostly from the LUMO+2 of the undistorted free molecule which has moved to higher energy. In the case of adsorbed pentacene, the molecular orbitals broaden due to hybridization with the substrate states extending into overlapping energy ranges, hampering a similar analysis in terms of final states.

Figure 7 shows the simulated NEXAFS spectra for pentacene adsorbed at the B site in (a) p-polarization with the electric field perpendicular and (b) s-polarization with the electric field parallel to the surface. The long molecular axis is directed along the *x*-direction and the short one along the *y*-direction. There, we show the spectrum decomposed in terms of initial state effects, and we compare it to the experimental result (dashed line) [15]. Looking at the upper panel (a) of Figure 7, we can see a nice agreement between the experimental and simulated p-polarization (solid line) spectra. The simulated spectrum is arbitrarily aligned to the most prominent double peaked experimental feature centered at 285.5 eV which can be attributed to the π^* resonances. The first peak of the π^* resonance consists of contributions from all the atoms except C1 and C4. The second peak has contributions from all the atoms but with a larger weight from C4. It can be observed that the π^* resonances in Figure 7 have narrowed down compared to those of the V-shaped gas phase pentacene in Figure 6. It was mentioned before that the V-shaped structural deformation alone reduces the HOMO–LUMO gap of the free molecule by 0.5 eV which facilitates the filling of LUMO by getting electronic charge

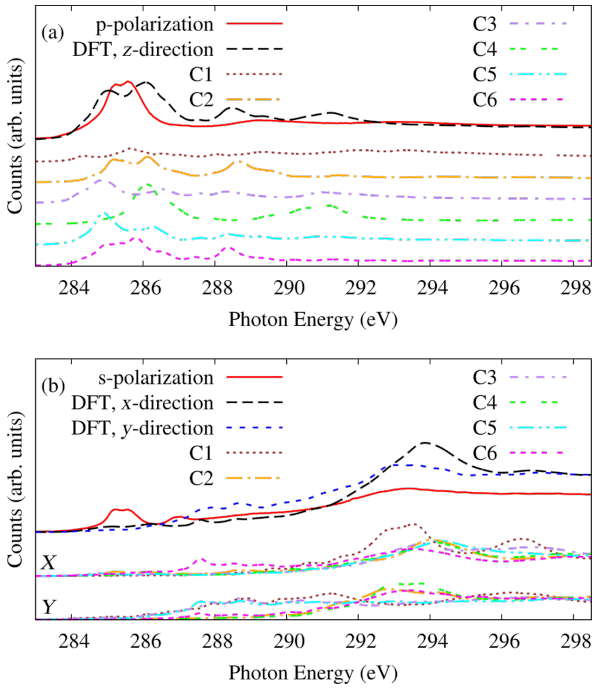

Figure 7: (a) Analysis of the initial state effects in the simulated NEXAFS spectrum and its comparison with the experimental one measured in p-polarization (electric field along *z*, i.e., perpendicular to the surface). (b) Same as (a), in s-polarization. Simulations are shown for electric field in the *x*- and *y*-directions, i.e., along the long and short molecular axes.

from aluminum and is hence absent in the NEXAFS spectrum [15]. In pentacene, C1 has the highest weight on LUMO but instead a node for LUMO+1 as can be seen in Figure 3. Hence, the absence of a significant contribution from C1 in the first peak of the π^* resonances in Figure 7 further confirms that it corresponds to the transitions to the LUMO+1 rather than the LUMO of the molecule.

Now let us look at the σ^* resonances of Figure 7b where the simulated NEXAFS computed for the molecule at the B site along the *x*- and *y*-directions (long and short molecular axes) are compared to the experimental NEXAFS in s-polarization. The experimental s-polarization has been averaged over the [110] and [001] surface azimuths, which provide very similar results as differently oriented domains are sampled. The experimental spectrum still displays some π^* resonance leftover centered at around 285.5 eV. This effect is not completely reproduced in the simulated spectrum even if we observe some non-zero contributions, which are due to the V-shaped molecules forming an angle of about 13° with the surface plane. Looking at the main σ^* peak centered at around 294 eV, we observe a small energy splitting between transitions with the electric field along the long and short molecular axes. This phenomenon called the azimuthal dichroism is much reduced, as compared to that of the free molecule. In the latter case, such energy splitting amounts to about 2 eV and was attributed equally to the intrinsic asymmetry of the molecule and to the shorter C–C bond lengths along the long molecular axis than that along the short one [31]. For adsorbed V-shaped molecules, the bond lengths along the two directions are more similar, as we reported in Table 1. Still the molecule being inherently anisotropic determines the residual azimuthal dichroism reduced to approx. 1 eV. Reporting the initial state contributions in this energy range, the *x*-direction spectrum has largest contributions by the core excitations from C1 whereas the *y*-direction one mainly by those from the carbon atoms C2, C4 and C6.

Conclusion

The pentacene/Al(001) system was studied by means of DFT methods in order to understand how the electronic structure of the V-shaped adsorbed molecule affects the XPS and the NEXAFS results. The rationale of the most stable configuration, the bridge one, where the molecule adsorbs by bending into V-shape with its long molecular axis along the [110] direction on the Al(001) with a V-angle of 155°, has been accounted for. By analyzing the molecule–surface bond charge and how this is modified to screen the core level excitation, we demonstrate that the similarity of the observed XPS spectrum for the adsorbed molecules results from the compensation between a line shape broadening induced by charge transfer, and a narrowing due to excitation site dependent screening. The latter effect would be absent for non-physical undistorted molecules. NEXAFS spectra, resolved into individual atomic initial states, show no contribution by the LUMO and provide evidence for hybridization and interchange of molecular orbitals facilitated by the V-shape. A smaller azimuthal dichroism in NEXAFS associated with the energy splitting of the sigma resonances, is computed and explained in terms of modified C–C bond lengths.

Computational Methods

The DFT calculations of the pentacene/Al(001) system were carried out using the Quantum-ESPRESSO package [34]. We choose the GGA as proposed by Perdew, Burke, and Ernzerhof (PBE) [35] for the exchange correlation functional. Plane waves and ultrasoft pseudopotentials generated with the Rappe, Rabe, Kaxiras, and Joannopoulos scheme [36] with a planewave cutoff of 27 Ry are used for relaxation and total energy calculations. The aluminum (001) surface is modeled by a slab with three layers of atoms, in a rectangular (8 × 5) surface unit cell. The repeated slab method is used with a vacuum space of 20 Å in the *z*-direction separating adjacent slabs. The surface Brillouin zone is integrated using a Monkhorst–Pack [37] set of special 2 × 3 grid of k-points and Methfessel–Paxton smearing [38] with a broadening of 0.02 Ry. The van der Waals interactions between the molecule and the surface are taken into account by adding semi empirical London dispersion forces in the Grimme approach [39] excluding the interactions within the Al atoms. The coordinates of pentacene deposited on only one side of the slab as well as the first layer of Al atoms were optimized as presented in Baby et al. [15] and are shown in Figure 1 for selected configurations (B and T sites). Modeling of the adsorption behavior of pentacene on the reconstructed Al surface has not been carried out as the molecule-induced reconstruction was found to be incommensurate and also because the accurate information about the surface structure is not available from the experiments. However calculations for the reconstructed surface are not expected to affect our computed XPS and NEXAFS spectra which are in very good agreement with experiments [15].

The XPS spectrum is computed in terms of the core level shifts (CLS) as defined in the text [40,41]. We remark that, differently from free molecules, the core hole in adsorbed molecules is eventually neutralized by the valence electrons from the metal substrate, so a globally neutral cell was used [42]. The corresponding core level shifts are computed with reference to the Fermi level of the substrate, as obtained in the experiments. The NEXAFS spectra are simulated using the xspectra code in Quantum-ESPRESSO [43,44]. We considered a half core hole in the carbon 1s orbital following the transition-potential

approach introduced by Triguero et al. [45] as such calculations can reproduce the main features of the spectral profiles [31,33]. For XPS and NEXAFS calculations, the core level excitations were modeled by carbon pseudopotentials with a full and half core hole, respectively, in the 1s orbital (requiring a higher plane wave cutoff of 59 Ry). By the pseudopotential approach, absolute transition energies are not accessible and as a consequence the simulated spectra have been aligned to the experimental ones.

Acknowledgements

We acknowledge support from the MIUR of Italy through PRIN project DSSCX (no. 20140XET32). This work has been developed under the European doctorate programme PCAM. Computational resources were made available in part by CINECA (application HP10CESYLM).

References

1. Lin, Y.-Y.; Gundlach, D. J.; Nelson, S. F.; Jackson, T. N. *IEEE Electron Device Lett.* **1997,** *18,* 606–608. doi:10.1109/55.644085
2. Nickel, B.; Fiebig, M.; Schiefer, S.; Göllner, M.; Huth, M.; Erlen, C.; Lugli, P. *Phys. Status Solidi A* **2008,** *205,* 526–533. doi:10.1002/pssa.200723372
3. Witte, G.; Wöll, C. *J. Mater. Res.* **2004,** *19,* 1889–1916. doi:10.1557/JMR.2004.0251
4. Rolin, C.; Steudel, S.; Myny, K.; Cheyns, D.; Verlaak, S.; Genoe, J.; Heremans, P. *Appl. Phys. Lett.* **2006,** *89,* 203502. doi:10.1063/1.2388864
5. Kelley, T. W.; Baude, P. F.; Gerlach, C.; Ender, D. E.; Muyres, D.; Haase, M. A.; Vogel, D. E.; Theiss, S. D. *Chem. Mater.* **2004,** *16,* 4413–4422. doi:10.1021/cm049614j
6. Facchetti, A. *Mater. Today* **2007,** *10,* 28–37. doi:10.1016/S1369-7021(07)70017-2
7. Pandey, A. K.; Shaw, P. E.; Samuel, I. D. W.; Nunzi, J.-M. *Appl. Phys. Lett.* **2009,** *94,* 103303. doi:10.1063/1.3098472
8. Steudel, S.; Myny, K.; Arkhipov, V.; Deibel, C.; De Vusser, S.; Genoe, J.; Heremans, P. *Nat. Mater.* **2005,** *4,* 597–600. doi:10.1038/nmat1434
9. Nádaždy, V.; Durný, R.; Puigdollers, J.; Voz, C.; Cheylan, S.; Gmucová, K. *Appl. Phys. Lett.* **2007,** *90,* 092112. doi:10.1063/1.2710203
10. Kim, C.; Jeon, D. *J. Korean Phys. Soc.* **2010,** *57,* 1702–1706. doi:10.3938/jkps.57.1702
11. Lee, Y. S.; Park, J. H.; Choi, J. S. *Opt. Mater.* **2003,** *21,* 433–437. doi:10.1016/S0925-3467(02)00178-7
12. Tondelier, D.; Lmimouni, K.; Vuillaume, D.; Fery, C.; Haas, G. *Appl. Phys. Lett.* **2004,** *85,* 5763–5765. doi:10.1063/1.1829166
13. Simeoni, M.; Picozzi, S.; Delley, B. *Surf. Sci.* **2004,** *562,* 43–52. doi:10.1016/j.susc.2004.05.015
14. Saranya, G.; Nair, S.; Natarajan, V.; Kolandaivel, P.; Senthilkumar, K. *J. Mol. Graphics Mod.* **2012,** *38,* 334–341. doi:10.1016/j.jmgm.2012.06.008
15. Baby, A.; Fratesi, G.; Vaidya, S. R.; Patera, L. L.; Africh, C.; Floreano, L.; Brivio, G. P. *J. Phys. Chem. C* **2015,** *119,* 3624–3633. doi:10.1021/jp512337y
16. Schroeder, P. G.; France, C. B.; Park, J. B.; Parkinson, B. A. *J. Appl. Phys.* **2002,** *91,* 3010–3014. doi:10.1063/1.1445286
17. Müller, K.; Seitsonen, A. P.; Brugger, T.; Westover, J.; Greber, T.; Jung, T.; Kara, A. *J. Phys. Chem. C* **2012,** *116,* 23465–23471. doi:10.1021/jp308058u
18. Ferretti, A.; Baldacchini, C.; Calzolari, A.; Di Felice, R.; Ruini, A.; Molinari, E.; Betti, M. G. *Phys. Rev. Lett.* **2007,** *99,* 046802. doi:10.1103/PhysRevLett.99.046802
19. Chu, Y.-H.; Hsu, C.-H.; Lu, C.-I.; Yang, H.-H.; Yang, T.-H.; Luo, C.-H.; Yang, K.-J.; Hsu, S.-H.; Hoffmann, G.; Kaun, C.-C.; Lin, M.-T. *ACS Nano* **2015,** *9,* 7027–7032. doi:10.1021/acsnano.5b03117
20. Zade, S. S.; Zamoshchik, N.; Reddy, A. R.; Fridman-Marueli, G.; Sheberla, D.; Bendikov, M. *J. Am. Chem. Soc.* **2011,** *133,* 10803–10816. doi:10.1021/ja106594v
21. Zhou, Z.; Parr, R. *J. Am. Chem. Soc.* **1989,** 7371–7379. doi:10.1021/ja00201a014
22. Geerlings, P.; De Proft, F.; Langenaeker, W. *Chem. Rev.* **2003,** *103,* 1793–1873. doi:10.1021/cr990029p
23. Cheng, M.-F.; Li, W.-K. *Chem. Phys. Lett.* **2003,** *368,* 630–638. doi:10.1016/S0009-2614(02)01955-3
24. Howard, S. T.; Krygowski, T. M. *Can. J. Chem.* **1997,** *75,* 1174–1181. doi:10.1139/v97-141
25. Von Ragué Schleyer, P.; Manoharan, M.; Jiao, H.; Stahl, F. *Org. Lett.* **2001,** *3,* 3643–3646. doi:10.1021/ol016553b
26. Steiner, E.; Fowler, P. W. *Int. J. Quantum Chem.* **1996,** *60,* 609–616. doi:10.1002/(SICI)1097-461X(1996)60:1<609::AID-QUA58>3.0.CO;2-1
27. Wiberg, K. B. *J. Org. Chem.* **1997,** *62,* 5720–5727. doi:10.1021/jo961831j
28. Ossowski, J.; Rysz, J.; Krawiec, M.; Maciazek, D.; Postawa, Z.; Terfort, A.; Cyganik, P. *Angew. Chem., Int. Ed.* **2015,** *54,* 1336–1340. doi:10.1002/anie.201406053
29. Löwdin, P.-O. *J. Chem. Phys.* **1950,** *18,* 365–375. doi:10.1063/1.1747632
30. Löwdin, P. O. On the Nonorthogonality Problem. *Advances in Quantum Chemistry;* Elsevier, 1970; pp 185–199.
31. Fratesi, G.; Lanzilotto, V.; Floreano, L.; Brivio, G. P. *J. Phys. Chem. C* **2013,** *117,* 6632–6638. doi:10.1021/jp312569q
32. Cabellos, J. L.; Mowbray, D. J.; Goiri, E.; El-Sayed, A.; Floreano, L.; de Oteyza, D. G.; Rogero, C.; Ortega, J. E.; Rubio, A. *J. Phys. Chem. C* **2012,** *116,* 17991–18001. doi:10.1021/jp3004213
33. Fratesi, G.; Lanzilotto, V.; Stranges, S.; Alagia, M.; Brivio, G. P.; Floreano, L. *Phys. Chem. Chem. Phys.* **2014,** *16,* 14834–14844. doi:10.1039/c4cp01625d
34. Giannozzi, P.; Baroni, S.; Bonini, N.; Calandra, M.; Car, R.; Cavazzoni, C.; Ceresoli, D.; Chiarotti, G. L.; Cococcioni, M.; Dabo, I.; Dal Corso, A.; de Gironcoli, S.; Fabris, S.; Fratesi, G.; Gebauer, R.; Gerstmann, U.; Gougoussis, C.; Kokalj, A.; Lazzeri, M.; Martin-Samos, L.; Marzari, N.; Mauri, F.; Mazzarello, R.; Paolini, S.; Pasquarello, A.; Paulatto, L.; Sbraccia, C.; Scandolo, S.; Sclauzero, G.; Seitsonen, A. P.; Smogunov, A.; Umari, P.; Wentzcovitch, R. M. *J. Phys.: Condens. Matter* **2009,** *21,* 395502. doi:10.1088/0953-8984/21/39/395502
35. Perdew, J. P.; Burke, K.; Ernzerhof, M. *Phys. Rev. Lett.* **1996,** *77,* 3865–3868. doi:10.1103/PhysRevLett.77.3865
36. Rappe, A. M.; Rabe, K. M.; Kaxiras, E.; Joannopoulos, J. D. *Phys. Rev. B* **1990,** *41,* 1227–1230. doi:10.1103/PhysRevB.41.1227
37. Pack, J. D.; Monkhorst, H. J. *Phys. Rev. B* **1977,** *16,* 1748–1749. doi:10.1103/PhysRevB.16.1748
38. Methfessel, M.; Paxton, A. T. *Phys. Rev. B* **1989,** *40,* 3616–3621. doi:10.1103/PhysRevB.40.3616

39. Grimme, S. *J. Comput. Chem.* **2004,** *25,* 1463–1473. doi:10.1002/jcc.20078
40. Pehlke, E.; Scheffler, M. *Phys. Rev. Lett.* **1993,** *71,* 2338–2341. doi:10.1103/PhysRevLett.71.2338
41. Bianchettin, L.; Baraldi, A.; De Gironcoli, S.; Lizzit, S.; Petaccia, L.; Vesselli, E.; Comelli, G.; Rosei, R. *Phys. Rev. B* **2006,** *74,* 045430. doi:10.1103/PhysRevB.74.045430
42. García-Gil, S.; García, A.; Ordejón, P. *Eur. Phys. J. B* **2012,** *85,* 239. doi:10.1140/epjb/e2012-30334-5
43. Taillefumier, M.; Cabaret, D.; Flank, A.-M.; Mauri, F. *Phys. Rev. B* **2002,** *66,* 195107. doi:10.1103/PhysRevB.66.195107
44. Gougoussis, C.; Calandra, M.; Seitsonen, A. P.; Mauri, F. *Phys. Rev. B* **2009,** *80,* 075102. doi:10.1103/PhysRevB.80.075102
45. Triguero, L.; Pettersson, L. G. M.; Ågren, H. *Phys. Rev. B* **1998,** *58,* 8097–8110. doi:10.1103/PhysRevB.58.8097

License and Terms

BEILSTEIN JOURNAL OF NANOTECHNOLOGY

Orthogonal chemical functionalization of patterned gold on silica surfaces

Francisco Palazon[*1,§], Didier Léonard[2], Thierry Le Mogne[3], Francesca Zuttion[1], Céline Chevalier[4,5], Magali Phaner-Goutorbe[1], Éliane Souteyrand[1], Yann Chevolot[*1] and Jean-Pierre Cloarec[*1]

Letter

Open Access

Address:
[1]Université de Lyon, Institut des Nanotechnologies de Lyon, site École Centrale de Lyon, CNRS UMR 5270, 36 Avenue Guy de Collongue, 69134 Écully, France, [2]Université de Lyon, Institut des Sciences Analytiques, Université Claude Bernard Lyon 1 / CNRS / ENS de Lyon, CNRS UMR 5280, 5 rue de la Doua, 69100 Villeurbanne, France, [3]Université de Lyon, École Centrale de Lyon, Laboratoire de Tribologie et Dynamique des Systèmes, CNRS UMR 5513, 36 Avenue Guy de Collongue, 69134 Écully, France, [4]Laboratoire Nanotechnologies & Nanosystèmes (UMI-LN2 3463), Université de Sherbrooke - CNRS - INSA de Lyon - ECL - UJF-CPE Lyon, Université de Sherbrooke, 3000 Boulevard de l'Université, Sherbrooke, Québec J1K 0A5, Canada, and [5]LTM/CNRS/RENATECH, 17 rue des martyrs, 38054 Grenoble, France

Email:
Francisco Palazon[*] - francisco.palazon@iit.it;
Yann Chevolot[*] - yann.chevolot@ec-lyon.fr;
Jean-Pierre Cloarec[*] - jean-pierre.cloarec@ec-lyon.fr

* Corresponding author
§ Current address: Nanochemistry Department, Istituto Italiano di Tecnologia, Via Morego 30, 16163 Genova, Italy

Keywords:
characterization; self-assembled monolayer; surface functionalization; ToF–SIMS; XPS

Beilstein J. Nanotechnol. **2015,** *6,* 2272–2277.
doi:10.3762/bjnano.6.233

Received: 06 October 2015
Accepted: 11 November 2015
Published: 01 December 2015

This article is part of the Thematic Series "Organized films".

Guest Editor: M. Canepa

Abstract

Single-step orthogonal chemical functionalization procedures have been developed with patterned gold on silica surfaces. Different combinations of a silane and a thiol were simultaneously deposited on a gold/silica heterogeneous substrate. The orthogonality of the functionalization (i.e., selective grafting of the thiol on the gold areas and the silane on the silica) was demonstrated by X-ray photoelectron spectroscopy (XPS) as well as time-of-flight secondary ion mass spectrometry (ToF–SIMS) mapping. The orthogonal functionalization was used to immobilize proteins onto gold nanostructures on a silica substrate, as demonstrated by atomic force microscopy (AFM). These results are especially promising in the development of future biosensors where the selective anchoring of target molecules onto nanostructured transducers (e.g., nanoplasmonic biosensors) is a major challenge.

Introduction

The orthogonal self-assembly of different molecules onto a patterned substrate was first demonstrated in 1989 by Whitesides and co-workers [1]. Recently, especially with the development of localized surface plasmon resonance (LSPR) biosensors, this topic has become a major focus [2-8]. Indeed, LSPR transduction is expected to yield enhanced signal as compared to classical SPR transduction. However, the enhancement of the LSPR limit of detection is effective only if the molecular targets reach the surface of the metallic LSPR active zones. When dealing with a low concentration of molecular targets, it is necessary to reduce nonspecific adsorption of targets outside of these LSPR active zones, and to increase the specific capture of targets onto LSPR hot spot areas. Orthogonal surface chemical functionalization appears to enable such directed anchoring of target biomolecules (Figure 1) [6,8,9].

Despite the aforementioned publications, there is still much to be investigated regarding the orthogonal functionalization of patterned metal on dielectric surfaces for even greater enhancement of LSPR-based biosensors. First, the orthogonality of the functionalization is often assumed from "end of process measurements" (i.e., SPR signal readout occurs after target immobilization) rather than directly characterized prior to target immobilization. Second, while biotinylated poly(ethylene glycol) [5-8] may be well suited to immobilize some biomolecules (avidin derivatives), it is worth considering other surface chemistries. For instance, carboxylic acid-based [10-21], amine-based [22-26] or other [27,28] self-assembled monolayers may provide a higher diversity of potential biomolecules to immobilize. Shorter spacer chains (e.g., short alkyl chains) may also be useful to immobilize the target as close to the metal surface (i.e., the maximum intensity of the evanescent field) as possible. If the molecules used for the orthogonal functionalization are truly selective for each material, it can be expected that the functionalization of both may be performed simultaneously, thus simplifying the whole process.

Therefore, this paper presents a facile single-step orthogonal functionalization protocol to selectively bind different thiols and silanes (mixed in organic solvent at room temperature) onto the gold and silica areas of a patterned surface. The chemical functionalization was verified by direct characterization using XPS and ToF–SIMS mapping. To this end, microscale gold structures were used to evaluate the different materials separately (especially for XPS characterization, whose spatial resolution is on the order of 10 µm) and combined with perfluorinated thiols and silanes that give a strong fluorine signal both in XPS and ToF–SIMS measurements. Finally, an orthogonal functionalization with biologically pertinent molecules (antifouling poly(ethylene glycol) silane and biotinylated thiols) was used for the selective immobilization of proteins onto metallic nanostructures relevant to the development of LSPR

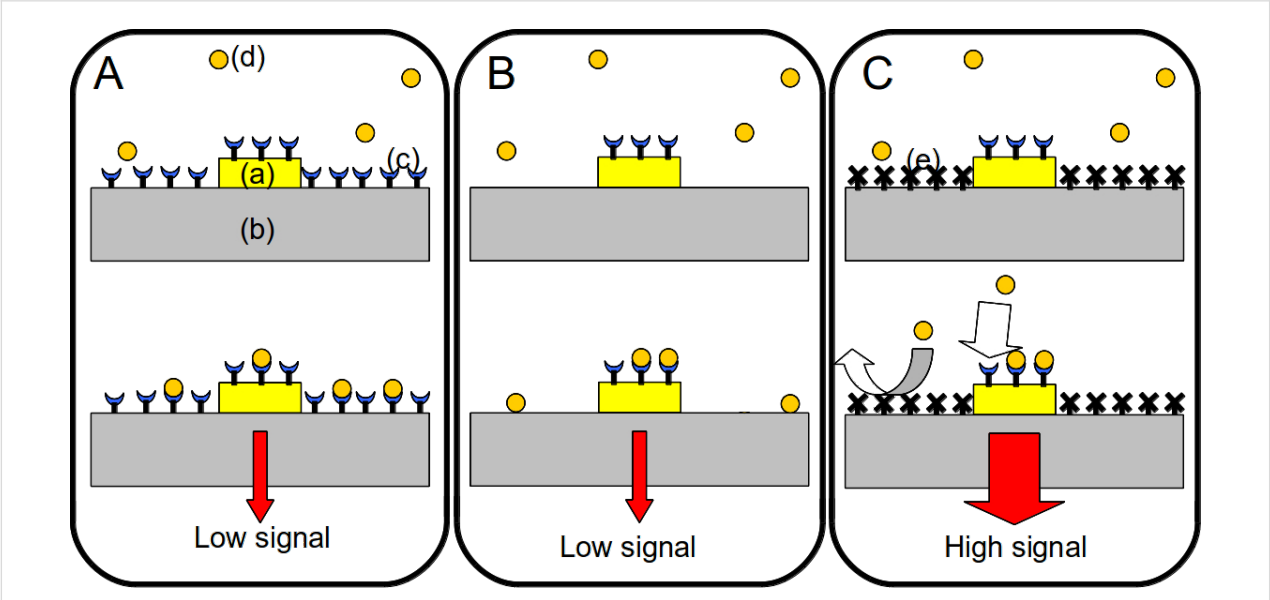

Figure 1: Schematic representation of the use of orthogonal functionalization techniques to enhance the sensitivity of a plasmonic biosensor (with a constant number of molecules). (A) Functionalization is uniform over the entire surface. The immobilization of probes (c) onto the entire surface, including the LSPR zone (a) and silica substrate (b). The targets (d) are captured far from the LSPR area. (B) Only the nanotransducer is functionalized. Selective immobilization of probes onto the LSPR area (a) only. The targets can absorb onto the silica substrate (b) far from the LSPR zone. (C) Orthogonal functionalization on the nanotransducer and surrounding surface. Selective immobilization of probes onto the LSPR area only, and selective nonfouling treatment (e) on the silica substrate. The targets only bind to the enhanced detection area.

biosensors and characterized by atomic force microscopy (AFM).

Results and Discussion

Micropatterned gold on a silica substrate (with features of ≈100 µm) functionalized with either (1) 1*H*,1*H*,2*H*,2*H*-perfluorodecanethiol and 2-[methoxy(polyethyleneoxy)propyl]trimethoxysilane (F-thiol + PEG/Si) or (2) trichloro(1*H*,1*H*,2*H*,2*H*-perfluorooctyl)silane and 11-mercapto-1-undecanoic acid (F-silane + MUA) were analyzed using XPS. For both surfaces, an initial image was acquired using scanning X-ray imaging (SXI; X-ray beam induced secondary electron images). This allows the gold microsquares (brighter) and surrounding silica areas (darker) to be visualized, as shown in Figure 2 and Figure 3. Then, two different analysis areas (≈10 µm in diameter) corresponding to the gold and silica

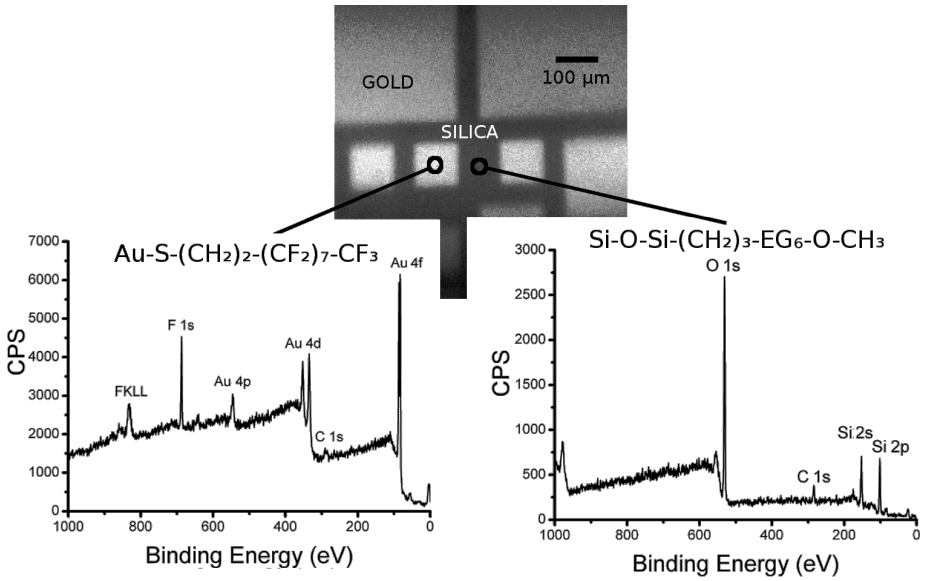

Figure 2: An SXI image and XPS spectra of a micropatterned gold on silica substrate sample, orthogonally functionalized with F-thiol and PEG/Si. The analyzed areas for the spectra were roughly 10 µm and their approximate localization is indicated on the image. The scale bar in the image is 100 µm.

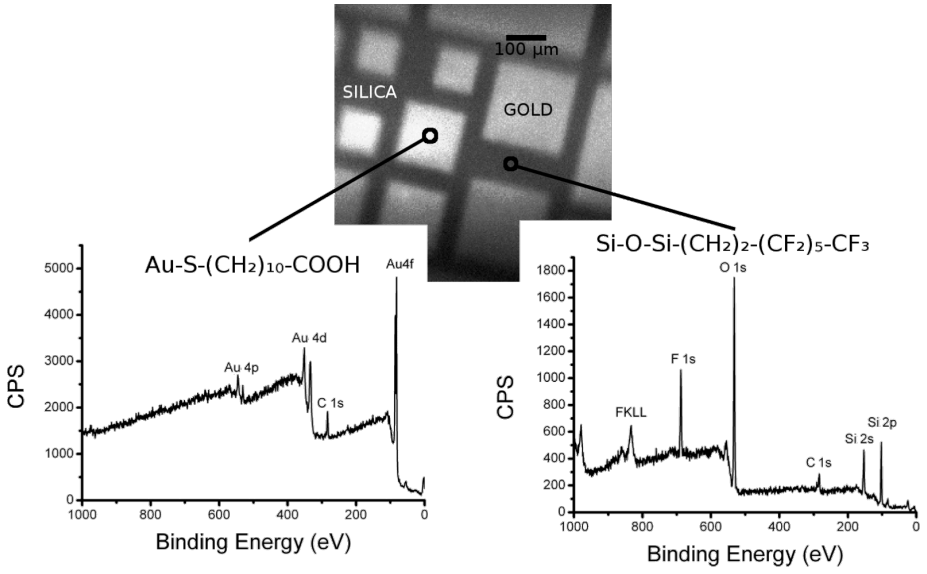

Figure 3: An SXI image and XPS spectra of a micropatterned gold on silica substrate sample, orthogonally functionalized with MUA and F-silane. The analyzed areas for the spectra were roughly 10 µm and their approximate localization is indicated on the image. The scale bar in the image is 100 µm.

surfaces were selected to perform a survey spectrum. High-resolution spectra of the different peaks could not be obtained due to the low signal from the small analysis areas. These spectra show the following:

– When the sample was simultaneously functionalized with a perfluorinated thiol and a PEG/silane (Figure 2)

1. On gold (left spectrum), fluorine is clearly present as evidenced by the F 1s and F KLL peaks, showing the presence of the perfluorinated thiol (F-thiol, molecular structure given above the spectrum). Furthermore, no Si 2s or O 1s peaks were detected, verifying the absence of PEG/silane. This suggests that, on the gold areas, F-thiol is specifically grafted while PEG/Si is not adsorbed.

2. On silica (right spectrum), fluorine is clearly absent as evidenced by the lack of F 1s or F KLL peaks, verifying the absence of the F-thiol. The presence of PEG/silane cannot be assessed by the silicon or oxygen-related peaks since these are present on the silica substrate. However, the presence of the C 1s peak seems to suggest that the silane is indeed grafted, though a contribution from other sources of carbon cannot be ruled out.

– When the sample is simultaneously functionalized with F-silane and an alkylthiol (Figure 3), the orthogonality of the functionalization is proven by the same arguments as above, the main one being the presence of fluorine on silica and not on gold.

We also conducted fluorine mapping on similar orthogonally functionalized surfaces using ToF–SIMS, which has been shown to be especially well-suited for the characterization of chemically patterned surfaces [29,30]. Figure 4 shows the presence of fluorine in both cases (F-thiol + PEG/Si and F-silane + MUA). In each case, only fluorine is present (or is very predominant) on the gold microsquares (Figure 4a) or the surrounding silica (Figure 4b) but not on both, which demonstrates the good orthogonality of the single-step orthogonal functionalization.

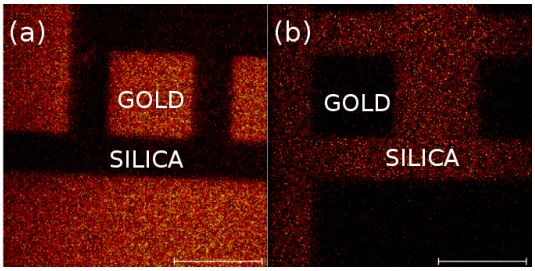

Figure 4: ToF–SIMS fluorine mapping of patterned gold on silica surfaces, orthogonally functionalized with F-thiol + PEG/Si (a) and F-silane + MUA (b). The scale bars are 100 µm.

Additionally, a nanostructured gold-on-silica substrate was functionalized with biotinylated thiols and antifouling PEG/silanes. A similar approach was already used to direct the immobilization of streptavidin-coated nanoparticles [31] onto the gold nanostructures. Here, “single” (i.e., not adsorbed on beads) proteins were immobilized as shown in Figure 5.

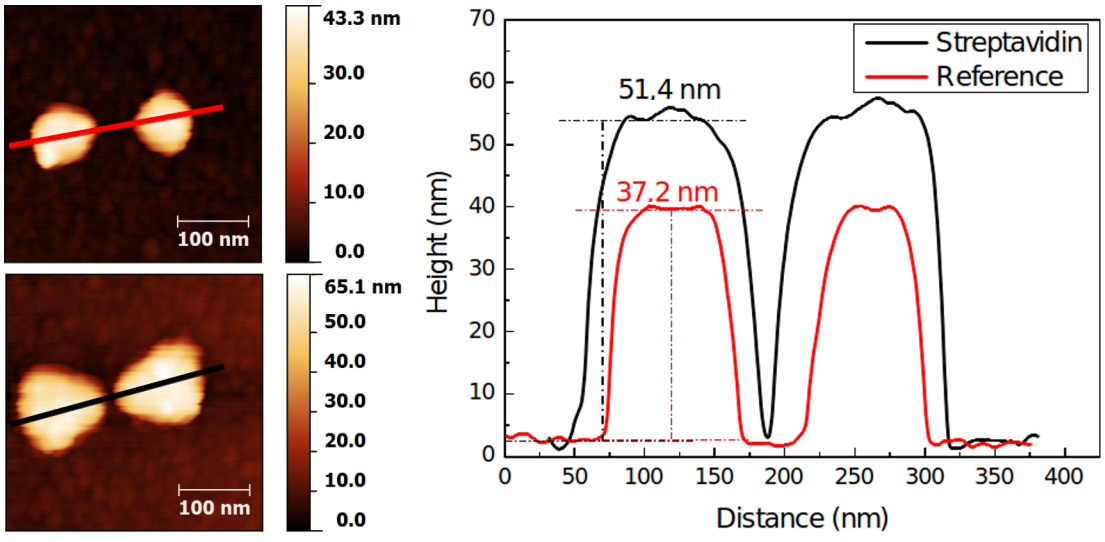

Figure 5: AFM height profiles of gold nanostructures on silica. The reference sample (red) was not functionalized or subjected to protein incubation and shows a height consistent with the deposition of 8 nm Ti + 30 nm Au. The streptavidin sample (black) was orthogonally functionalized and subjected to protein immobilization. The increase in size is indicative of the binding of streptavidin on the nanostructure.

Conclusion

The orthogonal chemical functionalization of patterned metal on dielectric surfaces appears to be a key process to direct target biomolecules onto individual nanostructures. This can be useful in different fields of nanotechnology, especially in the development of LSPR-based biosensors. In this paper, we reported different single-step functionalization procedures of patterned gold on silica surfaces with alkylthiols and silanes. The direct chemical characterization using XPS and ToF–SIMS provided evidence of the orthogonality, and AFM topography measurements showed the utility of this approach for biomolecule immobilization. Current work is being undertaken to implement this methodology into LSPR biosensors.

Experimental

Substrate patterning

A silica thin film (100 nm) was sputtered onto clean silicon wafers. UV lithography was used to define different patterns (lines, squares) with typical dimensions ranging from 2 to 100 µm. Electron beam lithography was used to develop the gold nanostructures (typical dimensions of 100 nm). Titanium (8 nm) and gold (30 nm) were deposited by electron beam evaporation. After lift-off, the samples were cleaned by oxygen plasma treatment (Anatech) at 400 sccm of oxygen, 350 W of forward power (10 W reflected), 90 Pa, for 5 min to ensure that no residual resist remained on the surface.

Surface functionalization

HS-$(CH_2)_{11}$-NH-C(O)-Biotin 95% (MU-Biot) was purchased from ProChimia. 1*H*,1*H*,2*H*,2*H*-Perfluorodecanethiol (F-thiol) 97% was purchased from Sigma-Aldrich. Trichloro(1*H*,1*H*,2*H*,2*H*-perfluorooctyl)silane (F-silane) 97% and 2-[methoxy(polyethyleneoxy)propyl]trimethoxysilane 90% (PEG/Si, MW = 460 g/mol) were purchased from abcr. Dichloromethane (DCM) 99.9% was purchased from Sigma-Aldrich then degassed and dried over molecular sieves. The thiols and silanes were dissolved in dry DCM at room temperature in different proportions, as given in Table 1.

After plasma cleaning, the resulting gold oxide is unstable and the samples were allowed to deoxidize for 24 h in fluoroware. Then, the samples were immersed in thiol/silane solutions under nitrogen and allowed to react for 48 h. The samples were then rinsed two times with fresh DCM for 5 min under sonication (Branson, 42 kHz, 100 W) followed by a stream of ultrapure water and dried with nitrogen.

Characterization

XPS

XPS characterization was conducted using an ULVAC-PHI VersaProbe II spectrometer equipped with a monochromatic Al Kα X-ray source (1486.6 eV). The analysis area can be adjusted from 200 µm to 10 µm and the energy scale was calibrated with reference to the C 1s line at a binding energy of 284.8 ± 0.1 eV (C–C/C–H). The charging effect is controlled by a dedicated neutralizer using a combination of ions and electrons at very low energy (0.1 eV). The X-ray spot can be scanned with a field of view of 1300 µm. This instrument allows for the recording of both XPS spectra and SXI images.

ToF–SIMS

ToF–SIMS measurements were performed with a Physical Electronics (Chanhassen, USA), TRIFT III instrument operated with a pulsed 22 keV Au ion gun (ion current of 2 nA). Areas of 300 × 300 µm were scanned. Under the present operation conditions, the lateral resolution is on the order of 1 µm. Submicron resolution can be achieved, albeit hindering mass resolution. The ion dose was kept below the static conditions limits. The data were analyzed using WinCadence software. The mass calibration was performed on hydrocarbon secondary ions.

Acknowledgements

The ANR P2N, ANR-12-NANO-0016 (PIRANEX project) is greatly acknowledged for financial support.

References

1. Laibinis, P. E.; Hickman, J. J.; Wrighton, M. S.; Whitesides, G. M. *Science* **1989,** *245,* 845–847. doi:10.1126/science.245.4920.845
2. Dodson, S.; Haggui, M.; Bachelot, R.; Plain, J.; Li, S.; Xiong, Q. *J. Phys. Chem. Lett.* **2013,** *4,* 496–501. doi:10.1021/jz302018x
3. Gschneidtner, T. A.; Chen, S.; Christensen, J. B.; Käll, M.; Moth-Poulsen, K. *J. Phys. Chem. C* **2013,** *117,* 14751–14758. doi:10.1021/jp402002n
4. Lalander, C. H.; Zheng, Y.; Dhuey, S.; Cabrini, S.; Bach, U. *ACS Nano* **2010,** *4,* 6153–6161. doi:10.1021/nn101431k
5. Feuz, L.; Jönsson, P.; Jonsson, M. P.; Höök, F. *ACS Nano* **2010,** *4,* 2167–2177. doi:10.1021/nn901457f

Table 1: Thiol/silane mixtures used for orthogonal functionalization in 25 mL of DCM.

Compound	Quantity	Molar concentration (approx.)
MUA + F-silane	50 mg/10 µL	9 mM/1 mM
F-thiol + PEG/Si	100 µL/10 µL	14 mM/1 mM
MU-Biot + PEG/Si	50 mg/10 µL	5 mM/1 mM

6. Feuz, L.; Jonsson, M. P.; Höök, F. *Nano Lett.* **2012,** *12,* 873–879. doi:10.1021/nl203917e
7. Kumar, K.; Dahlin, A. B.; Sannomiya, T.; Kaufmann, S.; Isa, L.; Reimhult, E. *Nano Lett.* **2013,** *13,* 6122–6129. doi:10.1021/nl403445f
8. Zhang, N.; Liu, Y. J.; Yang, J.; Su, X.; Deng, J.; Chum, C. C.; Hong, M.; Teng, J. *Nanoscale* **2014,** *6,* 1416–1422. doi:10.1039/C3NR04494G
9. Penzo, E.; Palma, M.; Wang, R.; Cai, H.; Zheng, M.; Wind, S. J. *Nano Lett.* **2015,** *15,* 6547–6552. doi:10.1021/acs.nanolett.5b02220
10. Afara, N.; Omanovic, S.; Asghari-Khiavi, M. *Thin Solid Films* **2012,** *522,* 381–389. doi:10.1016/j.tsf.2012.08.025
11. Briand, E.; Gu, C.; Boujday, S.; Salmain, M.; Herry, J. M.; Pradier, C. M. *Surf. Sci.* **2007,** *601,* 3850–3855. doi:10.1016/j.susc.2007.04.102
12. Choi, S.; Chae, J. *J. Micromech. Microeng.* **2010,** *20,* 075015. doi:10.1088/0960-1317/20/7/075015
13. Morel, A.-L.; Volmant, R.-M.; Méthivier, C.; Krafft, J.-M.; Boujday, S.; Pradier, C.-M. *Colloids Surf., B* **2010,** *81,* 304–312. doi:10.1016/j.colsurfb.2010.07.021
14. Kim, I.; Junejo, I.-u.-R.; Lee, M.; Lee, S.; Lee, E. K.; Chang, S.-I.; Choo, J. *J. Mol. Struct.* **2012,** *1023,* 197–203. doi:10.1016/j.molstruc.2012.04.031
15. Bellon, S.; Buchmann, W.; Gonnet, F.; Jarroux, N.; Anger-Leroy, M.; Guillonneau, F.; Daniel, R. *Anal. Chem.* **2009,** *81,* 7695–7702. doi:10.1021/ac901140m
16. El Khoury, G.; Laurenceau, E.; Chevolot, Y.; Souteyrand, E.; Cloarec, J.-P. *Biosens. Bioelectron.* **2010,** *26,* 1320–1325. doi:10.1016/j.bios.2010.07.032
17. Campos, M. A. C.; Trilling, A. K.; Yang, M.; Giesbers, M.; Beekwilder, J.; Paulusse, J. M. J.; Zuilhof, H. *Langmuir* **2011,** *27,* 8126–8133. doi:10.1021/la200932w
18. Sam, S.; Touahir, L.; Salvador Andresa, J.; Allongue, P.; Chazalviel, J. N.; Gouget-Laemmel, A. C.; Henry de Villeneuve, C.; Moraillon, A.; Ozanam, F.; Gabouze, N.; Djebbar, S. *Langmuir* **2010,** *26,* 809–814. doi:10.1021/la902220a
19. Wang, C.; Yan, Q.; Liu, H.-B.; Zhou, X.-H.; Xiao, S.-J. *Langmuir* **2011,** *27,* 12058–12068. doi:10.1021/la202267p
20. Touahir, L.; Chazalviel, J.-N.; Sam, S.; Moraillon, A.; Henry de Villeneuve, C.; Allongue, P.; Ozanam, F.; Gouget-Laemmel, A. C. *J. Phys. Chem. C* **2011,** *115,* 6782–6787. doi:10.1021/jp200150m
21. Palazon, F.; Benavides, C. M.; Léonard, D.; Souteyrand, É.; Chevolot, Y.; Cloarec, J.-P. *Langmuir* **2014,** *30,* 4545–4550. doi:10.1021/la5004269
22. Halpern, A. R.; Chen, Y.; Corn, R. M.; Kim, D. *Anal. Chem.* **2011,** *83,* 2801–2806. doi:10.1021/ac200157p
23. Bedford, E. E.; Boujday, S.; Humblot, V.; Gu, F. X.; Pradier, C.-M. *Colloids Surf., B* **2014,** *116,* 489–496. doi:10.1016/j.colsurfb.2014.01.031
24. Brockman, J. M.; Frutos, A. G.; Corn, R. M. *J. Am. Chem. Soc.* **1999,** *121,* 8044–8051. doi:10.1021/ja991608e
25. Wegner, G. J.; Lee, H. J.; Corn, R. M. *Anal. Chem.* **2002,** *74,* 5161–5168. doi:10.1021/ac025922u
26. Smith, E. A.; Thomas, W. D.; Kiessling, L. L.; Corn, R. M. *J. Am. Chem. Soc.* **2003,** *125,* 6140–6148. doi:10.1021/ja034165u
27. Canepa, M.; Maidecchi, G.; Toccafondi, C.; Cavalleri, O.; Prato, M.; Chaudhari, V.; Esaulov, V. A. *Phys. Chem. Chem. Phys.* **2013,** *15,* 11559–11565. doi:10.1039/c3cp51304a
28. Toccafondi, C.; Prato, M.; Barborini, E.; Vinati, S.; Maidecchi, G.; Penco, A.; Cavalleri, O.; Bisio, F.; Canepa, M. *Bionanosci.* **2011,** *1,* 210–217. doi:10.1007/s12668-011-0024-3
29. Priest, C.; Stevens, N.; Sedev, R.; Skinner, W.; Ralston, J. *J. Colloid Interface Sci.* **2008,** *320,* 563–568. doi:10.1016/j.jcis.2008.01.042
30. Brito e Abreu, S.; Skinner, W. *Langmuir* **2012,** *28,* 7360–7367. doi:10.1021/la300352f
31. Palazon, F.; Rojo-Romeo, P.; Chevalier, C.; Géhin, T.; Belarouci, A.; Cornillon, A.; Zuttion, F.; Phaner-Goutorbe, M.; Souteyrand, É.; Chevolot, Y.; Cloarec, J.-P. *J. Colloid Interface Sci.* **2015,** *447,* 152–158. doi:10.1016/j.jcis.2014.11.028

License and Terms

BEILSTEIN JOURNAL OF NANOTECHNOLOGY

Fabrication of hybrid graphene oxide/polyelectrolyte capsules by means of layer-by-layer assembly on erythrocyte cell templates

Joseba Irigoyen[1], Nikolaos Politakos[1], Eleftheria Diamanti[1], Elena Rojas[1], Marco Marradi[1], Raquel Ledezma[2], Layza Arizmendi[2], J. Alberto Rodríguez[2], Ronald F. Ziolo[2] and Sergio E. Moya[*1]

Full Research Paper

Open Access

Address:
[1]Soft Matter Nanotechnology, CIC biomaGUNE, Paseo Miramón 182 C, 20009 San Sebastian, Spain and [2]Departamento de Materiales Avanzados, Centro de Investigación en Química Aplicada, Blvd. Enrique Reyna Hermosillo No.140 C.P. 25294 Saltillo, Coahuila, México

Email:
Sergio E. Moya[*] - smoya@cicbiomagune.es

* Corresponding author

Keywords:
capsules; erythrocytes; graphene; layer by layer; polyelectrolyte membranes

Beilstein J. Nanotechnol. **2015,** *6,* 2310–2318.
doi:10.3762/bjnano.6.237

Received: 01 September 2015
Accepted: 02 November 2015
Published: 04 December 2015

This article is part of the Thematic Series "Organized films".

Guest Editor: M. Canepa

Abstract

A novel and facile method was developed to produce hybrid graphene oxide (GO)–polyelectrolyte (PE) capsules using erythrocyte cells as templates. The capsules are easily produced through the layer-by-layer technique using alternating polyelectrolyte layers and GO sheets. The amount of GO and therefore its coverage in the resulting capsules can be tuned by adjusting the concentration of the GO dispersion during the assembly. The capsules retain the approximate shape and size of the erythrocyte template after the latter is totally removed by oxidation with NaOCl in water. The PE/GO capsules maintain their integrity and can be placed or located on other surfaces such as in a device. When the capsules are dried in air, they collapse to form a film that is approximately twice the thickness of the capsule membrane. AFM images in the present study suggest a film thickness of approx. 30 nm for the capsules in the collapsed state implying a thickness of approx. 15 nm for the layers in the collapsed capsule membrane. The polyelectrolytes used in the present study were polyallylamine hydrochloride (PAH) and polystyrenesulfonate sodium salt (PSS). Capsules where characterized by transmission electron microscopy (TEM), atomic force microscopy (AFM), dynamic light scattering (DLS) and Raman microscopy, the constituent layers by zeta potential and GO by TEM, XRD, and Raman and FTIR spectroscopies.

Introduction

The past decades have witnessed explosive growth in research on low-dimensional carbon forms with graphene and carbon nanotubes in the forefront [1-3]. The unique electrical, mechanical, thermal and optical properties of graphene in particular, and of its derivatives, continue to be explored theoretically and experimentally in physics, chemistry, engineering and biology with emerging potential applications of societal importance [4-7]. The unique properties of graphene (G), which forms super strong sheets of carbon a single atom thick [8], result from its planar nature and the sp^2 hybridization of its carbon atoms.

Single layer, bi- and few-layer graphene are difficult to work with in soft matter or wet chemical applications because of dispersibility issues and the tendency to form multi-layered agglomerates, which begin to acquire the properties of graphite [9-11]. Because of these difficulties, most studies of graphene, whether for layered assembly or other investigations, have been performed on graphite oxide or its exfoliated form, graphene oxide (GO), which bears a mix of sp^2 and sp^3 hybridized carbons in an overall planar structure. These derivatives of graphene can also possess unique and often controllable properties and have the potential to be reduced to what is called a reduced form of graphene oxide, rGO, by chemical or physical means, which can lead to materials with properties more like G than GO [12-15]. The derivatization of G to form GO leads to easily dispersible and stable systems containing GO with an overall surface charge while exfoliated, for example, in water [16]. The use of GO sheets in the formation of hierarchical structures and assemblies is a subject of current interest, and if done by procedures involving wet chemical techniques, offers much potential for the development of advanced and composite layered materials.

The assembly of GO in thin films on the basis of its surface charge can be accomplished using the layer-by-layer technique (LbL). Although the technique was originally developed for the alternating assembly of polyelectrolytes (PE) of opposite charge, LbL can be and has been extended to include particles, 2D layered materials, nanostructures, and lipid vesicles, which provide charged surfaces, or, which can have complementary interactions with another material that can lead to a subsequent or alternating assembly [17]. There are examples in literature of the assembly of GO with polycations using LbL as a promising tool for the incorporation of GO into nanoscale organized thin films and the subsequent electrochemical reduction of the GO to rGO [18,19].

Using LbL, we explored the assembly of exfoliated GO into 3D structures and developed micrometre-sized capsules on the basis of GO and polyelectrolytes using chicken erythrocyte cells as templates. Template cells have been used in the past as capsule templates on the basis of a simple protocol, which includes the oxidation of the cell components to leave a thin polymer film in the form of a capsule that mimics the dimensions and topological features of the cell template [20-22]. We show that by incorporating GO within the LbL assembly on top of the erythrocytes, 3D closed films containing walls of PE/GO and an empty volume can be produced.

Capsules based on GO can have applications in drug delivery, especially for topical applications, as the LbL capsules provide low degradability and high stability through the GO. The use of GO in the fabrication of capsules was reported by J. Hong et al. [23] and by Kurapati et al. [24], the last one with a focus on drug delivery. The authors, however, use a different protocol and templates for their fabrication. In the present work, we produce continuous GO capsules with the shape of cells and show the presence and location of the GO by Raman confocal microscopy. Another potential application of these capsules is for the production of PE/GO films with a high concentration of GO, which was achievable in the present study by employing a high concentration of exfoliated GO during the layer by layer assembly. This is due to the coating protocol employed in which the cells are suspended in a GO solution and then centrifuged. Under these conditions, a high concentration of GO is achieved on the cell surface leading to a continuous coating.

Once dried, the capsules collapse by losing internal volume and form planar films with nanoscale thicknesses. Such films could be used to build additional hierarchical structures or for integration into devices; moreover, by the judicious choice of reagents, the GO may be further reduced to form rGO to alter particularly the electronic, mechanical and optical properties of the films.

Results and Discussion

Graphene oxide was prepared by the strong acid oxidation of powdered graphite by a modified Hummer's method [25,26]; characterization data are shown in Figure 1. Multiple TEM images formed from exfoliated GO in water and dried on lacey carbon grids show micrometre-size, few-layer GO sheets with some gentle folds and ripples (Figure 1a,b). The SAED inset in panel b shows diffraction spots indicative of hexagonal patterns [27]. Raman spectroscopy (Figure 1c) shows the expected prominent peaks for GO at 1349 and 1601 cm^{-1}, with a D/G ratio of 0.8. The D resonance corresponds to the vibration of sp^2 carbon while G corresponds to sp^3 carbon and defects associated with vacancies and grain boundaries [28]. The peaks at higher wavenumbers are also characteristic of graphene oxide.

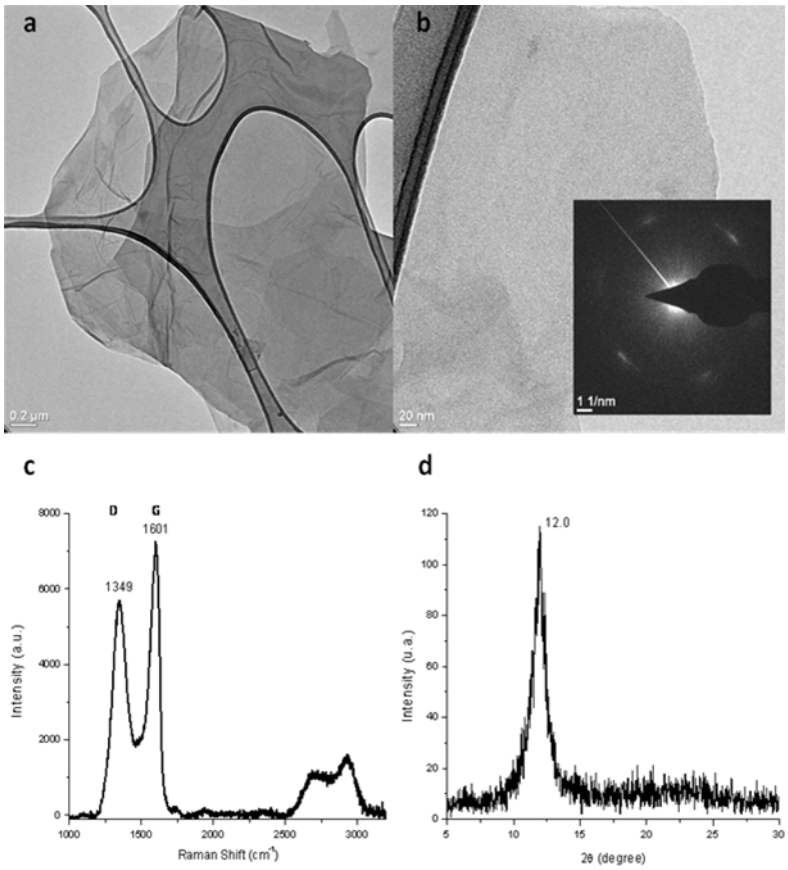

Figure 1: GO data; a) and b) TEM images of graphene oxide on lacey carbon, inset: SAED showing diffraction spots of hexagonal patterns; c) Raman spectrum with 532 nm excitation d) XRD pattern showing (002) with *d* = 0.737 nm.

XRD results (Figure 1d) indicate the absence of graphite and show the prominent (002) peak at 12.0 degrees 2θ, indicating an inter-planar GO sheet distance of 0.737 nm [29]. Prominent FTIR bands for GO were observed at 3415, 1723, 1623, 1394 and 1050 cm^{-1} as reported in [30].

A scheme of the layer-by-layer assembly applied on the erythrocytes for the deposition of GO and polymers, as well as for the subsequent NaOCl oxidation and capsule generation, is represented in Figure 2. In the first step, the red blood cells are crosslinked with glutaraldehyde. The crosslinking is necessary to insure that the polyelectrolytes will not disrupt the erythrocyte membrane. Erythrocytes were chosen because of their simple structure that lacks a nucleus, which makes the degradation of the whole cell content with NaOCl solution easier. Before the coating with GO, four layers of PSS/PAH were assembled on top of the cell. Despite the erythrocytes have a slightly negative charged surface the first assembled layer was PSS, which is also negative. We have observed earlier that the PSS assembles better as first layer on the cells causing significantly less aggregation of the cells [19]. The coating of the cells with an initial film of PSS/PAH is done to ensure a homogenously charged surface prior to the GO deposition. The assembly of the polyelectrolytes in the first layers and between the GO was done in 0.5 M NaCl as in these salt conditions the polymers assemble in a denser and compact structure, due to the optimal coiled conformation of the PEs at this ionic strength.

The assembly of exfoliated GO was done in water at pH 10 to avoid the screening of the charges on the GO. If present, screening the GO charges could lead to a stronger interaction between GO sheets in solution leading to aggregation. Charge screening would also eventually reduce the electrostatic interaction between the GO and the polyelectrolyte on the cell, which would be unfavourable for assembly. Between each GO deposition, we deposited either one layer of PAH or three layers of PAH/PSS/PAH. Since the assembly of one layer of PAH between the GO layers may not be sufficient to lead to a complete coating of the surface and full recharging, we additionally prepared capsules assembling three polyelectrolyte layers in between the GO layers. The addition of three polyelectrolyte layers on top of the GO layer makes the procedure more time consuming but we observe a major improvement in the stability of the coated cell, thus reducing aggregation.

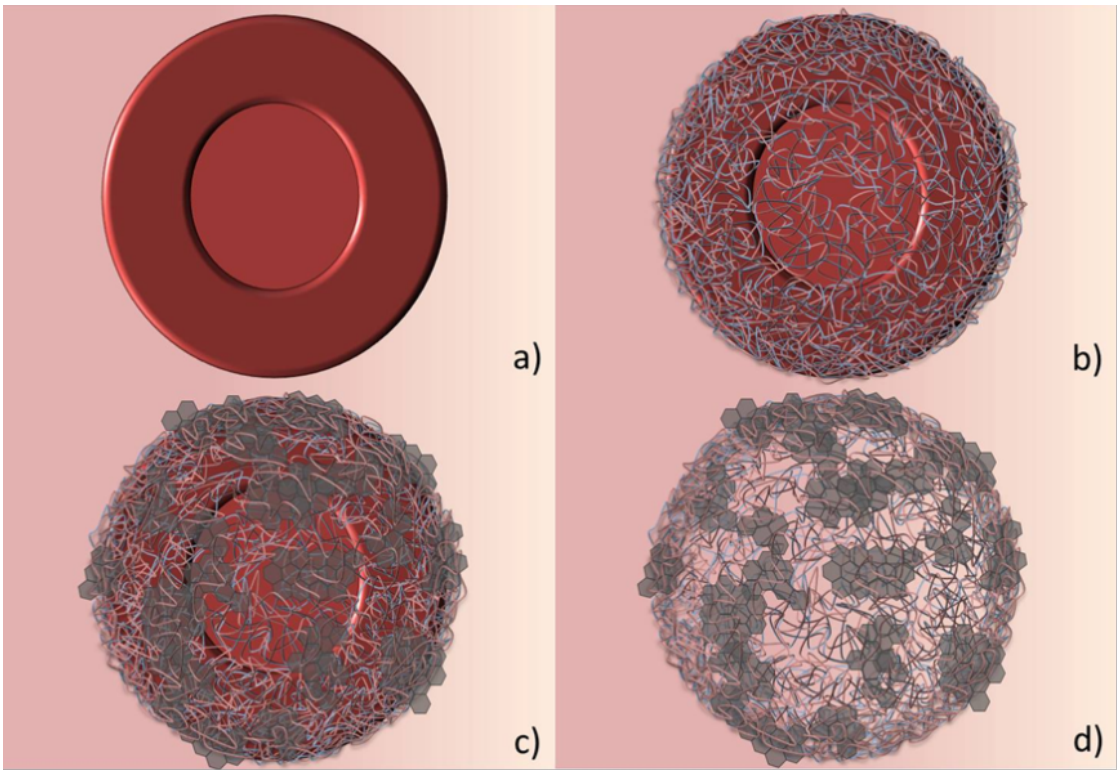

Figure 2: Schematic illustrations of a) the glutaraldehyde fixed red blood cells, b) the fixed erythrocytes coated with four layers of PSS/PAH, c) the fixed cells in (b) coated with additional GO/polyelectrolyte layers and d) the hybrid GO/polyelectrolyte capsule after NaOCl oxidation of the cell.

The removal of the cell interior by NaOCl is based on the oxidation of the cell content, which is mainly proteins, which become defragmented and are easily eliminated during centrifugation and washing cycles with NaCl and water. Oxidation also affects the PAH within the layers but a thin polymer film remains as was shown previously [31]. The possible oxidation of the GO with NaOCl would increase the percentage of negative charge on the GO surface.

The morphology and structural characteristics of the capsules were first studied by TEM which also provided proof of the core removal. Figure 3a shows an image of the capsules prepared as a control which do not contain GO. They clearly retain the shape of the erythrocytes used as templates. The capsules contain only water and collapse in the dry state to ellipsoid shaped films. The drying process is responsible for the appearance of edges on the capsule surface.

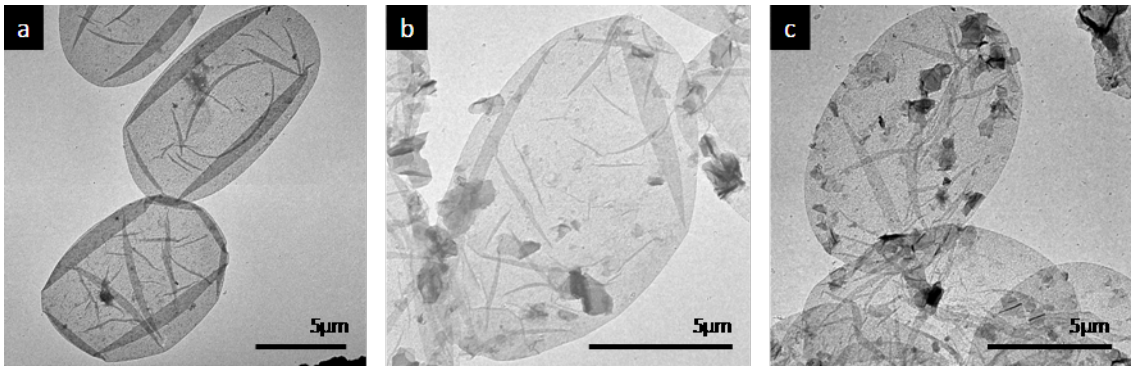

Figure 3: TEM micrographs of a) sample 1: $(PSS/PAH)_{4.5}^{0.5M}$, b) sample 2: $(PSS/PAH)_2^{0.5M}$ + [GO/$(PAH/PSS/PAH)^{0.5M}$ /GO] + $(PSS/PAH)^{0.5M}$, c) sample 3 $(PSS/PAH)_2^{0.5M}$ + $[GO/PAH]_{2.5}$ + $(PSS/PAH)^{0.5M}$ using a concentration of 0.1 mg/mL of GO during the assembly.

In Figure 3b,c we observe two examples of capsules fabricated with GO at a 0.1 mg/mL concentration with one PAH layer and three PAH/PSS/PAH layers in between the GO. As for the polyelectrolyte capsules, the GO capsules also retain the shape and size of the cells used as templates. The GO capsules are also empty as they are in a collapsed state after drying. On the capsule wall we can recognize the presence of a structure of patches, with dimensions between a few hundred of nanometers and one micrometre. GO is recognized in the structure but embedded within the polyelectrolyte materials. GO is present on some random spots in the capsule, the rest of the capsule structure is very similar to the control capsules. The patches have the characteristic of GO sheets in the range of micrometres.

We decided to increase the concentration of GO to 0.2 mg/mL in order to increase the GO coating. For this GO concentration TEM imaging reveals that indeed the GO coating has become visible all over the surface of the capsules as can be appreciated in Figure 4.

In Figure 4a,b the capsules are prepared as in Figure 3a,b but with a GO concentration of 0.2 mg/mL instead of 1 mg/mL. Figure 4c,d are magnifications of a selected area from the corresponding capsules represented in Figure 4a,b, respectively. The GO sheets can be recognized all over the surface. Presumably, there is more GO deposited in the areas that show more contrast. The presence of these darker areas could imply that there may be GO stacking on top of previously assembled GO but still separated by PEs. The TEM images also confirm that by increasing the GO concentration, there is a complete coverage of the capsules with GO, which is not observed at the concentration of 1 mg/mL. The TEM images also proves the formation of a complete and continuous coating of the capsule surface with GO with only three layers of GO being assembled, which, interestingly, is not obtained for the same number of layers on a planar surface. The use of a layer of PAH or three polyelectrolyte layers between the GO assemblies does not seem to affect the integrity of the capsules. Accordingly, we proceeded with the assembly with just one intermediate polyelectrolyte layer, which results in

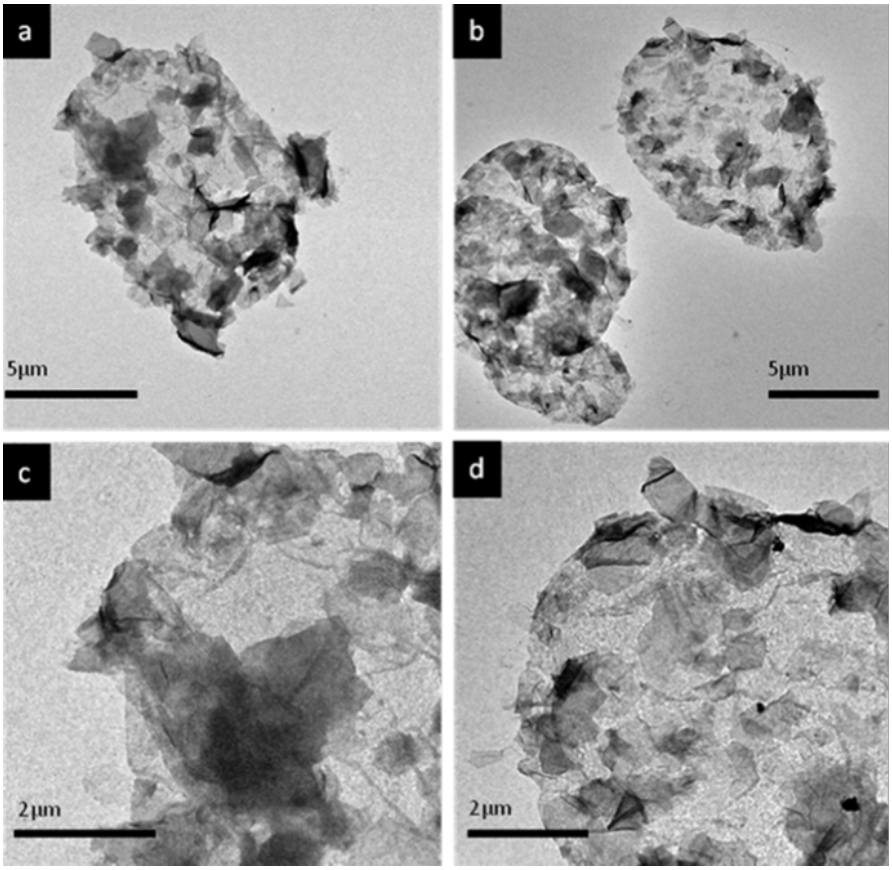

Figure 4: TEM micrographs of a) sample 2: $(PSS/PAH)_2^{0.5M}$ + [GO/$(PAH/PSS/PAH)^{0.5M}$/GO] + $(PSS/PAH)^{0.5M}$, b) sample 3: $(PSS/PAH)_2^{0.5M}$ + $[GO/PAH]_{2.5}$ + $(PSS/PAH)^{0.5M}$, c and d) magnification of samples 2 and 3, respectively. GO concentration was 0.2 mg/mL.

a reduced number of steps during the assembly for ease of fabrication.

Although the GO sheets can be recognized by their characteristic shape, we performed confocal Raman microscopy imaging to provide additional proof that the patches on the capsule wall correspond to GO. A representative scan of one capsule is shown in Figure 5a.

The surface of the capsule was scanned point by point. At each point, the Raman spectra revealed the presence of characteristic and strong bands at 1353 and 1598 cm^{-1}, which are characteristic for the GO and graphene structures and which cannot be detected in the capsules prepared solely with polyelectrolytes. The peaks in the Raman spectra of the capsules correspond to the G and D bands observed in the pristine GO (vide supra), with the typical shift in the G band to higher frequencies for GO with respect to graphite [28].

In order to determine the thickness of the capsule walls we performed AFM imaging of the capsules in the collapsed state. From the AFM images (Figure 6a) an estimated maximal thickness of about 30 nm could be determined for the capsules, implying a thickness of the order of 10–19 nm for the walls of

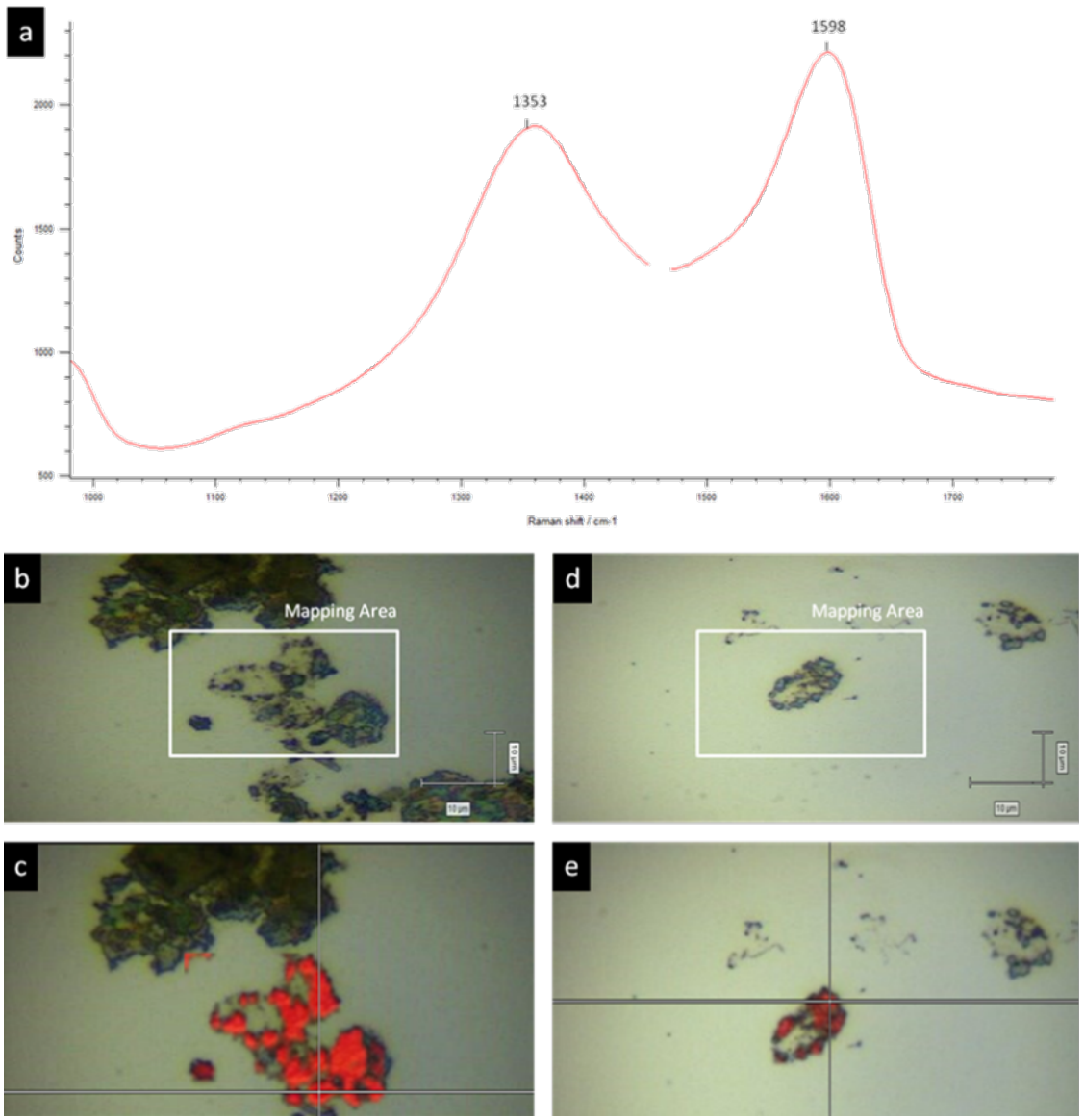

Figure 5: Raman of the GO-capsules. a) Raman spectra of GO sheets, G band located at 1598 cm^{-1} and D band at 1353 cm^{-1}. b) Image of the sample 2: $(PSS/PAH)_2^{0.5M}$ + [GO/$(PAH/PSS/PAH)^{0.5M}$ /GO] + $(PSS/PAH)^{0.5M}$ capsules onto Si wafer with the selected area to be analysed. c) Mapping by intensity of the G band at 1598 cm^{-1} of the area selected in b. d) Image of sample 3 $(PSS/PAH)_2^{0.5M}$ + $[GO/PAH]_{2.5}$ + $(PSS/PAH)^{0.5M}$ capsules onto Si wafer with the selected area to be analysed. e) Mapping by intensity of the G band at 1598 cm^{-1} of the area selected in d.

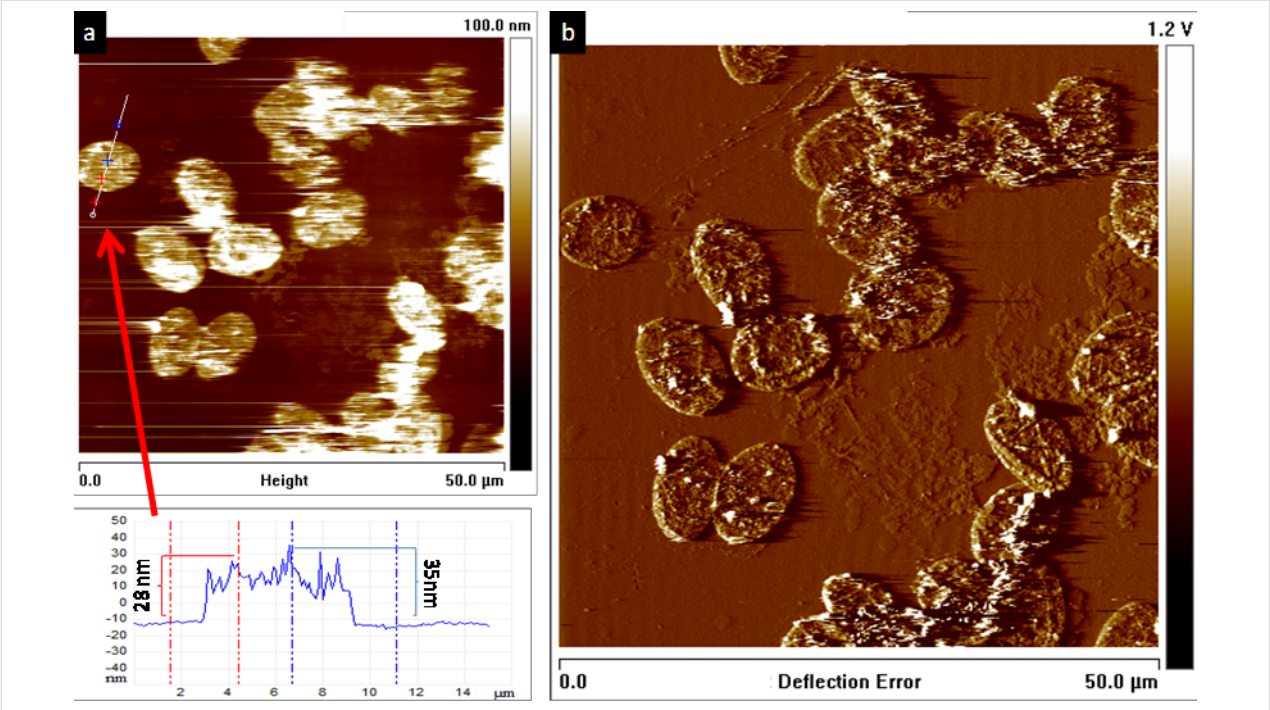

Figure 6: Atomic force microscope images of dried hybrid PE/GO capsules. a) Height image of a 50 × 50 µm scan, with a profile corresponding to the line drawn in the image. b) Deflection image of the same area analysed in a).

the capsule in the dry state. These values are obtained assuming that the thickness of the collapsed capsule is twice the thickness of the capsule wall since the capsule loses internal volume when drying. These values are taken from the maximal and minimal thickness measured for the capsule. AFM imaging also confirmed the stability of the capsules, which retain their shape and integrity after collapsing in air (Figure 6b).

Experimental

Materials

Polyallylamine hydrochloride, (PAH, M_w 15 kg/mol), polystyrenesulfonate sodium salt, (PSS, M_w 70 kg/mol), sodium hypochlorite with active chlorine 13%, phosphate buffered saline 10× (PBS), glutaraldehyde solution grade II 25% in water, Hank´s balanced salt solution 10×, sodium chloride and graphite powder (<45 µm, ≥99.99% trace metals basis) were obtained from Sigma–Aldrich. Lymphocytes isolation solution (Ficoll) was purchased from Rafer Zaragoza, Spain. Full blood chicken collected in Alsever's anticoagulant solution was purchased from Harlan Laboratories Models S.L., Barcelona, Spain.

Methods

Erythrocytes

Erythrocytes were separated from the chicken blood and the rest of the plasma components by centrifugation. Chicken blood conserved in Alsever´s solution was diluted with (Ca, Mg) Hank´s solution and carefully poured onto a Ficoll solution to avoid mixing. Afterwards the resulting solution was centrifuged at 800*g* for 30 min at 4 °C depositing the erythrocytes at the bottom and the rest of the plasma in different phases above them. Only the erythrocytes were obtained and cleaned twice with Hank´s solution by centrifugation under the same conditions as before. Cells were then fixed for 1 h at 4 °C with glutaraldehyde at a concentration of 2.5% in filtered PBS buffer. After fixation, they were centrifuged and washed in 0.9% NaCl several times at 10 °C and kept refrigerated.

Graphene oxide

Graphene oxide was prepared by strong acid oxidation of graphite using Hummer's method [25] as modified in [26] where the dispersion was water washed to neutral pH. Following this, we washed with dilute HCl followed again by water washes to neutral pH. The graphene oxide was exfoliated via ultra-sonication and microwave irradiation. FTIR spectra were taken with a Nexus 470 Spectrometer over 4000–400 cm^{-1} using multiple scans and 4 cm^{-1} resolution in transmission mode.

Layer-by-layer assembly

The LbL assembly of GO and polyelectrolytes was performed on the fixed erythrocytes. Previous to the GO assembly, two bilayers of PSS/PAH were assembled. The polyelectrolytes were assembled at a concentration of 1 mg/mL in 0.5 M NaCl.

Two washings were performed with water between each layer assembly by centrifugation at 67.08*g* for 2 min. The first assembled layer on top of the cells was always PSS since it was already shown that it assemblies better using a polyanion rather than a polycation on the erythrocytes, despite the negative charge of the cells [32]. After the fourth layer was assembled, GO is deposited in a concentration of 0.1 or 0.2 mg/mL in water (pH 10). The assembly of GO is performed without NaCl as the salt would screen the charges of the GO and lead to aggregation. The incubation time for polyelectrolytes and GO was always 2 min. After GO deposition, the cells were also washed in water by centrifugation. GO was assembled alternating with PAH or with three polyelectrolyte layers; PAH/PSS/PAH, until a total number of eleven layers was achieved in both cases. Also, another sample with just nine layers of PEs, without GO, was assembled as a control, following the same procedure described above.

Capsule fabrication

Once the GO/polyelectrolyte multilayer was assembled on top of the cells, they were exposed to aqueous 1% NaOCl. The oxidizing solution degrades the cells by breaking their protein constituents through oxidation. After NaOCl treatment, samples were washed first in NaCl and then in water for several cycles to remove the products of oxidation.

Electron transmission (TEM) and X-ray diffraction measurements

Transmission electron microscopy images were taken using a JEOL JEM-1400PLUS (40–120 kV) equipped with a GATAN US1000 CCD camera. An aliquot of 5 µL of each sample was deposited on grids of carbon film 400 mesh Cu, (50/bx) and left to evaporate. The grid was previously stained with uranyl acetate.

TEM imaging of the GO was done using an FEI Titan 80–300 kV field emission gun microscope, which has a symmetrical condenser-objective lens type S-TWIN (with an spherical aberration $C_s \approx 1.25$ mm). The images were acquired with a CCD camera of samples prepared from water dispersions cast on lacey carbon grids.

X-ray diffraction

XRD data for GO were obtained using a Siemens D-5000 operated at 35 kV and 25 mA and Cu Kα radiation.

Raman spectroscopy and confocal Raman microscopy

Raman analysis was performed using a Renishaw inVia Raman microscope with a 100× objective, a 532 nm laser excitation and a 1800 mm^{-1} grating. The system was calibrated to the spectral line of crystalline silicon at 520.7 cm^{-1}. A drop of a diluted solution containing the capsules was placed onto a silicon wafer and left evaporating overnight.

Atomic force microscopy (AFM)

Atomic force microscopy studies were performed using a Veeco Multimode AFM attached to a Nanoscope V controller. The samples were imaged in contact mode in air, using a TESP-V2 silicon probe with $k = 42$ N/m. A drop of a diluted solution with the capsules was placed on a glass substrate with a thin layer of Au deposited on top. The sample was left evaporating and afterwards imaged.

Conclusion

We have shown that 3D micrometre-sized objects in the form of capsules can be fabricated on the basis of the LbL assembly of GO and polyelectrolytes on top of fixed erythrocyte cells as templates. TEM imaging revealed a surface structure composed of GO sheets when the GO assembly was performed with a high GO concentration. The presence of GO was confirmed by Raman spectro-microscopy that revealed the presence of the GO in the capsule structure. AFM revealed that the capsule walls are thin films with a thickness of approx. 15 nm. Our result shows an alternative method for the fabrication of capsules entailing GO in a dense arrangement that could eventually have applications in drug delivery and optoelectronics by developing hybrid thin polymer films containing graphene oxide or its reduced form rGO.

Acknowledgements

This work was financially supported by the Marie Curie project *"Higraphen, Hierarchical functionalization and assembly of Graphene for multiple device fabrication"* (HiGRAPHEN) (Grant ref: 612704). The authors also acknowledge the project MAT2013-48169-R from the Spanish Ministry of Economy (MINECO).

References

1. Morris, J. E.; Iniewski, K., Eds. *Graphene, Carbon Nanotubes, and Nanostructures: Techniques and Applications;* Taylor & Francis: Boca Raton, Florida, 2013.
2. Wolf, E. L., Ed. *Graphene: A New Paradigm in Condensed Matter and Device Physics;* Oxford University Press: UK, 2014.
3. Hong, J.; Han, J. Y.; Yoon, H.; Joo, P.; Lee, T.; Seo, E.; Char, K.; Kim, B.-S. *Nanoscale* **2011,** *3,* 4515–4531. doi:10.1039/c1nr10575b
4. Ziolo, R. F.; Avila, C.; Arizmendi-Galaviz, L. Chapter 4. Graphene, Carbon Nanotubes and other BCN Materials. In *Isotopes in Nanoparticles: Fundamentals & Applications;* Llop Roig, J.; Gomez-Vallejo, V.; Gibson, P. N., Eds.; Pan Stanford Publishing Pte. Ltd., 2016.
5. Li, J.; Zeng, X.; Ren, T.; van der Heide, E. *Lubricants* **2014,** *2,* 137–161. doi:10.3390/lubricants2030137

6. Enoki, T.; Ando, T., Eds. *Physics and Chemistry of Graphene: Graphene to Nanographene;* Pan Stanford, 2013. doi:10.1201/b14396
7. Wolf, E. L., Ed. *Applications of Graphene, An Overview;* Springer International Publishing, 2014. doi:10.1007/978-3-319-03946-6
8. Blees, M. K.; Barnard, A. W.; Rose, P. A.; Roberts, S. P.; McGill, K. L.; Huang, P. Y.; Ruyack, A. R.; Kevek, J. W.; Kobrin, B.; Muller, D. A.; McEuen, P. L. *Nature* **2015,** *524,* 204–207. doi:10.1038/nature14588
9. Tasis, D.; Papagelis, K.; Spiliopoulos, P.; Galiotis, C. *Mater. Lett.* **2013,** *94,* 47–50. doi:10.1016/j.matlet.2012.12.027
10. Nicolosi, V.; Chhowalla, M.; Kanatzidis, M. G.; Strano, M. S.; Coleman, J. N. *Science* **2013,** *340,* 1226419. doi:10.1126/science.1226419
11. Hernandez, Y.; Lotya, M.; Rickard, D.; Bergin, S. D.; Coleman, J. N. *Langmuir* **2010,** *26,* 3208–3213. doi:10.1021/la903188a
12. Dreyer, D. R.; Park, S.; Bielawski, C. W.; Ruoff, R. S. *Chem. Soc. Rev.* **2010,** *39,* 228–240. doi:10.1039/B917103G
13. Si, Y.; Samulski, E. T. *Nano Lett.* **2008,** *8,* 1679–1682. doi:10.1021/nl080604h
14. Hassouna, F.; Kashyap, S.; Laachachi, A.; Ball, V.; Chapron, D.; Toniazzo, V.; Ruch, D. *J. Colloid Interface Sci.* **2012,** *377,* 489–496. doi:10.1016/j.jcis.2012.03.054
15. Gao, X.; Jang, J.; Nagase, S. *J. Phys. Chem. C* **2010,** *114,* 832–842. doi:10.1021/jp909284g
16. Du, W.; Jiang, X.; Zhu, L. *J. Mater. Chem. A* **2013,** *1,* 10592–10606. doi:10.1039/c3ta12212c
17. Decher, G. *Science* **1997,** *277,* 1232–1237. doi:10.1126/science.277.5330.1232
18. Yang, M.; Hou, Y.; Kotov, N. A. *Nano Today* **2012,** *7,* 430–447. doi:10.1016/j.nantod.2012.08.006
19. Kotov, N. A.; Dékány, I.; Fendler, J. H. *Adv. Mater.* **1996,** *8,* 637–641. doi:10.1002/adma.19960080806
20. Donath, E.; Moya, S.; Neu, B.; Sukhorukov, G. B.; Georgieva, R.; Voigt, A.; Bäumler, H.; Kiesewetter, H.; Möhwald, H. *Chemistry* **2002,** *8,* 5481–5485. doi:10.1002/1521-3765(20021202)8:23<5481::AID-CHEM5481>3.0.CO;2-8
21. Moya, S. E.; Georgieva, R.; Bäumler, H.; Richter, W.; Donath, E. *Med. Biol. Eng. Comput.* **2003,** *41,* 504–508. doi:10.1007/BF02348097
22. Georgieva, R.; Moya, S.; Hin, M.; Mitlöhner, R.; Donath, E.; Kiesewetter, H.; Möhwald, H.; Bäumler, H. *Biomacromolecules* **2002,** *3,* 517–524. doi:10.1021/bm010164n
23. Hong, J.; Char, K.; Kim, B.-S. *J. Phys. Chem. Lett.* **2010,** *1,* 3442–3445. doi:10.1021/jz101441a
24. Kurapati, R.; Raichur, A. M. *Chem. Commun.* **2012,** *48,* 6013–6015. doi:10.1039/c2cc32248j
25. Hummers, W. S., Jr.; Offeman, R. E. *J. Am. Chem. Soc.* **1958,** *80,* 1339. doi:10.1021/ja01539a017
26. Kovtyukhova, N. I.; Ollivier, P. J.; Martin, B. R.; Mallouk, T. E.; Chizhik, S. A.; Buzaneva, E. V.; Gorchinskiy, A. D. *Chem. Mater.* **1999,** *11,* 771–778. doi:10.1021/cm981085u
27. Kim, T.-Y.; Kang, H. C.; Tung, T. T.; Lee, J. D.; Kim, H.; Yang, W. S.; Yoon, H. G.; Suh, K. S. *RSC Adv.* **2012,** *2,* 8808–8812. doi:10.1039/c2ra21400h
28. Kudin, K. N.; Ozbas, B.; Schniepp, H. C.; Prud'homme, R. K.; Aksay, I. A.; Car, R. *Nano Lett.* **2008,** *8,* 36–41. doi:10.1021/nl071822y
29. Jeong, H.-K.; Lee, Y. P.; Lahaye, R. J. W. E.; Park, M.-H.; An, K. H.; Kim, I. J.; Yang, C.-W.; Park, C. Y.; Ruoff, R. S.; Lee, Y. H. *J. Am. Chem. Soc.* **2008,** *130,* 1362–1366. doi:10.1021/ja076473o
30. Lee, D. W.; De Los Santos, V. L.; Seo, J. W.; Leon, F. L.; Bustamante, D. A.; Cole, J. M.; Barnes, C. H. W. *J. Phys. Chem. B* **2010,** *114,* 5723–5728. doi:10.1021/jp1002275
31. Moya, S.; Dähne, L.; Voigt, A.; Leporatti, S.; Donath, E.; Möhwald, H. *Colloids Surf., A* **2001,** *183–185,* 27–40. doi:10.1016/S0927-7757(01)00537-4
32. Gao, C.; Leporatti, S.; Moya, S.; Donath, E.; Möhwald, H. *Chem. – Eur. J.* **2003,** *9,* 915–920. doi:10.1002/chem.200390113

License and Terms

BEILSTEIN JOURNAL OF NANOTECHNOLOGY

Nanostructured surfaces by supramolecular self-assembly of linear oligosilsesquioxanes with biocompatible side groups

Maria Nowacka, Anna Kowalewska* and Tomasz Makowski

Full Research Paper

Open Access

Address:
Centre of Molecular and Macromolecular Studies, Polish Academy of Sciences, Sienkiewicza 112, 90-363 Łódź, Poland

Email:
Anna Kowalewska* - anko@cbmm.lodz.pl

* Corresponding author

Keywords:
atomic force microscopy; hydrophilicity; oligosilsesquioxanes; self-assembly; surface

Beilstein J. Nanotechnol. **2015,** *6,* 2377–2387.
doi:10.3762/bjnano.6.244

Received: 09 September 2015
Accepted: 27 November 2015
Published: 11 December 2015

This article is part of the Thematic Series "Organized films".

Guest Editor: M. Canepa

Abstract

Linear oligomeric silsesquioxanes with polar side moieties (e.g., carboxylic groups and derivatives of *N*-acetylcysteine, cysteine hydrochloride or glutathione) can form specific, self-assembled nanostructures when deposited on mica by dip coating. The mechanism of adsorption is based on molecule-to-substrate interactions between carboxylic groups and mica. Intermolecular cross-linking by hydrogen bonds was also observed due to the donor–acceptor character of the functional groups. The texture of supramolecular nanostructures formed by the studied materials on mica was analysed with atomic force microscopy and their specific surface energy was estimated by contact angle measurements. Significant differences in the surface roughness, thickness and the arrangement of macromolecules were noted depending on the kind of functional groups on the side chains. Specific changes in the morphology of the surface layer were observed when mica was primed with a monolayer of small organic compounds (e.g., *N*-acetylcysteine, citric acid, thioglycolic or acid). The adsorption of both silsesquioxane oligomers and organic primers was confirmed with attenuated total reflectance infrared spectroscopy. The observed physiochemical and textural variations in the adsorbed materials correlate with the differences in the chemical structure of the applied oligomers and primers.

Introduction

The modification of surface properties can be used as a versatile tool in materials engineering for biological and medical purposes [1-4]. The focus has been more recently shifted towards hydrophilic surfaces due to their antifouling properties [5]. Cell biology applications also require new materials that could mimic the natural biological environment of cells and resemble the natural extracellular matrix (ECM). The surface chemical composition and topography that define the free energy [6-9] also impact the pre-adsorbed protein layer and can mediate cell–substrate interactions [3,10-21]. Substrates bearing COOH groups can be used to control the cell behaviour via interactions with the underlying matrix. For example, surfaces

carrying COOH groups were applied for studies on the effect of surface wettability on protein adsorption and adhesion of human umbilical vein endothelial cells (HUVECs) and HeLa cells [3], human fibroblasts [14], human mesenchymal stem cells [15,22], corneal epithelial cells [23], fibroblasts [24], myoblasts [25] and endothelial cells [26]. Substrates with COOH groups were also used to elucidate the role of chemistry-dependent differences in cell differentiation owing to specific binding to proteins adsorbed on the surface [25,27,28].

Well-defined substrates made of small molecule self-assembled monolayers (SAMs) [3,14,23-30] and self-assembled polymer monolayers (PSAMs) [12,31-33] are thus promising candidates for such purpose-tailored bioengineering tools. The structure of the SAMs and PSAMs strongly depends on the operating mechanism of adsorption [34,35]. These two types of monolayers can differ significantly due to conformational variabilities observed for macromolecular chains. On the other hand, PSAMs offer improved surface stability, ease in processing, unique chemical specificity and tunable surface energy [12,31-33,36].

We have recently found that linear oligosilsesquioxanes functionalized with 2-(carboxymethylthio)ethyl side groups (LPSQ-COOH) can adsorb from their solutions and spontaneously form well-ordered and stable, PSAM-type, 2D nanolayers at the surface of muscovite mica, which renders the surface exceptionally hydrophilic [37,38]. Muscovite mica, chosen as a substrate for the present study, is a layered aluminosilicate [$KAl_2(Si_3AlO_{10})(OH)_2$] that exhibits interesting surface properties and chemical specificity. Potassium ions electrostatically bind the alternating aluminosilicate sheets in the lamellar structure of mica. The mineral can be easily cleaved along the plane located in the K^+ layer to expose a perfectly smooth surface [39] that can serve as a very good AFM imaging substrate for studies on biomaterials [40,41] and polymers [42,43]. Upon exfoliation, K^+ becomes accessible to acidic molecules and can be involved in the formation of surface salts. For example, potassium carboxylates generated on the surface of mica assist the process of adsorption of fatty acids [44-47] and their derivatives [48].

The character of the interactions between the oligomers and the substrate also defines the structure of the assemblies of LPSQ-COOH on mica [37]. It was thus of interest to study if the morphology of the surface layer of PSAMs and its physicochemical properties can be changed by alteration of the mechanism of adsorption on mica. The structure of the PSAMs was engineered both by alteration of the functional groups on the surface as well as those belonging to the side chains of LPSQ. In this report we present the modification of mica with linear oligomeric silsesquioxanes (LPSQ-COOH/X) with side groups bearing 2-(carboxymethylthio)ethyl where the X-groups are derivatives of *N*-acetylcysteine (NAC), cysteine hydrochloride (Cys-HCl) and glutathione (GSH). Such self-assembled PSAMs based on polysilsesquioxane materials are attractive for surface nanopatterning and bioengineering, including preparation of surfaces rich in organic groups typical of the extracellular matrix in living organisms (e.g., CH_3, OH, NH_2 and COOH).

We have investigated the effect of the kind of functional groups in side chains of LPSQ-COOH/X on the structure (e.g., surface roughness, thickness and arrangement of macromolecules within the coated layer) of the prepared PSAMs. Native mica was used bare or primed, prior to the coating with LPSQ-COOH/X, with a monolayer of *N*-acetylcysteine, citric acid or thioglycolic acid. The primers are bound to mica by ionic bonds (carboxylates) and simultaneously provide the substrate with new organic functions capable of hydrogen bonding [49].

Atomic force microscopy (AFM) and attenuated total reflectance infrared spectroscopy (ATR-FTIR) were used as analytic tools for the studies. The changes in the free surface energy of the prepared hydrophilic surfaces were also investigated for all LPSQ-COOH/X adsorbed on native and primed mica. The obtained results suggest that both the composition of side polymer chains and the kind of functional groups on the surface are key factors defining the structure and properties of PSAMs based on LPSQ-COOH/X.

Results and Discussion

Supramolecular assemblies of LPSQ-COOH/X on native mica

Functionalized ladder-like silsesquioxanes (LPSQ-COOH/X) were prepared (Scheme 1, Table 1) by the two-step addition of organic thio-derivatives, i.e., thioglycolic acid, *N*-acetylcysteine (NAC), glutathione (GSH) and cysteine hydrochloride (Cys-HCl), to the side chains of vinyl-containing LPSQ precursors obtained by polycondensation of cyclic tetravinylsiloxanetetraols [50]. The thiol-ene additions were photoinitiated by 2,2-dimethoxy-2-phenylacetophenone (DMPA) (full experimental data can be found in Supporting Information File 1). Thin layers of LPSQ-COOH/X were deposited onto freshly cleaved mica substrates by dip coating from their diluted solutions and the morphology of the coated samples was studied with AFM (Figure 1).

AFM studies of LPSQ-COOH/X coated on native mica

The structure and reactivity of LPSQ-COOH/X makes the polymers suitable for the formation of planar PSAMs on various reactive surfaces. Side carboxylic groups in LPSQ-COOH/X

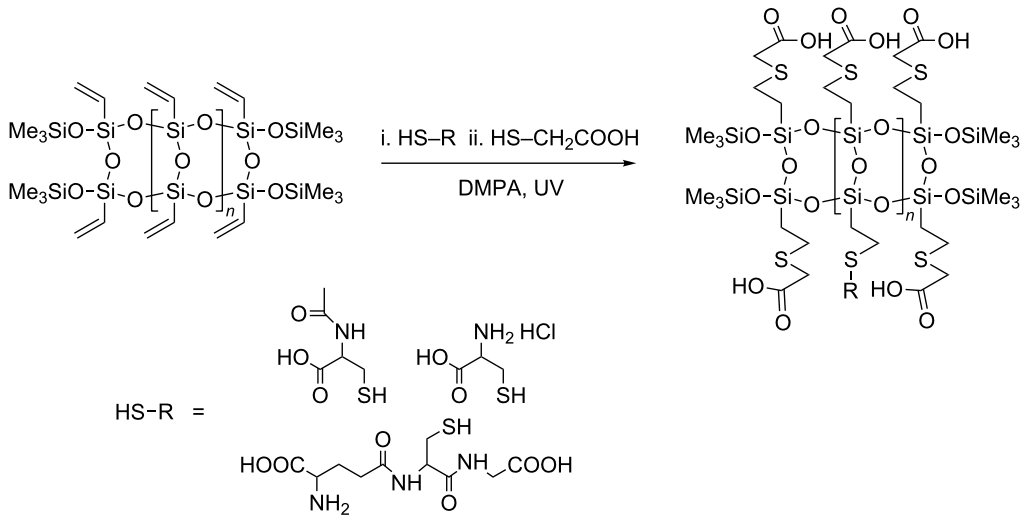

Scheme 1: Synthesis of LPSQ-COOH/X.

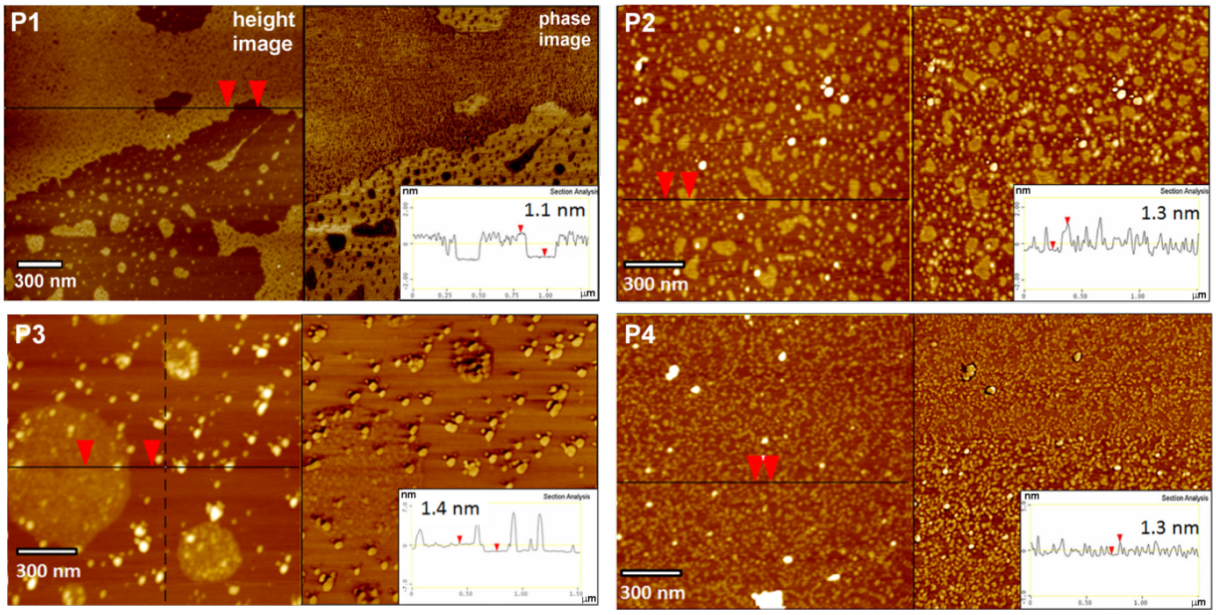

Figure 1: AFM height and phase images and the corresponding surface profiles of P1, P2, P3 and P4, dip-coated on bare mica. P1, P3 and P4: 0.045 wt % solutions in THF; P2: 0.045 wt % solution in MeOH; immersion time t_i = 5 s.

Table 1: Composition of the prepared LPSQ-COOH/X.

Sample	Side group amount (mol %)			
	COOH	Cys-HCl	GSH	NAC
P1	100	–	–	–
P2	80	20	–	–
P3	80	–	20	–
P4	80	–	–	20

allow for a very efficient polymer anchoring on the surface due to both multipoint ionic substrate–adsorbate interactions and adsorbate–adsorbate hydrogen bonding [37]. The formation of ordered SAMs and PSAMs at the liquid–solid interface can occur only if it is energetically allowed by entropy–enthalpy compensation [51-53]. Thus, the mechanism of adsorption of LPSQ-COOH/X on mica should be discussed with respect to possible intermolecular interactions between polymer chains and their relations with the substrate. Macromolecules consisting of surface-reactive repeating units can made for a

special case of PSAMs – the one not anchored at the end point but adsorbed parallel to the surface [31]. The thickness of such PSAMs depends on the flexibility of the polymer backbone and its affinity for the surface [54]. In the case of high-affinity adsorption and rigid polymers, it is close to the chain width.

The results obtained for LPSQ-COOH/X using AFM (topographic images and height profiles) suggest a specific packing of the chains on the surface of mica. LPSQ-COOH can form fine nanolayers (Figure 1) of thickness that correlates well with the estimated macromolecule width. This was estimated to be about 1.6 nm, as calculated for the structure of a LPSQ-COOH oligomer constructed on HyperChem platform and modelled in vacuum using a molecular mechanics force field MM+ method (Polak–Ribiere/conjugate gradient optimization algorithm) and a semi-empirical PM3 method (single point energy calculations [37]. However, macromolecules of LPSQ-COOH/GSH, LPSQ-COOH/Cys-HCl and LPSQ-COOH/NAC do not easily extend parallel to the mica substrate. The surface of coated samples is covered with globular nano-objects (Figure 1) that can be possibly formed by single oligomers (or their clusters) that are coiled due to intramolecular hydrogen bonding between the compatible side groups. ATR-FTIR spectra (Supporting Information File 1) confirmed that COOH groups in all the studied polymers are involved in the formation of adsorbed surface structures (a substantial decrease of the $\nu_{C=O}$ band at ≈1700 cm^{-1} and emergence of diffuse bands in the formed PSAMs was observed).

Surface energy of LPSQ-COOH/X coated on native mica

The surface free energy (γ_S) of each studied PSAM sample was determined by measuring the contact angle of water and glycerol as reference liquids (sessile drop technique and Owens–Wendt geometric mean Equation S1 described in Supporting Information File 1 [55]). We have previously reported [37,38] that the very good wettability of mica coated with LPSQ-COOH is a result of the structure of adsorbed nanolayers and the fact that carboxylic groups attached to oligomers of LPSQ-COOH adopt a specific conformation at the interface with air. We have analysed the wettability of samples covered with other LPSQ-COOH/X schemes (Figure 2) to find that, in spite of their different morphology, they exhibit almost the same surface energy and the ratio between polar and dispersive forces. The COOH moieties in these polymers bind to the surface of native mica but the remaining polar groups can interact with neighbouring substituents (e.g., dimerization of COOH, or formation of amine salts (–$COO^-NH_2^+$– and –$COO^-NH_3^+$–)) and establish a network of hydrogen bonds. The slightly poorer wettability of P4 can be ascribed to the presence of the acetyl group, protecting the NH_2 function of NAC.

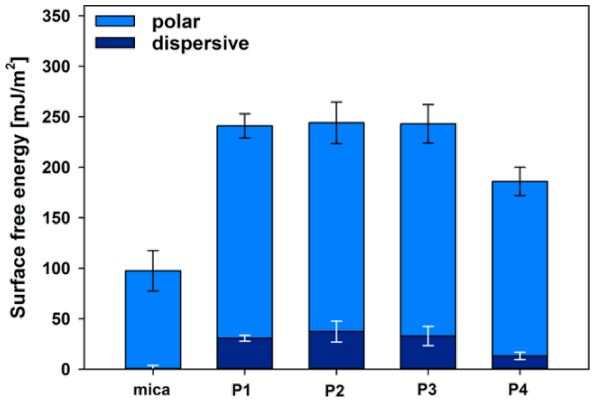

Figure 2: Surface free energy of LPSQ-COOH/X coated on native mica determined by wetting angle measurements.

We have analysed the effect of surface roughness on changes in γ_S (Figure 1, Figure 2, and Figures S1a, S2a, S3a, S4a and Table S1 in Supporting Information File 1). All surfaces are smooth (with root mean squared roughness factor, R_q = 0.03 nm for native mica and ≈0.1 ÷ 0.25 nm for PSAMs). No correlation could be found between R_q and γ_S. The increase of γ_S observed for all studied PSAMs can be tentatively linked to the presence of specific side groups in the adsorbed polymers, capable of effective hydrogen bonding.

Supramolecular assemblies of LPSQ-COOH/X on primed mica

The adsorption of LPSQ-COOH/X on native mica is governed by the formation of surface salts–potassium carboxylates. It was of interest to alter these ionic interactions between LPSQ and mica and block the K^+ ions by adsorption of small molecules [49]. They should be simultaneously capable of the formation of surface salts and hydrogen bonds with functional groups in side chains of LPSQ-COOH/X. Consequently, thioglycolic acid (TG), citric acid (CA) and *N*-acetylcysteine (NAC) were selected and used as primers to modify the surface properties of mica (Scheme 2). They were adsorbed from their diluted solutions in THF or MeOH. The excess of the primer compound was removed by washing the sample with THF.

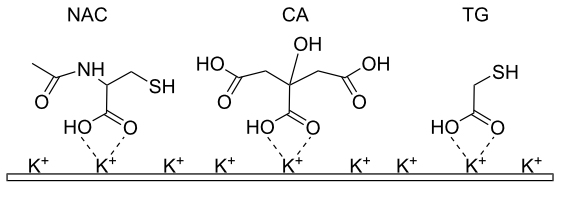

Scheme 2: Functionalization of native mica by adsorption of *N*-acetylcysteine (NAC), citric acid (CA) and thioglycolic acid (TG).

The formation of surface salts (potassium carboxylates) by the used primers was confirmed by ATR-FTIR analysis (Figure 3). Comparison of the FTIR spectra in the region characteristic to COOH groups shows almost complete disappearance of $\nu_{C=O}$ bands observed for the native compounds and formation of diffuse bands characteristic for carboxylates [56]. The only exception is citric acid, which due to the geometric constraints, cannot adsorb on the surface with all of three COOH groups present in the molecule. As expected, part of the COOH groups of adsorbed CA is still available for macromolecules adsorbed as PSAMs. The carboxylic groups of TG are completely transformed into carboxylates. Quite interestingly, two FTIR bands characteristic of the amide bond in NAC (amide I at 1567 cm^{-1} (stretching vibrations of the amide C=O bond) and amide II at 1523 cm^{-1} (bending vibrations of the N–H bond)) disappeared after its adsorption on mica. This phenomenon can be ascribed to changes in geometry of NAC and possible interactions of C=O in the amide unit with K^+ on the surface of mica.

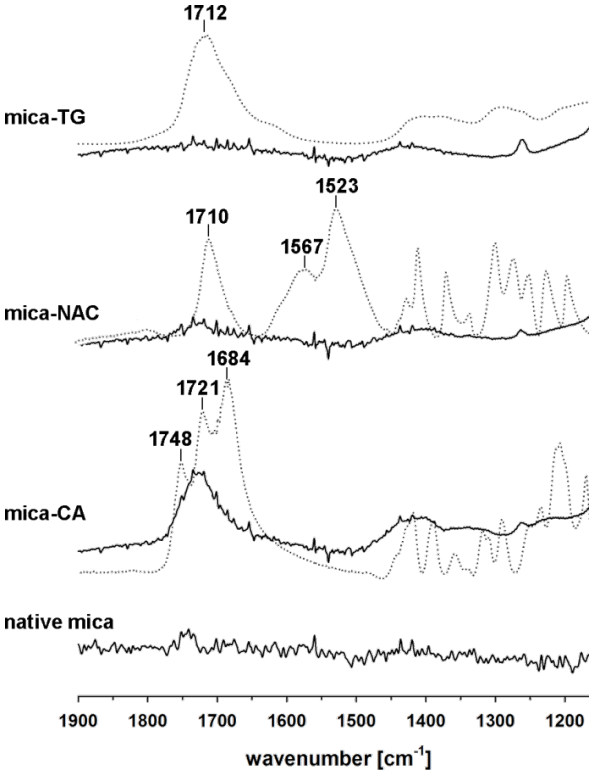

Figure 3: ATR-FTIR spectra (1900–1150 cm^{-1} region) of TG, NAC and CA before (dotted lines) and after their adsorption on muscovite mica.

AFM was used to analyse the structure of coated samples (Figure 4). We found that the priming compounds evenly cover the surface. The adherence of the used molecules to mica is very high. Dewetting of the adsorbed materials was not observed and the upper layer was not removed or mechanically deformed with the probing tip of the cantilever during the measurement. For NAC and CA, specific structures that suggest formation of multilayered assemblies due to the presence of hydrogen bond accepting groups were observed. The AFM

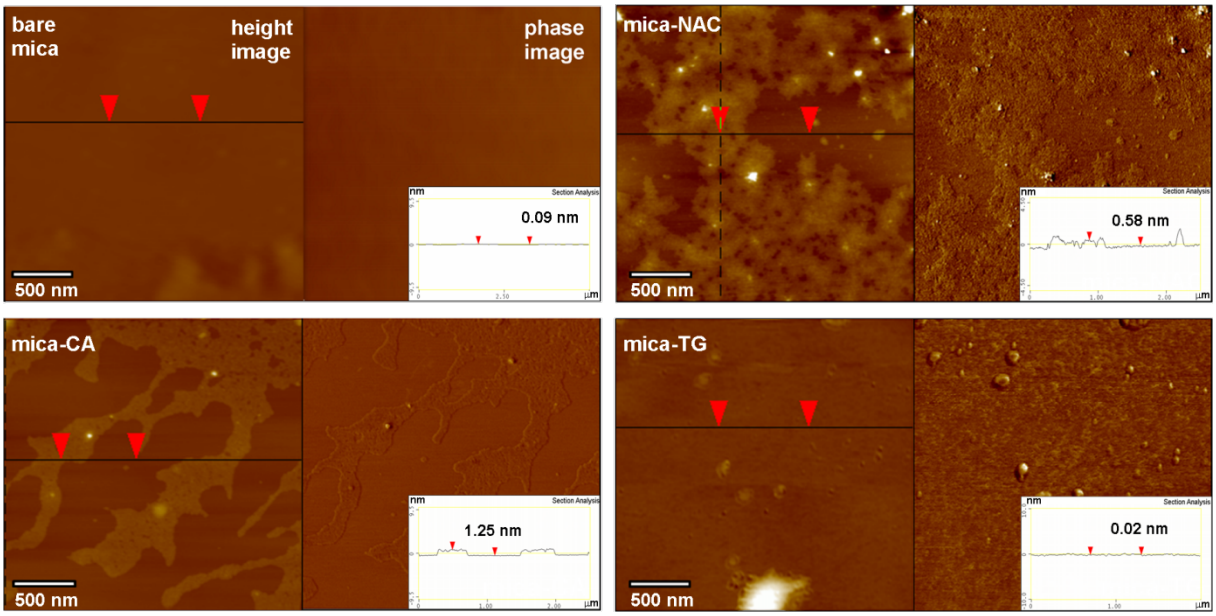

Figure 4: AFM height and phase images of bare mica and mica modified with *N*-acetylcysteine (mica-NAC), citric acid (mica-CA) and thioglycolic acid (mica-TG). The modified samples were prepared by immersion (t_i = 15 min) of mica in 0.002 M solutions of primers in THF, followed by washing the excess primer by immersion in pure THF (t_i = 5 s).

micrographs (Figure 4) show that the top layers have thickness of 0.58 ÷ 1.25 nm, whereas the thickness of a single layer should be close to 0.5 nm (Supporting Information File 1, Figure S6). The R_q parameter estimated with AFM for these substrates is low (0.24 nm and 0.095 nm for the topmost layers, respectively). For both compounds patches of base layers can be observed that are more smooth (R_q = 0.077 and 0.047 nm). They do not exhibit clear phase contrast and it cannot be asserted whether they are areas of well-packed molecules or bare mica (R_q = 0.032 nm for bare mica). The surface of mica covered with TG bearing thiol functions (less effective in hydrogen bonding) is uniform and very smooth (R_q = 0.117 nm) except for visible drops of excess primer. Priming mica with NAC, CA and TG thus yields smooth, chemo-specific, hydrophilic supports (see later also Figure 9a and Discussion). The abundance of hydroxyl and carboxyl groups on mica treated with CA is responsible for its exceptionally high surface energy.

AFM studies of LPSQ-COOH/X adsorbed on primed mica

After priming, the mica tiles were air-dried and then the polymer layer was adsorbed from diluted solutions of functionalized LPSQ-COOH/X and analysed with AFM and ATR-FTIR. The structure of PSAMs adsorbed on primed mica depends both on the type of primer and the chemical structure of adsorbed macromolecules. The mechanism of adsorption and the character of formed hydrogen bonds is different than that of bare mica. In spite of this, the surface and interlayer adherence is good. The morphology of the samples prepared on muscovite mica treated with citric acid (mica-CA, Figure 5) is governed by the presence of the residual carboxyl groups. The homopolymer P1 (LPSQ-COOH) can form very smooth assemblies on native mica but on mica-CA it tends to coil into fine particles. This can be ascribed to the preferential formation of dimeric hydrogen bonds (intra/intermolecular and surface-P1) involving carboxyl moieties and the lack of predominant, chain-straightening interactions with mica. This phenomenon illustrates the importance of strong surface–adsorbate interactions for the formation of well-assembled PSAMs (Figure 6).

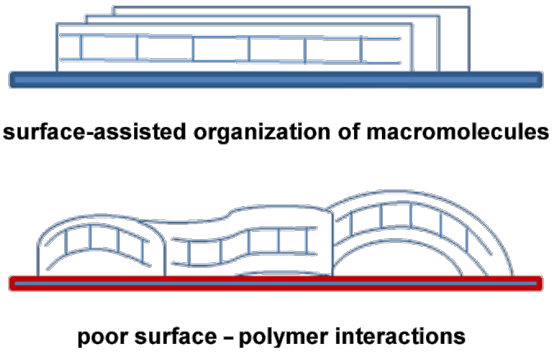

Figure 6: Structure of PSAMs based on LPSQ-COOH/X defined by surface–polymer interactions (composition of side polymer chains and the kind of functional groups on the surface).

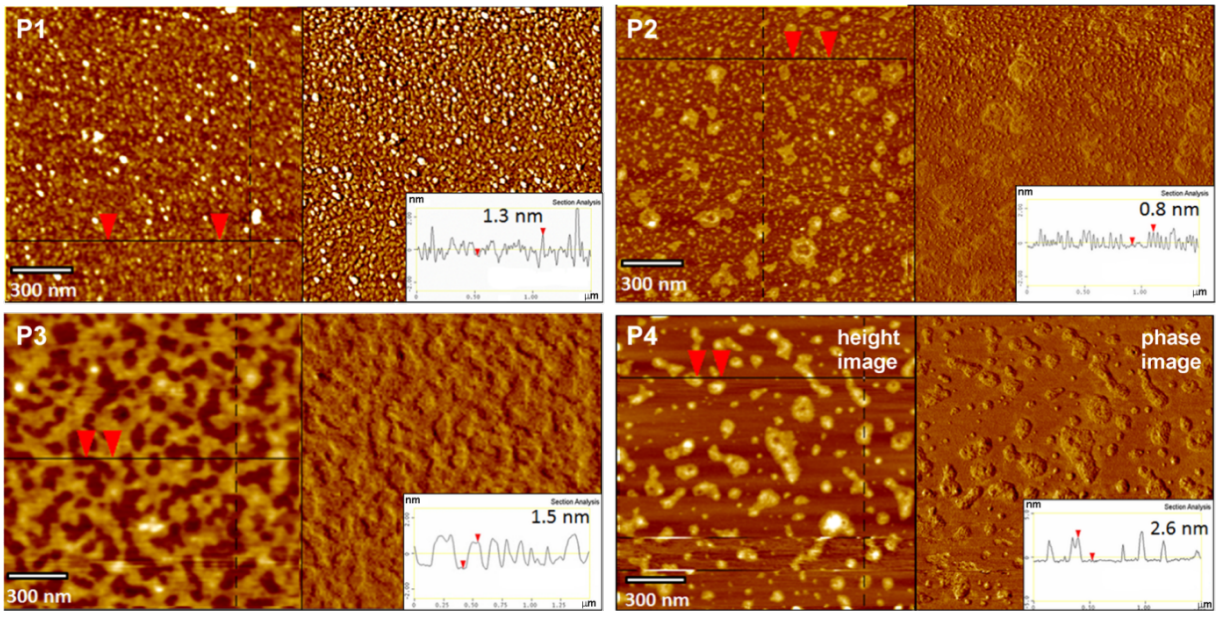

Figure 5: AFM height and phase images and the corresponding surface profiles of P1, P2, P3 and P4, dip-coated on mica modified with citric acid. P1, P3 and P4: 0.045 wt % solutions in THF; P2: 0.045 wt % solution in MeOH; immersion time t_i = 5 s.

ATR-FTIR studies in the sensitive region (1900–1150 cm^{-1}) indicate a significant alteration in the nature of interactions between the studied macromolecules and the surface (Figure 7 and Supporting Information File 1). The most clear changes can be observed for sample P1 (Figure 7) that binds to the native mica through ionic bonds with the K^+ layer, and the rest of the COOH groups involved in the intermolecular interactions form a network of hydrogen bonds arranged mostly in linear (catemeric) structures resulting in a characteristic FTIR $\nu_{C=O}$ band at ≈1720 cm^{-1} [37]. The thermally induced reshuffling of the catemeric form into an arrangement with dimeric –COOH···HOOC– units results in a shift of the $\nu_{C=O}$ band to 1600 cm^{-1} [38]. A similar shift can be found for P1 adsorbed on primed mica. It correlates with the difference in the topographic structure observed by AFM for P1 adsorbed on native and primed mica (Figure 1, Figure 5, Figure 8 and Figure 9). It can be surmised that LPSQ-COOH is anchored on the primed surface (formation of hydrogen bonds with C=O, SH and NH moieties) but instead of producing lamellar structures bound by hydrogen bonds (linear catemeric structures) it adheres to mica as clusters of polymeric chains cross-linked by –COOH···HOOC– dimers or amine salts (–$COO^-NH_2^+$– and –$COO^-NH_3^+$–).

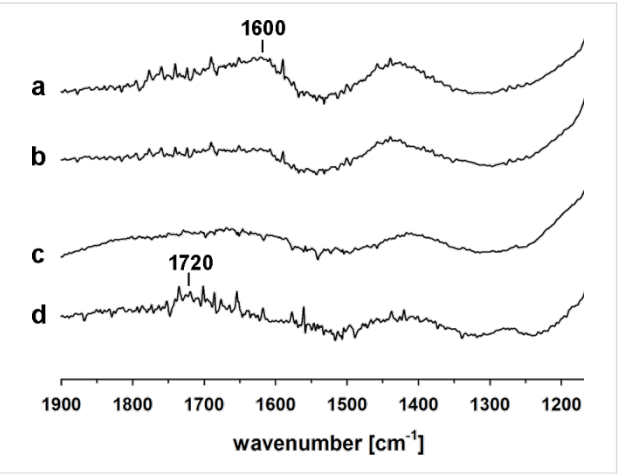

Figure 7: ATR-FTIR spectra (1900–1150 cm^{-1} region) of P1 adsorbed on (a) mica-CA, (b) mica-TG, (c) mica-NAC and (d) native mica.

Species P2, P3 and P4, having donor/acceptor NH/NH_2 units, can adsorb on mica-CA via formation of complementary hydrogen bonds with COOH groups, which results in a change of the surface morphology (Figure 5). P3 bearing GSH units forms different structures than P2 and P4, which can be explained by better accessibility of donor/acceptor units in GSH molecules. Cys-HCl and NAC in P2 and P4 are more hindered by the polymer matrix.

A similar trend can be observed for samples adsorbed on supports pretreated with mica-TG or mica-NAC (Figure 8 and Figure 9). Thiol groups are present on both surfaces. Thiols are more nucleophilic than hydroxyls and thus their ability for the formation of hydrogen bonds is different. P1 produces well-ordered layers on mica-TG and multilayered globular formations on mica-NAC. P2 and P4 are well-dispersed on surfaces

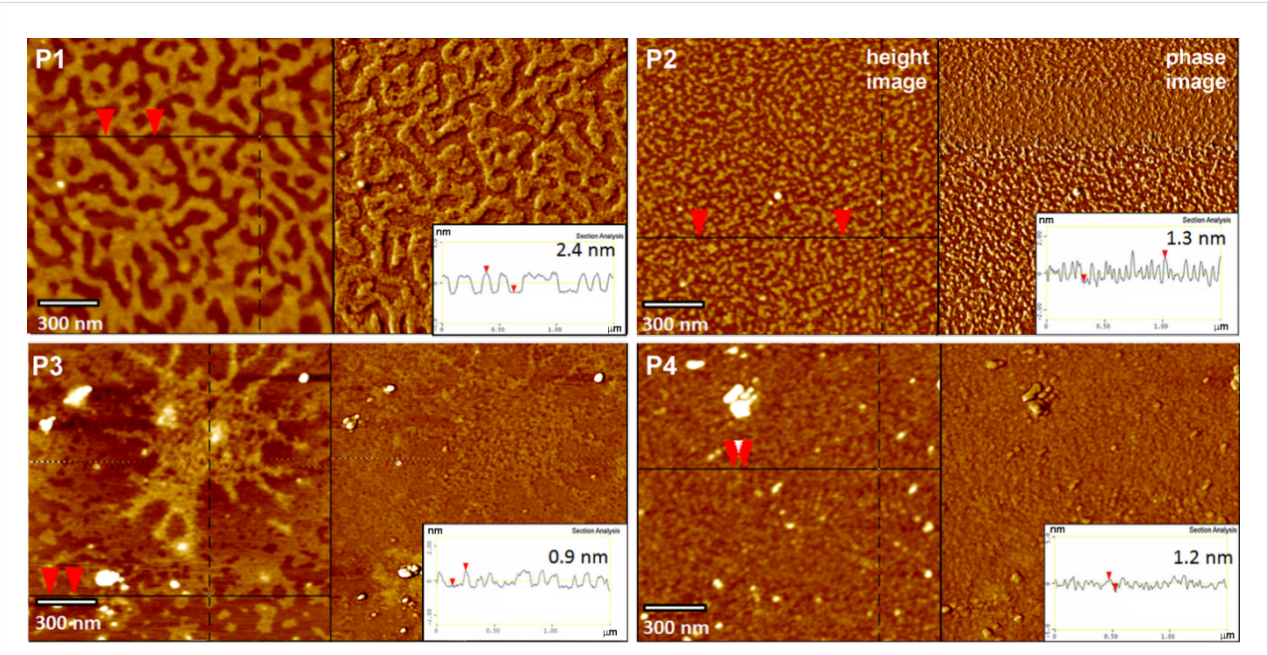

Figure 8: AFM height and phase images and the corresponding surface profiles of P1, P2, P3 and P4, dip-coated on mica modified with thioglycolic acid. P1, P3 and P4: 0.045 wt % solutions in THF; P2: 0.045 wt % solution in MeOH; immersion time t_i = 5 s.

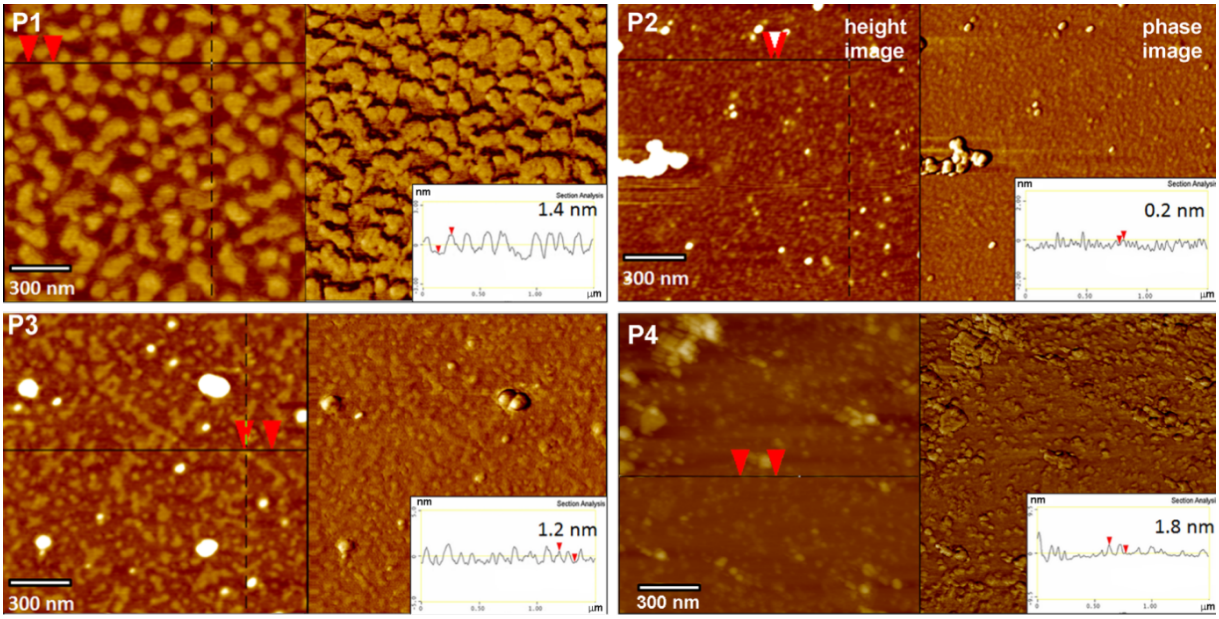

Figure 9: AFM height and phase images and the corresponding surface profiles of P1, P2, P3 and P4, dip-coated on mica modified with *N*-acetylcysteine. P1, P3 and P4: 0.045 wt % solutions in THF; P2: 0.045 wt % solution in MeOH; immersion time t_i = 5 s.

obtained with those supports. The morphology of surfaces covered with P3 suggests good interaction between GSH units in the polymer and thiol groups on mica.

Surface energy of LPSQ-COOH/X coated on primed mica

The surface free energy measurements (Figure 10) proved the proposed model of adsorption of NAC, CA and TG (Scheme 2) by ionic interactions of COOH substituents with K^+ ions on the surface of mica. Such an arrangement of the multifunctional primers exposes reactive polar groups (e.g., SH, NH, OH and COOH). Their ability for the formation of hydrogen bonds with probe liquids (H_2O and glycerol) defines the wettability and chemical specificity of the modified supports (Figure 10a). The results are in accordance with ATIR-FTIR data (Figure 3). Citric acid, which was shown to adsorb on mica with part of its COOH moieties, gives the most hydrophilic surface.

The analysis of the surface roughness and changes in the free surface energy did not indicate any defined trend that could indicate an effect of surface structure on its wettability. It must be stressed that all the prepared samples exhibit R_q < 0.5 nm, which is characteristic of smooth surfaces.

The modification of mica-CA by adsorption of LPSQ-COOH/X results in a decrease of the surface free energy (Figure 10b). The most significant effect was observed for P1. It can be explained by the formation of dimeric structures by COOH groups, which was recently reported as the cause for the decrease of surface wettability [38]. The extent of the surface-guided organization of P1 directs its arrangement on the support and changes of the surface energy (Figure 10b,c). P2, in spite of the apparent lack of lamellar organization on the surface, exhibits the highest surface free energy among the studied samples (Figure 10b–d), which can be explained by the presence of the polar amine function. When NH_2 is protected by an acetyl group (polymer P4), the wettability of the coated samples is lower.

Conclusion

The structure and properties of PSAMs made of ladder-like oligosilsesquioxanes LPSQ-COOH/X on chemo-reactive supports (bare and functionalized muscovite mica) have been analysed. The AFM studies showed that linear oligomers adsorb on the surface of mica and form various types of structures, depending both on the morphology of LPSQ-COOH/X and the chemical specificity of the support. The functional groups in side chains have a significant impact on the arrangement of macromolecules, surface pattern and hydrophilicity. The distribution of the studied macromolecules within the adsorbed PSAMs is a consequence of both polymer–substrate as well as inter- and intramolecular bonding. The homopolymer LPSQ-COOH can form the smoothest layers with macromolecules arranged horizontally in the monolayer due to the specific mechanism of their adsorption on mica. An alternative adsorption mechanism and the shifting of the orientation of the

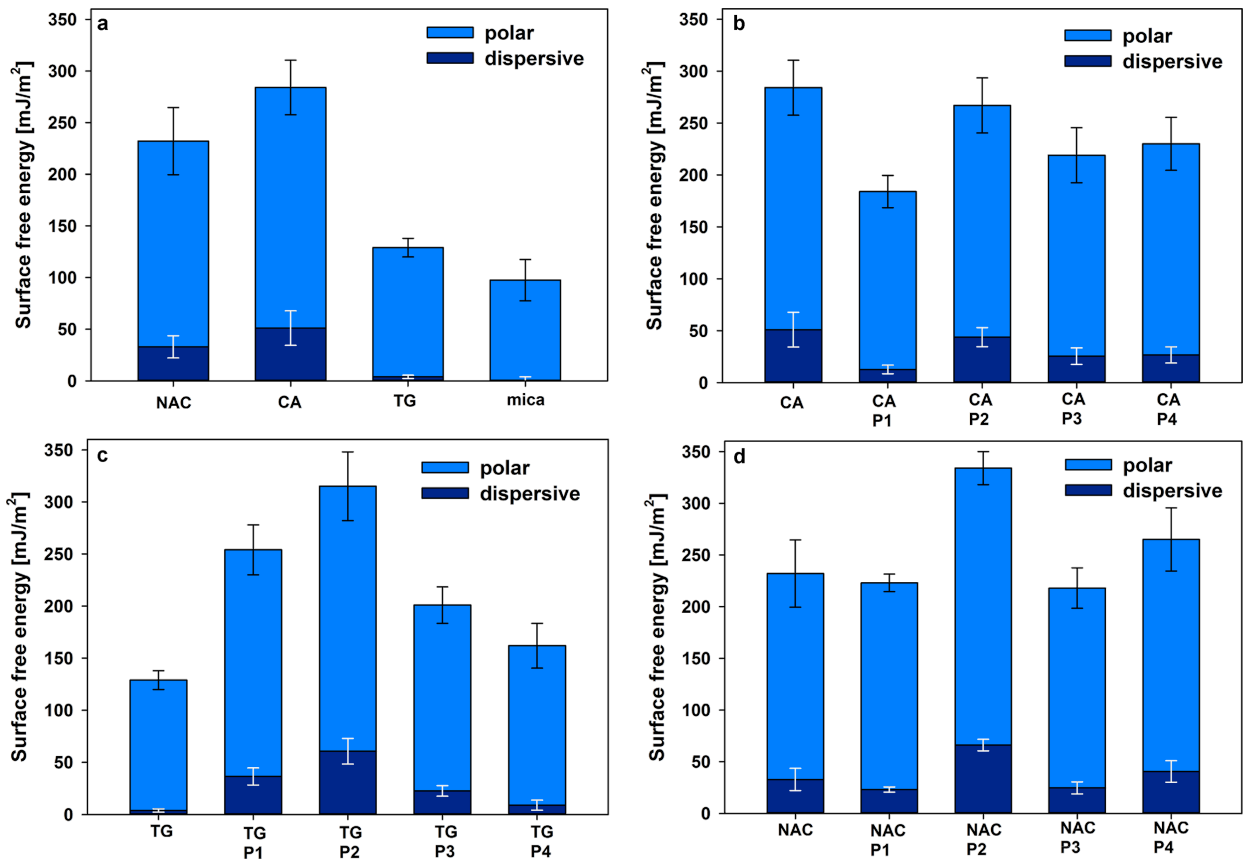

Figure 10: Surface energy of (a) mica pretreated with NAC, CA and TG; (b) P1, P2, P3 and P4 adsorbed on mica-CA; (c) P1, P2, P3 and P4 adsorbed on mica-TG; and (d) P1, P2, P3 and P4 adsorbed on mica-NAC, as determined by wetting angle measurements.

silsesquioxane chains towards more mushroom-like shapes allows for the possibly for other LPSQ-COOH/X schemes. It was also found that priming the substrate with small organic compounds can alter the structure of the adsorbed polymeric films due to the change of specific interactions between the polymer and the surface. The presented, simple approach for the preparation of hydrophilic, nanopatterned surfaces rich in organic polar groups can be especially useful in bioengineering.

Supporting Information

The supporting information features all experimental procedures, characterization methods, and NMR spectral data for the prepared LPSQ-COOH/X materials in addition to the ATR-FTIR spectra of P1, P2, P3 and P4, adsorbed on mica-CA, mica-TG and mica-NAC.

Supporting Information File 1

Experimental part.
[http://www.beilstein-journals.org/bjnano/content/supplementary/2190-4286-6-244-S1.pdf]

Acknowledgements

The authors thank the Polish National Science Centre for the financial support within grant DEC-2011/03/B/ST5/02672 ‘‘Studies on preparation and structurization of new hybrid materials’’. We also acknowledge the assistance of Adam Michalski in recording ATR-FTIR spectra.

References

1. Somorjai, G. A.; Li, Y. *Proc. Natl. Acad. Sci. U. S. A.* **2011,** *108,* 917–924. doi:10.1073/pnas.1006669107
2. Hudalla, G. A.; Murphy, W. L. *Soft Matter* **2011,** *7,* 9561–9571. doi:10.1039/c1sm05596h
3. Arima, Y.; Iwata, H. *Biomaterials* **2007,** *28,* 3074–3082. doi:10.1016/j.biomaterials.2007.03.013
4. Palacio, M. L. B.; Bhushan, B. *Philos. Trans. R. Soc., A* **2012,** *370,* 2321–2347. doi:10.1098/rsta.2011.0483
5. Drelich, J.; Chibowski, E.; Meng, D. D.; Terpilowski, K. *Soft Matter* **2011,** *7,* 9804–9828. doi:10.1039/c1sm05849e
6. Azimi, G.; Dhiman, R.; Kwon, H.-M.; Paxson, A. T.; Varanasi, K. K. *Nat. Mater.* **2013,** *12,* 315–320. doi:10.1038/nmat3545
7. Yilgor, I.; Bilgin, S.; Isik, M.; Yilgor, E. *Langmuir* **2012,** *28,* 14808–14814. doi:10.1021/la303180k
8. Mendes, P. M. *Chem. Soc. Rev.* **2008,** *37,* 2512–2529. doi:10.1039/B714635N

9. Liu, X.; Wang, S. *Chem. Soc. Rev.* **2014,** *43,* 2385–2401. doi:10.1039/C3CS60419E
10. Higuchi, A.; Ling, Q.-D.; Chang, Y.; Hsu, S.-T.; Umezawa, A. *Chem. Rev.* **2013,** *113,* 3297–3328. doi:10.1021/cr300426x
11. Rashidi, H.; Yang, J.; Shakesheff, K. M. *Biomater. Sci.* **2014,** *2,* 1318–1331. doi:10.1039/C3BM60330J
12. Li, D.; Zheng, Q.; Wang, Y.; Chen, H. *Polym. Chem.* **2014,** *5,* 14–24. doi:10.1039/C3PY00739A
13. Schaap-Oziemlak, A. M.; Kühn, P. T.; van Kooten, T. G.; van Rijn, P. *RSC Adv.* **2014,** *4,* 53307–53320. doi:10.1039/C4RA07915A
14. Faucheux, N.; Schweiss, R.; Lützow, K.; Werner, C.; Groth, T. *Biomaterials* **2004,** *25,* 2721–2730. doi:10.1016/j.biomaterials.2003.09.069
15. Curran, J. M.; Chen, R.; Hunt, J. A. *Biomaterials* **2006,** *27,* 4783–4793. doi:10.1016/j.biomaterials.2006.05.001
16. Ren, Y.-J.; Zhang, H.; Huang, H.; Wang, X.-M.; Zhou, Z.-Y.; Cui, F.-Z.; An, Y.-H. *Biomaterials* **2009,** *30,* 1036–1044. doi:10.1016/j.biomaterials.2008.10.028
17. Lee, J. H.; Jung, H. W.; Kang, I.-K.; Lee, H. B. *Biomaterials* **1994,** *15,* 705–711. doi:10.1016/0142-9612(94)90169-4
18. Lee, J. H.; Khang, G.; Lee, J. W.; Lee, H. B. *J. Colloid Interface Sci.* **1998,** *205,* 323–330. doi:10.1006/jcis.1998.5688
19. Tamada, Y.; Ikada, Y. *J. Colloid Interface Sci.* **1993,** *155,* 334–339. doi:10.1006/jcis.1993.1044
20. Rodríguez Patino, J. M.; Rodríguez Niño, M. R.; Carrera Sánchez, C. *Curr. Opin. Colloid Interface Sci.* **2007,** *12,* 187–195. doi:10.1016/j.cocis.2007.06.003
21. Zhai, J. L.; Day, L.; Aguilar, M.-I.; Wooster, T. J. *Curr. Opin. Colloid Interface Sci.* **2013,** *18,* 257–271. doi:10.1016/j.cocis.2013.03.002
22. Curran, J. M.; Chen, R.; Hunt, J. A. *Biomaterials* **2005,** *26,* 7057–7067. doi:10.1016/j.biomaterials.2005.05.008
23. Franco, M.; Nealey, P. F.; Campbell, S.; Teixeira, A. I.; Murphy, C. J. *J. Biomed. Mater. Res., Part A* **2000,** *52,* 261–269. doi:10.1002/1097-4636(200011)52:2<261::AID-JBM4>3.0.CO;2-2
24. McClary, K. B.; Ugarova, T.; Grainger, D. W. *J. Biomed. Mater. Res., Part A* **2000,** *50,* 428–439. doi:10.1002/(SICI)1097-4636(20000605)50:3<428::AID-JBM18>3.0.CO;2-H
25. Lan, M. A.; Gersbach, C. A.; Michael, K. E.; Keselowsky, B. G.; García, A. J. *Biomaterials* **2005,** *26,* 4523–4531. doi:10.1016/j.biomaterials.2004.11.028
26. Tidwell, C. D.; Ertel, S. I.; Ratner, B. D.; Tarasevich, B. J.; Atre, S.; Allara, D. L. *Langmuir* **1997,** *13,* 3404–3413. doi:10.1021/la9604341
27. Keselowsky, B. G.; Collard, D. M.; García, A. J. *Proc. Natl. Acad. Sci. U. S. A.* **2005,** *102,* 5953–5957. doi:10.1073/pnas.0407356102
28. Lee, M. H.; Ducheyne, P.; Lynch, L.; Boettiger, D.; Composto, R. J. *Biomaterials* **2006,** *27,* 1907–1916. doi:10.1016/j.biomaterials.2005.11.003
29. Ulman, A. *Chem. Rev.* **1996,** *96,* 1533–1554. doi:10.1021/cr9502357
30. Marmisollé, W. A.; Capdevila, D. A.; de la Llave, E.; Williams, F. J.; Murgida, D. H. *Langmuir* **2009,** *29,* 5351–5359. doi:10.1021/la304730q
31. Park, J.-W.; Kim, H.; Han, M. *Chem. Soc. Rev.* **2010,** *39,* 2935–2947. doi:10.1039/b918135k
32. Senaratne, W.; Andruzzi, L.; Ober, C. K. *Biomacromolecules* **2005,** *6,* 2427–2448. doi:10.1021/bm050180a
33. Welch, M. E.; Ober, C. K. *J. Polym. Sci., Part B: Polym. Phys.* **2013,** *51,* 1457–1472. doi:10.1002/polb.23356
34. Love, J. C.; Estroff, L. A.; Kriebel, J. K.; Nuzzo, R. G.; Whitesides, G. M. *Chem. Rev.* **2005,** *105,* 1103–1170. doi:10.1021/cr0300789
35. Maroni, P.; Montes Ruiz-Cabello, F. J.; Cardoso, C.; Tiraferri, A. *Langmuir* **2015,** *31,* 6045–6054. doi:10.1021/acs.langmuir.5b01103
36. Kobayashi, M.; Terayama, Y.; Yamaguchi, H.; Terada, M.; Murakami, D.; Ishihara, K.; Takahara, A. *Langmuir* **2012,** *28,* 7212–7222. doi:10.1021/la301033h
37. Kowalewska, A.; Nowacka, M.; Tracz, A.; Makowski, T. *Soft Matter* **2015,** *11,* 4818–4829. doi:10.1039/C5SM00787A
38. Kowalewska, A.; Nowacka, M.; Makowski, T.; Michalski, A., Thermal Stability of Self-Assembled Surfaces and Micropatterns Made of Ladder Polysilsesquioxanes; submitted for publication, 2015.
39. Liberelle, B.; Banquy, X.; Giasson, S. *Langmuir* **2008,** *24,* 3280–3288. doi:10.1021/la703522u
40. Leow, W. W.; Hwang, W. *Langmuir* **2011,** *27,* 10907–10913. doi:10.1021/la2018055
41. Loo, R. W.; Goh, M. C. *Langmuir* **2008,** *24,* 13276–13278. doi:10.1021/la803041v
42. Rojas, O. J. Adsorption of polyelectrolytes on mica. In *Encyclopedia of Surface and Colloid Science;* Hubbard, A. T., Ed.; Marcel Dekker, Inc.: New York, 2002; Vol. 1, pp 517–535.
43. Zhao, F.; Du, Y.-K.; Yang, P.; Tang, J.; Li, X.-C. *Colloid Polym. Sci.* **2005,** *283,* 1361–1365. doi:10.1007/s00396-005-1321-6
44. Heredia-Guerrero, J. A.; San-Miguel, M. A.; Sansom, M. S. P.; Heredia, A.; Benítez, J. J. *Phys. Chem. Chem. Phys.* **2010,** *12,* 10423–10428. doi:10.1039/c0cp00163e
45. Heredia-Guerrero, J. A.; San-Miguel, M. A.; Sansom, M. S. P.; Heredia, A.; Benítez, J. J. *Langmuir* **2009,** *25,* 6869–6874. doi:10.1021/la9001412
46. Benítez, J. J.; Heredia-Guerrero, J. A.; Serrano, F. M.; Heredia, A. *J. Phys. Chem. C* **2008,** *112,* 16968–16972. doi:10.1021/jp805445z
47. Benítez, J. J.; Heredia-Guerrero, J. A.; Heredia, A. *J. Phys. Chem. C* **2007,** *111,* 9465–9470. doi:10.1021/jp070563y
48. Chen, J.; Murphy, A. R.; Esteve, J.; Ogletree, D. F.; Salmeron, M.; Fréchet, J. M. J. *Langmuir* **2004,** *20,* 7703–7710. doi:10.1021/la030395a
49. Kowalewska, A.; Nowacka, M.; Makowski, T. patent application P-411408 "Modyfikowana powierzchniowo mika oraz sposób jej wytwarzania / Surface modification of muscovite mica nad the method of prodcution thereof" submitted to Polish Patent Office 2015.
50. Kowalewska, A.; Nowacka, M. *Silicon* **2015,** *7,* 133–146. doi:10.1007/s12633-014-9209-z
51. Fleer, G. J.; Lyklema, J. In *Adsorption from Solution at the Solid/Liquid Interface;* Parfitt, G. D.; Rochester, C. H., Eds.; Academic Press: New York, 1983; pp 153–220.
52. Whitesides, G. M.; Mathias, J. P.; Seto, C. T. *Science* **1991,** *254,* 1312–1319. doi:10.1126/science.1962191
53. Liu, L.; Guo, Q.-X. *Chem. Rev.* **2001,** *101,* 673–696. doi:10.1021/cr990416z
54. Linse, P.; Källrot, N. *Macromolecules* **2010,** *43,* 2054–2068. doi:10.1021/ma902338m
55. Owens, D. K.; Wendt, R. C. *J. Appl. Polym. Sci.* **1969,** *13,* 1741–1747. doi:10.1002/app.1969.070130815
56. Smith, B. *Infrared Spectral Interpretation: A Systematic Approach;* CRC Press LLC: New York, 1999.

BEILSTEIN JOURNAL OF NANOTECHNOLOGY

Surface-enhanced Raman scattering by colloidal CdSe nanocrystal submonolayers fabricated by the Langmuir–Blodgett technique

Alexander G. Milekhin*[1,2], Larisa L. Sveshnikova[1], Tatyana A. Duda[1], Ekaterina E. Rodyakina[1,2], Volodymyr M. Dzhagan[3], Ovidiu D. Gordan[3], Sergey L. Veber[2,4], Cameliu Himcinschi[5], Alexander V. Latyshev[1,2] and Dietrich R. T. Zahn[3]

Full Research Paper

Open Access

Address:
[1]A.V. Rzhanov Institute of Semiconductor Physics, pr. Lavrentieva 13, Novosibirsk 630090, Russia, [2]Novosibirsk State University, Pirogov str. 2, Novosibirsk 630090, Russia, [3]Semiconductor Physics, Technische Universität Chemnitz, 09107 Chemnitz, Germany, [4]International Tomography Center SB RAS, Novosibirsk 630090, Russia, and [5]Institut für Theoretische Physik, TU Bergakademie Freiberg, 09596 Freiberg, Germany

Email:
Alexander G. Milekhin* - milekhin@isp.nsc.ru

* Corresponding author

Keywords:
CdSe nanocrystals; dimers; localized surface plasmon resonance; metal nanoclusters; phonons; surface-enhanced Raman spectroscopy

Beilstein J. Nanotechnol. **2015,** *6,* 2388–2395.
doi:10.3762/bjnano.6.245

Received: 31 August 2015
Accepted: 24 November 2015
Published: 14 December 2015

This article is part of the Thematic Series "Organized films".

Guest Editor: M. Canepa

Abstract

We present the results of an investigation of surface-enhanced Raman scattering (SERS) by optical phonons in colloidal CdSe nanocrystals (NCs) homogeneously deposited on both arrays of Au nanoclusters and Au dimers using the Langmuir–Blodgett technique. The coverage of the deposited NCs was less than one monolayer, as determined by transmission and scanning electron microscopy. SERS by optical phonons in CdSe nanocrystals showed a significant enhancement that depends resonantly on the Au nanocluster and dimer size, and thus on the localized surface plasmon resonance (LSPR) energy. The deposition of CdSe nanocrystals on the Au dimer nanocluster arrays enabled us to study the polarization dependence of SERS. The maximal SERS signal was observed for light polarization parallel to the dimer axis. The polarization ratio of the SERS signal parallel and perpendicular to the dimer axis was 20. The SERS signal intensity was also investigated as a function of the distance between nanoclusters in a dimer. Here the maximal SERS enhancement was observed for the minimal distance studied (about 10 nm), confirming the formation of SERS “hot spots”.

Introduction

Since its observation in 1974 [1], surface-enhanced Raman scattering (SERS) has become a powerful technique for detecting and studying ultra-low quantities of organic and biological substances [2-7] down to a single molecule [8,9]. The primary benefit of SERS is that the intensity of Raman scattering by vibrational modes in molecules is drastically increased (typically by a factor of 10^5–10^6) when the molecules are placed in the proximity of noble metal nanoclusters or on rough metal surfaces. The locally enhanced electromagnetic field induced by the localized surface plasmon resonance (LSPR) in the vicinity of metal surface is responsible for the Raman scattering intensity enhancement, which is proportional to the fourth power of the enhancement of the local field [3-7]. The progress in controlled nanostructuring of metal surfaces has led to the development of high-performance SERS substrates with an average SERS enhancement factor (EF) well above 10^6 (EF > 10^8) for ultrasensitive analysis of organic substances [10-12]. It was also shown that for single molecular detection, the EF can reach an ultimate value of 10^{14}–10^{15} [8,9].

However, with few exceptions (such as carbon-based materials [13-16]), inorganic nanostructures have been much less investigated by SERS. It was already shown that several types of semiconductor NCs, including CdS [17,18], CdTe [19], CdSe [20-24], ZnO [25-28], GaN [26], and Cu_xS [29,30], reveal the SERS effect by optical phonons when placed in close proximity of Au or Ag nanoclusters.

Among those, CdSe NCs have attracted much attention for SERS experiments for at least two reasons. From one side, colloidal CdSe NCs are already used in commercial applications [31]. The information on the crystal structure of the NCs, their size, shape, and mechanical strain (which can be derived from the frequencies of the Raman phonon modes as seen in SERS spectra) is crucial for device performance. From other side, CdSe NCs are resistant against intense laser irradiation and have a direct band transition energy located in the same (red) spectral range as that for LSPR in Au nanoclusters and are therefore considered as a model system for resonant SERS experiments.

SERS by optical phonons was previously observed for several CdSe-based NCs, including pure CdSe and core–shell CdSe/CdZnS NCs deposited on Au or Ag substrates of various morphology [20-23]. Resonant SERS enables the observation of LO phonon modes of the CdSe core in a monolayer of core–shell CdSe/ZnS NCs deposited on commercially available SERS substrates [20]. However, the usage of conventional SERS conditions provides a SERS enhancement that is insufficient for investigation of an individual nanostructure.

Very recently, it was demonstrated that the phonon spectrum of individual CdSe nanoplatelets can be probed by SERS when the semiconductor nanostructure is placed in the gap between a gold nanocluster and a gold surface (the so-called “hot spot”) [32]. As in the case of metal nanoclusters in close proximity, the plasmonic gap supports electromagnetic fields confined in the gap much that are stronger (typically a few orders of magnitude depending on the gap size) than the field located near a single metal nanocluster or a metal surface [33]. SERS enhancement benefits from the implementation of this experimental geometry. In particular, it allows the influence of the spatial confinement and the structure anisotropy on optical phonon modes in individual CdSe nanoplatelets to be investigated [33].

For the investigation of resonant SERS, it is vitally important to have metal nanocluster arrays with controlled and intentionally varied structural parameters as well as homogeneous NC coverage. While metal nanocluster arrays can be fabricated by means of electron-beam lithography [34,35], nanoimprint lithography [36,37], or nanosphere lithography [38,39], the deposition of homogeneous films of CdSe NCs is possible by using Langmuir–Blodgett (LB) technology [40-43].

In this paper we report on the study of resonant SERS by CdSe NC coverage of less than one monolayer deposited onto regular arrays of Au nanoclusters, with a particular focus on Au dimer arrays.

Experimental

Colloidal CdSe NCs with a diameter of 5.2 nm purchased from Lumidot were homogeneously deposited on specially prepared plasmonic substrates by means of the LB technique, which is traditionally used for the fabrication of both highly ordered organic films [44] and NCs with controlled areal density [18] on a solid substrate [24,29]. The periodic Au nanocluster arrays were fabricated by direct electron beam writing (Raith-150, Germany) on (001)-oriented Si substrates and served as SERS-active substrates. They were fabricated with two areas of Au nanoclusters with pitch of 150 and 200 nm (Figure 1a). Each area contained 30 square, 10 × 10 μm^2 lattices with different diameters of Au nanoclusters for each lattice, as described in [24,29]. The fabrication details of regular arrays of Au nanoclusters and dimers on a Si substrate are presented in [29]. In addition to regular arrays of Au nanoclusters, arrays of paired Au nanoclusters or dimers were fabricated by electron beam lithography on a Si substrate covered with 75 nm of SiO_2. The silicon dioxide layer was implemented to combine the benefits of interference-enhanced Raman scattering and SERS for further enhancement of the Raman signal [30]. It is worth mentioning that for regular nanocluster arrays, a silica spacer

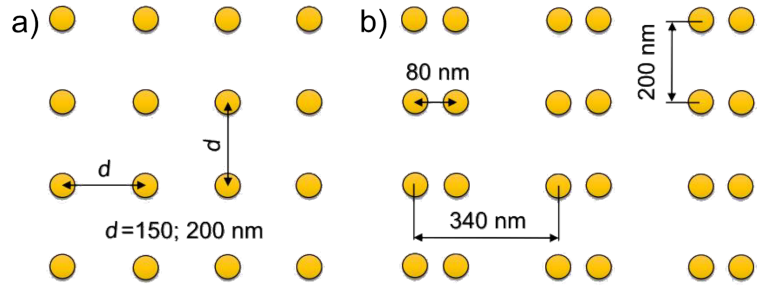

Figure 1: A sketch representing (a) a regular Au nanocluster array and (b) a Au dimer array.

causes an undesirable shift of LSPR energy from the resonant conditions due to the change of dielectric function of the surrounding media. However, as will be shown later for dimers that have LSPR energy distinct from individual nanoclusters, the resonant conditions are again fulfilled. The distance between the centers of nanoclusters in a dimer was fixed at 80 nm, while the pitch of dimers in the orthogonal directions was 200 and 340 nm, as shown in Figure 1b. The nanocluster size for a dimer was gradually varied from 71 to 40 nm from array to array. Thus, the gap size between the adjacent nanoclusters in a dimer was in the range between 9 and 40 nm. The accuracy in the determination of nanocluster size and gap size between the adjacent nanoclusters in a dimer in the experiments was about ±5 nm, limited by the statistical fluctuation and size of the gold grains (about 10 nm).

The size, shape, and areal density of CdSe NCs were determined by SEM using the same Raith-150 system at 10 kV acceleration voltage, 30 µm aperture, and 6 mm working distance. The high-resolution transmission electron microscopy (HR-TEM) experiments were performed using a JEM-400EX (JEOL) electron microscope with an accelerating voltage of 400 keV. The point resolution was 0.165 nm.

The LSPR energy in Au dimer arrays was determined from reflection measurements carried out using a Bruker Vertex 80v Fourier transform infrared spectrometer supplied with a Hyperion 2000 infrared microscope in the spectral range from 400–1000 nm with an aperture of 10 µm. The reflection from a part of the same substrate but without dimer arrays was used as a reference.

Micro-Raman experiments were performed with a LabRam spectrometer in backscattering geometry at 300 K. The excitation wavelength of λ_{exc} = 632.8 nm (provided by a He–Ne laser) was used in the Raman experiments. The laser light incident on the sample surface was focused to a ≈1 µm spot diameter with a power of about 0.5 mW. Raman experiments of CdSe NCs deposited on dimer arrays were carried out with the incident and scattered light polarized parallel or perpendicular to the long axis of the dimers.

Results and Discussion

CdSe NCs on regular arrays of Au nanoclusters

Typical SEM and HR-TEM images of a single monolayer of CdSe NCs deposited by the LB technique on the plasmonic substrate and on a carbon-coated Cu grid are shown in Figure 2. This demonstrates a dense, homogeneous coverage of the NCs for both the Si substrate with a Au nanocluster array and the Cu grid. The Raman spectrum acquired from the area where CdSe NCs are deposited on the Si substrate reveals only features inherent to crystalline Si.

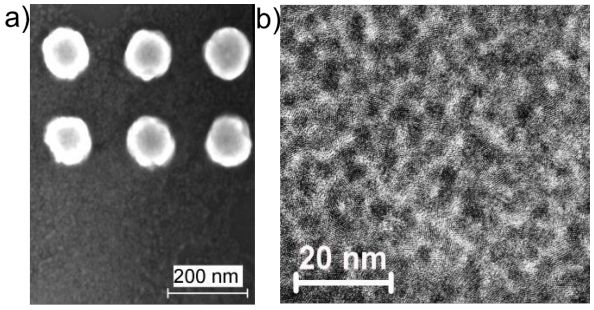

Figure 2: (a) SEM image of a single monolayer of CdSe NCs deposited on Si (bottom) and Au nanocluster arrays with a pitch of 200 nm (top). (b) HR-TEM image of a single monolayer of CdSe NCs formed on a carbon-coated Cu grid.

However, the Raman spectra of CdSe NCs deposited on the nanocluster arrays (Figure 3a) reveal a pronounced peak at about 207.5 cm^{-1} (denoted as 1LO in Figure 3a) and weaker peaks at multiple frequencies (about 415 and 623 cm^{-1}), which are attributed to a confined longitudinal optical (LO) mode and its overtones from CdSe NCs [45]. From this point on, the variation of 1LO phonon mode in CdSe NCs deposited on various

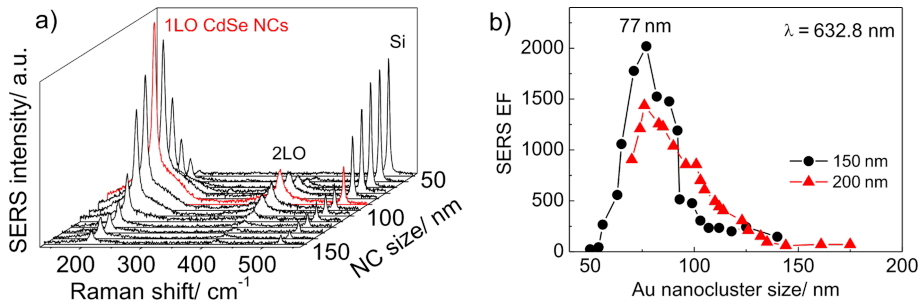

Figure 3: (a) SERS spectra of a single monolayer of CdSe NCs deposited on the nanocluster arrays with decreasing Au nanocluster size. (b) The SERS EF of LO phonon modes in CdSe NCs as a function of Au nanocluster size for Au nanocluster arrays with a pitch of 150 and 200 nm.

substrates does not exceed 0.6 cm^{-1}. The appearance of new Raman peaks illustrates the SERS effect by optical phonons in CdSe NCs. The mode at 520.5 cm^{-1} originates from the optical phonons of the Si substrate. With decreasing Au nanocluster size, the SERS intensity of CdSe-related modes shows a maximum resonant behavior for a Au nanocluster size of about 77 nm, while the intensity of the Si phonon mode gradually increases. The behavior of the 1LO mode of the CdSe NCs deposited on the Au nanocluster arrays of different nanocluster pitches (d = 150 and 200 nm) is rather similar (Figure 3b) and confirms the resonant character of SERS by optical phonons in CdSe NCs. As was shown from the micro-ellipsometry measurements [24], the LSPR energy in the array of 77 nm Au nanoclusters was about 625 nm. This value is very close to the excitation energy used in the SERS experiment (632.8 nm) that leads to the resonant SERS. Note that in the case of CdSe NCs on Au nanocluster arrays, the double resonance condition is fulfilled when the excitation energy matches both the transition energy in the NCs (2.03 eV or 610 nm) and the LSPR energy in the Au nanoclusters.

The increase of the Si phonon mode intensity with decreasing Au nanocluster size is due to a larger proportion of bare (not covered with Au nanoclusters) Si surface for the arrays with Au nanoclusters of smaller size.

A broad band between 170 and 260 cm^{-1} which appears pronounced in the SERS spectra (Figure 3a) measured in the resonant conditions will be further discussed in detail. From this point, a constant background was subtracted from the SERS spectra.

The resonance behavior of SERS by optical phonons for different excitation wavelengths in regular Au arrays with a period of 150 nm was investigated in detail in our previous work [24]. It was previously shown [24] that the SERS EF (determined for Au nanocluster arrays with a pitch of 150 nm) as a function of nanocluster size has a maximum of about 2×10^3. By increasing the nanocluster pitch up to 200 nm, the SERS intensity decreases due to the decreased number of Au nanoclusters. Note that for both Au array periods, the maximal EF is observed for a Au nanocluster size of 77 nm indicating the noninteracting character of neighboring Au nanoclusters [24]. The Raman intensity of the 1LO phonon mode in the spectra of CdSe NCs deposited with the same process on a Si substrate without Au nanoclusters was below the noise level. A detectable Raman phonon intensity was obtained when the acquisition time was increased up to 60 s and was further used as a reference.

CdSe NCs on Au dimer arrays

To achieve further SERS enhancement, CdSe NCs were deposited on arrays of Au dimers (Figure 4a). The SERS experiments with Au dimer arrays allow for the reduction of the areal density of the CdSe NC coverage (as shown in Figure 4b) without reduction of the SERS signal. This is due to the formation of localized electric field hot spots within the dimer gap, which is partially filled with CdSe NCs.

In comparison with Au nanocluster arrays, a dimer array represents an anisotropic plasmonic structure which is characterized by two coupled resonance plasmon modes when excited perpendicular to the structure surface [46]. The longitudinal LSPR mode (which is polarized along the long dimer particle axis) red-shifts with decreasing gap between the nanoclusters in a dimer. The other, transverse plasmon mode (polarized in the orthogonal polarization) blue-shifts very slightly with decreasing gap.

The LSPR energy in the Au dimer arrays was determined by micro-reflection measurements using linearly polarized light. The reflection spectra taken from Au dimer arrays with the same distance between the nanocluster centers (80 nm) (but different nanocluster sizes and, thus, different gaps between

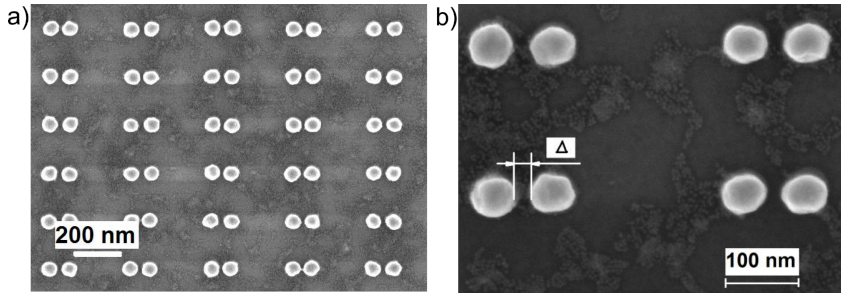

Figure 4: (a) SEM image of submonolayer coverage of CdSe NCs deposited on a Au dimer array. (b) An enlarged fragment of the SEM image of the structure shown in (a). The dimer gap is denoted as Δ.

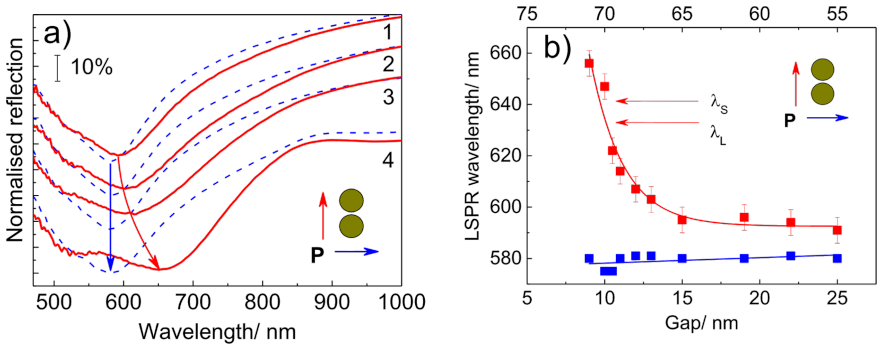

Figure 5: (a) The representative reflection spectra of Au dimer arrays with decreasing gap size (Δ = 15 cm, 1; Δ = 13 cm, 2; Δ = 10 cm, 3; Δ = 8 cm, 4) measured with light polarized parallel to (solid) and perpendicular to (dashed) the long dimer axis. (b) The dependence of the LSPR wavelength on the gap size, Δ, between dimers. The arrows show the laser excitation wavelength, λ_L, and the wavelength of the scattered photons, λ_S.

dimers) are presented in Figure 5a. The reflection spectra taken on areas without Au nanocluster arrays measured with the corresponding polarizations were used as reference spectra. One can see from the figure that the reflection spectra measured with polarization parallel to the long axis of the dimers reveal a pronounced minimum at about 590 nm for Δ = 15 nm. This corresponds to a red-shift with decreasing gap size, reaching a value of about 655 nm for Δ = 8 nm. However, the minimum at 580 nm measured with the polarization perpendicular to the long dimer axis for dimers with a nanocluster size of 65 nm and a gap size Δ = 15 nm barely changes when the gap size is varied. These minima are attributed to the coupled LSPR modes in dimers as described above. The variation of the LSPR wavelength with gap size agrees well with the universal scaling behavior previously reported [46]. The shoulder seen in the reflection spectra at about 520 nm (2.38 eV) for both polarizations is due to the interband transitions in gold [47].

The data on the LSPR wavelength derived from the reflection measurements are summarized in Figure 5b. As can be seen, the LSPR wavelength of the dimers with the smallest gap size (about 10 nm) is very close to the excitation wavelength (λ_L = 632.8 nm). Relative to that of the LO phonon mode frequency of 207.5 cm^{-1} (about 26 meV), the wavelength of the scattered photons is somewhat higher (λ_S = 641.4 nm) and even closer to the LSPR wavelength (Figure 5b). Consequently, between these two values, λ_L and λ_s, the conditions for the ultimate resonant SERS are fulfilled for which the maximal SERS enhancement factor is expected [48].

Indeed, the SERS spectra of CdSe NCs on Au dimers with the smallest gap between nanoclusters measured with 632.8 nm excitation wavelength and light polarized parallel to the long dimer axis reveal the most intense LO phonon mode. This mode appears at 207.5 cm^{-1} (Figure 6) superimposed with a broad background between 170 and 260 cm^{-1} and a weaker feature due to 2LO scattering near 414 cm^{-1}. The intensity of the LO mode decreases by a factor of 20 in the orthogonal geometry (calculated after background subtraction). The background was fit by two Lorentzian curves centered at about 190 and

230 cm^{-1}. The first can be attributed to scattering by surface optical modes, which was previously well-investigated in CdSe NCs [45,49,50]. The latter may originate from SERS by amorphous selenium formed on the NC surface due to partial photodegradation of CdSe NCs under laser illumination [51,52]. This mode has somewhat different intensity and shape for different Au arrays and depends on the sample preparation history. The Lorentzian curves obtained as a result of the fitting procedure are shown in Figure 6.

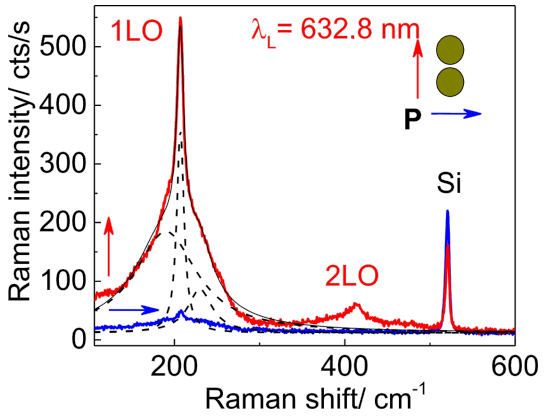

Figure 6: SERS spectra of a submonolayer of CdSe NCs deposited on the dimer array with a gap size of about 10 nm measured at λ_L = 632.8 nm with parallel (vertical arrow) and perpendicular (horizontal arrow) polarized light with respect to the long dimer axis. The Lorentzian curves used for the fit of the Raman spectra as well as the fitting result are shown by dashed and solid lines, respectively.

Interestingly, the intensity of the Si phonon mode seen in the spectra polarized parallel to the dimer axis is 30% weaker than that for the orthogonal polarization. This effect could be explained by the resonant absorption of the laser light by the longitudinal plasmon near Au dimers that reduces the Raman scattering signal from the underlying Si. The observed anisotropy of both CdSe- and Si-related phonon modes gradually decreases with increasing the gap size and disappears for gap sizes above 20 nm. This means that dimer arrays with relatively large gap sizes behave very similar to the regular Au nanocluster arrays.

The intensity of the LO mode for the excitation polarized parallel to the long dimer axis as well as its overtone, 2LO, decreases with increasing gap size between Au nanoclusters (Figure 7a,b). The decrease of the CdSe phonon modes is accompanied by an increase of Si peak by 43% for Au nanocluster size of 55 nm. The decreasing intensity of the LO mode in CdSe is associated with a reduction of the electromagnetic field in the gap between Au nanoclusters responsible for the SERS effect and with detuning the SERS resonance. The relatively large increase of the Si peak cannot be explained only by the decreasing size of the Au nanoclusters (from 70 to 55 nm) and thus larger illuminated area of the bare Si substrate taking part in the Raman process. The Raman signal from Si should be proportional to this area. Simple geometrical consideration gives an increase of the illuminated area with decreasing Au nanoclusters of about 12%, which is sufficiently smaller than the experimentally observed value of intensity increase (43%). This effect can again be explained by the resonant absorption of the laser light by the longitudinal plasmon near the Au dimers with the smallest gap. This causes an increase of the "effective" Au nanocluster size (or extinction cross-section) of up to about 100 nm, and thus the reduction of the Raman scattering signal from the underlying Si. This conclusion is consistent with previously reported results [53] confirming that for noble metal nanoclusters the extinction cross-section can be up to 10 times larger than their geometrical cross-section. The absorption by the plasmon is reduced with decreasing Au nanocluster size, as can be seen in the experiment.

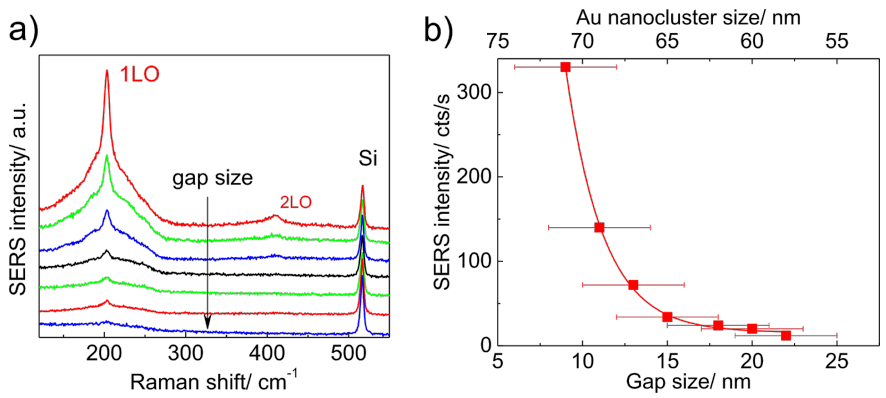

Figure 7: (a) SERS spectra of a submonolayer of CdSe NCs deposited on dimer arrays with increasing gap size measured at λ_L = 632.8 nm with light polarized parallel to the long dimer axis. (b) The dependence of SERS intensity on the gap size and Au nanocluster size.

Conclusion

LB technology was successfully applied for the formation of a homogeneous, submonolayer coverage of CdSe NCs on ordered plasmonic structures fabricated by direct electron beam writing.

The pronounced enhancement of the Raman scattering intensity by optical phonons in the CdSe NC ensembles deposited on regular arrays of Au nanoclusters and Au dimers, which resonantly depends on Au nanocluster size and laser excitation wavelength, provides evidence of the resonant character of the surface-enhanced Raman scattering effect. A maximal SERS enhancement by optical phonons in CdSe NCs was achieved for arrays of Au dimers with a minimal gap between nanoclusters in a dimer resonantly excited with the light polarized parallel to the long dimer axis where hot spots are realized.

Acknowledgements

This study was supported by the Russian Science Foundation (project n. 14-12-01037), Grant No. GRK 1215 “Materials and Concepts for Advanced Interconnects”, and the Ministry of Education and Science of the Russian Federation. The authors are thankful to Dr. A. K. Gutakovskii for providing HR-TEM images.

References

1. Fleishman, M.; Hendra, P. J.; McQuillan, A. J. *Chem. Phys. Lett.* **1974,** *26,* 163–166. doi:10.1016/0009-2614(74)85388-1
2. Moskovits, M. *Rev. Mod. Phys.* **1985,** *57,* 783–826. doi:10.1103/RevModPhys.57.783
3. Otto, A. Surface-enhanced Raman scattering: classical and chemical origins. In *Light Scattering in Solids IV;* Cardona, M.; Guentherodt, G., Eds.; Springer-Verlag: Berlin, 1984.
4. Aroca, R. *Surface-enhanced vibrational spectroscopy;* John Wiley & Sons Ltd.: Chichester, England, 2006.
5. Schluecker, S., Ed. *Surface Enhanced Raman Spectroscopy;* Wiley-VCH: Weinheim, Germany, 2011.
6. Le Ru, E.; Etchgoin, P. *Principles of surface-enhanced Raman spectroscopy and related plasmonic effects;* Elsevier: Amsterdam, The Netherlands, 2000.
7. Kneipp, K.; Moskovits, M.; Kneipp, H., Eds. *Surface-Enhanced Raman Scattering, Physics and Applications;* Springer-Verlag: Berlin, Heidelberg, 2006.
8. Kneipp, K.; Wang, Y.; Kneipp, H.; Perelman, L. T.; Itzkan, I.; Dasari, R. R.; Feld, M. S. *Phys. Rev. Lett.* **1997,** *78,* 1667–1670. doi:10.1103/PhysRevLett.78.1667
9. Nie, S.; Emory, S. R. *Science* **1997,** *275,* 1102–1106. doi:10.1126/science.275.5303.1102
10. Camden, J. P.; Dieringer, J. A.; Wang, Y.; Masiello, D. J.; Marks, L. D.; Schatz, G. C.; Van Duyne, R. P. *J. Am. Chem. Soc.* **2008,** *130,* 12616–12617. doi:10.1021/ja8051427
11. Alexander, K. D.; Hampton, M. J.; Zhang, S.; Dhawan, A.; Xu, H.; Lopez, R. *J. Raman Spectrosc.* **2009,** *40,* 2171–2175. doi:10.1002/jrs.2392
12. Kleinman, S. L.; Frontiera, R. R.; Henry, A.-I.; Dieringer, J. A.; Van Duyne, R. P. *Phys. Chem. Chem. Phys.* **2013,** *15,* 21–36. doi:10.1039/C2CP42598J
13. Schedin, F.; Lidorikis, E.; Lombardo, A.; Kravets, V. G.; Geim, A. K.; Grigorenko, A. N.; Novoselov, K. S.; Ferrari, A. C. *ACS Nano* **2010,** *4,* 5617–5626. doi:10.1021/nn1010842
14. Lefrant, S.; Baltog, I.; Baibarac, M.; Mevellec, J. Y.; Chauvet, O. *Carbon* **2002,** *40,* 2201–2211. doi:10.1016/S0008-6223(02)00089-1
15. Kneipp, K.; Kneipp, H.; Corio, P.; Brown, S. D. M.; Shafer, K.; Motz, J.; Perelman, L. T.; Hanlon, E. B.; Marucci, A.; Dresselhaus, G.; Dresselhaus, M. S. *Phys. Rev. Lett.* **2000,** *84,* 3470–3473. doi:10.1103/PhysRevLett.84.3470
16. Perevedentseva, E.; Karmenyan, A.; Chung, P.-H.; He, Y.-T.; Cheng, C.-L. *Surf. Sci.* **2006,** *600,* 3723–3728. doi:10.1016/j.susc.2006.01.074
17. Honma, I.; Sano, T.; Komiyama, H. *J. Phys. Chem.* **1993,** *97,* 6692–6695. doi:10.1021/j100127a020
18. Milekhin, A. G.; Yeryukov, N. A.; Sveshnikova, L. L.; Duda, T. A.; Kosolobov, S. S.; Latyshev, A. V.; Surovtsev, N. V.; Adichtchev, S. V.; Himcinschi, C.; Zenkevich, E. I.; Jian, W.-B.; Zahn, D. R. T. *J. Phys. Chem. C* **2012,** *116,* 17164–17168. doi:10.1021/jp210720v
19. Wang, Y.; Li, M.; Jia, H.; Song, W.; Han, X.; Zhang, J.; Yang, B.; Xu, W.; Zhao, B. *Spectrochim. Acta, Part A: Mol. Spectrosc.* **2006,** *64,* 101–105. doi:10.1016/j.saa.2005.07.003
20. Hugall, J. T.; Baumberg, J. J.; Mahajan, S. *Appl. Phys. Lett.* **2009,** *95,* 141111. doi:10.1063/1.3243982
21. Chursanova, M. V.; Dzhagan, V. M.; Yukhymchuk, V. O.; Lytvyn, O. S.; Valakh, M. Ya.; Khodasevich, I. A.; Lehmann, D.; Zahn, D. R. T.; Waurisch, C.; Hickey, S. G. *Nanoscale Res. Lett.* **2010,** *5,* 403–409. doi:10.1007/s11671-009-9496-2
22. Lee, Y.-B.; Lee, S. H.; Lee, S.; Lee, H.; Kim, J.; Joo, J. *Appl. Phys. Lett.* **2013,** *102,* 033109. doi:10.1063/1.4788926
23. Todescato, F.; Minotto, A.; Signorini, R.; Jasieniak, J. J.; Bozio, R. *ACS Nano* **2013,** *7,* 6649–6657. doi:10.1021/nn402022z
24. Sheremet, E.; Milekhin, A. G.; Rodriguez, R. D.; Weiss, T.; Nesterov, M.; Rodyakina, E. E.; Gordan, O. D.; Sveshnikova, L. L.; Duda, T. A.; Gridchin, V. A.; Dzhagan, V. M.; Hietschold, M.; Zahn, D. R. T. *Phys. Chem. Chem. Phys.* **2015,** *17,* 21198–21203. doi:10.1039/C4CP05087H
25. Wang, X.; Kong, X.; Yu, Y.; Zhang, H. *J. Phys. Chem. C* **2007,** *111,* 3836–3841. doi:10.1021/jp064118z
26. Liu, C. Y.; Dvoynenko, M. M.; Lai, M. Y.; Chan, T. H.; Lee, Y. R.; Wang, J.-K.; Wang, Y. L. *Appl. Phys. Lett.* **2010,** *96,* 033109. doi:10.1063/1.3291041
27. Milekhin, A. G.; Yeryukov, N. A.; Sveshnikova, L. L.; Duda, T. A.; Zenkevich, E. I.; Kosolobov, S. S.; Latyshev, A. V.; Himcinski, C.; Surovtsev, N. V.; Adichtchev, S. V.; Feng, Z. C.; Wu, C. C.; Wuu, D. S.; Zahn, D. R. T. *J. Exp. Theor. Phys.* **2011,** *113,* 983–991. doi:10.1134/S1063776111140184
28. Rumyantseva, A.; Kostcheev, S.; Adam, P.-M.; Gaponenko, S. V.; Vaschenko, S. V.; Kulakovich, O. S.; Ramanenka, A. A.; Guzatov, D. V.; Korbutyak, D.; Dzhagan, V.; Stroyuk, A. L.; Shvalagin, V. V. *ACS Nano* **2013,** *7,* 3420–3426. doi:10.1021/nn400307a
29. Milekhin, A. G.; Yeryukov, N. A.; Sveshnikova, L. L.; Duda, T. A.; Rodyakina, E. E.; Sheremet, E. S.; Ludemann, M.; Gordan, O. D.; Latyshev, A. V.; Zahn, D. R. T. *Thin Solid Films* **2013,** *543,* 35–40. doi:10.1016/j.tsf.2013.03.070

30. Milekhin, A. G.; Yeryukov, N. A.; Sveshnikova, L. L.; Duda, T. A.; Rodyakina, E. E.; Gridchin, V. A.; Sheremet, E. S.; Zahn, D. R. T. *Beilstein J. Nanotechnol.* **2015,** *6,* 749–754. doi:10.3762/bjnano.6.77
31. Rogach, A. *Semiconductor nanocrystal quantum dots: synthesis, assembly, spectroscopy, and applications;* Springer: New York, 2008. doi:10.1007/978-3-211-75237-1
32. Sigle, D. O.; Hugall, J. T.; Ithurria, S.; Dubertret, B.; Baumberg, J. J. *Phys. Rev. Lett.* **2014,** *113,* 087402. doi:10.1103/PhysRevLett.113.087402
33. Etchegoin, P. G.; Le Ru, E. C. *Phys. Chem. Chem. Phys.* **2008,** *10,* 6079–6089. doi:10.1039/b809196j
34. Kahl, M.; Voges, E.; Kostrewa, S.; Viets, C.; Hill, W. *Sens. Actuators, B* **1998,** *51,* 285–291. doi:10.1016/S0925-4005(98)00219-6
35. Gunnarsson, L.; Bjerneld, E. J.; Xu, H.; Petronis, S.; Kasemo, B.; Käll, M. *Appl. Phys. Lett.* **2001,** *78,* 802–804. doi:10.1063/1.1344225
36. Chou, S. Y. *MRS Bull.* **2001,** *26,* 512–517. doi:10.1557/mrs2001.122
37. Choi, C. J.; Xu, Z.; Wu, H.-Y.; Liu, G. L.; Cunningham, B. T. *Nanotechnology* **2010,** *21,* 415301–415307. doi:10.1088/0957-4484/21/41/415301
38. Hulteen, J. C.; Van Duyne, R. P. *J. Vac. Sci. Technol., A* **1995,** *13,* 1553–1558. doi:10.1116/1.579726
39. Haynes, C. L.; Van Duyne, R. P. *J. Phys. Chem. B* **2001,** *105,* 5599–5611. doi:10.1021/jp010657m
40. Dabbousi, B. O.; Murray, C. B.; Rubner, M. F.; Bawendi, M. G. *Chem. Mater.* **1994,** *6,* 216–219. doi:10.1021/cm00038a020
41. Cordero, S. R.; Carson, P. J.; Estabrook, R. A.; Strouse, G. F.; Buratto, S. K. *J. Phys. Chem. B* **2000,** *104,* 12137–12142. doi:10.1021/jp001771s
42. Gattás-Asfura, K. M.; Constantine, C. A.; Lynn, M. J.; Thimann, D. A.; Ji, X.; Leblanc, R. M. *J. Am. Chem. Soc.* **2005,** *127,* 14640–14646. doi:10.1021/ja0514848
43. Munechika, K.; Chen, Y.; Tillack, A. F.; Kulkarni, A. P.; Plante, I. J.-L.; Munro, A. M.; Ginger, D. S. *Nano Lett.* **2010,** *10,* 2598–2603. doi:10.1021/nl101281a
44. Peterson, I. R. *J. Phys. D* **1990,** *23,* 379–395. doi:10.1088/0022-3727/23/4/001
45. Dzhagan, V. M.; Valakh, M. Ya.; Raevskaya, A. E.; Stroyuk, A. L.; Kuchmiy, S. Ya.; Zahn, D. R. T. *Nanotechnology* **2007,** *18,* 285701. doi:10.1088/0957-4484/18/28/285701
46. Jain, P. K.; Huang, W.; El-Sayed, M. A. *Nano Lett.* **2007,** *7,* 2080–2088. doi:10.1021/nl071008a
47. Christensen, N. E.; Seraphin, B. O. *Phys. Rev. B* **1971,** *4,* 3321–3344. doi:10.1103/PhysRevB.4.3321
48. Stiles, P. L.; Dieringer, J. A.; Shah, N. C.; Van Duyne, R. P. *Annu. Rev. Anal. Chem.* **2008,** *1,* 601–626. doi:10.1146/annurev.anchem.1.031207.112814
49. Hwang, Y.-N.; Park, S.-H.; Kim, D. *Phys. Rev. B* **1999,** *59,* 7285–7288. doi:10.1103/PhysRevB.59.7285
50. Baranov, A. V.; Rakovich, Ya. P.; Donegan, J. F.; Perova, T. S.; Moore, R. A.; Talapin, D. V.; Rogach, A. L.; Masumoto, Y.; Nabiev, I. *Phys. Rev. B* **2003,** *68,* 165306–165307. doi:10.1103/PhysRevB.68.165306
51. Baganich, A. A.; Mikla, V. I.; Semak, D. G.; Sokolov, A. P.; Shebanin, A. P. *Phys. Status Solidi B* **1991,** *166,* 297–302. doi:10.1002/pssb.2221660133
52. Raevskaya, A. E.; Stroyuk, A. L.; Kuchmiy, S. Ya.; Dzhagan, V. M.; Zahn, D. R. T.; Schulze, S. *Solid State Commun.* **2008,** *145,* 288–292. doi:10.1016/j.ssc.2007.11.003
53. Garcia, M. A. *J. Phys. D: Appl. Phys.* **2011,** *44,* 283001–283020. doi:10.1088/0022-3727/44/28/283001

License and Terms

BEILSTEIN JOURNAL OF NANOTECHNOLOGY

Two step formation of metal aggregates by surface X-ray radiolysis under Langmuir monolayers: 2D followed by 3D growth

Smita Mukherjee[1], Marie-Claude Fauré[1,2], Michel Goldmann[1,2,3] and Philippe Fontaine[*3]

Full Research Paper

Open Access

Address:
[1]Sorbonne Universités, Université Pierre et Marie Curie (Paris 06), Institut des NanoSciences de Paris, CNRS-UMR 7588, 4 place Jussieu, 75005 Paris, France, [2]Faculté des Sciences Fondamentales et Biomédicales, Université Paris Descartes, 45 rue des Saints Peres, 75006 Paris, France and [3]Synchrotron SOLEIL, L'Orme des Merisiers, Saint-Aubin, BP 48, 91192 Gif-sur-Yvette, France

Email:
Philippe Fontaine[*] - philippe.fontaine@synchrotron-soleil.fr

* Corresponding author

Keywords:
GIXD; Langmuir monolayers; silver clusters; TXRF; X-ray radiolysis

Beilstein J. Nanotechnol. **2015,** *6,* 2406–2411.
doi:10.3762/bjnano.6.247

Received: 20 October 2015
Accepted: 27 November 2015
Published: 15 December 2015

This article is part of the Thematic Series "Organized films".

Guest Editor: M. Canepa

Abstract

In order to form a nanostructured metallic layer below a Langmuir monolayer, radiolysis synthesis was carried out in an adapted geometry that we call surface X-ray radiolysis. In this procedure, an X-ray beam produced by a synchrotron beamline intercepts the surface of an aqueous metal-ion solution covered by a Langmuir monolayer at an angle of incidence below the critical angle for total internal reflection. Underneath the organic layer, the X-ray beam induces the radiolytic synthesis of a nanostructured metal–organic layer whose ultrathin thickness is defined by the vertical X-ray penetration depth. We have shown that increasing the X-ray flux on the surface, which considerably enhances the kinetics of the silver layer formation, results in a second growth regime of silver nanocrystals. Here the formation of the oriented thin layer is followed by the appearance of a 3D powder of silver clusters.

Introduction

Formation of metal nanoclusters and ultrathin metal–organic systems is an active research field. Indeed, due to their adjustable optical, magnetic, electronic, and catalytic properties these systems demonstrate many applications [1,2]. The usual approach for the synthesis of this type of material is the chemical reduction of metal-ion precursors. The radiolysis induced by reduction of metal ions is generally considered as an efficient method to control this synthesis in solution as it leads to the formation of monodisperse, tailored, metal nano-objects [3]. The synthesis route involves the irradiation of a metal-ion aqueous

solution that induces the radiolysis of water. This results in the formation of various radicals (e.g., $H^{\bullet}$, $HO^{\bullet}$, e^{-}_{aq}). In the presence of a radical scavenger, $H^{\bullet}$ and e^{-}_{aq} induce reduction of the metal ions into atoms that further aggregate in the solution to form metallic clusters. Usually γ rays or electrons [3] and more recently X-rays [4,5] are used to perform the irradiation.

In order to increase the variety of shapes of the formed nano-objects and to vary their properties, we have proposed a technique that brings together the advantages of both – the radiolytic reduction of metal ions to atoms and the self-assembly properties of surfactant molecules in solution. By the choice of the organic molecule, we can tune the surface charge of the formed self-assembly in order to attract the ions in their vicinity. Therefore, we expect that during the irradiation process, the aggregation of the reduced atoms takes place around the organic templates.

We have previously applied this strategy to a spherical and a planar geometry. In the first case, we observed the formation of silver nanoshells upon irradiation of an aqueous solution of linoleic acid micelles that contained silver ions [6,7]. In the latter case, we were able to form a dense, metallic silver layer anchored underneath an organic monolayer by irradiating with an X-ray beam in grazing incidence geometry, a Langmuir monolayer (mono-molecular layer of insoluble surfactant molecules) deposited on the free surface of a silver-ion aqueous solution. The thickness of the formed layer (here, 4.5 nm thick) created with this process is determined by the penetration depth of the X-ray evanescent wave [4]. Hence, we termed this method surface X-ray radiolysis. Based on the analysis of the intensity and the shape of the diffraction peaks that emerge in the spectra during the radiolysis process, we proved that the metal layer anchored to the organic monolayer consisted of silver atoms organized in thin crystallites oriented by the interface [4]. We also studied the kinetics of formation of this silver layer by total reflection X-ray fluorescence (TRXF) and grazing incidence off-specular scattering [8]. However, the X-ray source was the experimental limitation. The experiments were performed on the “difliq” beamline at Laboratoire pour l'Utilisation du Rayonnement Électromagnétique (LURE), which was a first generation synchrotron source with flux around 10^8–10^9 photons/s. Nowadays, third generation sources deliver about three orders of magnitude higher flux, at least 10^{12} photons/s.

In the present paper, we have used the new SIRIUS beamline equipped with a liquid surface diffractometer at the SOLEIL synchrotron [9] to perform X-ray surface radiolysis with a much higher X-ray flux and follow the evolution of the process for higher irradiation doses.

Results and Discussion

Figure 1 presents the X-ray fluorescence measurement over the course of at least 16 h of irradiation for a behenic acid Langmuir monolayer deposited on silver sulphate and ethanol aqueous solution (alcohol is added as an $HO^{\bullet}$ radical scavenger), and compressed up to a surface pressure of 10 mN/m. The incident photon flux is approximately 10^{12} photons/s at the working energy 10.5 keV. In Figure 1a,b presents a typical fluorescence spectrum (split in two energy ranges) measured during the irradiation. Figure 1a is the L fluorescence emission due to the presence of silver atoms at the interface within the irradiated depth. The signal is analyzed by determining the weight of the individual fluorescence peaks, fitted by a Gaussian function, centered at each emission energy maximum, as reported in the literature [10]. Each time-stamped fluorescence spectrum is then fitted by the sum of these Gaussian functions weighted by the coefficients previously determined and a proportionality coefficient, $A_f(t)$. This coefficient is proportional to the amount of the excited element (here silver) in the irradiated volume. Therefore, its evolution reflects the change in the silver concentration. At high energy

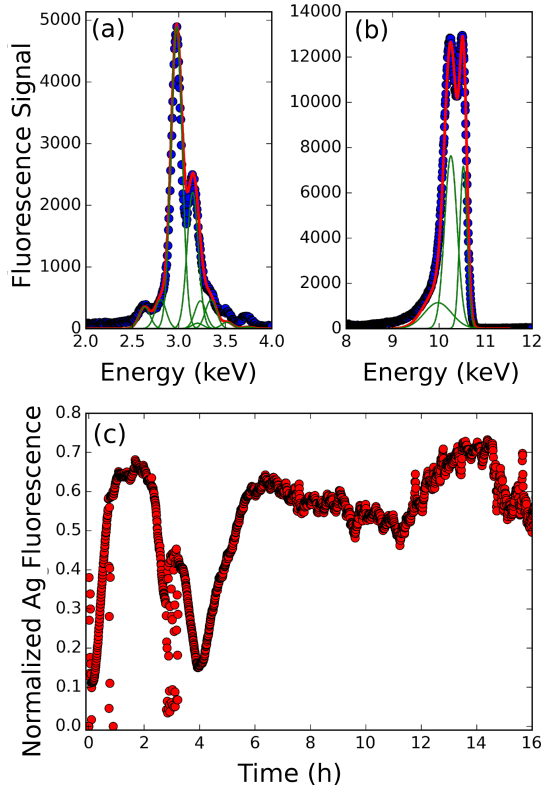

Figure 1: (a) X-ray fluorescence spectrum in the L-line energy range of Ag, where the green lines are the individual L line components, and the red is the fit by the sum of all lines. (b) Elastic and Compton peak analysis of the fluorescence spectrum. (c) Time evolution of the silver fluorescence intensity during 16 h of irradiation of a behenic acid Langmuir monolayer deposited on a silver sulphate aqueous solution. The signal is normalized by the elastic peak intensity.

(Figure 1b), one observes the elastic peak and two peaks at slightly lower energy, which correspond to Compton scattering [11]. The three peaks are adjusted by a Gaussian function, where the elastic peak is centered at 10.5 keV and the intensity defines the $A_e(t)$ parameter for normalization.

The time evolution of the normalized fluorescence intensity, A_f/A_e is depicted in Figure 1c. The first hours are characterized by an initial and fast increase of the fluorescence intensity for about 30 min after the irradiation started, followed by a constant fluorescence signal. The fluorescence intensity remains constant for about 2.5 h and then decreases suddenly down to almost its initial value at the beginning of the irradiation. Then, it rises up again up almost to its previous value but also shows strong fluctuations.

The first regime associated with the fluorescence intensity increase can be associated with an increase of the amount of silver atoms in the irradiated volume, defined by the X-ray footprint (1×50 mm^2) and the penetration depth (4.6 nm) of X-rays. Comparing this curve to the result obtained from the previous experiment performed on a first generation synchrotron source with a much lower flux (10^9 photons/s) [8], a distinct difference is first observed in the time needed to reach saturation. This is reduced from 5 h at the LURE down to 30 min at SIRIUS, demonstrating a significant increase of radiolysis kinetics, which is of course related to the increase of the dose rate directly related to the source intensity.

Such a reduction of the saturation time (one order of magnitude) makes the observation of the film transformation accessible when irradiation continues after the saturation is reached. The evolution exhibits two main features: a huge fluctuation ending with an increase back to the first saturated value of the fluorescence intensity, which is followed by a slow decrease and then increase resulting in a 15% fluctuation of the signal around the saturation value. This indicates the lack of a strong variation in the silver concentration in the probed volume in this second regime.

Two explanations can be proposed for the huge fluctuation: the first one is associated with the observation of a decrease of the surface pressure down to zero as the irradiation proceeds. One can then consider that the fluidity of the monolayer is enhanced, increasing the in-plane mobility of the patches of irradiated material. Thus, the surface region initially irradiated could drift in and out of the footprint area, leading to various thickness of the silver film and thus inducing the observed fluctuations. The second explanation is associated with the loss of silver patches (that can submerge into the sub-phase) followed by the formation of new ones by the incident beam.

In order to obtain information about the structure of the formed layer at the air–water interface, we record the fluorescence signal (TRXF) simultaneously with the grazing incidence X-ray diffraction signal (GIXD) over a broad q-range covering the scattering wave vector transfer for the expected diffraction peak of 2D and 3D silver crystals. Figure 2, Figure 3 and Figure 4 present the diffraction spectra at different times over the course of the 16 h irradiation period of Figure 1. During the first 30 min of irradiation, the evolution previously measured at the LURE was recovered [4,8]. The two peaks (one in-plane at 14.38 nm^{-1} and one out-of-plane at 13.87 nm^{-1}) assigned to the L2 phase of Langmuir monolayers of fatty acids [12] are observed at the beginning of the irradiation (Figure 2). Upon further irradiation, these peaks vanish (as the surface pressure decreases) and two new peaks located at $q_{xy} = 13.65$ nm^{-1} and $q_{xy} = 15.52$ nm^{-1} appear whose intensity grows with time (Figure 3). The q_z profile of these peaks appears as is characteristic of a 2D powder, that is, the crystallites present the same lattice plane parallel to the surface but random in plane orientation. This result is identical to that previously observed [4]. However, in the q-range of the 3D silver structure, the appearance of weaker peaks is observed, although they are presented as vertical rods characteristic of a 2D structure.

At longer time ($t > 30$ min), the lower q-range only exhibits some intensity fluctuations of the 2D diffraction peaks. The more striking feature is the appearance and growth in the high q-range of two diffraction rings for $q = 19.60$ nm^{-1} and $q = 22.64$ nm^{-1} (Figure 4). Such rings are characteristic of a 3D powder. These q-values do not correspond to that expected for the structure of bulk silver crystals, which are located at higher q-values (e.g., 26.6 nm^{-1} for the 111 reflection). However, smaller q-values corresponding to a larger feature size have been reported for small silver clusters exhibiting a crystal structure different from fcc [13,14]. The final picture of the system (after 16 h of irradiation) results in the co-existence of a 2D structure that grows rapidly after the initial irradiation and a 3D crystal powder that appears after the completion of the formation of the 2D layer at a longer irradiation time.

Conclusion

Increasing the photon flux allows us to probe the formation kinetics of the inorganic film at longer time scales when irradiating the surface of a silver solution covered by a Langmuir monolayer. We evidenced that the growth of silver crystal continues with transformation of the film structure, even after the saturation concentration of the silver atoms is reached in the irradiation volume. However, in this second step, one observes the growth of clusters that are no longer oriented by the interface, as demonstrated by the appearance of a 3D powder. The key point of this study is that the appearance of late 3D silver

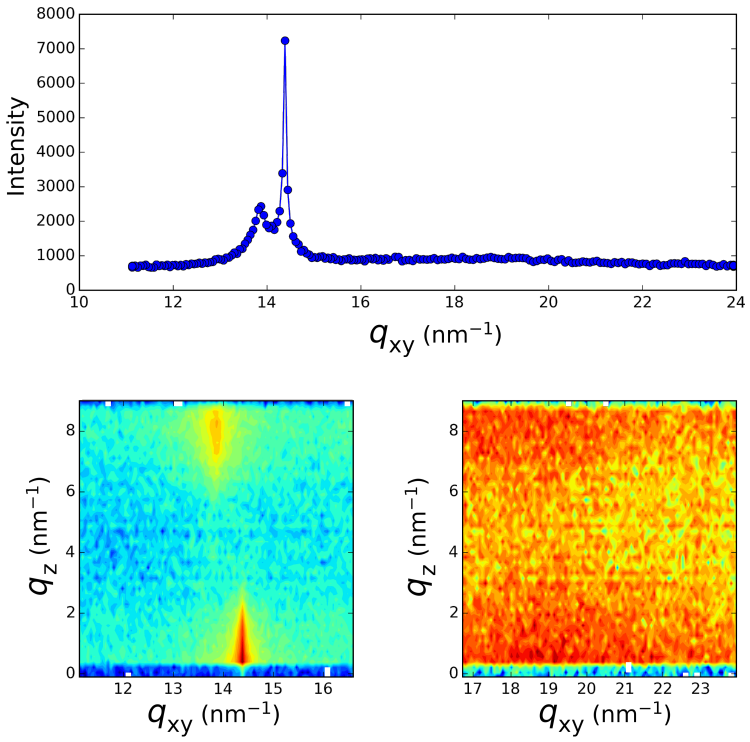

Figure 2: Grazing incidence X-ray diffraction spectrum taken at the beginning of the irradiation process of Figure 1c. Top: q_z integrated spectrum, Bottom: q_{xy}–q_z intensity maps.

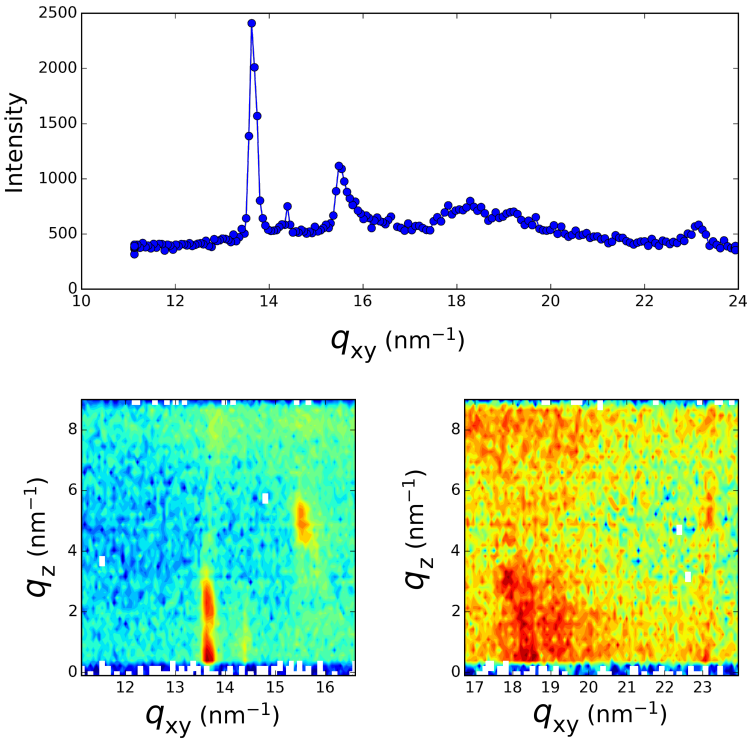

Figure 3: Grazing incidence X-ray diffraction spectrum taken after two hours into the irradiation process of Figure 1c. Top: q_z integrated spectrum, Bottom: q_{xy}–q_z intensity maps.

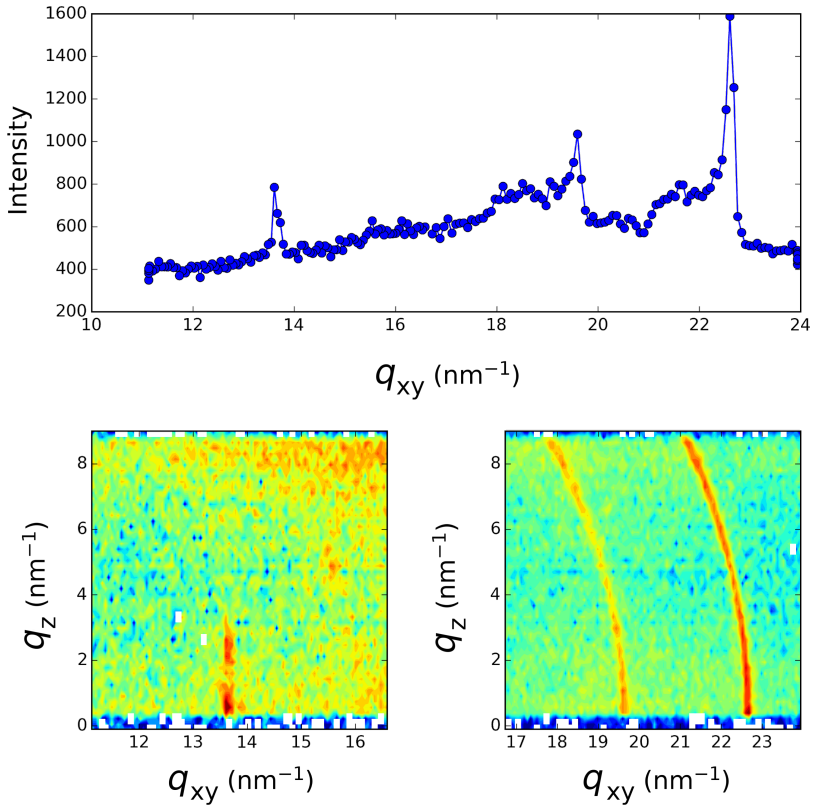

Figure 4: Grazing incidence X-ray diffraction spectrum taken after 15 h into the irradiation process of Figure 1c. Top: q_z integrated spectrum, Bottom: q_{xy}–q_z intensity maps.

crystal growth seems only to appear in the fluorescence signal with an increase of the fluctuations. This indicates that, under irradiation, these disoriented crystallites replace the previously oriented ones. We underline that the probed thickness is defined by the penetration depth of the X-ray evanescent wave, and thus, the silver film can be thicker for the latter case. This could be related to the observation of the evolving FWHM of the 2D peaks under irradiation. We previously observed [8] that the in-plane coherence length of the 2D crystal growth (deduced form the FWHM) is continuous under irradiation, even after the saturation of the fluorescence intensity is reached. This indicates that when the irradiated volume is completely filled with oriented 2D crystals, the irradiation induced the in-plane coalescence of these 2D crystals. One then obtains a 2D crystal with a surface area of approximately 10 µm^2 with thickness of about 4.5 nm (equal to the X-ray penetration depth) [4]. However, the surface energy of the two surfaces of this platelet should differ since the interfaces are different (water/Ag below and organic molecule/air above). Such difference should induce a curvature of the platelet, which could rupture when the surface energy reaches a critical value. This could lead to the disorientation of the platelets and the formation of the 3D structures, which are then thicker than the X-ray penetration depth.

Experimental

The sample preparation procedure was previously described in detail [4,8]. Droplets of 5 mmol·L^{-1} of behenic acid solution ($C_{21}H_{43}COOH$, Sigma-Aldrich) in chloroform ($CHCl_3$) were spread onto the silver-ion solution in a Langmuir trough of 700 cm^2 area and 1 cm depth. The temperature of the subphase was maintained at $T = 20 \pm 1$ °C. The monolayer was slightly compressed up to $\pi = 10$ mN·m^{-1}, the surface pressure at which the irradiation process is started. The Langmuir trough is enclosed in a gas-tight box flushed by helium gas. This allows the deoxygenation of the aqueous phase over the course of the experimental time scale and prevents bulk oxygenation by air during the radiolytic process.

The monolayer subphase is made by dissolving silver sulfate, Ag_2SO_4 (Sigma-Aldrich, purity 99%), in ultrapure water (Millipore system, 18 MΩ·cm) at a silver concentration of $1.5 \cdot 10^{-4}$ mol·L^{-1}. Ethanol (CH_3CH_2OH) was added at a concentration of 0.2 mol·L^{-1} as a radical scavenger [15]. Indeed, irradiation of deoxygenated water leads to the formation of three radicals, HO$^\bullet$, H$^\bullet$ and hydrated electrons, e^-_{aq}. By addition of ethanol to the aqueous solution, HO$^\bullet$ radical species are readily scavenged and lead to secondary radical creation,

$CH^{\bullet}_3CH_2OH$. The remaining e^-_{aq}, $H^{\bullet}$ and $CH^{\bullet}_3CH_2OH$ are strong reductive agents and thus induce silver-ion reduction into atoms, which coalesce and finally form the silver aggregates.

The X-ray irradiation and scattering measurements were performed on the SIRIUS beamline at the SOLEIL synchrotron. The details and optics of the facility are described elsewhere [9]. The incident X-ray energy used was 10.5 keV (λ = 0.118 nm) and the beam size was 0.1 × 1 mm^2 (V × H) at the sample position. The water surface was illuminated at an incident angle of 1.8 mrad below the critical angle of the air–water interface (2.04 mrad at 10.5 keV), so that the incident wave was totally reflected, while the refracted wave became evanescent, exploring a layer of several nanometers beneath the interface. The scattered intensity was collected on a very low noise, position sensitive, 1D gas detector, with 2048 channels on 150 mm. A custom-built Langmuir trough was enclosed in a temperature-controlled, sealed chamber and flushed with helium during data collection to reduce gas scattering and to avoid beam damage to the monolayer. GIXD was used to obtain in-plane information about the molecular structure of the surface. The spectra were obtained by varying the X-ray, momentum transfer, in-plane component q_{xy} that is parallel to the air–water interface. The scattered intensity was measured as a function of the angle, 2θ, between the incident and diffracted beam projected onto the horizontal plane.

The X-ray fluorescence signal was measured using a one-element, silicon drift detector (Brüker, Germany) equipped with a collimator and mounted at 30° with respect to the vertical direction towards the X-ray source in order to reduce the elastic peak that would otherwise saturate the detector.

Acknowledgements

S. Mukherjee is grateful to Mairie de Paris (Paris City Council) for the postdoctoral fellowship.

References

1. Wilcoxon, J. P.; Abrams, B. L. *Chem. Soc. Rev.* **2006,** *35,* 1162–1194. doi:10.1039/b517312b
2. Schaming, D.; Remita, H. *Found. Chem.* **2015,** *17,* 187–205. doi:10.1007/s10698-015-9235-y
3. Remita, H.; Remita, S. Metal Clusters and Nanomaterials: Contribution of Radiation Chemistry. In *Recent Trends in Radiation Chemistry;* Wishart, J. F.; Rao, B. S. M., Eds.; World Scientific Publishing, 2010; pp 347–383. doi:10.1142/9789814282093_0013
4. Muller, F.; Fontaine, P.; Remita, S.; Fauré, M.-C.; Lacaze, E.; Goldmann, M. *Langmuir* **2004,** *20,* 4791–4794. doi:10.1021/la049534u
5. Remita, S.; Fontaine, P.; Lacaze, E.; Borensztein, Y.; Sellame, H.; Farha, R.; Rochas, C.; Goldmann, M. *Nucl. Instrum. Methods Phys. Res., Sect. B* **2007,** *263,* 436–440. doi:10.1016/j.nimb.2007.06.032
6. Remita, S.; Fontaine, P.; Rochas, C.; Muller, F.; Goldmann, M. *Eur. Phys. J. D* **2005,** *34,* 231–233. doi:10.1140/epjd/e2005-00149-x
7. Attia, J.; Rémita, S.; Jonic, S.; Lacaze, E.; Fauré, M.-C.; Larquet, E.; Goldmann, M. *Langmuir* **2007,** *23,* 9523–9526. doi:10.1021/la701366f
8. Fontaine, P.; Fauré, M.-C.; Remita, S.; Muller, F.; Goldmann, M. *Eur. Phys. J. Special Topics* **2009,** *167,* 157–162. doi:10.1140/epjst/e2009-00952-5
9. Fontaine, P.; Ciatto, G.; Aubert, N.; Goldmann, M. *Sci. Adv. Mater.* **2014,** *6,* 2312–2316. doi:10.1166/sam.2014.2189
10. Elam, W. T.; Ravel, B. D.; Sieber, J. R. *Radiat. Phys. Chem.* **2002,** *63,* 121–128. doi:10.1016/S0969-806X(01)00227-4
11. Van Gysel, M.; Lemberge, P.; Van Espen, P. *X-Ray Spectrom.* **2003,** *32,* 139–147. doi:10.1002/xrs.628
12. Kaganer, V. M.; Möhwald, H.; Dutta, P. *Rev. Mod. Phys.* **1999,** *71,* 779–819. doi:10.1103/RevModPhys.71.779
13. Reinhard, D.; Hall, B. D.; Ugarte, D.; Monot, R. *Phys. Rev. B* **1997,** *55,* 7868–7881. doi:10.1103/PhysRevB.55.7868
14. Marks, L. D. *Rep. Prog. Phys.* **1994,** *57,* 603–649. doi:10.1088/0034-4885/57/6/002
15. Elliott, A. J.; Simsons, A. S. *Radiat. Phys. Chem.* **1984,** *24,* 229–231. doi:10.1016/0146-5724(84)90056-6

License and Terms

BEILSTEIN JOURNAL OF NANOTECHNOLOGY

pH-Triggered release from surface-modified poly(lactic-*co*-glycolic acid) nanoparticles

Manuel Häuser[1,2], Klaus Langer[2] and Monika Schönhoff*[1]

Full Research Paper

Open Access

Address:
[1]Institute of Physical Chemistry, University of Muenster, Corrensstraße 28/30, 48149 Münster, Germany and [2]Institute of Pharmaceutical Technology and Biopharmacy, University of Muenster, Corrensstraße 48, 48149 Münster, Germany

Email:
Monika Schönhoff* - schoenho@uni-muenster.de

* Corresponding author

Keywords:
layer-by-layer self-assembly; pH-triggered release; PLGA nanoparticles; polyelectrolyte multilayers; weak polyelectrolyte

Beilstein J. Nanotechnol. **2015,** *6,* 2504–2512.
doi:10.3762/bjnano.6.260

Received: 15 October 2015
Accepted: 11 December 2015
Published: 30 December 2015

This article is part of the Thematic Series "Organized films".

Guest Editor: M. Canepa

Abstract

Nanoparticles (NP) of poly(lactic-*co*-glycolic acid) (PLGA) represent a promising biodegradable drug delivery system. We suggest here a two-step release system of PLGA nanoparticles with a pH-tunable polymeric shell, providing an initial pH-triggered step, releasing a membrane-toxic cationic compound. PLGA nanoparticles are coated by polyelectrolytes using the layer-by-layer self-assembly technique, employing poly(acrylic acid) (PAA) as a pH-sensitive component and poly(diallyldimethylammonium chloride) (PDADMAC) as the releasable polycation. The pH during multilayer deposition plays a major role and influences the titration curve of the layer system. The pH-tunability of PAA is intensively investigated with regard to the pH region, in which the particle system becomes uncharged. The isoelectric point can be shifted by employing suitable deposition pH values. The release is investigated by quantitative ^{1}H NMR, yielding a pH-dependent release curve. A release of PDADMAC is initiated by a decrease of the pH value. The released amount of polymer, as quantified by ^{1}H NMR analysis, clearly depends on the pH value and thus on the state of deprotonation of the pH-sensitive PAA layer. Subsequent incubation of the nanoparticles with high concentrations of sodium chloride shows no further release and thus demonstrates the pH-driven release to be quantitative.

Introduction

The use of nanoparticles as drug delivery systems has been intensively investigated and important progress has been made within the past decades, establishing reliable methods for particle preparation and characterization. Formation of nanostructures based on different materials, such as metals [1], mineral compounds [2], proteins [3], and a large variety of polymers [4] is widely used in numerous scientific fields. The assembly of biocompatible nanoparticle preparation deserves special attention, if the aim is to apply these nanoparticles as drug delivery systems in vivo. A commonly used polymer fulfilling this criterion is poly(lactic-*co*-glycolic acid) (PLGA), a copolymer consisting of lactic acid and glycolic acid, which

has been approved by the authorities to be suitable for pharmaceutical application [5]. Nanoparticles of an appropriate size can be reliably assembled via an emulsion diffusion method, using poly(vinyl alcohol) (PVA) as a stabilizing agent [6]. A part of the stabilizer remains associated with the nanoparticles even after intensive purification procedures because PVA forms an interconnected network with the polymer at the interface [7,8]. PLGA is well-known for its outstanding biocompatibility and its hydrolytic biodegradability which varies in dependence of the relative molar ratio of the monomeric compounds [9]. Subsequent optimization of PLGA-based nanostructures is generally required in order to add specific properties, such as reduced opsonisation [10], a prolonged half-life [11] or improved drug targeting. These optimization procedures are generally performed after particle assembly, since the nanoparticle formation is influenced by many parameters and often limited by minor changes in the experimental setup. However, several further surface modifications are well established these days, such as covalent ligand binding via crosslinking agents [12,13] and different adsorption strategies [14].

The layer-by-layer (LbL) self-assembly technique, introduced by Decher and Hong in the early 1990s [15] has proven to be an outstandingly valuable method for the fabrication of ultrathin polyelectrolyte multilayers (PEM) with well adjustable properties and architecture. Layer build-up is based on alternating adsorption of cationic and anionic compounds, such as polyelectrolytes [15], proteins [16], nucleic acids [17,18], dyes [19], and even colloids [14] onto the surface of charged substrates. The most common and therefore best investigated multilayer build-up involves two oppositely charged polyelectrolytes. Weak polyelectrolytes, such as polyacrylic acid (PAA), with a pH-dependent charge density can be used to add pH-tunable properties to the nanoparticle surface to which they are adsorbed. In case of PAA, a shift of acidity has been reported by several research groups, comparing free polyelectrolyte chains in solution to PAA in multilayers [20], and also the growth behaviour of the layer was shown to depend strongly on the pH value [21]. In the meantime, polyelectrolyte multilayers have already in various cases been applied for pH-driven release, based on weak polyelectrolyte components [22-27].

Nanoparticles can be used as carrier systems for the transport of drugs to cells and tissues. Once getting in contact with cells nanoparticles can be taken up by endocytosis. During the process of endocytosis, nanoparticular drug carriers most often end up in endolysosomes with a reduced internal pH value. In order to provide improved accessibility of the drug to the whole cell, membrane destruction of the endolysosomal bilayer would be beneficial. We present here the idea of a two-step delivery system consisting of core–shell nanoparticles. The outer shell is susceptible to changes of the pH value, such that the release of a membrane-toxic cationic compound is triggered by a reduced pH value in the endolysosomal compartment of the cells. The idea is that this mechanism might in the future trigger a disruption of endosomal membranes and therefore enhance the intracellular distribution of the nanoparticles and the drug that is incorporated in the particle core. In the present work, we employ biodegradable PLGA nanoparticles, which are modified by successive adsorption of four polyelectrolyte layers in total, containing in particular the weak polyanion PAA. We demonstrate that an appropriate pH stimulus induces a controlled release of the polycationic species poly(diallyldimethylammonium chloride) (PDADMAC). The successful pH-triggered release of PDADMAC is concluded from ^{1}H NMR spectroscopy. Although ^{1}H NMR spectroscopy lacks sensitivity, it has significant advantages with respect to selectivity and robustness compared to current state of the art analytical methods, such as chromatography and titration strategies [28], which are commonly applied to detect anionic polymers [29] or dyes [30]. The obtained release data reveal valuable information about the pH-tunability of PAA in the complexed state within a polyelectrolyte multilayer. The quantification of released PDADMAC is a direct evidence of PEM decomposition and marks their stability limits. In particular, we find the stability limits and the released amount of PDADMA to be dependent on the assembly pH of the multilayers.

Results and Discussion

Nanoparticle coating

Successful nanoparticle synthesis can be concluded from measurements of particle size, polydispersity index (PDI), and zeta potential. PLGA nanoparticles were (249 ± 4) nm in diameter, showing a narrow size distribution (PDI 0.04 ± 0.02) and a zeta potential of (−53 ± 1) mV. After adsorption of the initial layer of polyethylenimine (PEI), the particles were washed as described in the Experimental section. The obtained PLGA–PEI nanoparticles showed only a minor increase in particle diameter (266 ± 4) nm and no significant increase in PDI (0.07 ± 0.03), which indicates no aggregation of nanoparticles taking place during adsorption or washing. The zeta potential was inverted to a positive value of (+35 ± 4) mV, which could be attributed to successful adsorption of the cationic PEI layer.

pH-Sensitivity of the PAA layer in dependence on the adsorption pH value

PAA, as a weak polyelectrolyte with a charge density depending on pH, can be easily adsorbed onto positively charged substrates, such as PLGA nanoparticles with an adsorbed layer of PEI. In order to investigate the effect of the linear charge density of adsorbing chains on the resulting layer properties, PAA from solutions adjusted to three different

pH values, respectively, was adsorbed to PLGA–PEI nanoparticles. Regarding the ionization degree, the titration curve of PAA shows a typical polyelectrolyte behaviour, since instead of a steep slope at the pK_a value, the degree of ionization smoothly varies over several pH units [20]. The following experiment was carried out adsorbing from PAA solutions adjusted to pH 3 (degree of ionization ≈ 10%), pH 5 (degree of ionization ≈30%), and pH 7 (degree of ionization ≈ 80%), respectively. PAA adsorption was successful in all cases, which can be concluded from the inversion of the zeta potential from positive to negative values (Table 1).

Table 1: Zeta potential (ζ) and hydrodynamic radii (R_H) of PAA-coated PLGA-PEI nanoparticles in dependence on pH during PAA adsorption. Nanoparticle radii were obtained in ultrapure water (H_2O) and 1 mM sodium hydroxide solution (NaOH), respectively. All experiments were performed in triplicate, average values ± standard deviations are shown.

pH (PAA)	ζ/mV (H_2O)	R_H/nm (H_2O)	R_H/nm (NaOH)
3	−59 ± 1	130 ± 2	250 ± 2
5	−40 ± 2	126 ± 1	142 ± 2
7	−30 ± 6	126 ± 2	134 ± 5

As shown in Table 1, an obvious trend comparing the zeta potential after adsorption to the pH of PAA during adsorption can be extracted. Adsorption of PAA with a low charge density (pH 3) leads to a highly charged nanoparticle system after removal of excess polyelectrolyte. During the washing process using ultrapure water (pH approx. 6), the adsorbed PAA chains become more deprotonated, resulting in a highly charged polyelectrolyte layer on the nanoparticle surface. An opposite effect can be observed considering PAA adsorption at pH 7. Here, the PAA chain is highly charged and therefore adsorbs in a flat, stretched conformation on the particle surface. Incubation with ultrapure water during the washing procedure (pH approx. 6) is not significantly influencing the charge density of PAA on the particle surface, hence leading to considerably lower absolute value of the zeta potential for PAA adsorption at pH 7 as compared to pH 3. This trend can be underlined considering the adsorption of PAA at pH 5, resulting in nanoparticles showing a zeta potential in between the two described cases for PAA adsorption at pH 3 and pH 7, respectively. Regarding nanoparticle radii, no significant differences can be observed by only comparing the determined particle sizes in ultrapure water. In contrast, measurements performed in sodium hydroxide solution (pH 11), show a drastic swelling behaviour for PAA adsorbed at pH 3, but only a slight increase in particle size for PAA adsorbed at pH 5 and pH 7, respectively. This observation can be attributed to different chain conformations of PAA during adsorption, in analogy to the conformation in solution: Due to repulsive forces between the charge-carrying deprotonated carboxylic functions, the PAA chain assumes a stretched conformation under conditions of high pH values and low salt concentrations. On the other hand, a low pH value or the presence of higher amounts of counterions in the polyelectrolyte solution leads to a coiled conformation. Many multilayer studies show that in the former case thin layers are formed, while the latter case yields thicker layers [31]. Several studies have dealt in detail with the influence of salt on layer thickness of polyelectrolyte multilayers [15,32-35] while others described the influence of pH on weak polyelectrolyte layer build-up [36,37]. General concepts of the relevance of the solution conformation have been derived [31]. Concerning charge diluted chains it can be argued that charge compensation, required to compensate the charge density of the terminating layer, determines the surface charge density of the subsequently adsorbing layer. Thus, an adsorbing charge-diluted chain requires a larger amount of mass, yielding thicker films [21,38]. At pH 3, PAA is weakly charged, and therefore adsorbs in a coiled conformation to yield a thick film. In ultrapure water (pH approx. 6), the degree of dissociation in the outermost PAA layer is increasing, causing a layer swelling due to electrostatic self-repulsion. Particularly noteworthy is the massive increase in hydrodynamic radius by more than 100 nm, see Table 1. This implies a significant stretching of single chains after adsorption rather than a swelling of a compact film, as schematically depicted in Figure 1. This behaviour is in agreement with earlier work, where it was shown that particle radii can increase by values on the order of the contour length, when the terminating layer is transferred from high salt to low salt conditions [39].

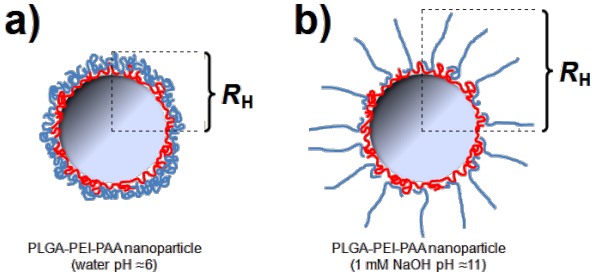

Figure 1: Sketch of terminating layer conformation for PLGA-PEI-PAA nanoparticles prepared at pH 3 in a) ultrapure water (pH approx. 6) and b) in NaOH (pH approx. 11), where PAA is fully charged.

When adsorbing PAA at higher pH values (i.e., pH 5 or pH 7), the hydrodynamic radii do not differ much compared to neutral and basic conditions. This can be attributed to the fact that the PAA chains are notably stretched at pH 5 and pH 7 and therefore already adsorb as a flat polymer layer, which remains tightly adsorbed even under basic conditions. Further characterization of the PLGA-PEI-PAA nanoparticles with varying

adsorption pH was performed by recording titration curves, where the particle dispersions were titrated with hydrochloric acid (25 mM). By plotting the zeta potential versus pH, the isoelectric point (IEP) can easily be determined. The IEP corresponds to a state of charge neutrality, where ζ is zero. Thus, it is an important parameter characterizing the pH region, in which the particle system is potentially sensitive for pH-triggering. An IEP of unmodified PLGA nanoparticles can be determined in the region of pH 2.2 (data not shown). For coated particles, the IEP depends strongly on the adsorption pH, as shown in Figure 2.

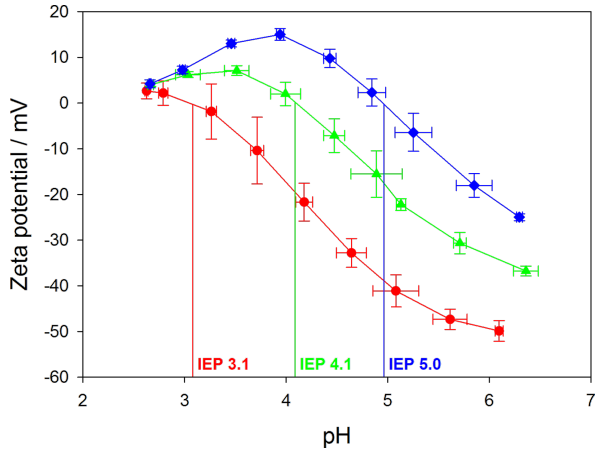

Figure 2: Titration of PLGA–PEI–PAA nanoparticles with HCl (25 mM) for different pH values during assembly of PAA. PAA assembly at pH 7 (blue), PAA assembly at pH 5 (green), PAA assembly at pH 3 (red). Experiments were performed in triplicate, average values ± standard deviations are shown.

In order to explain the mechanism behind this data, the properties of the PAA layers adsorbed at different pH values have to be taken into account. Considering adsorption at pH 3, PAA adsorbs as a slightly charged chain, forming a thick layer of coiled chains with a high surface coverage of carboxylic functions, as previously explained. The IEP strongly depends on the surface coverage of carboxylic functions. A higher carboxylic surface coverage requires a larger proton concentration in solution to yield neutralisation of the surface layer. On the other hand, at high pH values during adsorption of the PAA layer, a low surface coverage of carboxylic functions is resulting, which can be neutralized already at a higher pH value. The overall probability for complete neutralization of the considered segment on the particle surface at a certain pH value is therefore higher for lower amounts of carboxylic functions in this segment, which can be directly correlated to the pH of PAA during adsorption. In case of the titration curves obtained for PAA adsorbed at pH 5 and pH 7, respectively, a decrease of surface potential is observed after reaching its maximum value (see Figure 2). This can be attributed to surface charge compensation effects induced by the increasing ionic strength, when adding more hydrochloric acid during the titration experiment. In summary, the pH-tunable range of the obtained nanoparticles can be controlled by adjusting the adsorption pH of PAA. It is thus feasible to impose a desired IEP value in the range between pH 3 and pH 5 onto the resulting particle system by choosing an appropriate pH value during assembly.

PDADMAC adsorption

After intense investigation of the effects concerning PAA modification on the particle system, PDADMAC is subsequently adsorbed in a layer-by-layer fashion. For further layer build-up, the PAA layer has been chosen to be adsorbed at pH 5, forcing the particle system to show an IEP in the region of pH 4. PDADMAC, as a strong polycation, has a charge density that does not depend on the pH value. However, its adsorption might depend on the state of charge of the terminating PAA layer. Therefore, PDADMAC solutions, as well as the PLGA-PEI-PAA nanoparticle dispersions, have been adjusted to pH 5, pH 7, and pH 9, respectively. After adsorption and subsequent washing, nanoparticles are characterized by the hydrodynamic radius and the zeta potential, as determined at pH 6. The dependence of the PDADMAC layer on the pH value during adsorption is shown in Figure 3. All particle samples show a monodisperse size distribution, indicated by a low polydispersity index (PDI ≤ 0.1).

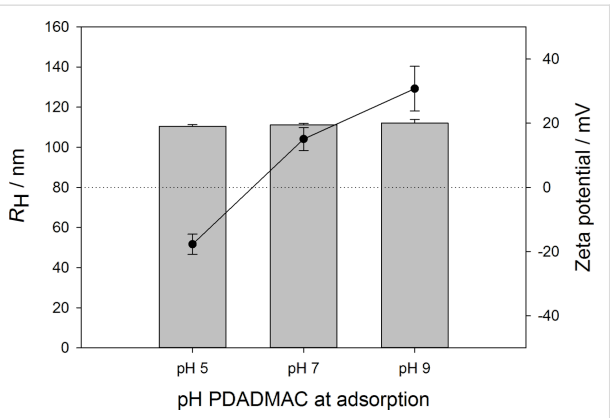

Figure 3: Particle radii (bars) and zeta potential (line plot) of PLGA-PEI-PAA-PDADMAC nanoparticles in dependence of the pH value during PDADMAC adsorption. All experiments were performed in triplicate, average values ± standard deviations are shown.

As expected, the nanoparticle size does not depend on the pH value during adsorption of PDADMAC, since the polymer chain conformation of PDADMAC is independent of the pH and therefore always adsorbs as a flat, highly charged layer. In contrast to the particle size, there is a strong influence of the pH value on the zeta potential of PLGA-PEI-PAA-PDADMAC

nanoparticles. The pH value of the nanoparticle dispersion before adsorption determines the degree of ionization of PAA on the particle surface and therefore leads to differently pronounced electrostatic attraction to the oppositely charged PDADMAC. The PLGA-PEI-PAA nanoparticle system shows negative zeta potentials at pH 5, pH 7, and pH 9, respectively (data not shown). Adsorption of PDADMAC at pH 5 yields a slightly decreased zeta potential, which still has a negative value of (−18 ± 3) mV, when measured in ultrapure water at pH 6. Apparently, the PAA charge coverage at pH 5 is too low to bind a sufficient amount of PDADMAC, which could neutralize even the charge density of PAA present at pH 6. Only choosing a pH ≥7 during adsorption leads to positive zeta potentials of (+15 ± 4) mV for PDADMAC adsorption at pH 7 and (+31 ± 7) mV for adsorption at pH 9. In summary, PDADMAC adsorption onto PLGA-PEI-PAA nanoparticles significantly depends on the adsorption pH, due to a varying state of deprotonation of the PAA layer on the particle surface, even though PDADMAC provides a charge density of the chain that does not depend on the pH value.

Terminating PAA layer adsorption

The third polymer layer of PDADMAC is followed by another layer of PAA, terminating the particle preparation. Figure 4 shows the resulting particle sizes and zeta potentials after each step of the nanoparticle modification, which underlines the successful preparation, demonstrated by a constant size and an inversion of the zeta potential after each adsorption step.

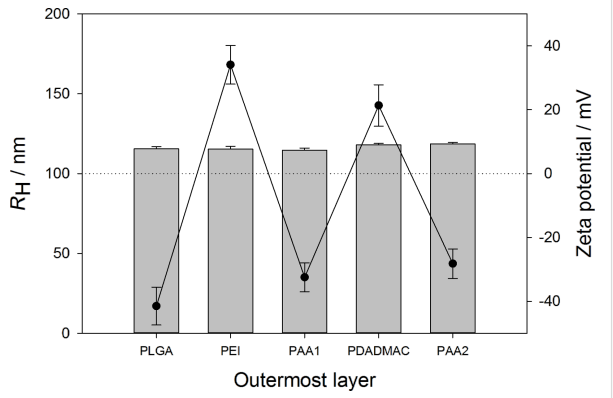

Figure 4: Hydrodynamic radii (bars) and zeta potential (line plot) in dependence of the number of polymer layers for the sequence PLGA-PEI(pH10)-PAA(pH5)-PDADMAC(pH9)-PAA(pH5). All experiments were performed in triplicate, average values ± standard deviations are shown.

Release of PDADMAC

To probe pH-tunability after adsorption of the second PAA layer, a titration experiment using HCl (25 mM) was carried out, as described in the Experimental section. PDADMAC desorption was monitored by quantitative ^{1}H NMR spectroscopy, using an external standard of resorcinol in D_2O as a reference substance. In Figure 5, ^{1}H NMR spectra of all polymeric components are shown, except for PLGA, which is insoluble in D_2O. Recorded spectra are stacked as a guide to the eye, while each polymer spectrum is normalized to the signal of residual water protons (HDO), calibrated by a chemical shift of 4.8 ppm.

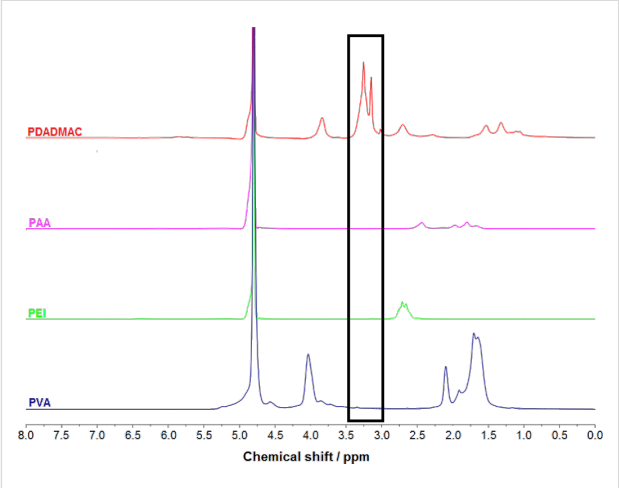

Figure 5: ^{1}H NMR spectra of solutions (50 mM monomer conc.) of PDADMAC, PAA, PEI, and PVA (from top to bottom). Quantification of PDADMAC in particle dispersion is based on the absence of signals between 2.9 and 3.4 ppm for any other polymer than PDADMAC.

Typical broad polymer resonances are observed, where two characteristic signals for PDADMAC occur at chemical shifts of 3.15 and 3.25 ppm in a region where all other polymers show now signal, which makes a quantification of PDADMAC possible using ^{1}H spectra. Quantification of PEI or PAA is difficult due to the comparatively lower signal intensities and some spectral overlap. The reference spectrum of resorcinol (data not shown) shows only chemical shifts higher than 4.8 ppm, which do not interfere with any polymer signal. For quantification, the integral of the resorcinol signal at a chemical shift of 7.1 ppm is used and related to the integrals of the PDADMAC signals at 3.15 and 3.25 ppm, respectively.

In order to assure the detection of the ^{1}H NMR signal of the polymers, the nanoparticles have been prepared using D_2O as solvent in the two final washing steps. For desorption experiments, the prepared nanoparticle dispersions were adjusted to pH values between pH 7.4 and pH 0.9 before acquisition of ^{1}H NMR spectra. As a first step, PLGA-PEI(pH 10)-PAA(pH 5)-PDADMAC(pH 9)-PAA(pH 5) nanoparticles were investigated. Alternatively, PLGA-PEI(pH 10)-PAA(pH 5)-PDADMAC(pH 9) nanoparticles have been prepared, lacking the terminating PAA layer and therefore

offering the possibility to investigate the influence of the outer PAA layer on the PDADMAC desorption process. The desorbed amount of PDADMAC in dependence of the adjusted pH is related to the total particle surface and given in Figure 6.

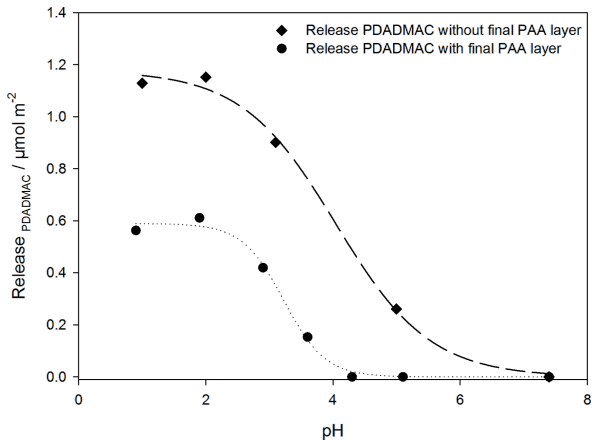

Figure 6: Released amount of PDADMAC per surface area in dependence of the pH. The amount of released PDADMAC was related to the total particle surface to yield the released amount per surface area.

An obvious dependence of the released amount of PDADMAC on the pH can be concluded, as a decrease in pH leads to the release of PDADMAC for both nanoparticle systems investigated. For the nanoparticle system including a terminating PAA layer, the release process starts at pH ≤4 and the released amount reaches a maximum plateau value at about pH 2. The data follow almost exactly a sigmoidal curve and as a release point the pH at 50% release can be determined as 3.2. Interestingly, this release only starts at much lower pH values than expected from previous titration experiments, which show charge neutrality of the PAA layer for the PLGA-PEI(pH 10)-PAA(pH 5) nanoparticle system at pH 4.1, see Figure 2. Since polyelectrolyte layers are dynamic systems of more or less penetrable polyelectrolyte chains, there will always be an amount of charge contributing from underlying layers to the overall electrostatic properties of the polyelectrolyte film. Overall, the total amount of negative charges present at the isoelectric point (IEP) can be concluded to be sufficient in order to preserve a stable PEM, hence preventing PDAMAC to be desorbed from the nanoparticle surface at pH values greater than 4. The release curve for the nanoparticle system lacking the terminating PAA layer also follows a sigmoidal release curve, but PDADMAC desorption already starts at significantly higher pH values compared to the PLGA-PEI(pH 10)-PAA(pH 5)-PDADMAC(pH 9)-PAA(pH 5) nanoparticle system. Additionally, the total amount of released PDADMAC is found to be increased by a factor of almost two. This can be explained considering the degree of ionization of the PAA layer in either nanoparticle system: During build-up of the PLGA-PEI(pH 10)-PAA(pH 5)-PDADMAC(pH 9)-PAA(pH 5) nanoparticles, the pH is reduced from pH 9 after adsorption of PDADMAC to pH 5 during adsorption of the final PAA layer, hence a fraction of PDADMAC may already be released because of the pH decrease during the adsorption of PAA. This also explains that the PDADMAC release is starting at lower pH values in case of the nanoparticle system containing the terminating PAA layer, since the formerly adsorbed amount of PDADMAC is already desorbed during build-up of the terminating PAA layer.

After pH-induced release of the polyelectrolyte we tested for complete release by adding sodium chloride to each sample solution, such that a final concentration of 2 M was reached. Dubas and Schlenoff had previously reported a complete destruction of PDADMAC/PAA multilayers at high salt concentrations (above 0.6 M) [40]. In our systems there was no additional release of PDADMAC observed after the increase of the ionic strength, thus we conclude that a quantitative release can be achieved by pH treatment alone.

Conclusion

In the present work, we successfully implemented a pH-tunable entity onto biocompatible PLGA nanoparticles using the LbL self-assembly technique and demonstrated ways to control the pH window, in which the nanoparticle surface is pH-sensitive. Successive adsorption of PDADMAC as a cationic compound was accomplished, illustrating the importance to choose adsorption conditions allowing an overcompensation of the nanoparticle surface charge. Furthermore, adsorbed PDADMAC was successfully released after application of an appropriate pH-stimulus, leading to well fitted desorption isotherms. Furthermore, desorption data obtained after omitting the previous adsorption of a terminating PAA layer clearly show a partial desorption of PDADMAC during assembly of the terminating PAA layer, emphasising the pH-sensitivity of PEM consisting of weak polyelectrolytes, such as PAA. The obtained data not only reveal important information about pH-tunability, but also about the absolute stability of polyelectrolyte multilayers and will therefore facilitate future development of applications in the field of pH-sensitive nanostructure assembly.

Experimental

Materials: Poly(lactic-*co*-glycolic acid) (PLGA, Resomer® RG 502H) was purchased from Evonik Industries AG (Darmstadt, Germany). Resorcinol (analytical grade), ethyl acetate (reagent grade; >99.5%), deuterium oxide (D_2O) (99.9% isotope purity), poly(vinyl alcohol) (PVA) (87–89% hydrolysed; $M_w \approx 67{,}000$ g/mol), as well as aqueous solutions of poly-

ethylenimine (PEI) ($M_w \approx$ 50,000–60,000 g/mol; 50 wt %) and polyacrylic acid (PAA) ($M_w \approx$ 100,000 g/mol; 35 wt %) were purchased from Sigma–Aldrich (Steinheim, Germany). An aqueous solution of poly(diallyldimethylammonium chloride) (PDADMAC) ($M_w \approx$ 8,500 g/mol; 28 wt %) was purchased from Polysciences (Eppelheim, Germany). Adjustments of pH values were performed by addition of sodium hydroxide solution (1 mol/L) or hydrochloric acid (1 mol/L), which were purchased from Waldeck (Münster, Germany). Washing and dilution steps were carried out using ultrapure water, having a resistivity of at least 18.2 MΩ·cm. All chemicals were used as received without further purification.

Solutions: An amount of 500 mg of PVA was dissolved in 50 mL of ultrapure water using gentle heating (60 °C) and magnetic stirring at 500 rpm. The PVA solution was cooled to room temperature and filtered (0.22 µm, cellulose acetate filter unit) directly before use. Additionally, 500 mg of PLGA were dissolved in 5 mL ethyl acetate. Polyelectrolyte solutions were diluted to concentrations of 10 mmol/L (PAA and PDADMAC) and 20 mmol/L (PEI), respectively. All polyelectrolyte concentrations were calculated with respect to the monomeric unit of the corresponding compound. If needed, pH was adjusted by addition of 1 molar hydrochloric acid (HCl) and 1 molar sodium hydroxide solution (NaOH).

Dynamic light scattering (DLS): Average particle size, polydispersity, and zeta potential were determined using a Zetasizer Nano ZS (Malvern Instruments, UK). All measurements were performed at ambient temperature of (22 ± 0.1) °C in ultrapure water as dispersant, unless mentioned otherwise. For titration experiments, a multi-purpose titration device MPT-2 (Malvern Instruments, UK) was connected to the Zetasizer Nano ZS. Titrations were carried out by diluting 5 mg nanoparticles (calculated as dry solids content) with ultrapure water to a final volume of 12 mL. Hydrochloric acid (25 mM) was chosen as the corresponding titration agent. During titration experiments, the pH was decreased step-wise to a final value of 2.5, while particle diameter, polydispersity, and zeta potential were monitored for each pH step.

Gravimetric analysis: Determination of nanoparticle concentration in dispersion was carried out by gravimetric analysis using a Sartorius SE2 Ultra microbalance (Sartorius AG, Göttingen, Germany). An aliquot (20.0 µL) of homogenized nanoparticle dispersion was transferred to a disposable aluminium weighing dish, which was weighted previously. The filled weighing dish was dried for at least four hours in a drying cabinet (Thermo Fisher Scientific Inc., USA) at 80 °C. The particle concentration of the initial dispersion was derived from the weight of the solids content.

Nuclear magnetic resonance (NMR) spectroscopy: ^{1}H NMR experiments were performed using a 400 MHz Avance spectrometer (Bruker, Rheinstetten, Germany). All measurements were carried out at room temperature (295 K) and all sample solutions were prepared in D_2O. For quantitative NMR measurements of PDADMAC, a solution of resorcinol in D_2O was used as an external standard. It was filled into a melting point capillary, which was flame-sealed on both ends and inserted on the central axis of an NMR tube containing the sample solution. A calibration was carried out by relating the resorcinol signal at 7.1 ppm to the PDADMAC signals (at 3.15 and 3.25 ppm) of solutions with known PDADMAC concentrations (1 mM and 2 mM). This obtained calibration was used to determine the amount of PDADMAC desorbed from nanoparticles after applying a pH stimulus.

Nanoparticle preparation: PLGA nanoparticles were prepared by a modified emulsion diffusion method. The addition of a stabilizing agent is generally favoured due to increased final particle stability. Here, poly(vinyl alcohol) (PVA) was used for particle preparation since it has proven to have outstanding emulsification properties and a low toxicity at the same time. In brief, 500 mg of PLGA was dissolved in 5 mL ethyl acetate. After addition of 10 mL aqueous PVA solution (10 mg/mL), the obtained emulsion was mixed using an Ultra Turrax T25 homogenization device (IKA Werke GmbH & Co KG, Staufen, Germany) at 17,000 rpm for 5 min to ensure a small and homogeneous droplet formation. The obtained emulsion was added to 40 mL of PVA solution (10 mg/mL) and stirred at 550 rpm at room temperature for at least 12 h in order to completely evaporate the ethyl acetate phase, leading to final nanoparticle precipitation. After particle formation, the dispersion was washed by centrifugation (Centrifuge 5242, Eppendorf, Germany) and removal of the supernatant containing excess PVA. The procedure was followed by redispersion in ultrapure water, treatment by a vortexing device (VWR VV3, Darmstadt, Germany) and gentle sonication (Bandelin Sonorex PK 102 H, Berlin, Germany), if necessary. The washing step was performed three times in order to completely remove the PVA from the aqueous phase.

Layer-by-layer (LbL) self-assembly: Polyelectrolyte multilayers were adsorbed to PLGA nanoparticles using the LbL self-assembly technique, as described elsewhere [15,41,42]. For each adsorption step, polymer solution was stirred at 700 rpm using a magnetic stirrer, while an equal volume of nanoparticle dispersion (10 mg/mL) was added dropwise. To ensure complete polymer adsorption, an incubation time of 20 min was chosen. Excess polymer was washed out by centrifugation at 4,000*g* for 20 min and removal of the supernatant. The particles were then redispersed in ultrapure water, using sonication

and a vortexer, if necessary. By this procedure, particle dispersions were washed twice after each adsorption step.

Acknowledgements

This work was funded by the Faculty Networking Program (Bonusprogramm) of the University of Münster.

References

1. Kimling, J.; Maier, M.; Okenve, B.; Kotaidis, V.; Ballot, H.; Plech, A. *J. Phys. Chem. B* **2006,** *110,* 15700–15707. doi:10.1021/jp061667w
2. Morel, M.; Martinez, F.; Mosquera, E. *J. Magn. Magn. Mater.* **2013,** *343,* 76–81. doi:10.1016/j.jmmm.2013.04.075
3. Langer, K.; Anhorn, M. G.; Steinhauser, I.; Dreis, S.; Celebi, D.; Schrickel, N.; Faust, S.; Vogel, V. *Int. J. Pharm.* **2008,** *347,* 109–117. doi:10.1016/j.ijpharm.2007.06.028
4. Quintanar-Guerrero, D.; Allémann, E.; Fessi, H.; Doelker, E. *Drug Dev. Ind. Pharm.* **1998,** *24,* 1113–1128. doi:10.3109/03639049809108571
5. Wacker, M. *Int. J. Pharm.* **2013,** *457,* 50–62. doi:10.1016/j.ijpharm.2013.08.079
6. Astete, C. E.; Sabliov, C. M. *J. Biomater. Sci., Polym. Ed.* **2006,** *17,* 247–289. doi:10.1163/156856206775997322
7. Sahoo, S. K.; Panyam, J.; Prabha, S.; Labhasetwar, V. *J. Controlled Release* **2002,** *82,* 105–114. doi:10.1016/S0168-3659(02)00127-X
8. Spek, S.; Haeuser, M.; Schaefer, M. M.; Langer, K. *Appl. Surf. Sci.* **2015,** *347,* 378–385. doi:10.1016/j.apsusc.2015.04.071
9. Shive, M. S.; Anderson, J. M. *Adv. Drug Delivery Rev.* **1997,** *28,* 5–24. doi:10.1016/S0169-409X(97)00048-3
10. Storm, G.; Belliot, S. O.; Daemen, T.; Lasic, D. D. *Adv. Drug Delivery Rev.* **1995,** *17,* 31–48. doi:10.1016/0169-409X(95)00039-A
11. Gref, R.; Domb, A.; Quellec, P.; Blunk, T.; Müller, R. H.; Verbavatz, J. M.; Langer, R. *Adv. Drug Delivery Rev.* **1995,** *16,* 215–233. doi:10.1016/0169-409X(95)00026-4
12. Tosi, G.; Rivasi, F.; Gandolfi, F.; Costantino, L.; Vandelli, M. A.; Forni, F. *Biomaterials* **2005,** *26,* 4189–4195. doi:10.1016/j.biomaterials.2004.10.025
13. Weiss, B.; Schneider, M.; Muys, L.; Taetz, S.; Neumann, D.; Schaefer, U. F.; Lehr, C.-M. *Bioconjugate Chem.* **2007,** *18,* 1087–1094. doi:10.1021/bc060342f
14. Westcott, S. L.; Oldenburg, S. J.; Lee, T. R.; Halas, N. J. *Langmuir* **1998,** *14,* 5396–5401. doi:10.1021/la980380q
15. Decher, G.; Hong, J. D.; Schmitt, J. *Thin Solid Films* **1992,** *210,* 831–835. doi:10.1016/0040-6090(92)90417-A
16. Lvov, Y.; Ariga, K.; Kunitake, T. *Chem. Lett.* **1994,** *23,* 2323–2326. doi:10.1246/cl.1994.2323
17. Lvov, Yu.; Decher, G.; Sukhorukov, G. *Macromolecules* **1993,** *26,* 5396–5399. doi:10.1021/ma00072a016
18. Ren, K.; Wang, Y.; Ji, J.; Lin, Q.; Shen, J. *Colloids Surf., B* **2005,** *46,* 63–69. doi:10.1016/j.colsurfb.2005.09.004
19. Ariga, K.; Lvov, Y.; Kunitake, T. *J. Am. Chem. Soc.* **1997,** *119,* 2224–2231. doi:10.1021/ja963442c
20. Choi, J.; Rubner, M. F. *Macromolecules* **2005,** *38,* 116–124. doi:10.1021/ma048596o
21. Bieker, P.; Schönhoff, M. *Macromolecules* **2010,** *43,* 5052–5059. doi:10.1021/ma1007489
22. Hashide, R.; Yoshida, K.; Hasebe, Y.; Seno, M.; Takahashi, S.; Sato, K.; Anzai, J.-I. *J. Nanosci. Nanotechnol.* **2014,** *14,* 3100–3105. doi:10.1166/jnn.2014.8562
23. Kempe, K.; Ka Fung, N.; Sher Leen, N.; Müllner, M.; Caruso, F. *Polymer* **2014,** *55,* 6451–6459. doi:10.1016/j.polymer.2014.09.074
24. Zhuk, I.; Jariwala, F.; Attygalle, A. B.; Wu, Y.; Libera, M. R.; Sukhishvili, S. A. *ACS Nano* **2014,** *8,* 7733–7745. doi:10.1021/nn500674g
25. Du, P.; Zhao, X.; Zeng, J.; Guo, J.; Liu, P. *Appl. Surf. Sci.* **2015,** *345,* 90–98. doi:10.1016/j.apsusc.2015.03.151
26. Mandapalli, P. K.; Venuganti, V. V. K. *J. Pharm. Invest.* **2015,** *45,* 131–141. doi:10.1007/s40005-014-0153-0
27. Yoshida, K.; Ono, T.; Kashiwagi, Y.; Takahashi, S.; Sato, K.; Anzai, J.-i. *Polymers (Basel, Switz.)* **2015,** *7,* 1269–1278. doi:10.3390/polym7071269
28. Wilson, J. Properties and Analysis of POLYDADMAC for Water Purification. Ph.D. Thesis, Stellenbosch University, Stellenbosch, South Africa, 2008.
29. Hanasaki, T.; Ohnishi, H.; Nikaidoh, A.; Tanada, S.; Kawasaki, K. *Bull. Environ. Contam. Toxicol.* **1985,** *35,* 476–481. doi:10.1007/BF01636541
30. Parazak, D. P.; Burkhardt, C. W.; Mccarthy, K. J. *Anal. Chem.* **1987,** *59,* 1444–1445. doi:10.1021/ac00137a015
31. Schönhoff, M. *J. Phys.: Condens. Matter* **2003,** *15,* R1781–R1808. doi:10.1088/0953-8984/15/49/R01
32. Lösche, M.; Schmitt, J.; Decher, G.; Bouwman, W. G.; Kjaer, K. *Macromolecules* **1998,** *31,* 8893–8906. doi:10.1021/ma980910p
33. Dubas, S. T.; Schlenoff, J. B. *Macromolecules* **1999,** *32,* 8153–8160. doi:10.1021/ma981927a
34. Steitz, R.; Leiner, V.; Siebrecht, R.; von Klitzing, R. *Colloids Surf., A* **2000,** *163,* 63–70. doi:10.1016/S0927-7757(99)00431-8
35. Ladam, G.; Schaad, P.; Voegel, J. C.; Schaaf, P.; Decher, G.; Cuisinier, F. *Langmuir* **2000,** *16,* 1249–1255. doi:10.1021/la990650k
36. Shiratori, S. S.; Rubner, M. F. *Macromolecules* **2000,** *33,* 4213–4219. doi:10.1021/ma991645q
37. Yoo, D.; Shiratori, S. S.; Rubner, M. F. *Macromolecules* **1998,** *31,* 4309–4318. doi:10.1021/ma9800360
38. Rusu, M.; Kuckling, D.; Möhwald, H.; Schönhoff, M. *J. Colloid Interface Sci.* **2006,** *298,* 124–131. doi:10.1016/j.jcis.2005.12.027
39. Dubois, M.; Schönhoff, M.; Meister, A.; Belloni, L.; Zemb, T.; Möhwald, H. *Phys. Rev. E* **2006,** *74,* 051402. doi:10.1103/PhysRevE.74.051402
40. Dubas, S. T.; Schlenoff, J. B. *Macromolecules* **2001,** *34,* 3736–3740. doi:10.1021/ma001720t
41. Sukhorukov, G. B.; Donath, E.; Lichtenfeld, H.; Knippel, E.; Knippel, M.; Budde, A.; Möhwald, H. *Colloids Surf., A* **1998,** *137,* 253–266. doi:10.1016/S0927-7757(98)00213-1
42. Schwarz, B.; Schönhoff, M. *Langmuir* **2002,** *18,* 2964–2966. doi:10.1021/la015636y

BEILSTEIN JOURNAL OF NANOTECHNOLOGY

Controlled graphene oxide assembly on silver nanocube monolayers for SERS detection: dependence on nanocube packing procedure

Martina Banchelli[1], Bruno Tiribilli[2], Roberto Pini[1], Luigi Dei[3], Paolo Matteini[*1] and Gabriella Caminati[*3]

Full Research Paper

Open Access

Address:
[1]Institute of Applied Physics, National Research Council - Via Madonna del Piano 10, I-50019 Sesto Fiorentino, Italy, [2]Institute for Complex Systems, National Research Council, Via Madonna del Piano 10, I-50019 Sesto Fiorentino, Italy and [3]Department of Chemistry and CSGI, University of Florence, Via della Lastruccia 3–13, I-50019 Sesto Fiorentino, Italy

Email:
Paolo Matteini[*] - p.matteini@ifac.cnr.it; Gabriella Caminati[*] - gabriella.caminati@unifi.it

* Corresponding author

Keywords:
graphene oxide; quartz crystal microbalance; sensing application; SERS; silver nanocubes

Beilstein J. Nanotechnol. **2016,** *7,* 9–21.
doi:10.3762/bjnano.7.2

Received: 15 October 2015
Accepted: 21 December 2015
Published: 06 January 2016

This article is part of the Thematic Series "Organized films".

Guest Editor: M. Canepa

Abstract

Hybrid graphene oxide/silver nanocubes (GO/AgNCs) arrays for surface-enhanced Raman spectroscopy (SERS) applications were prepared by means of two procedures differing for the method used in the assembly of the silver nanocubes onto the surface: Langmuir–Blodgett (LB) transfer and direct sequential physisorption of silver nanocubes (AgNCs). Adsorption of graphene oxide (GO) flakes on the AgNC assemblies obtained with both procedures was monitored by quartz crystal microbalance (QCM) technique as a function of GO bulk concentration. The experiment provided values of the adsorbed GO mass on the AgNC array and the GO saturation limit as well as the thickness and the viscoelastic properties of the GO film. Atomic force microscopy (AFM) measurements of the resulting samples revealed that a similar surface coverage was achieved with both procedures but with a different distribution of silver nanoparticles. In the GO covered LB film, the AgNC distribution is characterized by densely packed regions alternating with empty surface areas. On the other hand, AgNCs are more homogeneously dispersed over the entire sensor surface when the nanocubes spontaneously adsorb from solution. In this case, the assembly results in less-packed silver nanostructures with higher inter-cube distance. For the two assembled substrates, AFM of silver nanocubes layers fully covered with GO revealed the presence of a homogeneous, flexible and smooth GO sheet folding over the silver nanocubes and extending onto the bare surface. Preliminary SERS experiments on adenine showed a higher SERS enhancement factor for GO on Langmuir–Blodgett films of AgNCs with respect to bare AgNC systems. Conversely, poor SERS enhancement for adenine resulted for GO-covered AgNCs obtained by spontaneous adsorption. This indicated that the assembly and packing of AgNCs obtained in this way, although more homogeneous over the substrate surface, is not as effective for SERS analysis.

Introduction

Organized films composed of metal nanoparticles have been extensively studied in recent years owing to their enormous potential in fields as diverse as photoelectrochemistry [1,2], optoelectronics [3], energy-harvesting applications [4], cancer imaging and therapy [5], sensing and biosensing applications [6,7]. In particular, sensors based on arrays of noble metal nanoparticles have become increasingly popular for the ultrasensitive detection of a variety of species ranging from small molecules to large proteins by means of surface-enhanced Raman spectroscopy (SERS) [8,9]. Furthermore, these arrays offer additional sensing capabilities based on the localized surface plasmon resonance (LSPR) sensitivity to subtle changes in the refractive index of the surrounding molecular environment [10,11].

Nanoparticle arrays differing in chemical composition, size, shape and bidimensional morphology have been extensively studied [8,9,12] in the past decades. The existing literature has revealed that not only the shape and size of metal nanoparticles determine their physicochemical and optical properties but also their bidimensional packing affects their properties. Among others, silver nanocubes (AgNCs) have been demonstrated to provide an intense and reproducible amplification of the Raman signal when densely assembled in ordered 2D structures on solid supports [13-15]. The large SERS effect has been demonstrated to be strictly dependent on the gap distance of adjacent nanostructures, commonly termed "hot spots", and many different approaches have been proposed for their production. Early methods rely on the random aggregation of silver or gold nanoparticles induced by a salt [16] whereas more recently external magnetic field were employed to dynamically control the interparticle spacing of a nanoparticle monolayer at the hexane/water interface [17]; however, the fabrication of controllable hot spots still remains a remarkable challenge.

The outstanding SERS capability of metal nanoparticle arrays may be further extended by a proper pairing with graphene or graphene derivatives due to their exclusive chemical, electronic and mechanical properties [18]. Graphene oxide (GO) is derived in the form of single-atom sheets of conjugated sp^2 carbon atoms with abundant oxygen-containing functionalities, which confer to the system additional features including great chemical stability in aqueous media and superior ability of capturing and retaining molecules.

Reports on nanoparticle/graphene hybrid nanocomposites showed that SERS signals arising from graphene/metal hybrid structures are higher compared to those of the individual components [19]. Several methods have been proposed for the fabrication of hybrid composites incorporating plasmonic nanoparticles and graphene [20]; preliminary results from this group evidenced that large SERS enhancement factors were obtained for rhodamine 6G adsorbed on a combination of graphene oxide and AgNCs arrays [21]. In a closely related paper by our group [22], we investigated the influence of thickness and structuring of the graphene oxide layer covering a Langmuir–Blodgett film of silver nanocubes on SERS detection, in the same paper [22] we compared the experimental results with theoretical simulations obtained by a finite element method (FEM).

In the present paper, we adopt a previously reported procedure for AgNC preparation [22] but we systematically explore the interplay between graphene oxide coverage and the morphology of the underlying AgNC arrays and how the resulting differences in the structural features of the hybrid system affect the spectroscopic properties and eventually SERS enhancement. Different approaches have been explored to assemble nanoparticles, including vacuum deposition, electrochemical deposition, electrostatic layer-by-layer adsorption and formation of nanoparticle films at the liquid−liquid interface [23-26]. In the latter case, assembly of uncapped nanoparticles generally leads to the formation of loosely packed aggregates and linking functionalities must be employed to decrease the interparticle distance, which in turns results in rigid arrays with suppressed elasticity and scarce resistance to mechanical stress. Nevertheless, the fabrication of large-scale homogeneous layers required for SERS detection has not been fully achieved. In this work we assembled closely packed AgNCs arrays with two different approaches: Langmuir–Blodgett (LB) transfer onto the solid support of a floating monolayer of AgNCs (procedure A) and sequential self-assembly of AgNCs by physisorption onto the surface (procedure B). The standard LB technique implies the preparation of a stable floating monolayer at liquid–air interface followed by controlled transfer onto the surface of a solid substrate [24]. The LB procedure was already employed in a related paper [22] for the deposition of AgNCs onto solid substrates, here we extended the preparation protocol investigating in detail the influence of hysteresis effect and monolayer fluidity on the packing of the resulting LB film. The monolayer is prepared by deposition and compaction of the nanoparticles onto water surface, to this aim different approaches can be chosen depending on particle functionalization: particles surrounded by a hydrophobic ligand shell can be deposited directly onto water surfaces [27] either alone or mixed with organic molecules that act as dispersants in the case of scarce particle stability at the interface [28]. Other strategies include choice of non-aqueous monolayer subphases [29] and formation of the monolayer at water–oil interfaces [27]. Although the encouraging successful results in SERS amplification of LB

samples, reports on the fabrication procedure are often contradictory and fine experimental control of the resulting structure is not always satisfactory. Self-assembly of metal nanoparticles through surface adsorption has received much less attention [30-32] due to the lack of direct monitoring of the assembly process in situ. In this work, we followed the formation of an adlayer of AgNCs on silicon oxide surfaces by means of a quartz crystal microbalance with dissipation monitoring as a function of time and AgNCs concentration, obtaining information on the kinetics and the mechanism of adsorption as well as the thickness and viscoelastic properties of the 2D structure at surface saturation.

Coverage of the resulting nanocube arrays with a graphene oxide layer was accomplished by spontaneous adsorption of GO. Although fabrication of GO-covered nanoparticles has been explored using several methods such as voltammetric co-reduction [33], formation of composite graphene oxide/PAMAM–silver nanoparticles through self-assembly followed by microwave irradiation [34] and GO drop-casting onto amino-functionalized Ag nanoparticles [19], detailed information on the GO coating step is not systematically studied and validated. Since the Raman scattering enhancement is strictly dependent on the geometry of the system at the nanoscale, controlling how GO affects the distribution of the AgNCs arrays is a key-step for the realization of efficient SERS substrates. Here we monitored the adsorption of GO onto AgNCs with a controlled step-by-step strategy by direct QCM monitoring of the adsorption process, a method that revealed both the mechanism and kinetics of the composite formation onto the AgNCs-covered SiO_2 surface. The hybrid samples were further characterized by means of atomic force microscopy that differences in the local morphology of the GO/AgNCs clusters.

The relationship between surface coverage and morphology and SERS activity of the GO/AgNCs hybrid structures was addressed characterizing the SERS behaviour of an extensively studied model probe such as adenine adsorbed on the resulting arrays. Preliminary results show that higher SERS intensities are detected from the GO/AgNCs hybrid nanostructures as compared to pure Ag nanoparticles for both nanoparticle packing procedures. Interestingly, we found that although similar GO coverage was found for both systems, which leads to similar quantities of adsorbed probe, the morphology of the nanoparticle layer dictates the effective Raman enhancement behaviour.

Results and Discussion

Assembly of silver nanocube monolayers

Silver nanocubes (AgNCs) were synthesized through a polyol synthesis, in the presence of poly(vinylpyrrolidone) (PVP) as a stabilizing agent, adopting an established literature protocol [35]. The resulting nanocube samples were mainly monodisperse with 45 nm average size and contained only a negligible fraction of Ag rods and irregular aggregates [36]. AgNC arrays were prepared with two different approaches: Langmuir–Blodgett (LB) transfer onto the solid support of a floating monolayer of AgNC (procedure A) and sequential self-assembly of AgNCs by physisorption onto the surface (procedure B).

Procedure A. Controlled assembly of AgNCs by Langmuir–Blodgett technique

The dispersion of silver nanocubes was spread at the water–air interface from a chloroform solution in a Langmuir trough to fabricate a monolayer of Ag nanoparticles. In agreement with the pioneering work by El-Sayed [37], we found that AgNCs are easily spread at the water–air interface to obtain ordered floating monolayers, in addition we observed that the shape and position of π–A isotherms strongly depend on factors such as the time allowed for solvent evaporation before starting compression, the amount of substance spread at the interface and the compression speed. Careful optimization of these parameters generated reproducible isotherms up to $\pi = 20$ mN/m, compression beyond this value leads to unstable monolayers due to incipient collapse of the film and formation of 3D structure. A typical π–A isotherm for AgNCs is reported in Figure 1a together with the behaviour of the surface compressional modulus as a function of surface area.

Surface pressure was found to increase monotonically as available surface area decreases showing a subtle phase transition more evident after a first expansion–compression cycle (see Supporting Information File 1, Figure S1) located at $\pi = 4$ mN/m in contrast with what reported previously [29,37]. We computed the surface compressional modulus from the experimental π–A data using Equation 1

$$C_s^{-1} = -A(d\pi / dA) \quad (1)$$

The surface compressional modulus is related to the elasticity and fluidity of the monolayer [38] and its value identifies the different monolayer phases: C_s^{-1} values lower than 50 mN/m correspond to a liquid-expanded phase, whereas for highly condensed phases values as high as 300 mN/m can be observed. Interestingly, the C_s^{-1} value remains constant as surface pressure increases revealing the presence of a wide domain where the mechanical features of the film remain unchanged. The small C_s^{-1} values described in Figure 1a, reveal fluid and elastic phase of the AgNC monolayer, similar low values of the surface compressional modulus ($C_s^{-1} < 50$ mN/m) were found

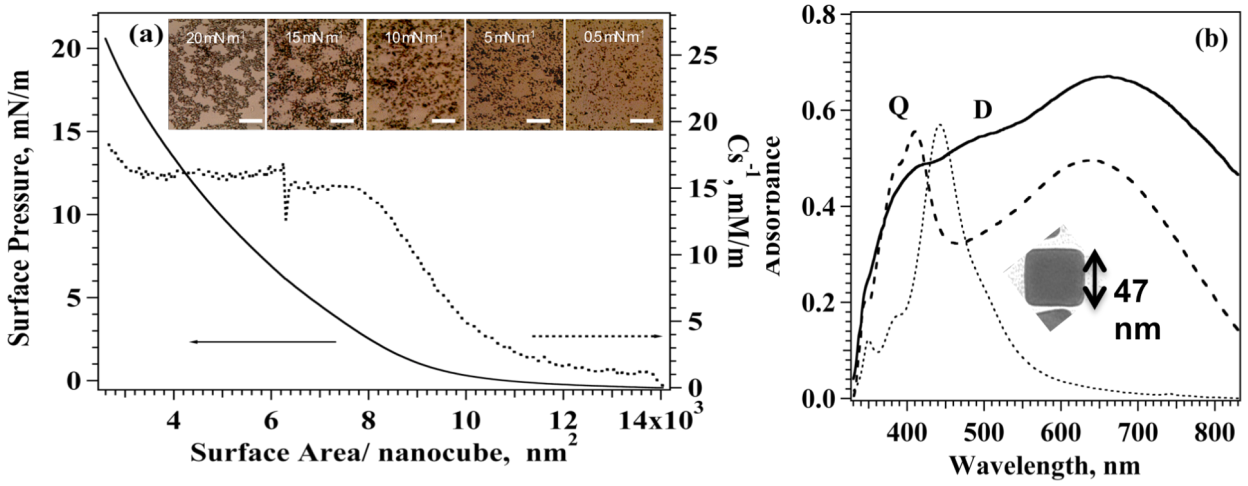

Figure 1: Procedure A. Formation of AgNC arrays by means of the Langmuir–Blodgett technique. (a) π–A and C_s^{-1}–A isotherm for AgNCs at the water–air interface. Optical images (650 × 750 μm) of the LB film of AgNC transferred at different surface pressures along the isotherm. (b) Absorption spectra of AgNC dispersion (dotted line) of a 1 LB layer of AgNC transferred onto glass at 15 mN/m (dashed line) and 20 mN/m (solid line). Inset: Transmission electron microscopy image of a representative single AgNC.

for nanoparticles trapped at the air–water interface also by other authors [39] who demonstrated the underlying correlation between the observed macroscopic transitions in mechanical properties and the microscopic dynamical phase transitions. Compression-expansion cycles were performed on AgNC monolayers arresting compression below 20 mN/m, the results (reported in Supporting Information File 1, Figure S1) show a small hysteresis that vanishes completely after the second cycle. These findings exclude loss of material in the subphase upon compression and support the formation of elastic arrays of AgNCs that quickly recover their closely-packed morphology after expansion thanks to the presence of the PVP polymer surrounding the nanoparticles. These features also warrant a successful transfer of the film from the water subphase to the solid support (Supporting Information File 1, Figure S2), fast reorganization of the nanocubes at the interface when the material is transferred to the solid substrate is evidenced by the stable value of surface pressure along the transfer process. Langmuir–Blodgett layers were transferred onto glass and silicon supports at different target surface pressures spanning from 0.5 mN/m to 20 mN/m (see Figure 1a), the transfer ratio (Supporting Information File 1, Figure S2), which reports on the quality of the transferred layer, was homogenous over the entire surface and close to one for all the selected surface pressures. Interestingly, conventional amphiphiles cannot be transferred successfully at low surface pressure whereas for AgNC significant transfer was obtained also at 0.5 mN/m although with low nanocube density. Such behaviour, reported also by other authors for mixed AgNC/phospholipid systems [40], is likely due to the stabilizing effect of PVP cushion capping the surface of the nanocubes.

Optical microscopy in reflection mode of LB monolayers of AgNCs transferred on silicon oxide, reported in Figure 1a, shows that as the transfer surface pressure increases, the particle density and the average size of the nanocube clusters increase, until a near-continuous monolayer is established around 15 mN/m. Images of the sample collected at 20 mN/m reveal the presence of 3D clusters of nanocubes supporting the hypothesis of incipient monolayer collapse at this surface pressure.

The principal structural features characterizing the AgNC assembly obtained with procedure A are summarized in Table 1 together with the results obtained for procedure B.

The data show that the LB layer transferred at 15 mN/m has an average thickness δ = 50 nm demonstrating the formation of a single layer of silver nanotubes. The surface density determined for QCM measurements for LB transferred directly on the QCN sensor was 41 NC/μm^2 which resulted in an average interparticle distance over the entire sensor surface of 100 nm, we recall that direct measurement of nanocube density at the water–air interface is vitiated by the presence of capping PVP molecules which cannot be directly quantified. Local interparticle distance estimated by AFM results [40] evidenced much smaller gaps of 1–3 nm between face-to-face nanocubes nm within the AgNC clusters.

Extinction spectra were collected for all transferred samples. Two typical spectra of 1 LB layer transferred at 15 and 20 mN/m together with the spectrum obtained for the dispersion of AgNCs are reported in Figure 1b. AgNC dispersion exhibits a sharp peak around 450 nm that, according to previous

Table 1: Structural parameters for AgNC arrays on silicon oxide.

AgNC packing procedure	Surface density, NC/μm^2	Interparticle distance, nm	δ, nm	$\Delta D \times 10^{-6}$
procedure A ($\pi_{transfer}$ = 15 mN/m)	41[a]	100[a]	50[b]	—
procedure B, sequential adsorption	35[a]	119[a]	32 ± 10[a]	18[a]

[a]Values extracted from analysis of QCM measurements. [b]Values extracted from analysis of AFM data.

reports [41,42], can be ascribed to the LSPR of nanocubes with 50 nm edge size in agreement with our TEM results and our preliminary findings [21] on different nanocube dispersions. Two minor peaks (348 and 380 nm) are also observed for the disperse NCs, likely due to the small fraction of Ag particles of different size and shape in the dispersion as reported earlier [42]. Spectra obtained for LB monolayers transferred at 15 and 20 mN/m exhibited a red-shifted shoulder at 490 nm together with the appearance of a new peak at 412 nm and a broader signal centred at 640 nm; similar spectral features were already reported for metal nanoparticles on dielectric support [31,43].

These experimental and theoretical studies demonstrate that the degeneracy of the localized surface plasmon resonance (LSPR) mode is split in two orthogonal electron oscillations with respect to the surface plane when a strong near-field interaction between AgNPs occurs in the 2D array. The cubic geometry of the nanoparticles provides a large nanoparticle–substrate contact area, leading to efficient hybridization of dipolar (D) and quadrupolar (Q) plasmonic resonances, which appear in the spectra as two separate D and Q peaks with the new Q band blue-shifted with respect to the D band due to dipolar modes. Therefore, a regular Ag nanocube array is expected to show an intense quadrupolar resonance and a dipolar red-shift relative to the solution of AgNCs, and this effect can be enhanced, or quenched, by controlling the particle size, the surrounding dielectric medium and the interparticle distance [27], namely the Q band is enhanced as the interparticle distance in the AgNC array decreases [44]. Other groups studied LB arrays of DOPC/AgNC of similar sizes [43] and AgNP assembly transferred from the hexane/water interface [44], these authors assigned the signal observed at 414 nm and 390 nm to quadrupolar coupling modes and observed a red shift of the dipolar contribution in agreement with our results. We also observed the appearance of a broad intense band due to strong interparticle dipole–dipole coupling centred at 642 nm and 665 nm for LB films transferred at 15 mN/m and 20 mN/m, respectively. Experimental and theoretical studies [45] on two dimensional (2D) arrays of AgNPs with the different edge-to-edge distances showed that delocalized long range LSPR results in a broad band centred at 640 nm for interparticle distance d = 3 nm and that the band red-shifts with increasing d. Although a definite assignment in the short wavelength region is hindered by the superposition of the signal of non-cubic aggregates to quadrupolar bands, our results show that regular arrangement of close-packed AgNPs contributes to the efficient coupling of dipole modes and that such coupling is less efficient for samples transferred at 20 mN/m, likely due to crystalline fusion in the collapsed 3D microdomains found in this samples. These results support our findings that a larger interparticle distance and higher aggregated fraction occur as transfer surface pressure is increased in the case of procedure A.

Procedure B. Controlled assembly of AgNCs by spontaneous adsorption on the surface

Spontaneous self-assembly of AgNC on silicon oxide surfaces was monitored in situ by means of a quartz crystal microbalance as the nanocubes approach the substrate and adsorb on the surface. In this experiment, the change in frequency, ΔF, related to the adsorbed mass, and the change of the dissipation factor, ΔD, related to the viscoelastic properties of the adsorbed film, were measured simultaneously as a function of time. Aliquots of a 0.3 mg mL^{-1} dispersion of AgNC were added sequentially in the measuring chamber, additions were made after adsorption equilibrium was established and after the excess of AgNC in solution was removed by water rinsing. This procedure was repeated until no further changes were recorded, indicating that surface saturation was reached. Typical results for the change in normalized frequency and dissipation factor for the third harmonic obtained for a single addition are reported in Figure 2. The plot shows how both $\Delta f_3/3$ and ΔD_3 change with time reaching a constant value only after 2 hours.

Interestingly, the kinetics of each adsorption step cannot be described by a simple Langmuir adsorption model but includes both a surface adsorption phase, with a significant change in $\Delta f_3/3$ and ΔD_3 and a rearrangement step at the surface where the adsorbed mass changes only slightly. Along the rearrangement step, the dissipation factor does not change significantly and oscillates around 7 × 10^{-6}, a value that is usually asso-

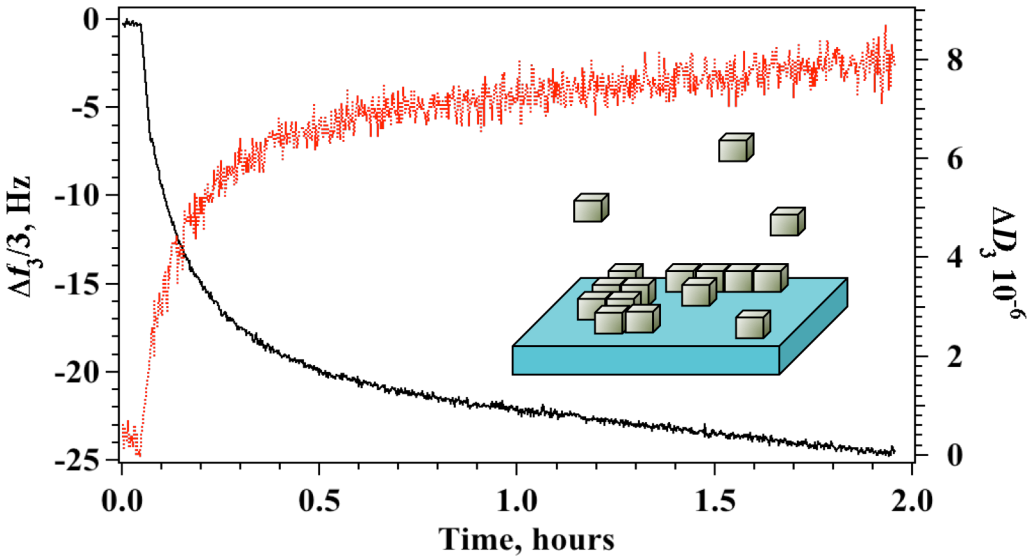

Figure 2: Procedure B. Formation of AgNC arrays by means of sequential physisorption. $\Delta f_3/3$ (black curve, left axis) and ΔD_3 (red curve, right axis) as a function of time after a single addition of AgNC in the QCM measuring chamber.

ciated with quasi-rigid layers. As adsorption proceeds in the following additions, the dissipation increases to values characteristic of elastic films. The structural parameters obtained at surface saturation for the AgNC layer fabricated with procedure B are reported in Table 1 together with the thickness of the adsorbed layer that was extracted by the analysis of all overtones as reported elsewhere [40,46].

The spontaneous adsorption method yields nanostructures with average interparticle spacing of 119 nm and an average layer thickness of 32 nm, comparison with the corresponding parameters obtained for procedure A (see Table 1) shows that both the adsorbed mass and the average thickness obtained with this procedure are slightly smaller suggesting lower surface coverage. In both cases formation of complete bilayers can be excluded although the presence of domains of 3D clusters cannot be discarded at this stage. The value of the nanocube surface density is in agreement with other studies on AgNC. Sisco and Murphy [47] studied AuNCs electrostatically immobilized on 4-MBA SAM and obtained a NC surface density ranging from 5.5 to 22 cubes/μm^2 with larger fraction of aggregated structures at higher surface densities (≈51%). Wang et al. [48] studied the formation of AgNC arrays by the dropping method as a function of AgNC concentration obtaining surface densities in the range 4.5–32.5 cubes/μm^2, whereas LB transfer of the same nanocubes provided larger surface densities of 19 to 49 AgNCs/μm^2 with increasing transfer surface pressure. The same authors also demonstrated that maximum Raman intensity of the R6G probe and enhancement factor are obtained for the large surface densities, i.e., 32.5 AgNC/μm^2.

Absorbance spectra for the AgNC arrays obtained with procedure B were tentatively acquired for glass and silicon oxide substrates, respectively. Typical results on glass (see Supporting Information File 1, Figure S3) show that absorbance for samples obtained with procedure B is very small due the lower surface coverage and stability obtained through physisorption. Weak shoulders are visible at 412 nm and 500 nm, as in the case of LB transfer, but the long-range dipolar contribution at 600 nm is suppressed. Although the weak absorbance does not allow for an unequivocal conclusion, similar results were recently obtained also by Park et al. [49] for NC horizontal transfer on silicon oxide substrates from the liquid–liquid interface. In the absence of a suitable linking functionality the authors observed the formation of loosely-packed arrays that exhibited a modest red-shift of the position of the dipole surface plasmon mode and a very broad extinction profile from 420 to 1200 nm without significant features. Electron microscopy in the early work by Malynych and Chumanov [50] also revealed no long-range order within the assembly of nanoparticles when 2D array of 100 nm AgNP were assembled by direct adsorption of the NP onto modified surfaces.

Adsorption of graphene oxide on AgNC arrays

Different fabrication methods have been developed for SERS-active surfaces involving graphene derivatives and nanoparticles including metal evaporation, electrochemical deposition and layer-by-layer self-assembly techniques [51]. Zarbin's group [20] directly synthesized and assembled silver nanoparticle/graphene oxide nanocomposites at a water/toluene

liquid–liquid interface whereas Wang et al. [52] proposed to assemble silver nanoparticles to graphene oxide sheets employing electrostatic interactions and a polymer, as adhesive agent, to impart greater stability against aggregation of AgNPs. Previous investigations are generally focused on spherical nanoparticles and only recently Fan et al. reported a work on single-particle SERS efficiencies of Ag nanooctahedra/GO hybrids built with drop-cast/adsorption method [19]. Most of these studies report on the fabrication of AgNC onto GO layers, without any control in situ of the AgNP packing density and of the morphology of the GO coverage. We adopted a different approach overlaying GO sheets on prepacked AgNC layers in the search for a reliable method that allows conjugation of AgNPs with desired morphologies (densities, sizes and shapes) with graphene oxide continuous covering. GO forms stable colloidal dispersions in water thanks to the presence of negatively charged carboxylic groups on its edges [53]. It has also been shown that GO flakes posses non-negligible surface activity that allows for the formation of spreading monolayers at the water–air interface and for its use in interfacial and flotation applications [54]. These features suggest that efficient coating of AgNC layers with graphene oxide may be obtained by direct adsorption from solution to the AgNC monolayer interface but a reproducible fabrication protocol of GO layers with controlled surface density and thickness necessitates a detailed knowledge of the mechanism and the kinetics of the process. To this end, the adsorption of graphene oxide flakes on the surface of the AgNC arrays was studied monitoring the change in adsorbed mass and thickness of the process by means of a quartz crystal microbalance. Preliminary studies demonstrated [21] that a decrease in frequency upon addition of GO was observed for GO bulk concentration as low as 4 mg L^{-1} with no mass loss upon water rinsing, the result indicates stable mass adsorption on the AgNC coated sensor surface even at low surface density. The same study [21] also evidenced that rapid increase in adsorbed mass was recorded up to 40 mg L^{-1}, after this concentration further addition of GO produced only a smaller increase in GO surface density. Typical results obtained for sequential adsorption of a 40 mg L^{-1} solution of GO on AgNC assemblies obtained with procedure A are reported in Figure 3.

The plots in Figure 3a show a continuous variation in time of the adsorbed mass in a Langmuir-type behaviour [21]. Interestingly, the increase in mass was paralleled by an increase in ΔD_3 value, which correlates with an increase in the viscoelastic properties of the adsorbed GO layer.

Analogously, QCM experiments were run to study the process of deposition of GO on top of AgNC layers assembled with procedure B, typical plots obtained for [GO] = 40 mg L^{-1} are

Table 2: Main physico-chemical parameters for GO layer on AgNC arrays.

AgNC array packing procedure	Surface density, ng/cm^2	δ, nm	$\Delta D \times 10^{-6}$
procedure A ($\pi_{transfer}$ = 15 mN/m)	1006	9 ± 1[a] 8[b]	80[a]
procedure B	1598	8 ± 1[a] 7[b]	125[a]

[a]Values extracted from analysis of QCM with dissipation monitoring measurements. [b]Values extracted from analysis of AFM data.

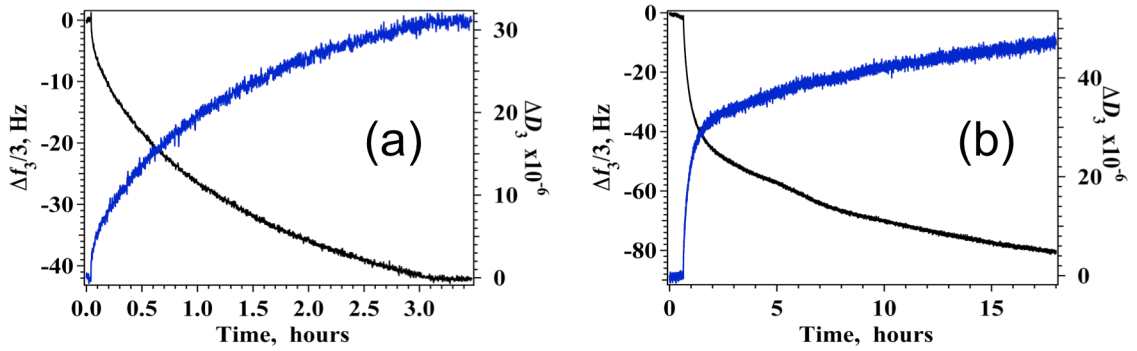

Figure 3: Change in $\Delta f_3/3$ (black curve, left *y*-axis) and ΔD_3 (blues curve, right *y*-axis) upon addition of graphene oxide from aqueous solution to 1 LB layer of silver nanocubes transferred at 15 mN/m (a) and to silver nanocubes arrays assembled by spontaneous adsorption (b). In all experiments [GO] = 40 mg L^{-1} and T = 20 °C.

reported in Figure 3b. Also in this case we observe a prompt decrease of frequency accompanied by an important increase in the dissipation factor, the behaviour of these two parameters with time is not continuous but reveals steps with different slopes that could be associated to a reorganization of the adsorbed GO flakes after arrival on the AgNC surface. For comparison we also recorded the adsorption behaviour of GO on bare silicon oxide surfaces, the results (Supporting Information File 1, Figure S4) revealed that GO adsorption is totally suppressed in the absence of the AgNC layer. Analysis of the experimental QCM results obtained for all overtones allowed for the determination of the surface density and thickness of the adsorbed GO layer, the values for the samples obtained with both procedures A and B at the same GO concentration, [GO] = 40 mg L^{-1}, are summarized in Table 2.

The data reveal that similar GO surface densities are obtained for both procedures, although larger values are found in the case of AgNC arrays obtained for spontaneous adsorption. The average QCM thickness is similar in both cases and corresponds to values much larger than 1 nm, a value previously ascribed to single flat GO layer [55]. These results could be explained either in terms of multilayer stacking or, more likely, with the folding of the GO sheet on the surface, this latter process is in agreement also with the large dissipation factor observed. Dissipation changes are large in both cases indicating that, as the surface density of adsorbed GO increases, the GO sheets do not adsorb flat onto the AgNCs surface but behave as an elastic, flexible and continuous layer.

The viscoelastic behaviour of graphene derivatives appear particularly important also for an emergent class of new graphene-derived metamaterials as reported also in a recent paper [56] where McEuen and coworkers describe graphene kirigami, robust microscale structures with tunable mechanical properties. Possibility to obtain these structures relies on the ratio between the in-plane stiffness and out-of-plane bending stiffness: large values of this parameter translate in membrane-like material that more easily bend and crumple. Optical microscopy in reflection mode images (Figure 4) of the two systems disclose quite different morphologies although with similar overall nanocube surface coverage. GO/AgNC assembly obtained with the LB technique is characterized by densely packed regions alternated to empty surface areas whereas the entire sensor surface is more homogeneously covered for GO/AgNC obtained with procedure B.

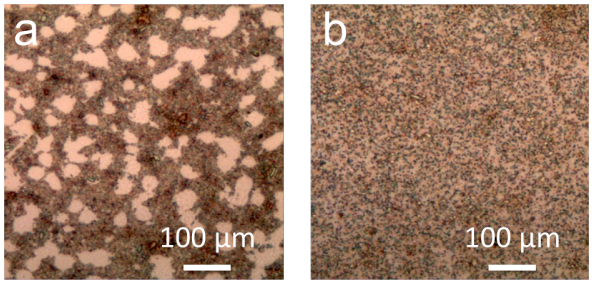

Figure 4: Optical images of GO-covered AgNCs prepared with procedure A (a) and B (b).

The larger amount of GO obtained with procedure B (see Table 2) is therefore strictly related to the smaller fraction of bare silicon oxide surface exposed. In both cases GO adsorbs through interactions with the silver surface anchoring exclusively to the outer face of the nanocube, with the large GO flakes extending and folding on the remaining nanocubes of the clusters or on the SiO_2 surface. This rationale is supported also by high resolution AFM images reported in Figure 5, the samples exhibit very similar structuring of the GO sheet over the AgNC assembly.

Figure 5c refers to graphene oxide deposits on silicon oxide obtained by simple drop casting followed by evaporation and shows, as expected, the presence of irregularly shaped sheets of lateral dimension ranging from a few nanometres to micrometres with nonuniform thickness ranging from 1.0 nm for single layers to 3.6 nm for GO terraces where the flakes partly overlap. AFM data confirm that folding of GO is prompted only by specific GO–AgNC interactions that anchor the larger GO

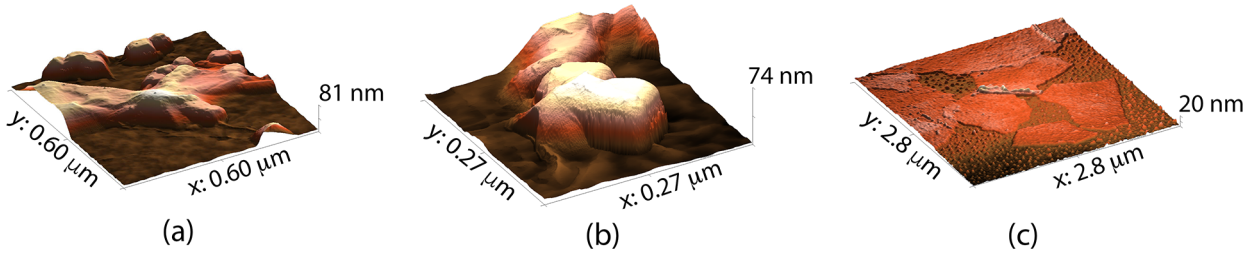

Figure 5: (a) AFM image of GO-covered silver nanocubes obtained from Langmuir–Blodgett transfer at 15 mN/m. (b) AFM image of GO-covered silver nanocubes obtained from direct sequential adsorption. (c) AFM image of the GO flakes on silicon oxide surfaces.

sheets extending the coverage also on the uncovered surface. AFM analysis (see Table 2) revealed that adsorbed GO has an average thickness of 7 nm for both procedures. Such high thickness values are in accordance with the formation of folded geometries of single GO sheets after anchoring to the nanoparticle surface. Nevertheless, AFM measurements reveal a smaller thickness compared to QCM for the same samples. This was expected since QCM values are always affected by the presence of water when hydrophilic substance are involved, as is the case of GO. Moreover, the presence of multiple GO folds offers inner surfaces where bound water can be confined, a phenomenon that escapes AFM detection but may be promptly revealed by gravimetric measurements.

Visible spectra for GO covered AgNCs on silicon oxide were collected in reflection mode using an integrating sphere for samples obtained with both procedure A and B are reported in Figure S5 of Supporting Information File 1. The spectra show that the dipole long-range coupling is broader and red-shifted for both packing procedures, although a red shift in the presence of GO was expected due to the higher refractive index of GO, the visible spectra of GO covered LB films evidenced only a modest red-shift to 670 nm. The larger shift observed in the present study may be explained considering that the use of the integrating sphere allows for the collection of reflected light coming from all angles and deriving from excitation at different incident angles with respect to the interface, therefore suggesting that in-plane and out-of-plane ordering of the nanocubes obtained with the two procedures are significantly different. Although the nanocubes are in a single layer with controlled interparticle distance they have a random rotational alignment perpendicular to the substrate and give an average response that includes all alignments. A strong angle dependence of the extinction and reflection spectra was observed also by other authors [57] and precludes a clear-cut spectral assignment at this stage.

SERS experiments

We analysed the SERS performances of the GO/AgNCs assemblies fabricated using procedure A (LB film of AgNCs) and B (sequential adsorption of AgNCs) and the results were compared with those obtained on pristine AgNCs LB films, excitation wavelength was fixed at 638 nm for both systems for the sake of comparison. The SERS experiments were conducted by using adenine as model probe because of its well-known SERS response and potential to establish interactions with both noble metal and graphene surfaces [58].

In Figure 6 the SERS spectra of adenine adsorbed from a 9×10^{-7} M incubation solution on AgNCs (B) and hybrid GO/AgNCs substrates (C, D) is displayed. Overall, the signals exhibit similar spectroscopic features (frequencies, S/N ratio, intensity), which suggests the occurrence of comparable interactions between the probe and the different substrates. Interestingly, the SERS spectrum of adenine features more detailed information in the presence of a GO layer, allowing even weaker Raman peaks (e.g., within the 750–1200 cm^{-1} region) to be resolved (Figure 6A, system C) possibly due to more favourable interactions between the adenine molecules and the substrate and/or a higher local concentration of adenine molecules retained by the GO layer as compared to those adsorbed on the naked nanoparticle substrates.

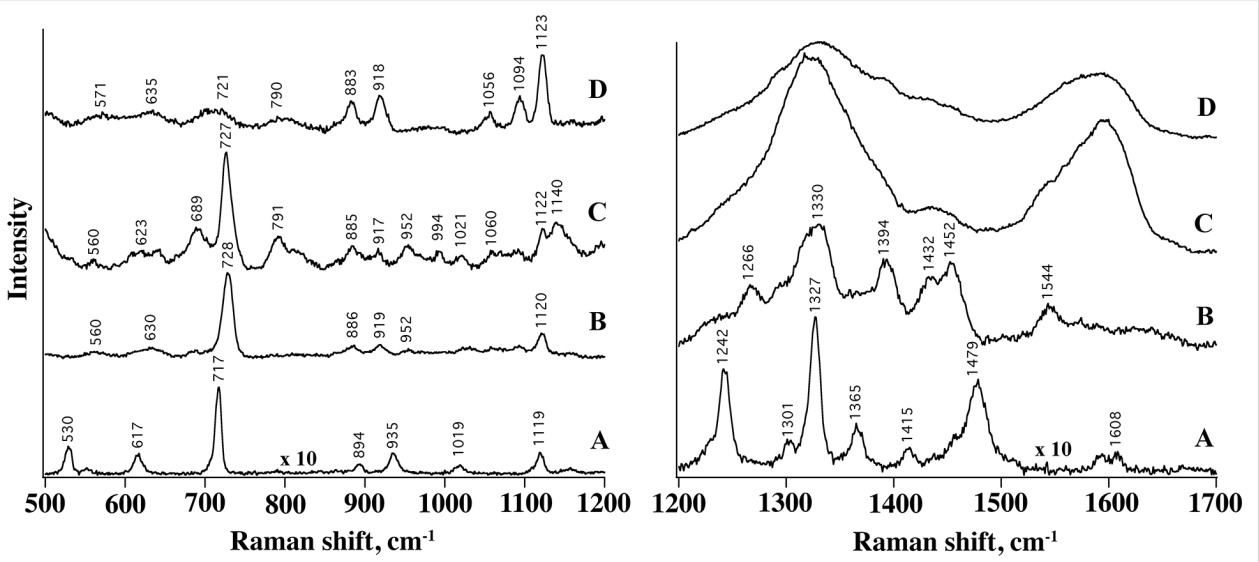

Figure 6: SERS spectra of Adenine (9×10^{-7} M) adsorbed on single LB layer of AgNCs (B), on GO/AgNCs obtained with procedure A (C) and with procedure B (D). Raman profile from adenine powder is also shown (A). Left: 500–1200 cm^{-1} Raman shift. Right: 1200–1799 cm^{-1} Raman shift.

The SERS spectra closely resemble the Raman profile of adenine (A) in the region between 500 and 1200 cm^{-1}, including the intense ring breathing peak at 730 cm^{-1}, which undergoes a 10 cm^{-1} blue shift ascribed to the interaction with the metal and GO surfaces. This peak is markedly weaker in the case of GO/AgNCs obtained with procedure B, which we attributed to a looser distribution of AgNPs and in turn to a reduced interparticle electromagnetic coupling and number of hot spots within the illuminated sample volume. Here the most intense bands observed are assigned to residual PVP molecules on the AgNCs surface (Supporting Information File 1, Figure S6).

The characteristic GO bands centred at 1601 cm^{-1} (G band) and at 1365 cm^{-1} (D band), and corresponding to the tangential stretching mode of the E_{2g} phonon of sp^2 atoms and to the breathing mode of κ-point phonons [59], respectively, dominate the Raman shift region between 1200 and 1700 cm^{-1} of the hybrid substrates (Figure 6 right) at the expense of the adenine signals. These bands are electromagnetically 50-fold enhanced by the underlying silver layer and this effect appears more pronounced for the GO/AgNCs assemblies obtained with procedure A (Supporting Information File 1, Figure S7).

When the samples are incubated with a more concentrated adenine solution, i.e., [adenine] = 9×10^{-4} M, a contribution from pure Raman occurs (see Figure 7) and overlaps with the SERS signals and this effect is more pronounced for GO/AgNCs samples obtained with procedure B. For example, the SERS contribution to the 730 cm^{-1} band reduces from 65% to 31% passing from type A to type B GO/AgNCs nanoarrays (Figure 7a), which again highlights how the non-homogenous assembly obtained with the Langmuir–Blodgett technique confers superior SERS activity compared with the samples obtained by spontaneous adsorption. Accordingly, the Raman signals of adenine can be detected against the prevailing GO bands in the GO/AgNCs substrate obtained by procedure B, which is not the case of that obtained by procedure A (Figure 7b).

The spectra in Figure 7 suggest that procedure A is the preferred approach for the production of reproducible SERS-active substrates although larger GO coverage and uniformity are obtained when AgNCs are assembled by spontaneous adsorption. This behaviour can be rationalized on the basis of the different clusters distribution obtained with the two procedures, as shown in the cartoon in Figure 8.

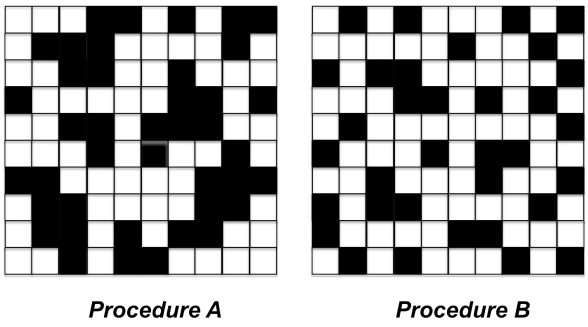

Figure 8: Checkboard model for AgNCs arrays on SiO_2 obtained with procedure A (surface density = 41 NC/μm^2) and procedure B (surface density = 35 NC/μm^2).

The scheme in Figure 8 describes a check board representation of the two systems, the overall number of nanocubes correlates with the experimental surface coverage reported in Table 1. Although the average intercube distance found from QCM data is similar in the two systems, AFM data reveal that a large frac-

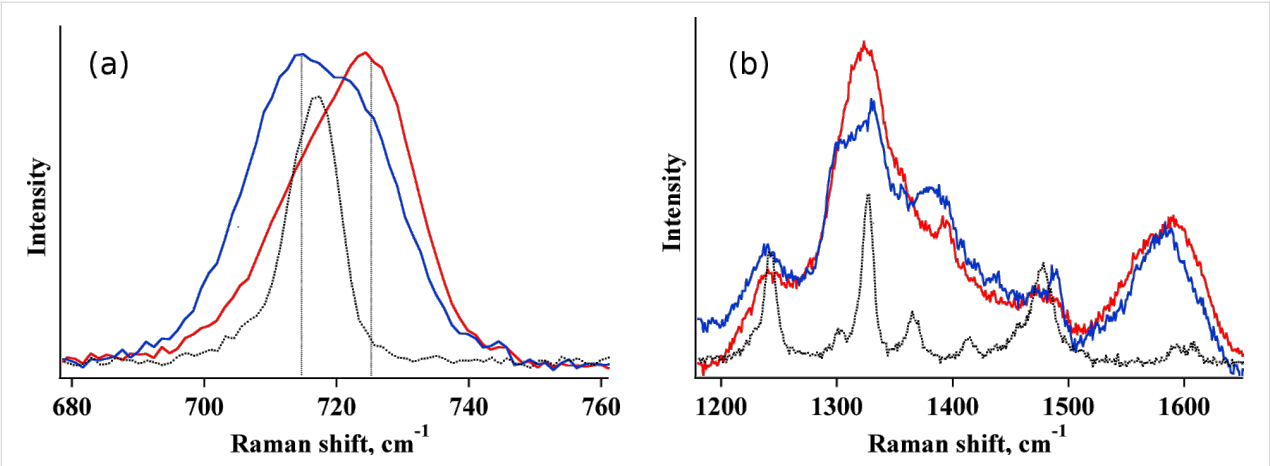

Figure 7: SERS spectra of Adenine (9×10^{-4} M) adsorbed on GO/AgNCs obtained with procedure A (red curve) and with procedure B (blue curve). The Raman spectrum (×10) of adenine powder is also reported (black curve).

tion of the nanocubes are grouped together in the case of procedure A with an average spacing of a few nanometers. Conversely, self-assembled nanocubes obtained from procedure B are uniformly dispersed as single nanocubes with larger spacing and only sparse NCs clusters. In the example reported in Figure 8, we can estimate that in the case of procedure B only 14% of nanocubes are closely packed but this fraction increases to 38% for samples obtained with procedure A. This picture may explain SERS results considering that the presence of a large fraction of AgNCs clusters with small interparticle distance permits the creation of an efficient hot spot distribution. Additionally, recent experiments on localized surface plasmon emission via delayed femtosecond laser pulses confirmed that small clusters lead to a plasmonic response that provides the highest peak intensity [60].

Conclusion

Here we stress how a different packing geometry between assembled silver nanocubes can affect the SERS signal detected on the surface of a GO covering layer used to improve the SERS response. A detailed QCM study revealed that GO coating of the nanocubes resulted in similar GO surface coverage and thickness for different AgNC arrays as long as their surface densities are equivalent. Structural characterization of the samples evidenced that GO/AgNCs arrays exhibit a strikingly different distribution of the GO veiled nanocubes that is reflected in distinct SERS response. While a spontaneous physisorption of cubes favours the formation of homogeneously distributed nanoparticle arrays, the method severely limits the construction of reproducible SERS-active substrates due to a large fraction of cubes with a large separation distance. Instead, a Langmuir–Blodgett transfer of a floating monolayer of silver cubes produces a large fraction of particle clusters with small interparticle distance, which generates an efficient hot spot distribution.

Experimental

Materials. Ethylene Glycol (EG, ≥99%) was obtained from Scharlab. Sodium sulfide nonahydrate, PVP (M_W = 55000), silver nitrate and GO solution (4 mg mL^{-1}) were obtained by Sigma-Aldrich. Aqueous solutions were prepared using ultrapure Milli-Q water. Silicon wafers (n-type, no dopant) were purchased from Sigma-Aldrich.

Synthesis of AgNCs. EG (10 mL) was placed into a flask and heated under magnetic stirring in an oil bath at 150 °C for 1 h under a nitrogen flow. Then, 0.175 mL of a 0.72 mg mL^{-1} sodium sulfide solution and 3.75 mL of a 20 mg mL^{-1} PVP solution in EG were subsequently added to the flask. The flask was thermostated for additional 10 min, until a temperature of 150 °C was again established. A silver nitrate solution (1.25 mL) in EG with a concentration of 48 mg mL^{-1} was added dropwise to the reaction flask at a rate of approximately 1 mL min^{-1}. The reaction was stopped after 40 min by placing the flask in an ice-bath and by adding 30 mL of acetone. The nanoparticles were then centrifuged at 10000*g* for 30 min and then dispersed in ethanol or chloroform by using an ultrasonic bath. The washing procedure was repeated at least three times in order to ensure the complete removal of the reagents. The suspensions of AgNCs thus obtained were stored in centrifuge tubes at −20 °C.

Transmission electron microscopy measurements. TEM micrographs of the particles were acquired with a Philips CM-12 microscope running at 100 kV.

Langmuir–Blodgett film preparation. Langmuir monolayers were prepared in a symmetric compression trough (KSV3000 trough, KSV Instruments Ltd., Finland) filled with Milli-Q water (resistivity = 18 MΩ cm, pH 5.6 at 20 °C). A suspension of AgNCs in chloroform (volume = 1.65 mL, [AgNCs] = 3.1 mg mL^{-1}) was deposited dropwise over the water surface and 40 min were allowed for solvent evaporation before starting the compression. Surface pressure was measured with a platinum Wilhelmy plate as a function of the surface area at T = 20 ± 0.5 °C (Haake thermostatic bath, Germany). Continuous spreading isotherms and hysteresis cycles were obtained using the same barrier speed of 20 mm min^{-1} in both directions. The reported results are the average of at least three independent measurements. Langmuir–Blodgett films were transferred, after area cycling, onto quartz slides and SiO_2-covered QCM quartz sensors by vertical dipping at a rate of 2 mm min^{-1} at several target surface pressures in the range 5 mN/m ≤ π ≤ 20 mN/m. All substrates were rinsed with ethanol and treated in a plasma cleaner immediately before deposition; different substrates were simultaneously coated by the same AgNC layer.

Quartz crystal microbalance measurements. QCM experiments with impedance monitoring were performed on a QCM-Z500 (KSV Instruments Ltd) equipped with a thermoelectric (TE) module (Oven Instruments). The resonant frequency shift and the change in energy dissipation of a SiO_2-coated AT-cut 5 MHz quartz microcrystal were simultaneously measured at its resonant frequency and at the third, fifth, seventh, ninth and eleventh overtones. The temperature of the measuring cell was kept constant at 20 °C with a Peltier element connected to the TE module. For thin, uniform and rigid or quasi-rigid films in solution, the resonant frequency is linearly proportional to the mass density of the deposited film according to the Sauerbrey equation; for thicker or less rigid films a more complex analysis must be undertaken since the resonance frequency is affected not only by the mass attached to the surface but also by the

viscoelastic properties of the adsorbed layer. Frequency and admittance data were simultaneously recorded and taken into consideration for the analysis. The QCM experimental data were analysed by means of the commercial QCMBrowse analysis software to estimate adsorbed mass and film thickness [45].

AFM measurements. Non-contact AC mode atomic force microscopy (AFM) images were acquired in air using a PicoSPM microscope equipped with an AC-mode controller (Keysight Technologies, Inc formerly Molecular Imaging). For optimal resolution rectangular non-contact gold coated cantilever were used (model Hi'Res-C14 from MicroMash – http://www.spmtips.com), with typical resonance frequency of 160 kHz, and 1 nm tip radius. The nanocube dimensions were measured from the height statistics in the topographic AFM images. Image processing and pseudo 3D rendering was performed using Gwyddion 2.30 SPM data visualization tool (http://gwyddion.net/).

UV–vis measurements. UV–vis spectra of the nanocube suspension in ethanol and of monolayers deposited on quartz substrates were recorded using a Jasco V-6 UV–vis–NIR spectrophotometer with 1 nm slit and 200 nm min^{-1} scan rate. Reflection spectra were the average of 10 scans.

SERS measurements. Raman measurements were performed at room temperature on an XPlora Horiba MicroRaman with a 638 nm laser as excitation source. We used a 100× objective with accumulation times of 10 s per spectrum and a 70 μW power on the sample. The SERS substrates were pre-immersed in a 9×10^{-4} M or 9×10^{-7} M adenine solution for two hours to ensure that adsorption equilibrium was reached. The samples were rinsed with deionized water and dried under nitrogen flux before each SERS measurement.

Supporting Information

The Supporting Information features compression–expansion cycles and transfer ratios for LB transfer; absorbance and reflectance spectra for AgNC and GO/AgNC arrays for procedure A and B; QCM data for graphene oxide adsorption on bare silicon oxide surfaces; and SERS and Raman spectra for adenine, PVP and GO.

Supporting Information File 1

Additional thermodynamic and spectroscopic characterization.
[http://www.beilstein-journals.org/bjnano/content/supplementary/2190-4286-7-2-S1.pdf]

Acknowledgements

This work was partially supported by Tuscany Region and the European Community within the frame of the ERANET+ Project BI-TRE. MIUR (Italian Ministry of Education, Universities and Research) and CSGI (Centre for Colloids and Interface Science) are acknowledged for partial financial support.

References

1. Leonard, K.; You, J.; Takahashi, J.; Yonemura, H.; Kurawaki, J.; Yamada, S. *J. Phys. Chem. C* **2015,** *119,* 8829–8837. doi:10.1021/jp5114366
2. Lin, L.; Gao, G.-Q.; Zhu, Q.; Xu, A.-W. *J. Mater. Chem. A* **2015,** *3,* 12845–12851. doi:10.1039/C5TA01772F
3. Ruoli, W.; Pitzer, M.; Fruk, L.; Hu, D.; Schaadt, D. M. *J. Nanoelectron. Optoelectron.* **2012,** *7,* 322–327. doi:10.1166/jno.2012.1311
4. Kawawaki, T.; Wang, H.; Kubo, T.; Saito, K.; Nakazaki, J.; Segawa, H.; Tatsuma, T. *ACS Nano* **2015,** *9,* 4165–4172. doi:10.1021/acsnano.5b00321
5. Liu, Y.; Yin, J.-J.; Nie, Z. *Nano Res.* **2014,** *7,* 1719–1730. doi:10.1007/s12274-014-0541-9
6. Ma, H.; Zhang, X.; Li, X.; Li, R.; Du, B.; Wei, Q. *Talanta* **2015,** *143,* 77–82. doi:10.1016/j.talanta.2015.05.029
7. Yang, P.; Wang, L.; Wu, Q.; Chen, Z.; Lin, X. *Sens. Actuators, B* **2014,** *194,* 71–78. doi:10.1016/j.snb.2013.12.074
8. Polavarapu, L.; Pérez-Juste, J.; Xu, Q.-H.; Liz-Marzán, L. M. *J. Mater. Chem. C* **2014,** *2,* 7460–7476. doi:10.1039/C4TC01142B
9. Khlebtsov, B. N.; Khanadeev, V. A.; Panfilova, E. V.; Bratashov, D. N.; Khlebtsov, N. G. *ACS Appl. Mater. Interfaces* **2015,** *7,* 6518–6529. doi:10.1021/acsami.5b01652
10. Anker, J. N.; Hall, W. P.; Lyandres, O.; Shah, N. C.; Zhao, J.; Van Duyne, R. P. *Nat. Mater.* **2008,** *7,* 442–453. doi:10.1038/nmat2162
11. Jenkins, J. A.; Zhou, Y.; Thota, S.; Tian, X.; Zhao, X.; Zou, S.; Zhao, J. *J. Phys. Chem. C* **2014,** *118,* 26276–26283. doi:10.1021/jp508181g
12. Rao, V. K.; Radhakrishnan, T. P. *ACS Appl. Mater. Interfaces* **2015,** *7,* 12767–12773. doi:10.1021/acsami.5b04180
13. Matteini, P.; de Angelis, M.; Ulivi, L.; Centi, S.; Pini, R. *Nanoscale* **2015,** *7,* 3474–3480. doi:10.1039/C4NR05704J
14. Xu, W.; Meng, G.; Huang, Q.; Hu, X.; Huang, Z.; Tang, H.; Zhang, J. *Appl. Surf. Sci.* **2013,** *271,* 125–130. doi:10.1016/j.apsusc.2013.01.144
15. Keating, M.; Song, S.; Wei, G.; Graham, D.; Chen, Y.; Placido, F. *J. Phys. Chem. C* **2014,** *118,* 4878–4884. doi:10.1021/jp410116h
16. Kneipp, K.; Kneipp, H.; Itzkan, I.; Dasari, R. R.; Feld, M. S. *Chem. Rev.* **1999,** *99,* 2957–2976. doi:10.1021/cr980133r
17. Guo, Q.-H.; Zhang, C.-J.; Wei, C.; Xu, M.-M.; Yuan, Y.-X.; Gu, R.-A.; Yao, J.-L. *Spectrochim. Acta, Part A: Mol. Biomol. Spectrosc.* **2016,** *152,* 336–342. doi:10.1016/j.saa.2015.07.092
18. Xu, W.; Mao, N.; Zhang, J. *Small* **2013,** *9,* 1206–1224. doi:10.1002/smll.201203097
19. Fan, W.; Lee, Y. H.; Pedireddy, S.; Zhang, Q.; Liu, T.; Ling, X. Y. *Nanoscale* **2014,** *6,* 4843–4851. doi:10.1039/c3nr06316j
20. Mehl, H.; Oliveira, M. M.; Gorgatti Zarbin, A. J. *J. Colloid Interface Sci.* **2015,** *438,* 29–38. doi:10.1016/j.jcis.2014.09.068
21. Banchelli, M.; Tiribilli, B.; Pini, R.; Caminati, G.; Matteini, P. Graphene oxide/silver nanocube composites for SERS detection of biomolecules. In *International Conference on BioPhotonics (BioPhotonics),* May 20–22, 2015; IEEE: Florence, Italy, 2015; pp 1–3. doi:10.1109/BioPhotonics.2015.7304046

22. Banchelli, M.; Tiribilli, B.; de Angelis, M.; Pini, R.; Caminati, G.; Matteini, P. *ACS Appl. Mater. Interfaces* **2016,** accepted.
23. Chen, Q.; Bae, S. C.; Granick, S. *Nature* **2011,** *469,* 381–384. doi:10.1038/nature09713
24. Min, Y.; Akbulut, M.; Kristiansen, K.; Golan, Y.; Israelachvili, J. *Nat. Mater.* **2008,** *7,* 527–538. doi:10.1038/nmat2206
25. Akiyama, T.; Aiba, K.; Hoashi, K.; Wang, M.; Sugawa, K.; Yamada, S. *Chem. Commun.* **2010,** *46,* 306–308. doi:10.1039/B913284H
26. Suzuki, M.; Niidome, Y.; Terasaki, N.; Inoue, K.; Kuwahara, Y.; Yamada, S. *Jpn. J. Appl. Phys.* **2004,** *43,* No. 4B. doi:10.1143/JJAP.43.L554
27. Garbin, V.; Crocker, J. C.; Stebe, K. J. *J. Colloid Interface Sci.* **2012,** *387,* 1–11. doi:10.1016/j.jcis.2012.07.047
28. Dochter, A.; Pichon, B. P.; Fleutot, S.; Medard, N.; Begin-Colin, S. *Solid State Sci.* **2013,** *16,* 81–89. doi:10.1016/j.solidstatesciences.2012.10.015
29. Sanders, T. A., II; Sauceda, M. N.; Dahl, J. A. *Mater. Lett.* **2014,** *120,* 159–162. doi:10.1016/j.matlet.2014.01.056
30. Bottomley, A.; Prezgot, D.; Staff, A.; Ianoul, A. *Nanoscale* **2012,** *4,* 6374–6382. doi:10.1039/c2nr31885g
31. Petkov, P. V.; Danov, K. D.; Kralchevsky, P. A. *Langmuir* **2014,** *30,* 2768–2778. doi:10.1021/la500126d
32. Liu, J.-W.; Zhang, S.-Y.; Qi, H.; Wen, W.-C.; Yu, S.-H. *Small* **2012,** *8,* 2412–2420. doi:10.1002/smll.201200172
33. Nossol, E.; Nossol, A. B. S.; Guo, S.-X.; Zhang, J.; Fang, X.-Y.; Zarbin, A. J. G.; Bond, A. M. *J. Mater. Chem. C* **2014,** *2,* 870–878. doi:10.1039/C3TC32178A
34. Luo, Z.; Yuwen, L.; Han, Y.; Tian, J.; Zhu, X.; Weng, L.; Wang, L. *Biosens. Bioelectron.* **2012,** *36,* 179–185. doi:10.1016/j.bios.2012.04.009
35. Siekkinen, A. R.; McLellan, J. M.; Chen, J.; Xia, Y. *Chem. Phys. Lett.* **2006,** *432,* 491–496. doi:10.1016/j.cplett.2006.10.095
36. Sherry, L. J.; Chang, S.-H.; Schatz, G. C.; Van Duyne, R. P.; Wiley, B. J.; Xia, Y. *Nano Lett.* **2005,** *5,* 2034–2038. doi:10.1021/nl0515753
37. Mahmoud, M. A.; El-Sayed, M. A. *J. Phys. Chem. C* **2008,** *112,* 14618–14625. doi:10.1021/jp8040499
38. Roberts, G. *Langmuir-Blodgett Films;* Plenum Press: New York, 1990. doi:10.1007/978-1-4899-3716-2
39. Bhattacharya, R.; Basu, J. K. *J. Colloid Interface Sci.* **2013,** *396,* 69–74. doi:10.1016/j.jcis.2013.01.003
40. Prezgot, D.; Ianoul, A. *J. Phys. Chem. C* **2015,** *119,* 3293–3301. doi:10.1021/jp512142a
41. Baik, H. J.; Hong, S.; Park, S. *J. Colloid Interface Sci.* **2011,** *358,* 317–322. doi:10.1016/j.jcis.2011.03.041
42. Panfilova, E. V.; Khlebtsov, B. N.; Burov, A. M.; Khlebtsov, N. G. *Colloid J.* **2012,** *74,* 99–109. doi:10.1134/S1061933X11060147
43. Gao, Y.; Zhang, R.; Cheng, J.-C.; Liaw, J.-W.; Ma, C. *J. Quant. Spectrosc. Radiat. Transfer* **2013,** *125,* 23–32. doi:10.1016/j.jqsrt.2013.04.014
44. Kinnan, M. K.; Chumanov, G. *J. Phys. Chem. C* **2010,** *114,* 7496–7501. doi:10.1021/jp911411x
45. Toma, M.; Toma, K.; Michioka, K.; Ikezoe, Y.; Obara, D.; Okamoto, K.; Tamada, K. *Phys. Chem. Chem. Phys.* **2011,** *13,* 7459–7466. doi:10.1039/c0cp02953j
46. Gambinossi, F.; Banchelli, M.; Durand, A.; Berti, D.; Brown, T.; Caminati, G.; Baglioni, P. *J. Phys. Chem. B* **2010,** *114,* 7338–7347. doi:10.1021/jp100730x
47. Sisco, P. N.; Murphy, C. J. *J. Phys. Chem. A* **2009,** *113,* 3973–3978. doi:10.1021/jp810329j
48. Wang, L.; Sun, Y.; Li, Z. *Appl. Surf. Sci.* **2015,** *325,* 242–250. doi:10.1016/j.apsusc.2014.11.071
49. Yun, S.; Hong, S.; Acapulco, J. A. I., Jr..; Jang, H. Y.; Ham, S.; Lee, K.; Kim, S. K.; Park, S. *Chem. – Eur. J.* **2015,** *21,* 6165–6172. doi:10.1002/chem.201406454
50. Malynych, S.; Chumanov, G. *J. Am. Chem. Soc.* **2003,** *125,* 2896–2898. doi:10.1021/ja029453p
51. He, F.-A.; Fan, J.-T.; Song, F.; Zhang, L.-M.; Chan, H. L.-W. *Nanoscale* **2011,** *3,* 1182–1188. doi:10.1039/c0nr00672f
52. Zhu, Z.; Su, M.; Ma, L.; Ma, L.; Liu, D.; Wang, Z. *Talanta* **2013,** *117,* 449–455. doi:10.1016/j.talanta.2013.09.017
53. Guo, S.; Dong, S. *Chem. Soc. Rev.* **2011,** *40,* 2644–2672. doi:10.1039/c0cs00079e
54. Kim, J.; Cote, L. J.; Kim, F.; Yuan, W.; Shull, K. R.; Huang, J. *J. Am. Chem. Soc.* **2010,** *132,* 8180–8186. doi:10.1021/ja102777p
55. Matteini, P.; Tatini, F.; Cavigli, L.; Ottaviano, S.; Ghini, G.; Pini, R. *Nanoscale* **2014,** *6,* 7947–7953. doi:10.1039/c4nr01622j
56. Blees, M. K.; Barnard, A. W.; Rose, P. A.; Roberts, S. P.; McGill, K. L.; Huang, P. Y.; Ruyack, A. R.; Kevek, J. W.; Kobrin, B.; Muller, D. A.; McEuen, P. L. *Nature* **2015,** *524,* 204–207. doi:10.1038/nature14588
57. Bottomley, A.; Ianoul, A. *J. Phys. Chem. C* **2014,** *118,* 27509–27515. doi:10.1021/jp508629d
58. Bell, S. E. J.; Sirimuthu, N. M. S. *J. Am. Chem. Soc.* **2006,** *128,* 15580–15581. doi:10.1021/ja066263w
59. Ferrari, A. C.; Robertson, J. *Phys. Rev. B* **2000,** *61,* 14095–14107. doi:10.1103/PhysRevB.61.14095
60. Mittal, R.; Glenn, R.; Saytashev, I.; Lozovoy, V. V.; Dantus, M. *J. Phys. Chem. Lett.* **2015,** *6,* 1638–1644. doi:10.1021/acs.jpclett.5b00264

License and Terms

BEILSTEIN JOURNAL OF NANOTECHNOLOGY

Charge injection and transport properties of an organic light-emitting diode

Peter Juhasz, Juraj Nevrela, Michal Micjan, Miroslav Novota, Jan Uhrik, Lubica Stuchlikova, Jan Jakabovic, Ladislav Harmatha and Martin Weis*

Full Research Paper

Open Access

Address:
Slovak University of Technology, Ilkovicova 3, Bratislava 81219, Slovakia

Email:
Martin Weis* - martin.weis@stuba.sk

* Corresponding author

Keywords:
activation energy; impedance spectroscopy; organic light-emitting device

Beilstein J. Nanotechnol. **2016,** *7,* 47–52.
doi:10.3762/bjnano.7.5

Received: 15 October 2015
Accepted: 08 January 2016
Published: 14 January 2016

This article is part of the Thematic Series "Organized films".

Guest Editor: M. Canepa

Abstract

The charge behavior of organic light emitting diode (OLED) is investigated by steady-state current–voltage technique and impedance spectroscopy at various temperatures to obtain activation energies of charge injection and transport processes. Good agreement of activation energies obtained by steady-state and frequency-domain was used to analyze their contributions to the charge injection and transport. We concluded that charge is injected into the OLED device mostly through the interfacial states at low voltage region, whereas the thermionic injection dominates in the high voltage region. This comparison of experimental techniques demonstrates their capabilities of identification of major bottleneck of charge injection and transport.

Introduction

Since the discovery of organic electroluminescent (EL) materials such as tris(8-hydroxyquinolinato)aluminum(III) (Alq3), organic light-emitting devices (OLEDs) have drawn huge attention in electronics [1]. OLED devices are envisioned as future light sources because of possible flexibility, transparency, and low-cost large-area production; however, OLEDs have recent reached luminous efficacy over 130 lm/W [2,3] that is double of fluorescent tube efficacy (60–70 lm/W), which is the current benchmark for novel light sources [4].

Organic semiconductors have zero doping level and very low intrinsic charge density, therefore all charges in OLED device are injected from the electrodes. As a result, the energy band diagram analysis plays a key role in the study of the charge injection/transport phenomena. Although, these important ideas are well-accepted in the development of high-performance OLED devices, deep understanding of the physical processes regarding the injection and transport of charge carriers is needed for further device performance improvement. In details,

the organic–organic and metal–organic interfaces determine injection properties, whereas the conductivities of organic layers limit the charge transport properties. Charge transport in organic semiconductors has been widely studied by electrical characterization techniques such as steady-state current density–voltage characteristics [5,6], or measurement in time- or frequency-domain, such as transient currents [7] and impedance spectroscopy [8,9]. Furthermore, the measurements can be extended by the temperature dependence of electrical properties which reveal the thermally activated charge behavior [10]. It should be noted here that the electrical properties of organic devices are strongly dependent of device fabrication. Therefore, a detailed comparison of results obtained at various devices is not applicable although identical materials/structures are used. Hence, the correlation between obtained results of different characterization techniques is reliable only for the same device.

This study demonstrates charge transport properties in OLED devices formed by indium tin oxide (ITO)/*N*,*N*′-di-1-naphthyl-*N*,*N*'-diphenyl-1,1'-biphenyl-4,4'-diamine (α-NPD)/Alq3/Al system. The steady-state current–voltage characteristics recorded at various temperatures have been used to evaluate the activation energy of electric conductivity. Obtained results are compared with energy band diagram to identify major energy barriers limiting the current.

Experimental

The study of the charge transport properties of OLED devices has been done on the organic double-layer sandwiched between two electrodes ITO/α-NPD/Alq3/Al. The devices were grown on glass slides precoated with ITO with sheet resistance lower than 10 Ω/sq. The substrates were cleaned sequentially in ultrasonic bath by isopropanol and deionized water and then treated by oxygen plasma to remove organic residues. Prior to the organic material deposition the substrates were heated up to 200 °C during 30 min in vacuum better than 10^{-5} Pa. Devices were formed by sequential thermal evaporation of hole transport material α-NPD (Sigma-Aldrich) followed by a layer deposition of electroluminescent material Alq3 (Tokyo Chemical Industry). The thicknesses of α-NPD and Alq3 were 150 and 50 nm, respectively, deposited at constant deposition rate of 0.6 nm/min. The Al electrode of 100 nm in thickness has been deposited through the shadow mask. All deposition processes have been done without braking of vacuum to avoid unintended defects. The OLED active area of 4 mm^2 was formed by overlap of ITO and Al electrodes.

All electrical characterizations have been done under vacuum in temperature range from 200 to 325 K. The steady-state current–voltage characteristics have been recorded using an Agilent Semiconductor Parameter Analyzer 4155C in the voltage range from −0.5 to 10 V. The frequency measurements have been carried out by the MODULAB MTS system with offset from −0.5 to 8 V with the probe signal AC amplitude of 10 mV. The impedance magnitude and phase frequencies ranged from 10 Hz to 1 MHz.

Results and Discussion

Figure 1 depicts a set of current density–voltage (*J*–*V*) characteristics recorded at various temperatures from 200 to 325 K. The OLED device exhibits rectifying property with an on/off ratio of about 10^4 at room temperature. Note that in low-conduction materials, ohmic transport is common for the low-voltage region, whereas the space-charge limited current (SCLC) regime usually governs the carrier transport at higher voltage region. Since, the well-known Mott–Gourney square law $J \propto V^2$ is valid only for the single-carrier transport in trap-free material, in real OLED devices the power exponent of the voltage usually reaches values higher than 2. The voltage dependencies in a log–log scale can be apparently divided to three regions in accordance to the different power exponent represented by the slope of the *J*–*V* characteristics.

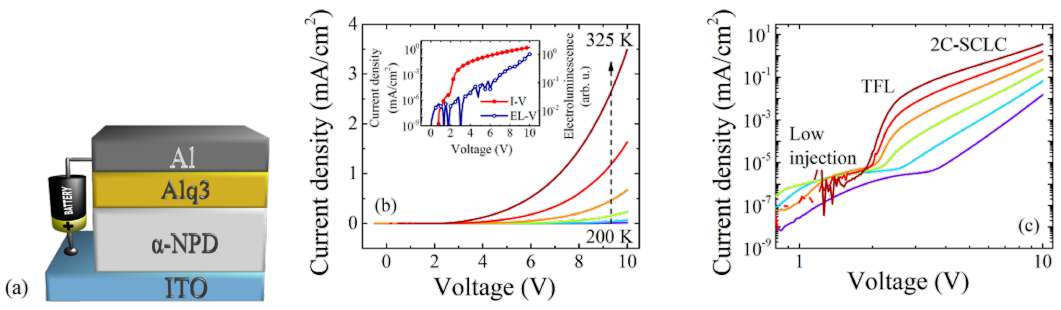

Figure 1: (a) Schematic diagram of the device ITO/α-NPD/Alq3/Al. Steady-state current–voltage characteristics (b) in linear scale, the inset shows current density–voltage characteristic and electroluminescence–voltage characteristic at 300 K in a semi-log scale, and (c) in log–log scale recorded over temperature range from 200 to 325 K. Abbreviations TFL and 2C-SCLC stand for trap-fill-limit and two-carrier space-charge limited conditions, respectively.

At voltages below 2 V the low charge injection region can be recognized, since the current density J follows applied voltage bias V linearly,

$$J = e \cdot n \mu_{\text{eff}} \frac{V}{L}, \quad (1)$$

where $e{\cdot}n$ is the charge density (e: elementary charge, n charge carrier density), μ_{eff} is the effective charge mobility, and L the organic film thickness. Note that the effective charge mobility μ_{eff} includes charge trapping phenomenon as follows,

$$\mu_{\text{eff}} = \mu_0 \left(\frac{n_{\text{mob}}}{n_{\text{mob}} + n_{\text{trap}}} \right), \quad (2)$$

where μ_0 is trap-free charge mobility, n_{mob} and n_{trap} are mobile and trapped charge carrier densities, respectively. In the voltage region from 2 to 3 V an abrupt increase of the current density is observed. Note that the significant rise of the current in certain voltage region only is usually assigned to the trap-filled-limit (TFL) voltage. In other words, the charge transport properties of organic films are changed due to filling of all localized states and charge carriers are no more influenced by the trapping mechanism. At voltages higher than 3 V the rise of current density slows down to $J \propto V^3$ and follows two-carrier space-charge limited conditions (2C-SCLC),

$$J = \frac{125}{18} \varepsilon \mu_e \mu_h \tau \frac{V^3}{L^5}, \quad (3)$$

where ε is the dielectric constant of the organic film, μ_e and μ_h are electron and hole mobilities, respectively, and τ is carrier lifetime [13]. However, the 2C-SCLC model is fully valid only if no injection barrier is present at metal–organic semiconductor interface. Previous studies revealed that observed current density–voltage characteristics can be also associated with thermionic emission or Fowler–Nordheim tunneling [14-16]. Hence, to distinguish between space-charge limited current and interface limited current is required more deep analysis.

The impedance spectroscopy is well-established characterization technique used to study the dielectric layers properties in frequency domain. It can be applied to investigate the dynamics of mobile charge carriers in the bulk of the layer or at the interfacial region between two layers. Here, the impedance spectroscopy has been applied for detail characterization of different charge transport regions estimated by current density–voltage measurements, since impedance spectroscopy is capable to distinguish charge relaxation processes with dissimilar relaxation times. Figure 2 illustrates impedance phase-shift spectra in all investigated voltage regions. Note that all spectra share a common decrease of the phase in high frequency region that originates from the parasitic series resistance of about 60 Ω. Interestingly, the low-injection region is represented by the impedance spectra that exhibit two transitions between different phases, as depicted in Figure 2a. Each transition of phases stands for a different relaxation process. However, due to the low current density the phase saturates in low frequency region at 90 degree that represents capacitor-like behavior. The relaxation processes are obviously thermally stimulated, and one of the processes is significantly more sensitive to a rise of temperature. In other words, two processes have strongly dissimilar activation energies. In the voltage range that has been assigned to TFL again two relaxations are observed. However, rising the current density induces saturation of the impedance phase at the value in between capacitor-like behavior (90 degree) and resistor-like behavior (0 degree). Surprisingly, at higher voltages only one charge-relaxation process is

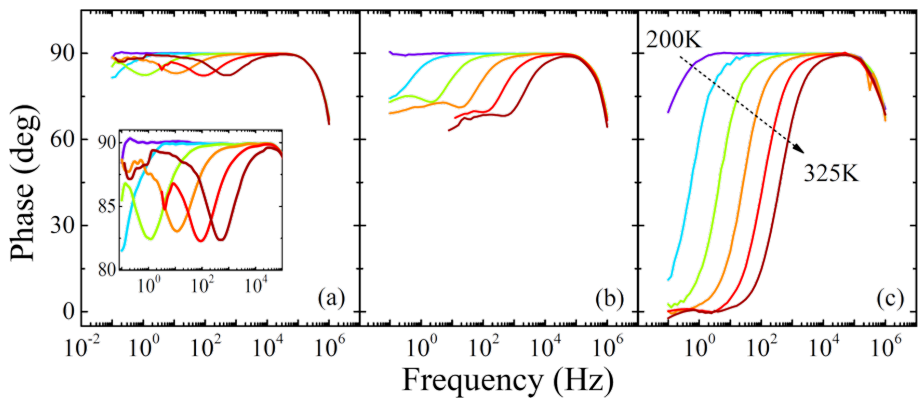

Figure 2: Impedance phase frequency spectra recorded in the temperature range from 200 to 325 K with the step of 25 K at voltage biases of (a) 1 V, (b) 2 V, and (c) 4 V. Inset depicts detail view of the phase spectra.

present and the device exhibits pure resistor-like behavior in the low-frequency region.

The evaluation has been done using electrical equivalent circuits shown in Figure 3a and fitting results have been found sufficient, see Figure 3b. Obtained values of equivalent electrical circuit elements are depicted in Figure 3c and Figure 3d. The resistances R_1 and R_2 are related to the charge injection/transport phenomena and exhibit strong voltage dependencies. Higher resistance stands for process representing major charge injection/transport limitation in low voltage region, but it diminishes at higher voltages. On the other hand, capacitances C_1 and C_2 consisting of a geometric capacitance (constant contribution of approx. 1 nF) and a differential capacitance (charge-dependent contribution) are almost independent of the voltage.

Since a high current density is a characteristic feature of the 2C-SCLC region, the major charge relaxation phenomenon should be related to the charge transport. Hence, in regions of a high applied voltage the relaxation time t_{relax} obtained from the impedance spectra analysis has been assigned to the transit time t_{tr} across the organic film as $t_{tr} \cong 0.72 t_{relax}$ [8]. The effective mobility can be evaluated in accordance to the time-of-flight model [9] as,

$$\mu_{eff} = \frac{4}{3}\frac{L^2}{V}\frac{1}{t_{tr}}. \quad (4)$$

The effective mobility value is in good agreement with hole mobility in Alq3 [9]. Since the hole mobility of α-NPD ranges from 10^{-4} to 10^{-3} $cm^2/V{\cdot}s$ [11,12], the hole mobility in Alq3 represents the charge transport bottleneck. It is interesting to note that estimated effective mobility follows the Poole–Frenkel dependence on the electric field,

$$\mu_{eff} = \mu_0 \exp\left(-\frac{E_a - \sqrt{\beta F}}{kT}\right), \quad (5)$$

where E_a is the activation energy of the relaxation process, $\beta = \sqrt{e^3/\pi\varepsilon}$ is the Schottky parameter, F is the intensity of electric field, and kT is the thermal energy (k: Boltzmann constant, T: thermodynamic temperature), as demonstrated in Figure 4. The electric field F is assumed as an average field across the device $F = V/L$, which is in good agreement with zero charge contribution to the capacitance. It should be mentioned here that the Poole–Frenkel model represents the charge-carrier hopping between localized states or thermionic emission through the energy barrier (the Schottky effect), where the energy barrier E_a is suppressed by the local electric field F [17]. Therefore, the evaluation of the activation energies is required for further understanding the charge-relaxation processes in OLED devices.

Charge injection/transport phenomena are thermally activated processes that follow the Boltzmann distribution. The Arrhenius

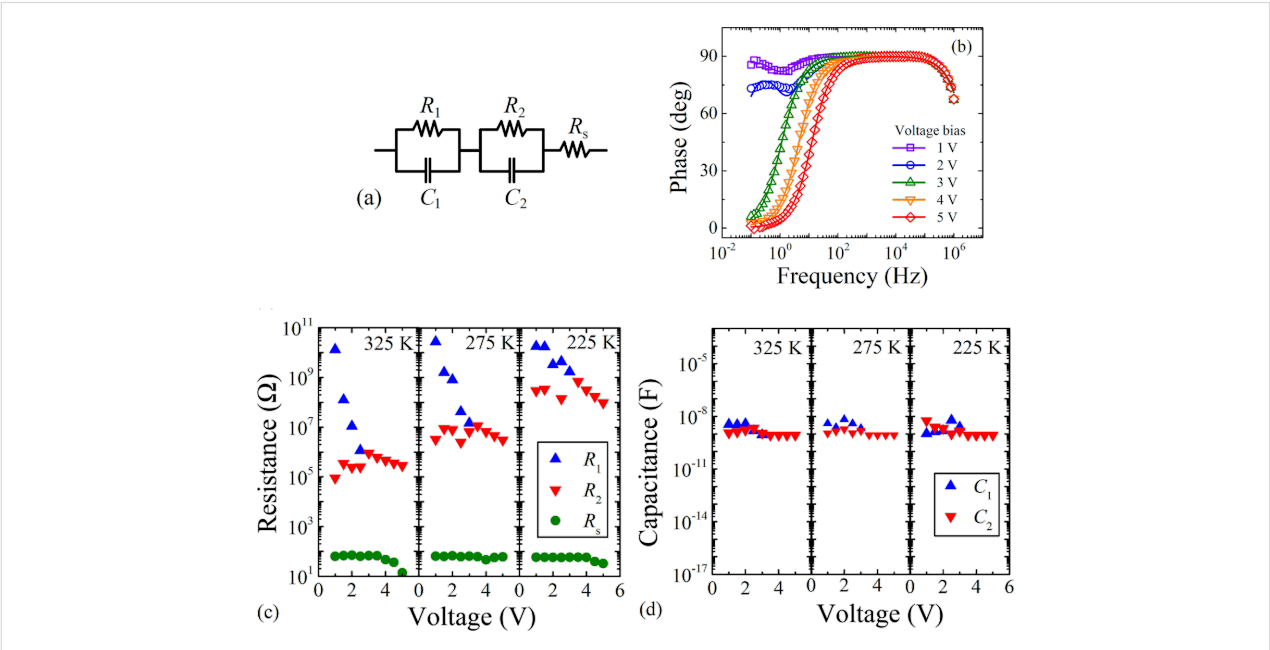

Figure 3: (a) Electrical equivalent circuit model used for data evaluation, (b) the comparison of recorded and fitted impedance phase spectra at temperature 250 K. Symbols represent the experiment, solid line show the equivalent circuit model evaluation. Obtained values of (c) resistances and (d) capacitances of equivalent electrical circuit.

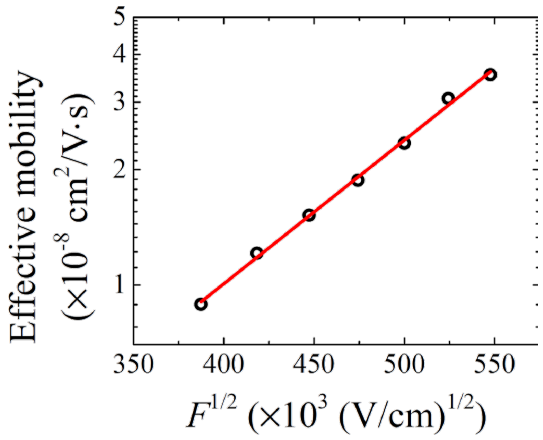

Figure 4: Electric field dependence of the effective mobility at the temperature of 300 K. The solid line represents the linear fit.

plots of conductivities have been used to evaluate activation energies, as shown in Figure 5a. Since the conductivity G is affected by charge density and carrier mobility,

$$G = e \cdot n \mu_{\text{eff}}, \quad (6)$$

it reflects the impact of charge traps on the carrier transport as well as that of energy barriers on the carrier injection. Figure 5b depicts the voltage dependence of the activation energies estimated from the steady-state current–voltage and impedance spectroscopy conductivities. In the low-injection region two relaxations with different activation energies are observed. Note that the activation energy of about 0.5 eV is voltage-independent up to the 2C-SCLC region (3 V or higher voltage), while the other one is gradually increasing with the rise of the voltage. In the 2C-SCLC region the activations energies estimated from the steady-state and frequency analyses are in good agreement. It should be mentioned here that the decay of the activation energy in 2C-SCLC region follows the square root of the electric field as predicted by the Poole–Frenkel or thermionic emission model. As a result, this charge relaxation can be assigned to an injection of the charge over the energy barrier lowered by the external field. On the other hand, the other relaxation in the low-injection region is ascribed to the charge injection through the interfacial states. An increase of the voltage causes a gradual filling of states that represents rise of the activation energy. After the filling of all interfacial states the charge is injected only over the interfacial barrier, which stands for second charge relaxation. This assumption is supported by diminishing of interfacial state relaxation after reaching of TFL region. Since steady-state methods are sensitive only to the major bottleneck of the charge injection/transport, we can conclude that the charge is injected into the OLED device mostly through the interfacial states in the low-voltage region, whereas the thermionic injection dominates in the high-voltage region.

The energy band diagram reconstruction is required for further identification of the energy barrier origin. The work function of cleaned ITO electrodes is at a level of 4.9 eV [18,19], while the

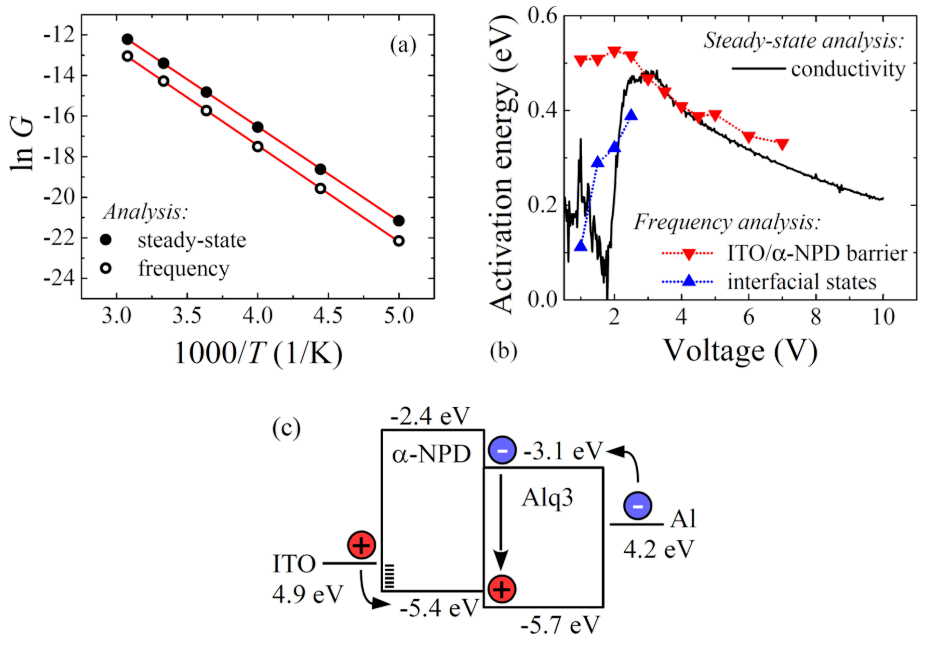

Figure 5: (a) Arrhenius plot of conductivities estimated from steady-state current density–voltage measurement and impedance spectroscopy spectra at voltage bias of 4 V and (b) evaluated voltage dependence of activation energies. (c) Energy band diagram model.

Al electrode reaches only 4.2 eV [20]. The energies of the highest occupied molecular orbitals (HOMO) and lowest unoccupied molecular orbitals (LUMO) of α-NPD and Alq3 are also known [21,22]. As a result, in accordance with the energy band diagram of the investigated OLED device, see Figure 5c, the only interface that satisfies these requirements is the ITO/α-NPD interface. Therefore, we can conclude that hole injection properties determine the performance of the ITO/α-NPD/Alq3/Al device. Furthermore, it is known that the high electron-injection barrier at the Alq3/Al interface suppresses the electron density in the OLED device and the hole density dominates in the OLED device [23]. Therefore, the holes are the main contribution to the charge injection/transport processes and activation energies of electron-related processes are not observable.

Conclusion

This paper suggests methodology suitable for study of charge transport properties in OLED device structure ITO/α-NPD/Alq3/Al by steady-state current density-voltage measurement and impedance spectroscopy spectra. The current density-voltage characteristics revealed presence of three different regions: (i) low injection region, (ii) trap-fill-limit region, and (iii) two-carrier space-charge limited current region. The analysis of impedance spectroscopy spectra found two charge relaxations in low injection region, while the only one at higher applied voltages. The detail analysis of activation energies voltage dependence suggested that at low voltages the charge is injected by hopping through interfacial localized states, while at high voltages is dominant thermionic injection.

Acknowledgements

The work has been supported by the Scientific Grant Agency of the Ministry of Education, Science, Research and Sport of the Slovak Republic and of the Slovak Academy of Sciences (project 1/0776/15) and the Slovak Research and Development Agency (APVV-14-0739 and APVV-14-0740).

References

1. Tang, C. W.; VanSlyke, S. A. *Appl. Phys. Lett.* **1987,** *51,* 913–915. doi:10.1063/1.98799
2. Kato, K.; Iwasaki, T.; Tsujimura, T. *J. Photopolym. Sci. Technol.* **2015,** *28,* 335–340. doi:10.2494/photopolymer.28.335
3. Cheng, G.; Kui, S. C. F.; Ang, W.-H.; Ko, M.-Y.; Chow, P.-K.; Kwong, C.-L.; Kwok, C.-C.; Ma, C.; Guan, X.; Low, K.-H.; Su, S.-J.; Che, C.-M. *Chem. Sci.* **2014,** *5,* 4819–4830. doi:10.1039/C4SC01105H
4. Reineke, S.; Lindner, F.; Schwartz, G.; Seidler, N.; Walzer, K.; Lüssem, B.; Leo, K. *Nature* **2009,** *459,* 234–238. doi:10.1038/nature08003
5. Malliaras, G. G.; Salem, J. R.; Brock, P. J.; Scott, C. *Phys. Rev. B* **1998,** *58,* R13411–R13414. doi:10.1103/PhysRevB.58.R13411
6. Fujimoto, H.; Potscavage, W. J., Jr.; Edura, T.; Adachi, C. *Org. Electron.* **2014,** *15,* 2783–2791. doi:10.1016/j.orgel.2014.08.021
7. Ruhstaller, B.; Carter, S. A.; Barth, S.; Riel, H.; Riess, W.; Scott, J. C. *J. Appl. Phys.* **2001,** *89,* 4575–4586. doi:10.1063/1.1352027
8. Okachi, T.; Nagase, T.; Kobayashi, T.; Naito, H. *Jpn. J. Appl. Phys.* **2008,** *47,* 8965–8972. doi:10.1143/JJAP.47.8965
9. Ishihara, S.; Hase, H.; Okachi, T.; Naito, H. *Thin Solid Films* **2014,** *554,* 213–217. doi:10.1016/j.tsf.2013.08.022
10. Karg, S.; Steiger, J.; von Seggern, H. *Synth. Met.* **2000,** *111–112,* 277–280. doi:10.1016/S0379-6779(99)00445-2
11. Naka, S.; Okada, H.; Onnagawa, H.; Yamaguchi, Y.; Tsutsui, T. *Synth. Met.* **2000,** *111–112,* 331–333. doi:10.1016/S0379-6779(99)00358-6
12. Nguyen, N. D.; Schmeits, M.; Loebl, H. P. *Phys. Rev. B* **2007,** *75,* 075307. doi:10.1103/PhysRevB.75.075307
13. Lampert, M. A.; Mark, P. *Current Injection in Solids;* Academia Press: New York, 1970.
14. Arkhipov, V. I.; von Seggern, H.; Emelianova, E. V. *Appl. Phys. Lett.* **2003,** *83,* 5074–5076. doi:10.1063/1.1633967
15. Kumar, P.; Jain, S. C.; Kumar, V.; Misra, A.; Chand, S.; Kamalasanan, M. N. *Synth. Met.* **2007,** *157,* 905–909. doi:10.1016/j.synthmet.2007.08.021
16. López Varo, P.; Jiménez Tejada, J. A.; López Villanueva, J. A.; Deen, M. J. *Org. Electron.* **2014,** *15,* 2526–2535. doi:10.1016/j.orgel.2014.05.039
17. Kao, K. C. *Dielectric Phenomena in Solids;* Elsevier Academic Press: San Diego, 2004.
18. Kim, J. S.; Lägel, B.; Moons, E.; Johansson, N.; Baikie, I. D.; Salaneck, W. R.; Friend, R. H.; Cacialli, F. *Synth. Met.* **2000,** *111–112,* 311–314. doi:10.1016/S0379-6779(99)00354-9
19. Jiang, X.; Wong, F. L.; Fung, M. K.; Lee, S. T. *Appl. Phys. Lett.* **2003,** *83,* 1875–1877. doi:10.1063/1.1605805
20. Lide, D. R. *CRC Handbook of Chemistry and Physics;* CRC Press, 2004.
21. Meerheim, R.; Scholz, S.; Olthof, S.; Schwartz, G.; Reineke, S.; Walzer, K.; Leo, K. *J. Appl. Phys.* **2008,** *104,* 014510. doi:10.1063/1.2951960
22. Nalwa, H. S. *Handbook of Surfaces and Interfaces of Materials;* Academic Press: San Diego, 2001. doi:10.1016/b978-012513910-6/50003-7
23. Tutiš, E.; Berner, D.; Zuppiroli, L. *J. Appl. Phys.* **2003,** *93,* 4594–4602. doi:10.1063/1.1558208

License and Terms

BEILSTEIN JOURNAL OF NANOTECHNOLOGY

Surface-site reactivity in small-molecule adsorption: A theoretical study of thiol binding on multi-coordinated gold clusters

Elvis C. M. Ting, Tatiana Popa and Irina Paci*

Full Research Paper

Open Access

Address:
Department of Chemistry, University of Victoria, Victoria, BC, V8W 3V6, Canada

Email:
Irina Paci* - ipaci@uvic.ca

* Corresponding author

Keywords:
coordination; gold clusters; methylthiol; sulfur–gold interactions; thiol adsorption

Beilstein J. Nanotechnol. **2016,** *7,* 53–61.
doi:10.3762/bjnano.7.6

Received: 15 October 2015
Accepted: 29 December 2015
Published: 18 January 2016

This article is part of the Thematic Series "Organized films".

Guest Editor: M. Canepa

Abstract

Background: The adsorption of organic molecules on metal surfaces has a broad array of applications, from device engineering to medical diagnosis. The most extensively investigated class of metal–molecule complexes is the adsorption of thiols on gold.

Results: In the present manuscript, we investigate the dependence of methylthiol adsorption structures and energies on the degree of unsaturation at the metal binding site. We designed an Au_{20} cluster with a broad range of metal site coordination numbers, from 3 to 9, and examined the binding conditions of methylthiol at the various sites.

Conclusion: We found that despite the small molecular size, the dispersive interactions of the backbone are a determining factor in the molecular affinity for various sites. Kink sites were preferred binding locations due to the availability of multiple surface atoms for dispersive interactions with the methyl groups, whereas tip sites experienced low affinity, despite having low coordination numbers.

Introduction

The interactions between organic molecules and metallic surfaces have been the subject of significant interest in recent years, because of their fundamental relevance in a broad array of nanoscience applications. One area of interfacial research has focused on the binding properties of aminoacids and peptides on metal substrates [1-12], due to the relevance of these interactions in device fabrication for biological sensors [13-16], for in vivo nanoparticle imaging, tagging and tracing [17-20], and for developing a general understanding of nanoparticle biosafety [21,22], among other issues. The sulfur-containing aminoacids cysteine, homocysteine and methionine are often targeted for such investigations, because of the binding affinity of sulfur-based groups to metal atoms.

Much is known of the adsorption behavior of sulfur-containing aminoacids on low-Miller-index [(111), (100), (110)] gold and

silver surfaces [3,23-35], though many questions regarding binding modes and condensed phase behavior still remain. Quantum calculations have been used to examine the behavior of single molecules or small molecular clusters on ideal surfaces [23-27,33,34,36,37]. Several classical simulation studies also exist, generally focused investigating peptide behavior at a metal surface [38-40]. A still outstanding issue is the change in aminoacid or peptide behavior upon adsorption on non-ideal surfaces, i.e., substrates with adatoms, high-Miller-index facets or surface curvature have been examined individually [41-45], but no rigorous studies of the dependence of surface binding on site reactivity or coordination have so far been done for aminoacids.

That unsaturated metal atoms bind more strongly to adsorbates has been long established in the literature, particularly as a result of nanoparticle–molecule studies. Several thorough studies by Nørskov and co-workers [46-48] investigated site coordination effects on the catalytic oxidation on Pt and Au nanoclusters, seeking to elucidate the experimentally observed dependence of catalytic activity on nanoparticle size and shape. A recent experimental study by Mostafa et al. [49] convincingly argued that the catalytic activity of Pt nanoparticles for the oxidation of 2-propanol was positively correlated to not only the average unsaturation of the surface metal atoms, but also to the fraction of edge and corner atoms, which present the lowest coordination.

With an end goal of developing a coordination-dependent description of aminoacid-surface interactions, we focus, in the current work, on the surface-binding groups. To this end, we replaced molecular backbones with methyl groups, in order to remove factors such as lone-pair or charge-group surface interactions, and the overall backbone–surface interaction. We designed a 20-atom Au cluster, with gold atom sites spanning an array of coordination numbers N_i, with i = 3–9, and investigated the binding behavior of single molecules of methylthiol in its non-dissociated and dissociated forms, as a model for the surface-binding group of physisorbed and chemisorbed thiols. The cluster itself was built to model various coordination sites that may be found on planar substrates, or along the surface of much larger Au clusters, and was thus held unoptimized, as discussed in some detail below.

The adsorption of methylthiol, and other thiols, at Au substrates has been the focus of a large number of studies, given its broad relevance in spectroscopy, sensing, nanotechnology and biophysics. Many reviews have been written in the last two decades on the topic of thiol adsorption on gold flat surfaces and clusters [50-62], and on that of aminoacid–gold binding [3,10,63-69]. We refer the reader interested in the broader field to these works, as well as many article collections and dedicated journals, and discuss here primarily those studies directly related to the principal focus of the current work: the dependence of binding structures and stabilities on metal site coordination, in the reduced model of methylthiol–Au_{20} interaction. We find that, despite the limited size of the adsorbate, dispersive interactions play an important role in determining preferred adsorption sites. The strongest adsorption occurred at sites that were relatively unsaturated, but also provided sufficient neighboring surface atoms available to interact dispersively to the molecular backbone.

Experimental

Configurational sampling. Zero-temperature DFT calculations suffer from an inability to broadly sample the configurational space, and are often trapped close to the initial (user input) configuration. This limitation can be particularly problematic in cases where there is an overwhelming contributor to the potential energy surface such as in the case of molecule–surface interactions [70]. An elegant workaround is to use thermal energy as provided by an ab initio molecular dynamics methodology, but this is computationally unfeasible except for small systems. Our group has chosen to provide a broad set of input geometries, often selected via a separate set of classical calculations [23].

Here, we perform a systematic scan of possible initial structures by sampling the configurational space through four variables: the distance from the adsorbate headgroup to a gold binding site d, the polar angle θ (the angle between the principal axis of the adsorbate and the axis normal to the binding surface), the azimuthal angle ϕ (describing the in-plane orientation of the projection of the adsorbate principal axis), and the relative location of the headgroup with respect to the substrate atoms (Figure 1). Three initial molecule–surface distances were used for all adsorbates (4.1, 4.3 and 4.5 Å), equilibrating to an average S–Au distance of 2.5 Å. Initial configurations were parallel to the surface plane (θ = 90°), and the in-plane angle ϕ was sampled in 12 increments of 30°. Initial headgroup locations were considered at both bridge and atop sites. On the Au_{20} cluster, ten atop sites and 18 bridge sites were considered for each molecule. Overall, 672 initial structures were considered for each of methylthiol and methylthiolate. Additional calculations were performed for low-coordinated binding sites, to ensure proper sampling of the configurational space. The most stable equilibrated configurations, their binding energies and bond lengths for the different binding sites are discussed in the following pages.

The small Au cluster was designed as a cut from an ideal Au fcc lattice, built to exhibit a variety of kink, edge and surface

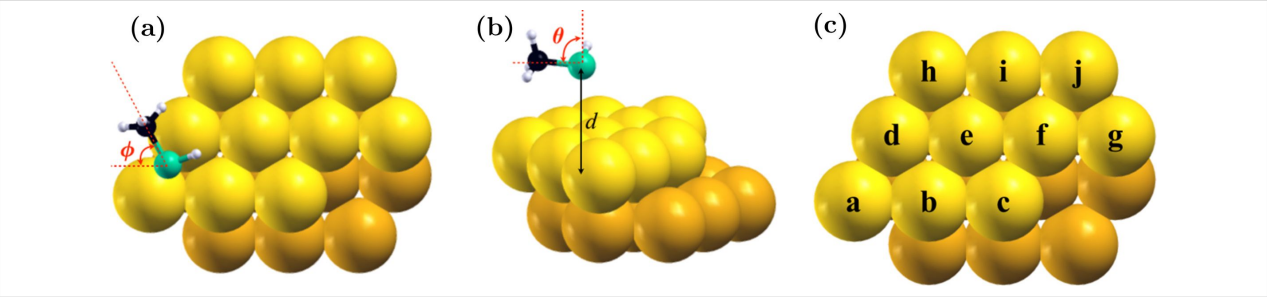

Figure 1: Configurational variables sampled and cluster geometry. In (a) and (b), *d* is the sulfur–gold distance, θ is the polar angle (90° in each initial configuration), and ϕ is the azimuthal angle. In (c), the site nomenclature is given in letters.

binding sites, with a broad array of coordination numbers. In order to preserve the designed coordination numbers, the cluster was held unoptimized in the calculations presented here. This approximation neglects the significant relaxation effect of the adsorbate on substrate geometry, but was necessary in order to avoid reorganization of the cluster to a more spherical shape. Such reorganization would preclude the study of the site coordination dependence of adsorption energies and structures, which is the subject of the present work. Below, the coordination number (CN) refers to the numbers of gold-atom neighbors around a particular gold atom. For example, a CN(9) binding site (a central atom on a (111) surface) has nine gold atoms around the central gold atom. On the Au_{20} cluster, only the 10 gold binding sites on the top layer were studied (labeled a–j in Figure 1c).

Density functional theory (DFT) methodology. Calculations were performed using the generalized gradient approximation-based Perdew–Burke–Ernzerhof (PBE) functional [71] with and without dispersion corrections, in the SIESTA 3.2 package [72,73]. Core electrons were described in terms of the core pseudopotentials constructed in the scheme of Troullier and Martins [74] with relativistic corrections for the gold atoms. Valence electrons were described using pseudo-atomic orbitals with a polarized triple-ζ (TZP) basis set. The pseudo-atomic orbitals (PAOs) in SIESTA are strictly localized and fall to zero outside a given cut-off radius, chosen by specifying a value of energy shift. Previous calculations by our group and others [36,75] suggested 1 mRy energy shift (equivalent to 6 Å for the cutoff radius of the carbon PAO with the smallest ζ).

A Grimme-type medium range van der Waals correction was included in the PBE-D2 calculations [76]. Dispersion coefficients and van der Waals radii for H, C, N, and S were taken from the original Grimme paper [76], and those for Au, from Liu et al. [77]. The addition of the dispersion correction enhanced non-dissociative binding energies in MeSH by 0.2 to 0.7 eV, and moderately increased chemisorption energies (MeS) by 0.2 to 0.5 eV.

Non-dissociative adsorption. The binding energy in non-dissociative adsorption was calculated as the enthalpy of the binding process:

$$\Delta E_{\text{binding}} = E_{\text{MeSH-Au}_{20}} - \left(E_{\text{Au}_{20}} + E_{\text{MeSH}}\right). \quad (1)$$

For unbound systems, the basis set superposition error (BSSE) was estimated using a counterpoise (CP) correction:

$$E_{\text{BSSE,Au}} = E^{\text{MeSH–Au}_{20}}_{\text{Au}_{20},\text{f}} - E^{\text{Au}_{20}}_{\text{Au}_{20},\text{f}}, \quad (2)$$

$$E_{\text{BSSE,MeSH}} = E^{\text{MeSH–Au}_{20}}_{\text{MeSH,f}} - E^{\text{MeSH}}_{\text{MeSH,f}}, \quad (3)$$

where f indicates the final geometry, subscripts indicate the molecule being considered, and the superscripts indicate the basis set in which each energy was evaluated. E_{BSSE} is a negative value. Applying the CP correction to the binding energy, one gets

$$E^{\text{CP}}_{\text{binding}} = E_{\text{binding}} - \left(E_{\text{BSSE,Au}} + E_{\text{BSSE,MeSH}}\right). \quad (4)$$

Dissociative adsorption. Calculated binding energies for the dissociative adsorption took into account the release of hydrogen as H_2:

$$E_{\text{binding}} = \left(E_{\text{MeS-Au}_{20}} + \frac{1}{2}E_{\text{H}_2}\right) - \left(E_{\text{Au}_{20}} + E_{\text{MeSH}}\right). \quad (5)$$

BSSE corrections were not calculated for the dissociative adsorption case, as considering the complex in the molecular (gold + adsorbate) basis set is appropriate in the context of chemical bonding of the two.

Results and Discussion

Dissociative binding of methyl thiol on the Au_{20} cluster

Despite the small size of the molecular backbones considered in this study, dispersive interactions held an important place in determining binding methylthiolate/Au binding strengths. As illustrated by the binding data in Table 1, the adsorption energy did not follow a direct, monotonous relationship with the degree of unsaturation of the gold atoms at the binding site. Instead, a convolution of site reactivity and van der Waals attraction was found to determine the preference of methylthiolate to one or another binding site. As a result, adsorption was strongest at the kink sites (**cf** and **fg**), at edge sites where strong methyl-Au dispersive interactions could be established with the bottom layer (**bc**), and at sites where strong unsaturation was supplemented by favorable but weaker dispersive interactions (**ij**, **hi** and **dh**). On the other hand, strongly unsaturated tip sites with fewer neighboring gold atoms (**ab**, **ad** and **jg**) adsorbed weakly.

The strongest binding arose at the relatively well-coordinated kink site, **cf**, with the methyl group aligned in an equatorial position, and interacting with the bottom layer of the cluster. Coordination numbers at site **cf** were relatively high (6 and 8), with 7 neighboring atoms located at less than 5 Å of the methyl group and available for dispersive interactions. In contrast, the low-coordinated tip site **ad** had coordination numbers 3 and 6, with only 4 neighboring atoms (see Figure 1) within 5 Å of the carbon atom, but showing weak dispersive and overall binding energies. The importance of dispersive interactions of the methyl group in establishing binding site preference is illustrated by the strong correlation between the overall binding energy (E_b in Table 1) and the additional dispersive interaction of the PBE-D2 formalism (E_m in Table 1) in this case.

Regardless of binding site, the thiol group adsorbed to the Au_{20} cluster in a two-bond, off-bridge configuration. In general, Au–S bond lengths were between 2.4 and 2.5 Å (see Table 1), with the sulfur atom generally located roughly along one of the gold lattice planes that intersect the two layers. The relative location of the thiolate group was determined to a great degree by the optimization of the methyl group interactions. The structures of the most stable configurations reported in Table 1 are shown in Figure 2.

Methyl groups experienced weak dispersive binding to Au atoms in the facets neighboring the binding site, with nearest C–Au distances around 3.3–3.7 Å in the most stable configurations. Table 1 includes the number of neighboring Au atoms (atoms within 5 Å of a methyl group), and their average C–Au distance. Several minima were found within thermal energy of the most stable adsorption configuration, with very different methyl group orientations, but similar binding distances. At the strongly binding **cf** kink site, a configuration with the methyl group pointing away from the kink, but interacting with the top layer of surface atoms, experienced only a 0.04 eV energy penalty, whereas slight changes in the location of the methyl group relative to the surface carried a 0.02 eV penalty (see Figure 2a–c). It should be specified that, although multiple low-energy configurations could be found for each site, with the methyl group interacting with various regions of the substrate,

Table 1: Binding energies and relevant distances for methylthiolate–gold adsorption.

site[a]	CN (Au)	E_b (eV)[b]	(d_1,d_2) (Å)[c]	$N_{neigh.}$[d]	$d_{C-Au;avg}$ (Å)[e]	E_m (eV)[f]
ab	3, 7	−0.62	(2.46, 2.49)	4	3.82	−0.30
ab	3, 7	−0.60	(2.45, 2.49)	3	3.54	−0.28
ab	3, 7	−0.58	(2.44, 2.47)	3	3.61	−0.26
bc	7, 6	−1.06	(2.45, 2.43)	4	3.54	−0.40
cf	6, 8	−1.16	(2.42, 2.49)	7	3.80	−0.57
cf	6, 8	−1.14	(2.40, 2.46)	6	3.71	−0.52
cf	6, 8	−1.12	(2.44, 2.47)	5	3.91	−0.43
fg	8, 4	−0.92	(2.53, 2.44)	7	3.79	−0.55
ad	3, 6	−0.65	(2.44, 2.49)	4	3.74	−0.29
dh	6, 4	−0.95	(2.47, 2.41)	4	3.73	−0.30
hi	4, 5	−0.95	(2.42, 2.46)	4	4.03	−0.21
ij	5, 4	−1.00	(2.47, 2.40)	4	3.72	−0.28
gj	4, 4	−0.78	(2.41, 2.48)	3	3.46	−0.28

[a]The indices of the gold atoms are as indicated in Figure 1c. Several equilibrated structures are indicated for some of the binding sites, in decreasing order of their binding energies. [b]Binding energy calculated by Equation 5. [c]Distances from the sulfur atom to the two Au binding sites. [d]Number of neighboring atoms (at less than 5 Å from the methyl group) available for dispersive interactions. This number includes the two Au atoms bound to the sulphur. [e]Average distance from the carbon atom to the neighboring Au atoms. [f]The Molecular Mechanics energy as reported by SIESTA, describing overall dispersive interactions.

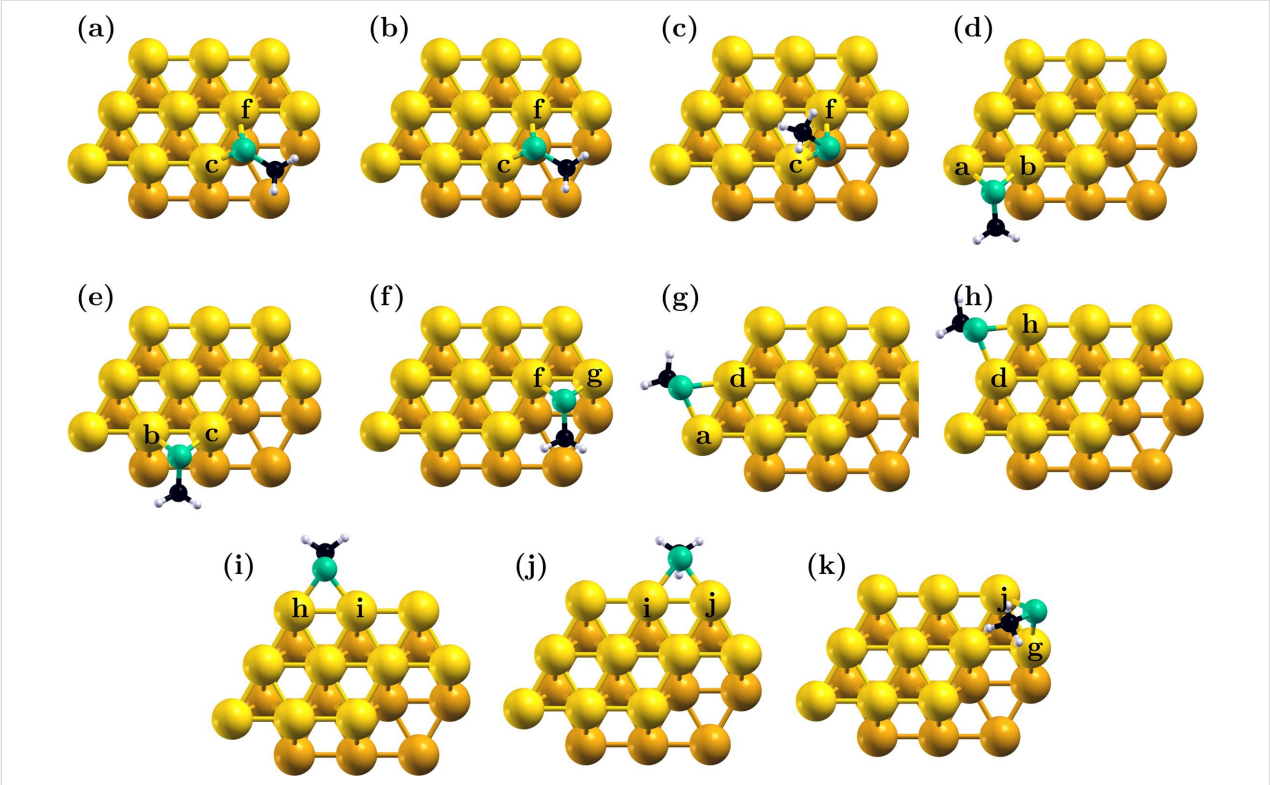

Figure 2: The most stable binding configurations for binding sites on the model Au_{20} cluster. The figures indicate structure for sites **cf** (a–c), **ab** (d), **bc** (e), **fg** (f), **ad** (g), **dh** (h), **hi** (i), **ij** (j) and **gj** (k). For site **cf**, the three most stable configurations are presented in panels a–c, in the order of decreasing stability. Binding site atoms are indicated in the figure.

the full methyl group desorption (an upright configuration still bound at the thiol end) carried an energetic cost between 0.8 and 1.2 eV. This was consistent with experimental and computational reports of methane adsorption on gold surfaces [78,79].

The importance of dispersive corrections in chemisorbed systems

Given the importance of dispersive interactions in the adsorption behavior of methylthiolate on Au as emphasized in the previous section, it was deemed necessary to incorporate dispersive corrections in the DFT formalism we employed. However, uncorrected DFT also includes some dispersion. To understand the actual impact of the correction on the observed adsorption behavior, a series of binding energies obtained using PBE without the van der Waals correction were also calculated and are provided in Table 2. As illustrated in the table, binding energies obtained using the pure PBE functional were weaker and much more homogeneous across the various binding sites.

Whereas S–Au binding distances were relatively unchanged from the PBE-D2 methodology discussed above, the methyl group experienced significant location changes in the PBE approach: A case in point is made by the comparison of the PBE ground state of the **cf**-bound methylthiolate, which had the methyl group located above the surface. This structure was somewhat similar to the third-lowest binding configuration of the PBE-D2-calculated complex (also with the methyl group above the cluster top facet, see Figure 2c and Table 1). In the uncorrected PBE **cf** structure, 5 nearest neighbors could be found within 0.5 Å of the carbon atom, but the structure was more upright, with a larger average C–Au distance (by 0.15 Å). Despite the empirical character of DFT-D2 methods, these results indicate that inclusion of dispersion terms is essential in

Table 2: Methylthiolate–gold binding energies estimated without dispersive corrections.

site[a]	E_b (eV)
ab	−0.33
bc	−0.65
cf	−0.71
fg	−0.45
ad	−0.42
dh	−0.69
hi	−0.74
ij	−0.75
gj	−0.56

[a]Headings are identical to those described in Table 1.

order to obtain reasonable binding strengths and molecular orientations, for even the simplest molecule–surface complexes.

Non-dissociative adsorption: the methylthiol form

Depending on adsorption conditions, and particularly on less reactive surfaces, many thiols maintain their mercapto group undissociated [80,81]. The thiol group then binds to the gold substrate through a single surface atom [23]. We examined here the behavior of complexes of undissociated methylthiol and our Au_{20} cluster. The single-bond configuration provided significantly more orientational freedom to the adsorbate, as illustrated in Figure 3. This in turn allowed both the methyl group and the mercapto hydrogen to approach the surface closely, resulting in overall stronger dispersive interactions relative to the thiolate case (See E_m in Table 1 and Table 3).

The case of thiol (non-dissociative) adsorption is a clear example of the duality of thiol group–methyl group binding in these systems. The weaker thiol–gold bond, with single coordi-

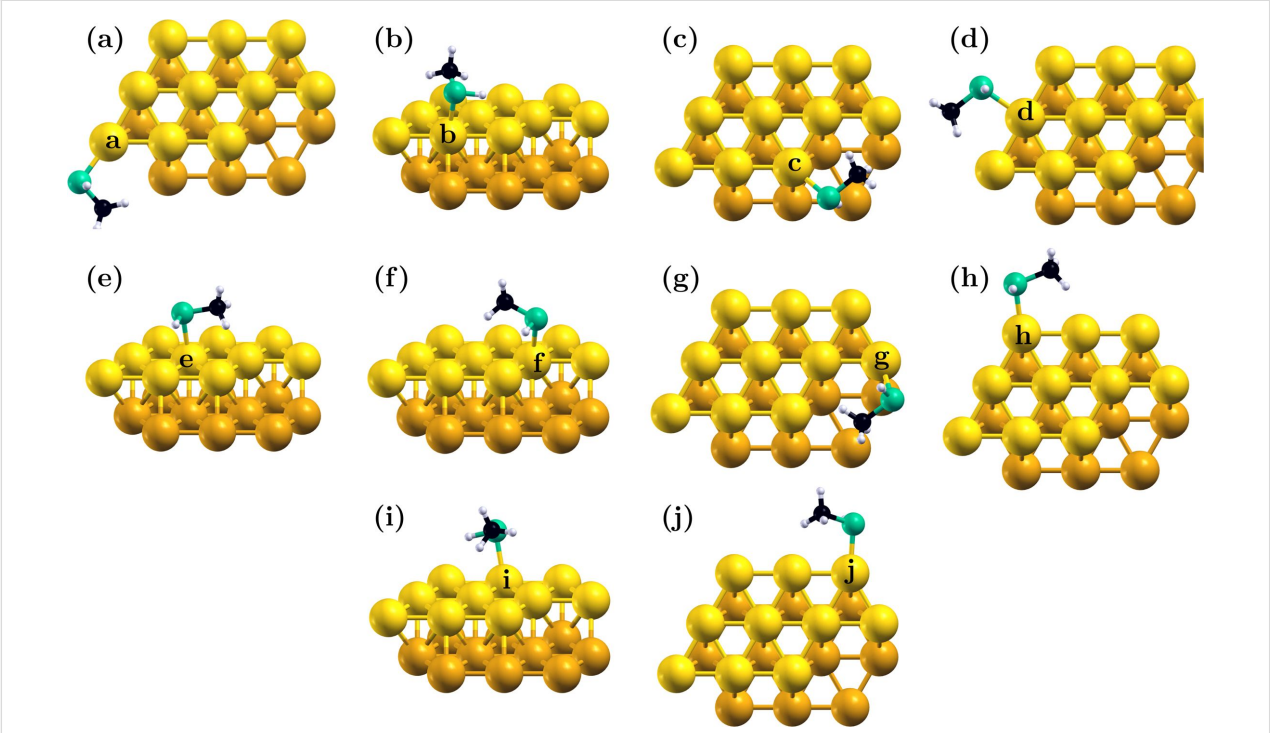

Figure 3: The most stable binding configurations for binding sites on the model Au_{20} cluster. The figures indicate structure for sites **a–j** (panels (a–j), respectively). Binding site atoms are indicated in the figure.

Table 3: Binding energies and relevant distances for methylthiol–gold physical adsorption.

site[a]	CN (Au)	E_b (eV)[b]	d (Å)	$N_{neigh.}$	$d_{C-Au;avg}$	E_m (eV)
a	3	−1.04	2.44	4	4.16	−0.23
b	7	−1.08	2.51	6	3.96	−0.57
c	6	−1.43	2.48	7	3.90	−0.68
d	6	−0.70	2.56	3	3.95	−0.31
e	9	−0.74	2.67	5	3.88	−0.63
f	8	−0.92	2.55	6	4.06	−0.57
g	4	−1.26	2.46	6	3.69	−0.54
h	4	−0.94	2.47	2	3.45	−0.26
i	5	−0.75	2.64	5	3.91	−0.47
j	4	−1.03	2.45	2	3.44	−0.27

[a]If not otherwise specified, headings are they same as in Table 1. [b]Binding energies were calculated by Equation 4.

nation, was more free to move in response to favorable methyl binding conditions. This was apparent in a disconnect between the dispersive added energy (E_m) and the binding energy trends, which had been well correlated in the case of thiolate adsorption. As shown in Table 3, systems where dispersive forces were relatively high could be overall more weakly bound when compared to systems where dispersive interactions are relatively weak: for example, binding at atoms **h** and **i**, in Table 3, where the dispersive and binding energies were negatively correlated. On the other hand though, strong dispersive forces in the **i**-bound thiol were due primarily to methyl–surface interactions, as the relatively long bond length indicated that the thiol group had moved away from the surface. Similar observations can be made for binding at sites **d**, **e** and **f**, with strong overall dispersive forces but relatively long binding distances. The strongest bonds were formed when both of the groups could be satisfied (at sites **c** and **g**, for example.)

In thiol adsorption, the use of dispersion corrections becomes important for describing both the thiol group and the methyl group interaction with the substrate. As shown in Figure 4, uncorrected PBE provides good estimates of bonding strengths and bond lengths only in those systems characterized by relatively strong S–Au bonds (and therefore short S–Au bond distances). The length of weaker bonds was overestimated by uncorrected PBE, as well as the strength of the surface interactions of the methyl group, leading to significant structural changes between the two methodologies.

Conclusion

In order to develop an understanding of thiol binding on complex-structured metal surfaces, we pursued an investigation of dissociative and non-dissociative adsorption at a model 20-atom Au cluster. The cluster model presented a series of distinct available binding sites, with coordination numbers between 3 and 9. To limit the set of competing interactions involved in the adsorption process, we examined methylthiol–Au complexes in a broad examination of their configurational space. We found that, even for small molecules such as methylthiol, dispersive interactions provide an important component of binding affinity. The molecules bound preferentially to kink sites that provided a maximum number of neighboring substrate atoms available for methyl group stabilization. Despite known issues with the empirical nature of dispersive corrections, their inclusion in calculations was essential in order to access reasonable binding structures, particularly for more weakly-bound molecular groups. In effect, a direct parallel between binding preference and the coordination of the adsorption site cannot be drawn without first examining the binding environment and backbone interactions, for even the simple molecules considered here.

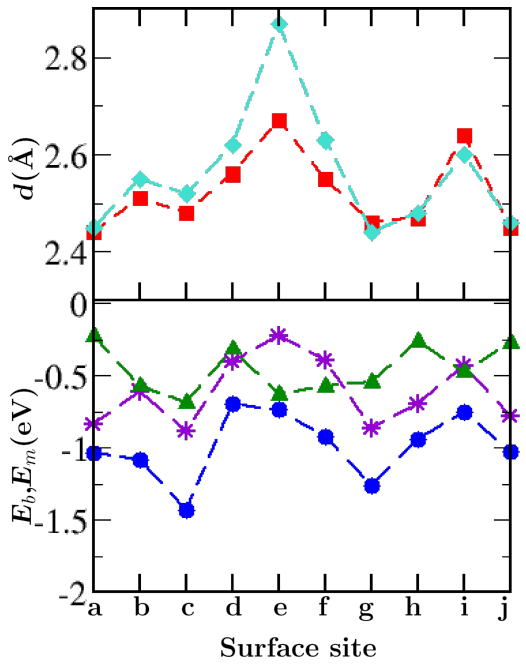

Figure 4: The importance of dispersive corrections in non-dissociative adsorption. Site symbols are given on the abscissa. D2 corrected and uncorrected S–Au bond lengths are shown by red squares and turquoise diamonds, respectively, in the top graph. vdW-Corrected bond energies, uncorrected bond energies and the D2 contribution to the corrected energy are shown by blue circles, purple stars and green triangles, respectively, in the bottom graph.

Acknowledgements

Research was funded through a National Science and Engineering Research Council Discovery Grant. This work was enabled in part by support provided by WestGrid (http://www.westgrid.ca) and Compute Canada/Calcul Canada (http://www.computecanada.ca).

References

1. Stobiecka, M.; Deeb, J.; Hepel, M. *Biophys. Chem.* **2010,** *146,* 98–107. doi:10.1016/j.bpc.2009.11.001
2. Barlow, S. M.; Raval, R. *Surf. Sci. Rep.* **2003,** *50,* 201. doi:10.1016/S0167-5729(03)00015-3
3. Kühnle, A. *Curr. Opin. Colloid Interface Sci.* **2009,** *14,* 157. doi:10.1016/j.cocis.2008.01.001
4. Maier, N. M.; Franco, P.; Lindner, W. *J. Chromatogr. A* **2001,** *906,* 3–30. doi:10.1016/S0021-9673(00)00532-X
5. Isky, E. V.; Tierney, H. L.; Jewell, A. D.; Sykes, E. C. H. *Chem. – Eur. J.* **2011,** *17,* 7205–7211. doi:10.1002/chem.201100268
6. Bombis, C.; Weigelt, S.; Knudsen, M. M.; Nørgaard, M.; Busse, C.; Lægsgaard, E.; Besenbacher, F.; Gothelf, K. V.; Linderoth, T. R. *ACS Nano* **2010,** *4,* 297–303. doi:10.1021/nn9012803
7. Gellman, A. J. *ACS Nano* **2010,** *4,* 5–11. doi:10.1021/nn901885n
8. Raval, R. *J. Mol. Catal. A* **2009,** *305,* 112. doi:10.1016/j.molcata.2008.11.032
9. Wenzel, B.; Fischer, S.; Brust, P.; Steinbach, J. *J. Chromatogr. A* **2010,** *1217,* 3855–3861. doi:10.1016/j.chroma.2010.04.018

10. Mallat, T.; Orglmeister, E.; Baiker, A. *Chem. Rev.* **2007,** *107,* 4863–4890. doi:10.1021/cr0683663
11. James, J. N.; Sholl, D. S. *Curr. Opin. Colloid Interface Sci.* **2008,** *13,* 60–64. doi:10.1016/j.cocis.2007.08.012
12. Sholl, D. S.; Gellman, A. J. *AIChE J.* **2009,** *55,* 2484–2490. doi:10.1002/aic.12036
13. Bantz, K. C.; Meyer, A. F.; Wittenberg, N. J.; Im, H.; Kurtuluş, Ö.; Lee, S. H.; Lindquist, N. C.; Oh, S.-H.; Haynes, C. L. *Phys. Chem. Chem. Phys.* **2011,** *13,* 11551–11567. doi:10.1039/c0cp01841d
14. Weng, Z.; Wang, H.; Vongsvivut, J.; Li, R.; Glushenkov, A. M.; He, J.; Chen, Y.; Barrow, C. J.; Yang, W. *Anal. Chim. Acta* **2013,** *803,* 128–134. doi:10.1016/j.aca.2013.09.036
15. Miao, L.-J.; Xin, J.-W.; Shen, Z.-Y.; Zhang, Y.-J.; Wang, H.-Y.; Wu, A.-G. *Sens. Actuators, B* **2013,** *176,* 906–912. doi:10.1016/j.snb.2012.10.070
16. Hussain, A. M. P.; Sarangi, S. N.; Kesarwani, J. A.; Sahu, S. N. *Biosens. Bioelectron.* **2011,** *29,* 60–65. doi:10.1016/j.bios.2011.07.066
17. Jain, P. K.; Lee, K. S.; El-Sayed, I. H.; El-Sayed, M. A. *J. Phys. Chem. B* **2006,** *110,* 7238–7248. doi:10.1021/jp057170o
18. Wang, A.; Vangala, K.; Vo, T.; Zhang, D.; Fitzkee, N. C. *J. Phys. Chem. C* **2014,** *118,* 8134–8142. doi:10.1021/jp411543y
19. Kogot, J. M.; England, H. J.; Strouse, G. F.; Logan, T. M. *J. Am. Chem. Soc.* **2008,** *130,* 16156–16157. doi:10.1021/ja8064717
20. Tong, L.; Cheng, J.-X. *Nanomedicine* **2009,** *4,* 265–276. doi:10.2217/nnm.09.4
21. Larson, T. A.; Joshi, P. P.; Sokolov, K. *ACS Nano* **2012,** *6,* 9182–9190. doi:10.1021/nn3035155
22. Dreaden, E. C.; Alkilany, A. M.; Huang, X.; Murphy, C. J.; El-Sayed, M. A. *Chem. Soc. Rev.* **2012,** *41,* 2740. doi:10.1039/c1cs15237h
23. Popa, T.; Ting, E. C. M.; Paci, I. *Surf. Sci.* **2014,** *629,* 20–27. doi:10.1016/j.susc.2014.01.018
24. Zhao, Y.; Zhou, F.; Zhou, H.; Su, H. *Phys. Chem. Chem. Phys.* **2013,** *15,* 1690–1696. doi:10.1039/C2CP42830J
25. Fajín, J. L. C.; Gomes, J. R. B.; Cordeiro, M. N. D. S. *Langmuir* **2013,** *29,* 8856–8862. doi:10.1021/la401057f
26. Buimaga-Iarinca, L.; Calborean, A. *Phys. Scr.* **2012,** *86,* 035707. doi:10.1088/0031-8949/86/03/035707
27. Askerka, M.; Pichugina, D.; Kuz'menko, N.; Shestakov, A. *J. Phys. Chem. A* **2012,** *116,* 7686–7692. doi:10.1021/jp303001x
28. Kühnle, A.; Linderoth, T. R.; Besenbacher, F. *Top. Catal.* **2011,** *54,* 1384–1390. doi:10.1007/s11244-011-9765-z
29. Kühnle, A.; Linderoth, T. R.; Besenbacher, F. *J. Am. Chem. Soc.* **2006,** *128,* 1076–1077. doi:10.1021/ja0568751
30. Kühnle, A.; Linderoth, T. R.; Hammer, B.; Besenbacher, F. *Nature* **2002,** *415,* 891–893. doi:10.1038/415891a
31. Kühnle, A.; Linderoth, T. R.; Besenbacher, F. *J. Am. Chem. Soc.* **2003,** *125,* 14680–14681. doi:10.1021/ja0377403
32. Kühnle, A.; Linderoth, T. R.; Schunack, M.; Besenbacher, F. *Langmuir* **2006,** *22,* 2156–2160. doi:10.1021/la052564s
33. Di Felice, R.; Selloni, A. *J. Chem. Phys.* **2004,** *120,* 4906–4914. doi:10.1063/1.1645789
34. Di Felice, R.; Seloni, A.; Molinari, E. *J. Phys. Chem. B* **2003,** *107,* 1151–1156. doi:10.1021/jp0272421
35. Grönbeck, H.; Curioni, A.; Andreoni, W. *J. Am. Chem. Soc.* **2000,** *122,* 3839. doi:10.1021/ja993622x
36. Chapman, C. R. L.; Ting, E. C. M.; Kereszti, A.; Paci, I. *J. Phys. Chem. C* **2013,** *117,* 19426–19436. doi:10.1021/jp405478n
37. Mateo-Martí, E.; Rogero, C.; Gonzalez, C.; Sobrado, J. M.; de Andrés, P. L.; Martin-Gago, J. A. *Langmuir* **2010,** *26,* 4113. doi:10.1021/la903230t
38. Verde, A. V.; Acres, J. M.; Maranas, J. K. *Biomacromolecules* **2009,** *10,* 2118–2128. doi:10.1021/bm9002464
39. Wright, L. B.; Rodger, P. M.; Corni, S.; Walsh, T. R. *J. Chem. Theory Comput.* **2013,** *9,* 1616–1622. doi:10.1021/ct301018m
40. Corni, S.; Hnilova, M.; Tamerler, C.; Sarikaya, M. *J. Phys. Chem. C* **2013,** *117,* 16990–17003. doi:10.1021/jp404057h
41. Horvath, J. D.; Koritnik, A.; Kamakoti, P.; Sholl, D. S.; Gellman, A. J. *J. Am. Chem. Soc.* **2004,** *126,* 14988. doi:10.1021/ja045537h
42. Horvath, J. D.; Gellman, A. J. *J. Am. Chem. Soc.* **2002,** *124,* 2384. doi:10.1021/ja012182i
43. Sholl, D. S.; Asthagiri, A.; Power, T. D. *J. Phys. Chem. B* **2001,** *105,* 4771. doi:10.1021/jp004524x
44. Rampulla, D. M.; Francis, A. J.; Knight, K. S.; Gellman, A. J. *J. Phys. Chem. B* **2006,** *110,* 10411. doi:10.1021/jp060508+
45. Ahmadi, A.; Attard, G.; Feliu, J.; Rodes, A. *Langmuir* **1999,** *15,* 2420. doi:10.1021/la9810915
46. Nørskov, J. K.; Bligaard, T.; Hvolbæk, B.; Abild-Pedersen, F.; Chorkendorff, I.; Christensen, C. H. *Chem. Soc. Rev.* **2008,** *37,* 2163. doi:10.1039/b800260f
47. Christensen, C. H.; Nørskov, J. K. *J. Chem. Phys.* **2008,** *128,* 182503. doi:10.1063/1.2839299
48. Mavrikakis, M.; Stoltze, P.; Nørskov, J. K. *Catal. Lett.* **2000,** *64,* 101. doi:10.1023/A:1019028229377
49. Mostafa, S.; Behafarid, F.; Croy, J. R.; Ono, L. K.; Li, L.; Yang, J. C.; Frenkel, A. I.; Cuenya, B. R. *J. Am. Chem. Soc.* **2010,** *132,* 15714–15719. doi:10.1021/ja106679z
50. Larsson, J. A.; Nolan, M.; Greer, J. C. *J. Phys. Chem. B* **2002,** *106,* 5931–5937. doi:10.1021/jp014483k
51. Zeng, C.; Jin, R. Gold Nanoclusters: Size-Controlled Synthesis and Crystal Structures. *Structure and Bonding;* Springer Science Business Media: Berlin, Germany, 2014; pp 87–115.
52. Zhao, P.; Li, N.; Astruc, D. *Coord. Chem. Rev.* **2013,** *257,* 638–665. doi:10.1016/j.ccr.2012.09.002
53. Pensa, E.; Cortés, E.; Corthey, G.; Carro, P.; Vericat, C.; Fonticelli, M. H.; Benítez, G.; Rubert, A. A.; Salvarezza, R. C. *Acc. Chem. Res.* **2012,** *45,* 1183–1192. doi:10.1021/ar200260p
54. Eckermann, A. L.; Feld, D. J.; Shaw, J. A.; Meade, T. J. *Coord. Chem. Rev.* **2010,** *254,* 1769–1802. doi:10.1016/j.ccr.2009.12.023
55. Maksymovych, P.; Voznyy, O.; Dougherty, D. B.; Sorescu, D. C.; Yates, J. T., Jr. *Prog. Surf. Sci.* **2010,** *85,* 206–240. doi:10.1016/j.progsurf.2010.05.001
56. Cao, R., Jr.; Díaz-García, A. M.; Cao, R. *Coord. Chem. Rev.* **2009,** *253,* 1262–1275. doi:10.1016/j.ccr.2008.08.010
57. Schmid, G. *Chem. Soc. Rev.* **2008,** *37,* 1909. doi:10.1039/b713631p
58. Heimel, G.; Romaner, L.; Zojer, E.; Bredas, J.-L. *Acc. Chem. Res.* **2008,** *41,* 721–729. doi:10.1021/ar700284q
59. Bilić, A.; Reimers, J. R.; Hush, N. S. *J. Chem. Phys.* **2005,** *122,* 094708. doi:10.1063/1.1850455
60. Chaki, N. K.; Vijayamohanan, K. *Biosens. Bioelectron.* **2002,** *17,* 1–12. doi:10.1016/s0956-5663(01)00277-9
61. Poirier, G. E. *Chem. Rev.* **1997,** *97,* 1117–1128. doi:10.1021/cr960074m
62. Schlenoff, J. B.; Li, M.; Ly, H. *J. Am. Chem. Soc.* **1995,** *117,* 12528–12536. doi:10.1021/ja00155a016

63. Barlow, S. M.; Raval, R. *Curr. Opin. Colloid Interface Sci.* **2008,** *13,* 65. doi:10.1016/j.cocis.2007.08.006
64. Humblot, V.; Barlow, S. M.; Raval, R. *Prog. Surf. Sci.* **2004,** *76,* 1–19. doi:10.1016/j.progsurf.2004.04.001
65. Zaera, F. *J. Phys. Chem. C* **2008,** *112,* 16196–16203. doi:10.1021/jp804588v
66. González-Campo, A.; Amabilino, D. B. Biomolecules at Interfaces: Chiral, Naturally. *Biochirality;* Springer Science Business Media: Berlin, Germany, 2013; pp 109–156.
67. Mark, A. G.; Forster, M.; Raval, R. *ChemPhysChem* **2011,** *12,* 1474–1480. doi:10.1002/cphc.201001034
68. Gautier, C.; Bürgi, T. *ChemPhysChem* **2009,** *10,* 483–492. doi:10.1002/cphc.200800709
69. Weissbuch, I.; Lahav, M. *Chem. Rev.* **2011,** *111,* 3236–3267. doi:10.1021/cr1002479
70. Chapman, C.; Paci, I. *J. Phys. Chem. C* **2010,** *114,* 20556–20563. doi:10.1021/jp104967e
71. Perdew, J. P.; Burke, K.; Ernzerhof, M. *Phys. Rev. Lett.* **1996,** *77,* 3865. doi:10.1103/PhysRevLett.77.3865
72. Sánchez-Portal, D.; Ordejón, P.; Artacho, E.; Soler, J. M. *Int. J. Quantum Chem.* **1997,** *65,* 453. doi:10.1002/(SICI)1097-461X(1997)65:5<453::AID-QUA9>3.0.CO;2-V
73. Soler, J. M.; Artacho, E.; Gale, J. D.; García, A.; Junquera, J.; Ordejón, P.; Sánchez-Portal, D. *J. Phys.: Condens. Matter* **2002,** *14,* 2745. doi:10.1088/0953-8984/14/11/302
74. Troullier, N.; Martins, J. L. *Phys. Rev. B* **1991,** *43,* 1993. doi:10.1103/PhysRevB.43.1993
75. Lee, K.; Yu, J.; Morikawa, Y. *Phys. Rev. B* **2007,** *75,* 045402. doi:10.1103/PhysRevB.75.045402
76. Grimme, S. *J. Comput. Chem.* **2006,** *27,* 1787–1799. doi:10.1002/jcc.20495
77. Liu, W.; Ruiz, V. G.; Zhang, G.-X.; Santra, B.; Ren, X.; Scheffler, M.; Tkatchenko, A. *New J. Phys.* **2013,** *15,* 053046. doi:10.1088/1367-2630/15/5/053046
78. Lang, S. M.; Bernhardt, T. M.; Barnett, R. N.; Landman, U. *ChemPhysChem* **2010,** *11,* 1570–1577. doi:10.1002/cphc.200900844
79. Wetterer, S. M.; Lavrich, D. J.; Cummings, T.; Bernasek, S. L.; Scoles, G. *J. Phys. Chem. B* **1998,** *102,* 9266–9275. doi:10.1021/jp982338+
80. Canepa, M.; Lavagnino, L.; Pasquali, L.; Moroni, R.; Bisio, F.; De Renzi, V.; Terreni, S.; Mattera, L. *J. Phys.: Condens. Matter* **2009,** *21,* 264005. doi:10.1088/0953-8984/21/26/264005
81. De Renzi, V.; Lavagnino, L.; Corradini, V.; Biagi, R.; Canepa, M.; del Penino, U. *J. Phys. Chem. C* **2008,** *112,* 14439. doi:10.1021/jp802206r

License and Terms

BEILSTEIN JOURNAL OF NANOTECHNOLOGY

Counterion effects on nano-confined metal–drug–DNA complexes

Nupur Biswas[1,2], Sreeja Chakraborty[3], Alokmay Datta[*1], Munna Sarkar[3], Mrinmay K. Mukhopadhyay[1], Mrinal K. Bera[4] and Hideki Seto[5]

Full Research Paper

Open Access

Address:
[1]Surface Physics and Material Science Division, Saha Institute of Nuclear Physics, 1/AF Bidhannagar, Kolkata 700064, India, [2]present affiliation: Soft Condensed Matter Department, Raman Research Institute, Bangalore 560080, India, [3]Chemical Science Division, Saha Institute of Nuclear Physics, 1/AF Bidhannagar, Kolkata 700064, India, [4]Center for Advanced Radiation Sources, University of Chicago, Chicago, Illinois 60637, USA and [5]KENS & CMRC, Institute of Materials Structure Science, High Energy Accelerator Research Organization, Tsukuba 305-0801, Japan

Email:
Alokmay Datta[*] - alokmay.datta@saha.ac.in

* Corresponding author

Keywords:
confinement; metal–drug–DNA composites; polyelectrolyte; X-ray scattering

Beilstein J. Nanotechnol. **2016,** *7,* 62–67.
doi:10.3762/bjnano.7.7

Received: 17 September 2015
Accepted: 11 January 2016
Published: 19 January 2016

This article is part of the Thematic Series "Organized films".

Guest Editor: M. Canepa

Abstract

We have explored morphology of DNA molecules bound with Cu complexes of piroxicam (a non-steroidal anti-inflammatory drug) molecules under one-dimensional confinement of thin films and have studied the effect of counterions present in a buffer. X-ray reflectivity at and away from the Cu K absorption edge and atomic force microscopy studies reveal that confinement segregates the drug molecules preferentially in a top layer of the DNA film, and counterions enhance this segregation.

Introduction

Condensed state behaviour of DNA, the best-known biopolymer, in a confined space is a matter of interest due to its relevance in living systems. Within cells DNA molecules remain in a confined space crowded by other molecules and ions. Thus, there are three aspects of the situation, which demand elucidation – the role of the ions, of the molecules (especially macromolecules) and of the confinement in the length scales of nanometers and micrometers – in maintaining the stability and homogeneity of the phase of the mixture [1-4] as well as of the structure of the DNA molecules [5]. Studies on the first aspect have established that depending on counterion concentrations and valencies, DNA molecules in bulk solution exhibit isotropic to liquid crystalline phase transition and under extreme conditions they can form crystalline states [6]. Again, a mixture of DNA and other macromolecules undergoes spontaneous segregation and organization under micrometre-scale confinement [7]. Regarding confinement effects at the nanometer scale, we have observed that in absence of counterions DNA molecules

form layered structures aligned laterally to the film surface, whereas in case of films prepared from buffered solution there is no such layering due to the increased orientational entropy of entangled shorter DNA molecules [8,9]. This indicates that both confinement and presence of charged and neutral species in the environment dictates the structure and dynamics of DNA aggregation and lead us to explore the confinement effect on other biologically relevant DNA composites.

We have focussed on the effect of one such biologically active molecule, piroxicam, which is an enolic acid. It is used as a nonsteroidal anti-inflammatory drug (NSAID) for symptomatic relief from rheumatoid arthritis, osteoarthritis and spondylitis [10]. However, the metal-complexes of this molecule form another group of drugs of even greater interest due to their anticancer activity [11,12]. In this context, the attachment of these drugs to DNA molecule gains special importance, since this determines their biofunctionality [13,14]. It is already reported that a Cu(II) complex of piroxicam intercalates within the DNA backbone [15-17]. Motivated by these observations, we have studied effect of counterions on the confined state of metal–drug–DNA complexes, because within living systems such complexes exist in the presence of various salt ions, in a highly confined state.

Here we report structural studies of a metal–drug–DNA complex within thin films, i.e., under one-dimensional confinement and of the influence of counterions on this confined system. Specifically, we have studied thin films comprising of composites of DNA and a Cu(II) complex of piroxicam in presence and absence of buffer molecules. Using anomalous X-ray reflectivity we have probed its out-of-plane structure whereas atomic force microscopy has provided us its in-plane morphology.

Experimental

Polymerized calf thymus DNA (Sisco Research Laboratory, India) dissolved in triple-distilled water formed a pristine stock solution. The absorbance ratio A_{260}/A_{280} of the solution at 260 and 280 nm being in the range $1.8 < A_{260}/A_{280} < 1.9$, indicated that no further deproteinization of the solution was necessary. The nucleotide concentration of the stock solution, assuming $\varepsilon_{260} = 6600\ M^{-1}cm^{-1}$, was found to be 1.8 mM. The stock solution was diluted to the desired concentration of 800 μM in triple distilled water. 10 mM of sodium cacodylate (Merck, Germany) solution in triple-distilled water was adjusted to the desired pH of 6.7 with hydrochloric acid and was used as stock buffer solution. Each molecule of sodium cacodylate effectively contributes one Na^+ ion.

The Cu–piroxicam complex was synthesized following an established protocol [18] and was characterized by FTIR, EPR, and elemental analysis as described in a previous work [19]. Figure 1 shows the structure of the piroxicam molecule along with its Cu(II) complex. Piroxicam was purchased from Sigma Chemicals and was used without further purification. A stock solution of piroxicam of strength 0.5 mM was prepared in spectroscopic grade ethanol, because of poor solubility of piroxicam in water. $CuCl_2$ was purchased from Sigma Chemicals and stock solution was prepared by dissolving it in water. Concentration of stock Cu(II)–piroxicam solution was maintained at 37.4 μM. This stock solution was mixed with DNA stock solution of concentration 800 μM resulting in a fraction of 0.046 of drug–metal complex in DNA. We have worked with two solutions of drug–metal complexes mixed with DNA, one in presence and the other in absence of buffer. When mixed with DNA-buffer solution, the buffer concentration was maintained at 10 mM.

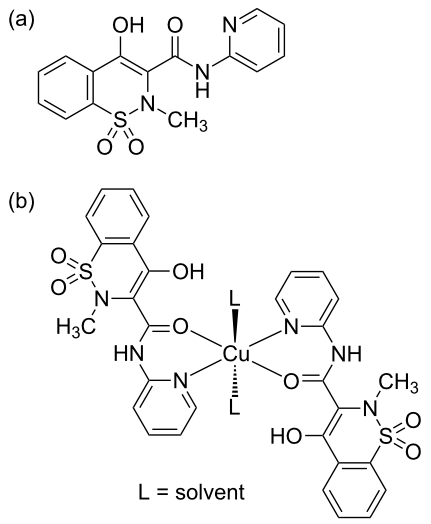

Figure 1: Structure of (a) piroxicam molecule and (b) Cu(II)–piroxicam complex.

Films were prepared by spin-coating the solution on amorphous fused quartz substrates at ambient condition using a spin-coater (Headway Research Inc., USA). Before spin-coating the fused quartz (Alfa Aesar, USA) substrates were cleaned and hydrophilized by boiling in 5:1:1 $H_2O/H_2O_2/NH_4OH$ solution for 10 min, followed by sonication in acetone and ethanol respectively, then rinsing by Millipore water (resistivity ≈ 18.2 MΩ·cm) and subsequent removal of water by spinning the substrate at high speed (4000 rpm).

To extract out-of-plane information specular X-ray reflectivity profiles of these thin films were recorded with step size 5 mdeg at the Indian Beamline (BL-18B) at Photon Factory, High Energy Accelerator Research Organization (KEK), Japan. Both

anomalous and normal X-ray reflectivity data was collected to check the spatial distribution of Cu along the film depth. Cu has two absorption edges in X-ray regime which are at 8.98 keV (K1 edge) and 1.096 keV (L1 edge). As Indian Beamline operates within 6–20 keV, anomalous reflectivity data was taken at K1 absorption edge of Cu (at wavelength 1.38 Å, energy 8.98 keV). For normal X-ray reflectivity we chose a wavelength which is away from the absorption edge. So we shifted to energy 11.736 keV which corresponds to wavelength 1.08 Å. To avoid radiation damage the sample was kept in nitrogen atmosphere. To analyse all XRR data we have used Minpack fitting package [20] based on Levenberg–Marquardt algorithm. It provides the local minimum of nonlinear least squares functions of several variables. Here an iterative process continues and termination occurs when the relative error between two consecutive iterates is below 10^{-9}. Atomic force microscope (AFM) images recorded in tapping mode using Nanonics MultiView1000 with glass tips of about 20 nm diameter, provides in-plane information. The images were analyzed using WSxM software [21].

Results and Discussion

Figure 2 shows the topography of the film surfaces as obtained from AFM. The top surface of the film comprising drug–metal–DNA complex has a lower height variation (rms roughness 4.28 Å) whereas the film with added buffer has an increased roughness (rms roughness 8.97 Å). We took several images from different regions of the sample. Here we are reporting the average roughness values from five such different images. For Cu(II)–piroxicam–DNA film rms roughness is 4.51 Å with a standard deviation of 0.41 Å. For Cu(II)–piroxicam–DNA–buffer film rms roughness is 8.35 Å with a relatively high standard deviation of 1.08 Å.

This is also apparent from the typical line profiles shown in Figure 2. The phase images shown inset indicate the clear presence of clusters of a material different from the film at the base of the buffered film, whereas such clustering is not so pronounced in the unbuffered film. We have carried out X-ray reflectivity (XRR) experiments of the films, which provide us electron density profiles (EDP) of the film along its depth. To analyze the anomalous reflectivity profiles we have used the distorted wave Born approximation (DWBA) method [22,23], which only requires an ansatz of the average electron density of the film and provides the electron densities of different "layers" of the film (of thickness decided by the spatial resolution) through Fourier transforms [24]. In contrast to the usual anomalous scattering analysis formalism [25] here we have not considered any interfacial width between the "layers". The reflectivity profiles of the films and EDPs along the depth of the film extracted from the fits are shown in Figure 3. It is to be mentioned that in the DWBA model "layers" do not extend into the substrate. To plot EDP, as shown in Figure 3b and Figure 3d, we have further convoluted the DWBA EDP with the average electron density of the substrate and of air ($\rho_s = 0.68$ and $\rho_{air} = 0$) and as well as with the roughnesses of those interfaces ($\sigma_{af} \approx 10$ Å and $\sigma_{fs} \approx 7$ Å). The values of these parameters were obtained from the DWBA fit and during fit it was always taken care that the roughness values do not exceed the "layer" thickness.

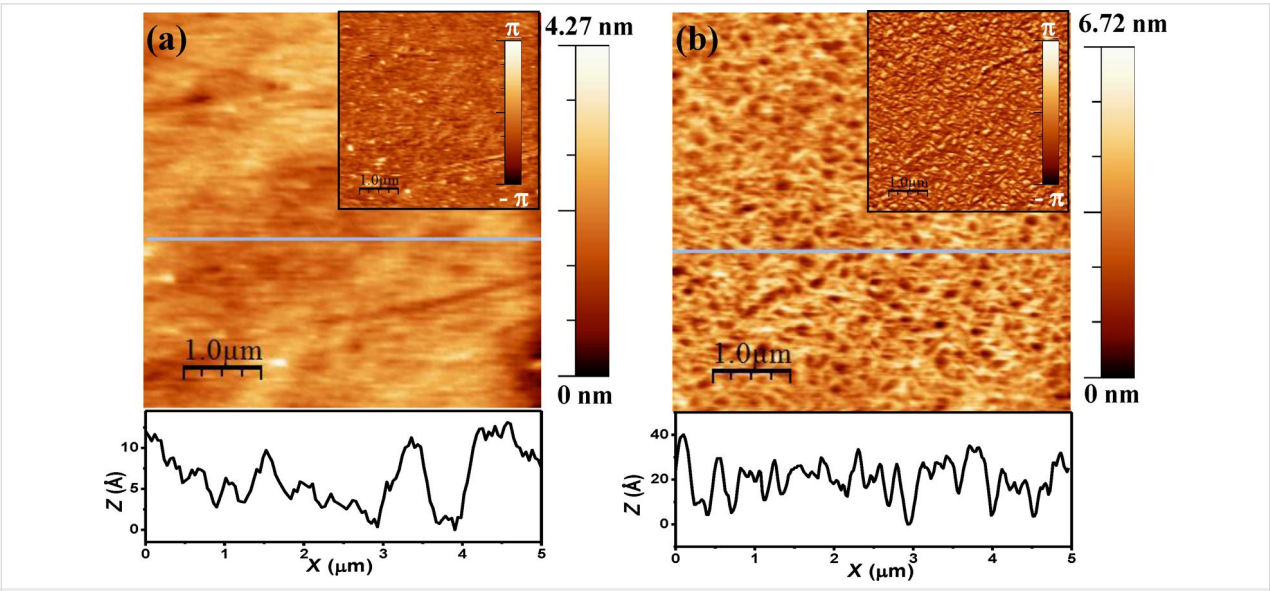

Figure 2: AFM height image of (a) Cu(II)-piroxicam-DNA film (scan size 5 μm × 5 μm) and (b) Cu(II)–piroxicam–DNA–buffer film (scan size 5 μm × 5 μm). Insets (a) and (b) show corresponding phase images. Lower panel shows the corresponding line profiles along the blue lines drawn on respective height images.

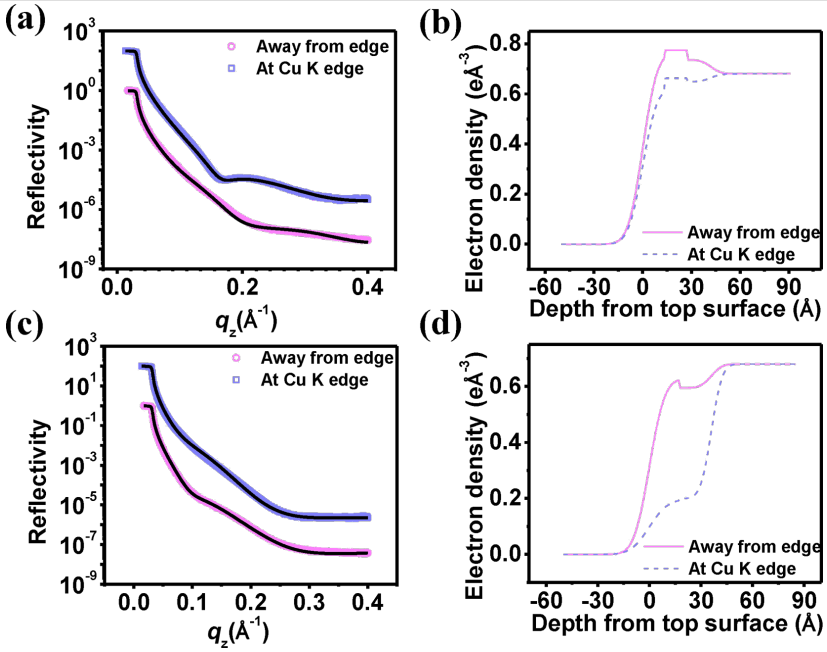

Figure 3: X-ray reflectivity data at and away from Cu absorption edge (up shifted for clarity). Symbols: experimental data points; line: fit with DWBA formalism. (a) Reflectivity profiles of Cu(II)–piroxicam–DNA film, (b) corresponding EDPs. (c) Reflectivity profiles of Cu(II)–piroxicam–DNA–buffer film, (d) corresponding EDPs.

We observe that the film prepared from a solution containing no counterions has a thickness of 42 Å, whereas the film prepared from solution with added buffer has a lower thickness of 36 Å. These small thickness values establish that we have succeeded in creating a confined state of this complex. A reduction of the film thickness after addition of buffer can be explained through a better neutralization of DNA molecules by the buffer molecules. This in turn reduces the persistence length of the DNA molecules, makes them softer and more entangled and hence more compact [26]. Considering the fact that DNA molecules have a diameter of 22–26 Å, the magnitude of the film thicknesses suggests a lateral alignment of DNA molecules within the film similar to the case of film formed from "pristine" DNA molecules [8].

Anomalous X-ray scattering data provides us the distribution of an effective density of Cu atoms along the film depth. Within any material X-rays interact with electrons only. Hence, the presence of a particular element is observed by X-ray, when the X-ray energy matches with any absorption edge of that element and the radiation is absorbed. As the beam is no more scattered by the the electrons of that element, the scattered beam provides a lower value of electron density. The effective electron densities for X-ray energies away from edge ($\rho^a(z)$) and at the edge ($\rho^e(z)$) of an element, Cu in our case, is given by [27],

$$\rho^{a}(z) = N_{Cu}(z) Z^{a}_{eff} \quad (1)$$

and

$$\rho^{e}(z) = N_{Cu}(z) Z^{e}_{eff}\,, \quad (2)$$

where $N_{Cu}(z)$ is the atomic density of the element Cu. It is independent of energy and effective atomic number Z_{eff} of the element as observed by X-ray. Hence, the difference yields the effective electron density for the element Cu,

$$\rho^{a}(z) - \rho^{e}(z) = N_{Cu}(z)\Delta Z_{eff} = \Delta\rho^{eff}_{Cu}(z)\,, \quad (3)$$

where $\Delta Z_{eff} = Z^{a}_{eff} - Z^{e}_{eff}$. The difference in electron densities, $\Delta\rho^{eff}_{Cu}$ represents the abundance of Cu. Figure 4a shows this variation along the film depth for both films. We observe a relative abundance of Cu near the air–film interface suggesting a Cu-rich upper layer for both films. This effect is more enhanced in the case of the buffer film, indicating counterions enhance the Cu proportion in this layer. This suggests that a drug–DNA segregation occurs with buffering leaving more drug–metal composites at the surface increasing its roughness and clustering as observed from AFM topography (Figure 2). In Figure 4b we have compared the line profiles drawn over two images. The horizontal lines denote corresponding average height of the profiles (6.38 Å and 20.37 Å for without buffer and with buffer films, respectively). Their difference of

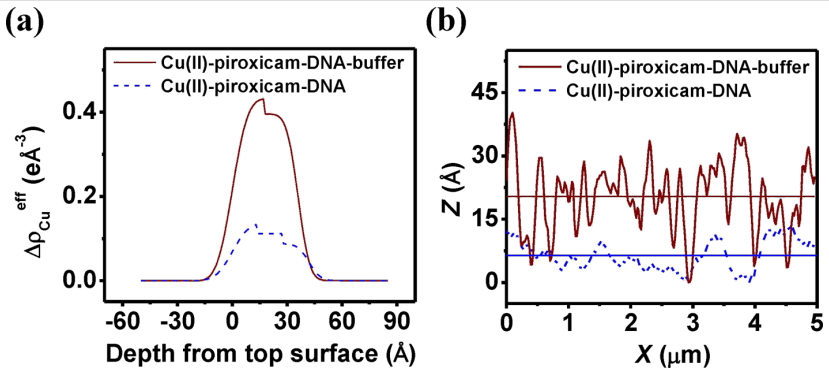

Figure 4: (a) Variation of $\Delta\rho_{Cu}^{eff}$ along the film depth for both Cu(II)–piroxicam–DNA and Cu(II)–piroxicam–DNA–buffer films. (b) Comparison of the line profiles along the blue lines drawn on respective height images of Figure 2. The horizontal lines denote corresponding average heights of the profiles.

approx. 14 Å matches closely with the lateral width of piroxicam molecules [28,29].

The structures of piroxicam molecule and Cu(II)–piroxicam complex as depicted in Figure 1 show a planar structure of the complex which intercalates in a DNA backbone parallel to the bases in solution [28]. In our case we observe an asymmetric distribution of Cu atoms with respect to the DNA molecules aligned laterally over the hydrophilic substrate leading to a preferential enrichment at the top surface of the films. It was observed earlier [8,19,30] that the negatively charged phosphate groups of DNA also attach with the hydroxyl-terminated hydrophilic quartz substrate through short-range interactions such as hydrogen bonds that dominating over the long-range but weak, screened Coulomb attraction. Due to this short-range interaction, the hydroxyl-terminated substrate prefers DNA molecules rather than the neutral metal–drug complex. On the other hand, at the surface, due to the absence of any such short-range interactions, the intercalation of the Cu(II) complex of piroxicam is allowed, quite similar to the case of bulk solution. This is shown in Figure 5a. In presence of counterions, the phosphate groups of the DNA backbone get neutralized. This causes two effects, (a) the short-range interactions become even more dominant causing a stronger adhesion to substrate, (b) the presence of counterions in buffer solution neutralizes the polyanionic DNA backbone to some extent. Charge neutralization of the backbone reduces the persistence length of DNA, making it more floppy. A floppy DNA is better accommodated nearer to the surface as shown in Figure 5b. Enhanced segmental flexibility of DNA in presence of buffer promotes not only closer approach to the surface but also helps in orienting the Cu-bearing drug molecule more towards the top. These considerations qualitatively explain the enrichment of the Cu–drug complex at the surface and the reduced thickness of the film made from solution with added buffer. This is shown in Figure 5b.

It is to be noted that we have explored the role of very high salt concentrations (500 mM) in case of pristine DNA thin films, as reported in [9]. At such high salt concentrations, we observed salt crystals over the film. Also at concentrations above 100 mM the persistence length of DNA molecules saturates to approx. 50 nm due to complete neutralization of DNA backbone. At salt concentrations of approx. 10 mM DNA is the onset of full neutralization. To explore counterion effects we have restricted ourselves to this onset regime [31].

Conclusion

We have carried out a preliminary exploration of the morphological effects of counterions on a metal–drug–DNA complex within a thin film. The metal–drug complex intercalates within

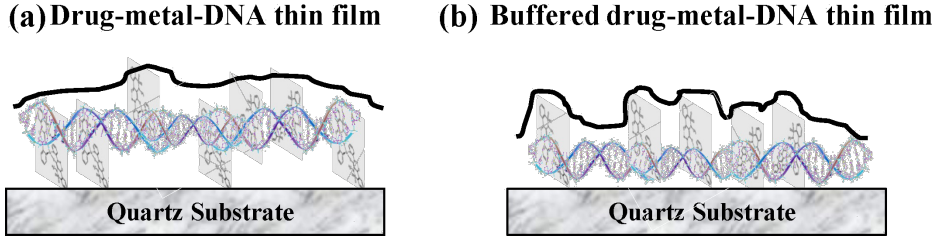

Figure 5: Schematic of (a) metal–drug–DNA film and (b) metal–drug–DNA–buffer film.

the DNA backbone and prefers to remain near the top surface of the film. Addition of buffer molecules results in the presence of more metal–drug composites at the top surface of the film and a reduction of the film thickness. We have explained these findings qualitatively, invoking enhanced short-range drug–DNA and substrate–DNA interactions that are influenced by the buffer.

Acknowledgements

We would like to acknowledge Heiwa-Nakajima Foundation, Japan for providing financial support and Department of Science and Technology, Government of India for sponsoring Indian beamline project at Photon Factory, KEK, Japan. Authors N. B. and S. C. thank Council of Scientific and Industrial Research (CSIR), Government of India and Director, SINP for their research fellowships.

References

1. Ésio Bessa Ramos, J., Jr.; de Vries, R.; Neto, J. R. *J. Phys. Chem. B* **2005,** *109,* 23661–23665. doi:10.1021/jp0527103
2. Saito, T.; Iwaki, T.; Yoshikawa, K. *Chem. Phys. Lett.* **2008,** *465,* 40–44. doi:10.1016/j.cplett.2008.09.040
3. Krotova, M. K.; Vasilevskaya, V. V.; Makita, N.; Yoshikawa, K.; Khokhlov, A. R. *Phys. Rev. Lett.* **2010,** *105,* 128302. doi:10.1103/PhysRevLett.105.128302
4. Kankia, B. I.; Buckin, V.; Bloomfield, V. A. *Nucleic Acids Res.* **2001,** *29,* 2795–2801. doi:10.1093/nar/29.13.2795
5. Evdokimov, Yu. M.; Platonov, A. L.; Tikhonenko, A. S.; Varshavsky, Ya. M. *FEBS Lett.* **1972,** *23,* 180–184. doi:10.1016/0014-5793(72)80335-1
6. Livolant, F.; Leforestier, A. *Prog. Polym. Sci.* **1996,** *21,* 1115–1164. doi:10.1016/S0079-6700(96)00016-0
7. Biswas, N.; Ichikawa, M.; Datta, A.; Sato, Y. T.; Yanagisawa, M.; Yoshikawa, K. *Chem. Phys. Lett.* **2012,** 539–540. doi:10.1016/j.cplett.2012.05.033
8. Biswas, N.; Chakraborty, S.; Datta, A.; Sarkar, M.; Mukhopadhyay, M. K.; Bera, M. K.; Seto, H. *arXiv* **2014,** No. 1404.
9. Biswas, N.; Chakraborty, S.; Datta, A.; Sarkar, M.; Mukhopadhyay, M. K.; Bera, M. K.; Seto, H. *AIP Conf. Proc.* **2012,** *1447,* 189–190. doi:10.1063/1.4709944
10. Brogden, R. N.; Heel, R. C.; Speight, T. M.; Avery, G. S. *Drugs* **1981,** *22,* 165–187. doi:10.2165/00003495-198122030-00001
11. Weder, J. E.; Dillon, C. T.; Hambley, T. W.; Kennedy, B. J.; Lay, P. A.; Biffin, J. R.; Regtop, H. L.; Davies, N. M. *Coord. Chem. Rev.* **2002,** *232,* 95–126. doi:10.1016/S0010-8545(02)00086-3
12. Marzano, C.; Pellei, M.; Tisato, F.; Santini, C. *Anti-Cancer Agents Med. Chem.* **2009,** *9,* 185–211. doi:10.2174/187152009787313837
13. Denda, A.; Endoh, T.; Kitayama, W.; Tang, Q.; Noguchi, O.; Kobayashi, Y.; Akai, H.; Okajima, E.; Tsujiuchi, T.; Tsutsumi, M.; Nakae, D.; Konishi, Y. *Carcinogenesis* **1997,** *18,* 1921–1930. doi:10.1093/carcin/18.10.1921
14. Mohammed, S. I.; Bennett, P. F.; Craig, B. A.; Glickman, N. W.; Mutsaers, A. J.; Snyder, P. W.; Widmer, W. R.; DeGortari, A. E.; Bonney, P. L.; Knapp, D. W. *Cancer Res.* **2002,** *62,* 356–358.
15. Roy, S.; Banerjee, R.; Sarkar, M. *J. Inorg. Biochem.* **2006,** *100,* 1320–1331. doi:10.1016/j.jinorgbio.2006.03.006
16. Hadadzadeh, H.; Salimi, M.; Weil, M.; Jannesari, Z.; Darabi, F.; Abdi, K.; Khalaji, A. D.; Sardari, S.; Ahangari, R. *J. Mol. Struct.* **2012,** *1022,* 172–180. doi:10.1016/j.molstruc.2012.04.094
17. Çeşme, M.; Gölcü, A.; Demirtaş, I. *Spectrochim. Acta, Part A* **2015,** *135,* 887–906. doi:10.1016/j.saa.2014.06.144
18. Cini, R.; Giorgi, G.; Cinquantini, A.; Rossi, C.; Sabat, M. *Inorg. Chem.* **1990,** *29,* 5197–5200. doi:10.1021/ic00351a012
19. Majumdar, A.; Chakraborty, S.; Sarkar, M. *J. Phys. Chem. B* **2014,** *118,* 13785–13799. doi:10.1021/jp5086087
20. More, J. J.; Garbow, B. S.; Hillstrom, K. E. *User guide for MINPACK-1;* Argonne National Laboratory: Lemont, IL, U.S.A., 1980. doi:10.2172/6997568
21. Horcas, I.; Fernández, R.; Gómez-Rodríguez, J. M.; Colchero, J.; Gómez-Herrero, J.; Baro, A. M. *Rev. Sci. Instrum.* **2007,** *78,* 013705. doi:10.1063/1.2432410
22. Sinha, S. K.; Sirota, E. B.; Garoff, S.; Stanley, H. B. *Phys. Rev. B* **1988,** *38,* 2297–2311. doi:10.1103/PhysRevB.38.2297
23. Basu, J. K.; Sanyal, M. K. *Phys. Rep.* **2002,** *363,* 1–84. doi:10.1016/S0370-1573(01)00083-7
24. Tolan, M. *X-ray Scattering from Soft Matter Thin Films;* Springer: Berlin, Germany, 1999.
25. Ohkawa, T.; Yamaguchi, Y.; Sakata, O.; Sanyal, M. K.; Datta, A.; Banerjee, S.; Hashizume, H. *Physica B* **1996,** *221,* 416–419. doi:10.1016/0921-4526(95)00960-4
26. Baumann, C. G.; Smith, S. B.; Bloomfield, V. A.; Bustamante, C. *Proc. Natl. Acad. Sci. U. S. A.* **1997,** *94,* 6185–6190. doi:10.1073/pnas.94.12.6185
27. Banerjee, S.; Park, Y. J.; Lee, D. R.; Jeong, Y. H.; Lee, K.-B.; Yoon, S. B.; Choi, H. M.; Park, J.-C.; Roh, J. S.; Sanyal, M. K. *Appl. Surf. Sci.* **1998,** *136,* 41–45. doi:10.1016/S0169-4332(98)00324-9
28. Abu-Eittah, R. H.; Zordok, W. A. *J. Mol. Struct.: THEOCHEM* **2010,** *951,* 14–20. doi:10.1016/j.theochem.2010.03.034
29. Cini, R.; Giorgi, G.; Cinquantini, A.; Rossi, C.; Sabat, M. *Inorg. Chem.* **1990,** *29,* 5197–5200. doi:10.1021/ic00351a012
30. Qiao, B.; Cerdà, J. J.; Holm, C. *Macromolecules* **2011,** *44,* 1707–1718. doi:10.1021/ma1026109
31. Manning, G. S. *Biophys. J.* **2006,** *91,* 3607–3616.

License and Terms

BEILSTEIN JOURNAL OF NANOTECHNOLOGY

Fabrication and characterization of novel multilayered structures by stereocomplexion of poly(D-lactic acid)/ poly(L-lactic acid) and self-assembly of polyelectrolytes

Elena Dellacasa[‡1], Li Zhao[‡2], Gesheng Yang[3], Laura Pastorino[1] and Gleb B. Sukhorukov[*2]

Full Research Paper

Open Access

Address:
[1]Department of Informatics, Bioengineering, Robotics and Systems Engineering, University of Genova, Via all' Opera Pia 13, 16145 Genova, Italy, [2]School of Engineering and Materials Science, Queen Mary University of London, Mile End Road, E1 4NS London, UK, and [3]State Key Laboratory for Modification of Chemical Fibers and Polymer Materials, College of Material Science and Engineering, Donghua University, Shanghai 201620, P. R. China

Email:
Gleb B. Sukhorukov[*] - g.sukhorukov@qmul.ac.uk

* Corresponding author ‡ Equal contributors

Keywords:
biocompatibility; layer-by-layer assembly; microcapsules; poly(lactic acids); stereocomplex

Beilstein J. Nanotechnol. **2016,** *7,* 81–90.
doi:10.3762/bjnano.7.10

Received: 14 October 2015
Accepted: 07 January 2016
Published: 21 January 2016

This article is part of the Thematic Series "Organized films".

Guest Editor: M. Canepa

Abstract

The enantiomers poly(D-lactic acid) (PDLA) and poly(L-lactic acid) (PLLA) were alternately adsorbed directly on calcium carbonate ($CaCO_3$) templates and on poly(styrene sulfonate) (PSS) and poly(allylamine hydrochloride) (PAH) multilayer precursors in order to fabricate a novel layer-by-layer (LBL) assembly. A single layer of poly(L-lysine) (PLL) was used as a linker between the $(PDLA/PLLA)_n$ stereocomplex and the cores with and without the polymeric $(PSS/PAH)_n$/PLL multilayer precursor (PEM). Nuclear magnetic resonance (NMR) and gel permeation chromatography (GPC) were used to characterize the chemical composition and molecular weight of poly(lactic acid) polymers. Both multilayer structures, with and without polymeric precursor, were firstly fabricated and characterized on planar supports. A quartz crystal microbalance (QCM), attenuated total reflection Fourier transform infrared spectroscopy (ATR-FTIR) and ellipsometry were used to evaluate the thickness and mass of the multilayers. Then, hollow, spherical microcapsules were obtained by the removal of the $CaCO_3$ sacrificial template. The chemical composition of the obtained microcapsules was confirmed by differential scanning calorimetry (DSC) and wide X-ray diffraction (WXRD) analyses. The microcapsule morphology was evaluated by scanning electron microscopy (SEM) and transmission electron microscopy (TEM) measurements. The experimental results confirm the successful fabrication of this innovative system, and its full biocompatibility makes it worthy of further characterization as a promising drug carrier for sustained release.

Introduction

The polycationic/polyanionic layer-by-layer (LBL) deposition on surfaces has been widely studied since the first description by Decher et al. [1-3]. The alternate adsorption of negatively and positively charged poly(styrene sulfonate) (PSS) and poly(allylamine hydrochloride) (PAH) on sacrificial templates have been the most widely characterized and applied materials for the production of hollow microcapsules [4-6]. The potential of these multilayer structures for biotechnological and biomedical applications, such as biosensors and carriers for drug delivery, led researchers to extend this technique beyond multilayer structure fabrication based on electrostatic interactions [7-11].

Over the years, other interactions such as covalent bonding [12-14], hydrogen bonding [15-17] and hydrophobic interaction [18-20] have been investigated, and also non-water-soluble polymers, viruses [21], proteins [22-26], and amphiphiles [27-29] have been used in LBL multilayers.

Among the non-water-soluble polymers, the aliphatic polyester poly(lactic acid) (PLA) has been widely used in the biomedical field due to its extraordinary biocompatibility, biodegradability and mechanical properties [19,30-33]. Lactic acid, which is the degraded product from PLA, is fully biocompatible in human bodies, and therefore medical materials made from PLA, such as surgical suture, implants, as well as drug carriers, are in high demand. Recently PLA-based polymers have been used for the fabrication of drug carriers by a LBL self-assembly technique [15,17,34]. As an example, the stepwise assembly of poly(L-lactic acid) (PLLA) and poly(D-lactic acid) (PDLA) enantiomers, forming a racemic crystal called a stereocomplex, has been successfully realized [35]. However, PLA capsules made by the LBL technique with an entirely biocompatible procedure remain a challenge [36-38].

The possibility to assemble these polymers, as well as other biocompatible polymers such as poly(methyl methacrylate) (PMMA) [39-41], poly(lactic-*co*-glycolic acid) (PLGA) [42] and poly-ε-caprolactone (PCL) [43,44], is extremely interesting for the fabrication of innovative multilayer structures to be used in drug delivery applications.

In this work, we proposed the LBL assembly of PDLA/PLLA layers onto a $(PSS/PAH)_n$/PLL precursor (PEM) [45,46]. This innovative configuration, involving both water-soluble and non-water-soluble polymers, could represent a promising drug carrier model. The multilayer structure was first characterized on planar supports, and then transferred onto spherical sacrificial templates, in order to build hollow microcapsules. Nuclear magnetic resonance (NMR) and gas permeation chromatography (GPC) were used to characterize the chemical composition and molecular weight of synthetic PLA polymers. Ellipsometry and quartz crystal microbalance (QCM) were used to monitor the step-by-step assembly and to evaluate the thickness and the mass of the multilayers. The use of ellipsometry to characterize the layer growth gave us information about the thicknesses of the films compared to the previously used QCM technique, which only gave information about mass change [35]. Attenuated total reflection Fourier transform infrared spectroscopy (ATR-FTIR) was used to verify the stereocomplex formation and its effective adsorption onto the polyelectrolyte precursor. Differential scanning calorimetry (DSC) and wide X-ray diffraction (WXRD) analyses were also used to confirm the stereocomplex formation. The multilayer structure was then built on spherical sacrificial templates and then morphologically characterized by scanning electron microscopy (SEM) and transmission electron microscopy (TEM).

Results and Discussion

Chemical composition and molecular weight of PLA polymers

The chemical structure of PDLA and PLLA was characterized by ^{1}H NMR. As can be seen in Figure 1a, the peak at 1.61 ppm belongs to the methyl group while the 5.19 ppm peak was assigned to the protons of the CH_2 group. The small peak between 7–8 ppm was assigned to the deuterated chloroform ($CDCl_3$) solvent. The spectra of Figure 1a and Figure 1b appear very similar, meaning that two polymers with the same chemical composition were synthesized.

GPC curves shown in Figure 2 confirm that both PDLA and PLLA (having a relatively narrow molecular weight distribution) were obtained via ring-opening polymerization. The molecular weight of PDLA and PLLA are 37511 and 59223 g/mol, respectively. This was suitable for our usage due to the use of polymers with similar molecular weights in LBL assembly [46]. Thus, these polymers were used for LBL assembly directly after synthesis and purification.

QCM measurements

As a first step, the LBL assembly of PEM and PLA polymers was carried out on QCM electrodes in order to monitor the effective multilayer growth. The QCM frequency shift, due to the deposition of material onto the electrode surface, was measured and the related adsorbed mass was calculated. Two kind of samples were compared, PLL/$(PDLA/PLLA)_3$ multilayers deposited on $(PAH/PSS)_4$/PSS multilayer precursor or directly on the crystal surface (Figure 3).

Figure 3 shows the step-by-step mass growth of the multilayer as a function of each deposited layer. Since the quartz crystal

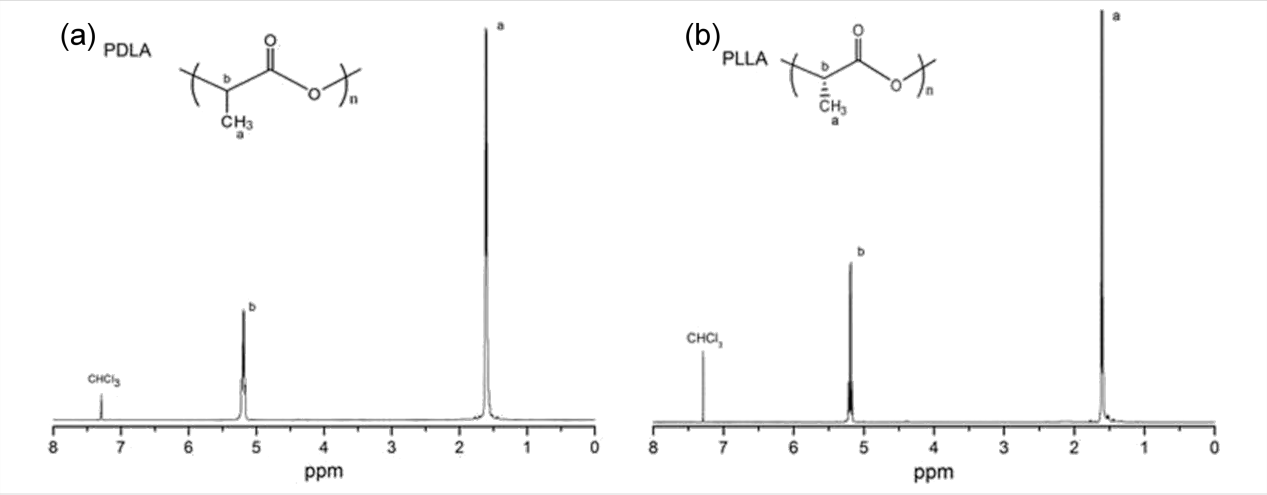

Figure 1: The NMR spectra for PDLA (a) and PLLA (b).

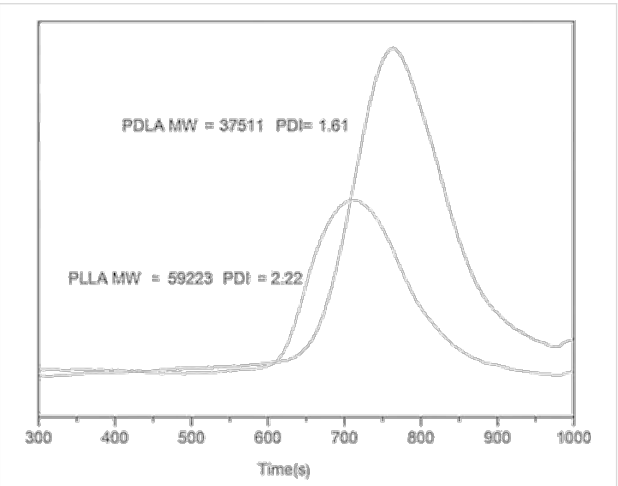

Figure 2: GPC curves of the synthesized PLLA and PDLA.

surface is mostly negatively charged, PAH was deposited as the first layer. The PEM structure shows a mean mass of 85.38 ng, with a mean frequency shift of 155.4 Hz. The total mass of adsorbed PLA layers with PEM precursor was found to be 1468 ng with a mean mass of 245 ng/layer (Figure 3a). Additionally, the total mass of the PLA layers without PEM precursor was found to be 1400 ng with a mean mass of 233 ng/layer (Figure 3b). The gradual growth of the PLA layers confirmed the successful deposition of the polymers in both cases. Comparing the two structures, no significant differences were found in terms of amount of deposited material, indicating that the PEM structure has no particular influence on the PLA adsorption (Figure 3c). However, some observations can be made about the PLA adsorption dynamics, which are better highlighted in Figure 3c. As shown in Figure 3c, in the presence of PEM precursor, the adsorbed mass of the first layer of PDLA is higher with respect to the successive layers. A similar behavior can be observed without the presence of the PEM precursor as it relates to the second PDLA layer. These differences may be due to the presence of the PEM precursor, which could have greater adsorption capability compared to the bare crystal. A higher amount of PLL adsorbed mass was also registered in the presence of the precursor (data not shown). However, no significant influence of this dynamic was observed on the final structure.

Ellipsometry

The kinetics of the growth of PLA films on a flat silicon substrate was also studied. Two samples were compared, a

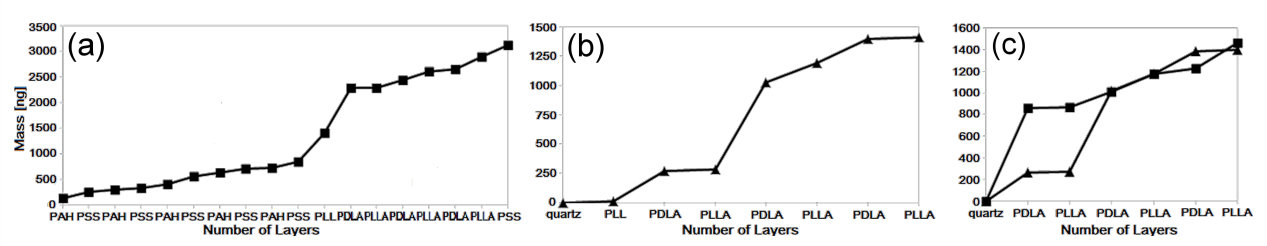

Figure 3: PLL/(PDLA/PLLA)$_3$ multilayer deposition with (PAH/PSS)$_4$/PSS precursor (a) and without (b), and (c) comparison of PLL/(PDLA/PLLA)$_3$ multilayer deposition, with and without (PAH/PSS)$_4$/PSS precursor.

PLL/(PDLA/PLLA)$_5$ multilayer deposited onto (PAH/PSS)$_4$ precursor and onto bare silicon. The thickness of the PLL/(PDLA/PLLA)$_5$ multilayers deposited onto the precursor as shown in Figure 4a was found to be 22.84 nm while the thickness of the PLL/(PDLA/PLLA)$_5$ multilayers deposited onto bare silicon (Figure 4b) was found to be 23.5 nm, indicating again that the polyelectrolyte multilayer precursor has no particular effect on the thickness of the PLA multilayer. This is different from the results of other research on the behavior of the growth of conventional polyelectrolyte multilayers, where the underlying precursor was shown to have some influence [47].

Another phenomenon that was observed is that an odd number of PLA layers is always thicker than an even number of layers. This is due to the "dotted-structure" formation during the PLA layer deposition [35]. As the process of each PLA deposition takes longer than the polyelectrolyte assembly, each odd number layer can hardly cover the whole substrate surface uniformly within each deposition. Hence, the next even number layer deposits on the uncovered surface during the formation of the stereocomplex with the former layer, which is reflected as a thinner layer after its deposition.

Coating of microparticles and fabrication of capsules out of stereocomplex

ATR-FTIR measurements

The PDLA/PLLA stereocomplex formation was monitored by ATR-FTIR. Figure 5a shows the PDLA/PLLA stereocomplex spectrum obtained by mixing 1:1 solutions at 50 °C. As previously reported [48], the 1:1 blend of low molecular weight PLLA and PDLA solutions in acetonitrile is desired for the

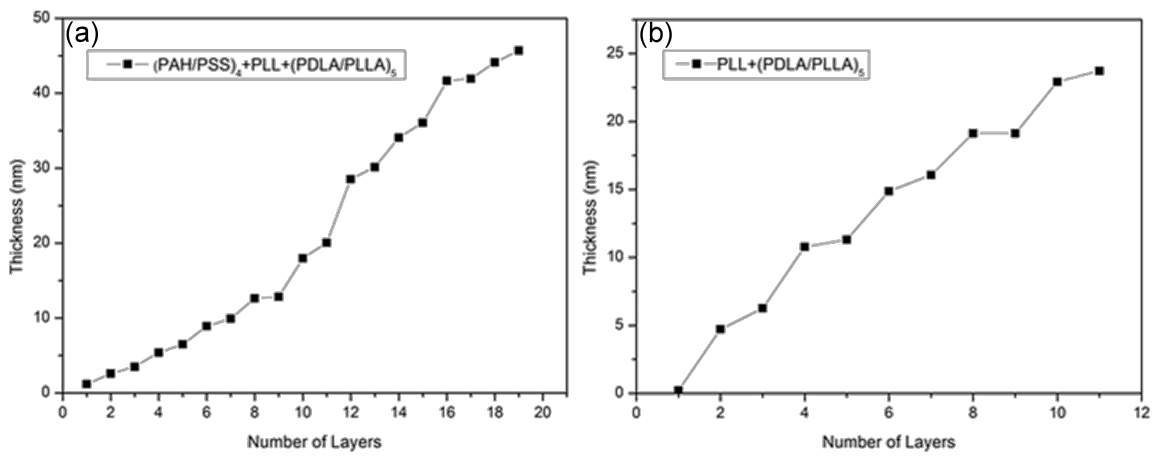

Figure 4: Kinetics study on the thickness of the PLL/(PDLA/PLLA)$_5$ multilayer on a silicon substrate with (PAH/PSS)$_4$ precursor (a) and without (b).

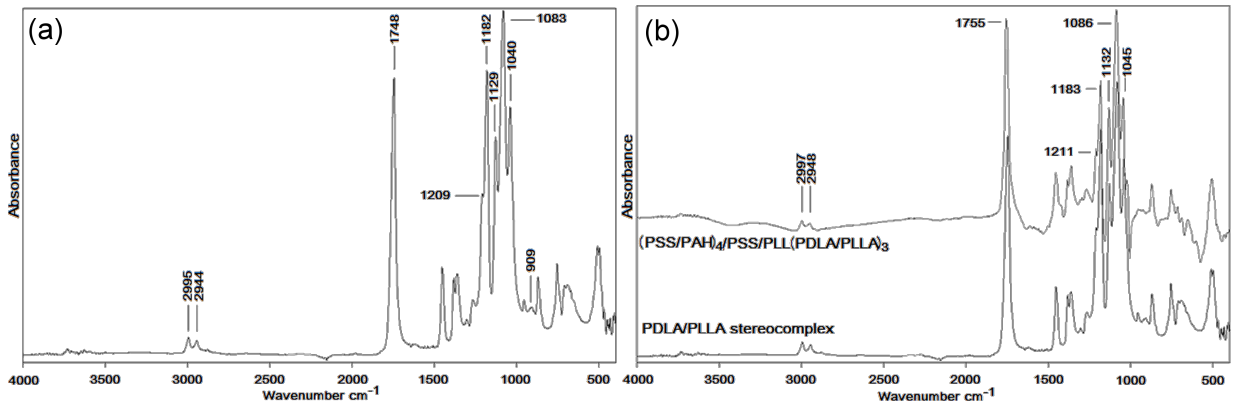

Figure 5: PDLA/PLLA stereocomplex spectrum by simple mixing (a) and comparison with PLA capsules with (PAH/PSS)$_4$/PSS/PLL precursor (b).

stereocomplex crystallite formation. The crystallization promotes the ν(C=O) spectral band at 1748 cm^{-1}, clearly visible in Figure 5a. Furthermore, two peaks at 909 and 1040 cm^{-1} can be identified, which are the characteristic bands of the PDLA/PLLA stereocomplex. C–O–C and C–C peaks were also visible at 1182 and 1209 cm^{-1}, respectively. Finally, bands at 2995 and 2944 cm^{-1} can be assigned to the CH_3 asymmetric stretching and CH_2 stretching, respectively, which confirmed the successful stereocomplex formation [49,50].

Figure 5b shows the comparison between the spectra of the PDLA/PLLA stereocomplex and the capsules with PDLA/PLLA stereocomplex as outer layers. In this case, PDLA and PLLA were not mixed but rather adsorbed onto the PEM capsules by the LBL technique. The characteristic peaks of the stereocomplex were detected, confirming the successful LBL deposition of PLAs on the polyelectrolyte capsule shell.

WXRD curves

Since the change in crystallinity is one of the differences that occurred during the formation of the stereocomplex polymer, WXRD was used to confirm the successful formation of the PLA stereocomplex modified microcapsules [51]. It can be seen in Figure 6 that PDLA and PLLA polymers have the same diffraction peaks in the spectrum which are at θ = 15.1°, 16.5°, and 18.1° and are the typical peaks of poly(lactic acid). The diffraction peaks of the PDLA/PLLA film are at θ = 12° and 22.1° (which is an overlap of the peaks at 20.8° and 24.1°). The peaks of the microcapsules situate at θ = 12°, 20.8° and 24.1°, which are uniquely assigned to PLA stereocomplex, demonstrating that the PLA microcapsules assembled are in the structure of stereocomplex [52].

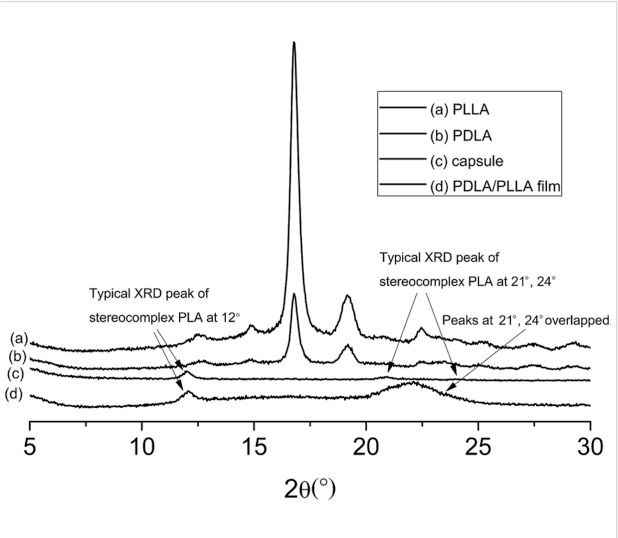

Figure 6: The WXRD spectra of PDLA, PLLA, PDLA/PLLA complex film and PDLA/PLLA complex microcapsules.

DSC curves

It is known that the melting point will shift to a higher degree once two enantiomeric polymers have formed their stereocomplex polymer due to the increased crystallinity. This is because the enantiomeric polymers attract each other with van der Waals force, creating a more complementary and rigid structure, which leads to a higher melting point.

In order to know whether the PDLA/PLLA complex had been formed after the PLA microcapsules were obtained, DSC was used to measure the melting points of four different samples (Figure 7). As described in the literature, the melting points for PDLA and PLLA are approximately 170 °C, which is very close to the melting points of the PLA polymers measured in our experiment [35]. The melting points for PDLA/PLLA films and microcapsules are 213.4 °C and 213.1 °C, respectively. This result indicated that the PLA complex microcapsules had been obtained during the LBL process as the melting point of the PDLA/PLLA stereocomplex is at approximately 220 °C [35].

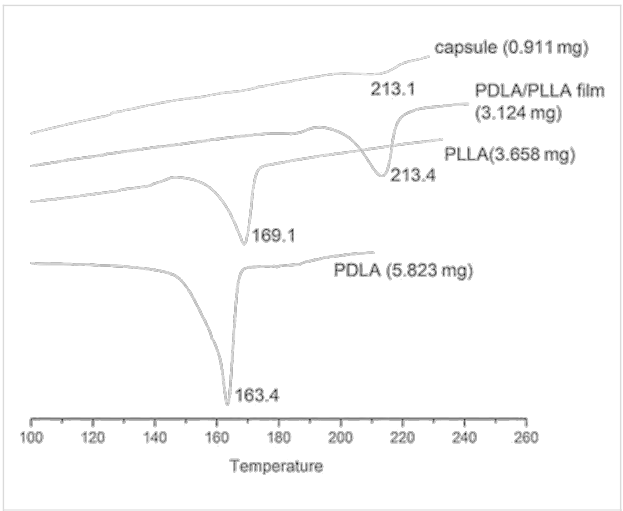

Figure 7: The DSC curves of PDLA, PLLA, PDLA/PLLA complex film and PDLA/PLLA complex microcapsules.

SEM measurements

A qualitative characterization was also carried out by SEM measurements. Figure 8 shows two different shell structures, specifically $(PSS/PAH)_4$/PSS/PLL (Figure 8a) and $(PSS/PAH)_4$/PSS/PLL$(PDLA/PLLA)_3$ (Figure 8b) on cores. The images clearly present different morphologies. A polyelectrolyte shell on cores, without PLA layers, shows a significant greater roughness when compared to the shell on cores with the addition of PLA. The shell with PLA layers, in fact, seems to be smoother and presents more gentle features with respect to the only PEM structure. Furthermore, from observation of Figure 8b, the shell can be considered rather homogeneous.

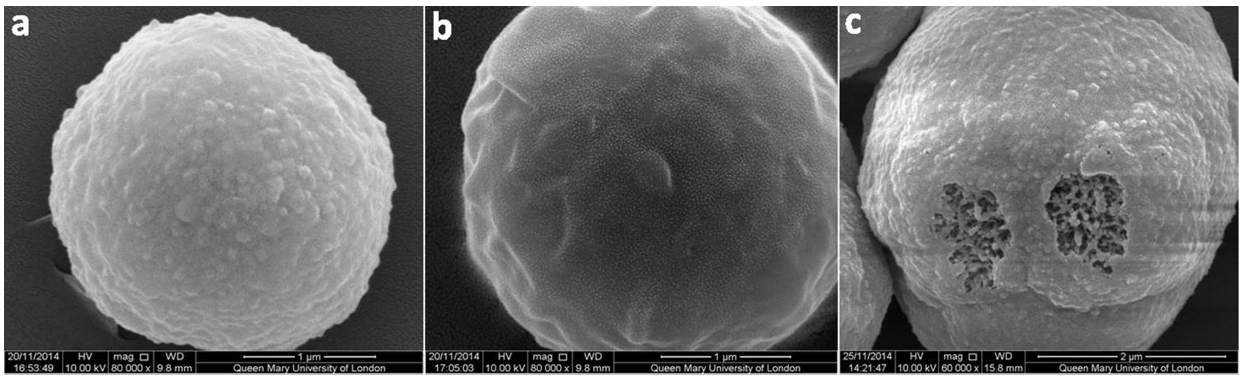

Figure 8: $(PSS/PAH)_4/PSS/PLL$ (a), $(PSS/PAH)_4/PSS/PLL(PDLA/PLLA)_3$ (b) and $(PSS/PAH)_4/PSS/PLL(PDLA/PLLA)_3/PSS$ (c) multilayer structures on cores.

Finally, Figure 8c confirms the effective LBL deposition. The multilayer structure $(PSS/PAH)_4/PSS/PLL(PDLA/PLLA)_3/PSS$ was built on calcium carbonate cores, and then moved from acetonitrile to water. A drop of the aqueous dispersion was let to evaporate at room temperature. In this sample, the structure of the calcium carbonate core is visible in some points where no shell is present. The different morphologies between the bare calcium carbonate core and the coated surface can be clearly noticed, confirming the successful assembly of the capsule shell. Since particles coated with $(PSS/PAH)_4/PSS/PLL(PDLA/PLLA)_3$ and $(PSS/PAH)_4/PSS/PLL(PDLA/PLLA)_3/PSS$ have different terminating layers, which usually have different surface morphologies, they look different in the SEM image. As demonstrated in previous studies, particle coating layers that terminate with PLA appear smoother [53], while those with PSS as the outmost layer appear rough [54].

TEM measurements

Hollow microcapsules with the multilayer structure $PLL(PDLA/PLLA)_{10}$ as the shell were characterized by TEM measurements. Figure 9a shows that most of the microcapsules look intact and flat, without evident defects, which indicates the proper core removal without damage. In addition, as can be seen in Figure 9b, the thickness of the $PLL/(PDLA/PLLA)_{10}$ multilayer is approximately 100 nm. Hence, the thickness of each PDLA/PLLA bilayer is estimated to be 10 nm. Interestingly, the thickness of the PLA layers on the silicon substrate (see Ellipsiometry) was not as thick as that of the microcapsules. A reasonable explanation is that for the microcapsules, the layers were adsorbed on $CaCO_3$ templates where the surfaces are more porous and able to accommodate more polymer within the pores of $CaCO_3$. In contrast, the smooth silicon substrate is less able to adsorb polymer molecules.

pH stability of microcapsules is indeed very important as some polyelectrolytes microcapsules are sensitive to pH change. We examined our PLA microcapsules at pH 1 and 13, and no obvious change was found after 30 min of treatment with hydrochloride acid and sodium hydroxide, meaning that these PLA stereocomplex microcapsules are stable in acidic or basic conditions. This is due to the lack of pH-sensitive functional groups on the PLA polymers.

Conclusion

PLA stereocomplex microcapsules were successfully fabricated by the LBL technique using $CaCO_3$ as a sacrificial template and

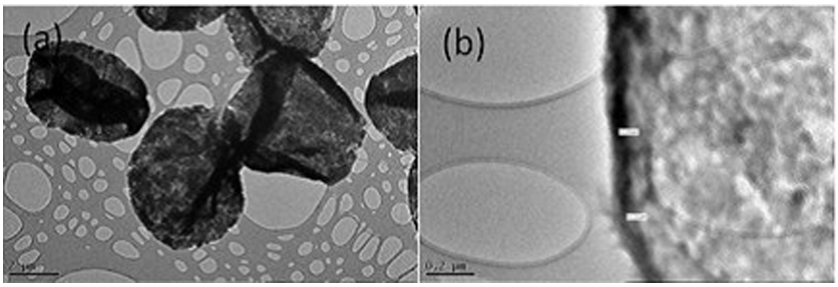

Figure 9: $PLL(PDLA/PLLA)_{10}$ hollow microcapsules (a) and magnification of the $PLL(PDLA/PLLA)_{10}$ hollow microcapsule shell (b).

enantiomeric PLAs with and without PEM precursor as the shell material. This is the first attempt at fabricating PLA stereocomplex microcapsules through a fully biocompatible process.

The kinetics study and the gravimetric measurements of PLA layer adsorption on flat substrates showed a successful deposition. The presence of the PEM precursor does not seem to have a particular effect on the growth of the PLA stereocomplex layers as there was no evident difference in the thickness and mass of the PLA. The change in the melting point and crystallinity of the obtained microcapsules indicated that the stereocomplex was obtained. The presence of the stereocomplex was also confirmed by the IR measurements. The SEM images showed a qualitative difference in the template surfaces coated with PLA and PEM layers respect to those coated only with PEM precursor. The characterization by TEM confirmed a successful template removal, resulting in intact, hollow capsules.

In conclusion, a novel, multilayer structure, involving both water- and non-water-soluble polymers, was successfully fabricated. The use of the highly suitable LBL technique as a simple and inexpensive assembly technique allowed for the fabrication of stable, hollow microcapsules as promising drug delivery carriers for biomedical applications. The combination of the physical and mechanical properties of such materials could make it possible to modify characteristic features, such as surface morphology, in order to modulate important delivery factors, like permeability and release rate.

Experimental

Materials

Sodium carbonate, calcium chloride, poly(styrene sulfonate) (PSS, MW 70,000), poly(allylamine hydrochloride) (PAH, MW 58,000), poly(L-lysine-hydrobomide) (MW = 30,000–70,000), L-lactide, D-lactide, tannous octoate, ethylenediaminetetraacetic acid (EDTA) were obtained from Sigma-Aldrich and used without any further purification. HPCL gradient grade acetonitrile, dichloromethane and diethyl ether were purchased from Fisher Chemical and were used as received. The water used in the experiments and for the preparation of solutions was purified by a Milli-Q system and had a resistance of 18.2 MΩ·cm.

Methods

Synthesis and characterization of PLLA and PDLA

Typically, 10 g of lactide and 0.5% tannous octoate (as a catalyst) were added to a conical flask. Then the conical flask was place into a vacuum oven at 180° after being sealed and the ring-opening polymerization lasted for 12 h. Afterwards, the crude polymer was dissolved in dichloromethane and precipitated in diethyl ether and this process was repeated three times to get rid of impurities and small molecules.

^{1}H NMR characterization was carried out using a Bruker AV spectrometer at a frequency of 400 MHz at room temperature. $CDCl_3$ and tetramethylsilane were used as solvents for the samples and internal reference, respectively. The sample concentrations were all fixed at 5 mg/mL.

The molecular weight and polydispersity index of synthesized PLAs were measured by GPC. THF was used as the eluent at a flow rate of 1.0 mL/min, while 2% of triethylamine was added to the solvent before dissolving the samples to avoid the tailing and adsorption phenomenon. The concentration of the polymer samples were all at 2 mg/mL.

Microcapsule preparation

Calcium carbonate microparticles (3 μm in diameter) were synthetized by mixing at 900 rpm with volumes of 0.33 M calcium chloride and 0.33 M sodium carbonate solutions according to the following reaction [55,56]:

$$CaCl_2 + Na_2CO_3 \rightarrow CaCO_3 + 2NaCl \qquad (1)$$

Calcium carbonate microparticles were used as sacrificial microtemplates for the assembly of polymeric microcapsules. As soon as the microparticles were synthetized, the adsorption steps (15 min in duration) of anionic PSS (2 mg/mL in 0.5 M NaCl) and cationic PAH (2 mg/ml in Milli-Q water) followed. After each adsorption step, three washings in Milli-Q water (1500 rpm for 1 min) were carried out. Once the four bilayer structures were deposited, one layer of PLL (5 mg/mL in Milli-Q water) was let to adsorb for 30 min on the top of the (PSS/PAH) multilayer, and again three washings followed. At this point, the coated templates were transferred in acetonitrile for the next PLA adsorption steps. PDLA and PLLA (5 mg/ml in 45 °C Acetonitrile) were let to adsorb for 1 h in acetonitrile at 45 °C, and each adsorption step was followed by three washing steps in acetonitrile. The process was carried out until three (PDLA/PLLA) bilayers were adsorbed, and the final structure $(PSS/PAH)_4/PSS/PLL(PDLA/PLLA)_3$ was obtained.

The same procedure was used for the fabrication of the multilayer structure $PLL(PDLA/PLLA)_n$ directly on calcium carbonate microtemplates. The obtained PLA-coated particles were then transferred back to water after washing off the organic solvent and the $CaCO_3$ cores were solubilized by 0.2 M EDTA solution. The hollow microcapsules were redispersed in water and were stored in a refrigerator at 4 °C.

Quartz crystal microbalance

A homemade quartz crystal microbalance (QCM) with a resonance frequency of 10 MHz was used for measurements. Before the multilayer deposition, the quartz electrodes were cleaned with piranha solution (H_2SO_4:30% H_2O_2 aqueous solution, 3:1 in volume) for 2 min, followed by two washing steps in pure water and a final drying step in nitrogen flux. The amount of polymer adsorbed, Δm, could be calculated by measuring the frequency decrease in the QCM, ΔF, using the following equation:

$$-\Delta F(\mathrm{Hz}) = 0.55\Delta m(\mathrm{ng}), \quad (2)$$

derived from Sauerbrey's equation [57],

$$-\Delta F(\mathrm{Hz}) = \frac{2F_0^2}{A\sqrt{\mu_q \rho_q}}\Delta m(\mathrm{ng}), \quad (3)$$

where F_0 is the resonance frequency of the quartz crystal oscillator, A is the area of the electrode (0.205 cm^2), ρ_q is the quartz density (2.648 g/cm^3), and μ_q is its shear modulus ($2.947 \cdot 10^{11}$ $g/cm \cdot s^2$).

The cleaned electrodes were immersed into aqueous solutions of PSS and PAH (2 mg/mL) for 15 min and PLL (5 mg/mL) for 30 min, then taken out, rinsed thoroughly with pure water, and dried with N_2. Since the quartz crystal surface is mostly negatively charged, PAH was deposited as the first layer.

The QCM was then immersed into acetonitrile solutions of PDLA and PLLA (5 mg/mL) for 1 h at 45 °C. Again, after removal from the PLA solutions, the coated electrodes were rinsed thoroughly with acetonitrile at 45 °C and dried with N_2. The deposition steps were repeated until the desired multilayers, with and without PEM precursor, were obtained.

Ellipsometry

The thickness of the PLA films deposited on silicon substrates was measured by a J. A. Woollam alpha-SE ellipsometer. A proper model should be chosen before the measurement to fit the given substrate and to minimize the error.

Before deposition of PLA, PLL was deposited on the silicon substrate to establish an interaction with PLA to form multilayers [45]. In detail, a 1 × 1 cm silicon substrate was immersed in a polylysine solution at a concentration of 5 mg/mL at 25 °C for 30 min. After the washing and drying steps, the substrate was alternately incubated in the PDLA/PLLA solutions for a similar deposition process. The measurement of thickness was recorded after the substrate was completely dried, after each deposition step.

ATR-FTIR measurements

Attenuated total reflection Fourier transform infrared spectroscopy (ATR-FTIR) spectra were obtained with a Bruker A225/Q device equipped with a Bruker MCT detector. Each spectrum was recorded with a total of 32 scans at a 4 cm^{-1} resolution. The PDLA/PLLA stereocomplex was obtained by mixing 1:1, 5 mg/mL solutions at 50 °C. The samples were prepared by pouring drops of the stereocomplex and the microcapsules on glass slides. The solvent was allowed to evaporate at room temperature for at least 48 h before measurement.

Differential scanning calorimetry

The melting point of different PLA samples was characterized by a Mettler Toledo DSC822e instrument. The polymer powder was first filled into a steel sample holder and then was sealed by immobilizing a cap before being put into the instrument.

Wide X-ray diffraction

Wide angle X-ray diffraction spectrometry was employed to analyze the crystallinity of the polymers with a Siemens D5000 X-ray powder diffractometer ranging from 5° to 30°.

Scanning electron microscope

SEM measurements were carried out with an Inspect FEI instrument from Oxford Instruments at an operation voltage of 10 kV. A drop of the sample solution was placed onto a glass wafer, dried overnight at room temperature, and sputtered with gold before analysis.

Transmission electron microscope

A JEOL 2010 TEM was applied to observe the inner morphology of PLA microcapsules as well as roughly measuring the thickness of their shell. The diluted microcapsule solution was pipetted onto a copper grid and left to dry in air overnight before measurement.

References

1. Decher, G. *Science* **1997,** *277,* 1232–1237. doi:10.1126/science.277.5330.1232
2. Decher, G.; Hong, J.-D. *Makromol. Chem., Macromol. Symp.* **1991,** *46,* 321–327. doi:10.1002/masy.19910460145
3. Decher, G.; Hong, J. D. *Ber. Bunsen-Ges. Phys. Chem.* **1991,** *95,* 1430–1434. doi:10.1002/bbpc.19910951122
4. Lvov, Y. M.; Decher, G. *Crystallogr. Rep.* **1994,** *39,* 628–647.
5. Caruso, F.; Niikura, K.; Furlong, D. N.; Okahata, Y. *Langmuir* **1997,** *13,* 3422–3426. doi:10.1021/la960821a

6. Lösche, M.; Schmitt, J.; Decher, G.; Bouwman, W. G.; Kjaer, K. *Macromolecules* **1998,** *31,* 8893–8906. doi:10.1021/ma980910p
7. De Geest, B. G.; De Koker, S.; Sukhorukov, G. B.; Kreft, O.; Parak, W. J.; Skirtach, A. G.; Demeester, J.; De Smedt, S. C.; Hennink, W. E. *Soft Matter* **2009,** *5,* 282–291. doi:10.1039/B808262F
8. Sukhorukov, G. B.; Möhwald, H. *Trends Biotechnol.* **2007,** *25,* 93–98. doi:10.1016/j.tibtech.2006.12.007
9. Pastorino, L.; Erokhina, S.; Erokhin, V. *Curr. Org. Chem.* **2013,** *17,* 58–64. doi:10.2174/138527213805289088
10. Antipov, A. A.; Sukhorukov, G. B. *Adv. Colloid Interface Sci.* **2004,** *111,* 49–61. doi:10.1016/j.cis.2004.07.006
11. Pastorino, L.; Dellacasa, E.; Noor, M. R.; Soulimane, T.; Bianchini, P.; D'Autilia, F.; Antipov, A.; Diaspro, A.; Tofail, S. A. M.; Ruggiero, C. *PLoS One* **2014,** *9,* e112192. doi:10.1371/journal.pone.0112192
12. Feng, Z.; Wang, Z.; Gao, C.; Shen, J. *Adv. Mater.* **2007,** *19,* 3687–3691. doi:10.1002/adma.200700541
13. Ochs, C. J.; Such, G. K.; Yan, Y.; van Koeverden, M. P.; Caruso, F. *ACS Nano* **2010,** *4,* 1653–1663. doi:10.1021/nn9014278
14. Usov, D.; Sukhorukov, G. B. *Langmuir* **2010,** *26,* 12575–12584. doi:10.1021/la1018949
15. Stockton, W. B.; Rubner, M. F. *Macromolecules* **1997,** *30,* 2717–2725. doi:10.1021/ma9700486
16. Sunkhishvili, S. A.; Granick, S. *J. Am. Chem. Soc.* **2000,** *122,* 9550–9551. doi:10.1021/ja002410t
17. Kozlovskaya, V.; Ok, S.; Sousa, A.; Libera, M.; Sukhishvili, S. A. *Macromolecules* **2003,** *36,* 8590–8592. doi:10.1021/ma035084l
18. Xu, L.; Zhu, Z.; Sukhishvili, S. A. *Langmuir* **2011,** *27,* 409–415. doi:10.1021/la1038014
19. Zhang, M.; Su, L.; Mao, L. *Carbon* **2006,** *44,* 276–283. doi:10.1016/j.carbon.2005.07.021
20. Al-Hariri, L. A.; Reisch, A.; Schlenoff, J. B. *Langmuir* **2011,** *27,* 3914–3919. doi:10.1021/la104109f
21. Lvov, Y.; Haas, H.; Decher, G.; Möhwald, H.; Mikhailov, A.; Mtchedlishvily, B.; Morgunova, E.; Vainshtein, B. *Langmuir* **1994,** *10,* 4232–4236. doi:10.1021/la00023a052
22. Ladam, G.; Schaaf, P.; Decher, G.; Voegel, J.-C.; Cuisinier, F. J. G. *Biomol. Eng.* **2002,** *19,* 273–280. doi:10.1016/S1389-0344(02)00031-X
23. Lvov, Y.; Ariga, K.; Kunitake, T. *Chem. Lett.* **1994,** *23,* 2323–2326. doi:10.1246/cl.1994.2323
24. Lvov, Y.; Ichinose, I.; Ariga, K.; Kunitake, T. *J. Am. Chem. Soc.* **1995,** *117,* 6117–6123. doi:10.1021/ja00127a026
25. Ariga, K.; McShane, M.; Lvov, Y. M.; Ji, Q.; Hill, J. P. *Expert Opin. Drug Delivery* **2011,** *8,* 633–644. doi:10.1517/17425247.2011.566268
26. Komatsu, T.; Qu, X.; Ihara, H.; Fujihara, M.; Azuma, H.; Ikeda, H. *J. Am. Chem. Soc.* **2011,** *133,* 3246–3248. doi:10.1021/ja1096122
27. Ichinose, I.; Fujiyoshi, K.; Mizuki, S.; Lvov, Y.; Kunitake, T. *Chem. Lett.* **1996,** *25,* 257–258. doi:10.1246/cl.1996.257
28. Sohling, U.; Schouten, A. J. *Langmuir* **1996,** *12,* 3912–3919. doi:10.1021/la950433t
29. Nagasaki, Y.; Okada, T.; Scholz, C.; Iijima, M.; Kato, M.; Kataoka, K. *Macromolecules* **1998,** *31,* 1473–1479. doi:10.1021/ma971294k
30. Zeng, J.; Xu, X.; Chen, X.; Liang, Q.; Bian, X.; Yang, L.; Jing, X. *J. Controlled Release* **2003,** *92,* 227–231. doi:10.1016/S0168-3659(03)00372-9
31. Akagi, T.; Fujiwara, T.; Akashi, M. *Langmuir* **2014,** *30,* 1669–1676. doi:10.1021/la404162h
32. Ding, A. G.; Shenderova, A.; Schwendeman, S. P. *J. Am. Chem. Soc.* **2006,** *128,* 5384–5390. doi:10.1021/ja055287k
33. Lim, J. Y.; Hansen, J. C.; Siedlecki, C. A.; Hengstebeck, R. W.; Cheng, J.; Winograd, N.; Donahue, H. J. *Biomacromolecules* **2005,** *6,* 3319–3327. doi:10.1021/bm0503423
34. Kharlampieva, E.; Kozlovskaya, V.; Tyutina, J.; Sukhishvili, S. A. *Macromolecules* **2005,** *38,* 10523–10531. doi:10.1021/ma0516891
35. Serizawa, T.; Yamashita, H.; Fujiwara, T.; Kimura, Y.; Akashi, M. *Macromolecules* **2001,** *34,* 1996–2001. doi:10.1021/ma001705o
36. Kenawy, E.-R.; Bowlin, G. L.; Mansfield, K.; Layman, J.; Simpson, D. G.; Sanders, E. H.; Wnek, G. E. *J. Controlled Release* **2002,** *81,* 57–64. doi:10.1016/S0168-3659(02)00041-X
37. Makadia, H. K.; Siegel, S. J. *Polymers (Basel, Switz.)* **2011,** *3,* 1377–1397. doi:10.3390/polym3031377
38. Matsusaki, M.; Ajiro, H.; Kida, T.; Serizawa, T.; Akashi, M. *Adv. Mater.* **2012,** *24,* 454–474. doi:10.1002/adma.201103698
39. Serizawa, T.; Hamada, K.-i.; Kitayama, T.; Katsukawa, K.-i.; Hatada, K.; Akashi, M. *Langmuir* **2000,** *16,* 7112–7115. doi:10.1021/la000241k
40. Hamada, K.-i.; Serizawa, T.; Kitayama, T.; Fujimoto, N.; Hatada, K.; Akashi, M. *Langmuir* **2001,** *17,* 5513–5519. doi:10.1021/la0101898
41. Serizawa, T.; Hamada, K.-i.; Kitayama, T.; Fujimoto, N.; Hatada, K.; Akashi, M. *J. Am. Chem. Soc.* **2000,** *122,* 1891–1899. doi:10.1021/ja9913535
42. Li, M.; Rouaud, O.; Poncelet, D. *Int. J. Pharm.* **2008,** *363,* 26–39. doi:10.1016/j.ijpharm.2008.07.018
43. Sinha, V. R.; Bansal, K.; Kaushik, R.; Kumria, R.; Trehan, A. *Int. J. Pharm.* **2004,** *278,* 1–23. doi:10.1016/j.ijpharm.2004.01.044
44. Kim, B.-S.; Park, S. W.; Hammond, P. T. *ACS Nano* **2008,** 386–392. doi:10.1021/nn700408z
45. Ogawa, Y.; Arikawa, Y.; Kida, T.; Akashi, M. *Langmuir* **2008,** *24,* 8606–8609. doi:10.1021/la800788e
46. Heuberger, R.; Sukhorukov, G.; Vörös, J.; Textor, M.; Möwald, H. *Adv. Funct. Mater.* **2005,** *15,* 357–366. doi:10.1002/adfm.200400063
47. Porcel, C.; Lavalle, P.; Ball, V.; Decher, G.; Senger, B.; Voegel, J.-C.; Schaaf, P. *Langmuir* **2006,** *22,* 4376–4383. doi:10.1021/la053218d
48. Zhang, J.; Tashiro, K.; Tsuji, H.; Domb, A. J. *Macromolecules* **2007,** *40,* 1049–1054. doi:10.1021/ma061693s
49. Zhang, J.; Sato, H.; Tsuji, H.; Noda, I.; Ozaki, Y. *Macromolecules* **2005,** *38,* 1822–1828. doi:10.1021/ma047872w
50. Chen, C.-C.; Chueh, J.-Y.; Tseng, H.; Huang, H.-W.; Lee, S.-Y. *Biomaterials* **2003,** *24,* 1167–1173. doi:10.1016/S0142-9612(02)00466-0
51. Kida, T.; Mouri, M.; Akashi, M. *Angew. Chem.* **2006,** *118,* 7696–7698. doi:10.1002/ange.200602116
52. Hasırcı, V.; Lewandrowski, K.; Gresser, J. D.; Wise, D. L.; Trantolo, D. J. *J. Biotechnol.* **2001,** *86,* 135–150. doi:10.1016/S0168-1656(00)00409-0
53. Kondo, K.; Kida, T.; Ogawa, Y.; Arikawa, Y.; Akashi, M. *J. Am. Chem. Soc.* **2010,** *132,* 8236–8237. doi:10.1021/ja1020537
54. Lei, M.; Tang, W. H.; Cao, L. Z.; Li, P. G.; Yu, J. G. *J. Cryst. Growth* **2006,** *294,* 358–366. doi:10.1016/j.jcrysgro.2006.06.029
55. Volodkin, D. V.; Larionova, N. I.; Sukhorukov, G. B. *Biomacromolecules* **2004,** *5,* 1962–1972. doi:10.1021/bm049669e
56. Volodkin, D. V.; Petrov, A. I.; Prevot, M.; Sukhorukov, G. B. *Langmuir* **2004,** *20,* 3398–3406. doi:10.1021/la036177z
57. Sauerbrey, G. *Z. Phys. A* **1959,** *155,* 206–222. doi:10.1007/BF01337937

BEILSTEIN JOURNAL OF NANOTECHNOLOGY

3D solid supported inter-polyelectrolyte complexes obtained by the alternate deposition of poly(diallyldimethylammonium chloride) and poly(sodium 4-styrenesulfonate)

Eduardo Guzmán[*1,§], Armando Maestro[2], Sara Llamas[3], Jesús Álvarez-Rodríguez[4], Francisco Ortega[1], Ángel Maroto-Valiente[4] and Ramón G. Rubio[*1,5,¶]

Full Research Paper

Open Access

Address:
[1]Departamento de Química Física I-Facultad de Ciencias Químicas, Universidad Complutense de Madrid, Ciudad Universitaria s/n, 28040 Madrid, Spain, [2]Department of Physics - Cavendish Laboratory, University of Cambridge, J. J. Thomson Avenue, CB3 0HE Cambridge, United Kingdom, [3]Istituto per l'Energetica e le Interfasi - U.O.S. Genova, Consiglio Nazionale delle Ricerche, Via De Marini 6, 16149 Genova, Italy, [4]Departamento de Química Inorgánica y Química Técnica - Facultad de Ciencias Universidad Nacional de Educación a Distancia, C/ Senda del Rey 9, 28040 Madrid and [5]Instituto Pluridisciplinar, Universidad Complutense de Madrid Avda. Juan XXIII 1, 28040 Madrid, Spain

Email:
Eduardo Guzmán[*] - eduardogs@quim.ucm.es; Ramón G. Rubio[*] - rgrubio@quim.ucm.es

* Corresponding author
§ Tel: +34 91 3944107; Fax: +34 91 3944135
¶ Tel: +34 91 3944123; Fax: +34 91 3944135

Keywords:
charge compensation; hydration; polyelectrolyte multilayers; stratification; swelling

Beilstein J. Nanotechnol. **2016,** *7,* 197–208.
doi:10.3762/bjnano.7.18

Received: 21 September 2015
Accepted: 19 January 2016
Published: 05 February 2016

This article is part of the Thematic Series "Organized films".

Guest Editor: M. Canepa

Abstract

This work addresses the formation and the internal morphology of polyelectrolyte layers obtained by the layer-by-layer method. A multimodal characterization showed the absence of stratification of the films formed by the alternate deposition of poly(diallyldimethylammonium chloride) and poly(sodium 4-styrenesulfonate). Indeed the final organization might be regarded as three-dimensional solid-supported inter-polyelectrolyte films. The growth mechanism of the multilayers, followed using a quartz crystal microbalance, evidences two different growth trends, which show a dependency on the ionic strength due to its influence onto the polymer conformation. The hydration state does not modify the multilayer growth, but it contributes to the total adsorbed mass of the film. The water associated with the polyelectrolyte films leads to their swelling and plastification. The use of X-ray photoelectron spectroscopy has allowed for deeper insights on the internal structure and composition of the polyelectrolyte multilayers.

Introduction

The new requirements of science and technology have created an increasing interest for the fabrication of materials with reduced dimensionality for their application in several fields, including optics, electronics, coatings and biomaterials (drug delivery and tissue engineering). In order to create the aforementioned materials, the development of new bottom-up techniques, which allow one to control the properties and structure of the materials at the sub-micrometric scale, has become necessary [1-3]. Among these techniques, the layer-by-layer (LbL) self-assembly has become probably one of the most promising [4,5], due to its high versatility and low costs [6,7]. Furthermore, a very broad range of compounds can be assembled through LbL: synthetic polyelectrolytes, biopolymers – such as peptides, proteins and nucleic acids – colloidal particles, carbon nanotubes, and/or microgels [8-10], which confers to this method an almost unlimited chemical versatility. Even though the method frequently makes use of electrostatic interactions, the multilayers can also be built based on other intermolecular forces, for instance hydrogen bonds, acid–base reactions, covalent cross-linking and host–guest interactions [11,12].

Polyelectrolyte multilayers can be considered an example of non-equilibrium materials, because the corresponding soluble or insoluble complexes are more stable from the thermodynamic point of view [13]. Thus, the structure and properties of the final film are expected to be strongly dependent on the experimental protocol followed for its fabrication. Many variables have strong influence on the final structure of LbL films, hence to know their role during film formation is critical for controlling the structure and physicochemical properties of the films [13]. Among the most relevant variables are the charge density of the molecules, the concentration of the solution used, ionic strength, solvent quality for the molecules, pH, and temperature [13].

In the last years, a lot of theoretical and experimental research effort has been spent to understand the different growth mechanisms that appear during the alternate deposition of the layers, the quantification of the adsorbed amount of material in each adsorption cycle, as well as the developments of technological applications for the manufactured systems [3]. Despite the extensive research, certain aspects that play an important role in the applications for these systems still remain unclear [14]. Among these aspects the internal composition of the multilayers (ionic composition and water content), the internal structure of the films and their mechanical properties are probably the most important [15-19].

This work studies polyelectrolyte multilayers formed by poly(diallyldimethylammonium chloride) (PDADMAC) and poly(sodium 4-styrenesulfonate) (PSS) from solutions of different ionic strength [19-22]. This system is well-studied in literature and can be considered as a paradigm for the study of the multilayer behavior even though their practical applications are limited [16,19,23-25]. We have performed a study to analyze the effect of the ionic strength on the internal structure and composition of polyelectrolyte multilayers with a variety of techniques. Following this approach, we have contributed to solve some controversial aspects related to the role and distribution of the ions and water within the films, i.e., the internal composition of the films, as well as to the internal morphology of the films, i.e., the absence of stratification. Furthermore, the comparative study of multilayers as prepared and after drying has allowed us to deepen the understanding about the physicochemical foundations that govern the formation and properties of polyelectrolyte films.

Experimental

Chemicals

The poly(sodium 4-styrenesulfonate) (PSS) used had a molecular weight of 70 kDa. The poly(diallyldimethylammonium chloride) (PDADMAC) had a molecular weight in the range of 200–350 kDa. Both polymers were purchased from Sigma-Aldrich (Germany) and used without further purification. The ionic strength of the solutions was controlled by adding NaCl (Sigma-Aldrich, purity > 99.9%). The water used for all the experiments was of Milli-Q quality (Millipore RG model). All the experiments were done at (298.1 ± 1.0) K.

Layer-by-layer assembly

In a similar manner as described in [8], the multilayers were formed from polyelectrolyte solutions of different ionic strengths, *I*. Between the adsorption of successive layers, the multilayers were rinsed with the solvent used for preparing the polyelectrolyte solutions. The rinsing process removed the polymer chains that were not strongly adsorbed. Thus the fabrication of the films follows a typical adsorption sequence polycation–rinsing–polyanion–rinsing. All the adsorption steps were performed under static conditions, without any stirring in the adsorption cell.

For some of the studies performed, the drying of the multilayers was carried out between the rinsing and the deposition of the second polyelectrolyte layer following the above described procedure. For this purpose, the films were exposed to highly purified nitrogen flow after each adsorption–rinsing cycle.

Dissipative quartz crystal microbalance (QCM-D)

We have used a dissipative quartz-crystal microbalance (QCM-D) from KSV (Model QCM Z-500, Finland) for the study of the

wet films, and an impedance/gain phase analyzer from Hewlett-Packard (HP4194A, U.S.A.) coupled to a QCM electrode for the study of the dry films. In similar manner as described in [19], the gold coated AT-cut quartz crystals were cleaned with piranha solution (70% H_2SO_4/30% H_2O_2) over a period of thirty minutes and then thoroughly rinsed with pure water. The characteristic frequency of the quartz crystal in vacuum was $f_0 \approx 5$ MHz. A self-assembled monolayer of sodium 3-mercapto-1-propanesulfonate was initially formed on the surface of the gold electrode of the quartz crystal, in order to obtain a charged substrate [19]. QCM-D provided the impedance spectra of the crystal for the fundamental resonance frequency and for its odd overtones, ν, up to 11 [26].

Ellipsometry

An imaging null-ellipsometer from Nanofilm (Model EP^3, Germany) was used; all the experiments were carried out on a solid–liquid cell at a fixed angle of 60°. Silicon wafers (Siltronix, France) were used as the substrates. In order to obtain the ellipsometric thickness, h_{op}, and the refractive index, n_f, of the layers a four layer model has been used, as in a previous work [20]. From the results obtained from ellipsometry it was possible to calculate the mass adsorbed on the substrate, Γ, using De Feijter's equation [27],

$$\Gamma = \frac{\left(n_f - n_l\right) h_{op}}{\left(dn/dc\right)_T}, \quad (1)$$

where n_f and n_l, are the refractive index of the film and solvent, respectively. The $(dn/dc)_T$ values measured for PDADMAC and PSS are 0.213 and 0.178 cm^3/g, respectively [20].

X-ray reflectivity

The reflectivity experiments were performed using silicon as substrates. X-ray experiments were made in a conventional diffractometer X'Pert Pro MRD from Panalytical (Netherlands). The analysis of X-ray reflectivity data was made using the software Package Parrat 32 from HMI (Berlin, Germany).

X-ray photoelectron spectroscopy

Surface chemical analysis of the samples was carried out by X-ray photoelectron spectroscopy (XPS) by using an ESCAPROBE P (Omnicron) spectrometer. The measurements were carried out with a Mg Kα (1253.6 eV) source operated at 150 W. The residual pressure was lower than 10^{-7} Pa during the collection of the spectra. The hemispherical analyzer EA 125 operated in constant analyzer energy mode and the pass energy was switched to 20 eV for transitions C 1s, Cl 2p, N 1s, Na 1s, O 1s and S 2p. Under these conditions the FWHM of the Ag $3d_{5/2}$ peak at 368.1 eV was 1.0 eV. Angle resolved spectra were collected at five sequentially increased electron emission angles to the normal of 10° from 0 to 40°, without modification of the source-to-detector configuration. This methodology provides information in depth equal to the cosine of the angle between the surface normal and the analysis direction. Data analysis of core level XPS spectra was conducted with Casa-XPS software, Relative sensitivity factors (RSF) employed: C 1s (1); Cl 2p (1.48); N 1s (1.77); Na 1s (7.99); O 1s (2.85); and S 2p (1.25).

Surface potential measurements

A Kelvin probe from Trek, Inc. (U.K.), located approximately 2 mm above the substrate, was used in order to measure the surface potential (ΔV) of the multilayer in the dry state after each cycle of deposition. The surface potential measurements are referenced to the value of ΔV of the bare solid–air interface.

Atomic force microscopy

AFM measurements were performed in air at room temperature using a Nanoscope III (Digital Instruments, USA) in the tapping mode. A silicon tip, model RTESP (Veeco Instrument Inc, USA), was used for the measurements. The AFM images were processed using the software WSxM from Nanotec Electronica [28].

Results and Discussion

Wet films vs dry films

The growth of polyelectrolyte multilayers of (PDADMAC + PSS)$_N$ was followed by monitoring the frequency shift (Δf) of the QCM-D normalized by the overtone number (ν), $-\Delta f/\nu$, as a function of the number of bilayers (N) [19,29]. It is well known that the adsorbed mass calculated using Sauerbrey's equation underestimates the real mass of viscoelastic films [30-32]. Figure 1 shows the frequency shift as a function of N for wet and dry multilayers (PDADMAC + PSS)$_N$. The differences between wet and dry multilayers are consequence of differences in the preparation method (see section "Layer-by-layer assembly"). The introduction of a drying step is expected to have a strong effect on the multilayer growth.

From the results shown in Figure 1 it is possible to evaluate different aspects of the behavior of the multilayers related mainly to their growth. The adsorbed mass increases (higher decrease in the resonance frequency of the overtones) with the ionic strength, I, in both wet and dry films. This is explained considering the conformational changes of the polyelectrolyte chains due to the modification of the ionic strength [19]. In fact, the increase of I leads to a screening of the charge of the chains that leads to the change from an extended to a coiled conformation. Thus the number of molecules that can be adsorbed to coat the surface increases and consequently the surface coverage increases. Furthermore, the increase in I provokes the transition

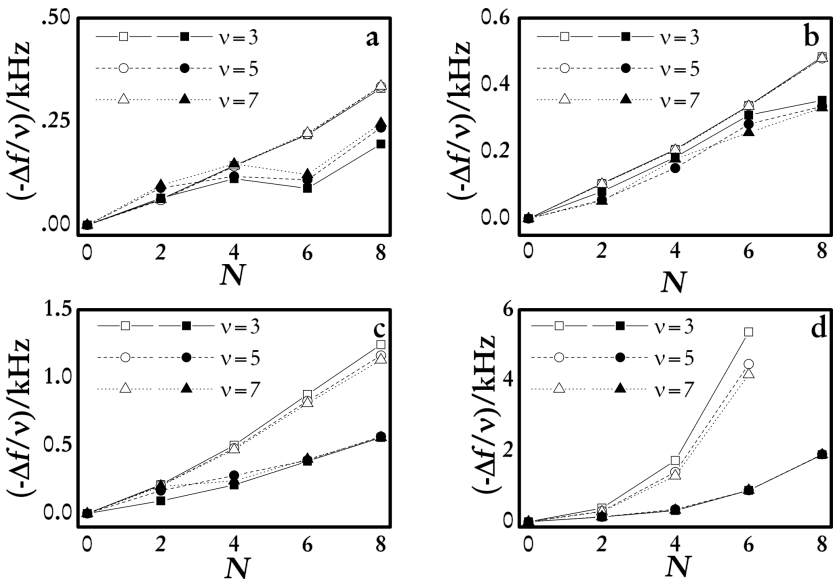

Figure 1: The reduced frequency of the quartz crystal for the different overtones measured (overtones ν = 3, 5 and 7) as a function of *N* for multilayers (PDADMAC + PSS)$_N$ formed from solutions with different ionic strength. (a) 0.05 M (b) 0.10 M (c) 0.30 M (d) 1.00 M. In all the plots: Wet multilayers (open symbols) and dry multilayers (solid symbols).

from a linear dependence of the mass on *N* to a non-linear one, in accordance with previous results [19,23-25]. High values of *I* lead to the adsorption of coiled chains, increasing the area available to the adsorption in the successive deposition cycles and consequently the growth dependence on *N* becomes supralinear. This is also associated with an increase of roughness of the films (roughness data for different (PDADMAC + PSS)$_N$ are reported in Table 1) as it can also be seen in the AFM image analysis in Figure 2.

Table 1: Roughness for (PDADMAC + PSS)$_N$ multilayers at different ionic strengths (dry films).

c_{NaCl} [*M*]	*N*	roughness [nm]	technique
	3	6 ± 2	X-ray reflectivity
	6	3.8 ± 0.5	AFM
	6	6 ± 1	X-ray reflectivity
0.10	9	4 ± 1	X-ray reflectivity
	12	5 ± 1	X-ray reflectivity
	15	7.8 ± 0.5	AFM
	15	6 ± 2	X-ray reflectivity
0.50	12	12.1 ± 0.5	neutron reflectivity
1.00	7	17.8 ± 0.5	AFM

The AFM images (Figure 2) show a more inhomogeneous topology and a higher roughness for the film built using solutions with high ionic strength. Recent works have shown that the increase of roughness is deeply related to the non-linear growth [21,22,30,31,33]. But this influence of the increasing roughness on the transition between different growth mechanisms does not allow us to rule out the contributions associated with inter-diffusion of the polymers [10,34,35]. However, a quantitative discussion of the potential effect of the inter-diffusion to the multilayer growth on the basis of equilibrium results is difficult, and no additional discussion related to this aspect will be included.

It is worth mentioning that the growth trend, i.e., the dependency of the adsorbed mass on *N*, is not modified by the drying of the films. This allows us to suggest that the growth trend is determined exclusively by the specific interactions occurring in the system and the polymer conformation, without effects due to the hydration/swelling phenomena associated with the uptake/release of water.

Even though the *N* dependence of the adsorbed mass is not changed by the drying process, other aspects are strongly modified by the film drying, among them the most evident is the adsorbed mass (see Figure 1). Because the QCM-D detects both the polymer adsorbed and the hydration water, drying of the films reduces the adsorbed mass (lower resonance frequency shift). The drying process makes the polymer matrix shrink, which is critically related to the mechanical properties of the film. In fact, from the separation of the values of $-\Delta f/\nu$ for the different overtones found in the QCM-D results [30-32], it is possible to predict the existence of modifications in the mechanical behavior of the films due to the drying process.

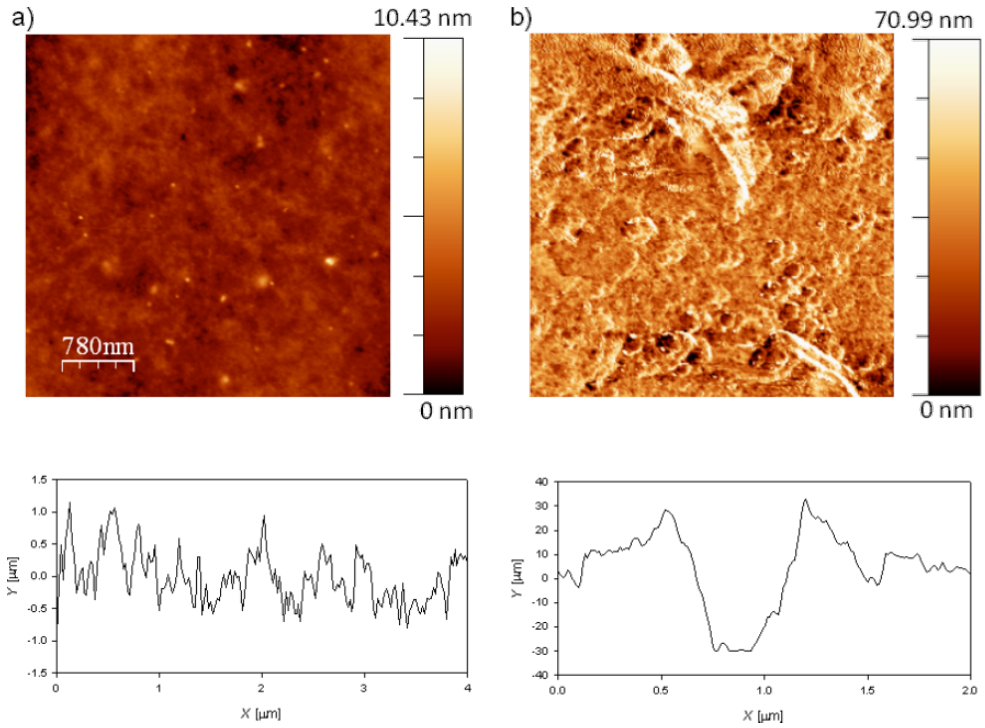

Figure 2: AFM images and height profiles taken along the diagonal of the images for multilayers (PDADMAC + PSS)$_N$ built using solutions with two different ionic strength. (a) 0.10 M (N = 15). (b) 1.00 M (N = 7).

The dependence of the normalized frequency on the number of the overtone allows us to make a qualitative discussion about the viscoelastic character of the layers [36]. The drying process leads to the collapse of the different overtones of the quartz crystal in a master curve. This is related to the transition from a viscoelastic behavior (lacked overlapping of the overtones) to a rigid one (Sauerbrey limit where the overtones define a master curve) [31]. Thus, it is possible to ascribe this change in the mechanical behavior of the layers to the release of water that leads to an increase of the ionic pairing and consequently to an increased rigidity of the multilayers in agreement with the results by Nolte and co-workers [37]. The presence of water induces a plastification of the film with the corresponding effect on the mechanical response of the multilayer. In addition, the increase of the ionic strength increases the viscoelastic character of the films, which is correlated to the formation of layers with more swollen chains [19]. It is expected that these swollen chains trap higher amounts of water, which leads to the most important plastifying effects [19]. We have calculated the water content using QCM-D and ellipsometry data following the method proposed by Vöros [19,38-41]. Figure 3 shows the water weight fraction, X_w, for (PDADMAC + PSS)$_N$ films.

The water content decreases as N increases, which agrees with the behavior reported for other films [42,43]. This behavior is due to the fact that the first layers adsorbed form an inhomogeneous film, forming isolated island that coalesce as N increases [33,44,45]. This mechanism is also supported by the theoretical considerations based on the electrostatic interaction of charged objects onto opposite charged surfaces [46]. The results in Figure 3 point out that X_w slightly increases with ionic strength, as expected from the adsorption of more hydrated chains at higher values of ionic strength. Multilayers with high N present

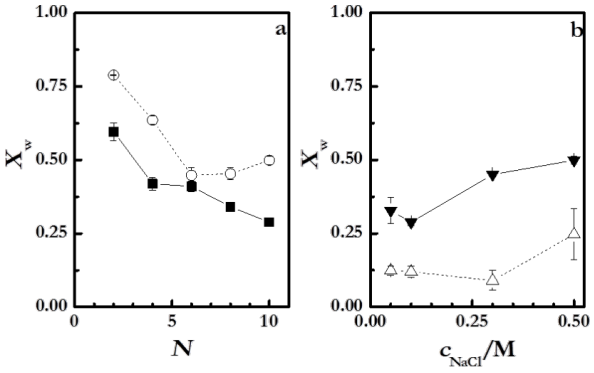

Figure 3: (a) Weight fraction of water as a function of N, obtained following the methodology proposed by Vöros [38], for (PDADMAC + PSS)$_N$ films formed at two different ionic strengths: 0.10 M (solid squares) and 0.50 M (open circles). (b)) Weight fraction of water as a function of the ionic strength for (PDADMAC + PSS)$_N$ films: obtained through the methodology proposed by Vöros [38] (solid triangles) and through XPS (open triangles). The solid lines are to guide the eye.

always average values of water content around the 20–60% of the total weight of the multilayer. Figure 3b shows that XPS technique leads to the same qualitative trend. Even though, the water content is not directly obtained from XPS measurements, it is possible to estimate it as

$$[H_2O] = [\text{oxygen}] - 3 \cdot [\text{sulfur}]. \quad (2)$$

It is worth mentioning that the water content estimates from XPS refer to the water molecules that remain trapped in the multilayer after the drying process [47]. This allows for explaining the differences observed in the results obtained using the two procedures described above (see Figure 3b). The residual water that remains in the multilayer is more or less half of the quantity that exists under wet conditions, and it is related to the increase of the relative proportion of counterions in the multilayer with ionic strength as will be discussed in the following.

The swelling ratio of the films can be calculated following Schönhoff et al. [48] according to

$$S = \frac{h_{\text{op}} - h_{\text{X-ray}}}{h_{\text{op}}}, \quad (3)$$

where h_{op} is the thickness calculated from ellipsometry for wet films, and $h_{\text{X-ray}}$ the value obtained using X-ray reflectivity for dry multilayers. The results are shown in Figure 4.

For multilayers obtained at an ionic strength of 0.10 M, S is in the range of 20–35% and slightly increases with N, which is qualitatively similar to what was found by Dodoo and co-workes [49]. This is in agreement with a transition from an intrinsic compensation to an extrinsic one with the increase of N [50,51] that has a strong influence on the viscoelastic character of the film (Figure 1) [36] due to the reduction of the ionic cross-linking between chains in adjacent layers associated with the transition between intrinsic to extrinsic compensation. Table 2 reports the swelling ratio for multilayers formed at two different ionic strengths with $N = 12$.

The degree of swelling of the multilayers can be related to the rigidification of the films upon drying (Figure 1). It is expected that films with low degree of swelling exhibit a strong ionic cross-linking under hydrated conditions with their rigidity almost unaffected during the drying process. On the other side, the films with the higher degree of swelling (under conditions of high ionic strength) are expected to exhibit a low level of ionic cross-linking, which leads to their rigidification upon dehydration. This is in accordance with the results obtained by Secrist and Nolte for spin-coated multilayers of (poly(allylamine) + poly(acrylic acid))$_N$ [52].

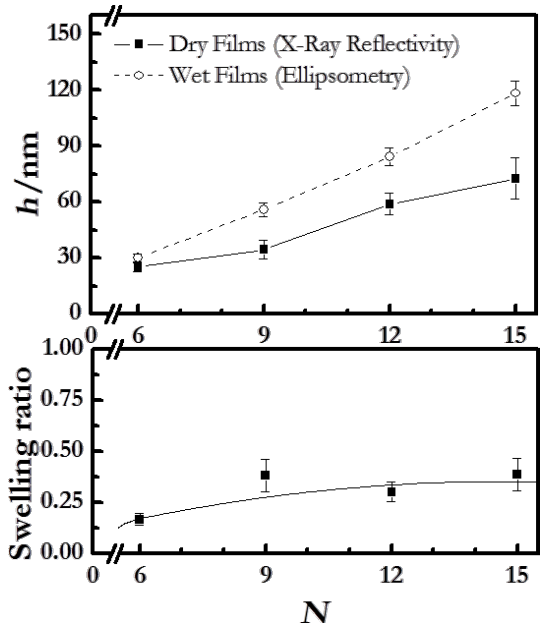

Figure 4: (a) Multilayer thickness of (PDADMAC + PSS)$_N$ films formed at an ionic strength of 0.10 M as a function of N, measured under wet conditions (ellipsometry) and dry conditions (X-ray reflectivity). (b) Swelling ratio as a function of N for the multilayers of part a. The lines are to guide the eye.

Table 2: Thicknesses (ellipsometry (wet films), h_{op}, and X-ray reflectivity (dry films), $h_{\text{X-ray}}$) and swelling ratio, S, for (PDADMAC + PSS)$_N$ multilayers (N = 12) formed from solutions with two different ionic strengths.

c_{NaCl} [M]	wet films h_{op} [nm]	dry films $h_{\text{X-ray}}$ [nm]	S
0.10	84 ± 5	59 ± 3	0.30 ± 0.05
0.50	316 ± 5	95 ± 13	0.67 ± 0.03

Internal structure: evidence of a non-stratified system

X-ray photoelectron spectroscopy (XPS) provides valuable information about the surface chemistry of the samples. A method to provide depth profiles (with different penetration depths, x) is angle-resolved XPS. In this method the electron path through the solid, i.e., three times the inelastic mean free path, is related to the change of the emission angle, φ,

$$x = 3\lambda \cdot \cos\varphi. \quad (4)$$

At higher emission angles (with respect to the normal angle) a higher surface sensitivity is achieved. In order to obtain insights

on the internal structure of the LbL films, we collected spectra at different emission angles while recording two different element representing each of the polymers, nitrogen for PDADMAC and sulfur for PSS. Thus, XPS can reveal information about a lamellar or disordered structure of the samples. Figure 5a and Figure 5b report the dependence of the element content of nitrogen and sulfur in the films on the ionic strength for different emission angles.

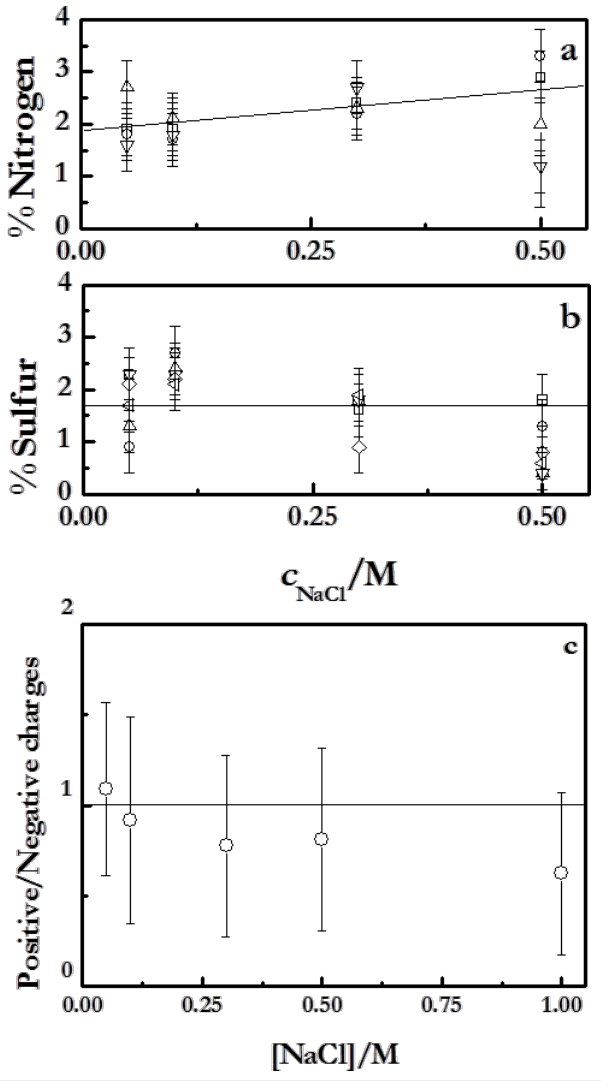

Figure 5: (a) Dependence on the salt concentration of the atomic fraction of nitrogen in $(PDADMAC + PSS)_N$ films, obtained by XPS measurement at different angles of electron emission: (squares) −40°, (circles) −30°, (upward triangles) −20°, (downward triangles) −10°, (diamonds) 0°, (leftward triangles) 10°. The solid lines are to guide the eye. (b) Dependence on the salt concentration of the atomic fraction of sulfur in $(PDADMAC + PSS)_N$ films, obtained by XPS measurement at different angles of electron emission: (squares) −40°, (circles) −30°, (upward triangles) −20°, (downward triangles) −10°, (diamonds) 0°, (leftward triangles) 10°. The solid lines are to guide the eye.
(c): Dependence on the salt concentration for the ratio between positive and negative charges in $(PDADMAC + PSS)_N$ films, obtained by XPS measurement at normal angle of incidence and 0° emission angle. The solid line is to guide the eye.

The atomic content remains almost constant with increasing ionic strength. Indeed, the atomic fractions of nitrogen and sulfur are both independent of the angle of incidence. This confirms the strong interdigitation of the successively adsorbed layers; PDADMAC and PSS form quasi-homogeneous mixed films. It is expected that this absence of stratification in the multilayer define the interactions within the film and the properties of the manufactured materials. Additional evidence of this absence of stratification can be obtained from the XPS measurements following the method proposed by Raposo and co-workers [47]. We have measured the ratio between the total content of positive (sodium and nitrogen) and negative charges (sulfur and chloride) in the multilayers. Values of this ratio close to unity indicate non-stratified films whereas values higher or lower than unity evidence the stratification of the multilayers [47]. Figure 5c shows the dependence of this ratio for $(PDADMAC + PSS)_N$ multilayers on the ionic strength. These results confirm the absence of stratification of the films, in agreement with previous studies based on reflectivity techniques (X-Ray and neutrons) [19,21,22], and contrast with the stratification found for $[poly(allylamine) + PSS]_N$ multilayers [17,18].

Moreover, a more detailed analysis of the XPS results in Figure 5a and Figure 5b provides additional insights in the adsorption of the different polymers in the multilayers. It is observed that the nitrogen content slightly increases with the ionic strength, while the content of sulfur remains constant, which means that the ionic strength affects the adsorption of PDADMAC but has a negligible effect on the adsorption of PSS. As it will discussed below this conclusion agrees with ellipsometry results.

Ellipsometry is a technique that evaluates the adsorbed mass through the refractive index contrast between the adsorbed layers [53] and allows one to obtain the adsorbed mass of each layer. Figure 6a shows the thickness change, Δh_{op}, for the adsorption of each layer for wet multilayers $(PDADMAC + PSS)_N$ under different assembly conditions (linear and non-linear growth). They show a clear odd–even effect in the successive adsorption cycles [19,54]. These results confirm the dependence on the ionic strength of the adsorbed amount of PDADMAC discussed above (the change from 0.10 M to 0.50 M leads to a thickening of the PDADMAC layers by a factor of six), whereas the adsorption of PSS does not show any significant change. This reflects the importance of the assembly conditions in the control of the multilayers fabrication.

The ellipsometric thickness can be related to the number of polymeric chains by a simple modification of de Feijter's equation (Equation 1) as we have discussed in a previous publica-

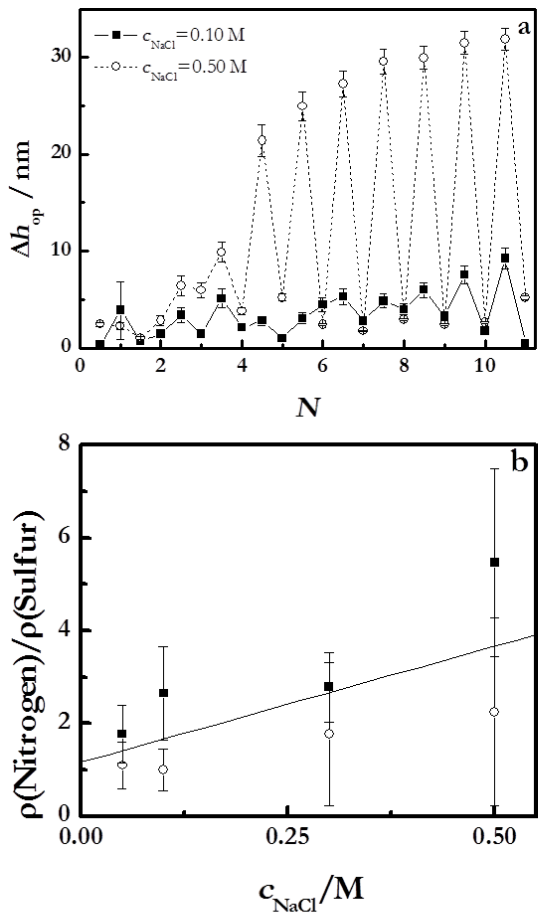

Figure 6: (a) Variation of thickness, obtained using ellipsometry for the adsorption of single layers, as a function of *N* for (PDADMAC + PSS)$_N$ films formed at two different ionic strengths: 0.10 M and 0.50 M. (b) Dependence on the salt concentration of the ratio between nitrogen and sulfur contents in (PDADMAC + PSS)$_N$ films obtained from ellipsometry (solid squares) measurements average over 12 bilayers and by XPS (open circles) measurements at 0°. The solid line is to guide the eye.

tion [42]. Following this approach it is possible to assume that the monomer surface density, $\rho_{monomer}$, for each single layer can be obtained as

$$\rho_{monomer} = \frac{N_A \Gamma}{M_w}, \quad (5)$$

where N_A is the Avogadro constant, Γ the surface concentration obtained by de Feijter's equation (Equation 1) and M_w is the molecular weight of the monomers. Equation 5 quantifies the surface density of the marker atoms $\rho(X) = \rho_{monomer}$ (X = nitrogen or sulfur). Considering this, we can define the ratio between the atomic contents of nitrogen and sulphur in the multilayer directly by the following expression,

$$\phi = \frac{\rho(\text{nitrogen})}{\rho(\text{sulfur})}. \quad (6)$$

Figure 6b reports the average ratio between the atomic contents of nitrogen and sulphur in the multilayer obtained from ellipsometry. For this purpose, the average value obtained over twelve bilayers will be considered. The ratio obtained from XPS results obtained at normal emission angle is reported together to the average ratio calculated from Equation 6 based in ellipsometric measurements. The results obtained using both techniques show a good qualitative agreement. In both cases, an increasing trend is observed in the atomic ratio with the increase of the ionic strength.

Chemical composition of the multilayers

The XPS report allows one to perform a detailed chemical characterization of the multilayers. Figure 7 shows the chemical composition of the main components of the multilayers in rela-

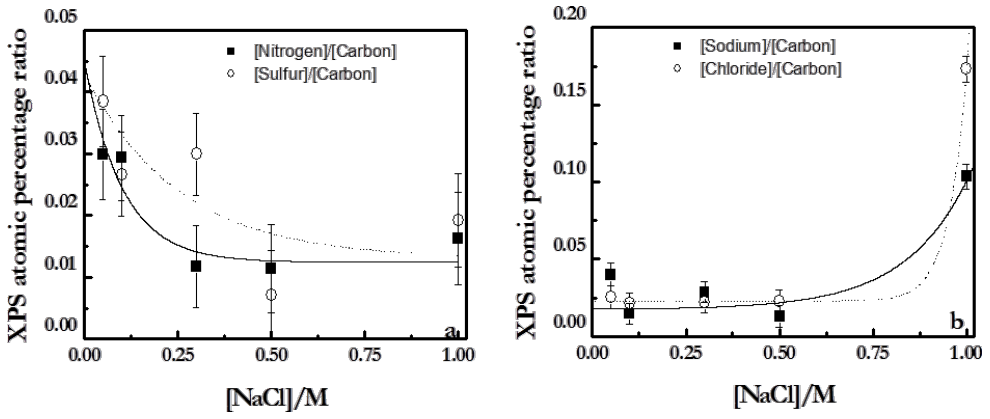

Figure 7: Atomic ratios obtained from XPS measurements at an angle of electron emission of 0°. (a) Ratios of [nitrogen]/[carbon] and [sulfur]/[carbon]. (b) Ratios [sodium]/[carbon] and [chloride]/[carbon]. The solid line is to guide the eye.

tion to those of the carbon, since it is expected that the carbon content is not sensitive to *N*.

The contents of sulphur and nitrogen decrease with increasing ionic strength, whereas those of the counterions increase, in qualitative good agreement with the results of Raposo et al. [47] for multilayers of PSS + poly(*o*-methoxyaniline) emeraldine salt. This behavior is explained by the co-deposition of counterions with the polymer chains, which becomes more prominent as the ionic strength increases. This type of behavior is on the basis of a charge compensation mechanism that will be discussed below. The compensation mechanism is related to the relative proportion between the number of polymer chains defined by the nitrogen and sulfur contained in the multilayers and the number of counterions (sodium and chloride). Considering this fact, the simultaneous deposition of counterions and polymer chains from the bulk govern the ionic pairing between adjacent layers.

Charge in polyelectrolyte multilayers

The charge of polyelectrolyte multilayers is one of the most critical aspects for the understanding of the physicochemical phenomena occurring in these soft systems. When we speak about the charge in polyelectrolyte multilayers, it is necessary to consider two different aspects that influence the film assembly: the charge inversion (overcompensation) that occurs during the deposition of the successive layers, and the charge compensation that ensures the neutrality of the supramolecular architecture.

The charge inversion or overcompensation has been traditionally considered as the main driving force for the assembly of polyelectrolyte films obtained by LbL methods [16,55]. In order to evaluate the charge inversion due to the sequential adsorption of layers with opposite charge, measurements of the changes of the surface potential, ΔV, have been performed (Figure 8a). The surface potential value changes between positive and negative values for the alternated adsorption of polycation and polyanion layers, respectively. Note that even the changes of the surface potential with *N* are similar to those expected for the ζ-potential; the absolute values measured by the Kelvin probe are referred directly to the potential on the surface whereas conventional measurements of ζ-potential are referred to an average charge within a larger area of the surface layer [56]. Figure 8a shows the surface potential of multilayers $(PDADMAC + PSS)_N$ adsorbed at different ionic strength as a function of *N*.

The ΔV values for the polyelectrolyte multilayers do not show any dependence on the ionic strength, which indicates the existence of a self-limited adsorption determined by the specific

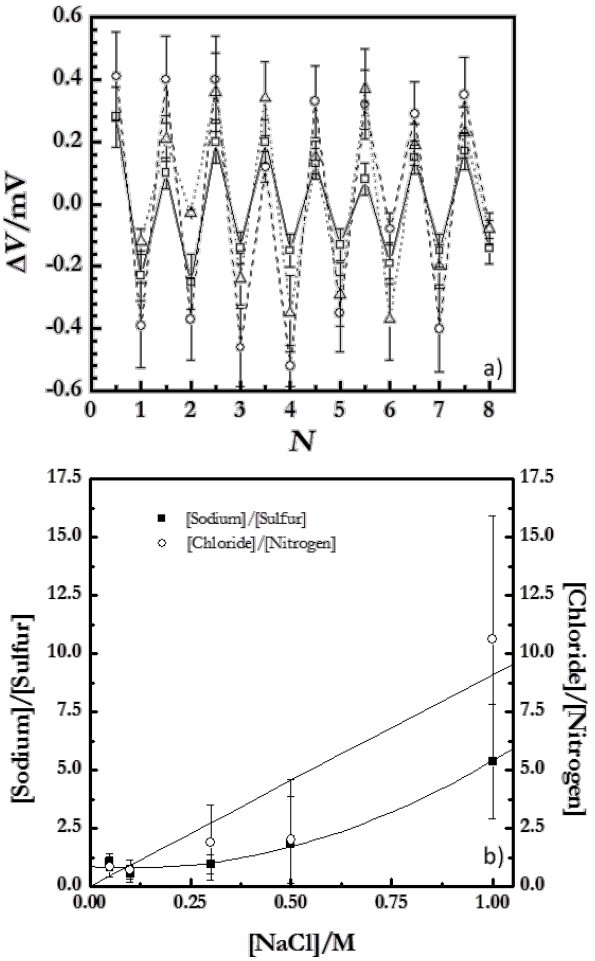

Figure 8: (a) Changes in the surface potential, ΔV, as a function of *N* for $(PDADMAC + PSS)_N$ films formed at different ionic strengths. The different symbols represent different ionic strengths: (open squares) 0 M, (open circles) 0.05 M, (open triangles) 1.00 M. (b) Ratios of [sodium]/[sulfur] and [chloride]/[nitrogen] as a function of the ionic strength obtained for dry multilayers from XPS spectra. The lines are to guide the eye.

nature of the polyelectrolyte pair [22,57], i.e., the adsorption of a polyelectrolyte occurs until a certain degree of charge inversion is reached, independently of the assembly conditions. This is explained considering that the increase of the ionic strength reduces the effective charge density of the polyelectrolyte multilayers, thus the overcompensation threshold is reached for higher amounts of adsorbed polymer.

Despite the charge overcompensation, the multilayer must be neutral from a macroscopic point of view [15,16,58]. A quantitative evaluation of the compensation can be obtained from the ratio of monomers with positive and negative charge in adjacent layers as was described in [8,42]. This method showed the extrinsic compensation for the $(PDADMAC + PSS)_N$ system, independently of the ionic strength [19]. In addition, the content

in PDADMAC is always higher than that of PSS as discussed above. This allows one to conclude that the content of chloride anions must be higher than that of the sodium cations. This latter is related to differences of the type of compensation implied in polycation and polyanion layers in agreement with the results by Lehaf and co-workers [59]. They found that PDADMAC-capped multilayers evidence a strongly extrinsic compensation whereas PSS-ended films are intrinsically compensated.

Moreover, the increase of the compensation ratio with the ionic strength is ascribable to the effect of entropic factors on the adsorption of the polyelectrolyte multilayers [16,19,58]. For low ionic strengths, the release of counterions strongly increases the entropic contribution to the adsorption process. This makes the charge compensation by the ionic pairing between polyelectrolytes in adjacent layers more favorable than the compensation through condensation of counterions. On the other side, the increase of the ionic strength reduces the importance of the entropic factor with the subsequent increases of the extrinsic compensation with counterions association to the films. Additional insights related to the charge compensation can be obtained using XPS [47,60,61]. Figure 8b reports the ratios of [sodium]/[sulfur] and [chloride]/[nitrogen].

Figure 8b shows that the role of the extrinsic compensation in PDADMAC layers is significantly enhanced with the increase in the ionic strength. This is associated to the strong screening effect of NaCl on the charge of PDADMAC. This implies that the amount of counterions associated with the PDADMAC layers increases with the ionic strength. On the opposite side, PSS layers show different behavior with the ratio that defines the degree of extrinsic compensation of PSS layers being almost independent on the ionic strength up to values higher than 0.5 M, where a slightly increase of the ratio of [sodium]/[sulfur] occurs. This is a further confirmation of the reduced effect of NaCl on the adsorption of PSS for low and moderate ionic strengths. The different trends found for the ratios of [sodium]/[sulfur] and [chloride]/[nitrogen] agree with the conclusion obtained from ellipsometry.

Conclusion

The electrostatic self-assembly, using the LbL approach, of polyelectrolyte layers formed by PSS as polyanion and PDADMAC as polycation has been studied through different techniques that allowed for a better understanding of the multilayer internal composition and interactions. Different physicochemical aspects have been evaluated for this model system and it has been possible to conclude that the growth and properties of $(PDADMAC + PSS)_N$ films are mainly controlled by a complex interplay between three main parameters such as the hydration/swelling induced by the solvent, the charge compensation mechanism and the ionic pairing between polyelectrolytes in adjacent layers. The study of hydrated and dry films have demonstrated that the main physicochemical features of polyelectrolytes multilayers are similar independently of the hydration of the films with the water playing a key role in the swelling of the supramolecular architecture and adding mass to the hydrated films. The important contribution of the water as swelling agent of the films plays a central role for controlling the ionic cross-linking between adjacent layers, and consequently the mechanical properties of the films. The results have pointed out that swollen layers present always a most viscoelastic character than shrunk and dry films. The analysis of the structural aspects has pointed out the formation of intermixed layers of PDADMAC and PSS without evidences of stratification in the films.

Acknowledgements

This work was supported in part by MINECO under grant FIS 2012-28231-C02-01 and FIS 2014-62005-EXP, by ESA under grants FASES and PASTA, and by EU under grant Marie Curie ITN-CoWet, and carried out in the framework of the ESF-COST Actions CM1101 and MP1106. The authors are grateful to the CAI of Spectroscopy and of X-ray diffraction both of the Complutense University of Madrid for the use of their facilities. EG and AM want to thank to the MINECO and RSC for the JdC contract and the Newton Fellowship, respectively.

References

1. Lehn, J.-M. *Science* **2002,** *295,* 2400–2403. doi:10.1126/science.1071063
2. Lehn, J.-M. *Proc. Natl. Acad. Sci. U. S. A.* **2002,** *99,* 4763–4768. doi:10.1073/pnas.072065599
3. Decher, G.; Schlenoff, J. B., Eds. *Multilayer Thin Films-Sequential Assembly of Nanocomposite Materials;* Wiley-VCH: Berlin, Germany, 2003.
4. Iler, R. K. *J. Colloid Interface Sci.* **1966,** *21,* 569–594. doi:10.1016/0095-8522(66)90018-3
5. Decher, G. *Science* **1997,** *277,* 1232–1237. doi:10.1126/science.277.5330.1232
6. Hammond, P. T. *AIChE J.* **2011,** *57,* 2928–2940. doi:10.1002/aic.12769
7. Schlenoff, J. B. *Langmuir* **2009,** *25,* 14007–14010. doi:10.1021/la901950c
8. Guzmán, E.; Chuliá-Jordán, R.; Ortega, F.; Rubio, R. G. *Phys. Chem. Chem. Phys.* **2011,** *13,* 18200–18207. doi:10.1039/c1cp21609k
9. Correa-Duarte, M. A.; Kosiorek, A.; Kandulski, W.; Giersig, M.; Liz-Marzán, L. M. *Chem. Mater.* **2005,** *17,* 3268–3272. doi:10.1021/cm047710e
10. Picart, C.; Mutterer, J.; Richert, L.; Luo, Y.; Prestwich, G. D.; Schaaf, P.; Voegel, J.-C.; Lavalle, P. *Proc. Natl. Acad. Sci. U. S. A.* **2002,** *99,* 12531–12535. doi:10.1073/pnas.202486099

11. Burke, S. E.; Barrett, C. J. *Langmuir* **2003,** *19,* 3297–3303. doi:10.1021/la026500i
12. Sukhishvili, S. A.; Granick, S. *Macromolecules* **2002,** *35,* 301–310. doi:10.1021/ma011346c
13. von Klitzing, R. *Phys. Chem. Chem. Phys.* **2006,** *8,* 5012–5033. doi:10.1039/B607760A
14. Lavalle, P.; Voegel, J.-C.; Vautier, D.; Senger, B.; Schaaf, P.; Ball, V. *Adv. Mater.* **2011,** *23,* 1191–1221. doi:10.1002/adma.201003309
15. Farhat, T.; Yassin, G.; Dubas, S. T.; Schlenoff, J. B. *Langmuir* **1999,** *15,* 6621–6623. doi:10.1021/la990631a
16. Schlenoff, J. B.; Dubas, S. T. *Macromolecules* **2001,** *34,* 592–598. doi:10.1021/ma0003093
17. Schmitt, J.; Griinewald, T.; Decher, G.; Pershan, P. S.; Kjaer, K.; Losche, M. *Macromolecules* **1993,** *26,* 7058–7063. doi:10.1021/ma00077a052
18. Lösche, M.; Schmitt, J.; Decher, G.; Bouwman, W. G.; Kjaer, K. *Macromolecules* **1998,** *31,* 8893–8906. doi:10.1021/ma980910p
19. Guzmán, E.; Ritacco, H.; Rubio, J. E. F.; Rubio, R. G.; Ortega, F. *Soft Matter* **2009,** *5,* 2130–2142. doi:10.1039/b901193e
20. Guzmán, E.; Ritacco, H.; Ortega, F.; Svitova, T.; Radke, C. J.; Rubio, R. G. *J. Phys. Chem. B* **2009,** *113,* 7128–7137. doi:10.1021/jp811178a
21. Guzmán, E.; Ritacco, H.; Ortega, F.; Rubio, R. G. *Colloids Surf., A* **2011,** *384,* 274–281. doi:10.1016/j.colsurfa.2011.04.005
22. Guzmán, E.; Ritacco, H. A.; Ortega, F.; Rubio, R. G. *J. Phys. Chem. C* **2012,** *116,* 15474–15483. doi:10.1021/jp304522t
23. Iturri Ramos, J. J.; Stahl, S.; Richter, R. P.; Moya, S. E. *Macromolecules* **2010,** *43,* 9063–9070. doi:10.1021/ma1015984
24. McAloney, R. A.; Sinyor, M.; Dudnik, V.; Goh, M. C. *Langmuir* **2001,** *17,* 6655–6663. doi:10.1021/la010136q
25. McAloney, R. A.; Dudnik, V.; Goh, M. C. *Langmuir* **2003,** *19,* 3947–3952. doi:10.1021/la026882s
26. Johannsmann, D. *Phys. Chem. Chem. Phys.* **2008,** *10,* 4516–4534. doi:10.1039/B803960G
27. De Feijter, J. A.; Benjamins, J.; Veer, F. A. *Biopolymers* **1978,** *17,* 1759–1772. doi:10.1002/bip.1978.360170711
28. Horcas, I.; Fernández, R.; Gómez-Rodríguez, J. M.; Colchero, J.; Gómez-Herrero, J.; Baro, A. M. *Rev. Sci. Instrum.* **2007,** *78,* 013705. doi:10.1063/1.2432410
29. Salomäki, M.; Kankare, J. *J. Phys. Chem. B* **2007,** *111,* 8509–8519. doi:10.1021/jp067344h
30. Sauerbrey, G. *Z. Phys.* **1959,** *155,* 206–222.
31. Johannsmann, D.; Mathauer, K.; Wegner, G.; Knoll, W. *Phys. Rev. B* **1992,** *46,* 7808–7815. doi:10.1103/PhysRevB.46.7808
32. Du, B.; Johannsmann, D. *Langmuir* **2004,** *20,* 2809–2812. doi:10.1021/la035965l
33. Haynie, D. T.; Cho, E.; Waduge, P. *Langmuir* **2011,** *27,* 5700–5704. doi:10.1021/la104516a
34. Jomaa, H. W.; Schlenoff, J. B. *Macromolecules* **2005,** *38,* 8473–8480. doi:10.1021/ma050072g
35. Lavalle, P.; Picart, C.; Mutterer, J.; Gergely, C.; Reiss, H.; Voegel, J.-C.; Senger, B.; Schaaf, P. *J. Phys. Chem. B* **2004,** *108,* 635–648. doi:10.1021/jp035740j
36. Steinem, C.; Janshoff, A., Eds. *Piezoelectric Sensors;* Springer: Berlin, Germany, 2007.
37. Nolte, A. J.; Treat, N. D.; Cohen, R. E.; Rubner, M. F. *Macromolecules* **2008,** *41,* 5793–5798. doi:10.1021/ma800732j
38. Vörös, J. *Biophys. J.* **2004,** *87,* 553–561. doi:10.1529/biophysj.103.030072
39. Guzmán, E.; Ortega, F.; Baghdadli, N.; Cazeneuve, C.; Luengo, G. S.; Rubio, R. G. *ACS Appl. Mater. Interfaces* **2011,** *3,* 3181–3188. doi:10.1021/am200671m
40. Guzmán, E.; Ortega, F.; Prolongo, M. G.; Starov, V. M.; Rubio, R. G. *Phys. Chem. Chem. Phys.* **2011,** *13,* 16416–16423. doi:10.1039/c1cp21967g
41. Guzmán, E.; Ortega, F.; Baghdadli, N.; Luengo, G. S.; Rubio, R. G. *Colloids Surf., A* **2011,** *375,* 209–218. doi:10.1016/j.colsurfa.2010.12.012
42. Guzmán, E.; Miguel, V. S.; Peinado, C.; Ortega, F.; Rubio, R. G. *Langmuir* **2010,** *26,* 11494–11502. doi:10.1021/la101043z
43. Wong, J. E.; Rehfeldt, F.; Hänni, P.; Tanaka, M.; von Klitzing, R. *Macromolecules* **2004,** *37,* 7285–7289. doi:10.1021/ma0351930
44. Kujawa, P.; Moraille, P.; Sanchez, J.; Badia, A.; Winnik, F. *J. Am. Chem. Soc.* **2005,** *127,* 9224–9234. doi:10.1021/ja044385n
45. Carrière, D.; Krastev, R.; Schönhoff, M. *Langmuir* **2004,** *20,* 11465–11472. doi:10.1021/la0486436
46. Grosberg, A. Yu.; Nguyen, T. T.; Shklovskii, B. I. *Rev. Mod. Phys.* **2002,** *74,* 329–345. doi:10.1103/RevModPhys.74.329
47. Raposo, M.; Lourenço, J. M. C.; Botelho do Rego, A. M.; Ferraria, A. M.; Ribeiro, P. A. *Colloids Surf., A* **2012,** *412,* 1–10. doi:10.1016/j.colsurfa.2012.05.005
48. Schönhoff, M.; Ball, V.; Bausch, A. R.; Dejugnat, C.; Delorme, N.; Glinel, K.; von Klitzing, R.; Steitz, R. *Colloids Surf., A* **2007,** *303,* 14–29. doi:10.1016/j.colsurfa.2007.02.054
49. Dodoo, S.; Balzer, B. N.; Hugel, T.; Laschewsky, A.; von Klitzing, R. *Soft Mater.* **2013,** *11,* 157–164. doi:10.1080/1539445X.2011.607203
50. Köhler, R.; Steitz, R.; von Klitzing, R. *Adv. Colloid Interface Sci.* **2014,** *207,* 325–331. doi:10.1016/j.cis.2013.12.015
51. Volodkin, D.; von Klitzing, R. *Curr. Opin. Colloid Interface Sci.* **2014,** *19,* 25–31. doi:10.1016/j.cocis.2014.01.001
52. Secrist, K. E.; Nolte, A. J. *Macromolecules* **2011,** *44,* 2859–2865. doi:10.1021/ma101983s
53. Azzam, R. M. A.; Bashara, N. M. *Ellipsometry and Polarized Light;* Elsevier: Amsterdam, Netherlands, 1987.
54. Nestler, P.; Block, S.; Helm, C. A. *J. Phys. Chem. B* **2012,** *116,* 1234–1243. doi:10.1021/jp208837m
55. Shin, Y.; Roberts, J. E.; Santore, M. M. *J. Colloid Interface Sci.* **2002,** *247,* 220–230. doi:10.1006/jcis.2001.8100
56. Ikuma, K.; Madden, A. S.; Decho, A. W.; Lau, B. L. T. *Environ. Sci.: Nano* **2014,** *1,* 117–122. doi:10.1039/C3EN00075C
57. Ladam, G.; Schaad, P.; Voegel, J. C.; Schaaf, P.; Decher, G.; Cuisinier, F. *Langmuir* **2000,** *16,* 1249. doi:10.1021/la990650k
58. Dubas, S. T.; Schlenoff, J. B. *Macromolecules* **1999,** *32,* 8153–8160. doi:10.1021/ma981927a
59. Lehaf, A. M.; Hariri, H. H.; Schlenoff, J. B. *Langmuir* **2012,** *28,* 6348–6355. doi:10.1021/la300482x
60. Lourenço, J. M. C.; Ribeiro, P. A.; Botelho do Rego, A. M.; Braz Fernandes, F. M.; Moutinho, A. M. C.; Raposo, M. *Langmuir* **2004,** *20,* 8103–8109. doi:10.1021/la049872v
61. Lourenço, J. M. C.; Ribeiro, P. A.; Botelho do Rego, A. M.; Raposo, M. *J. Colloid Interface Sci.* **2007,** *313,* 26–33. doi:10.1016/j.jcis.2007.04.040

BEILSTEIN JOURNAL OF NANOTECHNOLOGY

Characterisation of thin films of graphene–surfactant composites produced through a novel semi-automated method

Nik J. Walch*[1], Alexei Nabok[2], Frank Davis[1] and Séamus P. J. Higson[1,3]

Full Research Paper

Open Access

Address:
[1]Cranfield Biotechnology Centre, Cranfield University, College Road, Cranfield, MK43 0AL, UK, [2]Sheffield Hallam University, Materials & Engineering Research Institute, Howard Street, Sheffield, S1 1WB, UK and [3]The University of Chichester, College Lane, Chichester, West Sussex, PO19 6PE, UK

Email:
Nik J. Walch* - N.J.Walch@Cranfield.ac.uk

* Corresponding author

Keywords:
characterization; ellipsometry; graphene; ^{1}H NMR; surfactant

Beilstein J. Nanotechnol. **2016,** *7,* 209–219.
doi:10.3762/bjnano.7.19

Received: 31 August 2015
Accepted: 21 January 2016
Published: 08 February 2016

This article is part of the Thematic Series "Organized films".

Guest Editor: M. Canepa

Abstract

In this paper we detail a novel semi-automated method for the production of graphene by sonochemical exfoliation of graphite in the presence of ionic surfactants, e.g., sodium dodecyl sulfate (SDS) and cetyltrimethylammonium bromide (CTAB). The formation of individual graphene flakes was confirmed by Raman spectroscopy, while the interaction of graphene with surfactants was proven by NMR spectroscopy. The resulting graphene–surfactant composite material formed a stable suspension in water and some organic solvents, such as chloroform. Graphene thin films were then produced using Langmuir–Blodgett (LB) or electrostatic layer-by-layer (LbL) deposition techniques. The composition and morphology of the films produced was studied with SEM/EDX and AFM. The best results in terms of adhesion and surface coverage were achieved using LbL deposition of graphene(−)SDS alternated with polyethyleneimine (PEI). The optical study of graphene thin films deposited on different substrates was carried out using UV–vis absorption spectroscopy and spectroscopic ellipsometry. A particular focus was on studying graphene layers deposited on gold-coated glass using a method of total internal reflection ellipsometry (TIRE) which revealed the enhancement of the surface plasmon resonance in thin gold films by depositing graphene layers.

Introduction

Since its initial discovery and development by Novoselov et al. [1] graphene has been of great interest to the scientific community due to its interesting optical and electrical properties. Graphene is defined as a single layer of sp^2-hybridised carbon with no third dimension. The double-bonded structure of graphene is responsible for the electrical properties of the material as the movement of π-bonds between adjacent carbon atoms can be used to transmit an electrical current. Because of this electrical activity in particular, graphene is being examined as a base material in a number of different applications including

sensor applications, for use in flexible electronics [2] and graphene-based printable inks for printed electrical circuits [3].

Graphene has reportedly been produced in a number of different ways. The method chosen for this research is sonochemical exfoliation in water in the presence of a surfactant, as first reported by Notley et al. [4]. This method was chosen for a number of reasons; firstly, it does not require the use of hazardous chemicals such as sodium nitrate, sulfuric acid, potassium permanganate and hydrazine hydrate, which are used in the oxidation of graphite to graphite oxide and the subsequent reduction to graphene [5], and secondly it guarantees single-layer or few-layer graphene, rather than the potentially larger products or graphene sheets with an uneven size distribution that might be produced in other techniques such as mechanical exfoliation (the "scotch tape" method). The sonochemical method was carried out using a semi-automated apparatus designed specifically for the purposes of this research.

In previous work [6] we manufactured graphene–surfactant complexes using the Notley method and applied them to carbon electrodes, thereby enhancing their electrochemical activity. Further work was then carried out on optimising graphene production, characterising the products and also depositing graphene layers by more controlled techniques than simple casting.

In this work a semi-automated technology of graphene production by sonochemical exfoliation of graphite in the presence of ionic surfactants is described in detail. The composite graphene-surfactant materials produced were characterised with NMR and Raman spectroscopy to confirm the formation of graphene. Thin films of graphene composites were deposited using the techniques of Langmuir-Blodgett (LB) and electrostatic layer-by-layer (LbL) deposition. Films composed of these new graphene composite materials were then characterised using SEM, AFM, and spectroscopic ellipsometry. The study of SPR in gold films coated with graphene using total internal reflection ellipsometry was carried out for the first time.

Experimental

Semi-automated sonochemical exfoliation of graphene

Two different surfactants were used to synthesise graphene–surfactant complexes: sodium dodecyl sulfate (SDS) and cetyltrimethylammonium bromide (CTAB). Firstly the surfactant solutions were prepared by dissolving in water. The SDS solution was made to a concentration of 462.9 mg·mL^{-1} while the CTAB solution concentration was made up to 49.7 mg·mL^{-1}. These solutions were prepared and then placed into a water bath heated to 50 °C to aid dissolution.

Once dissolved, the surfactant solution was placed into the surfactant reservoir of the synthesiser. This solution was then pumped into the reactor during synthesis at a rate of 35 µL·min^{-1} giving an addition rate of 16.2 mg·min^{-1} for SDS and 1.74 mg·min^{-1} for CTAB. The addition rate was crucial to maintain a surface tension of 41 mJ·m^{-2}, which is both the optimum surface tension for graphene production and also the surface free energy of graphene. The graphite suspension (10–50%) was then placed into the reactor, and sonicated continuously for 120 min at a power of 50 W. A total of 3.15 mL of surfactant solution was added in each case over the course of the synthesis. The sonication step was carried out in a fume cabinet, as an aerosol containing potentially harmful graphene nanoparticles is produced at this stage. A schematic diagram of this apparatus is shown below (Figure 1).

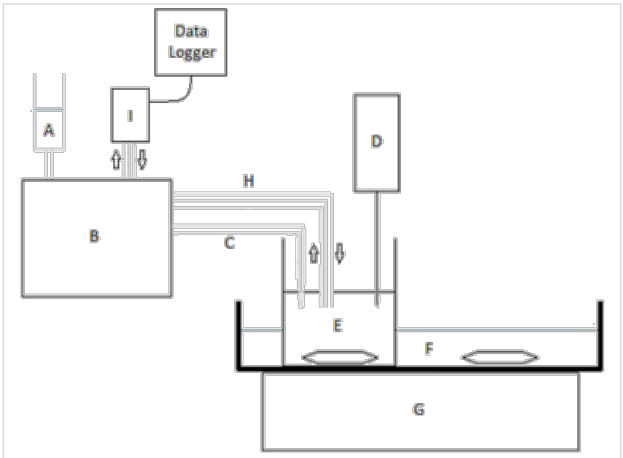

Figure 1: A schematic diagram of the apparatus used to synthesis graphene. (A) surfactant solution, (B) peristaltic pump, (C) heat, (D) ultrasonic probe, (E) reactor, (F) water, (G) magnetic stirring unit, (H) sampling loop, and (I) photometric flow cell.

The apparatus was designed to alleviate the time constraints of the Notley method. In that method, solid surfactant must be added every 5 min whilst continuous sonication is carried out. This method with its continuous addition of aqueous surfactant eliminates the need for constant supervision of the process as well as providing the reproducibility of automation. This is only semi-automated, however, as full automation would require the monitoring of surface tension throughout the synthesis as well as automatic adjustments to the surfactant flow rate to maintain this at the required level of 41 mJ·m^{-2}.

Figure 1 depicts the assembled apparatus, the function of which is explained here. The aqueous suspension of graphite is placed into the reactor (E). The graphite is kept in suspension throughout the procedure using a magnetic stirrer (G). The ultrasonic probe (D), operating at a power of 50 W, penetrates approximately 1 cm into the graphite suspension. The surfactant solu-

tion (A) is pumped into the reactor via a peristaltic pump (B). The reservoir containing the surfactant and the tubing carrying it to the reactor are heated to 50 °C in a water bath (C) to prevent precipitation of the surfactant from solution in the tubing. A water trough (F) is used as a heat sink to dissipate any heat produced in the reactor during synthesis, as the tip of the ultrasonic probe can reach temperatures of up to 100 °C during continuous operation. The heat sink is stirred continuously, also using the magnetic stirrer (G), to maximise cooling efficiency. A sampling loop (H) continuously cycles the liquid contents of the reactor through a photometric flow cell (I) which determines the concentration of graphene by measuring the absorbance at 650 nm. The concentration data is then recorded using a data logger.

Upon completion of the 120 min cycle, the contents of the reactor were removed and placed into a 50 mL centrifuge tube and spun at 3500 rpm for 20 min. The supernatant was then removed and the pellet (containing mostly unreacted graphite as well as some precipitated graphene) was re-suspended in 40 mL of deionised water. This was then centrifuged at 3500 rpm for 20 min. This process was repeated until no more graphene was contained in the supernatant. If a dry sample was required, then the graphene suspension was frozen and then placed into a freeze dryer (Labogene) for 3–4 days (depending on the sample size) and then subsequently into a vacuum oven at 70 °C overnight to remove all traces of water.

Characterisation of graphene-surfactant composite material

Graphene–surfactant complexes were characterised by using a range of different techniques. The presence of graphene was determined by Raman microscopy. The concentration of graphene in solution was obtained by spectrophotometry. The absorbance of a graphene solution at a wavelength of 650 nm was determined and the Beer–Lambert law applied, using an extinction coefficient of 13.9 $mg \cdot mL^{-1} \cdot cm^{-1}$ [7]. The interaction of the surfactant with the graphene surface was also analysed using NMR spectroscopy. Dried graphene–surfactant complex was dissolved in D_2O and placed into an NMR tube. Another tube containing the surfactant alone was also prepared. Both were scanned individually and then the spectra were compared to show shifts in peak position corresponding to interaction between the surfactant and the graphene. NMR experiments were performed on a Bruker 400 MHz spectrometer running topspin analysis software. This analysis works according to the nuclear Overhauser effect (NOE). The NOE, which is present in nuclear magnetic resonance (NMR) spectroscopy, can be used to determine the amount of contact between the surfactant and the graphene sheet. This is achieved by observing peak shifts that occur when two nuclei are within 5 Å of each other. The dried graphene sample was deposited onto a glass microscope slide and then scanned using a Renishaw In-Via Raman microscope at an excitation wavelength of 532 nm. Data were recorded between 100 and 3200 cm^{-1}.

Deposition of thin films of graphene-surfactant composites

Langmuir–Blodgett and Langmuir–Schaefer deposition

Both composite materials obtained, e.g., graphene(+)CTAB and graphene(−)SDS, appeared to be soluble in water due to the presence of ionic groups, NMe_3^+ and SO_3^-, respectively. Yet, the presence of alkyl chains and π-systems facilitated their solubility in chloroform, hence the use of the Langmuir–Blodgett (LB) technique (Nima 610 trough) was an obvious choice for the deposition of thin films. The standard LB procedure was applied [8]: a 1 $mg \cdot mL^{-1}$ solution of graphene(+)CTAB in chloroform was spread onto the surface of deionised water (Millipore). Surface pressure was then recorded using a Wilhelmy plate-based sensor. Because of the unknown ratio of graphene/surfactant within the complex the area per molecule (or repeated unit) was difficult to calculate, so the area was presented in actual units of cm^2. Another method known as Langmuir–Schaefer (LS) deposition [9] was also used to prepare monolayer films. In this technique the hydrophilic substrate is held horizontally to the assembled monolayer and then lowered slowly to gently touch water surface and the monolayer is then transferred onto the substrate surface. Organised monolayer films obtained in this fashion were then characterised by AFM (Nanoscope III) operating in tapping mode using Veeco cantilevers with silicon nitride tips having a radius of less than 10 nm.

Electrostatic LbL deposition

Much better results (in terms of adhesion and surface coverage) were obtained by using a simple technique of electrostatic layer-by-layer (LbL) deposition, a well-established technique developed first for polyelectrolytes [10] and later adapted for deposition of other objects, such as nanoparticles and biomolecules (proteins, antibodies, enzymes, DNA) [9,11]. Multi layered films of graphene were deposited onto gold-coated glass microscope slides by alternating layers of graphene–surfactant with oppositely charged polyelectrolytes, e.g., graphene(+)-CTAB layers alternated with polyanionic layers of sodium polystyrene sulfonate (PSS), while graphene(−)SDS was alternated with layers of polycationic species such as polyallylamine hydrochloride (PAH) or polyethyleneimine (PEI). Alternating layers of graphene(−)SDS and graphene(+)CTAB was also attempted. The films were deposited by consecutive dipping of gold-coated glass or silicon wafers into 1 $mg \cdot mL^{-1}$ solutions of the above materials in deionised water. The mutlilayered films

obtained were then characterised with scanning SEM combined with EDX (energy dispersing X-ray) elemental analysis (SEM NOVA) and AFM.

Optical characterisation of thin graphene-surfactant films

Spectroscopic ellipsometry study

UV–vis spectra of graphene–surfactant samples are featureless showing almost constant absorbance over the spectral range of 350–800 nm, while the main absorption band of graphene lies in the UV region at about 280 nm. Therefore, optical properties of novel graphene–surfactant composites were studied via spectroscopic ellipsometry using a J. A. Woollam M2000 instrument operating in the spectral range of 370–1000 nm. The measurements were performed on graphene–surfactant films deposited on different substrates, i.e., glass, silicon, and gold-coated glass. Experimental parameters were found by fitting data, the procedure for which is explained in the Results and Discussion section below.

For the LbL deposition of alternating layers of graphene(−)SDS and graphene(+)CTAB on gold-coated glass slides, a gold film of approximately 25 nm thickness was thermally evaporated onto a 3 nm under layer of chromium (which was used to improve adhesion between the gold and the glass). Metal evaporation was carried out in a vacuum of 10^{-6} Torr using an Edwards 360 unit. Prior to LbL deposition, gold-coated slides were treated overnight in cystamine hydrochloride solution in order to make the gold surface positively charged. Then LbL deposition started with the layer of graphene(−)SDS (negatively charged) followed by deposition of graphene(+)CTAB (positively charged). This procedure was repeated four times, so that four graphene bilayers were deposited. Layer by layer deposition onto other substrates was performed in a similar manner.

TIRE study

The surface plasmon resonance (SPR) phenomenon in graphene films deposited on thin films of gold was studied in more detail using the method of total internal reflection ellipsometry (TIRE), which was developed in the last decade [12-14]. TIRE experimental set-up (shown schematically below as inset in Figure 12) was built on the basis of a J. A. Woollam M2000 spectroscopic instrument, in which the light is coupled into a thin gold film deposited on glass through a 68° prism providing total internal reflection conditions. The cell attached underneath allows for measurements in different media. The advantage of using TIRE is a 10-fold sensitivity enhancement compared to traditional SPR [15]. The samples were constructed by electrostatic LbL deposition of PEI and graphene(−)SDS on chromium/gold-coated glass slides, as described above.

Results and Discussion

Characterisation of graphene–surfactant composite material

Graphene was synthesised using graphite suspensions of 10–50% using either SDS or CTAB as the surfactants. The concentration of the final graphene solution obtained from each synthesis was determined by spectrophotometry (Figure 2).

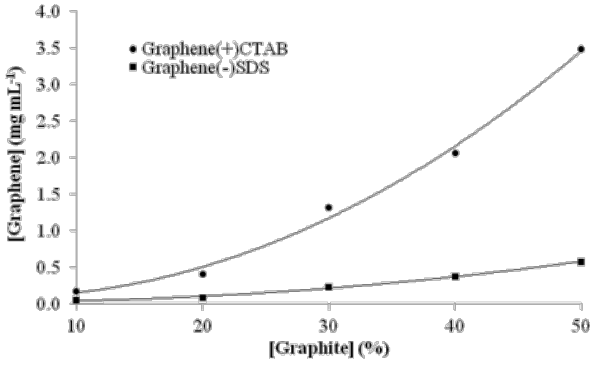

Figure 2: Effect of the initial graphite suspension concentration in water on the final graphene concentration after sonication for 120 min in the presence of different surfactants.

^{1}H NMR measurements of the graphene–surfactant complex, when compared to ^{1}H NMR measurements of the surfactant alone, shows shifting of peaks representing hydrogens involved in the complexation interaction (Figure 3). The data shows a peak shift towards the left for almost every peak. This is a shielding effect caused by the delocalised electrons in the graphene sheet, which only occurs when the proton is in close proximity (less than 5 Å) and involved in van der Waals interactions. This suggests that the hydrophobic chains of each surfactant lie flat against the graphene sheet with the exception of carbon-1 (the carbon attached directly to the polar head group),

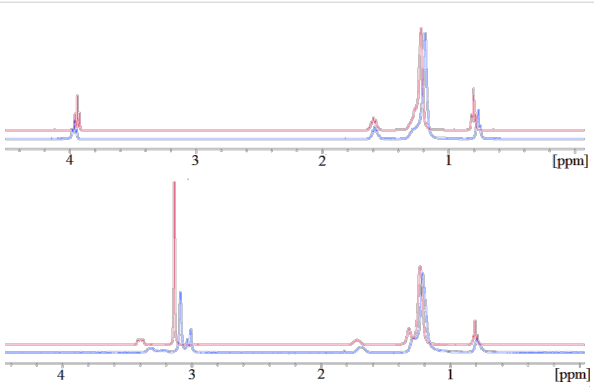

Figure 3: ^{1}H NMR spectra of the graphene–surfactant complexes (blue) stabilized with SDS (top) and CTAB (bottom) compared with the surfactant alone (red).

which is pulled away from it by the polar head group and therefore does not undergo as much of a shielding effect in the SDS–graphene complex.

Additionally, for the CTAB–graphene complex, two of the methyl groups on the quaternary amine are interacting with the graphene sheet. This is shown by the splitting of the peak into three peaks. This interaction causes the CTAB to lie much flatter against the graphene than SDS, resulting in the polar head being pulled closer to the sheet. This is why the peak for carbon-1 in the CTAB–graphene complex is displaced further towards the left than its equivalent in the SDS-stabilised graphene.

The peak representing carbon-1 in SDS (at around 4 ppm) is shifted downfield by complexation with the graphene. This means that the protons are deshielded by the presence of graphene. Since the carbon–sulfur bond is polar the electron density around the carbon atom is already lower than it would normally be in a carbon–carbon bond. Repulsion between the graphene and the sulfate group could cause lengthening of the carbon–sulfur bond. This could in turn lead to a lower electron density around the nuclei responsible for this peak [16].

The sample was also analysed using Raman spectroscopy (Figure 4) which, when compared to the spectrum for graphite, was used to verify the presence of graphene. The spectrum shows intense peaks at 1350 cm^{-1} (D) and 1620 cm^{-1} (G & D'). Additionally the peak labelled 2D is slightly broader, between 2650–2700 cm^{-1}. This is indicative of graphene flakes with a high number of edge defects [17].

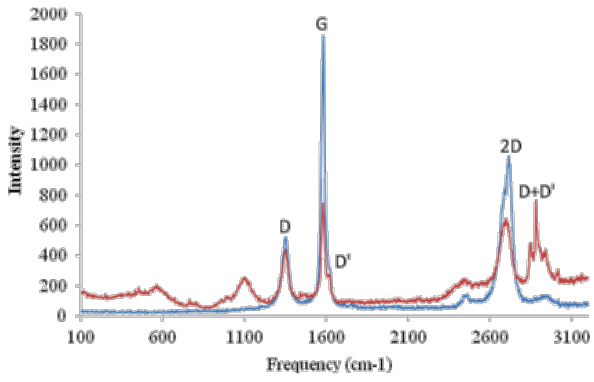

Figure 4: The Raman spectrum of surfactant-stabilised graphene (red) compared with the spectrum of graphite (blue).

The G band is present in all sp^2-hybridised carbon materials, and is caused by stretching of the C–C bond. The reduction in intensity in the graphene spectrum compared with the graphite spectrum is caused by the reduced number of layers. The D and D' bands are caused by disorder in the graphene flakes. The D' band is present when there are surface defects, such as charging or other impurities adsorbed onto the surface. The D band is caused by edge defects such as a "zig-zag" or "chair" shape on the edge. Edge defects provide an enhancement to electrochemical systems by increasing the total capacitance of the electrode surface. Both the D and the D' band are not present in pristine graphene with straight edges [17].

The 2D band is also present in many sp^2-hybridized systems and can be used to estimate the number of layers [18]. However the intensity is also dependant on the excitation laser frequency and so cannot be solely relied upon. Further details on the electrochemistry and usage of graphene produced by this method are detailed in another paper [6].

Deposition of thin films of graphene–surfactant composites

Langmuir–Blodgett (Langmuir–Schaefer) deposition

Typical surface pressure vs area diagrams of graphene(+)CTAB in Figure 5 showed the formation of a stable monolayer on the water surface, similar to that found for classical amphiphilic compounds. The consecutive compressions of the monolayer did not yield substantial losses of material caused either by the monolayer collapse or dissolving the material in water. Graphene(−)SDS composite showed a similar behaviour.

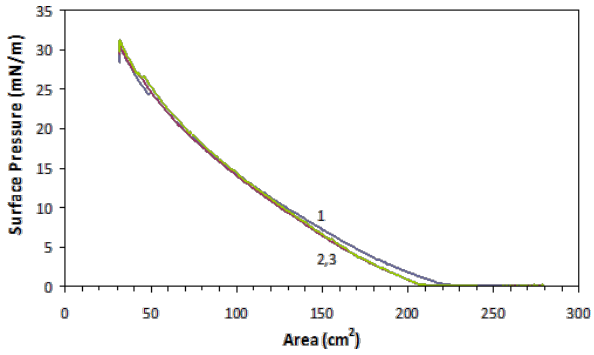

Figure 5: Surface pressure/area isotherms of graphene(+)CTAB monolayers on the water surface. Numbers 1, 2, and 3 indicate consecutive compressions of the monolayer.

However, for LB deposition onto hydrophilic substrates such as glass or oxidised silicon, which are slightly negatively charged due the presence of OH^- groups, positively charged graphene(+)CTAB was chosen; as this provided good adhesion between the substrate and monolayer.

Attempts at depositing thin films of graphene(+)CTAB using a traditional LB process, e.g., vertical dipping and withdrawing

the substrate through the monolayer, were not successful since the transfer ratio was poor. The first withdrawal yielded about 60%. After that the layer was shown to peel off during subsequent dipping cycles. The overall transfer ratio by area (when substrate surface area was compared with graphene LB isotherm) was 10–20%. The most significant cause of this was poor adhesion of the first graphene layer to hydrophilic substrates. This could be improved in future work through the use of substrates with surface modifications that either enhance the surface charge or make the surface more hydrophobic. Much better results were obtained using the horizontal lifting method known as Langmuir–Shaefer (LS) deposition [8], in which the hydrophilic substrate is held horizontally to the assembled monolayer and then lowered slowly to gently touch the water surface. The monolayer is then transferred onto the substrate surface. Only a single layer of graphene(+)CTAB could be deposited by LS deposition. Attempts to deposit multilayers by the LS technique failed, as the deposited layers began to peel off upon consecutive depositions.

Organised monolayer films obtained in this fashion were then characterised by using AFM (Nanoscope III) operating in tapping mode using Veeco cantilevers with silicon nitride tips having a radius of less than 10 nm. A typical AFM image of graphene(+)CTAB flakes deposited onto a piece of silicon wafer using LS method is shown in Figure 6. The larger scale image (a) shows a number of irregularly shaped graphene(+)CTAB flakes with gaps between; the flakes were sometimes shown to overlap, forming double and sometimes triple layers. Image (b) shows, a pseudo 3D image of a flat individual flake of about 500 nm in size with another smaller flake lying on top.

Sectional analysis of AFM image along the lines shown, allows for an estimation of the graphene(+)CTAB flake thickness at 2 nm, which is significantly higher than the reported thickness of pristine graphene of 0.355 nm [19]. The obtained value of 2 nm for an individual graphene(+)CTAB is likely due to the presence of surfactant molecules, CTAB in this case.

It is clear from these images that the surface coverage is not optimal. Additionally the graphene flakes were seen to change position and shape during scanning, suggesting poor adhesion to the silicon surface. This could potentially be overcome in future work by using surface-modified silicon wafers for sample deposition.

Electrostatic LbL deposition

The multi layered films obtained from layer-by-layer deposition method were characterised with scanning SEM combined with EDX (energy dispersing X-ray) elemental analysis (SEM NOVA) and AFM.

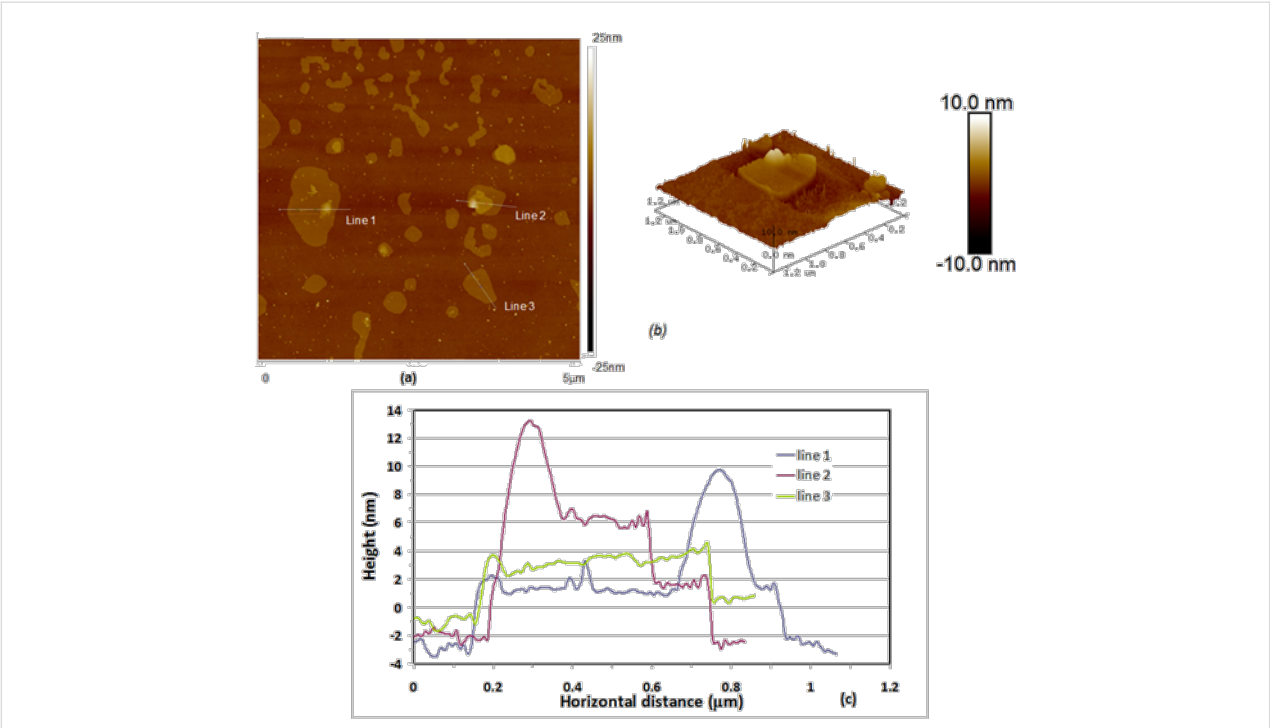

Figure 6: AFM images of the same sample of a graphene(+)CTAB layer deposited onto a silicon substrate using the LS method: (a) 2D image 5 µm; (b) pseudo-3D image of individual graphene flake. (c) Sectional analysis of the image in (a).

Not all alternating combinations worked well, however. For example, the most promising combination of graphene(+)CTAB with graphene(−)SDS was not successful, while the alternation of graphene(+)CTAB with PAH (or with PEI) proved to be optimal. Deposition on glass or silicon samples was performed by electrostatic adsorption of PAH (or PEI) for 20–30 min followed by dipping into a solution of graphene(−)SDS for 10–15 min. This sequence was repeated several times with a typical incubation time of 10–15 min.

Figure 7 shows an SEM image of alternating layers of PAH and graphene(−)SDS deposited onto a silicon substrate. Separate flakes are clearly visible, the largest of which is approximately 30 μm across. EDX spectral analysis (b) performed on a flake show a dominating peak of carbon while on the empty space (c) silicon is the dominant peak. This shows that the graphene flakes consist predominantly of carbon, with a few trace elements. Deposition of the first few layers gives a less than optimal coverage. The reason for this is likely poor adhesion between layers of graphene(−)SDS and PAH. Deposition of subsequent layers greatly improves the coverage by overlapping adjacent graphene flakes.

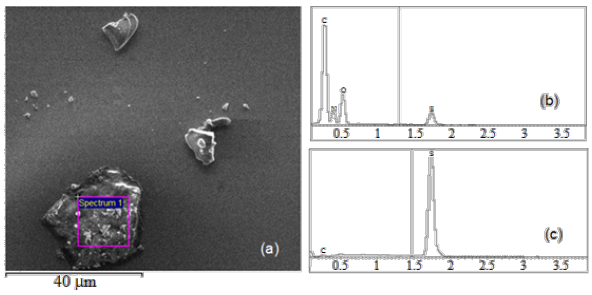

Figure 7: (a) SEM image of PAH/graphene(−)SDS layer on a silicon surface; (b) EDX spectra recorded on a graphene flake, and (c) an empty space.

Adhesion between graphene and substrate was greatly improved when using a branched polycation such as PEI. The AFM image of graphene(−)SDS deposited onto a layer of PEI in Figure 8 shows far better surface coverage. However it can be seen that graphene flakes overlap and form double and, in some cases, triple layers.

Sectional analysis performed on the sample shows the double and triple layers, and shows the thickness of a single flake at approximately 2.5 nm. This is a somewhat higher than that for LS films in Figure 6; the difference could potentially be caused by the presence of the PEI layer.

Optical characterisation of thin graphene-surfactant films

Spectroscopic ellipsometry study

The analysis of graphene films by spectroscopic ellipsometry has already been carried out by other groups, and so is fairly well described [20,21]. A typical set of spectra of Ψ and Δ of graphene(−)SDS deposited on Si by alternation with PAH are shown in Figure 9a. Numbers 1, 2, and 3 indicate the number of PAH/graphene bilayers deposited. It can be seen from the data that all Ψ spectra almost coincide with each other, while the Δ spectra shift downwards upon deposition of bilayers of PAH/graphene(−)SDS.

The thickness values (*d*) and dispersions, e.g., spectra of refractive index (*n*) and extinction coefficient (*k*) of graphene films can be found by fitting the above spectra to the model using the dedicated software by J. A. Woollam. In this particular case, the model of the reflecting system consists of the following three layers: (1) Si substrate; (2) the layer of native oxide (SiO_2) which is typically present on the surface of Si; (3) the deposited layer of PAH/graphene(−)SDS. The ambient was air. Optical parameters for Si and SiO_2 were taken from the J. A. Woollam database. The fitting was first performed for ellipsometric spec-

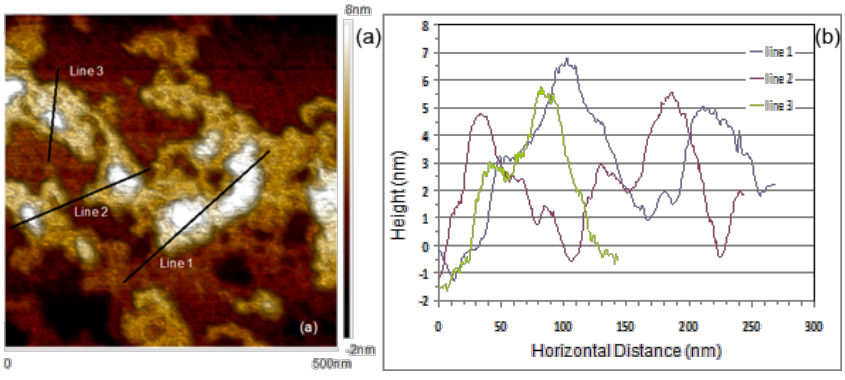

Figure 8: (a) AFM image (tapping mode) of a PEI/graphene(−)SDS film, and (b) a corresponding sectional analysis.

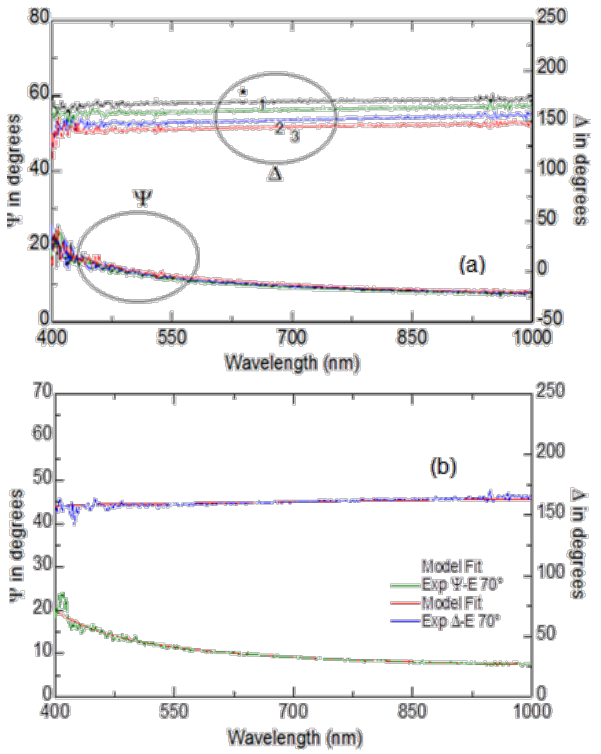

Figure 9: (a) Spectra of ellipsometric parameters Ψ and Δ recorded on a bare silicon surface (*) and on PAH/graphene(−)SDS films deposited on it (the numbers 1, 2, 3 correspond to the number of PAH/graphene bilayers); (b) The example of data fitting for one bilayer of PAH/graphene deposited on silicon using a three-layer model.

tra of the Si/SiO_2 substrate. For the set of data in Figure 9a, the fitting for the thickness of the native SiO_2 layer was performed first using the data for the bare Si substrate. The thickness of SiO_2 layer obtained (d = 3.2 nm) was then fixed for consecutive fittings. The PAH/graphene(−)SDS film was considered as one layer in the following fittings which is justified by the fact that aliphatic chains of SDS interlock with PAH and form a mixed composite layer of PAH/graphene(−)SDS. Several possible models were tried for fitting PAH/graphene(−)SDS layers, and the best results were achieved using a Lorentz oscillator model from the J. A. Woollam data analysis software, which is given below as a dispersion function of a complex dielectric permittivity, ε(hν):

$$\varepsilon(h\nu) = \varepsilon_{1\infty} + \sum_k \frac{A_k}{E_k^2 - (h\nu)^2 - jB_k h\nu},$$

where $\varepsilon_{1\infty}$ is the dielectric permittivity at infinite frequency, E_k, A_k and B_k are, respectively, the position, amplitude, and half-width of the k-th Lorentzian peak. There could be a number of peaks from 1 to k. The best fit was obtained with the use of a single Lorentzian with the following parameters: $\varepsilon_{1\infty}$ = 1.31, E_k = 0.625 eV, A_k = 1.759 $(eV)^2$, B_k = 3.86 eV. The presence of the Lorentz peak in the IR region gives a featureless dispersion of k for graphene–surfactant composite films in the visible spectral range similar to that reported in [22,23]. The absorption peak of graphene reported earlier [22,23] at about 260 nm is outside the spectral range of our ellipsometric instrument (370–1000 nm). The example of ellipsometry data fitting for one PAH/graphene bilayer deposited on Si is shown in Figure 9b with the dotted (fitting) lines almost perfectly reproducing the experimental spectra (solid lines). The thicknesses were found to be of 6.65, 9.3, and 10.88 nm for 1st, 2nd, and 3rd PAH/graphene bilayer, respectively. Although the d value of the first bilayer appeared to be too high, the average thickness increment Δd = 3.63 ± 2 nm is reasonable and close to that observed with AFM.

Spectroscopic ellipsometry measurements were carried out on samples after each layer was deposited and similarly to the previous experiments, Ψ spectra did not change much while the Δ spectra exhibited downward shifts upon deposition of the layers. The ellipsometry data fitting was performed in a similar way as described above using a three layer model containing the substrate glass, the chromium/gold layer, and the graphene layer. The ambient was air. The parameters d, $n(\lambda)$ and $k(\lambda)$ of the chromium/gold layer were found by fitting the data for uncoated samples, and then used as fixed parameters for subsequent fittings. The graphene layers were modeled through a Lorentz oscillator as before, the values for thickness obtained are plotted against the graphene layers deposited in Figure 10. As one can see the deposition is not consistent, the graphene layers started to peel off after 3rd deposition most likely because of poor adhesion between graphene layers. However, the thickness increment of 0.87 ± 0.03 nm in the middle of the graph is much smaller and corresponds to graphene–surfactant layers without intermediate polycation layers.

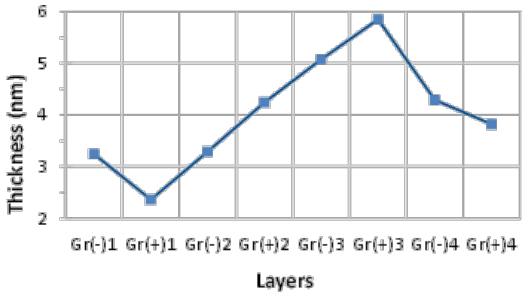

Figure 10: The variation of the film thickness upon deposition of alternating graphene(−)SDS and graphene(+)CTAB graphene layers on gold-coated glass slides.

As mentioned above, the use of PEI as a binding layer alternating with graphene(−)SDS improving the deposition of graphene. The ellipsometry spectra recorded on samples of PEI/

graphene(−)SDS deposited on gold-coated glass are shown in Figure 11a. Both Ψ and Δ spectra show the characteristic features at around 450 nm associated with surface plasmon oscillations in thin gold films. Also, the spectra shift upwards and downwards, respectively, upon deposition of PEI/graphene layers, which is consistent with the thickness increment of 2.5 nm obtained by fitting of the data in Figure 11a. Following the approach developed in [24], in Figure 11b we attempted to present these data as differential spectra of $\delta\Psi = \Psi - \Psi^*$, and $\delta\Delta = \Delta - \Delta^*$ (Ψ^* and Δ^* correspond to spectra of uncoated gold samples), which allows one to clearly distinguish a contribution of deposited layers.

It is quite remarkable to observe spectral features around the plasmon-resonance frequency of the gold substrate, which are not related to graphene itself [22,23] but rather appeared as a result of the interaction of π-electrons in graphene with free electrons in the gold film.

TIRE study

The samples were constructed by electrostatic LbL deposition of PEI and graphene(−)SDS on chromium/gold-coated glass slides, as described above. The results obtained are shown in Figure 12 as TIRE spectra of Ψ and Δ. The spectra of Ψ resemble a traditional SPR curve with the maximum corresponding to conditions of total internal reflection of light, while the minimum is the actual plasmon resonance. The spectra of Δ, which do not exist in traditional SPR, represent a new phase-related characteristic and show a sharp drop near the resonance wavelength.

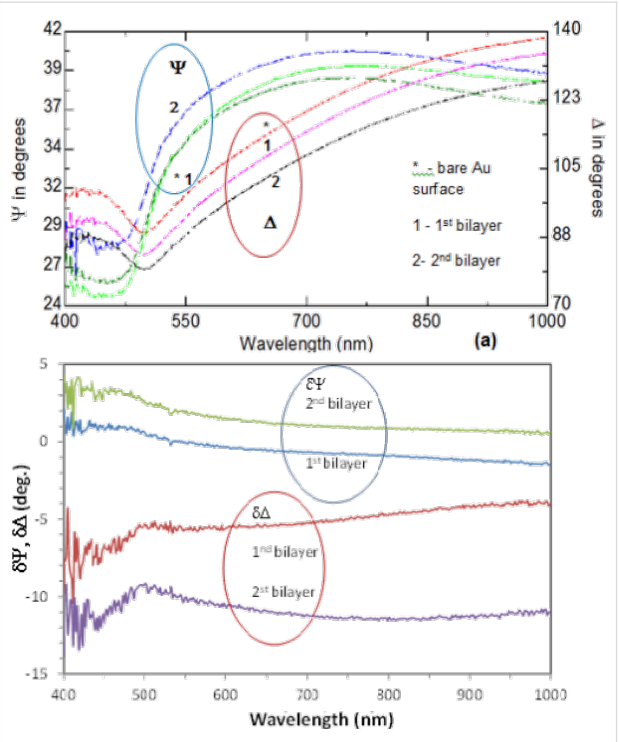

Figure 11: (a) Ψ, Δ and (b) δΨ, δΔ spectra of PEI/graphene(−)SDS films deposited on gold-coated glass slides.

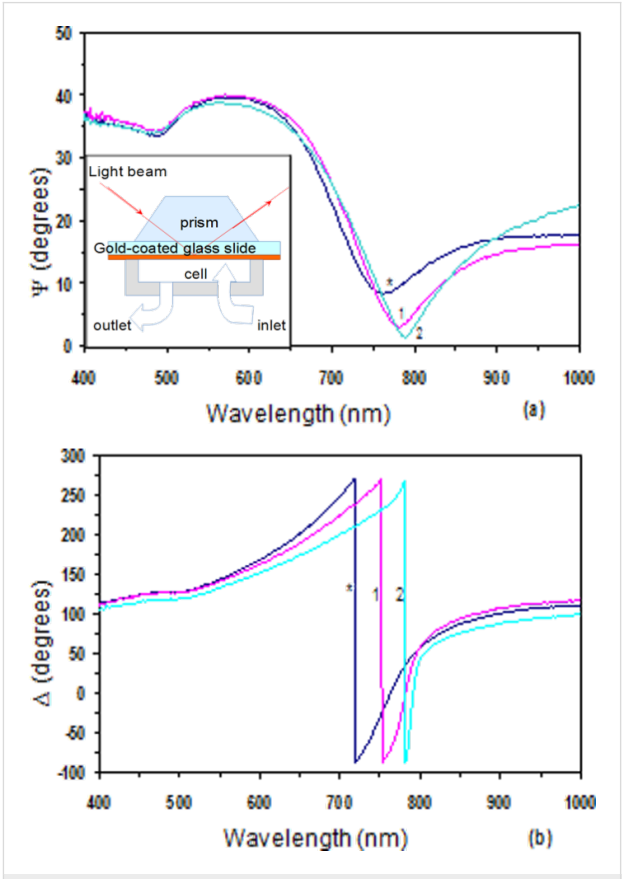

Figure 12: TIRE spectra of (a) Ψ, and (b) Δ recorded on a bare gold-coated glass slide (*) and after deposition of bilayers of PEI/graphene(−)SDS. Numbers 1, 2, and 3 indicate the number of bilayers deposited. The inset shows the geometry of TIRE set-up.

Deposition of graphene layers made the SPR minimum even lower on the Ψ spectra while causing an additional phase shift on Δ spectra. The enhancement of the SPR peak due to the deposition of graphene layers is observed for the first time. It is interesting to note that graphene itself does not show plasmonic behavior in the visible spectral range as was proven by ellipsometry measurements shown before (Figure 9). At the same time the interaction of π-electrons in graphene and free electrons in gold (which we suspected earlier) may lead to the enhancement of SPR in gold layers. The TIRE data fitting revealed a similar thickness increment of 2.5 nm per PEI/graphene bilayer which was reported earlier.

Conclusion

A simple semi-automated technique for graphene production by aqueous sonochemical exfoliation of graphite in the presence of

ionic surfactants, e.g., CTAB or SDS, was developed. Full automation could be potentially achieved by adding surface tension sensors to control the amount of surfactant being added to the reactor, thus maintaining a constant and optimum surface tension. The formation of individual graphene flakes and the interaction of alkyl chains of the surfactants with graphene were, respectively, confirmed with Raman spectroscopy and NMR measurements.

The two different graphene-surfactant complexes produced (graphene(+)CTAB and graphene(−)SDS) appeared to be soluble in water and thus suitable for electrostatic LbL deposition. Both compounds were also found to be amphiphilic and soluble in chloroform, hence it was possible to form stable monolayers on the water surface. Thin films of the above graphene composites were deposited onto different solid substrates, i.e., silicon, glass and gold-coated glass, using either electrostatic LbL or LB (LS) deposition techniques. SEM and AFM study showed that LB (or LS) films of graphene(+)CTAB had poor surface coverage and adhesion to the substrate. Electrostatic LbL deposition of graphene by alternation of graphene with oppositely charged polyelectrolytes was much more promising in these aspects. Several combinations of materials were tried including the alternation of graphene(+)CTAB and graphene(−)SDS. The best results were achieved by alternation of graphene(−)SDS with PEI. AFM study allowed the estimation the thickness of an individual graphene–surfactant flakes of about 2.0–2.5 nm.

The spectroscopic ellipsometry study of graphene thin films gave similar values for the thickness of the graphene–surfactant composite layer. While the dispersions of refractive index and extinction coefficient were modelled by a single Lorentzian peak lying in the IR region, the absorption peak of graphene at approximately 260 nm was outside the spectral range (370–1000 nm) of the ellipsometric instrument. Interesting results were obtained when studying the SPR effect in gold films coated with a few layers of graphene using both external and internal (TIRE) reflection ellipsometry. Even though graphene itself axhibits no spectral features associated with plasmon oscillations in the above spectral range, the deposition of graphene layers on gold progressively enhances the plasmon resonance in TIRE Ψ spectra and caused an extra phase shift in TIRE Δ spectra. This phenomenon can be explored in the future for enhancing the performance of SPR-based biosensors.

Acknowledgements

The authors would like to acknowledge Dr. Isaac Chang and Dr. Shei Su of the University of Birmingham for Raman measurements.

References

1. Novoselov, K. S.; Geim, A. K.; Morozov, S. V.; Jiang, D.; Zhang, Y.; Dubonos, S. V.; Grigorieva, I. V.; Firsov, A. A. *Science* **2004,** *306,* 666–669. doi:10.1126/science.1102896
2. Sharma, B. K.; Ahn, J.-H. *Solid-State Electron.* **2013,** *89,* 177–188. doi:10.1016/j.sse.2013.08.007
3. Torrisi, F.; Hasan, T.; Wu, W.; Sun, Z.; Lombardo, A.; Kulmala, T. S.; Hsieh, G.-W.; Jung, S.; Bonaccorso, F.; Paul, P. J.; Chu, D.; Ferrari, A. C. *ACS Nano* **2012,** *6,* 2992–3006. doi:10.1021/nn2044609
4. Notley, S. M. *Langmuir* **2012,** *28,* 14110–14113. doi:10.1021/la302750e
5. Hummers, W. S., Jr.; Offeman, R. E. *J. Am. Chem. Soc.* **1958,** *80,* 1339. doi:10.1021/ja01539a017
6. Walch, N. J.; Davis, F.; Langford, N.; Holmes, J. L.; Collyer, S. D.; Higson, S. P. J. *Anal. Chem.* **2015,** *87,* 9273–9279. doi:10.1021/acs.analchem.5b01829
7. Fan, J.; Shi, Z.; Ge, Y.; Wang, J.; Wang, Y.; Yin, J. *J. Mater. Chem.* **2012,** *22,* 13764–13772. doi:10.1039/c2jm31437a
8. Petty, M. C. *Langmuir–Blodgett Films. An introduction;* Cambridge University Press: Cambridge, United Kingdom, 1996. doi:10.1017/CBO9780511622519
9. Nabok, A. *Organic and Inorganic Nanostructures;* Artech House Publishers: London, United Kingdom, 2005.
10. Lvov, Y.; Decher, G.; Moehwald, H. *Langmuir* **1993,** *9,* 481–486. doi:10.1021/la00026a020
11. Lvov, Y.; Decher, G. *Crystallogr. Rep.* **1994,** *39,* 696–716.
12. Westphal, P.; Bornmann, A. *Sens. Actuators, B* **2002,** *84,* 278–282. doi:10.1016/S0925-4005(02)00037-0
13. Poksinski, M.; Arwin, H. *Sens. Actuators, B* **2003,** *94,* 247–252. doi:10.1016/S0925-4005(03)00382-4
14. Nabok, A. V.; Tsargorodskaya, A.; Hassan, A. K.; Starodub, N. F. *Appl. Surf. Sci.* **2005,** *246,* 381–386. doi:10.1016/j.apsusc.2004.11.084
15. Nabok, A.; Tsargorodskaya, A. *Thin Solid Films* **2008,** *516,* 8993–9001. doi:10.1016/j.tsf.2007.11.077
16. Webb, G. A. *Modern Magnetic Resonance: Applications in Chemistry, Biological and Marine Sciences;* Springer: Berlin, Germany, 2008.
17. Huang, C.-H.; Su, C.-Y.; Okada, T.; Li, L.-J.; Ho, K.-I; Li, P.-W.; Chen, I.-H.; Chou, C.; Lai, C.-S.; Samukawa, S. *Carbon* **2013,** *61,* 229–235. doi:10.1016/j.carbon.2013.04.099
18. Matthews, M. J.; Pimenta, M. A.; Dresselhaus, G.; Dresselhaus, M. S.; Endo, M. *Phys. Rev. B* **1999,** *59,* R6585–R6588. doi:10.1103/PhysRevB.59.R6585
19. Gupta, A.; Chen, G.; Joshi, P.; Tadigadapa, S.; Eklund, P. C. *Nano Lett.* **2006,** *6,* 2667–2673. doi:10.1021/nl061420a
20. Isić, G.; Jakovljević, M.; Filipović, M.; Jovanović, D.; Vasić, B.; Lazović, S.; Puač, N.; Petrović, Z. L.; Kostić, R.; Gajić, R.; Humlíček, J.; Losurdo, M.; Bruno, G.; Bergmair, I.; Hingerl, K. *Nanophotonics* **2011,** *5,* 051809. doi:10.1117/1.3598162
21. Losurdo, M.; Giangregorio, M. M.; Bianco, G. V.; Capezzuto, P.; Bruno, G. *Thin Solid Films* **2014,** *571,* 389–394. doi:10.1016/j.tsf.2014.03.057
22. Kravets, V. G.; Grigorenko, A. N.; Nair, R. R.; Blake, P.; Anissimova, S.; Novoselov, K. S.; Geim, A. K. *Phys. Rev. B* **2010,** *81,* 155413–155416. doi:10.1103/PhysRevB.81.155413
23. Weber, J. W.; Calado, V. E.; van de Sanden, M. C. M. *Appl. Phys. Lett.* **2010,** *97,* 91904. doi:10.1063/1.3475393
24. Prato, M.; Moroni, R.; Bisio, F.; Rolandi, R.; Mattera, L.; Cavalleri, O.; Canepa, M. *J. Phys. Chem. C* **2008,** *12,* 3899–3906. doi:10.1021/jp711194s

BEILSTEIN JOURNAL OF NANOTECHNOLOGY

Mismatch detection in DNA monolayers by atomic force microscopy and electrochemical impedance spectroscopy

Maryse D. Nkoua Ngavouka[‡1,2,3], Pietro Capaldo[‡1,3], Elena Ambrosetti[1,2,3], Giacinto Scoles[4], Loredana Casalis[1,2] and Pietro Parisse[*1,2]

Full Research Paper

Open Access

Address:
[1]Elettra-Sincrotrone Trieste S.C.p.A., s.s. 14 km 163.5 in Area Science Park, Basovizza, Trieste, Italy, [2]INSTM – ST Unit, s.s. 14 km 163.5 in Area Science Park, Basovizza, Trieste, Italy, [3]University of Trieste, Via Valerio 9, Trieste, Italy and [4]Department of Medical and Biological Sciences, University of Udine, Udine, Italy

Email:
Pietro Parisse[*] - pietro.parisse@elettra.eu

* Corresponding author ‡ Equal contributors

Keywords:
atomic force microscopy; DNA monolayers; electrochemical impedance spectroscopy; hybridization; mismatches

Beilstein J. Nanotechnol. **2016,** *7,* 220–227.
doi:10.3762/bjnano.7.20

Received: 19 October 2015
Accepted: 25 January 2016
Published: 09 February 2016

This article is part of the Thematic Series "Organized films".

Guest Editor: M. Canepa

Abstract

Background: DNA hybridization is at the basis of most current technologies for genotyping and sequencing, due to the unique properties of DNA base-pairing that guarantee a high grade of selectivity. Nonetheless the presence of single base mismatches or not perfectly matched sequences can affect the response of the devices and the major challenge is, nowadays, to distinguish a mismatch of a single base and, at the same time, unequivocally differentiate devices read-out of fully and partially matching sequences.

Results: We present here two platforms based on different sensing strategies, to detect mismatched and/or perfectly matched complementary DNA strands hybridization into ssDNA oligonucleotide monolayers. The first platform exploits atomic force microscopy-based nanolithography to create ssDNA nano-arrays on gold surfaces. AFM topography measurements then monitor the variation of height of the nanostructures upon biorecognition and then follow annealing at different temperatures. This strategy allowed us to clearly detect the presence of mismatches. The second strategy exploits the change in capacitance at the interface between an ssDNA-functionalized gold electrode and the solution due to the hybridization process in a miniaturized electrochemical cell. Through electrochemical impedance spectroscopy measurements on extended ssDNA self-assembled monolayers we followed in real-time the variation of capacitance, being able to distinguish, through the difference in hybridization kinetics, not only the presence of single, double or triple mismatches in the complementary sequence, but also the position of the mismatched base pair with respect to the electrode surface.

Conclusion: We demonstrate here two platforms based on different sensing strategies as sensitive and selective tools to discriminate mismatches. Our assays are ready for parallelization and can be used in the detection and quantification of single nucleotide mismatches in microRNAs or in genomic DNA.

Introduction

Most current technologies for genotyping and sequencing are based on DNA hybridization, exploiting the high grade of selectivity due to the unique properties of DNA base pairing. Although the understanding of the behaviour of nucleic acids on a solid surface has made huge progress from the seminal work of Southern [1] due to the rapid development of DNA microarray and DNA microarray-based techniques [2,3], there are still open questions and bottlenecks limiting the selectivity and the sensitivity of devices that are based on the hybridization of DNA [4]. One example is the detection of single nucleotide polymorphism (SNP) [5]. Single-base variations in a DNA/RNA sequence afflict 1 out of 1000 base pairs in the genome causing small differences in individuals belonging to the same species. This can lead to diseases [6-8] or drastically affect the response to pharmacological treatments [9]. SNPs are particularly relevant for applications in the field of pharmacogenomics and population genetics, as a diagnostic tool towards a personalized approach to diseases [10]. However, state-of-the-art devices still are not fully able to identify a single-base mismatch nor to unequivocally distinguish fully and partially matching sequences during hybridization [11,12].

The most common strategies for mismatch detection can be divided in three different categories: hybridization-based detection, detection based on thermal denaturation and protein-mediated detection [5]. For each strategy, different read-out systems and experimental designs have been reported, which include fluorescence [13], surface plasmon resonance [14,15], electrochemical [16,17], atomic force microscopy [18,19], colorimetric assays [20], Raman spectroscopy [21]. However, all these state-of-the-art technologies are limited in multiplexing implementation, mutation discrimination and/or sample throughput. Therefore the field is still open for an optimization of strategies to overcome the current limitations [22].

We present here two platforms, which are based on different sensing strategies, to detect mismatched and/or perfectly matched hybridization of complementary DNA strands into ssDNA oligonucleotide monolayers. The first platform exploits atomic force microscopy-based nanolithography (nanografting) to create ssDNA nano-arrays on gold surfaces and then AFM topography measurements to monitor the variation of the height of the nanostructures after loading the complementary/mismatched strands in the liquid cell. In the last years we optimized this nanomechanical approach, which is based in the different rigidity of ss- and dsDNA [23-25], enabling the ultrasensitive detection of biomarkers [26]. The second strategy exploits the change in capacitance during the hybridization process, measured at the interface between a ssDNA-functionalized gold electrode and the solution in an electrochemical cell. In a previous work we demonstrated the ability to follow the hybridization of perfectly matched sequences in real time through electrochemical impedance spectroscopy (EIS) measurements on extended ssDNA self-assembled monolayers (SAMs) [27]. Here we successfully tested EIS for the detection of mismatched sequences. From the analysis of hybridization kinetics we distinguished the presence of single or multiple mismatches and their relative position.

Both nanoarrays and EIS devices hold the premises for parallelization, multiplexing and low-volume analysis, making them amenable for point-of-care diagnostics of SNPs. Moreover a comparative analysis between the two techniques allows for a deep understanding of hybridization processes in the presence of single and multiple mismatches.

Experimental

Fabrication and measurement processes of AFM-based assays

Gold-coated substrates were immersed in 300 μM of top oligo(ethylene glycol)-terminated alkylthiols (TOEG6: $HS–(CH_2)_{11}–(OCH_2CH_2)_6–OH$) ethanol solutions, overnight, to allow for the adsorption and assembly of a full monolayer with bio-repellent characteristics [28]. The samples were then removed from the solution, rinsed with ethanol and water to remove loosely bound molecules and placed in a customised liquid cell for the AFM experiments.

All AFM experiments were carried out on a XE-100 Park Instruments with a customised liquid cell. Si cantilevers (NSC36B Mikromasch, spring constant: 0.6 N/m) were used for the nanografting experiments. Briefly, the AFM tip is scanned at high load (approx. 100 nN) over the TOEG6 SAM, operating in a buffer solution (10 mM Tris-HCl, 1 mM EDTA, (hereafter TE), 1 M NaCl, pH 7.1) containing 5 μM thiolated ssDNA oligonucleotides. The applied load is sufficient to displace the TOEG6 molecules from the gold surface, which are subsequently locally substituted by the thiolated ssDNA molecules, creating ssDNA patches embedded in the surrounding TOEG6 carpet. Exchanging the buffer and the thiolated ssDNA probes, it is possible to sequentially immobilize different sequences on the same substrate. The parameters for nanografting have been properly chosen to obtain a surface density of probes optimal for the detection of target hybridization, following previous works of our group [23-25]. After the immobilization the ssDNA patches are measured through AFM topographic imaging in soft contact with standard silicon cantilevers (CSC38 Mikromasch, spring constant: 0.06 N/m) at 1 Hz scan rate, applying a force of 0.1 nN. Hybridization was monitored after the addition of the required target solutions (1 μM target in

TE buffer 1 M NaCl) into the AFM liquid cell for 1 h. All DNA sequences used in the present work are listed in Table 1.

Fabrication and measurement processes for EIS-based assay

Detailed fabrication processes and layout of the electrochemical impedance spectroscopy experiments have been reported by Ianeselli and co-workers [27]. Briefly, the setup (a scheme is reported in Figure S1, Supporting Information File 1) consists of a glass slide with lithographically fabricated working (WE) and counter (CE) gold electrodes. The two electrodes are covered with insulating resist leaving exposed to the solution only the active part, to avoid spurious effects. To confine the drop of solution and to carefully position the reference electrode (a classical millimetre-sized Ag/AgCl pellet electrode) we placed around the electrodes a silicone circular cell (6 mm in diameter, 4 mm in height). The WE and CE electrodes were functionalized with thiolated ssDNA molecules using a well-established procedure for DNA SAMs on gold [23,29]. Initially the electrodes were wetted for 10 min with a drop of a high-ionic-strength buffer, TE 1 M NaCl, containing 1 μM thiolated ssDNA. In this way a low-density ssDNA SAM (about 2×10^{12} to 3×10^{12} molecules/cm^2) was obtained [29]. After DNA-functionalization the devices were rinsed with the buffer solution used for the measurements, 100 mM KCl, and the capacitance at the electrode/electrolyte interface was measured. In the hybridization step the cell is filled with a drop of the same hybridizing buffer solution, 100 mM KCl, containing the complementary or partially complementary DNA strand at different concentrations.

The electrochemical current I_{rms} is monitored between WE and CE with a Heka PG340 USB potentiostat upon application of a 10 mV AC voltage at 100, 200, 250 and 400 Hz. In this regime of frequencies the total impedance is dominated by the capacitance at the electrode/electrolyte interface, allowing for the extraction of the differential capacitance simply from a linear fit of I_{rms}. The functionalized electrodes can be regenerated after the hybridization process by means of a thermal treatment in TE buffer (pH 9) for 1 h in oven at a temperature 10 °C higher than the melting temperature of the used DNA sequence. The differential capacitance after the regeneration treatment maintains its original value within the error bars (Figure S2, Supporting Information File 1).

Results and Discussion

Atomic force microscopy-based assay

In Figure 1 we report a schematic representation of the AFM-based assay. We immobilize by means of nanografting on a gold surface two ssDNA sequences, differing by one base (reported as a red mark), and carefully measure the height of the DNA nanostructures with respect to the surrounding biorepellent self-assembled monolayer, this last serving as a constant reference for the height measurements (h_{ssDNA}, Figure 1a). Then we hybridize with a sequence that is perfectly complementary to one of the two sequences. We expect the perfect matched (PM) sequence and the one-base mismatched (MM) sequence hybridization to produce a similar increase in height, which follows the change in the nanomechanical properties from ssDNA to dsDNA configuration (h_{dsDNA}, Figure 1b). We then perform a thermal treatment to selectively de-hybridize only the MM sequences, as we can measure from the different height response of the two grafted ssDNA structures ($h_{after\ treatment}$, Figure 1c). Since the non-perfectly matching sequence will have a reduced melting temperature with respect to the perfectly matched (PM) sequence (T_m(MM) < T_m(PM)), its de-hybridization will be favoured upon annealing to a temperature (T_{ann}) close or slightly higher than the melting temperature of the perfect matched sequence (T_m(MM) < T_m(PM) ≤ T_{ann}). We have used our AFM-based nanomechanical approach to distinguish single mismatched DNA base pairs of single nucleotide polymorphisms (SNPs), in particular a T–G mismatch.

Table 1: List of the sequences used for the AFM and EIS experiments. The position of the mismatches are typeset in bold.

sequence name	sequence
HS-SNP-C	HS–$(CH_2)_6$–5'–tgataatcatta**c**aaaactgaaata–3'
HS-SNP-T	HS–$(CH_2)_6$–5'–tgataatcatta**t**aaaactgaaata–3'
SNP-coC	5'–tatttcagtttt**g**taatgattatca–3'
SNP-coT	5'–tatttcagtttt**a**taatgattatca–3'
HS_ssDNA	HS–$(CH_2)_6$–5'–caaaacagcagcaatccaaagatcagacacccgattacaaatgc–3'
cDNA_3MM	5'–**t**catttgtaatcgggtgtc**g**gatc**c**ttggattgctgctgttttg–3'
cDNA_PM	5'–gcatttgtaatcgggtgtctgatctttggattgctgctgttttg–3'
cDNA_2MM	5'–gcatttgtaatcgggtgtc**g**gatc**c**ttggattgctgctgttttg–3'
cDNA_DOWN	5'–tctttggattgctgctgttttg–3'
cDNA_UP	5'–gcatttgtaatcgggtgtctga–3'

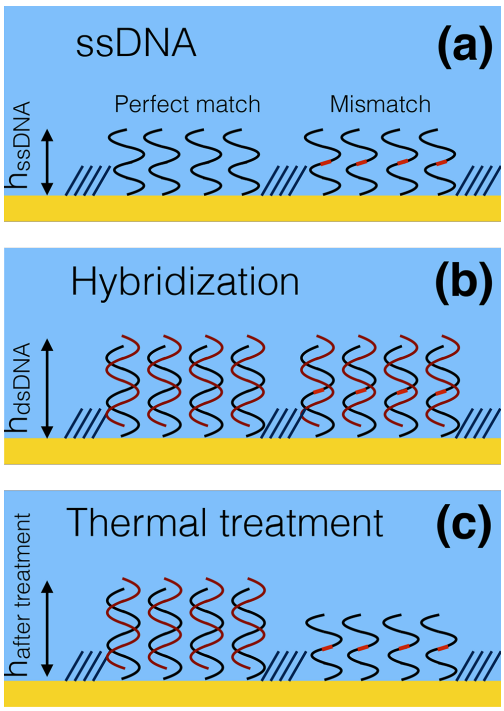

Figure 1: Schematics of the atomic force microscopy-based assay. We graft two sets of ssDNA nanostructures, whose sequences differ by one single base, highlighted by a red dot (panel a, b,c). By means of careful AFM topographic measurements, we record the height variation over the ssDNA nanostructures, (h_{ssDNA}, panel a) upon hybridization with a strand fully matching only the left grafted strand (h_{dsDNA} panel b), upon thermal treatment, ($h_{after\ treatment}$, panel c), evidencing the different de-hybridization behaviour of perfectly matched sequences vs mismatched sequences.

In particular, we chose to immobilize on the surface two 25 bases-long ssDNA sequences, HS-SNP-C and HS-SNP-T (see Table 1) differing from one cytosine vs one thymine. We produced by nanografting patches of each of the two ssDNA sequences into 1 μm^2 areas in the biorepellent TOEG6 SAM, using the same grafting parameters (Figure 2a). After grafting, the sample was incubated with the sequence SNP-coC fully matching one strand and matching the second one but for one base, originating a T/G polymorphism. In Figure 2b we report the AFM topographic image after incubation with SNP-coC targets for 1 h. The height variation ($\Delta h = h - h_{ssDNA}$) after the hybridization step is very similar for the two different sequences (Figure 2d), evidencing the impossibility to clearly distinguish the presence of the mismatched base only by means of height measurements. We therefore designed a melting experiment: we kept the sample in TE buffer, pH 9, for 1 h at 60 °C, a temperature slightly higher than the melting temperature of the PM sequence (T_m^{PM} = 57 °C, T_m^{MM} = 53 °C). In Figure 2c we report the AFM topographic image after the thermal treatment and in Figure 2d the relative height changes. We can observe a sensible height decrease in the HS-SNP-T probe only, matching almost completely the initial ssDNA value. This is the sign of a complete de-hybridization of the mismatched sequence, whereas the perfect match probe is only slightly perturbed by this thermal treatment.

These successful preliminary experiments demonstrate that our system has the ability to detect mismatches after precise

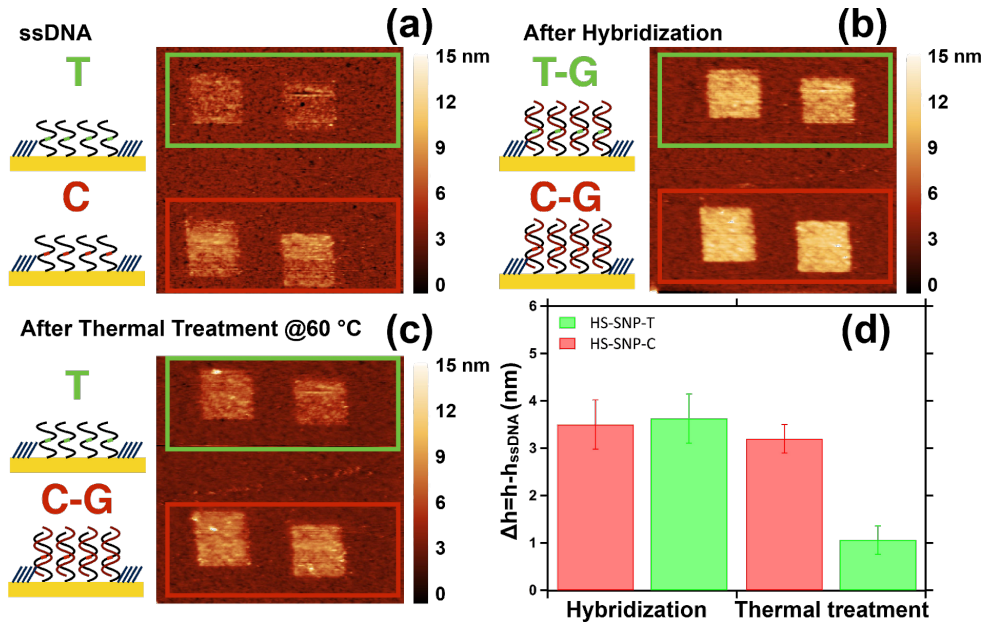

Figure 2: Schematic view and AFM topographic images of HS-SNP-C and HS-SNP-T nanografted patches (a) before and (b) after incubation with SNP-C for 1 h and (c) thermal treatment. (d) Histogram of the height variation with respect to the ssDNA patches ($\Delta h = h - h_{ssDNA}$) after the hybridization with SNP-C-Co sequence and after the thermal treatment (1 h at 60 °C).

annealing steps, as the ones used in current melting-based SNPs assays [30,31]. The novelty of our assay resides in the possibility of reducing the dimensions of the spots (below 1 μm^2) and to work multiplexing in small volumes. The use of locked nucleic acids or enzyme-based strategies [22] might improve sensitivity further possibly circumventing the annealing step.

Electrochemical impedance spectroscopy-based assay

Despite the high sensitivity, the AFM assay does not allow, at the moment, for a real-time investigation of binding events. In order to overcome such limitations, we tested in parallel another device developed in our laboratory [27], based on electrochemical impedance spectroscopy (EIS) [32]. The device exploits the capacitive effects at the interface between an electrode and an electrolytic solution. When a potential is applied to the gold electrode the free ions in solution will rearrange close to the surface creating the so-called double layer capacitance (C_{DL}) [33,34]. In presence of a molecular layer between the solution and the electrode, an additional capacitance in series has to be taken in account. In our case, similarly to the AFM experiments, we functionalized the electrode with a low density ssDNA monolayer that serves as a probe for hybridization studies. In Figure 3 we report a scheme of the device as a series of two capacitances, one due to the charged DNA strands, C_{ssDNA} and the other (C_{DL}) to the pure ionic solution [35]. The measurements of the total differential capacitance will be dominated by the smaller capacitance and, since C_{ssDNA} (densities of about 10 $\mu F/cm^2$) < C_{DL} (densities of about 40 $\mu F/cm^2$) [27], will give us a reasonable estimation of the C_{ssDNA}. In the approximation of parallel plate capacitance we can write C_{ssDNA} as $\varepsilon \cdot \varepsilon_0(A/d)$, where A is the area of the electrode, d the thickness of the ssDNA layer, and ε_0 and ε are the dielectric constant of vacuum and ssDNA layer, respectively. When we insert a complementary strand in the electrochemical cell, the molecular recognition between the two strands will cause a change in the capacitance at the interface, due to a combination of height changes, displacement of water molecules upon binding of new strands, and rearrangement of charge density, bringing to a new value for the capacitance, C_{dsDNA} [36]. Our device can follow the variation of capacitance in real time, allowing for the study of the kinetic of hybridization. Indeed, the eventual presence of a mismatch should change the kinetic of the binding, as already reported by pioneering work of Georgiadis's group [37,38]. Therefore, following in real time the variation of the capacitance we expect to distinguish the presence of mismatched sequences.

We functionalized the electrode with the HS-SNP-T probe and measured the capacitance at the electrode (red dots in Figure 3). The value of C_{ssDNA} is shown to be constant over an hour of continuous measurements, as already demonstrated by Ianeselli et al. [27]. After addition of the perfectly matching sequence SNP-coT (blue squares) in the electrochemical cell, we observed a fast decrease of the capacitance, followed by a subsequent slow decay that reaches a plateau at a value of capacitance 36% less than the initial value, as a sign of the occurred hybridization. When we insert on the regenerated electrode with the HS-SNP-T probe the mismatched sequence SNP-coC (green triangles) we observe a slower decay of the capacitance tending to a plateau much closer to the initial C_{ssDNA} value than the perfectly matched one (21% variation), confirming a different

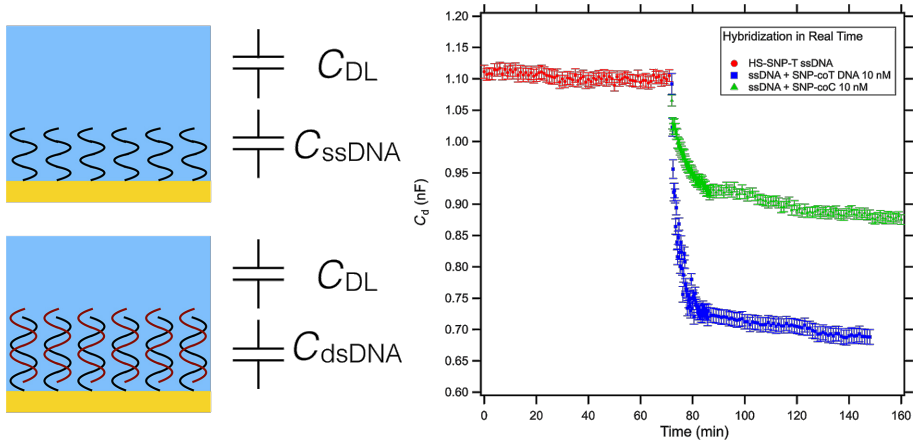

Figure 3: Schematic representation of the electrode/electrolyte interface. The first layer in contact with the gold electrode is the ssDNA self-assembled monolayer, modelled as a capacitance C_{ssDNA}. Then we have the ions present in solution that arrange in response to the gold and DNA charges forming the so-called double layer capacitance C_{DL}, in series with C_{ssDNA}. When hybridization occurs, the binding of the complementary strand will produce a change in capacitance due to height changes, substitution of water molecules in the biological layer, and changes in the electrical charge density. The capacitance, extracted from the impedance measured in our electrochemical setup, is plotted versus time for the ssDNA-functionalized electrode (red curve) and for the mismatched (green) and perfectly matching (blue) complementary sequences.

kinetic behaviour and a less efficient hybridization. Our results are in good agreement with previous reports of Georgiadis based on SPR measurements [38]. We can observe here that the EIS measurements allow for distinguishing the mismatched and perfectly matched sequences by observing a different kinetic behaviour and a different capacitance plateau, whereas AFM was not able to directly detect a height difference. Indeed, the changes of capacitance at the functionalized electrode are the results of a combination of changes of height in the molecular case and rearrangement of charge density. The distortions on the DNA structure due to the mismatched bases can modify the charge distribution inside the molecular layer [39], causing a change in the capacitance that is readable in the EIS measurement, even if does not significantly affect the height of the layer after the hybridization.

We further tested our device exposing a 44 bases ssDNA (HS_ssDNA_44) probe to five different sequences: a perfect match (cDNA_44_PM), a double mismatch (cDNA_44_2MM), a triple mismatch (cDNA_44_3MM), and two 22 bases sequences complementary to the bottom half (cDNA_44_DOWN) and top half (cDNA_44_UP) part of the ssDNA_44 sequence, respectively.

In Figure 4a we report the study of the kinetics of DNA hybridization in the presence of 2 MM (green triangles) and 3 MM (black markers) mismatches compared with the PM (blue squares) sequence. We can clearly distinguish the behaviour of the three differently matching sequences. As expected we measured a slower kinetics and a lower plateau value going from the PM (36% variation) to 2 MM (17% variation) and finally to 3 MM (10% variation). Analogously, we observe in Figure 4b the evolution of the differential capacitance in presence of two 22 bases-long sequences complementary to the bottom half (cDNA_44_DOWN) and top half (cDNA_44_UP) part of the ssDNA_44 sequence, respectively. The curves follow more or less the same trend: an initial fast decay and then a slow decay to an asymptotic value representative of the efficiency of the hybridization. The kinetics and the asymptotic value are, respectively, slower and lower for the two half sequences with respect to the PM. Notably, the kinetics and efficiency of hybridization is much lower for the down matching sequence than for the up matching sequence. The 44 bases probe brush can in fact hinder the hybridization of the bottom part, while the upper part is made more available for the target sequence. Noteworthy, we observe a sensible variation between up and down hybridization in the presence of as low as 20 nM target concentration. The increase in sensitivity with respect to previous results reported by Georgiadis group [38] can be attributed to the applied electric field during the EIS real time hybridization measurements. Such electric field can indeed favour the hybridization process, as already reported by [40], accelerating the kinetics and improving the efficiency of the hybridization.

Conclusion

We proposed here two different sensing strategies based on the use of ssDNA monolayers tethered to gold substrates, for the

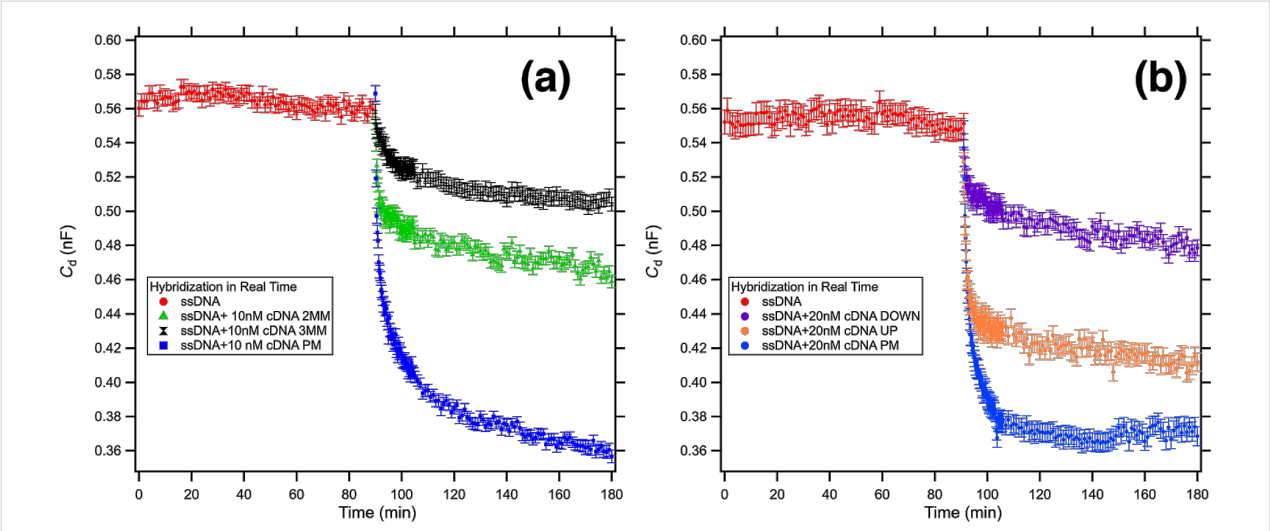

Figure 4: Differential capacitance measurements of the kinetics of DNA hybridization in presence of multiple mismatches (a) and in presence of partially complementary sequences (b). The red signal represents the differential capacitance of a low-density 44 bases ssDNA SAM functionalized WE measured in 100 mM KCl. (a) In blue we report the hybridization with the fully matching sequence, in green the hybridization with a sequence with 2 MMs, and in black the hybridization with a sequence with 3 MM. (b) In blue we report the hybridization with the fully matching sequence, in orange the hybridization with a 22mer sequence complementary with the upper part (far from the gold surface) of the target and in purple the hybridization with a 22mer sequence complementary with the lower part (close to the gold surface) of the target.

detection of mismatches in DNA oligonucleotides. Both the strategies are label-free and are sensitive enough to detect point mutations. In Table 2 we report a comparison between the performance of our two approaches (nano-mechanical and electrochemical) and current label-free surface-based biosensing strategies, according to recent literature. As we can see from the table, SPR strategies seem to be the most promising in terms of limit of detection. However, in these devices the surface area is larger, limiting multiplexing and small volume operations [14,15].

By contrast, the nano-mechanical approach on DNA nanoarrays although hampered by the time consuming processes of annealing and AFM height measurements (in line with benchmark of AFM-based assays reported in literature [11,18,19]), allows for a straightforward multiplexing. Ultimate sensitivity has been demonstrated for these arrays (100 pM, [41]), making them overall amenable to less invasive diagnostic analysis with a sensible reduction of the volume of the analyte till single cell [26].

Finally, our electrochemical measurements combine high sensitivity with real-time analysis, allowing for an accurate study of the kinetics and of the efficiency of the hybridization in mismatched targets. In our case, we were able to clearly distinguish the presence of single, or multiple mismatches and also the position with respect to the gold surface of the missing base-pairs. Due to the relatively simple geometry, the device could be easily further miniaturized and integrated in multiplexed arrays through microfluidic systems, allowing for point-of-care diagnostics. Our results demonstrated that nano-mechanical and EIS strategies are state of the art for the detection of SNP, confirming the relevance of immobilized DNA on solid supports in life science studies, including single cell RNA characterization, gene expression profile and genetic variability. Moreover, the complementarity of the two techniques (one more sensitive to the morphological and mechanical changes of the DNA layer, the other more sensitive to its charge density) let us conclude that the structural deformations related to a single mismatch have a strong influence on the charge distribution only, leaving the molecular structure not significantly affected.

Supporting Information

Supporting Information features a schematic view of the EIS setup, details of temperature stability of DNA nanobrushes for the AFM-based assays, and regeneration efficiency of ssDNA functionalized electrode for EIS measurements.

Supporting Information File 1

Additional experimental data.
[http://www.beilstein-journals.org/bjnano/content/supplementary/2190-4286-7-20-S1.pdf]

Acknowledgements

This work was supported by a FIRB 2011 grant “Nanotechnological approaches toward tumor theragnostic” (P.P., E.A., M.D.N.N. and L.C.), a grant from the Associazione Italiana per la Ricerca sul Cancro (AIRC) to L.C. and P.C. (AIRC 5 per mille 2011, no. 12214), and European Research Council (ERC) grant “Monalisa Quidproquo” (M.D.N.N and G.S.).

References

1. Maskos, U.; Southern, E. M. *Nucleic Acids Res.* **1992,** *20,* 1675–1678. doi:10.1093/nar/20.7.1675
2. Heller, M. J. *Annu. Rev. Biomed. Eng.* **2002,** *4,* 129–153. doi:10.1146/annurev.bioeng.4.020702.153438
3. Hoheisel, J. D. *Nat. Rev. Genet.* **2006,** *7,* 200–210. doi:10.1038/nrg1809
4. Harrison, A.; Binder, H.; Buhot, A.; Burden, C. J.; Carlon, E.; Gibas, C.; Gamble, L. J.; Halperin, A.; Hooyberghs, J.; Kreil, D. P.; Levicky, R.; Noble, P. A.; Ott, A.; Pettitt, B. M.; Tautz, D.; Pozhitkov, A. E. *Nucleic Acids Res.* **2013,** *41,* 2779–2796. doi:10.1093/nar/gks1358
5. Knez, K.; Spasic, D.; Janssen, K. P. F.; Lammertyn, J. *Analyst* **2014,** *139,* 353. doi:10.1039/c3an01436c
6. Paynter, N. P.; Chasman, D. I.; Buring, J. E.; Shiffman, D.; Cook, N. R.; Ridker, P. M. *Ann. Intern. Med.* **2009,** *150,* 65–72. doi:10.7326/0003-4819-150-2-200901200-00003
7. Tuupanen, S.; Turunen, M.; Lehtonen, R.; Hallikas, O.; Vanharanta, S.; Kivioja, T.; Björklund, M.; Wei, G.; Yan, J.; Niittymäki, I.; Mecklin, J.-P.; Järvinen, H.; Ristimäki, A.; Di-Bernardo, M.; East, P.; Carvajal-Carmona, L.; Houlston, R. S.; Tomlinson, I.; Palin, K.; Ukkonen, E.; Karhu, A.; Taipale, J.; Aaltonen, L. A. *Nat. Genet.* **2009,** *41,* 885–890. doi:10.1038/ng.406

Table 2: Comparison among different surface-based label free approaches for the detection of SNPs.

approach	detection limit	dimensions of the sensitive area	mutation discrimination	high throughput	multiplexing
AFM [11,18,19] and this work	100 pM to 1 μM	0.01–1 μm^2	yes	not foreseen	yes
electrochemical [16,17] and this work	0.1 pM to 10 nM	10000 μm^2	yes	yes, integrating with microfluidics	yes, integrating with microfluidics
surface plasmon resonance [14,15]	20 fM to 100 pM	more than 10000 μm^2	yes	limited	limited

8. Zacharova, J.; Chiasson, J.-L.; Laakso, M.; STOP-NIDDM Study Group. *Diabetes* **2005,** *54,* 893–899. doi:10.2337/diabetes.54.3.893
9. Carr, D. F.; Alfirevic, A.; Pirmohamed, M. *Genes* **2014,** *5,* 430–443. doi:10.3390/genes5020430
10. Lacy, E. R.; Cox, K. K.; Wilson, W. D.; Lee, M. *Nucleic Acids Res.* **2002,** *30,* 1834–1841. doi:10.1093/nar/30.8.1834
11. Han, W.-H.; Liao, J.-M.; Chen, K.-L.; Wu, S.-M.; Chiang, Y.-W.; Lo, S.-T.; Chen, C.-L.; Chiang, C.-M. *Anal. Chem.* **2010,** *82,* 2395–2400. doi:10.1021/ac902665c
12. Shen, W.; Tian, Y.; Ran, T.; Gao, Z. *TrAC, Trends Anal. Chem.* **2015,** *69,* 1–13. doi:10.1016/j.trac.2015.03.008
13. Kong, R.-M.; Zhang, X.-B.; Zhang, L.-L.; Huang, Y.; Lu, D.-Q.; Tan, W.; Shen, G. L.; Yu, R.-Q. *Anal. Chem.* **2011,** *83,* 14–17. doi:10.1021/ac1025072
14. Milkani, E.; Morais, S.; Lambert, C. R.; Grant McGimpsey, W. *Biosens. Bioelectron.* **2010,** *25,* 1217–1220. doi:10.1016/j.bios.2009.09.010
15. Knez, K.; Spasic, D.; Delport, F.; Lammertyn, J. *Biosens. Bioelectron.* **2015,** *67,* 394–399. doi:10.1016/j.bios.2014.08.067
16. Ji, H.; Yan, F.; Lei, J.; Ju, H. *Anal. Chem.* **2012,** *84,* 7166–7171. doi:10.1021/ac3015356
17. Zhang, J.; Wu, X.; Chen, P.; Lin, N.; Chen, J.; Chen, G.; Fu, F. *Chem. Commun.* **2010,** *46,* 6986–6988. doi:10.1039/c0cc02080j
18. Subramanian, H. K. K.; Chakraborty, B.; Sha, R.; Seeman, N. C. *Nano Lett.* **2011,** *11,* 910–913. doi:10.1021/nl104555t
19. Zhang, Z.; Zeng, D.; Ma, H.; Feng, G.; Hu, J.; He, L.; Li, C.; Fan, C. *Small* **2010,** *6,* 1854–1858. doi:10.1002/smll.201000908
20. Dong, J.; Cui, X.; Deng, Y.; Tang, Z. *Biosens. Bioelectron.* **2012,** *38,* 258–263. doi:10.1016/j.bios.2012.05.042
21. Hu, J.; Zhang, C.-y. *Anal. Chem.* **2010,** *82,* 8991–8997. doi:10.1021/ac1019599
22. Chang, K.; Deng, S.; Chen, M. *Biosens. Bioelectron.* **2015,** *66,* 297–307. doi:10.1016/j.bios.2014.11.041
23. Mirmontaz, E.; Castronovo, M.; Grunwald, C.; Bano, F.; Scaini, D.; Ensafi, A. A.; Scoles, G.; Casalis, L. *Nano Lett.* **2008,** *8,* 4134. doi:10.1021/nl802722k
24. Bosco, A.; Bano, F.; Parisse, P.; Casalis, L.; DeSimone, A.; Micheletti, C. *Nanoscale* **2012,** *4,* 1734. doi:10.1039/C2NR11662F
25. Nkoua Ngavouka, M. D.; Bosco, A.; Casalis, L.; Parisse, P. *Macromolecules* **2014,** *47,* 8748–8753. doi:10.1021/ma501712a
26. Bosco, A.; Ganau, M.; Palma, A.; Corvaglia, S.; Parisse, P.; Fruk, L.; Beltrami, A. P.; Cesselli, D.; Casalis, L.; Scoles, G. *Nanomedicine* **2015,** *11,* 293. doi:10.1016/j.nano.2014.04.006
27. Ianeselli, L.; Grenci, G.; Callegari, C.; Tormen, M.; Casalis, L. *Biosens. Bioelectron.* **2014,** *55,* 1–6. doi:10.1016/j.bios.2013.11.067
28. Solano, I.; Parisse, P.; Gramazio, F.; Cavalleri, O.; Bracco, G.; Castronovo, M.; Casalis, L.; Canepa, M. *Phys. Chem. Chem. Phys.* **2015,** *17,* 28774. doi:10.1039/C5CP04028K
29. Peterson, A. W.; Heaton, R. J.; Georgiadis, R. M. *Nucleic Acids Res.* **2001,** *29,* 5163–5168. doi:10.1093/nar/29.24.5163
30. Crews, N.; Wittwer, C. T.; Montgomery, J.; Pryor, R.; Gale, B. *Anal. Chem.* **2009,** *81,* 2053–2058. doi:10.1021/ac801495w
31. Knez, K.; Janssen, K. P. F.; Pollet, J.; Spasic, D.; Lammertyn, J. *Small* **2012,** *8,* 868–872. doi:10.1002/smll.201102209
32. Holford, T. R. J.; Davis, F.; Higson, S. P. J. *Biosens. Bioelectron.* **2012,** *34,* 12–24. doi:10.1016/j.bios.2011.10.023
33. Kornyshev, A. A.; Qiao, R. *J. Phys. Chem. C* **2014,** *118,* 18285–18290. doi:10.1021/jp5047062
34. Fedorov, M. V.; Kornyshev, A. A. *Chem. Rev.* **2014,** *114,* 2978–3036. doi:10.1021/cr400374x
35. Guiducci, C.; Stagni, C.; Zuccheri, G.; Bogliolo, A.; Benini, L.; Samori, B.; Ricco, B. A Biosensor for Direct Detection of DNA Sequences Based on Capacitance Measurements. In *Proceeding of the 32nd European Solid-State Device Research Conference,* Sept 24–26, 2002; 2002; pp 479–482. doi:10.1109/ESSDERC.2002.194972
36. Carrara, S.; Cavallini, A.; Leblebici, Y.; DeMicheli, G.; Bhalla, V.; Valle, F.; Samorì, B.; Benini, L.; Riccò, B.; Vikholm-Lundin, I. *Microelectron. J.* **2010,** *41,* 711–717. doi:10.1016/j.mejo.2010.01.007
37. Peterson, A. W.; Heaton, R. J.; Georgiadis, R. *J. Am. Chem. Soc.* **2000,** *122,* 7837–7838. doi:10.1021/ja0015489
38. Peterson, A. W.; Wolf, L. K.; Georgiadis, R. M. *J. Am. Chem. Soc.* **2002,** *124,* 14601. doi:10.1021/ja0279996
39. Rossetti, G.; Dans, P. D.; Gomez-Pinto, I.; Ivani, I.; Gonzalez, C.; Orozco, C. *Nucleic Acids Res.* **2015,** *43,* 4309–4321. doi:10.1093/nar/gkv254
40. Wong, I. Y.; Melosh, N. A. *Biophys. J.* **2010,** *98,* 2954–2963. doi:10.1016/j.bpj.2010.03.017
41. Nkoua Ngavouka, M. D. Conformational properties of variable density DNA nanobrushes. Ph.D. Thesis, University of Trieste, Trieste, Italy, 2015.

License and Terms

BEILSTEIN JOURNAL OF NANOTECHNOLOGY

Influence of calcium on ceramide-1-phosphate monolayers

Joana S. L. Oliveira*[1], Gerald Brezesinski[1], Alexandra Hill[2] and Arne Gericke[2]

Full Research Paper

Open Access

Address:
[1]Max Planck Institute of Colloids and Interfaces, Colloid Chemistry Department, Wissenschaftspark Potsdam-Golm, Am Mühlenberg 1, 14476 Potsdam, Germany and [2]Department of Biological Sciences, Kent State University, Kent, Ohio 44242, USA

Email:
Joana S. L. Oliveira* - joana.oliveira@mpikg.mpg.de

* Corresponding author

Keywords:
calcium; ceramide-1-phosphate; Langmuir monolayers; phase behaviour; structural properties

Beilstein J. Nanotechnol. **2016,** *7,* 236–245.
doi:10.3762/bjnano.7.22

Received: 16 October 2015
Accepted: 03 February 2016
Published: 12 February 2016

This article is part of the Thematic Series "Organized films".

Guest Editor: M. Canepa

Abstract

Ceramide-1-phosphate (C1P) plays an important role in several biological processes, being identified as a key regulator of many protein functions. For instance, it acts as a mediator of inflammatory responses. The mediation of the inflammation process happens due to the interaction of C1P with the C2 domain of $cPLA_{2\alpha}$, an effector protein that needs the presence of submicromolar concentrations of calcium ions. The aim of this study was to determine the phase behaviour and structural properties of C1P in the presence and absence of millimolar quantities of calcium in a well-defined pH environment. For that purpose, we used monomolecular films of C1P at the soft air/liquid interface with calcium ions in the subphase. The pH was varied to change the protonation degree of the C1P head group. We used surface pressure versus molecular area isotherms coupled with other monolayer techniques as Brewster angle microscopy (BAM), infrared reflection–absorption spectroscopy (IRRAS) and grazing incidence X-ray diffraction (GIXD). The isotherms indicate that C1P monolayers are in a condensed state in the presence of calcium ions, regardless of the pH. At higher pH without calcium ions, the monolayer is in a liquid-expanded state due to repulsion between the negatively charged phosphate groups of the C1P molecules. When divalent calcium ions are added, they are able to bridge the highly charged phosphate groups, enhancing the regular arrangement of the head groups. Similar solidification of the monolayer structure can be seen in the presence of a 150 times larger concentration of monovalent sodium ions. Therefore, calcium ions have clearly a strong affinity for the phosphomonoester of C1P.

Introduction

Ceramide-1-phosphate (C1P) is a sphingoid analogue of phosphatidic acid, which has a sphingoid base with a phosphomonoester head group (Figure 1). It is synthesized in the trans-Golgi network (TGN), where ceramide is phosphorylated into C1P in a reaction catalyzed by a ceramide kinase [1,2]. Several reviews about the function of C1P describe its role in a number of biological functions as cell growth, survival and mediation of macrophage migration and control of inflammatory responses [3-5].

According to the work of Chalfant and co-workers [6,7], C1P mediates inflammatory responses by activation of the cytosolic

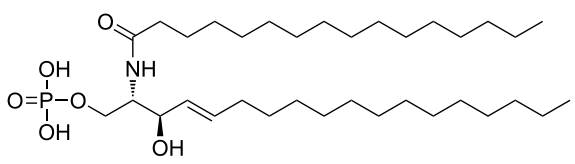

Figure 1: Chemical structure of fully protonated C1P.

phospholipase A2α (cPLA$_2$α). cPLA$_2$α is the major phospholipase that regulates eicosanoid synthesis in response to inflammatory agonists. The binding site for C1P was determined to be within the C2-domain of cPLA$_2$α, by a calcium-dependent mechanism [3,6,7].

For a better understanding of the mechanisms underlying the described biological functions, Langmuir monolayers at the soft air/water interface are convenient model systems. They can be especially used to study interactions at membrane surfaces. By changing the subphase conditions, such as pH, ionic strength, or/and the type of ions (Hofmeister effects), it is possible to study their influence on the phase state of the lipids. Having this in mind, Kooijman and co-workers [8] studied the behaviour of C1P monolayers in the absence and presence of Ca^{2+} and found interesting results. On pure water, C1P forms a condensed monolayer, while at pH 7.2 the electrostatic repulsion of the negatively charged phosphomonoester head groups becomes more important and the monolayer is in a less solid-like state. Also at pH 7.2, the monolayer has a higher charge density than on water. They also determined the pK_{a2} in presence of other lipids (DOPC and DOPE), and found that the environment has a strong influence on the charge state of the phosphomonoester head groups [9]. The pK_{a2} of C1P is in the range of physiological values (5 < pH < 8) and similar to the one of lyso-phosphatidic acid (LPA) [10].

Since the monolayer studies were performed in a non-defined protonation region, either water or pH 7.2, we studied the phase behaviour and structural properties at more extreme values, namely at pH 4, where C1P should be mostly protonated, and at pH 9, where we expect the C1P to be completely deprotonated. The aim of these experiments is to provide a complete physicochemical characterization of C1P towards a better understanding of the influence of pH and ions in the subphase. This study can lead to better comprehension of the mechanism and potential role of this important sphingolipid in biological membranes and cellular environment.

Results and Discussion

The C1P monolayer was studied at pH 4 and pH 9. While at pH 9 the head groups of C1P should be mostly deprotonated and therefore twofold negatively charged, these groups are highly protonated at pH 4. Figure 2 displays the surface pressure–area isotherms at pH 4 and pH 9 with and without calcium in the subphase.

For pH 9, a solution of 10 mM borax buffer has been used, and for pH 4, a 10 mM citric buffer. Either 150 mM NaCl was added to mimic the physiological environment and 1 mM EDTA to chelate traces of divalent cations, or the EDTA was substituted by 1 mM $CaCl_2$.

On the pH 9 subphase without calcium, the isotherms indicate an expanded phase (LE) at low lateral pressures and a first-order phase transition from LE to LC (condensed state). At 10 °C, this phase transition is not seen. As the temperature increases, the phase-transition pressure increases. This dependence is characteristic of a first-order transition. Unfortunately, the domains appearing in the two-phase coexistence region are too small for the lateral resolution of our BAM instrument (about 2 μm), and therefore we were not able to follow the nucleation and growth processes associated with the LE/LC phase transition (data not shown). The calculated critical temperature T_c (see section 1 in Supporting Information File 1) for this system, i.e., the temperature above which the LC phase cannot be reached anymore upon compression of the monolayer, was found to be about 38 °C, which is slightly lower than the transition temperature T_m of a gel to a liquid-crystalline phase obtained by Kooijman et al. [9] (ca. 44 °C) for the bulk system at pH 7.4. Most likely, the difference in temperatures can be attributed to a different protonation state of C1P in the two cases. Therefore, we might conclude that T_c and T_m are the same showing that the lateral packing in the monolayers and in the bilayers is identical [11].

At pH 4 without calcium, the isotherms have a shape characteristic of a condensed phase. The resublimation (transition from gas-analogous to condensed state) occurs at nearly zero pressure. As a first assumption, we expect the C1P head groups to be mostly deprotonated at pH 9. This leads to strong electrostatic repulsion between the twofold negatively charged phosphomonoester head groups favouring the disordered LE phase. In contrast, the head groups are expected to be mostly protonated at pH 4 allowing the molecules to pack in a tighter way, favouring the ordered LC phase.

When calcium is added, the isotherms of the pH 9 subphase change drastically. Now, the typical behaviour of a fully condensed monolayer even at low pressures can be seen. At pH 4, no pronounced changes are seen, and the monolayer is at all lateral pressures in the condensed state. The isotherm on water is also fully condensed (Figure S1, Supporting Informa-

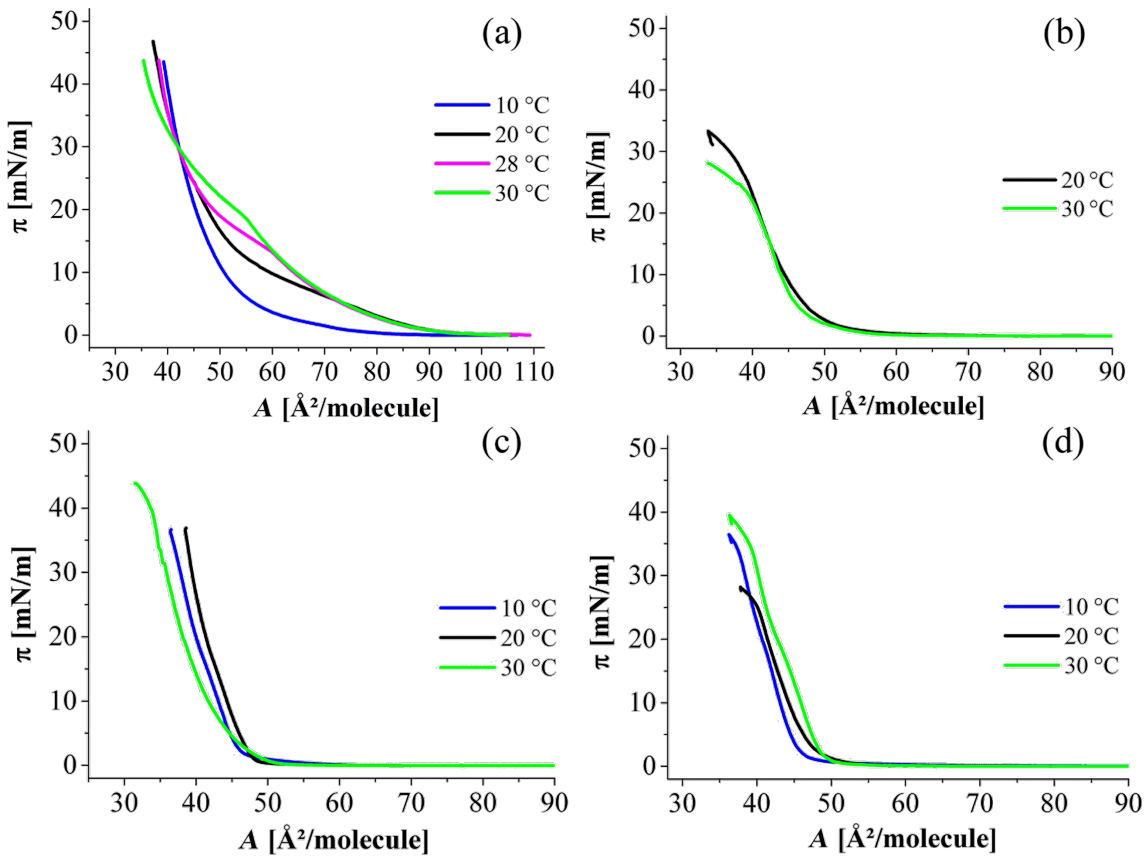

Figure 2: Surface pressure–area isotherms at (a) pH 9 without calcium (borax buffer with 150 mM NaCl and 1 mM EDTA), (b) pH 9 with calcium (borax buffer with 1 mM $CaCl_2$ and 150 mM NaCl), (c) pH 4 without calcium (citric buffer with 150 mM NaCl and 1 mM EDTA), and (d) pH 4 with calcium (citric buffer with 1 mM $CaCl_2$ and 150 mM NaCl) at different temperatures (indicated).

tion File 1), which is in perfect agreement with the isotherm obtained by Kooijman [8]. This is not surprising, since the pH of water saturated with CO_2 is around 6. All the condensed isotherms are supported by Brewster angle microscopy images. Figure 3 is shown as an example of a stiff and crystalline monolayer observed on a pH 4 subphase without calcium. At very low pressure, the image indicates some holes, which are removed by compression.

The monolayers in the condensed state are not perfectly reproducible concerning the areas per molecule (as already reported by Kooijman [8]). They exhibit hysteresis between compres-

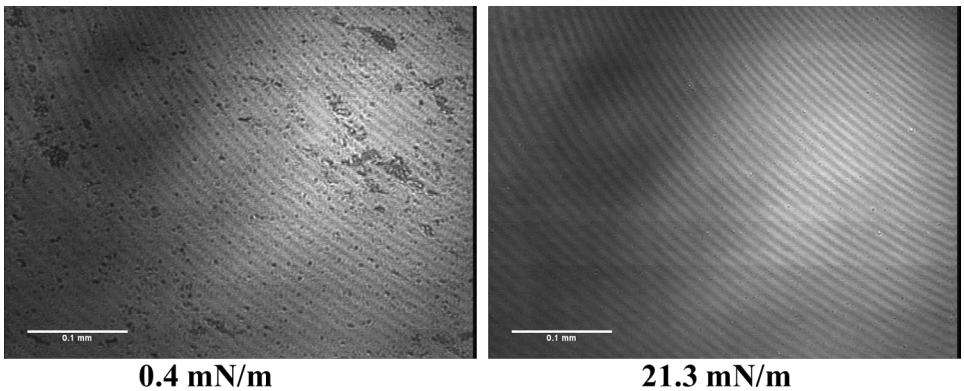

Figure 3: BAM pictures obtained at pH 4 without calcium (citric buffer with 150 mM NaCl and 1 mM EDTA) at selected surface pressures (indicated).

sion and decompression, which proves the highly crystalline state of these systems and leads to limitations in a precise determination of molecular areas. The isotherms were measured at several temperatures to investigate whether the first-order transition between LE and LC can be obtained. However, only condensed monolayers have been obtained in the accessible temperature range. Only at pH 4 without calcium, the isotherm measured at 30 °C is clearly shifted to smaller area values, most probably due to a slightly increased solubility of C1P in this subphase.

Infrared reflection–absorption spectroscopy (IRRAS) has been used to determine the phase state of the aliphatic chains on the different subphases. For this purpose, the CH_2 symmetric and asymmetric stretching vibration bands of IRRAS spectra have been carefully analyzed. If the chains are in an ordered condensed (all-*trans*) state, the corresponding characteristic bands are at wavenumbers $\nu \leq 2920$ cm^{-1} ($\nu_{asym}CH_2$) and $\nu \leq 2849$ cm^{-1} ($\nu_{sym}CH_2$). Wavenumbers $\nu \geq 2924$ cm^{-1} ($\nu_{asym}CH_2$) or $\nu \geq 2854$ cm^{-1} ($\nu_{sym}CH_2$) are characteristic for the liquid-like (*gauche*) state of the chains [12]. Figure 4 displays the wavenumbers of the $\nu_{asym}CH_2$ band of C1P on the different subphases.

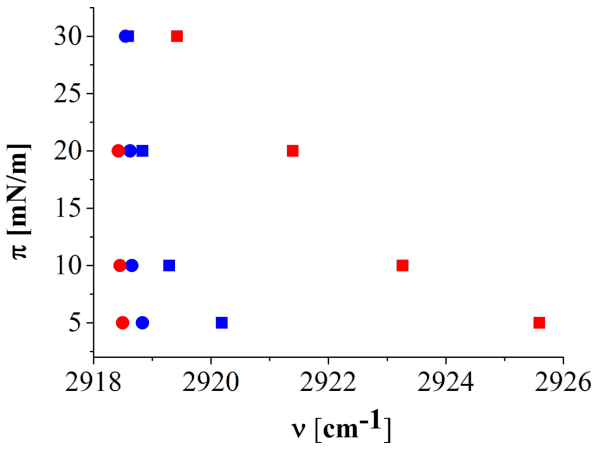

Figure 4: Wavenumbers of the CH_2 asymmetric stretching vibration band (incidence angle 40° and s-polarization) of C1P monolayers at 30 °C on different subphases: (red square) pH 9 without calcium (borax buffer with 150 mM NaCl and 1 mM EDTA), (red circles) pH 9 with calcium (borax buffer with 1 mM Ca^{2+} and 150 mM NaCl), (blue squares) pH 4 without calcium (citric buffer with 150 mM NaCl and 1 mM EDTA), and (blue circle) pH 4 with calcium (citric buffer with 1 mM Ca^{2+} and 150 mM NaCl), determined by IRRAS.

The IRRAS data show the same tendency as the isotherms. At pH 4 without calcium, C1P is in a condensed state with slightly higher wavenumbers at low pressures (less dense packing of molecules). Upon compression, the same low wavenumbers (approx. 2918.5 cm^{-1}) are reached as in the system with calcium (the packing and therefore the wavenumbers do not change upon compression). At pH 9 without calcium, high wavenumbers at low pressures (approx. 2926 cm^{-1}) indicate the disordered LE state, which upon compression undergoes the transition into the LC phase with lower wavenumbers (approx. 2920 cm^{-1}), but not as low as in the other systems. At pH 9, the electrostatic repulsion between the negatively charged head groups leads to an expanded state. These repulsive forces prevent a high packing density even at high lateral pressures. Interestingly, on the pH 9 subphase with calcium, the C1P chains are in a highly condensed state (all-*trans* conformation) with very low wavenumbers (approx. 2918.2 cm^{-1}). All temperatures studied show the same tendency (data of IRRAS measurements at 10 °C and 30 °C not shown).

C1P has three dissociation states due to its phosphomonoester head group. The equilibrium constants pK_{a1} and pK_{a2} determine the state of C1P, defining whether the molecule will be completely deprotonated, one-fold deprotonated or neutral (no deprotonation) at a certain pH. The pK_{a2} of C1P was determined by Kooijman et al. [9] to lie within pH 5 and 8. The dissociation behaviour of C1P was shown to be similar to the one of LPA, obeying the electrostatic/hydrogen bond switch model, and to a certain extent to the one of phosphatidic acid (PA) [10]. The pK_{a1} of LPA and PA is in the pH range between 2 and 4 [13]. To our knowledge, the pK_{a1} of C1P is not described in the literature. We expect C1P to be one-fold deprotonated at pH 4 and completely deprotonated at pH 9. In an attempt to get more information about the deprotonation state of the C1P monolayer, the phosphate vibration bands of IRRAS spectra were analyzed and are depicted in Figure 5. The asymmetrical and symmetrical stretching vibration bands of PO_3^{2-}

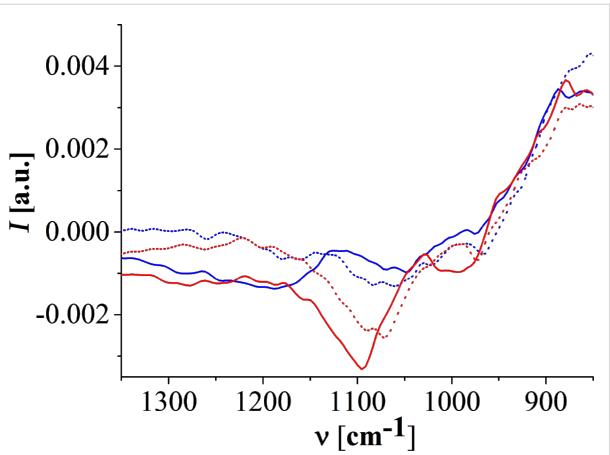

Figure 5: IRRAS spectra (incidence angle 40°, s-polarization) of C1P monolayers on the different subphases (red lines – pH 9 buffer; blue lines – pH 4 buffer; solid line – with calcium; dotted line – without calcium) at 20 mN/m and 30 °C. The spectra are shifted (*y*-axis) for better clarity.

are described to be located at approx. 1080 cm^{-1} and approx. 1000 cm^{-1} and the P–O–(H) stretching mode at approx. 925 cm^{-1} [14].

It is important to note that the phosphate bands region is noisy and the accurate analysis of the peak position of the bands is challenging. Therefore no fitting was performed, and the peak positions were defined by an eye analysis. Apart from the asymmetrical PO_3^{2-} band of C1P on the pH 9 subphase with calcium, which shows a pronounced intensity, the bands are either very broad or seem to be a doublet. Doublets were already described for phosphonic acid salts in IR [14]. However, the broadening of the bands could also indicate a superposition of bands due to different protonation states of the molecules in the system.

At pH 4 without calcium, a band at approx. 970 cm^{-1} and a very broad band composed of at least two contributions, one doublet around 1012 cm^{-1} and the other one around 1068 cm^{-1} are present. In comparison with LPA and PA, the pK_{a1} of C1P is expected to be in the range of $2 < pH < 4$, hence at pH 4 C1P should be one-fold deprotonated. The ionic strength of the subphase can influence the dissociation degree of the monolayer, since the counter-ions interact with the charged head groups. Usually the pK_a values decrease with increasing ionic strength. The doublets seem to indicate a coexistence of one-fold deprotonated and neutral C1Ps. When calcium is added to the system such bands change slightly the position to approx. 966 cm^{-1}, approx. 1007 cm^{-1} (very weak band) and one doublet around 1066 cm^{-1} (approx. 1052 and approx. 1079 cm^{-1}). The slightly lower wavenumbers and shape of the bands give an overall impression that almost all C1P molecules are now neutral. The wavenumbers of the acyl chains support this assumption: the monolayer without calcium has slightly lower wavenumbers (less condensed monolayer) due to electrostatic repulsions between the charged oxygen ions of the phosphomonoester head group. Interestingly, molecular dynamics simulations of dimyristoylphosphatidate ($DMPA^-$) monolayer in water environment (and therefore one-fold deprotonated) reported no difference between the effect of Ca^{2+} or Na^+ ions on the properties of a condensed phase monolayer [15].

At pH 9, C1P is expected to be completely deprotonated. The wavenumbers are shifted to higher values. The bands for the subphase without calcium are located at approx. 974 cm^{-1}, approx. 1011 cm^{-1} and a doublet (approx. 1072 and 1088 cm^{-1}). We assume C1P on the pH 9 subphase without calcium is most likely not 100% deprotonated since the doublet is still present. When calcium is added to the subphase the wavenumbers are even more shifted to higher wavenumbers and the asymmetrical PO_3^{2-} band is no longer a doublet. The bands are located at approx. 995 cm^{-1}, approx. 1045 cm^{-1} and 1100 cm^{-1}. Such clear shift to higher wavenumbers was already observed by Laroche et al. [14] in the case of a DMPA/Ca^{2+} complex, where the bridging of the head groups of neighbouring molecules mediated by calcium was found. Nevertheless, even if the phosphate bands indicate that Ca^{2+} ions have a stronger influence on the charge state of the monolayer (slightly deprotonated at pH 9) compared to a higher concentration of Na^+, no quantitative information about the deprotonation state of the monolayer is available. Again, at all temperatures and pressures studied the same tendency was found.

This interesting calcium dependence was further investigated by means of grazing incidence X-ray diffraction (GIXD) at synchrotron facilities. The Langmuir trough is in an air-tight container filled with helium to avoid signal reduction due to absorption and scattering of photons in air. The incident beam is at an angle below the critical angle for total external reflection. The diffraction pattern is then collected by a linear detector which is scanned in the in-plane direction. The parameters of the unit cell of the lipid chains can be calculated based on the Q_{xy} and Q_z values of the observed Bragg peaks. All the details of GIXD measurements and analysis can be found in [16-18].

Figure 6 is shown as an example of the results obtained for C1P at pH 4 with calcium in the subphase. The contour plots display the diffracted intensities versus the in-plane (Q_{xy}) and out-of-plane (Q_z) components of the scattering vector. Bragg peaks and Bragg rods can be extracted to yield structural information as the in-plane lattice, the tilt of the chains, the lattice distortion, and the cross sectional area (A_0) of one chain [16-18].

C1P on the pH 4 buffer at 10 mN/m shows three diffraction peaks indicative of the presence of an oblique in-plane lattice with a tilt of (18.6 ± 1.0)° and an area per molecule of (40.2 ± 0.8) $Å^2$, which transforms between 10 and 30 mN/m into a rectangular lattice of NN (nearest neighbour) tilted chains. At 40 mN/m, only one Bragg peak has been observed indicating a hexagonal packing of untilted chains. The extrapolated tilting transition pressure is 38.9 mN/m (see below and section 3 in Supporting Information File 1).

On water, the presence of two Bragg peaks at non-zero Q_z values demonstrates the existence of a rectangular unit cell with molecules tilted in the direction of next-nearest neighbours (NNN) and an area per molecule of (41.0 ± 0.8) $Å^2$. Above 5 mN/m, the super-liquid (LS) phase (hexagonal unit cell with non-tilted molecules) is observed. Interestingly, the results obtained by Kooijman et al. [8] show a different picture, since at 10 mN/m the tilt angle is (18 ± 1)°. In our experiments, at the same pressure, non-tilted molecules are observed. This could be

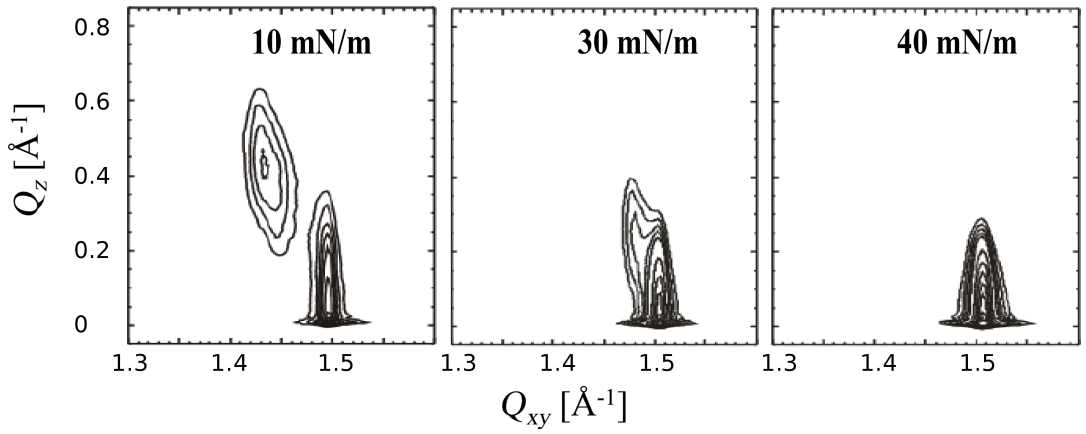

Figure 6: Contour plots of the corrected X-ray intensities plotted versus the in-plane (Q_{xy}) and out-of-plane (Q_z) components of the scattering vector for C1P monolayers on the pH 4 subphase with calcium (citric buffer with 1 mM Ca^{2+} and 150 mM NaCl) at 10 mN/m (left), 30 mN/m (middle) and 40 mN/m (right).

attributed to possible traces of divalent ions in the Millipore water used in our experiments with no addition of EDTA, and supports the finding that small amounts of divalent ions have a big influence on the behaviour of C1P.

Plotting 1/cos(t) versus the surface pressure (t is the tilt angle of the chains) allows for the determination of the tilting transition pressure. The only assumption one has to make is that the cross-sectional area of the chains remains constant on compression and that the isotherms show an almost linear relationship between area and pressure in the condensed state [19]. In Figure 7, the lines are linear fits to the experimental data. On water, the tilting transition occurs already at low lateral pressures (5.2 mN/m). As already discussed, at pH 4 with calcium the extrapolated tilting transition pressure is 38.9 mN/m.

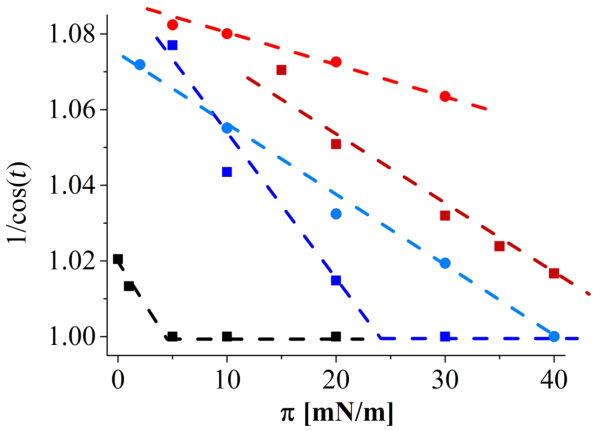

Figure 7: 1/cos(t) as a function of the surface pressure of C1P monolayers at 20 °C on (red circle) pH 9 with calcium; (red square) pH 9 without calcium; (blue circle) pH 4 with calcium; (blue square) pH 4 without calcium; and (black square) on water.

At the same pH but without calcium in the subphase, the chains are packed in an oblique in-plane lattice at 5 mN/m, but with a larger tilt angle of (21.8 ± 1)°. Consequently, the in-plane area per molecule is (42.2 ± 0.8) Å^2. The lattice transforms upon compression, and at 30 mN/m hexagonal packing of untilted chains is observed. The extrapolated transition pressure (23.1 mN/m) is lower than on the calcium containing subphase. Apparently, the presence of divalent calcium ions leads to a higher degree of dissociation compared to the monovalent sodium.

On the pH 9 subphase without calcium, a rectangular unit cell with chains tilted in the NNN direction is observed at low pressures. The tilt direction changes to NN at 30 mN/m, where the tilt amounts to (14.3 ± 1)° and the in-plane area per molecule is 42.4 Å^2. The extrapolated tilting transition pressure is much higher (46.8 mN/m). On the pH 9 subphase with calcium, the oblique structure is seen at all pressures investigated. The tilt changes only marginally on compression (21 ± 1)°. Therefore, the structure is very rigid and does almost not respond on compression of the film. Furthermore, the extrapolated tilting transition pressure is an unrealistic value of 114 mN/m. The divalent calcium ions are able to bridge the highly charged phosphate groups and solidify the monolayer structure, in contrast to all the other systems. Calcium seems to be the key element to bridge the charged head groups leading to a very rigid arrangement of the molecules. It is interesting to note that calcium has this strong effect even in the presence of a 150-fold larger concentration of monovalent sodium ions.

Plotting the lattice distortion as a function of the sinus square of the tilt (Figure 8) according to a modified Landau theory usually shows a linear dependence [17]. An extrapolated zero distortion at zero tilt indicates that the lattice distortion is

caused only by the tilt of the molecules [20]. However, this is not the case for the monolayer on the pH 9 subphase with calcium, since the distortion remains more or less constant at 0.18. The cross-sectional area is not extraordinarily small ((19.7 ± 0.04) Å^2 at 30 mN/m) but is clearly smaller compared to all the other systems. Even if the value is not yet the one observed for herringbone or pseudo-herringbone packing, which is usually the source for lattice distortion apart from the chain tilting, the packing has clearly a strong influence on the distortion. Strong interactions in the hydrophilic head group region mediated by the calcium ions bridge the negatively charged phosphate head groups and enhance the solid arrangement of the molecules to form a strongly condensed monolayer.

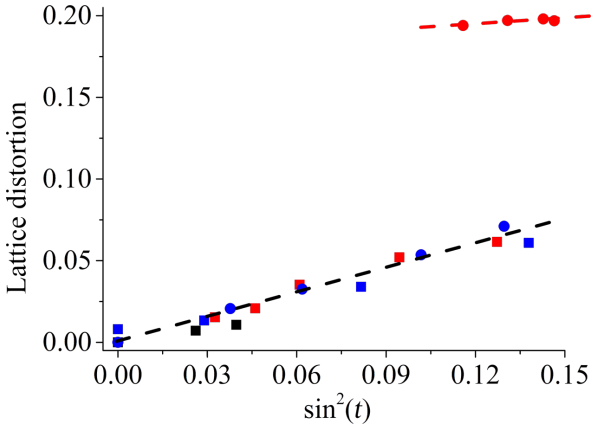

Figure 8: Lattice distortion as a function of sin^2(*t*) of C1P monolayers at 20 °C on (red circle) pH 9 with calcium; (red square) pH 9 without calcium; (blue circle) pH 4 with calcium; (blue square) pH 4 without calcium; and (black square) on water.

The differences in the tilt transition pressure are in agreement with all the other data. On the pH 4 subphase without calcium, the C1P monolayer presents a mixture of one-fold deprotonated and neutral molecules. The electrostatic repulsions between the slightly negatively charged head groups are responsible for the larger areas per molecule and larger tilt angles. Upon compression, the strong van der Waals forces between the acyl chains and the screening effect of sodium ions surpass the electrostatic repulsions allowing C1P to transform into the untilted state. On the pH 4 subphase with calcium, the head groups interacting with calcium ions obviously require a larger effective area. Therefore, a much higher lateral pressure is needed to observe the untilted state. However, calcium is not able to bridge the single-charged head groups in an effective way as observed for the system on the pH 9 subphase. In the case of the pH 9 subphase without calcium, the untilted state is reached at much higher lateral pressures due to stronger electrostatic interactions. The presence of calcium ions leads to a very rigid structure, which does not change upon compression.

In a study of the Chalfant group [21], the activation of cPLA$_2$α by C1P was found to be related with the chain length, showing an increase in activity with increasing chain length. It is known for other lipids that the chain length has an influence on the structural properties of the lipids. For example, in saturated fatty acids an expanded phase is dominantly found up to C_{12} chains, and lipids with longer chains exhibit only condensed phases [17]. Therefore, comparing the data of Chalfant and co-workers with our results, we suggest that the activation of cPLA$_2$α by C1P is connected with the rigidity of the C1P structure, which is enhanced in the presence of calcium ions.

Conclusion

The results presented clearly show the influence of the protonation degree of C1P head groups on its interaction with calcium ions. At higher pH without calcium ions, the C1P monolayer is at low lateral pressures in a liquid-expanded phase (LE) due to repulsive forces between the negatively charged phosphate head groups. At pH 4, the C1P head groups are either one-fold deprotonated or neutral (most probably a mixture of protonation states). The strong van der Waals forces between the chains allow the system to be in a condensed state. When calcium is added to the subphase, at both pH values, only a condensed phase state is observed. At pH 4, the systems with and without calcium are quite similar. However, the untilted state on the subphase with calcium is reached only at higher lateral pressures compared to the system without calcium. This intriguing behaviour let us believe that calcium is able to stabilize the one-fold deprotonated molecules in the system, even though less effectively than in the presence of two negative charges in the head groups. Sodium does not seem to be able to neutralize the negative charges so efficiently. At pH 9, when the C1P is mostly deprotonated, the divalent calcium interacts strongly with the negatively charged phosphate groups and bridges the head groups, enhancing a solid-like arrangement of the molecules in a condensed phase. The solidification effect of the monolayer by calcium ions is clear since the same effect is not seen with the 150-fold larger concentration of sodium ions.

This work shows clearly the affinity of calcium for the phosphomonoester of C1P and its big influence on the phase state of the lipid, which is pH-dependent (competition between repulsive electrostatic and attractive van der Waals forces). This result supports the calcium-mediated interaction of C1P with the C2 domain of cPLa2α (effector protein).

Since C1P is involved in many biological functions, its interaction with other ions could also be of interest. Furthermore, the potential to form solid-like domains (rafts) will critically depend on the intracellular pH and the presence of divalent

cations, therefore the information presented in this work will help to better understand some of these biological mechanisms.

Experimental

Materials

Ceramide-1-phosphate (*N*-hexadecanoyl-D-*erythro*-sphingosine-1-phosphate) was purchased from Matreya, LLC (PA, USA). EDTA (≥99.4%), NaCl (≥99.5%), NaOH (≥99.5%), $CaCl_2$ (≥99%) and HCl were purchased from Sigma Aldrich GmbH (Taufkirchen, Germany). Chloroform (≥99.9%) and citric acid monohydrate (≥99.5%) were purchased from Carl Roth GmbH (Karlsruhe, Germany) and methanol (≥99.9%) from VWR Chemicals (Fontenay-sous-Bois, France). Sodium tetraborate decahydrate (≥99.5%) was purchased from Merck KGaA (Darmstadt, Germany). NaCl was heated to 600 °C to remove potential organic impurities. All other chemicals and salts were used without further purification. For monolayer experiments, Milli-Q Millipore water with a specific resistance of 18.2 MΩ·cm and pH approx. 6.2 was used.

Monolayer experiments

For monolayer experiments, a stock solution with a concentration of around 1 mM of C1P was prepared in a chloroform/methanol/0.5 N HCl (2:0.9:0.1 v/v) mixture, and vortexed until the solution was completely limpid. This mixture of solvents has been proved previously to be the most adequate one to dissolve C1P [8]. A 10 mM citrate buffer solution was used as subphase for pH 4 and a 10 mM borax solution was used for pH 9 (pH adjusted with NaOH/HCl). NaCl in a concentration of 150 mM was added to mimic the physiological environment, and 1 mM EDTA to chelate traces of divalent cations in the buffer solution. In case of a subphase with calcium, the EDTA was replaced by 0.001 M $CaCl_2$.

The stock solutions were drop-wise given onto the subphase using a 100 µL micro-syringe, and 10 min were allowed for the evaporation of the solvent. The pressure–area isotherms were recorded on a computer interfaced custom-made Langmuir trough. The trough is equipped with a Wilhelmy balance using a glass plate. The compression speed was 3 $Å^2 \cdot molecule^{-1} \cdot min^{-1}$. The temperature was kept constant at the desired value with an accuracy of ±0.1 °C.

Infrared reflection–absorption spectroscopy (IRRAS)

Infrared reflection–absorption spectra were recorded on a Vertex 70 FTIR spectrometer (Bruker, Ettlingen, Germany). The setup includes a MCT detector cooled with liquid nitrogen and coupled to a film balance (R&K, Potsdam, Germany), placed in an enclosed container to allow for a constant water vapor atmosphere. A sample trough with two movable barriers and a reference trough (subphase without monolayer) allows for the fast recording of sample and reference spectra successively by a shuttle technique. The infrared beam is focused on the liquid surface by a set of mirrors. The angle of incidence normal to the surface can be varied by moveable arms. A KRS-5 wire grid polarizer is used to polarize the infrared radiation either in parallel (p) or perpendicular (s) direction. Reflectance–absorbance spectra were obtained by using $-\log(R/R_0)$, with R being the reflectance of the film covered surface and R_0 being the reflectance of the same subphase without the film. Each IRRAS experiment was started 1 h after spreading. FTIR spectra were collected with a scanning velocity of 20 kHz and a resolution of 8 cm^{-1}, using 200 scans for s-polarized light and 400 scans for p-polarized light and saved in OPUS 6.0®. For data analysis, spectra obtained with s-polarized light at 40° angle of incidence were used. IRRA spectra were shifted to zero between 1950 cm^{-1} and 2250 cm^{-1}. To determine the position of the asymmetric CH_2-stretching vibration band, a non-linear fit using Lorentz function in Origin 9® was used.

Brewster angle microscopy (BAM)

The morphology of the monolayer was imaged with a Brewster angle microscope, BAM2plus from NanoFilm Technologie (Göttingen, Germany), equipped with a miniature film balance from NIMA Technology (Coventry, UK). The microscope was equipped with a frequency-doubled Nd:YAG laser (532 nm, ca. 50 mW), a polarizer, an analyzer, and a CCD camera. When p-polarized light is directed onto the pure air/water interface at the Brewster angle (approx. 53.1°), zero reflectivity is observed. When a monolayer is added, the light starts to be reflected due to the change of the refractive index of the surface layer. This change is registered by the CCD camera after passing the analyzer. BAM images of 355 × 470 $µm^2$ were digitally recorded during compression of the monolayer. The lateral resolution is ca. 2 µm.

Grazing incidence X-ray diffraction (GIXD)

Grazing incidence X-ray diffraction (GIXD) experiments were performed at the beamlines BW1 at DESY, Hamburg, Germany, and ID10 at the ERSF, Grenoble, France. The setup includes a Langmuir trough, equipped with one moveable barrier and a Wilhelmy surface tension sensor. The temperature was kept at 20 °C by a thermostat. During experiments, the trough was kept hermetically sealed and flushed with He.

At BW1 (DESY, Hamburg) the synchrotron beam was monochromated through a beryllium(002) crystal to a wavelength of 1.304 Å (energy: 9.5 keV). The incidence angle at the liquid surface was 0.11°, which is around 85% of the critical angle for total external reflection for water at this X-ray wavelength. A Mythen detector (Paul Scherrer Institute, Villigen, Switzerland)

was rotated around the sample in order to detect the intensity of the diffracted beam as a function of the vertical scattering angle α_f and the horizontal scattering angle 2θ. A Soller collimator (JJ X-Ray, Denmark) was located between the sample and the detector.

At ID10 (ESRF, Grenoble) the synchrotron beam was monochromated by a germanium(111) crystal to a wavelength of 0.56 Å (energy: 22 keV). The incidence angle at the liquid surface was 0.033°, which is around 85% of the critical angle for total external reflection for water at this X-ray wavelength. A Mythen detector (Dectrys, Baden, Switzerland) was rotated around the sample in order to detect the intensity of the diffracted beam as a function of the vertical scattering angle α_f and the horizontal scattering angle 2θ. A Soller collimator (JJ X-Ray, Denmark) was located between the sample and the detector. The setup was already described elsewhere [22,23].

The accumulated position-resolved counts were corrected for polarization, effective area, and Lorentz factor. In the case of ID10 the contour plots of the corrected intensities were plotted as a function of the in-plane (Q_{xy}) and out-of-plane (Q_z) components of the scattering vector in PyMca and cuts representing the Bragg peaks of the in-plane and Bragg rods of the out-of-plane direction were determined. Model peaks (Lorentzian in the in-plane direction (Q_{xy}) and Gaussian in the out-of-plane direction (Q_z)) were fitted to the corrected intensities, and structural information, as the tilt, distortion, cross-sectional area (A_0) and the in-plane lattice area of one chain (A_{xy}) were extracted [16-18].

Supporting Information

Supporting Information File 1

Full experimental data.
[http://www.beilstein-journals.org/bjnano/content/supplementary/2190-4286-7-22-S1.pdf]

Acknowledgements

The financial support of the Deutsche Forschungsgemeinschaft is gratefully acknowledged. We thank DESY (Hamburg, Germany) and ESRF (Grenoble, France) for attributed beam time and excellent support. The authors thank Giovanni Li Destri for his help at ID10 and with data treatment.

References

1. Kolesnick, R. N.; Hemer, M. R. *J. Biol. Chem.* **1990,** *265,* 18803–18808.
2. Pettus, B. J.; Bielawska, A.; Subramanian, P.; Wijesinghe, D. S.; Maceyka, M.; Leslie, C. C.; Evans, J. H.; Freiberg, J.; Roddy, P.; Hannun, Y. A.; Chalfant, C. E. *J. Biol. Chem.* **2004,** *279,* 11320–11326. doi:10.1074/jbc.M309262200
3. Maceyka, M.; Spiegel, S. *Nature* **2014,** *510,* 58–67. doi:10.1038/nature13475
4. Arana, L.; Gangoiti, P.; Ouro, A.; Trueba, M.; Gómez-Muñoz, A. *Lipids Health Dis.* **2010,** *9,* 1–12. doi:10.1186/1476-511X-9-15
5. Chalfant, C. E.; Spiegel, S. *J. Cell Sci.* **2005,** *118,* 4605–4612. doi:10.1242/jcs.02637
6. Subramanian, P.; Stahelin, R. V.; Szulc, Z.; Bielawska, A.; Cho, W.; Chalfant, C. E. *J. Biol. Chem.* **2005,** *280,* 17601–17607. doi:10.1074/jbc.M414173200
7. Pettus, B. J.; Bielawska, A.; Spiegel, S.; Roddy, P.; Hannun, Y. A.; Chalfant, C. E. *J. Biol. Chem.* **2003,** *278,* 38206–38213. doi:10.1074/jbc.M304816200
8. Kooijman, E. E.; Vaknin, D.; Bu, W.; Joshi, L.; Kang, S.-W.; Gericke, A.; Mann, E. K.; Kumar, S. *Biophys. J.* **2009,** *96,* 2204–2215. doi:10.1016/j.bpj.2008.11.062
9. Kooijman, E. E.; Sot, J.; Montes, L.-R.; Alonso, A.; Gericke, A.; de Kruijff, B.; Kumar, S.; Goñi, F. M. *Biophys. J.* **2008,** *94,* 4320–4330. doi:10.1529/biophysj.107.121046
10. Kooijman, E. E.; Burger, K. N. J. *Biochim. Biophys. Acta, Mol. Cell Biol. Lipids* **2009,** *1791,* 881–888. doi:10.1016/j.bbalip.2009.04.001
11. Brezesinski, G.; Möhwald, H. *Adv. Colloid Interface Sci.* **2003,** *100–102,* 563–584. doi:10.1016/S0001-8686(02)00071-4
12. Mendelsohn, R.; Moore, D. J. *Chem. Phys. Lipids* **1998,** *96,* 141–157. doi:10.1016/S0009-3084(98)00085-1
13. Kooijman, E. E.; Carter, K. M.; van Laar, E. G.; Chupin, V.; Burger, K. N. J.; de Kruijff, B. *Biochemistry* **2005,** *44,* 17007–17015. doi:10.1021/bi0518794
14. Laroche, G.; Dufourc, E. J.; Dufourcq, J.; Pézolet, M. *Biochemistry* **1991,** *30,* 3105–3114. doi:10.1021/bi00226a018
15. Casares, J. J. G.; Camacho, L.; Martín-Romero, M. T.; Cascales, J. J. L. *ChemPhysChem* **2008,** *9,* 2538–2543. doi:10.1002/cphc.200800321
16. Kjaer, K. *Physica B* **1994,** *198,* 100–109. doi:10.1016/0921-4526(94)90137-6
17. Kaganer, V. M.; Möhwald, H.; Dutta, P. *Rev. Mod. Phys.* **1999,** *71,* 779–819. doi:10.1103/RevModPhys.71.779
18. Stefaniu, C.; Brezesinski, G. *Curr. Opin. Colloid Interface Sci.* **2014,** *19,* 216–227. doi:10.1016/j.cocis.2014.01.004
19. Bringezu, F.; Dobner, B.; Brezesinski, G. *Chem. – Eur. J.* **2002,** *8,* 3203–3210. doi:10.1002/1521-3765(20020715)8:14<3203::AID-CHEM3203>3.0.CO;2-6
20. Antipina, M. N.; Schulze, I.; Dobner, B.; Langner, A.; Brezesinski, G. *Langmuir* **2007,** *23,* 3919–3926. doi:10.1021/la062840i
21. Wijesinghe, D. S.; Subramanian, P.; Lamour, N. F.; Gentile, L. B.; Granado, M. H.; Bielawska, A.; Szulc, Z.; Gomez-Munos, A.; Chalfant, C. E. *J. Lipid Res.* **2009,** *50,* 1986–1995. doi:10.1194/jlr.M800367-JLR200
22. Li Destri, G.; Malfatti Gasperini, A. A.; Konovalov, O. *Langmuir* **2015,** *31,* 8856–8864. doi:10.1021/acs.langmuir.5b02054
23. Smilgies, D.-M.; Boudet, N.; Struth, B.; Konovalov, O. *J. Synchrotron Radiat.* **2005,** *12,* 329–339. doi:10.1107/S0909049505000361

BEILSTEIN JOURNAL OF NANOTECHNOLOGY

Case studies on the formation of chalcogenide self-assembled monolayers on surfaces and dissociative processes

Yongfeng Tong[‡1,2], Tingming Jiang[‡1,2,3], Azzedine Bendounan[2], Makri Nimbegondi Kotresh Harish[4], Angelo Giglia[5], Stefan Kubsky[2], Fausto Sirotti[2], Luca Pasquali[3,5,6], Srinivasan Sampath[7] and Vladimir A. Esaulov[*1]

Full Research Paper

Open Access

Address:
[1]Institut des Sciences Moléculaires d'Orsay, UMR 8214 CNRS-Université Paris Sud, Université Paris-Saclay, F-91405 Orsay, France, [2]Synchrotron Soleil, L'Orme des Merisiers, Saint-Aubin, BP 48, F-91192 Gif-sur-Yvette Cedex, France, [3]Dipartimento di Ingegneria 'E. Ferrari', Università di Modena e Reggio Emilia, Via Vignolese 905, 41125 Modena, Italy, [4]Acharya Institute of Technology, Bangalore 560 107, India, [5]CNR-IOM, s.s.14, km 163.5 in Area Science Park, 34012 Trieste, Italy, [6]Physics Department, University of Johannesburg, P.O. Box 524, Auckland Park 2006, South Africa, and [7]Department of Inorganic and Physical Chemistry, Indian Institute of Science, CV Raman Avenue, Bangalore 560 012, India

Email:
Vladimir A. Esaulov[*] - vladimir.esaulov@u-psud.fr

* Corresponding author ‡ Equal contributors

Keywords:
copper; nickel; palladium; reactivity; selenol; selenophene; self-assembly; thiol; thiophene

Beilstein J. Nanotechnol. **2016,** *7,* 263–277.
doi:10.3762/bjnano.7.24

Received: 08 October 2015
Accepted: 03 February 2016
Published: 17 February 2016

This article is part of the Thematic Series "Organized films".

Guest Editor: M. Canepa

Abstract

This report examines the assembly of chalcogenide organic molecules on various surfaces, focusing on cases when chemisorption is accompanied by carbon–chalcogen atom-bond scission. In the case of alkane and benzyl chalcogenides, this induces formation of a chalcogenized interface layer. This process can occur during the initial stages of adsorption and then, after passivation of the surface, molecular adsorption can proceed. The characteristics of the chalcogenized interface layer can be significantly different from the metal layer and can affect various properties such as electron conduction. For chalcogenophenes, the carbon–chalcogen atom-bond breaking can lead to opening of the ring and adsorption of an alkene chalcogenide. Such a disruption of the π-electron system affects charge transport along the chains. Awareness about these effects is of importance from the point of view of molecular electronics. We discuss some recent studies based on X-ray photoelectron spectroscopy that shed light on these aspects for a series of such organic molecules.

Introduction

In recent years research related to various applications such as catalysis, sensor development, hydrogen storage, thin films, and molecular electronics has focused on the study of self-assembled monolayers (SAMs) with different combinations of molecular architecture, and in particular, different molecule anchoring head groups. The latter determines the binding to the substrate and plays an important role in defining the molecular ordering and electronic coupling, which determines the charge flow between the molecular components and the substrate electrode. Much work on various aspects of assembly and its uses has been performed with sulfur head group (thiol) molecules [1-27], but interest in other head group atoms such as C [28,29], N [30] and other chalcogenides has also received increased attention. In particular, selenium head group SAMs have attracted much attention and significant research has resulted [31-43] for substrates such as Au and Ag. There is considerable discussion in the literature about the strength of the head group substrate bond [14,34,41] and whether or not it provides a better conductance pathway than sulfur. Besides the case of self-assembly on bulk metal surfaces, the knowledge of the physics and chemistry of chalcogenide SAMs on metal nanoparticle surfaces is also very important as they are widely used in different areas.

In this paper, we focus on recent work where the interaction with the substrate is strong and can lead to dissociative processes. This is, for instance, the case of copper and transition metals (Ni and Pd), which are characterized by a greater reactivity than gold. Thus, in the case of thiophene, dehydrogenation and desulfurization is well known to occur on transition metal surfaces [44,45]. A few years ago, the research groups of Nuzzo [46], Whitesides [46] and others [48] noted that for alkane thiol SAMs, the initial desulfurization occurs via S–C bond scission. This leads to the formation of a sulfidic interface layer, upon which a more or less ordered molecular layer can eventually form. This was noted for the case of alkanethiol SAMs on Pd and it was shown that this led to interesting consequences, such as greater resistance to corrosion by chemical etchants [46,47]. In biotechnology applications, a greater resistance to invasion by cells was observed in this case as opposed to the case of the same SAMs on gold [46,47]. Similarly, in some examples of thiol adsorption on Cu, there exists evidence [26] of S–C bond scission with sulfur remaining on the surface.

It is clear that such processes strongly affect the interface properties and in particular the characteristics of charge transport through such a sulfidic interface layer would be strongly affected.

In the context of the use of nanoparticles in various applications [49-52] such as in catalysis, sensing or hydrogen storage, capping the nanoparticles using thiols leads to important questions related to the nature of the interface layer. For instance, in the case of palladium nanoparticles there has been a controversy [53-55] about whether the thiol was adsorbed on the metal core or rather if the metal core was capped by a PdS layer on which the alkanethiol was formed. This has obvious implications in hydrogen storage applications, for example, where hydrogen permeation into Pd [52] is inhibited by a sulfidic layer.

While it might not seem surprising that such dissociative processes may take place on reactive substrates, it is noteworthy that this has been invoked for the case of thiol and selenol SAMs on Au [30], as well as in the case of ultrathin layers of thiophene derivatives on Au. In the latter case, S–C bond scission occurs, leading to the opening of the ring and observation of thiolate species [52-63]. The loss of aromaticity and planarity can thus occur and this interrupts the π-electron system and impairs charge transport along the chains. There are indications of the appearance of atomic S on the surface [60,61,63], i.e., complete desulfurization for these thiophenes.

Finally, experiments show that the presence of these reactive channels depends on the preparation method, e.g., vacuum versus liquid phase adsorption [56-58], or also deposition onto bulk metal versus evaporation of electrodes onto a molecular layer [64,65]. This point is of much importance when creating contacts to these organic species.

It should be noted that in many cases the conclusions of the above mentioned investigations of dissociation processes in thiol self-assembly rely on the knowledge of the characteristic S 2p core level binding energies (CLBEs) for atomic S adsorption and the thiolate sulfur. These are usually deduced from X-ray photoelectron spectroscopy (XPS) studies. Thus, it was noted in the Pd case that the S 2p region spectra differed significantly from those observed for Au and Ag substrates. This is because of contributions from both atomic and thiolate sulfur. The situation is in general complicated by the fact that molecular adsorption can occur on alternative or "unusual" adsorption sites, in the sense that they are not observed in well-ordered SAMs [27]. For these cases, it has been observed that the thiolate CLBE can be close to that of atomic S on Au and Ag. This engenders serious ambiguities. Interestingly, on transition metals such as Rh, W and Ni, there are observations of multicomponent S 2p spectra [66-68], which could be due to some type of interface sulfide layers. Understanding the interfaces in these situations is thus very important. A good knowledge of monolayer atomic chalcogen adsorption is obviously an important prerequisite, as well as information regarding the CLBEs of

S 2p (Se 3d, etc.) for such coverages is essential. This is still frequently unavailable, and obtaining precise spectroscopic information on this aspect is an essential complement to the investigation of other characteristics of molecular adsorption. Furthermore, there is currently much interest in nanostructured metal chalcogenides and ultrathin films, and in this context, this data is also of significant relevance.

In this progress report, we discuss recent work performed mainly in our groups on chalcogen SAM formation on reactive substrates, for which there exists few studies. We summarize selected, recently published work, as well as new data for alkane and aromatic chalcogenide molecules on Au, Cu, Pd and Ni surfaces. The main systems discussed are schematized in Figure 1. We chose alkane chalcogenide molecules that have been extensively studied on Au and a few aromatic molecules such as benzenedithiol, thiophene derivatives and selenophene that are of interest in molecular electronics.

Experimental

The experimental procedure has been outlined in detail in previous publications [22-24,26,27,43,48,69] and here we provide only essential points about new experiments relevant to this report.

Sample preparation

Sulfur and selenium adsorption was performed, as in an earlier study [69], by immersion into a 0.1 mM Na_2S or Na_2Se solution in 0.1 M aqueous NaOH. Na_2Se, alkanethiols, thiophenes and selenophene were purchased from Sigma-Aldrich and α,ω-dihexylquaterthiophene (DH4T) from SYNCOM, and all were used as supplied. DC6DSe ($((CH_3CH_2)_5Se)_2$ was synthesized according to the procedure described in an earlier publication [43] and in Supporting Information File 1.

Adsorption of DC6DSe was performed with a 1 mM solution in ethanol. It is known to lead to hexaneselenol adsorption on Au [37]. Thiophene and bithiophene adsorption was performed from a 1 mM ethanolic solution, whereas for DH4T, adsorption was performed from a 1 mM solution in dicholoromethane. In all cases a 24 h immersion time was used. Selenophene adsorption was performed from pure selenophene for 1 h.

The Au samples were prepared by evaporation onto hot mica that had been degassed for three hours at 300 °C. Au deposition was done at this temperature and then a brief heating to 550 °C was performed. The Cu(111), Pd(111) and Ni(111) monocrystals were purchased, oriented and polished, from Mateck or from the Surface Preparation Laboratories. In situ surface preparation was performed as usual by cycles of sputtering and annealing, and the surface cleanliness and crystallinity was checked by XPS and low energy electron diffraction (LEED).

The prepared samples were extracted from the ultra-high vacuum preparation chamber under N_2 flow and immediately immersed into the solutions. Thereafter, they were rinsed in the corresponding solvents and dried by N_2 gas. The samples were then immediately transferred into the analysis chamber.

Photoemission

The photoemission experiments were performed mainly on the BEAR beamline [22-24,26,27] at the Elettra (Trieste, Italy) synchrotron and the TEMPO beamline [43,48,69] at the Soleil (St. Auban, France) synchrotron. The experimental procedures are described in the indicated references. The energy resolution was about 50 meV and 200 meV on the TEMPO and BEAR beamlines, respectively. The measurements on thiophenes were performed using a VG-Microtech K-Alpha spectrometer incorporating a monochromatic X-ray source with an Al anode

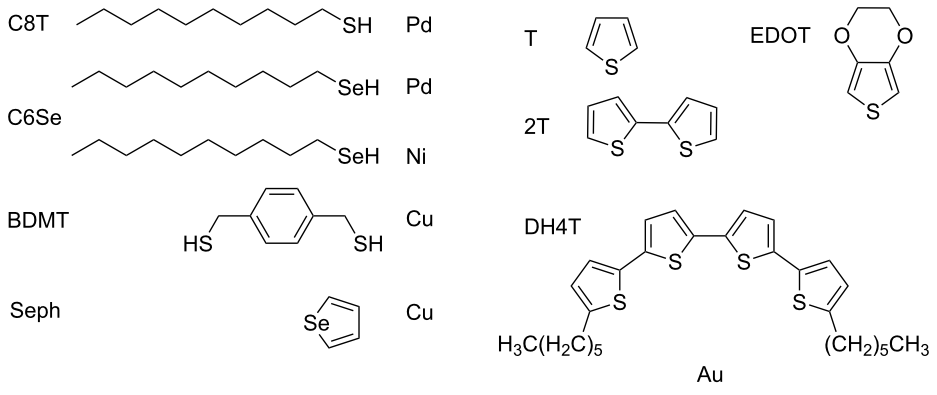

Figure 1: The main molecule–metal combinations discussed in this report: alkane chalcogenides (CnT), 1,4-benzenedimethanethiol (BDMT), selenophene (Seph), 3,4-ethylenedioxythiophene (EDOT), thiophene (T), bithiophene (2T), and α,ω-dihexylquaterthiophene (DH4T). Other examples of EDOT family compounds are mentioned later.

at the Orsay campus. In this case, the energy resolution was 500 meV.

The binding energy in the XPS spectra was calibrated with respect to the Au $4f_{7/2}$ peak, set at 84 eV. The calibration error is estimated to be 50 meV at TEMPO and about 100 meV at BEAR. With some exceptions (indicated later in the text), we used a photon energy corresponding to a final kinetic energy of ≈100 eV in order to maximize surface contributions.

Because X-ray irradiation is known to lead to alterations in the organic layers, particular care was taken to distinguish this effect. This was done by comparing the spectral shapes for successive scans and performing measurements on several points on the sample. A detailed discussion of this can be found in the original publications [26,48] and in the selenophene section below.

NEXAFS spectra presented here were recorded in partial yield mode by measuring the carbon Auger signal that appears consistent with the total yield measurements. We have used synchrotron light with 100% horizontal linear polarization. To probe the molecule orientation over the surface, we varied the polar angle by rotating the sample around the *z*-axis (the polarization is parallel to the surface plane for Θ = 90°).

Results and Discussion

1,4-Benzenedimethanethiol adsorption on copper surfaces

Dithiol SAMs have attracted attention in particular because the two thiol ends can be used as linkers between metal electrodes and thus metal–organic heterostructures can be constructed [70-74]. 1,4-Benzenedimethanethiol (BDMT) has been the object of several investigations on gold [21-25,75] and this dithiol was used in one of the first studies of molecular conductance [70]. Many of these studies use gold electrodes. It was interesting to extend these investigations to another prototype electrode metal: copper. This prompted the work described below. Studies of alkane and phenyl thiols do exist and they conclude that an ordered thiol layer is formed [76-78].

BDMT evaporative adsorption was studied on Au(111), Cu(100) and Cu(111) surfaces by Alarcón et al. [25,79] using time-of-flight ion scattering [80], which allows the study of the surface composition without inducing noticeable damage. It was observed that in the case of the copper surfaces, at the onset of adsorption, a substantial amount of sulfur on the surface appeared, while the carbon concentration remained small and increased only after addition of a much larger amount of BDMT. This could be interpreted as initial BDMT decomposition due to S−C bond scission that led to the presence of atomic S on the surface. This was surprising since such S–C bond scission was not observed for room temperature adsorption of alkanethiol and phenyl thiol [76-78].

To verify this, a high-resolution XPS study was performed [26] and S 2p spectra were recorded from low sub-monolayer coverage to very high exposures. Figure 2a shows the S 2p spectrum after exposure of a Cu(100) surface to 50 langmuir of BDMT. For dithiol adsorption on Au, in the case of well-ordered SAMs, one observes two doublets with the S 2p components located at about 162 eV and 163.1 eV. The former corresponds to thiolate sulfur (bound to Au) and the latter to the sulfur of the “free” SH end group on the top of an upright SAM. In the case of Cu at the lowest exposure, a strong component at 161.4 eV is observed. This could be due to an alternative adsorption site or to atomic S from dissociation. To clarify this, one needs information on the CLBEs for atomic S adsorption on Cu. Atomic S adsorption on Cu(100) and Cu(111) surfaces [81-87] leads to rather complex surface structures explored in several STM

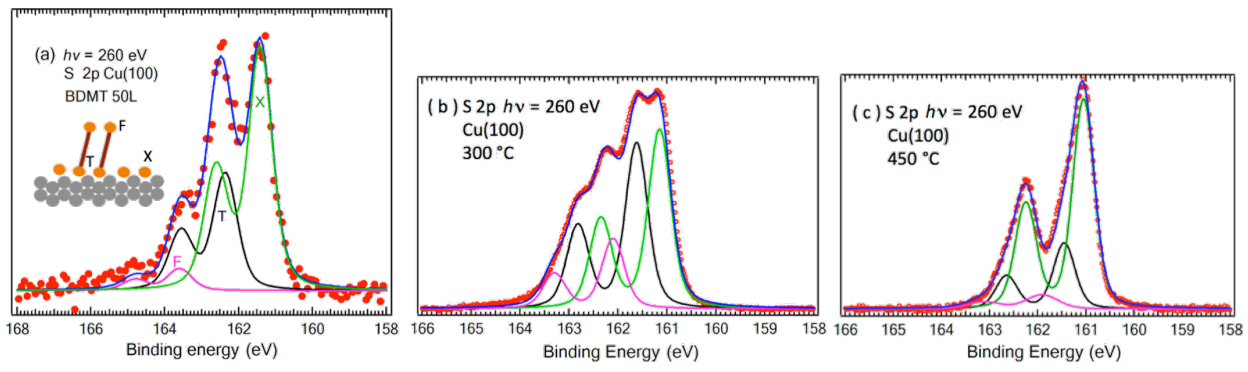

Figure 2: (a) S 2p XPS spectra for a small dose of BDMT evaporated [26] onto Cu(100). (b,c) S 2p spectra for S adsorption onto Cu(100) [82] from Na_2S. The solid lines are fits using Voigt contours and the appropriate spin–orbit splitting of the S $2p_{3/2}$ and S $2p_{1/2}$ components. Figure adapted with permission from [82], copyright 2014 American Chemical Society.

studies [81,84,85] and these are still being actively studied [82,86,87].

Although the S 2p binding energies for bulk copper sulfide are known, with a rare exception [83], there was previously not much information on CLBEs for sub-monolayer chemisorbed phases. A detailed photoemission study was therefore performed [82], revealing multicomponent S 2p spectra with different CLBEs corresponding to differently coordinated S atoms for different coverages (Figure 2b,c). The spectra in Figure 2b,c were taken after a pristine UHV prepared Cu surface was dipped into a Na_2S solution and then annealed to the indicated temperatures. This leads to the appearance of well-ordered structures that are identifiable by LEED. The 161.4 eV CLBE corresponds closely to one of the observed components for BDMT adsorption. It was also found [26] that annealing the BDMT-exposed Cu results in the molecular decomposition and appearance of residual S on the surface with this binding energy.

A careful analysis of the relative intensities of the C 1s and S 2p peaks in BDMT adsorption shows [26] that at this low 50 langmuir exposure, the amount of carbon present on the surface is much lower than could be expected. These measurements thus indicate that in the initial stages of adsorption, S–C bond scission occurs, leading to sulfidation of the Cu surface. Thereafter, when the surface is passivated, molecular adsorption occurs. The remaining molecular fragment after dissociation appears to leave the surface. Possibly [26], the loss of this fragment could be mediated by a H-atom transfer, leading to the formation of a less reactive, CH_3-terminated species and the sulfurized (Cu–S) surface:

$$Cu + HS–CH_2–R–CH_2–CH_3 \rightarrow Cu–S + CH_3–R–CH_2–CH_3$$

Alkanechalcogenides on Pd

The formation of alkanethiol SAMs on Pd was reported by several authors [46,47]. The research groups of Nuzzo and Whitesides concluded that alkanethiol SAMs [46,47] were not formed directly on the Pd(111) surface, but rather on a PdS interface layer. Similar conclusions were recently reached by others [88].

Let us first look at the adsorption of sulfur on Pd. Previous studies [81,89-92] showed the existence of several structures in the sub-monolayer range, namely: the (√3 × √3)R30° phase and the more complex (√7 × √7)R19.1° phase. The (√3 × √3)R30° forms at lower temperatures and corresponds to a simple sulfur overlayer. The (√7 × √7)R19.1° phase (for simplicity we shall call it the √7 phase) has been observed upon annealing sulfurized surfaces. The sulfur coverage in this case is estimated to be 3/7. A theoretical analysis [92] shows that this corresponds to a single PdS atomic overlayer as proposed by Liu et al. [89]. The S atoms lie at slightly off-bridge sites and are slightly below the Pd atom plane.

A theoretical study of thiol adsorption by Carro et al. [88] considered the formation of the thiol layer on a (√7 × √7)R19.1° PdS layer and concluded that upon thiol adsorption, some Pd adatoms are extracted from the PdS layer. The thiols attach to these “extracted adatoms”.

In order to shed light on characteristics of thiol adsorption, we first studied [48] sulfur adsorption on Pd(111) since CLBEs for S on the √7 phase were not known. Thereafter, dodecanethiol (C12T) adsorption was performed on pristine Pd. We also investigated C12T adsorption on both presulfurized and preselenized Pd surfaces, which allowed us to highlight characteristics of adsorption on a chalcogenide interface and distinguish between the thiol S and the interface chalcogen atom. We briefly summarize here the main findings of this study.

Figure 3a shows the measured XPS spectrum in the S 2p region. As observed in previous investigations, the spectrum is broad, without well-defined features. It was fitted with two main doublet components at 161.71 and 162.45 eV and significantly smaller structures at 163.26 and 164.26 eV. These values were similar to previous reports [46,47,88] in a low resolution study on polycrystalline Pd with components at 162.1 eV (or 162.3 eV) and 162.9 eV (or 163.2 eV). It was suggested [88] that the thiolate CLBE has the higher binding energy, whereas the lower one corresponds to the sulfide phase; although in many cases of thiol adsorption on metal, the thiolate S 2p CLBE is close to 162 eV.

The S 2p spectrum for a sulfurized surface prepared in a Na_2S aqueous solution followed by annealing to a few hundred Celsius (Figure 3b) was studied. The initial spectrum was found to be broad with a lower energy component. From angular measurements (i.e., normal and grazing emission), it was concluded that this component corresponds to atoms in an upper layer. Upon heating, essentially only one doublet component is left in the spectrum as shown in Figure 3b. LEED measurements indicate that under this condition, a well-defined √7 phase exists. A comparison with the thiol spectrum in Figure 3a then suggests that if this is really the underlying sulfide layer, the thiolate component lies at lower binding energies.

To explore this further, the √7 phase PdS surface was first prepared and then exposed to C12T. The result was remarkably similar to the one for direct C12T adsorption. Therefore, the fits to the C12T/PdS spectra suggest that the thiolate peak lies at

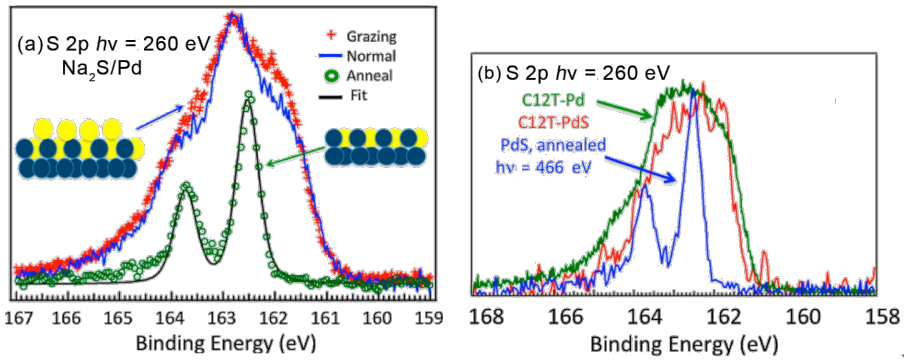

Figure 3: (a) XPS spectra [48] in the S 2p region before (blue, normal emission; red, grazing emission) and after annealing at 450 °C (green line). (b) Comparison of S 2p spectra [48] for the √7 PdS surface after annealing (blue line), PdS with adsorbed C12T molecules (red line), and clean Pd(111) with C12T molecules (green line). Figure adapted with permission from [48], copyright 2014 American Chemical Society.

161.8 eV. This results in the PdS S 2p peak being split into two main components at 162.35 and 162.96 eV, suggesting a restructuring occurs in the PdS layer (as would be expected from the model of Carro et al.) [88]. An important aspect in XPS analysis is potential radiation damage to molecular films. This was carefully checked and was found not to affect the above conclusions (see original publication [48] for details).

In a final twist in this investigation, we similarly prepared a selenized Pd surface in a Na_2Se solution and later adsorbed the thiols onto this surface [48]. This was done in order to distinguish between the thiol S and the interface chalcogen atom. The Se 3d XPS spectra of the selenized surface, after annealing to 500 °C, are shown in Figure 4a. Interestingly, in this case, on both the initial selenized surface and after annealing, we obtained multicomponent spectra. In both cases, from angular emission measurements the lower energy feature appears to correspond to outer lying Se atoms. The LEED results for the annealed surface [48] were akin to the √7 PdS phase, except that multiple spots suggested a more complex structure with widely spaced, rotated domains.

C12T adsorption on the annealed, selenized surface resulted in changes in intensity of the Se 3d features: a clear decrease of the outer lying Se 3d peak was especially noticeable, indicating changes in the layer occurred. The S 2p XPS spectrum (Figure 4b) had a prominent doublet at 161.8 eV, as was deduced for the PdS surface case, supporting the attribution of the peak to thiolate for C12T adsorption on Pd and PdS. The higher energy component was attributed to X-ray damage effects, while the 162.3 eV component may be a different thiolate energy at a different adsorption site.

Measurements were also more recently performed for C6DSe adsorption on pristine Pd(111). The Se 3d XPS spectrum is shown in Figure 4c. As for the case of alkanethiol adsorption, the spectrum is broad. Its shape can be reproduced by fitting with two main components at 54.1 eV and 54.8 eV in addition

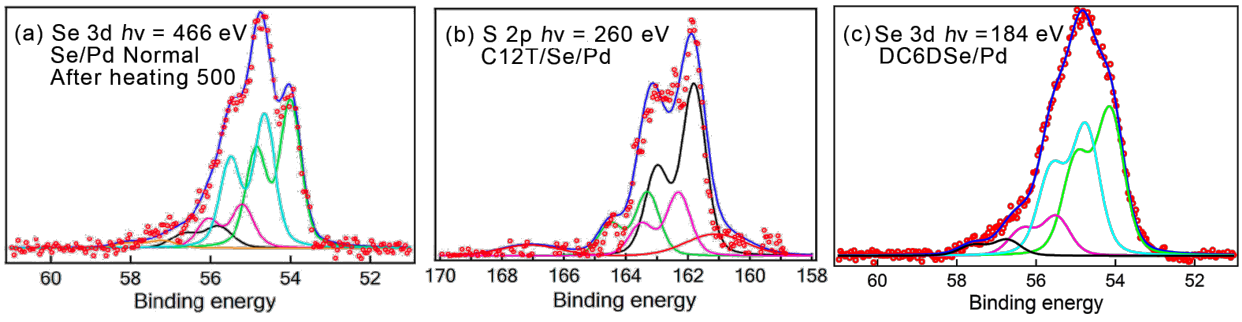

Figure 4: (a) XPS in the Se 3d region [48] after initial selenization of Pd with atomic selenium and heating to 500 °C. (b) XPS spectrum [48] in the S 2p region after C12T adsorption on the selenized surface (see text). (c) XPS in the Se 3d region after adsorption of DC6DSe (this work). Figure adapted with permission from [48], copyright 2014 American Chemical Society.

to two smaller ones at 55.5 and 56.7 eV. The spectrum is remarkably similar to that corresponding to atomic Se adsorption. Although a detailed study for C12T was not performed, this similarity strongly suggests that we are dealing with C6DT dissociation and formation of a PdSe interface, possibly with molecular adsorption on this interface layer.

Alkaneselenide and Se on Ni

The study of thiol and selenol SAM adsorption on Pd was extended here to the study of C6DSe adsorption on Ni and complemented by an investigation of Se interaction with Ni(111). We looked at Ni, since amongst other uses it can be employed as an electrode material. Additionally, Ni nanoparticles [93-97] are an example of magnetic nanoparticles [95] that are useful as catalysts [96], in magnetic fluids, as well as for binding and even magnetic separation of proteins [97]. As for other metals, undesirable oxidation has led to research into protection by chalcogenide SAMs, and while thiol adsorption has been investigated in some works [98], selenium head group molecule adsorption requires further study.

High-resolution XPS spectra were acquired on the Ni(111) surface selenized in the aqueous Na_2Se solution and also on the annealed selenized sample. LEED measurements were performed to ascertain existence of ordered phases on the annealed surface. We will only focus on the main Se 3d results here, but results of the other XPS and LEED measurements are given in Supporting Information File 1, Figures S1–S3.

The XPS spectrum in the Se 3d region after annealing the sample to 500 °C is shown in Figure 5 along with fits using Voigt contours (Supporting Information File 1, Table S1). The initial broad spectra obtained after immersion into solution and after heating to 300 °C are given in Supporting Information File 1, Figure S2 and Table S1. As shown in Supporting Information File 1, Figure S2, the spectrum peak positions shift and narrow upon heating. Heating to 500 °C leads to further decrease in width of the spectrum, which retains its main "B" component and has smaller features that appear to be remnants of contributions from differently coordinated Se atoms observed at lower temperatures (see Supporting Information File 1, Table S1). Indeed, LEED measurements on the heated samples show complex patterns that evolve with temperature (Supporting Information File 1, Figure S3).

High-resolution XPS measurements were performed for C6DSe adsorption from a millimolar solution in ethanol for an incubation time of one hour. Figure 5b shows the Se 3d region spectra for Ni(111). The spectrum, as was observed for Pd, is rather broad and can be fitted with several doublet components as shown in the figure (see Supporting Information File 1, Table S2). This suggests that here, as previously reported for thiol SAMs on Ni, we deal with Se–C bond breaking processes.

The attribution of the different components is challenging. In alkaneselenide adsorption on Au, the Se $3d_{5/2}$ CLBE of selenol for well-ordered SAMs is found to be close to 54.6 eV [32,37,39,43]. Here, however, as seen in Figure 5a, this energy corresponds to that of atomic Se on Ni for the case of an annealed surface (peak B). This comparison would lead to the tentative attribution of the two lower CLBE components (Figure 5b, A' and B') to the presence of atomic Se due to Se–C bond scission. The higher energy peak, C', could then be due to molecular Se, and the peak D' could possibly be due to a different atomic Se species.

As in the case of thiols on Pd, it is possible that in the initial stages of alkaneselenide adsorption we observed Se–C bond scission with the formation of a passivated Se–Ni surface. Thereafter, C6DSe adsorption occurs, which also leads to modifications in the structure of the Se–Ni surface layer as was the case for Pd. The attribution of the different components in the

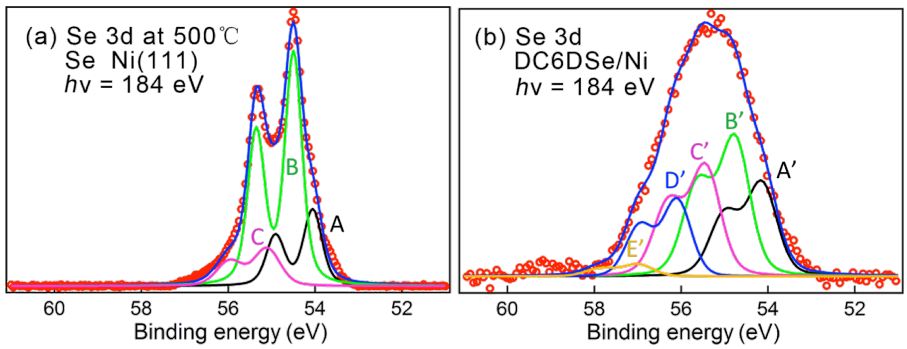

Figure 5: XPS in the Se 3d region after (a) initial selenization of Ni with atomic selenium and heating to 500 °C and (b) after adsorption of DC6DSe on Ni. See Supporting Information File 1, Tables S1 and S2 for peak positions.

spectrum is only tentative and a more in-depth analysis is still necessary.

Thiophene-family compounds

Thiophene derivative, π-conjugated systems have attracted much attention in molecular electronic applications [63-65,99-101] because of their interesting properties, structural versatility, intrinsic charge transport behavior with high carrier mobility, and high light harvesting efficiency. Their use includes application in field effect transistors, solar cells and light emitting diodes. A number of studies have been devoted to the assembly of these molecules on metallic electrodes [102-104] and in particular on gold surfaces [56-65]. They reveal peculiar features and differences in adsorption characteristics.

Evaporative assembly of thiophene onto Au(111) by Nambu et al. [56] at low temperatures (around 120 K) shows initial adsorption in a lying down configuration and then a transition to a more standing up configuration, until at high exposures a multilayer is formed. The S $2p_{3/2}$ CLBE for multilayer thiophene is about 164.5 eV whereas at monolayer coverage it was found to be 163.8 eV. This difference in position is due to the S Au surface interaction in the monolayer of the molecularly adsorbed thiophene. In liquid phase adsorption, on the other hand, a single doublet is observed with S 2p found at 162 eV, and this has been attributed to S–C bond scission leading to the appearance of a thiolate sulfur of an alkene chain. A shift to higher energy and broadening of the C 1s peak is also observed. In NEXAFS measurements, for molecular adsorption in vacuum, the spectrum is characterized by a sharp peak at about 285 eV related to the π*1 orbital of thiophene, which disappears for liquid phase adsorption, indicating breaking of the thiophene molecule.

The work of Noh and Hara's groups [57,58], however, found a main peak with S $2p_{3/2}$ CLBE near 162 eV and a smaller extra feature at 161 eV in liquid phase adsorption. The latter was tentatively attributed to atomic sulfur due to complete desulfurization of thiophene or possibly to adsorption at an alternative adsorption site. For thiols, this question of alternative adsorption sites was recently discussed by Jia et al. [27]. Interestingly, in the case of bithiophene adsorption [58], no significant dissociation was observed with the XPS spectrum composed of a single doublet S 2p at 163.4 eV. This led to the conclusion [58] that the adsorption state of the thiophenes depends on the number of units in the thiophene oligomer. Yet another conclusion was reached by Liu et al. [60], who reported for thiophene a S $2p_{3/2}$ binding energy of 163.4 eV for low temperature adsorption, whereas at room temperatures it was close to 161 eV. Thus there exist rather different accounts on thiophene adsorption on Au.

Studies of 3,4-ethylenedioxythiophene (EDOT) and its derivatives [62] (Figure 6a) on polycrystalline Au, Au(111) and Au nanoparticle (AuNP) surfaces from vapor phase and solution has also revealed complex S 2p spectra (Figure 6a) with components corresponding to molecular adsorption and the appearance of thiolate and possibly atomic sulfur. Thus, these components were observed with various degrees of intensity for EDOT, bi-EDOT, 3',4'-ethylenedioxy-2,2':5',2"-terthiophene (TET), and the polymer (PEDOT). The dissociation process would not, in this case, depend on the number of units.

A recent detailed study [63] was performed for the case of α,ω-dihexylquaterthiophene (DH4T) which, because of its high carrier mobility [63], is of great interest for organic electronics. We studied the assembly on Au surfaces from photoemission and XPS spectra in the S 2p region as shown in Figure 6B. For a thick, DH4T layer one observes the S $2p_{3/2}$ peak related to thiophene rings at about 164 eV (peak 1), while for the thin layer, the same feature shifts to 163.4 eV (peak 2). This is due to the presence of thiophenes at the close interface with Au. One also observes features at about 162 eV (peak 3) and 161 eV (peak 4), attributable to the strong reaction, leading to S–C bond breaking and the appearance of thiolate (peak 3) and possibly atomic S (or possibly molecules at a different adsorption site; peak 4). A similar spectrum is obtained when Au is evaporated onto the thick DH4T layer [63] and reactions likely occur at the diffuse interface. Indeed, the partial penetration of Au into the layer may occur, as this has been observed in metal evaporation onto organic samples. This was noted for Au, Ag and Cu electrode evaporation onto other thiophenic derivatives such as poly(3-hexylthiophene), where penetration of the metal into the layer was also suggested to occur [64,65].

New experiments were performed on adsorption of thiophene (1T), bithiophene (2T) and DH4T on Au(111) surfaces produced by evaporation of Au onto mica. Several sets of measurements were performed with variable results. The S 2p XPS spectra are shown in Figure 7 along with fits using Voigt contours. They show the existence of multiple doublet components with S 2p at 163.5, 162 and 161.5 eV, corresponding to: a) peak 2 - the thiophene molecule interacting with Au, b) peak 3 - a thiolate S of an alkene chain of the broken thiophene molecule and c) peak 4 - a large component either due to atomic sulfur or an alternative adsorption site of the molecules, respectively. Here we use the same notation as in Figure 6B [63]. For 1T we only see components corresponding to fragments from dissociation. In the case of 2T and DH4T, there is a component corresponding to adsorbed thiophene interacting with Au. The 2T result differs from that reported earlier [58], where the XPS study concluded that there was no dissociation. We were able to obtain such spectra quite systematically. Finally, for 2T the

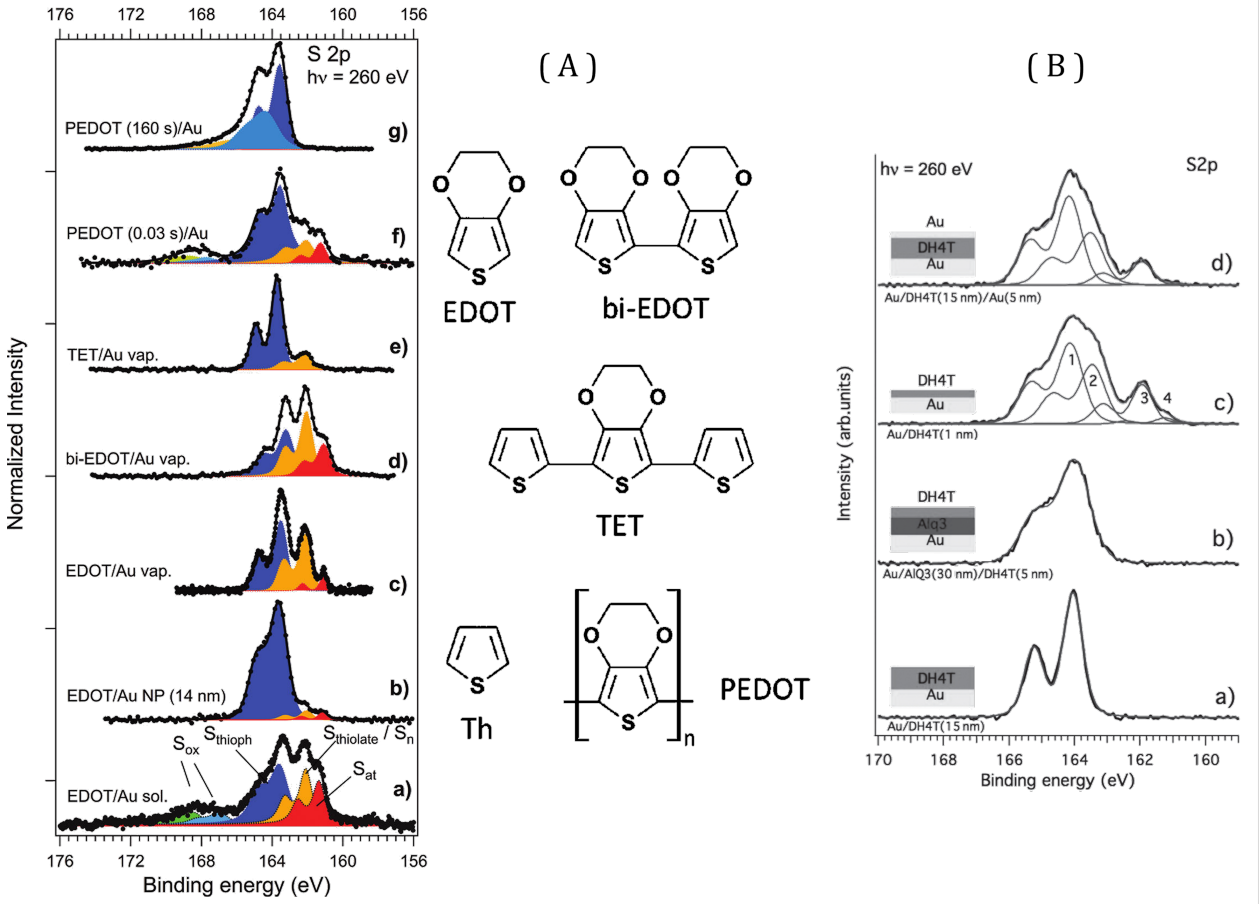

Figure 6: (A) EDOT-related molecules and XPS S 2p spectra for these cases [62]. Figure adapted with permission from [62], copyright 2011 American Chemical Society. (B) XPS spectra for DH4T [63] on gold for different cases of deposition as indicated for each curve. In this panel, the spectra refer to: a) 15 nm thick layer of DH4T on Au, b) DH4T layer on AlQ3 film on Au, c) a 1 nm DH4T layer on Au and c) a 5 nm layer of Au evaporated onto a 15 nm DH4T layer on Au. Figure adapted with permission from [63], copyright 2014 John Wiley & Sons, Inc.

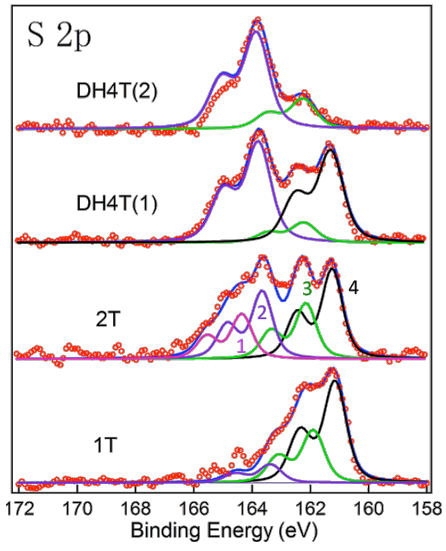

Figure 7: XPS S 2p spectra for 1T, 2T and DH4T adsorption on Au films on mica. The DT spectra are shown for two different samples prepared in the same manner.

spectrum was fitted with a higher energy component (peak 1) ascribed to thiophene not interacting with Au, and for which the CLBE is similar to the one found for a thick molecular layer of thiophene (Figure 6B, peak 1).

The DH4T spectrum shows the same components as in the preceding study, albeit with different relative intensities and without the multilayer component (peak 1, Figure 6B). Here, for DH4T, we show data for two different samples, prepared under the same conditions, but which give very different results. We emphasize this variability, which we attribute to differences in the surface characteristics that can lead to differences in reactivity and changes in the relative intensity of components related to dissociation channels. This can also explain the difference between the characteristics of the spectra shown here and earlier works. Note also that as mentioned above and shown for thiols [27], adsorption of the S atom of the alkene chain at different adsorption sites could lead to different CLBEs close to 162 and 161.5 eV. This may depend on the order and packing density of the molecules.

From these results, one sees that on Au (which is considered to be nonreactive), thiophene and its various derivatives undergo S–C bond scission. The catalytic activity and electron transfer processes for Au have been extensively investigated in recent years and are shown to be quite large on nanoclusters [105-110]. This has been related to low coordination sites [109,110] and to the density of steps and different kinds of surface defects. Variability, to the extent of dissociation processes, could thus be expected depending upon the structure of the surface.

Selenophene on Cu(111)

Selenophene (Seph)-based compounds are considered interesting alternatives [111] to thiophene. Selenophene adsorption on Au surfaces in vacuum and from liquid was reported by Kondoh et al. [112], who, as for thiophene, reported molecular adsorption of selenophene in UHV, but dissociative adsorption from liquid phase adsorption. This was deduced from changes in the Se 3p peak positions and strong differences in NEXAFS spectra. In adsorption in UHV, a strong peak due to the selenophene π orbital was observed, whereas it was very strongly reduced for liquid phase adsorption.

Along the lines of the other studies, we first examined Se adsorption on Cu(111) from a Na_2Se solution, with the objective of determining the Se CLBEs on Cu surfaces for ordered sub-monolayer structures. The photoemission data concerning Cu 2p and Cu 3p levels and the Cu Auger results are very similar to the case of sulfur adsorption [82] and we do not go into them here. The XPS spectrum in the Se 3d region after initial adsorption is broad with the Se $3d_{5/2}$ peak at 54.3 eV. The resulting spectra after annealing to 300 and 500 °C are shown in Figure 8, which includes fits using Voigt profiles. After the first annealing step, two main components are observed with Se $3d_{5/2}$ CLBEs of 53.9 eV (A) and 54.2 eV (B) and a small feature (C) at 54.5 eV, indicating differently coordinated Se atoms. After the second annealing, component A dominates the spectrum. These changes are also reflected in LEED images, where rather different structures are observed after annealing. These will not be discussed in this short report.

High-resolution XPS and NEXAFS spectra for selenophene adsorption onto Cu(111) are shown in Figure 9. We show the results of two sets of measurements (Figure 9a,b and Figure 9c,d, corresponding to what we later call Sample 1 and Sample 2, respectively). In both cases, the Cu(111) surface preparation and incubation in pure selenophene was performed in the same manner.

The XPS spectra display a considerable variability as for the thiophene case. In general, a broad Se 3d spectrum is observed, which can be fitted with three with Se 3d components located at 54.3 eV (A), 54.85 eV (B) and 55.8 eV (C). The relative intensities of these components vary greatly between the two measurements sets.

On the basis of a comparison with the Se 3d spectra for atomic Se adsorption on Cu and with the CLBE of selenol adsorption on Au, we could ascribe the different components in the Se 3d spectrum to: a) presence of Seph Se 3d components, b) Seph dissociation, leading to alkene-selenol-like CLBEs and c) possible atomic Se or molecules adsorbed on different adsorption sites. The CLBE for atomic Se adsorption lies at lower energies after high temperature annealing (Figure 9), but we cannot entirely rule out its presence in this spectrum, because one does see higher energy components at the lower temperature.

Further information comes from NEXAFS spectra shown in Figure 9b,d. In Figure 9b, for Sample 1, the NEXAFS spectrum is dominated by a peak at 285.5 eV ascribable to the π*1 orbital of selenophene. For Sample 2 this peak is much weaker. We also see that for Sample 1 in the XPS 3d spectrum, the B peak is most intense, whereas for Sample 2 it is the A peak that dominates the spectrum. In this case, there is also a more prominent

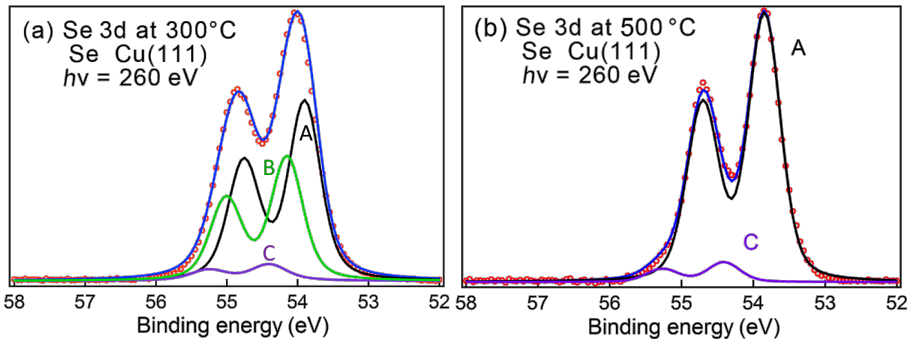

Figure 8: Se adsorption on Cu(111) from a Na_2Se solution and after heating to the indicated temperatures.

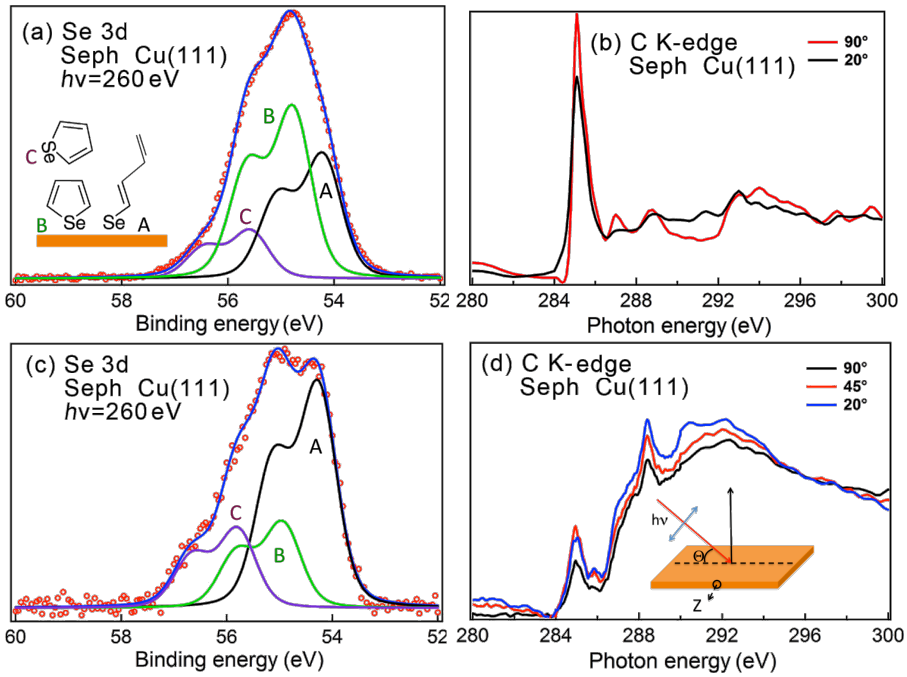

Figure 9: Selenophene (Seph) adsorption on Cu(111). (a,c) Se 3d spectra and (b,d) NEXAFS spectra for the indicated angles.

peak at 288.4 eV and a shoulder at 292.2 eV, which could be related to the alkene chain. We rule out that this difference in Sample 2 is due to X-ray irradiation effects since measurements as a function of scanning did not reveal any significant changes (see Supporting Information File 1, Figure S4).

On the basis of these results, it would seem reasonable to ascribe peak B to selenophene interacting with the surface. Furthermore, peak A can be related to Se adsorption corresponding to one Se–C bond breaking, leading to an alkene chain appearance. Finally, the higher energy C component can be related to residual (after rinsing) selenophene remaining on the surface (e.g., on top of the rest of the molecular film) and not reacting strongly with Cu. This is schematically illustrated in the inset of Figure 9a. These attributions follow the scheme for thiophene described above. The peaks in the fit are somewhat broad, which may reflect presence of atomic Se at the lower energy end of the spectrum and also different bonding configurations of molecules. The NEXAFS spectra suggest, in both cases, that the molecules are either strongly tilted from the surface normal or that a large fraction of the layer is disordered.

Selenophene adsorption thus shows the possibility of dissociation with Se–C bond scission and underlines again the variability, which could be related with surface morphology, different probabilities of reactive bond breaking or different adsorption configurations.

Conclusion

The results presented here show that in a number of cases in self-assembly of chalcogenide molecules on metal surfaces, dissociation processes are observed that correspond to chalcogen-atom/C-bond scission. While in case of the more reactive transition metals this may not appear surprising, these processes are also observed on the less reactive coinage metal surfaces, including gold.

In the case of the copper surface, earlier studies of alkanethiol and phenyl thiol adsorption did not reveal existence of any dissociation process, but we see that in the case of BDMT S–C bond scission is observed at room temperature. This occurs in the early stages of adsorption, corresponding to the lying down phase, leading to formation of a sulfurized surface on which molecules are later adsorbed after its passivation. There are, until now, no theoretical studies that would help to understand these differences and in what way the presence of the methylene unit promotes dissociation, as opposed to the case of alkane and phenyl thiols. Such studies in the early phase of adsorption would be most interesting.

In the case of Pd and Ni, we see that also chalcogenide molecule adsorption is accompanied by formation of a chalcogenized interface layer on which molecules are then adsorbed. One can expect that capping nanoparticles with these molecules would lead to formation of metal–metal chalcogenide,

core/shell nanoparticles, which has been shown to have interesting specific properties.

In the case of chalcogenophene molecules, we also observed that even for gold, S–C (Se–C) bond scission occurs, leading to opening of the ring and loss of aromaticity. This interrupts the π-electron system and impairs charge transport along the chains, which is a problem in molecular electronics. There are indications of the appearance of atomic S/Se on the surface that corresponds to complete removal (dechalcogenation) of the molecules. It has been suggested that this may be accompanied by metallocycle formation [56,112].

In general, such dissociation processes leading to formation of chalcogenide interface layers accompanied by changes in molecular properties can adversely affect charge transport. In metal deposition on dithiol SAMs, which has been considerably discussed, the reaction with the metal with S–C bond scission would result in cutting the link with the rest of the molecule. In molecular electronics applications, this would result in a disruption of current flow.

In this work, we have strived to underline the variability in the adsorption results, where we see that under seemingly similar preparation conditions, quite different results are obtained with significant dissociation occurring in some cases, even though the preparation procedures appear to be reasonably good. We would relate this at least partly to surface morphology, since reactivity can be large at low coordination sites and depends on the density of steps and different kinds of surface defects. It is important to delineate this from the point of view of creation of metal contacts in organic electronic devices. This should be taken into account in general, including the case of evaporative deposition or contact printing [72] by transfer from a stamp.

We hope that this report will stimulate further investigations of these reactive processes and be useful to researchers dealing with these systems in various applications mentioned here.

Supporting Information

Supporting Information File 1

Case studies of formation of chalcogenide self-assembled monolayers on surfaces and dissociative processes.
Selenide synthesis; XPS spectra for selenium on nickel and tables of Se 3d peak positions; LEED images for Se on Ni(111); X-ray damage verification for selenophene.
[http://www.beilstein-journals.org/bjnano/content/supplementary/2190-4286-7-24-S1.pdf]

Acknowledgements

T. Jiang and Y. Tong thank the Chinese Scholarship Council for their Ph.D. scholarships. We thank Diana Dragoe for her help with XPS measurements using the K-Alfa spectrometer, Karine Chaouchi for help in the Soleil chemistry laboratory and François Nicolas for help in the Soleil surface laboratory. The research leading to some of these results has received funding from the European Community's Seventh Framework Program (FP7/2007-2013) under grant agreement nº 312284.

References

1. Nuzzo, R. G.; Fusco, F. A.; Allara, D. L. *J. Am. Chem. Soc.* **1987,** *109,* 2358. doi:10.1021/ja00242a020
2. Tour, J. M.; Jones, L., II; Pearson, D. L.; Lamba, J. J. S.; Burgin, T. P.; Whitesides, G. M.; Allara, D. L.; Parikh, A. N.; Atre, S. V. *J. Am. Chem. Soc.* **1995,** *117,* 9529. doi:10.1021/ja00142a021
3. Schreiber, F. *Prog. Surf. Sci.* **2000,** *65,* 151. doi:10.1016/S0079-6816(00)00024-1
4. Love, J. C.; Estroff, L. A.; Kriebel, J. K.; Nuzzo, R. G.; Whitesides, G. M. *Chem. Rev.* **2005,** *105,* 1103. doi:10.1021/cr0300789
5. Maksymovych, P.; Voznyy, O.; Dougherty, D. B.; Sorescu, D. C.; Yates, J. T., Jr. *Prog. Surf. Sci.* **2010,** *85,* 206–240. doi:10.1016/j.progsurf.2010.05.001
6. Vericat, C.; Vela, M. E.; Benitez, G. A.; Martin Gago, J. A.; Torrelles, X.; Salvarezza, R. C. *J. Phys.: Condens. Matter* **2006,** *18,* R867. doi:10.1088/0953-8984/18/48/R01
7. Häkkinen, H. *Nat. Chem.* **2012,** *4,* 443–455. doi:10.1038/nchem.1352
8. Turchanin, A.; Gölzhäuser, A. *Prog. Surf. Sci.* **2012,** *87,* 108–162. doi:10.1016/j.progsurf.2012.05.001
9. Srisombat, L.; Jamison, A. C.; Lee, T. R. *Colloids Surf., A* **2011,** *390,* 1–19. doi:10.1016/j.colsurfa.2011.09.020
10. Jung, C.; Dannenberger, O.; Xu, Y.; Buck, M.; Grunze, M. *Langmuir* **1998,** *14,* 1103–1107. doi:10.1021/la9708851
11. Kato, H. S.; Noh, J.; Hara, M.; Kawai, M. *J. Phys. Chem. B* **2002,** *106,* 9655–9658. doi:10.1021/jp020968c
12. Ishida, T.; Hara, M.; Kojima, I.; Tsuneda, S.; Nishida, N.; Sasabe, H.; Knoll, W. *Langmuir* **1998,** *14,* 2092–2096. doi:10.1021/la971104z
13. Fuxen, C.; Azzam, W.; Arnold, R.; Witte, G.; Terfort, A.; Wöll, C. *Langmuir* **2001,** *17,* 3689–3695. doi:10.1021/la0018033
14. Rong, H.-T.; Frey, S.; Yang, Y.-J.; Zharnikov, M.; Buck, M.; Wühn, M.; Wöll, C.; Helmchen, G. *Langmuir* **2001,** *17,* 1582–1593. doi:10.1021/la0014050
15. Frey, S.; Stadler, V.; Heister, K.; Eck, W.; Zharnikov, M.; Grunze, M.; Zeysing, B.; Terfort, A. *Langmuir* **2001,** *17,* 2408–2415. doi:10.1021/la001540c
16. Prato, M.; Moroni, R.; Bisio, F.; Rolandi, R.; Mattera, L.; Cavalleri, O.; Canepa, M. *J. Phys. Chem. C* **2008,** *112,* 3899. doi:10.1021/jp711194s
17. Guo, G.; Zheng, W.; Hamoudi, H.; Dablemont, C.; Esaulov, V. A.; Bourguignon, B. *Surf. Sci.* **2008,** *602,* 3551. doi:10.1016/j.susc.2008.09.029
18. Ito, E.; Kang, H.; Lee, D.; Park, J. B.; Hara, M.; Noh, J. *J. Colloid Interface Sci.* **2013,** *394,* 522. doi:10.1016/j.jcis.2012.12.035
19. Subramanian, S.; Sampath, S. *Anal. Bioanal. Chem.* **2007,** *388,* 135–145. doi:10.1007/s00216-007-1184-4

20. Hamoudi, H.; Guo, Z. A.; Prato, M.; Dablemont, A.; Zheng, W. Q.; Bourguignon, B.; Canepa, M.; Esaulov, V. A. *Phys. Chem. Chem. Phys.* **2008,** *10,* 6836. doi:10.1039/b809760g
21. Hamoudi, H.; Prato, M.; Dablemont, C.; Cavalleri, O.; Canepa, M.; Esaulov, V. A. *Langmuir* **2010,** *26,* 7242–7247. doi:10.1021/la904317b
22. Pasquali, L.; Terzi, F.; Seeber, R.; Nannarone, S.; Datta, D.; Dablemont, C.; Hamoudi, H.; Canepa, M.; Esaulov, V. A. *Langmuir* **2011,** *27,* 4713–4720. doi:10.1021/la105063u
23. Pasquali, L.; Mukherjee, S.; Terzi, F.; Giglia, A.; Mahne, N.; Koshmak, K.; Esaulov, V.; Toccafondi, C.; Canepa, M.; Nannarone, S. *Phys. Rev. B* **2014,** *89,* 045401. doi:10.1103/PhysRevB.89.045401
24. Pasquali, L.; Terzi, F.; Zanardi, C.; Pigani, L.; Seeber, R.; Paolicelli, G.; Suturin, S. M.; Mahne, N.; Nannarone, S. *Surf. Sci.* **2007,** *601,* 1419–1427. doi:10.1016/j.susc.2007.01.007
25. Salazar Alarcón, L.; Jia, J.; Carrera, A.; Esaulov, V. A.; Ascolani, H.; Gayone, J. E.; Sánchez, E. A.; Grizzi, O. *Vacuum* **2014,** *105,* 80–87. doi:10.1016/j.vacuum.2014.01.017
26. Jia, J.; Giglia, A.; Flores, M.; Grizzi, O.; Pasquali, L.; Esaulov, V. A. *J. Phys. Chem. C* **2014,** *118,* 26866. doi:10.1021/jp509184t
27. Jia, J.; Kara, J.; Pasquali, L.; Bendounan, A.; Sirotti, F.; Esaulov, V. A. *J. Chem. Phys.* **2015,** *143,* 104702. doi:10.1063/1.4929350
28. Zhang, S.; Chandra, K. L.; Gorman, C. B. *J. Am. Chem. Soc.* **2007,** *129,* 4876–4877. doi:10.1021/ja0704380
29. Fracasso, D.; Kumar, D.; Rudolf, P.; Chiechi, R. C. *RSC Adv.* **2014,** *4,* 56026–56030. doi:10.1039/C4RA09880C
30. Bayati, M.; Schiffrin, D. J. *J. Phys. Chem. C* **2013,** *117,* 22746–22755. doi:10.1021/jp406370c
31. Canepa, M.; Giulia Maidecchi, G.; Chiara Toccafondi, C.; Cavalleri, O.; Prato, M.; Chaudhari, V.; Esaulov, V. A. *Phys. Chem. Chem. Phys.* **2013,** *15,* 11559–11565. doi:10.1039/c3cp51304a
32. Romashov, L. V.; Ananikov, V. P. *Chem. – Eur. J.* **2013,** *19,* 17640–17660. doi:10.1002/chem.201302115
33. Cometto, F. P.; Patrito, E. M.; Olivera, P. P.; Zampieri, G.; Ascolani, H. *Langmuir* **2012,** *28,* 13624–13635. doi:10.1021/la3024937
34. Ossowski, J.; Wächter, T.; Silies, L.; Kind, M.; Noworolska, A.; Blobner, F.; Gnatek, D.; Rysz, J.; Bolte, M.; Feulner, P.; Terfort, A.; Cyganik, P.; Zharnikov, M. *ACS Nano* **2015,** *9,* 4508–4526. doi:10.1021/acsnano.5b01109
35. Monnell, J. D.; Stapleton, J. J.; Jackiw, J. J.; Dunbar, T.; Reinerth, W. A.; Dirk, S. M.; Tour, J. M.; Allara, D. L.; Weiss, P. S. *J. Phys. Chem. B* **2004,** *108,* 9834–9841. doi:10.1021/jp037728x
36. Lee, S. Y.; Ito, E.; Kang, H.; Hara, M.; Lee, H.; Noh, J. *J. Phys. Chem. C* **2014,** *118,* 8322–8330. doi:10.1021/jp409531w
37. Subramanian, S.; Sampath, S. *J. Colloid Interface Sci.* **2007,** *312,* 413. doi:10.1016/j.jcis.2007.03.021
38. Mekhalif, Z.; Fonder, G.; Laffineur, F.; Delhalle, J. *J. Electroanal. Chem.* **2008,** *621,* 245–252. doi:10.1016/j.jelechem.2007.11.020
39. Shaporenko, A.; Ulmann, A.; Terfort, A.; Zharnikov, M. *J. Phys. Chem. B* **2005,** *109,* 3898–3906. doi:10.1021/jp045052f
40. Dischner, M. H.; Hemminger, J. C.; Feher, F. J. *Langmuir* **1997,** *13,* 4788–4790. doi:10.1021/la970397t
41. Adaligil, E.; Shon, Y.-S.; Slowinski, K. *Langmuir* **2010,** *26,* 1570–1573. doi:10.1021/la904180u
42. Chaudhari, V.; Kotresh, H. M. N.; Srinivasan, S.; Esaulov, V. A. *J. Phys. Chem. C* **2011,** *115,* 16518–16523. doi:10.1021/jp2042922
43. Prato, M.; Toccafondi, C.; Maidecchi, G.; Chaudhari, V.; Harish, M. N. K.; Sampath, S.; Parodi, R.; Esaulov, V. A.; Canepa, M. *J. Phys. Chem. C* **2012,** *116,* 2431–2437. doi:10.1021/jp207157m
44. Zaera, F.; Kollin, E. B.; Gland, J. L. *Surf. Sci.* **1987,** *184,* 75–89. doi:10.1016/S0039-6028(87)80273-X
45. Cheng, L. C.; Bocarsly, A. B.; Bernasek, S. L.; Ramanarayanan, T. A. *Surf. Sci.* **1997,** *374,* 357–372. doi:10.1016/S0039-6028(96)01200-9
46. Love, J. C.; Wolfe, D. B.; Haasch, R.; Chabinyc, M. L.; Paul, K. E.; Whitesides, G. M.; Nuzzo, R. G. *J. Am. Chem. Soc.* **2003,** *125,* 2597–2609. doi:10.1021/ja028692+
47. Love, J. C.; Wolfe, D. B.; Chabinyc, M. L.; Paul, K. E.; Whitesides, G. M. *J. Am. Chem. Soc.* **2002,** *124,* 1576. doi:10.1021/ja012569l
48. Jia, J.; Bendounan, A.; Chaouchi, K.; Kubsky, S.; Sirotti, F.; Pasquali, L.; Esaulov, V. A. *J. Phys. Chem. C* **2014,** *118,* 24983. doi:10.1021/jp507051q
49. Cookson, J. *Platinum Met. Rev.* **2012,** *56,* 83–98. doi:10.1595/147106712X632415
50. Yamauchi, M.; Ikeda, R.; Kitagawa, H.; Takata, M. *J. Phys. Chem. C* **2008,** *112,* 3294–3299. doi:10.1021/jp710447j
51. Mubeen, S.; Zhang, T.; Yoo, B.; Deshusses, M. A.; Myung, N. V. *J. Phys. Chem. C* **2007,** *111,* 6321–6327. doi:10.1021/jp067716m
52. Hamilton, H. *Platinum Met. Rev.* **2012,** *56,* 117–123. doi:10.1595/147106712X632460
53. Corthey, G.; Rubert, A. A.; Picone, A. L.; Casillas, G.; Giovanetti, L. J.; Ramallo-López, J. M.; Zelaya, E.; Benitez, G. A.; Requejo, F. G.; José-Yacamán, M.; Salvarezza, R. C.; Fonticelli, M. H. *J. Phys. Chem. C* **2012,** *116,* 9830–9837. doi:10.1021/jp301531n
54. Zelakiewicz, B. S.; Lica, G. C.; Deacon, M. L.; Tong, Y. *J. Am. Chem. Soc.* **2004,** *126,* 10053–10058. doi:10.1021/ja0491883
55. Ramallo-López, J. M.; Giovanetti, L.; Craievich, A. F.; Vicentin, F. C.; Marín-Almazo, M.; José-Yacaman, M.; Requejo, F. G. *Phys. B (Amsterdam, Neth.)* **2007,** *389,* 150–154. doi:10.1016/j.physb.2006.07.044
56. Nambu, A.; Kondoh, H.; Nakai, I.; Amemiya, K.; Ohta, T. *Surf. Sci.* **2003,** *530,* 101–110. doi:10.1016/S0039-6028(03)00383-2
57. Noh, J.; Ito, E.; Araki, T.; Hara, M. *Surf. Sci.* **2003,** *532–535,* 1116–1120. doi:10.1016/S0039-6028(03)00164-X
58. Ito, E.; Noh, J.; Hara, M. *Jpn. J. Appl. Phys.* **2003,** *42,* L852–L855. doi:10.1143/JJAP.42.L852
59. Terzi, F.; Pasquali, L.; Montecchi, M.; Nannarone, S.; Viinikanoja, A.; Aaritalo, T.; Salomaki, M.; Lukkari, J.; Doyle, B. P.; Seeber, R. *J. Phys. Chem. B* **2005,** *109,* 19397–19402. doi:10.1021/jp0530956
60. Liu, G.; Rodriguez, J. A.; Dvorak, J.; Hrbek, J.; Jirsak, T. *Surf. Sci.* **2002,** *505,* 295–307. doi:10.1016/S0039-6028(02)01377-8
61. Pasquali, L.; Terzi, F.; Doyle, B. P.; Seeber, R. *J. Phys. Chem. C* **2012,** *116,* 15010–15018. doi:10.1021/jp304758b
62. Terzi, F.; Pasquali, L.; Montecchi, M.; Nannarone, S.; Viinikanoja, A.; Aäritalo, T.; Salomaki, M.; Lukkari, J.; Doyle, B. P.; Seeber, R. *J. Phys. Chem. C* **2011,** *115,* 17836–17844. doi:10.1021/jp203219b
63. Capelli, R.; Dinelli, A.; Gazzano, M.; D'Alpaos, R.; Stefani, A.; Generali, G.; Riva, M.; Montecchi, M.; Giglia, A.; Pasquali, L. *Adv. Funct. Mater.* **2014,** *24,* 5603–5613. doi:10.1002/adfm.201400877
64. Lachkar, A.; Selmani, A.; Sacher, E.; Leclerc, M.; Mokhliss, R. *Synth. Met.* **1994,** *66,* 209–215. doi:10.1016/0379-6779(94)90069-8
65. Reeja-Jayan, B.; Manthiram, A. *Sol. Energy Mater. Sol. Cells* **2010,** *94,* 907–914. doi:10.1016/j.solmat.2010.01.021
66. Rufael, T. S.; Huntley, D. R.; Mullins, D. R.; Gland, J. L. *J. Phys. Chem.* **1995,** *99,* 11472–11480. doi:10.1021/j100029a027

67. Mullins, D. R.; Lyman, P. F. *J. Phys. Chem.* **1993,** *97,* 12008–12013. doi:10.1021/j100148a028
68. Mullins, D. R.; Lyman, P. F. *J. Phys. Chem.* **1993,** *97,* 9226–9232. doi:10.1021/j100138a026
69. Jia, J.; Bendounan, A.; Kotresh, H. M. N.; Chaouchi, K.; Sirotti, F.; Sampath, S.; Esaulov, V. A. *J. Phys. Chem. C* **2013,** *117,* 9835–9842. doi:10.1021/jp4007203
70. Andres, R. P.; Bein, T.; Dorogi, M.; Feng, S.; Henderson, J. I.; Kubiak, C. P.; Mahoney, W.; Osifchin, G. R.; Reifenberger, R. *Science* **1996,** *272,* 1323. doi:10.1126/science.272.5266.1323
71. Hamoudi, H.; Ariga, K.; Uosaki, K.; Esaulov, V. A. *RSC Adv.* **2014,** *4,* 39657–39666. doi:10.1039/C4RA05476H
72. Loo, Y.-L.; Lang, D. V.; Rogers, J. A.; Hsu, J. W. P. *Nano Lett.* **2003,** *3,* 7. doi:10.1021/nl034207c
73. Carlson, A.; Bowen, A. M.; Huang, Y.; Nuzzo, R. G.; Rogers, J. A. *Adv. Mater.* **2012,** *24,* 5284. doi:10.1002/adma.201201386
74. Hamoudi, H.; Esaulov, V. A. *Ann. Phys.* **2016**. doi:10.1002/andp.201500280
75. Pasquali, L.; Terzi, F.; Seeber, R.; Doyle, B. P.; Nannarone, S. *J. Chem. Phys.* **2008,** *128,* 134711. doi:10.1063/1.2876118
76. Beccaria, M.; Kanjilal, A.; Betti, M. G.; Mariani, C.; Floreano, L.; Cossaro, A.; Di Castro, V. *J. Electron Spectrosc. Relat. Phenom.* **2009,** *172,* 64–68. doi:10.1016/j.elspec.2009.03.004
77. Vollmer, S.; Witte, G.; Wöll, C. *Langmuir* **2001,** *17,* 7560–7565. doi:10.1021/la0107852
78. Denayer, J.; Delhalle, J.; Mekhalif, Z. *J. Electrochem. Soc.* **2011,** *158,* 100–108. doi:10.1149/1.3604529
79. Alarcón, L. S.; Cristina, L. J.; Shen, J.; Jia, J.; Esaulov, V. A.; Sánchez, E. A.; Grizzi, O. *J. Phys. Chem. C* **2013,** *117,* 17521–17530. doi:10.1021/jp403348s
80. Esaulov, V. A. Low Energy Ion Scattering and Recoiling Spectroscopy in Surface Science. In *Surface Science Techniques;* Braco, G.; Holst, B., Eds.; Springer Series in Surface Sciences, Vol. 51; Springer: Berlin, Germany, 2013; pp 423–460. doi:10.1007/978-3-642-34243-1_15
81. Ruan, L.; Stensgaard, I.; Besenbacher, F.; Lægsgaard, E. *Ultramicroscopy* **1992,** *42–44,* 498–504. doi:10.1016/0304-3991(92)90313-9
82. Jia, J.; Bendounan, A.; Chaouchi, K.; Esaulov, V. A. *J. Phys. Chem. C* **2014,** *118,* 24583–24590. doi:10.1021/jp5078517
83. Ma, Y.; Rudolf, P.; Chaban, E. E.; Chen, C. T.; Meigs, G.; Sette, P. *Phys. Rev. B* **1990,** *41,* R5424–5427. doi:10.1103/PhysRevB.41.5424
84. Colaianni, M. L.; Chorkendorff, I. *Phys. Rev. B* **1994,** *50,* 8798–8806. doi:10.1103/PhysRevB.50.8798
85. Foss, M.; Feidenshans'l, R.; Nielsen, M.; Findeisen, E.; Buslaps, T.; Johnson, R. L.; Besenbacher, F. *Surf. Sci.* **1997,** *388,* 5–14. doi:10.1016/S0039-6028(97)00071-X
86. Bradley, M. K.; Woodruff, D. P.; Robinson, J. *Surf. Sci.* **2013,** *613,* 21–27. doi:10.1016/j.susc.2013.02.018
87. Seema, P.; Behler, J.; Marx, D. *J. Phys. Chem. C* **2013,** *117,* 337–348. doi:10.1021/jp309728w
88. Carro, P.; Corthey, G.; Rubert, A. A.; Benitez, G. A.; Fonticelli, M. H.; Salvarezza, R. C. *Langmuir* **2010,** *26,* 14655–14662. doi:10.1021/la102505c
89. Liu, W.; Mitchell, K. A. R.; Berndt, W. *Surf. Sci.* **1997,** *393,* L119–L125. doi:10.1016/S0039-6028(97)00792-9
90. Speller, S.; Rauch, T.; Postnikov, A.; Heiland, W. *Phys. Rev. B* **2000,** *61,* 7297–7300. doi:10.1103/PhysRevB.61.7297
91. Grillo, M. E.; Stampfl, C.; Berndt, W. *Surf. Sci.* **1994,** *317,* 84–98. doi:10.1016/0039-6028(94)90255-0
92. Alfonso, D. R. *Surf. Sci.* **2005,** *596,* 229–241. doi:10.1016/j.susc.2005.09.021
93. Jing, Y.; Chen, Q.; Zheng, Y. *J. Phys. D: Appl. Phys.* **2008,** *41,* 205011. doi:10.1088/0022-3727/41/20/205011
94. Deo, N.; Bain, M. F.; Montgomery, J. H.; Gamble, H. S. *J. Mater. Sci.: Mater. Electron.* **2005,** *16,* 387–392. doi:10.1007/s10854-005-2302-8
95. Zhang, H. T.; Wua, G.; Chen, X. H.; Qiu, X. G. *Mater. Res. Bull.* **2006,** *41,* 495–501. doi:10.1016/j.materresbull.2005.09.019
96. Saxena, A.; Kumar, A.; Mozumdar, S. *J. Mol. Catal. A: Chem.* **2007,** *269,* 35–40. doi:10.1016/j.molcata.2006.12.042
97. Lee, I. S.; Lee, N.; Park, J.; Kim, B. H.; Yi, Y.-W.; Kim, T.; Kim, T. K.; Lee, I. H.; Paik, S. R.; Hyeon, T. *J. Am. Chem. Soc.* **2006,** *128,* 10658–10659. doi:10.1021/ja063177n
98. Bengió, S.; Fonticelli, M.; Benítez, G.; Creus, A. H.; Carro, P.; Ascolani, H.; Zampieri, G.; Blum, B.; Salvarezza, R. C. *J. Phys. Chem. B* **2005,** *109,* 23450–23460. doi:10.1021/jp052915b
99. Garnier, F.; Hajlaoui, R.; El Kassmi, A.; Horowitz, G.; Laigre, L.; Porzio, W.; Armanini, M.; Provasoli, F. *Chem. Mater.* **1998,** *10,* 3334–3339. doi:10.1021/cm970704g
100. Leydecker, T.; Trong Duong, T.; Salleo, A.; Orgiu, E.; Samori, P. *ACS Appl. Mater. Interfaces* **2014,** *6,* 21248–21255. doi:10.1021/am506245v
101. Mauldi, C. E.; Puntambekar, K.; Murphy, A. R.; Liao, F.; Subramanian, V.; Fréchet, J. M. J.; DeLongchamp, D. M.; Fischer, D. A.; Toney, M. F. *Chem. Mater.* **2009,** *21,* 1927–1938. doi:10.1021/cm900267v
102. Roberts, J. T.; Friend, C. M. *Surf. Sci.* **1987,** *186,* 201–218. doi:10.1016/S0039-6028(87)80043-2
103. Elfeninat, F.; Fredriksson, C.; Sacher, E.; Selmani, A. *J. Chem. Phys.* **1995,** *102,* 6153. doi:10.1063/1.469349
104. Netzer, F. P.; Bertel, E.; Goldmann, A. *Surf. Sci.* **1988,** *201,* 257–268. doi:10.1016/0039-6028(88)90610-3
105. Haruta, M.; Yamada, N.; Kobayashi, T.; Iijima, S. *J. Catal.* **1989,** *115,* 301–309. doi:10.1016/0021-9517(89)90034-1
106. Valden, M.; Lai, X.; Goodman, D. W. *Science* **1998,** *281,* 1647–1650. doi:10.1126/science.281.5383.1647
107. Canário, A. R.; Esaulov, V. A. *J. Chem. Phys.* **2006,** *124,* 224710. doi:10.1063/1.2205849
108. Shen, J.; Jia, J.; Bobrov, K.; Guillemot, L.; Esaulov, V. A. *J. Phys. Chem. C* **2015,** *119,* 15168–15176. doi:10.1021/acs.jpcc.5b02525
109. Caprile, L.; Cossaro, A.; Falletta, E.; Pina, C. D.; Cavalleri, O.; Rolandi, R.; Terreni, S.; Ferrando, R.; Rossi, M.; Floreano, L.; Canepa, M. *Nanoscale* **2012,** *4,* 7727–7734. doi:10.1039/c2nr32741d
110. Yim, W.-L.; Nowitzki, T.; Necke, M.; Schnars, H.; Nickut, P.; Biener, J.; Biener, M. M.; Zielasek, V.; Al-Shamery, K.; Klüner, T.; Bäumer, M. *J. Phys. Chem. C* **2007,** *111,* 445–451. doi:10.1021/jp0665729
111. Alghamdi, A. A. B.; Watters, D. C.; Yi, H. N.; Al-Faifi, S.; Almeataq, M. S.; Coles, D.; Kingsley, J.; Lidzey, D. G.; Iraqi, A. *J. Mater. Chem. A* **2013,** *1,* 5165–5171. doi:10.1039/c3ta00122a
112. Kondoh, H.; Nakai, I.; Nambu, A.; Ohta, T.; Nakamura, T.; Kimura, R.; Matsumoto, M. *Chem. Phys. Lett.* **2001,** *350,* 466–472. doi:10.1016/S0009-2614(01)01335-5

BEILSTEIN JOURNAL OF NANOTECHNOLOGY

Comparison of the interactions of daunorubicin in a free form and attached to single-walled carbon nanotubes with model lipid membranes

Dorota Matyszewska

Full Research Paper

Open Access

Address:
Faculty of Chemistry, Biological and Chemical Research Centre, University of Warsaw, Żwirki i Wigury 101, 02089 Warsaw, Poland

Email:
Dorota Matyszewska - dorota.matyszewska@chem.uw.edu.pl

Keywords:
daunorubicin (DNR); 1,2-dipalmitoyl-*sn*-glycero-3-phosphothioethanol (DPPTE); drug carriers; model lipid membranes; single-walled carbon nanotubes (SWCNTs)

Beilstein J. Nanotechnol. **2016,** *7,* 524–532.
doi:10.3762/bjnano.7.46

Received: 24 August 2015
Accepted: 29 March 2016
Published: 08 April 2016

This article is part of the Thematic Series "Organized films".

Guest Editor: M. Canepa

Abstract

In this work the interactions of an anticancer drug daunorubicin (DNR) with model thiolipid layers composed of 1,2-dipalmitoyl-*sn*-glycero-3-phosphothioethanol (DPPTE) were investigated using Langmuir technique. The results obtained for a free drug were compared with the results recorded for DNR attached to SWCNTs as potential drug carrier. Langmuir studies of mixed DPPTE–SWCNTs-DNR monolayers showed that even at the highest investigated content of the nanotubes in the monolayer, the changes in the properties of DPPTE model membranes were not as significant as in case of the incorporation of a free drug, which resulted in a significant increase in the area per molecule and fluidization of the thiolipid layer. The presence of SWCNTs-DNR in the DPPTE monolayer at the air–water interface did not change the organization of the lipid molecules to such extent as the free drug, which may be explained by different types of interactions playing crucial role in these two types of systems. In the case of the interactions of free DNR the electrostatic attraction between positively charged drug and negatively charged DPPTE monolayer play the most important role, while in the case of SWCNTs-DNR adducts the hydrophobic interactions between nanotubes and acyl chains of the lipid seem to be prevailing. Electrochemical studies performed for supported model membranes containing the drug delivered in the two investigated forms revealed that the surface concentration of the drug-nanotube adduct in supported monolayers is comparable to the reported surface concentration of the free DNR incorporated into DPPTE monolayers on gold electrodes. Therefore, it may be concluded that the application of carbon nanotubes as potential DNR carrier allows for the incorporation of comparable amount of the drug into model membranes with simultaneous decrease in the negative changes in the membrane structure and organization, which is an important aspect in terms of side effects of the drug.

Introduction

Daunorubicin (DNR) is an anthracycline antitumor drug, which finds application in the treatment of various types of cancer including leukemia, breast cancer, ovarian cancer, lung carcinoma and several sarcomas (Figure 1). Its mode of action consists in the intercalation into DNA double strand, which leads to the inhibition of the process of duplication and transcription of mRNA as well as DNA damage by the inhibition of topoisomerase II [1,2]. However, the second mechanism involving the increased production of ceramides inside cells has been recently postulated [3]. Application of this drug in the cancer treatment is limited because of serious side effects including drug-induced heart failure, which is mainly associated with the process of the reactive oxygen species formation as well as the formation of hydroxyl radicals by free iron cations in the Fenton reaction [4]. Therefore, numerous studies focus on the application of different drug delivery systems (DDS) to transport daunorubicin to cancer cells [5].

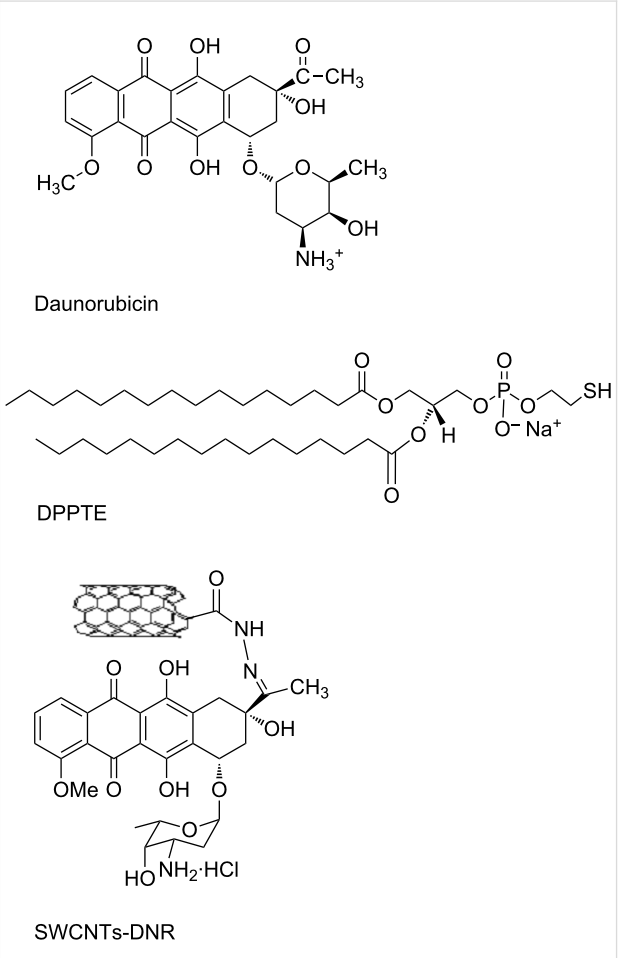

Figure 1: Structures of daunorubicin (DNR) and 1,2-dipalmitoyl-*sn*-glycero-3-phosphothioethanol (DPPTE) used as a component of model membranes and single-walled carbon nanotubes modified with daunorubicin (SWCNTs-DNR).

Drug delivery systems are aimed at providing enhanced transport of therapeutic agents directly to the targeted organs and tissues, which enables the elimination or significant decrease in the side effects of a drug. One of the most common type of drug nanocarriers includes liposomes, which are commercially available daunorubicin formulation (Daunoxome®) used in the treatment of Kaposi's sarcoma [6]. Despite that, there are still numerous studies on the improvement of this drug delivery system aiming at enhancing drug loading into cells by using specific interactions between targeting agents and their receptors, such as for example folates and transferrin [7,8]. Additionally, liposomes are also prepared in such a way that simultaneous loading of two drugs into a liposome in order to improve the efficiency of the treatment is possible [9]. Dual drug loading is also employed in case of other DDS such as biodegradable polymers, which co-assemble into composite micelles [10]. Another type of common drug carriers includes nanoparticles. Magnetic Fe_3O_4 nanoparticles are often employed because they give possibility to control the transport by applying external magnetic fields. Such magnetic nanoparticles conjugated with DNR were reported to induce apoptosis of cancer cell lines [11,12]. Other examples of nanoparticles include titanium dioxide (TiO_2) and gold nanoparticles (AuNPs) [13,14]. In the latter case the nanoparticles were also modified with aptamer – single-stranded DNA or RNA sequences showing high specificity and affinity to their targets, which were employed as molecular targeting agents for targeted drug transport.

Carbon nanotubes (CNTs) are among the promising drug delivery systems. They attract scientists' attention due to their properties such as stability, robustness, high drug carrying capacity and ability to penetrate cell membranes [15]. Although toxicity of the nanotubes is an issue, it strongly depends on the dimensions and type of functionalization, which may significantly increase their biocompatibility [16,17]. There are different mechanisms proposed to explain the cellular uptake of CNTs including the passive diffusion in a non-invasive manner (tiny nanoneedle mechanism) [18]. Carbon nanotubes have been successfully used to transport different types of anticancer agents including camptothecin, doxorubicin and daunorubicin [19]. The two main methods of attaching the drugs comprise either covalent attachment or physical adsorption based on π–π stacking interactions. There are a few reports in the literature on the preparation and characterization of CNTs-DNR adducts used as drug delivery systems. In those works daunorubicin was conjugated to either polyethylene glycol (PEG) functionalized single-walled carbon nanotubes (SWCNTs) [20] or to aptamer-wrapped SWCNTs via π–π interactions. In both cases the cytotoxicity of the conjugates was verified on the selected cancer cell lines.

In this study the influence of both free daunorubicin and daunorubicin attached via covalent bond to single-walled carbon nanotubes (SWCNTs, Figure 1) on model biological membranes was investigated using Langmuir technique. The model membranes were composed of 1,2-dipalmitoyl-*sn*-glycero-3-phosphothioethanol (DPPTE, Figure 1). This thiolipid has been used so far either as a tethering layer in tBLM systems employed, e.g., for studying ion-channel proteins on electrode surfaces or as a model membrane in the studies of a lipolytic enzyme, phospholipase A2, which was employed as a tool for modifying the structure of supported thiolipid layers in a controlled way [21,22]. Due to the presence of a thiol group in the polar headgroup region, this lipid has negative charge and it is possible to transfer monolayers onto solid support by means of both Langmuir–Blodgett method and self-assembly, which results in the differences in the packing of the thiolipid molecules in the supported layers depending on the mode of transfer [23]. Our previous results of Langmuir studies show that daunorubicin in a free form may easily incorporate into the DPPTE layers during their formation and significantly change the properties of the layers [24]. The effect of daunorubicin attached to carbon nanotubes as potential drug carrier on the properties of model membranes is compared to that reported for a free drug. In order to obtain more detailed information on the interactions between DNR in the two investigated forms the electrochemical techniques were also employed to study the supported lipid layers containing both free DNR and SWCNTs-DNR adducts.

Experimental

Langmuir monolayers at the air–water interface

Langmuir monolayers were prepared using a KSV LB trough 5000 (KSV Ltd., Finland) equipped with hydrophilic barriers and a Wilhelmy balance made of a filter paper used as a surface pressure sensor. The experiment was controlled with software version KSV 5000. 1,2-dipalmitoyl-*sn*-glycero-3-phosphothioethanol (sodium salt, DPPTE, Avanti Polar Lipids) was dissolved in chloroform to give 1 mg/mL stock solution. Carbon nanotubes used for the modification were commercial, oxidized nanotubes SWCNT(s)-COOH (CheapTubes, Brattleboro, USA) with the diameter of 1–2 nm and length of 5–30 μm. The modification at the ends of the nanotubes as well as in the defect sites was obtained by the formation of SWCNTs-end hydrazide, which was then mixed with daunorubicin to form hydrazone. The detailed procedure of the covalent end modification of single-walled carbon nanotubes with daunorubicin by the formation of hydrazone was inspired by the protocol previously described for side and end carboxylated SWCNTs modification [25]. Basing on the TGA analysis such modification procedure yields the functionalization degree in the order of approximately 1.25×10^{-7} mol of drug per 1 mg of carbon nanotubes (approximately 1.5×10^{-3} mol of drug per 1 mol of carbon). Mixed DPPTE–SWCNTs-DNR dispersion was prepared by weighing approximately 0.5 mg of modified nanotubes and adding the appropriate volume of DPPTE stock solution in order to obtain the desired weight ratio of carbon nanotubes to thiolipid. Prior to the deposition at the air–water interface, the mixed solutions were sonicated in the ultrasonic bath (Emag, Germany) for approximately 30 min to ensure carbon nanotubes dispersion. Langmuir monolayers were prepared on either Milli-Q ultra-pure water (resistivity 18.2 MΩ/cm) subphase (mixed DPPTE–SWCNTs-DNR monolayers) or subphase containing daunorubicin (AK Scientific, USA). After careful cleaning of the subphase, a few drops of the solution (DPPTE or mixed DPPTE–SWCNTs) were spread on the subphase using a Hamilton microsyringe and the solution was left for approximately 15 min for solvent evaporation. Barrier speed during compression was 10 mm/min (7.5 cm^2/min). Experiments were performed at room temperature (21 ± 1 °C).

Langmuir–Blodgett transfer

Supported DPPTE or mixed DPPTE–SWCNTs-DNR monolayers were prepared by means of Langmuir–Blodgett method. Prior to the transfer, gold electrodes (10 × 10 mm slides, Ssens, The Netherlands), which were 200 nm thick gold films evaporated onto borosilicate glass precoated with an underlayer of chromium, were flame annealed, cleaned in the mixture of $H_2O_2/NH_3/H_2O$ with 1:1:5 ratio at 70 °C for approximately 5 min and thoroughly rinsed with Milli-Q water. The DPPTE and mixed DPPTE–SWCNTs-DNR layers were deposited on the gold surface by vertical withdrawal of the electrode at the speed of 25 mm/min to give a transfer ratio of 1.0 ± 0.1. The target surface pressure, at which the layers were transferred was equal to 30 mN/m and 35 mN/m for DPPTE and mixed DPPTE–SWCNTs-DNR monolayers, respectively. After the LB deposition and before the electrochemical measurements, the electrodes were dried in air for approximately 2 h.

Electrochemical experiments

Electrochemical experiments were performed using AutoLab AUT 71819 with the GPES 4.9 software in the three electrode system with Ag/AgCl as a reference electrode and platinum foil (10 × 10 mm plate) as a counter electrode. Phosphate buffer (50 mM, pH 6.9) prepared from sodium phosphates (Avantor, Poland) was used as a supporting electrolyte.

Results and Discussion

Monolayer studies at the air–water interface

In order to study the influence of daunorubicin in a free form and attached to carbon nanotubes as potential drug carrier, Langmuir technique has been employed. Drug in a free form

was dissolved in the subphase, on which monolayers of DPPTE were formed. In case of DNR attached to carbon nanotubes, it was impossible to dissolve the carbon nanotube adducts in the subphase due to their insufficient solubility in water. Therefore, the mixed layers composed of DPPTE and SWCNTs-DNR adduct were prepared with either prevailing weight ratio of nanotubes or prevailing weight ratio of thiolipid. The isotherms are shown in Figure 2.

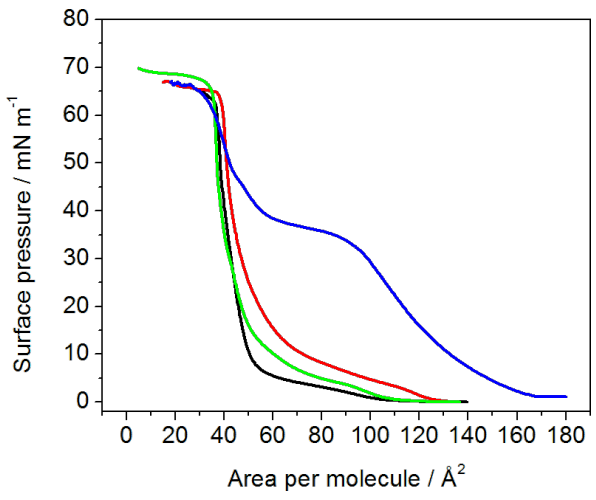

Figure 2: Surface pressure-area per molecule (π–A) isotherms of DPPTE monolayer on water subphase (black), mixed layers of DPPTE:SWCNTs-DNR weight ratio of 1:5 (red), mixed layers of DPPTE/SWCNTs-DNR weight ratio of 10:1 (green), DPPTE monolayer on subphase containing 10^{-5} DNR (blue).

Despite the fact that the experimental procedure differed in case of the two investigated forms of the drug (free drug was dissolved in the subphase, while drug-carbon nanotube adduct was mixed with thiolipid and administered as a mixture at the air–water interface), which makes the direct comparison more difficult, some interesting and new insight into such interactions may be still provided. It can be clearly observed that in the presence of daunorubicin in a free form in the subphase the shape of the isotherm changes significantly and the isotherm is shifted towards larger areas per molecule (Figure 2). As observed in our previous studies concerning the influence of DNR on thiolipid model membranes [24], characteristic parameters describing the properties of the monolayer are also significantly changed (Table 1). The area per molecule in a well-organized monolayer increases from the value of 44 Å^2 corresponding to the DPPTE monolayer formed on pure water subphase to the value of 74 Å^2 in the presence of the drug in the subphase. Such a significant increase is caused by the incorporation of DNR molecules into the thiolipid layer. Additionally, the shape of the isotherms is altered and the broad plateau region corresponding to the phase transition is clearly visible at relatively high surface pressure of 38 mN/m (Figure 2). Significant changes concern the compression modulus and its maximum value. The compression modulus is defined as [26]:

$$Cs^{-1} = -A\frac{d\pi}{dA} \quad (1)$$

where A is area per molecule, and π is surface pressure. Compression modulus gives information on the state, in which the monolayer is at a given surface pressure. The maximum value of compression modulus obtained for DPPTE monolayers formed on pure water subphase is equal to 395 mN/m, which corresponds to the solid state of the monolayer [27]. In the presence of DNR in the subphase the maximum value decreases to 80 mN/m (Table 1), which indicates liquid expanded phase of the monolayer (Figure 3).

Different situation occurs when daunorubicin attached to carbon nanotubes is introduced into DPPTE monolayers. In case of mixed DPPTE–SWCNTs-DNR layer the isotherms are only slightly altered. When the amount of drug carrier is relatively small compared to the prevailing amount of the lipid (DPPTE/SWCNTs-DNR weight ratio of 10:1), the isotherm shape is not significantly changed (Figure 2). The area per molecule increases by several angstroms from the value of 44 Å^2 corresponding to the DPPTE monolayer formed on pure water subphase to the value of 49 Å^2, but other characteristic parameters such as collapse area and collapse pressure do not change greatly (Table 1). Interestingly, the presence of small amount of SWCNTs leads to the increase in the maximum value of compression modulus compared to DPPTE monolayers formed

Table 1: Characteristic parameters of DPPTE Langmuir monolayers in the presence of free daunorubicin and daunorubicin attached to carbon nanotubes.

Substance	A_0/Å^2	A_{coll}/Å^2	π_{coll}/mN m^{-1}	Cs^{-1}/mN m^{-1}
DPPTE	44.5 ± 0.3	36.6 ± 0.2	65.2 ± 1.7	395 ± 25
DPPTE + 10^{-5} DNR	73.8 ± 2.6	33.5 ± 2.6	64.4 ± 2.0	80 ± 5
DPPTE/SWCNTs-DNR 1:5	50.4 ± 0.4	39.2 ± 0.3	64.7 ± 0.8	325 ± 15
DPPTE/SWCNTs-DNR 10:1	48.6 ± 0.7	39.0 ± 0.1	63.8 ± 0.3	450 ± 10

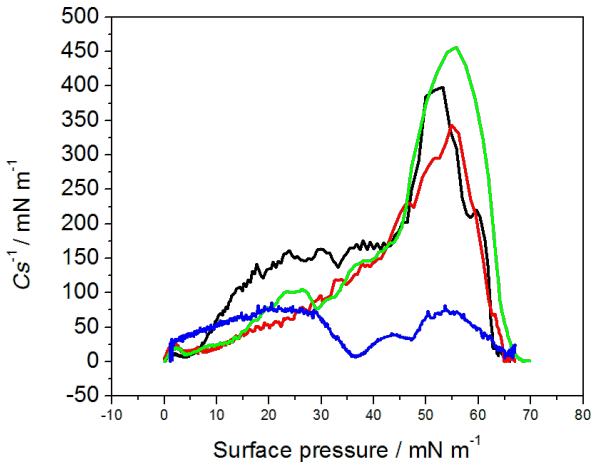

Figure 3: Compression modulus versus surface pressure plot for DPPTE monolayer on water subphase (black), mixed layers of DPPTE/SWCNTs-DNR weight ratio of 1:5 (red), mixed layers of DPPTE/SWCNTs-DNR weight ratio of 10:1 (green), DPPTE monolayer on subphase containing 10^{-5} DNR (blue).

on water subphase (Figure 3). However, the presence of bigger amounts of carbon nanotubes in the mixed layers (DPPTE/SWCNTs-DNR weight ratio of 1:5) affect the DPPTE monolayer more significantly. Although the increasing amount of carbon nanotubes in the mixed layer does not lead to a significant increase in the area per molecule compared to the value obtained for mixed DPPTE–SWCNTs-DNR monolayers with the prevailing amount of the lipid (Table 1), more pronounced changes are observed in case of the compression modulus. Its value decreases to 325 mN/m, which is 70 mN/m less than the value reported for pure DPPTE monolayer, but it is still in the range corresponding to the solid phase. It should be also noted that for the same weight ratio of the components there is no significant difference between the effect of the unmodified CNTs and CNTs–drug adducts in the mixed layer. Since the molar percentage of the DNR in the adduct is equal only to 0.15% (see Experimental section), the absence or presence of the drug on the nanotubes will not result in the detectable changes in the isotherms, as has been shown in control experiments. The isotherms obtained for mixed layers containing DPPTE and carbon nanotubes with and without drug are almost identical. The exemplary DPPTE isotherms recorded in the presence of nanotubes without and following modification with the drug are shown in Supporting Information File 1, Figure S1.

The observed changes in the DPPTE monolayer behavior in the presence of both free drug and drug attached to carbon nanotubes should be explained in terms of the different driving forces responsible for the interactions. In case of free daunorubicin interactions, such significant changes in the isotherm shape and dramatic decrease in the maximum value of compression modulus implies that upon the incorporation into DPPTE monolayer, DNR disorganizes the thiolipid monolayer and causes its fluidization. Changes in the properties of DPPTE membrane were attributed to the electrostatic interactions [24]. Since the thiolipid molecules are negatively charged and pKa of daunorubicin is equal to 8.4 [28], at the pH corresponding to pure water there is electrostatic attraction between the negatively charged polar heads of the lipid and positively charged drug. Obviously, hydrophobic interactions between the hydrophobic part of the drug and acyl chains of the lipids should be also taken into account, but electrostatic interactions seem to be playing the most important role, especially in case of the interactions at lower surface pressures, when the drug dissolved in the subphase first interacts with polar heads of the lipid. However, with the increasing surface pressure DNR molecules may penetrate deeper into the monolayer and then hydrophobic interactions also play important role. Consequently, those types of interactions result both in the observed changes in the Cs^{-1} values, as well as in the significant increase in the area per molecule in the organized layer (Table 1) as reported before [24].

In case of the effect of SWCNTs modified with DNR different explanation may be given. The unexpected increase in the maximum value of compression modulus for the mixed layers with the prevailing amount of thiolipid may be caused by the fact that due to the presence of relatively small amounts of carbon nanotubes in the monolayer the thiolipid molecules become more oriented with less tilted hydrocarbon chains, which leads to the observed increase in the maximum value of compression modulus. In the same time, the nanotubes occupy the interfacial area and therefore a small increase in the area per molecule is observed (Table 1). The increasing amount of the nanotubes in the mixed layer results in some fluidization of the DPPTE monolayer because the increasing number of nanotubes prevents from the hydrophobic interactions between acyl chains of the lipid and thus leads to the disorganization of the layer. However, this influence is not as significant as the influence of DNR in the free form and therefore it does not introduce the change of the phase of the monolayer. Additionally, the relatively small increase in the area per molecule with the increasing content of the nanotubes in the thiolipid monolayer (from 48.6 to 50.4 Å^2 for the prevailing weight ratio of the lipid and the nanotubes, respectively, Table 1) indicates that the nanotubes may form aggregates or bundles and do not distribute evenly within the thiolipid monolayer. They may be also squeezed out from the monolayer into the subphase or into the close vicinity of the monolayer. Alternatively, closing the barriers and increasing the surface pressure may lead to the above mentioned formation of aggregates or bundles. Moreover, in the presence of SWCNTs-DNR conjugates the isotherms are only slightly shifted towards larger areas per mole-

cule but their shape is not altered. Similar observation was made by Cancino et al., who studied the effect of carbon nanotubes-dendrimers nanoconjugates on DPPC monolayers [29]. The presence of such types of adducts did not significantly affect the properties of lipid monolayers.

In conclusion, the effect of the free drug and drug attached to the potential carrier on the properties of model thiolipid monolayer is different. Daunorubicin in the free form significantly changes the properties of DPPTE monolayers by increasing the area per molecule in the monolayer and causing their immense fluidization. The electrostatic interactions between positively charged drug and negatively charged polar headgroups of the lipid are most relevant in this case. The influence of carbon nanotubes modified with DNR on the properties of DPPTE monolayers is less pronounced. The observed areas per molecule are only slightly increased compared to pure DPPTE monolayer, which implies that although CNTs occupy the interfacial area, the change in the organization of the lipid molecules is not as big as in case of a free drug. It may be explained by a different mechanism responsible for the interactions in this case. Although the amine group of DNR attached to the ends of carbon nanotubes is protonated as in a free drug, which still gives the possibility of the electrostatic interactions, the hydrophobic interactions with nanotubes seem to play the crucial role. First of all, the drug modification of the nanotubes provides relatively small mole fraction of the drug with respect to the nanotube, as stated in the Experimental section. Secondly, the modification at the end (and defect sites) of the nanotubes leaves the sides of the nanotubes unmodified. Therefore, due to the strong hydrophobicity of the nanotubes one may suppose that although electrostatic interactions between the attached drug and polar heads of the lipid are still possible, the hydrophobic interactions between carbon nanotubes and acyl chains of the lipids will be determining the overall interactions in this case.

Electrochemical studies

Since daunorubicin is electroactive and undergoes $2e^-/2H^+$ redox process (Scheme 1), the interactions of the drug in a free form and attached to carbon nanotubes with model membranes may be also followed using electrochemistry. After the LB transfer described in detail in Experimental section, supported layers were characterized by electrochemical techniques. First, in order to verify the presence of daunorubicin attached to carbon nanotubes in the mixed layer on the electrode, cyclic voltammetry was performed. The reduction–oxidation peaks observed in voltammograms correspond to the electrode process of the quinone-hydroquinone group (Figure 4) [30]. Basing on the results obtained for the supported mixed DPPTE–SWCNTs-DNR monolayers with the prevailing amount of nanotubes it has been shown that the drug is present at the electrode surface. Additionally, the linear dependence of the peak current versus the scan rate proves the adsorptive character of the observed electrode process and thus confirms that the electroactive drug is covalently attached to the carbon nanotubes supported at the electrode surface.

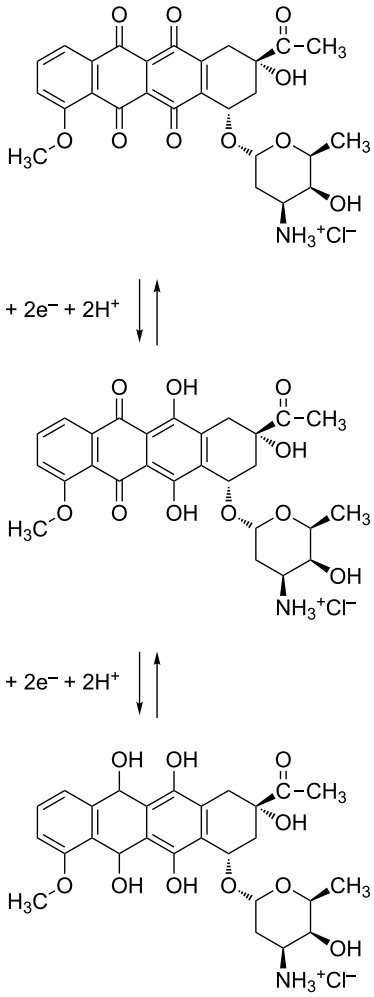

Scheme 1: The electrode processes of daunorubicin.

In order to assess the interactions of the free daunorubicin with model membranes, DPPTE monolayers were transferred by means of LB method onto gold electrodes and were exposed to 10^{-5} M DNR solutions for 600 s to ensure the incorporation of the drug into the model membrane. The optimal incubation time of the model membrane in the drug solution was based on our previous studies, which showed that after this time cyclic voltammograms become stable [24]. Alternatively, it is also possible to incorporate the drug into the model membrane during its formation and then transfer it onto the electrode [31]. It should be also stressed that the concentration used for the

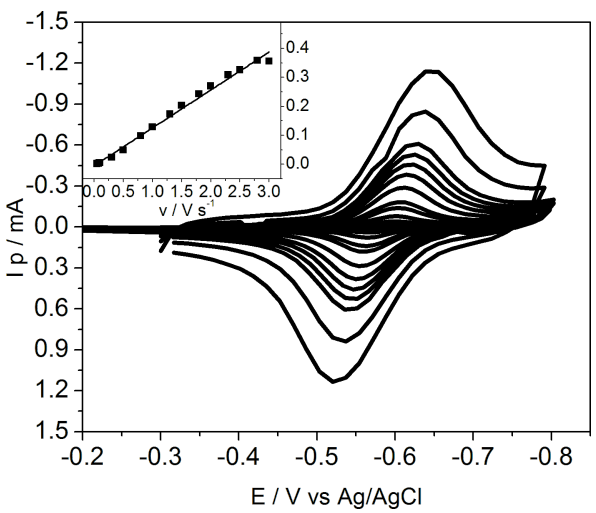

Figure 4: Cyclic voltammograms recorded at the increasing scan rate for mixed DPPTE/SWCNTs-DNR (1:5 w/w) layers transferred onto gold electrodes by means of LB method for end modification of nanotubes. Inset: dependence of peak current vs scan rate.

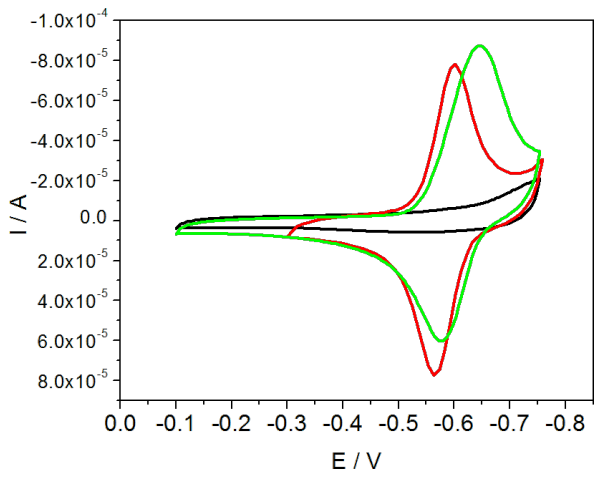

Figure 5: Cyclic voltammograms recorded for gold electrode modified with DPPTE monolayer (black), mixed DPPTE/SWCNTs-DNR (1:5 w/w) layer (red) and DPPTE monolayer exposed to 10^{-5} M DNR solution for 600 s (green). Scan rate: 500 mV/s.

incubation of the modified electrodes is consistent with the DNR concentration used in monolayer studies. Additionally, it corresponds to the concentrations used in the in vitro studies. The IC_{50} value, which is defined as the concentration of a drug that inhibits cell growth by 50%, given in the literature usually varies from 10^{-6} M to 10^{-5} M depending on the type of cell lines [32-34].

In the next step, voltammograms obtained after the incubation in DNR solution were compared with the voltammograms recorded for electrodes modified with DPPTE monolayer (before exposure to DNR) and electrodes modified with mixed DPPTE–SWCNTs-DNR monolayers (Figure 5). In case of both DPPTE monolayers exposed to DNR solution and mixed DPPTE–SWCNTs-DNR monolayers the oxidation–reduction peaks corresponding to the electrode process of daunorubicin are observed and the peak currents are similar. The control experiments on the effect of unmodified SWCNTs in the supported layers are not shown because in the absence of electroactive species such as daunorubicin attached to carbon nanotubes on the electrode surface, no reduction–oxidation peaks can be observed, since neither unmodified carbon nanotubes, nor thiolipid undergo reduction–oxidation processes in the potential range investigated. Therefore, in such case only the blocking of the electrode by the mixed DPPTE–SWCNTs-bare could be seen, similarly to the blocking of the electrode by the monocomponent DPPTE monolayer (Figure 5).

In order to compare the results for the two types of modified electrodes in a more detailed way, surface concentration of the drug may be calculated. The surface concentration of daunorubicin can be estimated using the following equation:

$$\Gamma = Q / nFA \quad (2)$$

where Γ is surface concentration (mol/cm^2), Q is charge under cathodic peak (C), n is number of electrons, F is Faraday constant and A is electrode area (cm^2). The surface concentration calculated based on the cyclic voltammogram for the electrode modified with mixed DPPTE–SWCNTs-DNR monolayer is equal to 0.67×10^{-10} mol/cm^2, while the value obtained for DPPTE supported monolayer exposed to DNR solution is equal to 0.60×10^{-10} mol/cm^2 as reported before [24]. Moreover, the values obtained for the mixed layer containing modified carbon nanotubes are comparable to the values reported for carbon nanotubes derivatized with antraquinone [35] and other types of electroactive species [36,37].

It is interesting to compare the surface concentrations of the drug incorporated into the supported model membranes in the two forms: free and attached to drug carriers. However, due to different solubilities, the experimental procedures are different: free drug is more soluble and, therefore, can be dissolved in the subphase from which it penetrates the lipid monolayer, while drug–carbon nanotube adduct is added to the thiolipid and chloroform and next the mixed sample is placed at the air–water interface. Therefore, the initial concentrations of the drugs cannot be easily compared. Our solution was to transfer the layer onto a solid substrate (electrode) and evaluate the amount of the drug present in the model membrane supported on the electrode by electrochemistry. In case of daunorubicin in the free form the estimation was based on the DNR concentration in

the subphase (10^{-5} M) and surface concentration of the drug incorporating into the model membrane precompressed to 30 mN/m [24], while in case of DNR attached to carbon nanotubes the content of DNR (1.25×10^{-7} mol of drug per 1 mg of carbon nanotubes) in the total amount of the DPPTE–SWCNTs-DNR adduct (with respect to the DPPTE/SWCNTs-DNR ratio) administered at the air–water interface as a mixed layer and transferred onto the electrode was taken into account. The estimated amount of daunorubicin in the supported model membrane is equal to 2.4×10^{-13} and 2.1×10^{-13} mol for the free drug and drug attached to carbon nanotubes, respectively. It should be noted that the surface concentration of DNR calculated based on electrochemical experiments is also the same for both mixed DPPTE–SWCNTs-DNR monolayer and incorporated drug in the free form. This proves that the amount of the drug in the model membrane is similar for both types of the drug delivery: direct or bound to the nanocarrier. However, basing on the results of monolayer studies, the effect of SWCNTs-DNR adducts on the properties of model DPPTE membranes is much smaller than the one observed for a free drug (Figure 2 and Figure 3). It is especially important in the view of the application of carbon nanotubes as drug carriers. These results prove that CNTs modified with DNR may provide the same amount of the therapeutic agent as the drug in the free form but in the same time they do not influence the organization and properties of the membranes to such extent as the free drug.

Conclusion

Interactions of anticancer drug daunorubicin with model thiolipid membranes were investigated using Langmuir technique and electrochemical methods. The drug was either in the free form dissolved in the subphase, on which the DPPTE monolayer was formed, or attached to single-walled carbon nanotubes, which are potential drug carriers. In this case, drug–carrier adducts were deposited onto the air–water interface forming the mixed layers of DPPTE with differing weight ratio of the components. Langmuir studies revealed that DNR influences the properties of the thiolipid monolayer leading to a significant increase in the area per molecule. Additionally, the organization of the monolayer changes: the maximum value of the compression modulus implies that upon incorporation of the drug in the free form, the layer changes its phase from solid to liquid. The observed differences in the properties of the monolayer are caused by the electrostatic interactions between the positively charged drugs and negatively charged polar heads of the lipid. Results of the studies with SWCNTs-DNR conjugates revealed that their influence on DPPTE monolayers is much less pronounced. The characteristic parameters such as area per molecule do not change as significantly as in case of a free drug. Moreover, the organization of the monolayer is not influenced to such a large extent and even at the higher weigh content of CNTs in the mixed layer, the monolayer retains its solid character. In this case hydrophobic interactions between the nanotubes and DPPTE molecules seem to play the most important role.

Electrochemistry was also employed to compare the model membranes containing daunorubicin in the two investigated forms. Cyclic voltammetry performed for the electrodes modified with DPPTE monolayers containing daunorubicin either in the free form or attached to carbon nanotubes proved the presence of the electroactive drug at the electrode surface. Moreover, it was shown that the surface concentration of the drug on the electrode surface is similar for both the drug in a free form and the drug–nanocarrier adduct. This observation proves that application of single-walled carbon nanotubes as drug delivery system allows for the transport of the comparable amount of the drug with respect to the drug in a free form but the influence of the drug–carrier adduct on the model membranes is much smaller. This conclusion is important from the point of view of side effects of the drug treatment and confirms the efficiency of the application of carbon nanotubes as drug delivery systems.

Supporting Information

Supporting Information File 1

DPPTE isotherms.
[http://www.beilstein-journals.org/bjnano/content/supplementary/2190-4286-7-46-S1.pdf]

Acknowledgements

Prof. Jan Biernat is acknowledged for providing CNTs-DNR conjugates. This work was supported by the Foundation for Polish Science with the POMOST/2011-3/6 project co-financed by the European Union, Regional Development Fund.

References

1. Yang, X.-L.; Wang, A. H.-J. *Pharmacol. Ther.* **1999,** *83,* 181–215. doi:10.1016/S0163-7258(99)00020-0
2. Gewirtz, D. A. *Biochem. Pharmacol.* **1999,** *57,* 727–741. doi:10.1016/S0006-2952(98)00307-4
3. Patel, A. G.; Kaufmann, S. H. *eLife* **2012,** *1,* e00387. doi:10.7554/eLife.00387
4. Minotti, G.; Menna, P.; Salvatorelli, E.; Cairo, G.; Gianni, L. *Pharmacol. Rev.* **2004,** *56,* 185–229. doi:10.1124/pr.56.2.6
5. Ma, P.; Mumper, R. J. *Nano Today* **2013,** *8,* 313–331. doi:10.1016/j.nantod.2013.04.006
6. Guaglianone, P.; Chan, K.; DelaFlor-Weiss, E.; Hanisch, R.; Jeffers, S.; Sharma, D.; Muggia, F. *Invest. New Drugs* **1994,** *12,* 103–110. doi:10.1007/BF00874439

7. Myhren, L.; Mostrøm Nilssen, L.; Nicolas, V.; Ove Døskeland, S.; Barratt, G.; Herfindal, L. *Eur. J. Pharm. Biopharm.* **2014,** *88,* 186–193. doi:10.1016/j.ejpb.2014.04.002
8. Ying, X.; Wen, H.; Lu, W.-L.; Dua, J.; Guo, J.; Tian, W.; Men, Y.; Zhang, Y.; Li, R.-J.; Yang, T.-Y.; Shang, D.-W.; Lou, J.-N.; Zhang, L.-R.; Zhang, Q. *J. Controlled Release* **2010,** *141,* 183–192. doi:10.1016/j.jconrel.2009.09.020
9. Fernandez-Fernandez, A.; Manchanda, R.; McGoron, A. J. *Appl. Biochem. Biotechnol.* **2011,** *165,* 1628–1651. doi:10.1007/s12010-011-9383-z
10. Xiao, H.; Li, W.; Qi, R.; Yan, L.; Wang, R.; Liu, S.; Zheng, Y.; Xie, Z.; Huang, Y.; Jing, X. *J. Controlled Release* **2012,** *163,* 304–314. doi:10.1016/j.jconrel.2012.06.004
11. Chen, B.; Lai, B.; Cheng, J.; Xia, G.; Gao, F.; Xu, W.; Ding, J.; Gao, C.; Sun, X.; Xu, C.; Chen, W.; Chen, W.; Liu, L.; Li, X.; Wang, X. *Int. J. Nanomed.* **2009,** *4,* 201–208. doi:10.2147/IJN.S7287
12. Ren, Y.; Zhang, H.; Chen, B.; Cheng, J.; Cai, X.; Liu, R.; Xia, G.; Wu, W.; Wang, S.; Ding, J.; Gao, C.; Wang, J.; Bao, W.; Wang, L.; Tian, L.; Song, H.; Wang, X. *Int. J. Nanomed.* **2012,** *7,* 2261–2269. doi:10.2147/IJN.S29357
13. Zhang, H.; Wang, C.; Chen, B.; Wang, X. *Int. J. Nanomed.* **2012,** *7,* 235–242. doi:10.2147/IJN.S27722
14. Danesh, N. M.; Lavaee, P.; Ramezani, P.; Abnous, K.; Taghdisi, S. M. *Int. J. Pharm.* **2015,** *489,* 311–317. doi:10.1016/j.ijpharm.2015.04.072
15. Peretz, S.; Regev, O. *Curr. Opin. Colloid Interface Sci.* **2012,** *17,* 360–368. doi:10.1016/j.cocis.2012.09.001
16. Yang, S.-T.; Luo, J.; Zhou, Q.; Wang, H. *Theranostics* **2012,** *2,* 271–282. doi:10.7150/thno.3618
17. Zhao, X.; Liu, R. *Environ. Int.* **2012,** *40,* 244–255. doi:10.1016/j.envint.2011.12.003
18. Mehra, N. K.; Jain, K.; Jain, N. K. *Drug Discovery Today* **2015,** *20,* 750–759. doi:10.1016/j.drudis.2015.01.006
19. Wong, B. S.; Yoong, S. L.; Jagusiak, A.; Panczyk, T.; Ho, H. K.; Ang, W. H.; Pastorin, G. *Adv. Drug Delivery Rev.* **2013,** *65,* 1964–2015. doi:10.1016/j.addr.2013.08.005
20. Liu, Z.; Sun, X.; Nakayama-Ratchford, N.; Dai, H. *ACS Nano* **2007,** *1,* 50–56. doi:10.1021/nn700040t
21. Jadhava, S. R.; Rao, K. S.; Zheng, Y.; Garavito, R. M.; Worden, R. M. *J. Colloid Interface Sci.* **2013,** *390,* 211–216. doi:10.1016/j.jcis.2012.09.031
22. Jabłonowska, E.; Więckowska, A.; Rogalska, E.; Bilewicz, R. *J. Electroanal. Chem.* **2011,** *660,* 360–366. doi:10.1016/j.jelechem.2011.03.018
23. Matyszewska, D.; Sek, S.; Bilewicz, R. *Langmuir* **2012,** *28,* 5182–5189. doi:10.1021/la2044027
24. Matyszewska, D.; Bilewicz, R. *Electrochim. Acta* **2015,** *162,* 45–52. doi:10.1016/j.electacta.2015.01.032
25. Nazaruk, E.; Sadowska, K.; Biernat, J. F.; Rogalski, J.; Ginalska, G.; Bilewicz, R. *Anal. Bioanal. Chem.* **2010,** *398,* 1651–1660. doi:10.1007/s00216-010-4012-1
26. Gaines, G. L., Jr. *Insoluble monolayers at liquid-gas interfaces;* Interscience: New York, 1966.
27. Harkins, W. D. *The Physical Chemistry of Surface Films;* Reinhold: New York, 1952.
28. Gallois, L.; Fiallo, M.; Garnier-Suillerot, A. *Biochim. Biophys. Acta* **1998,** *1370,* 31–40. doi:10.1016/S0005-2736(97)00241-1
29. Cancino, J.; Nobre, T. M.; Oliveira, O. N., Jr.; Machado, S. A. S.; Zucolotto, V. *Nanotoxicology* **2013,** *7,* 61–70. doi:10.3109/17435390.2011.629748
30. Komorsky-Lovrić, Š. *Bioelectrochemistry* **2006,** *69,* 82–87. doi:10.1016/j.bioelechem.2005.10.006
31. Matyszewska, D.; Brzezińska, K.; Juhaniewicz, J.; Bilewicz, R. *Colloids Surf., B* **2015,** *134,* 295–303. doi:10.1016/j.colsurfb.2015.07.001
32. Zhang, H.; Jiang, H.; Sun, F.; Wang, H.; Zhao, J.; Chena, B.; Wang, X. *Biosens. Bioelectron.* **2011,** *26,* 3361–3366. doi:10.1016/j.bios.2011.01.020
33. Taghdisi, S. M.; Lavaee, P.; Ramezani, M.; Abnous, K. *Eur. J. Pharm. Biopharm.* **2011,** *77,* 200–206. doi:10.1016/j.ejpb.2010.12.005
34. Yu, S.; He, C.; Ding, J.; Cheng, Y.; Song, W.; Zhuang, X.; Chen, X. *Soft Matter* **2013,** *9,* 2637–2645. doi:10.1039/c2sm27616j
35. Banks, C. E.; Wildgoose, G. G.; Heald, C. G. R.; Compton, R. G. *J. Iran. Chem. Soc.* **2005,** *2,* 60–64. doi:10.1007/BF03245781
36. Sadowska, K.; Roberts, K. P.; Wiser, R.; Biernat, J. F.; Jabłonowska, E.; Bilewicz, R. *Carbon* **2009,** *47,* 1501–1510. doi:10.1016/j.carbon.2009.01.044
37. Sadowska, K.; Stolarczyk, K.; Biernat, J. F.; Roberts, K. P.; Rogalski, J.; Bilewicz, R. *Bioelectrochemistry* **2010,** *80,* 73–80. doi:10.1016/j.bioelechem.2010.06.003

License and Terms

BEILSTEIN JOURNAL OF NANOTECHNOLOGY

Investigating organic multilayers by spectroscopic ellipsometry: specific and non-specific interactions of polyhistidine with NTA self-assembled monolayers

Ilaria Solano[1], Pietro Parisse[2], Ornella Cavalleri[*1], Federico Gramazio[1], Loredana Casalis[2] and Maurizio Canepa[1]

Full Research Paper

Open Access

Address:
[1]Dipartimento di Fisica, Università di Genova, Via Dodecaneso 33, Genova, Italy and [2]Elettra Sincrotrone Trieste S.C.p.A., s.s. 14 km 163,5 in Area Science Park, Basovizza, Trieste, Italy

Email:
Ornella Cavalleri[*] - cavalleri@fisica.unige.it

* Corresponding author

Keywords:
His-tag; nitrilotriacetic acid (NTA); protein binding; self-assembled monolayers (SAMs); spectroscopic ellipsometry

Beilstein J. Nanotechnol. **2016,** *7,* 544–553.
doi:10.3762/bjnano.7.48

Received: 02 December 2015
Accepted: 31 March 2016
Published: 13 April 2016

This article is part of the Thematic Series "Organized films".

Associate Editor: J. Lahann

Abstract

Background: A versatile strategy for protein–surface coupling in biochips exploits the affinity for polyhistidine of the nitrilotriacetic acid (NTA) group loaded with Ni(II). Methods based on optical reflectivity measurements such as spectroscopic ellipsometry (SE) allow for label-free, non-invasive monitoring of molecule adsorption/desorption at surfaces.

Results: This paper describes a SE study about the interaction of hexahistidine (His_6) on gold substrates functionalized with a thiolate self-assembled monolayer bearing the NTA end group. By systematically applying the difference spectra method, which emphasizes the small changes of the ellipsometry spectral response upon the nanoscale thickening/thinning of the molecular film, we characterized different steps of the process such as the NTA-functionalization of Au, the adsorption of the His_6 layer and its eventual displacement after reaction with competitive ligands. The films were investigated in liquid, and ex situ in ambient air. The SE investigation has been complemented by AFM measurements based on nanolithography methods (nanografting mode).

Conclusion: Our approach to the SE data, exploiting the full spectroscopic potential of the method and basic optical models, was able to provide a picture of the variation of the film thickness along the process. The combination of $\delta\Delta_{i+1,i}(\lambda)$, $\delta\Psi_{i+1,i}(\lambda)$ (layer-addition mode) and $\delta\Delta^{\dagger}_{i',i+1}(\lambda)$, $\delta\Psi^{\dagger}_{i',i+1}(\lambda)$ (layer-removal mode) difference spectra allowed us to clearly disentangle the adsorption of His_6 on the Ni-free NTA layer, due to non specific interactions, from the formation of a neatly thicker His_6 film induced by the Ni(II)-loading of the NTA SAM.

Introduction

The design of biosensing devices requires precise immobilization, with controlled orientation, of functional proteins on a surface, generally consisting of a substrate functionalized with a molecular receptor layer [1,2].

After seminal works [3], the interaction of chelated Ni ions with oligohistidine peptides has been largely implemented over the years for the affinity purification of recombinant proteins [4-6], and for the development of bioanalytical surfaces [7-12]. To this purpose, self-assembled monolayers (SAMs) terminated with the nitriloacetic acid (NTA) group, after loading with nickel ions (Ni(II)), provide platforms able to specifically bind his-tag proteins [13-18] and enzymes that retain their activity upon immobilization [19-21]. The affinity between the adsorbent surface and the protein can be modulated, e.g., by using multi-chelator constructs [22,23] or double hexahistidine tags [24].

Among applications, the NTA–Ni(II)–His coupling has been exploited for the functionalization of nanoparticles [25-27] and atomic force microscopy (AFM) tips [28] as well as for more biologically oriented applications such as the delivery of polymeric gene vehicles [29] or for the design of NTA-functionalized fluorescent probes able to track cellular events in situ by targeting specific His-tagged proteins [30,31].

Beyond selectivity, the reversibility of the NTA–Ni(II)-His coupling upon reaction with competitive ligands [32] makes this strategy a versatile system for the development of highly sensitive, specific and renewable sensing devices [33].

A high-performance sensor needs to integrate a specific binding scheme with a sensitive, non-destructive transduction of the binding event into a measurable signal. Optical methods based on optical reflectivity, such as surface plasmon resonance (SPR) and ellipsometry, allow for label-free, non-invasive, in situ monitoring of molecular adsorption/desorption at surfaces [34-40]. While SPR-based methods require supports with specific plasmonic properties, ellipsometry methods can be employed on a variety of reflecting solid surfaces. Spectroscopic ellipsometry (SE) can detect molecular adsorption on the receptor layer through the observation of thickness variations and, more specifically, through the spectroscopic characterization of UV–vis absorptions related to the analyte or to the receptor–analyte bond.

At variance with more traditional fields of application of SE [41-43], a reliable analysis of SE data on ultrathin films, at the nanometer scale thickness, must rely on the evaluation of the fine changes of the ellipsometry response upon the thickening/thinning of the molecular film. Such variations can be emphasized looking at so-called difference spectra [44], $\delta\Psi_{i+1,i}(\lambda)$, $\delta\Delta_{i+1,i}(\lambda)$, where the suffix labels the difference between the spectra taken after and before the addition of the $(i + 1)$-th layer in a multilayer stack.

Our approach, developed in recent years [45,46], aims to exploit, under an unconventional perspective, the full spectroscopic potential of difference spectra. Regarding the important class of thiolate SAMs on flat gold films, careful analysis of δ-spectra allowed us to disentangle spectral features related to the SAM and to the S–Au interface region [46] as well as to identify fingerprints of molecular UV–vis absorptions [47,48], with sub-monolayer sensitivity.

In a very recent work we successfully combined our approach with thickness determination based on AFM measurements exploiting smart nanolithography methods, such as the so-called nanoshaving [49], that considerably helped to reduce the uncertainty related to the correlation between thickness and refractive index that is typical of ultrathin films.

A step forward, we intend to apply the same methods to control the adsorption of the analyte layer (AL) on the receptor layer (RL), eventually distinguishing between specific and non-specific binding. In this article we describe a study about the interaction of His_6 on gold substrates functionalized with NTA (Figure 1). While on simple NTA-terminated films only non-specific adsorption of His_6 is expected, the loading with Ni(II) endows the RL with specific affinity towards His_6. We investigated the sequence of steps of the process (schematically sketched in Figure 1) beginning from the functionalization of Au until the final regeneration of the NTA layer through displacement of His_6. To this aim we will introduce convenient $\delta\Delta^{\dagger}_{i',i+1}(\lambda)$ and $\delta\Psi^{\dagger}_{i',i+1}(\lambda)$ difference spectra where the suffix labels the difference between the spectra taken after and before the removal of the $(i + 1)$-th layer in a multilayer stack.

The systems were investigated in situ in liquid, and ex situ in ambient air. The experiments aimed to explore the variation of film thickness after convenient stages of the process as well as to detect spectral features that could be eventually related to the specific NTA–Ni(II)–His_6 interaction. The SE investigation has been usefully complemented by AFM measurements based on SAM nanolitography (both shaving and grafting modes).

Results and Discussion

Substrate functionalization: the NTA-SAM

The first step of the experiment consisted of the formation and the characterization of the NTA-terminated precursor SAMs.

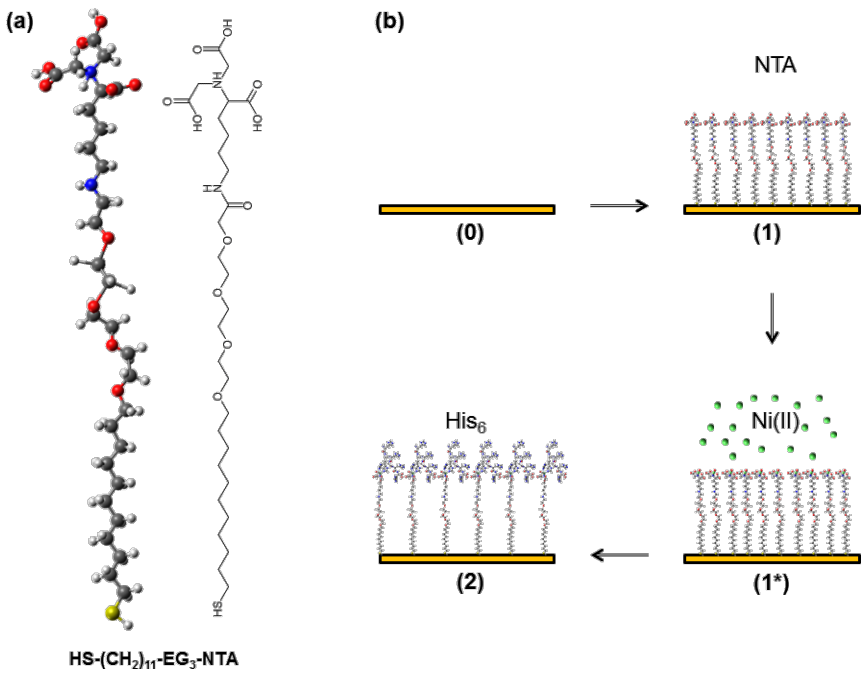

Figure 1: (a) Chemical structure of the HS-C11-EG3-NTA (NTA1) molecule; (b) sketch of the steps of sample preparation: (0) substrate preparation, (1) formation of the NTA SAM, (1*) Ni(II) loading and (2) adsorption of His_6. Step (1*) was skipped for a subset of samples in order to check non-specific His_6–NTA interactions. The ellipsometry analysis focused on steps (0), (1), (2).

Details on the preparation are reported in the Experimental section. Note that an accurate characterization of the precursor receptor SAM is a necessary prerequisite for a reliable interpretation of measurements about adsorption of analytes. Ex situ SE $\delta\Delta_{1,0}$ and $\delta\Psi_{1,0}$ spectra are presented in Figure 2 for two types of SAMs (HS-C11-EG3-NTA, NTA1, and HS-C16-EG3-NTA, NTA2). The suffixes 1 and 0 of $\delta\Delta_{1,0}$ and $\delta\Psi_{1,0}$ correspond to the SAM–Au and to the Au system, respectively. The results from NTA SAMs are compared with those obtained recently for oligo(ethylene glycol)-terminated alkanethiols, HS-C11-EG3 (T-OEG3) and HS-C11-EG6 (T-OEG6), for which the thicknesses were accurately determined by SE and AFM nanolithography [49].

The shape of the NTA spectra closely resembles that of T-OEG SAMS and does not show any evident features typical of intrinsic molecular optical absorptions [47,50]. Thus, the data are presented in comparison with a set of simulations based on the model of a transparent film (TF) onto the substrate (Au), assuming for TF a Cauchy-type dispersion formula [42]:

$$n = n_{\mathrm{TF}} + \frac{B\left[\mu\mathrm{m}^2\right]}{\lambda^2}; \quad \kappa = 0. \tag{1}$$

The shaded areas in Figure 2 span the representative range of $1.35 \leq n_{\mathrm{TF}} \leq 1.50$ [51], for three indicative values of the film thickness d_{TF}. The coefficient B was set to the value found in the analysis of T-OEG molecules (0.005) [49]. Note that the extension of the shaded bands provide an intuitive picture of the well-known correlation between refractive index and thickness that is typical for ultrathin films.

Systematic studies carried out in our group and, in particular, the analysis of the TF|Au model performed in [49] showed that $\delta\Delta_{1,0}$ and $\delta\Psi_{1,0}$ spectra provide a somewhat complementary information. While the $\delta\Delta_{1,0}$ spectra are sensitive to the properties of film + interface throughout the whole spectral range, the $\delta\Psi_{1,0}$ spectra show an interesting behavior in connection with the high reflectivity onset of Au which is evident in Ψ spectra (Figure 2b) between 500 and 550 nm.

Above this threshold, going towards the NIR, the TF|Au model predicts that Ψ tends to assume values close to 45° insensitive to transparent films: Simulated $\delta\Psi_{1,0}$ values vanish. Negative experimental $\delta\Psi_{1,0}$ values are due only to the absorptive properties of the interface layer, in connection with the formation of a strong molecule–gold bond [46,52].

In contrast, below the threshold, $\delta\Psi_{1,0}$ spectra bear substantial information only about the transparent part of the film [49].

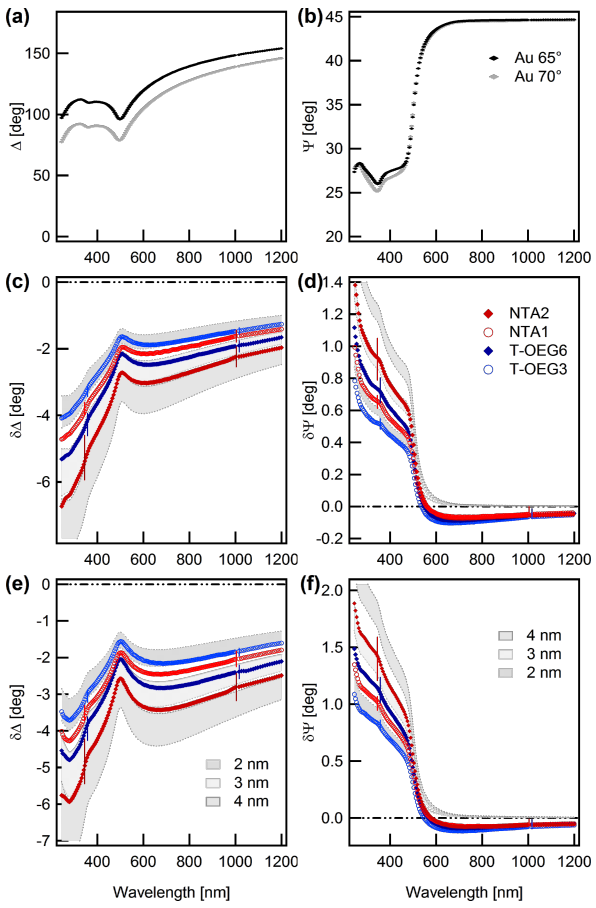

Figure 2: (a,b) Ex situ experimental SE spectra obtained on gold substrates. (c–f) Ex situ experimental difference spectra ($\delta\Delta_{1,0} = \Delta_1 - \Delta_0$, $\delta\Psi_{1,0} = \Psi_1 - \Psi_0$) obtained for NTA2 (red full diamonds) and NTA1 (red open circles) SAMs. Panels c and d: 65° angle of incidence, panels e and f: 70° angle of incidence. Data from T-OEG6 and T-OEG3 SAMs [49] are also shown for reference. Thin vertical bars represent the experimental uncertainty related to data dispersion over the investigated samples. Shaded areas illustrate the results of simulations based on the TF|Au model, for three values of the SAM thickness (d_{TF} = 2, 3 and 4 nm). For $\delta\Delta_{1,0}$ patterns (left) the top and bottom borders of the shadings correspond to n_{TF} = 1.35 and 1.50, respectively. For the $\delta\Psi_{1,0}$ spectra (right panels) the order is reversed.

Further, compared to the $\delta\Delta_{1,0}$ spectra, $\delta\Psi_{1,0}$ spectra are less affected by the correlation between n_{TF} and d_{TF}.

Thus, from careful inspection of the $\delta\Psi_{1,0}$ patterns in Figure 2, and considering the uncertainties of experiment and model, one can estimate d_{TF} values of 2.2 ± 0.3 and 3.1 ± 0.3 nm for the NTA1 and NTA2 SAMs, respectively. Negative $\delta\Psi_{1,0}$ values, which are substantially common to all the SAMs of Figure 2 and closely comparable to other well-structured thiolate–Au SAMs [46,47,53,54], can be effectively reproduced by simulations considering an effective interface layer [55] with effective thickness d_I of the order of 0.2 nm [46,49]. The sum D of d_I and d_{TF} (2.4 ± 0.3 and 3.3 ± 0.3 nm for the NTA1 and NTA2 SAMs, respectively) accounts for the total film thickness that is reflected in the $\delta\Delta_{1,0}$ spectra.

The AFM images of Figure 3a are representative of experiments of nanografting of T-OEG6 molecules in NTA SAMs. The latter were deposited with the same procedures applied in the SE measurements. The grafted areas are darker than the surrounding SAM carpet, indicating a lower height level. The histograms reported in Figure 3c show distributions that can be fitted by the superposition of two Gaussian curves. One, related to the T-OEG6 surface is taken as the reference; the second corresponds to the surface of the NTA SAM. The separation between the centers of the Gaussian curves provides $\Delta h_{NTA-TOEG6}$, the height difference between the NTA and T-OEG6 SAMs.

After repeating this procedure for ten grafted patches we were able to obtain an average value of $\Delta h_{NTA2-TOEG6}$ of 0.95 ± 0.15 nm (Figure 3d). Regarding NTA1 SAMs, the contrast with the nanografted T-OEG6 patches is much lower (Figure 3b). In this case the analysis of images provides $\Delta h_{NTA1-TOEG6}$ of 0.2 ± 0.1 nm (Figure 3d). Combining these findings with the AFM results regarding the height of T-OEG6 SAMs presented in [49], which amounted to 2.4 ± 0.3 nm, we obtain for the NTA1 and NTA2 films an AFM thickness of 2.6 ± 0.4 and 3.4 ± 0.5 nm, respectively.

The height difference between NTA2 and NTA1 SAMs measured with AFM ($\Delta h_{NTA2-NTA1}$ = 0.8 nm) and the thickness difference obtained by SE ($\Delta D_{NTA2-NTA1}$ = 0.9 nm) agree with the nominal length difference between the two molecules, of about 0.8 nm. However, although AFM and SE findings are compatible within the experimental uncertainty, the measurements by AFM yield height values that are systematically larger than the ellipsometry thickness. Small discrepancies between the two methods appear conceivable and even expected for several reasons. First of all, we need to consider that the NTA head is more charged than the OEG termination and can be responsible of an increased electrostatic repulsion and therefore of an increased height during the measurements in liquid. Moreover, we should consider systematic differences regarding the macroscopic area probed by the optical beam in SE vs the microscopic area probed by AFM and the different environment of the measurements (liquid for AFM, air for SE).

Note that SE does not provide direct information about molecular orientations in the SAM and about the SAM organization. Such properties should be probed through surface-sensitive infrared spectroscopy methods such as reflection–absorption infrared spectroscopy [56]. Nevertheless, the values of film thickness determined by SE and AFM testify the formation of

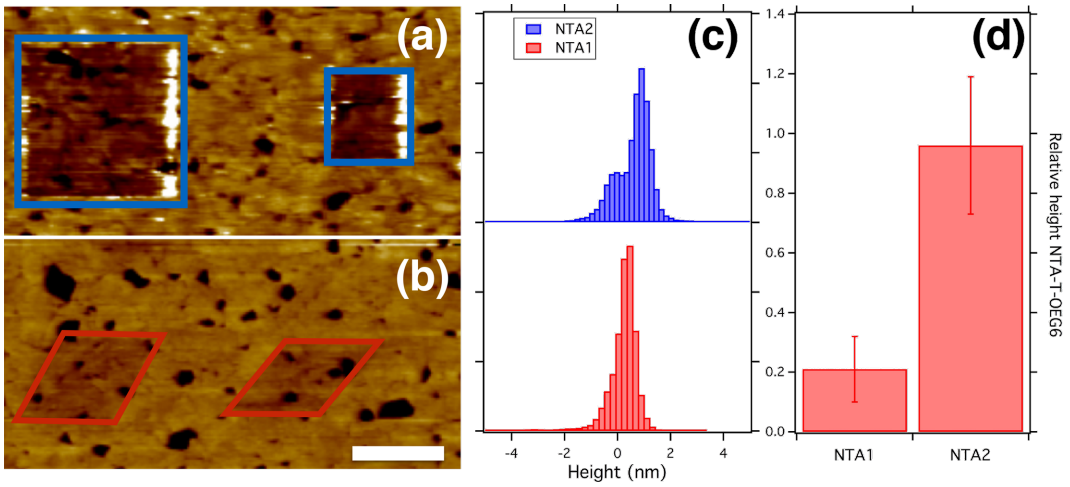

Figure 3: (a) Atomic force microscopy image showing two nanografted patches of T-OEG6 in a NTA2 SAM (b) the same for a NTA1 SAM. The white scale bar corresponds to 1 µm. (c) Height histograms corresponding to the AFM images in (a) and (b). The reference has been set at the center of the Gaussian distribution related to the squared dark areas in the images. (d) Synthesis of histogram analysis for the NTA1 and NTA2 samples investigated providing the average values of $\Delta h_{NTA-TOEG6}$ and $\Delta h_{NTA1-TOEG6}$ (for details see the text).

compact NTA SAMs, which can be used for second-layer adsorption experiments.

His_6–NTA interaction

Exploratory checks showed that the variations induced by Ni(II) loading on the NTA/Au SE spectra were very small. Thus, we decided to study the His_6 adsorption (step (2) in Figure 1) by referencing the difference spectra to the data of the NTA film. Specific or non-specific interactions of His_6 are therefore probed through a comparison of the results obtained with or without the Ni(II) pre-loading. We adopted preparation protocols described in literature [57], which are summarized in the Experimental section.

$\delta\Delta_{2,1}$ and $\delta\Psi_{2,1}$ difference spectra shown in Figure 4a,b are representative of the observed behavior. Despite the reduced refractive index mismatch between the film and the ambient and the use of cell windows tending to lower the signal-to-noise ratio, the emerging picture appears rather sharp.

In the case of Ni-free RL (light grey circles) we found very low $\delta\Psi_{2,1}$ and $\delta\Delta_{2,1}$ spectral values, over the whole wavelength range. These results suggest a very modest thickness increment. In facts, the formation of films uniformly spread on gold-like substrates, even if very thin, usually induces a well-defined relative maximum of $\delta\Delta_{i+1,i}$ at about 500 nm [46,52]. This is actually missing in the data, possibly indicating the formation of a low-coverage sub-monolayer [58], a situation that is compatible with non-specific His_6–NTA interactions, in accordance with literature [10].

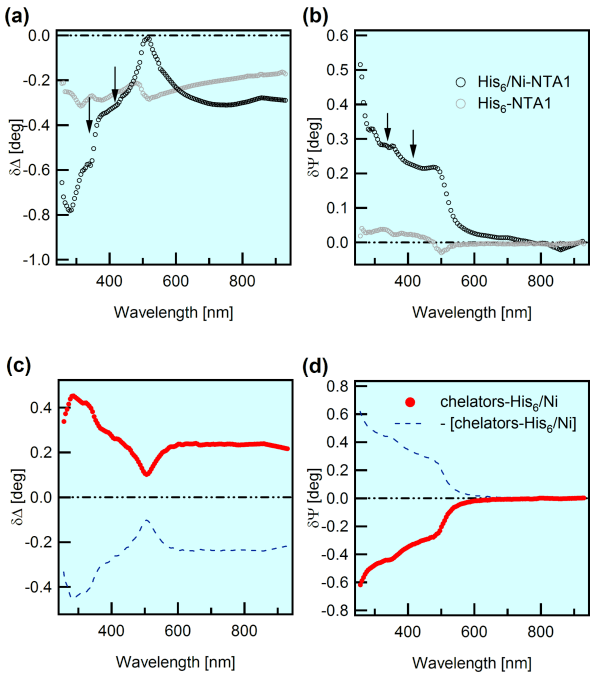

Figure 4: His_6 adsorption on the NTA/Au system and subsequent treatment with imidazole/EDTA. The SE data are derived from in situ (buffer) measurements at 65° angle of incidence. (a,b) $\delta\Delta_{2,1}$ and $\delta\Psi_{2,1}$ difference spectra; the suffixes 1 and 2 indicate the NTA1/Au system before and after the exposure to His_6 molecules, respectively. Black and light grey symbols refer to measurements with and without Ni(II) loading, respectively. Arrows indicate possible weak optical absorptions (see the text for details). (c,d) Red symbols: $\delta\Delta^{\dagger}_{1',2}$, $\delta\Psi^{\dagger}_{1',2}$ spectra; the suffixes 1' and 2 stand for the His_6/NTA1/Au system after and before the treatment with chelating agents. The blue dashed curves represent $-\delta\Delta^{\dagger}_{1',2}$ and $-\delta\Psi^{\dagger}_{1',2}$ spectra.

Conversely, well-structured spectra were observed after the interaction of His_6 with Ni-loaded NTA SAMs (black open circles), testifying the formation of a well-defined layer. Note in passing that Ni(II) loading and subsequent His_6 adsorption have very little influence on the $\delta\Psi_{2,1}$ values above 550 nm, which are overall positive and close to zero. This finding suggests that the percolation of Ni through the compact NTA SAM down to the S–Au interface is likely negligible.

In order to add confidence about the formation of the Ni(II)–His_6 complex, we analyzed its interaction with competitive chelating agents eventually leading to the regeneration of the NTA film. Representative difference between spectra measured after and before the imidazole/EDTA treatment, for brevity $\delta\Delta^{\dagger}_{1',2}$ and $\delta\Psi^{\dagger}_{1',2}$, are shown in Figure 4c,d (red open circles).

The graphic choice in panels c and d emphasizes that $\delta\Delta^{\dagger}_{1',2}$ and $\delta\Psi^{\dagger}_{1',2}$ spectra are specular (with respect to the null level) to $\delta\Delta_{2,1}$ and $\delta\Psi_{2,1}$ spectra which have been considered until now (and in all our previous works on SAMs on Au). $\delta\Delta_{i+1,i}$ and $\delta\Psi_{i+1,i}$, were always associated with the addition of a molecular layer (for example the NTA layer on the Au substrate or the His_6 layer on the NTA/Au system). In the case of Figure 4c,d, positive $\delta\Delta^{\dagger}_{1',2}$ and low-wavelength, negative $\delta\Psi^{\dagger}_{1',2}$ (red curves) indicate a neat decrease of the thickness, to be associated with the removal of molecular layer 2 (His_6).

Further insight into thickening or thinning of the films following specific adsorption and removal of His_6 was obtained from ex situ measurements. In Figure 5, $\delta\Delta_{2,1}$ and $\delta\Psi_{2,1}$ spectra (black symbols), related to the His_6 adsorption, are compared with $\delta\Delta_{1',1}$ and $\delta\Psi_{1',1}$ spectra (grey symbols) obtained after the completion of the imidazole/EDTA treatment. Note that these difference spectra are referenced to the NTA/Au film. In the figure, we also report the $\delta\Delta_{1,0}$ and $\delta\Psi_{1,0}$ spectra from Figure 2, referenced to the bare gold substrate. Ideally, $\delta\Delta_{1',1}$ and $\delta\Psi_{1',1}$ should present values close to the zero. Indeed, they appear significantly lower than the $\delta\Delta_{2,1}$ and $\delta\Psi_{2,1}$ spectra, indicating the thinning of the film.

The ex situ measurements are also useful for an estimate of the second layer thickness exploiting its rough proportionality with the NIR $\delta\Delta_{2,1}$ values, considering the NTA/Au film as reference and performing the same type of analysis as that in Figure 2. With a reasonable guess for the His_6 layer refraction index in the range of 1.35–1.40, the layer thickness is estimated in the range of 1.5–1.7 nm range. Analogously, we can also estimate that the imidazole/EDTA treatment removed ≈75% of the His_6 layer. The removal percentage could be even higher considering the conceivable effect of imidazole/EDTA residuals in $\delta\Delta_{1',1}$ and $\delta\Psi_{1',1}$ spectra. Therefore, the SE analysis of both in situ and ex situ data is able to follow the thickness variations induced by the addition/removal of the Ni(II)–His_6 layer.

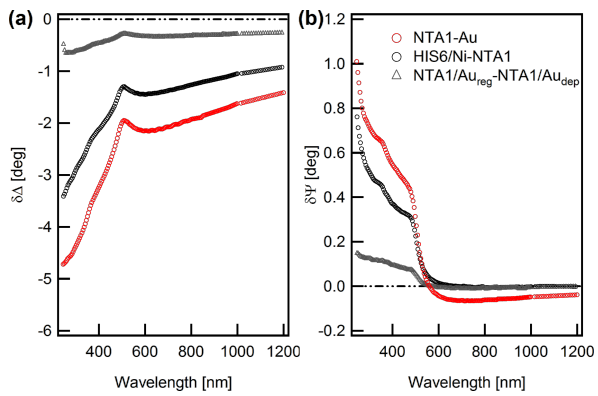

Figure 5: $\delta\Delta_{2,1}$ and $\delta\Psi_{2,1}$ spectra (black circles), related to the His_6 adsorption, are compared with $\delta\Delta_{1',1}$ and $\delta\Psi_{1',1}$ spectra (grey triangles) obtained after the completion of the imidazole/EDTA treatment. These difference spectra are referenced to the NTA/Au system. $\delta\Delta_{1,0}$ and $\delta\Psi_{1,0}$ spectra associated to the deposition of NTA1 on the Au substrate (red circles) are also reported for comparison.

An important step further would be the detection of spectral fingerprints of the Ni(II)–His_6 bond. In this respect, a comprehensive transmission spectroscopy study in solution reported optical absorptions of the Ni(II)–His_6 complex in the spectral range of 300–700 nm. Shape and intensity of absorption bands were found to depend on the Ni(II)/His_6 concentration ratio and the pH value of the solution [15]. Indeed, in previous SE works on other SAMs on gold, we could detect optical molecular fingerprints as characteristic narrow-band dips in difference spectra. Specific examples are the intense Soret band observed in in situ spectra of cytochrome C SAMs [48,50] or the UV absorptions of carbazole groups [47]. Detection of molecular fingerprints becomes definitely easier as the thickness scales up, as in the case of a 30 nm thick photochromic polymer film [59].

Due to index matching issues, observation of optical absorptions in SAMs becomes easier in liquid with refractive index close to that of the film [48,50]. A close look at in situ data (Figure 4) shows fine spectral features (indicated by arrows) which cannot be reproduced by a simple Cauchy model, and could be tentatively attributed to optical absorptions. However, these features are not intense and sharp enough for an unambiguous assignment, which would require, e.g., a check of K–K consistency, as it was possible in previous experiments on other molecular systems [48,50,59]. Therefore the direct spectroscopic detection of the Ni(II)–His_6 compound is still uncertain and will require further investigation.

Conclusion

We have applied spectroscopic ellipsometry to investigate the interaction of His_6 with gold surfaces functionalized with a thiolate, OEG SAM bearing the NTA end-group, a system which is of recognized relevance for the design of a whole class of bio-sensing devices.

Indeed, ellipsometry was already employed to study related systems. In [37], about mixed layers of bis-NTA thiols with inert OEG thiols, the authors thoroughly reported on imaging ellipsometry measurements at a single wavelength. They exploited variations of Δ and Ψ to obtain information about the thickness and homogeneity of the mixed layers while their functionalities were probed using imaging SPR. In [51] the NTA–Ni(II)-mediated immobilization of His_6-tagged green fluorescent protein on a silica surface was reported. Ellipsometry, at two wavelengths, was exploited mainly to characterize the precursor NTA SAM (about 15 nm thick) while the interactions with proteins of the NTA surface were studied by fluorescence methods. Spectroscopic ellipsometry was also frequently used on other NTA-related systems as an ancillary characterization method [10,60,61].

To our knowledge this is the first time that SE has been used to comprehensively address the process, from the characterization of the precursor NTA layer to the study of the Ni(II)-mediated His_6 absorption and the final regeneration of the NTA layer obtained by exposure to competitive chelating agents.

Our approach, progressively developed in recent years, is based on the careful analysis of SE difference spectra bearing information on the small changes of the ellipsometry response upon the thickening or thinning of molecular films with nanoscale thickness, and aims to fully exploit the rich broadband potential of SE, a point which marks the difference with single wavelength techniques, including SPR. Difference spectra, measured for hundreds of wavelengths ranging from the short UV to the NIR, proved able to show the variation of film thickness related to a complex process consisting of addition and removal of several organic layers.

Our investigation addressed the characterization of the NTA SAM on gold, exploiting the powerful cross-check with AFM measurements of the SAM height based on smart nanolitography methods. The SE data, which have been interpreted with basic models, provided a reliable evaluation of the thickness and optical properties of compact NTA SAMs. The accurate knowledge of the properties of the functionalizing SAMs constituted the necessary base for the second step of the experiment which regarded the investigation of the NTA reaction with His_6. The experiments were not conclusive regarding the direct spectroscopic detection of the NTA–Ni(II)–His_6 bond, which will deserve further investigation. Nonetheless, the combination of $\delta\Delta,\Psi_{i+1,i}(\lambda)$ (layer-addition mode) and $\delta\Delta,\Psi^{\dagger}_{i',i+1}(\lambda)$ (layer-removal mode) allowed us to clearly disentangle the formation of a His_6 film induced by Ni(II)-loading of the NTA SAM from the non-specific adsorption of His_6 on the Ni-free NTA layer.

This investigation is intended to form a solid analytical background towards the study of layered systems of greater complexity such as the interaction of NTA with His_6-tag proteins, or the DNA/DNA hybridization, which is ongoing in our laboratories. Further, this paper describes a quite general method, which can be applied to other forms of organized organic nano-multi layers on solid as well liquid reflecting substrates.

Experimental

Gold substrates and reagents

Gold films for optical measurements were purchased from Arrandee™ (200 nm thick, deposited on glass with a Cr primer). For AFM measurements Ulman-type [62] ultra-flat stripped gold surfaces were preferred. Ultra-flat gold samples were prepared by UHV deposition of gold onto a freshly cleaned Si(111) wafer. A silicon sample was then glued on the gold surface and cured overnight at 130 °C. Ultraflat and clean gold surfaces are obtained by mechanically stripping the silicon wafer substrate from the silicon gold sandwich [49,62].

(1-Mercaptoundec-11-yl)tri(ethylene glycol) and (1-mercaptoundec-16-yl)tri(ethylene glycol) with NTA (for brevity NTA1 and NTA2) were purchased from Prochimia Surfaces. Hexahistidine His_6 (840.85 g/mol) was purchased from GenScript. Ethylenediaminetetraacetic acid (EDTA), imidazole, tris(hydroxymethyl)aminomethane (Tris), NaCl and $NiCl_2$ were purchased from Sigma-Aldrich.

NTA SAM deposition and interaction with His_6

Clean Arrandee samples or freshly stripped Ulman gold samples were incubated for 24 h in 15 μM NTA1 (NTA2) solution, using ethanol as solvent. For ex situ optical measurements the NTA/Au samples were rinsed with ethanol and dried with N_2 flow. A subset of NTA/Au samples were transferred in a salt buffer solution (20 mM Tris and 150 mM NaCl, pH 7.4) for subsequent characterization and treatments. After a first optical characterization in the new medium, the samples were immersed in 0.5 M EDTA (pH 8.6) solution for 15 min in order to remove undesired divalent metal ions and rinsed in MilliQ water. Soaking the NTA samples in a solution of 10 mM $NiCl_2$ in 20 mM Tris (pH 7.4) for 5–10 min allowed for the coordination of NTA COOH groups with Ni^{2+} ions. The samples were

then immersed in the salt buffer solution containing a 170 μM concentration of His_6. A subsets of samples were exposed to His_6 without pre-emptive Ni loading. Finally the samples were rinsed with the buffer solution, characterized by SE in situ, rinsed in MilliQ water, fluxed with N_2 and characterized by SE ex situ. Regeneration of the NTA/Au surface was accomplished by rinsing the sample in 0.4 M imidazole in 20 mM Tris solution and then in 0.5 M EDTA (pH 8.6) solution.

Spectroscopic ellipsometry

SE measurements were performed on a rotating compensator instrument (M-2000, J.A.Woollam Co.Inc.). Ex situ data were collected at 65–70° angle of incidence. The presented spectra were obtained after the averaging over five samples and over four different zones of each sample. In situ measurements were conducted in a custom-made Teflon cell with 65° angle of incidence. The in situ data are presented in the transparency region of the solvent. Principles and applications of SE are detailed in books [42,43] and reviews [63,64]. Briefly, standard ellipsometry consists in the investigation of the coefficient $\rho = \tilde{r}_p / \tilde{r}_s = \tan \Psi \, e^{i\Delta}$ where $\tilde{r}_p$ and $\tilde{r}_s$ are the complex Fresnel reflection coefficients related respectively to p- and s-polarization. The ellipsometric analysis is performed through comparison between experimental and simulated data. Simulations are based on models that take into account optical and morphological properties of the layered sample.

AFM nanografting and imaging

AFM experiments were carried out with a XE100 (Park Instruments) instrument in custom liquid cells. For nanografting, the freshly prepared NTA SAM samples were glued in a custom liquid cell filled with a solution of 30 μM HS-C11-OEG6 (T-OEG6) in ethanol. During the nanografting process, we operated in contact mode with commercial AFM tips (NSC19 Mikromasch, k = 0.6 N/m), applying a high load (100 nN) in a confined (from 0.5 × 0.5 to 2 × 2 μm^2) scanning area. The applied load is sufficient to displace the NTA molecules that are substituted by the T-OEG6 molecules present in the ethanol solution [65,66]. The nanografted areas have been then imaged in soft contact mode in ethanol or in saline buffer (Tris-HCl 20 mM, NaCl 150 mM, pH 7.4) with commercial cantilevers (CSC38 Mikromasch, k = 0.03 N/m) at the minimum force detectable (0.1 nN). Images and data were analyzed with XEI (Park Instruments) and Igor Pro (Wavemetrics Inc.) software.

Acknowledgements

This work was supported by the Italian Ministry of Education (grant RBAP11ETKA-005). The authors thank Matteo Castronovo for useful hints in the initial stage of the work, B. Sanavio for clarifications on the preparation protocols, and G. Bracco for discussions.

References

1. Prime, K.; Whitesides, G. *Science* **1991,** *252,* 1164–1167. doi:10.1126/science.252.5009.1164
2. Hucknall, A.; Rangarajan, S.; Chilkoti, A. *Adv. Mater.* **2009,** *21,* 2441–2446. doi:10.1002/adma.200900383
3. Hochuli, E.; Döbeli, H.; Schacher, A. *J. Chromatogr. A* **1987,** *411,* 177–184. doi:10.1016/S0021-9673(00)93969-4
4. Gaberc-Porekar, V.; Menart, V. *Chem. Eng. Technol.* **2005,** *28,* 1306–1314. doi:10.1002/ceat.200500167
5. Jain, P.; Sun, L.; Dai, J.; Baker, G. L.; Bruening, M. L. *Biomacromolecules* **2007,** *8,* 3102–3107. doi:10.1021/bm700515m
6. Kim, S. H.; Jeyakumar, M.; Katzenellenbogen, J. A. *J. Am. Chem. Soc.* **2007,** *129,* 13254–13264. doi:10.1021/ja074443f
7. Zhen, G.; Falconnet, D.; Kuennemann, E.; Vörös, J.; Spencer, N. D.; Textor, M.; Zürcher, S. *Adv. Funct. Mater.* **2006,** *16,* 243–251. doi:10.1002/adfm.200500232
8. Shen, W.; Zhong, H.; Neff, D.; Norton, M. L. *J. Am. Chem. Soc.* **2009,** *131,* 6660–6661. doi:10.1021/ja901407j
9. Liu, Y. C.; Rieben, N.; Iversen, L.; Sørensen, B.; Park, J.; Nygrård, J.; Martinez, K. L. *Nanotechnology* **2010,** *21,* 245105. doi:10.1088/0957-4484/21/24/245105
10. Gautrot, J. E.; Huck, W. T. S.; Welch, M.; Ramstedt, M. *ACS Appl. Mater. Interfaces* **2010,** *2,* 193–202. doi:10.1021/am9006484
11. Maalouli, N.; Gouget-Laemmel, A. C.; Pinchemel, B.; Bouazaoui, M.; Chazalviel, J.-N.; Ozanam, F.; Yang, Y.; Burkhard, P.; Boukherroub, R.; Szunerits, S. *Langmuir* **2011,** *27,* 5498–5505. doi:10.1021/la2005437
12. Valenti, L. E.; Martins, V. L.; Herrera, E.; Torresi, R. M.; Giacomelli, C. E. *J. Mater. Chem. B* **2013,** *1,* 4921–4931. doi:10.1039/C3TB20769B
13. Wegner, G. J.; Lee, H. J.; Marriott, G.; Corn, R. M. *Anal. Chem.* **2003,** *75,* 4740–4746. doi:10.1021/ac0344438
14. Ataka, K.; Giess, F.; Knoll, W.; Naumann, R.; Haber-Pohlmeier, S.; Richter, B.; Heberle, J. *J. Am. Chem. Soc.* **2004,** *126,* 16199–16206. doi:10.1021/ja045951h
15. Valenti, L. E.; Pauli, C. P. D.; Giacomelli, C. E. *J. Inorg. Biochem.* **2006,** *100,* 192–200. doi:10.1016/j.jinorgbio.2005.11.003
16. Cheng, F.; Gamble, L. J.; Castner, D. G. *Anal. Chem.* **2008,** *80,* 2564–2573. doi:10.1021/ac702380w
17. Ley, C.; Holtmann, D.; Mangold, K.-M.; Schrader, J. *Colloids Surf., B* **2011,** *88,* 539–551. doi:10.1016/j.colsurfb.2011.07.044
18. Schartner, J.; Güldenhaupt, J.; Mei, B.; Rögner, M.; Muhler, M.; Gerwert, K.; Kötting, C. *J. Am. Chem. Soc.* **2013,** *135,* 4079–4087. doi:10.1021/ja400253p
19. Nakamura, I.; Makino, A.; Ohmae, M.; Kimura, S. *Macromol. Biosci.* **2010,** *10,* 1265–1272. doi:10.1002/mabi.201000189
20. Le, T. T.; Wilde, C. P.; Grossman, N.; Cass, A. E. G. *Phys. Chem. Chem. Phys.* **2011,** *13,* 5271–5278. doi:10.1039/C0CP02531C
21. Sosna, M.; Boer, H.; Bartlett, P. N. *ChemPhysChem* **2013,** *14,* 2225–2231. doi:10.1002/cphc.201300340
22. Tinazli, A.; Tang, J.; Valiokas, R.; Picuric, S.; Lata, S.; Piehler, J.; Liedberg, B.; Tampé, R. *Chem. – Eur. J.* **2005,** *11,* 5249–5259. doi:10.1002/chem.200500154
23. Valiokas, R.; Klenkar, G.; Tinazli, A.; Reichel, A.; Tampé, R.; Piehler, J.; Liedberg, B. *Langmuir* **2008,** *24,* 4959–4967. doi:10.1021/la703709a
24. Khan, F.; He, M.; Taussig, M. J. *Anal. Chem.* **2006,** *78,* 3072–3079. doi:10.1021/ac060184l

25. Hainfeld, J. F.; Liu, W.; Halsey, C. M. R.; Freimuth, P.; Powell, R. D. *J. Struct. Biol.* **1999,** *127,* 185–198. doi:10.1006/jsbi.1999.4149
26. Li, Y.-C.; Lin, Y.-S.; Tsai, P.-J.; Chen, C.-T.; Chen, W.-Y.; Chen, Y.-C. *Anal. Chem.* **2007,** *79,* 7519–7525. doi:10.1021/ac0711440
27. Xie, H.-Y.; Zhen, R.; Wang, B.; Feng, Y.-J.; Chen, P.; Hao, J. *J. Phys. Chem. C* **2010,** *114,* 4825–4830. doi:10.1021/jp910753f
28. Schmitt, L.; Ludwig, M.; Gaub, H. E.; Tampé, R. *Biophys. J.* **2000,** *78,* 3275–3285. doi:10.1016/S0006-3495(00)76863-9
29. Wang, C.-H. K.; Jiang, S.; Pun, S. H. *Langmuir* **2010,** *26,* 15445–15452. doi:10.1021/la1025203
30. Uchinomiya, S.; Nonaka, H.; Wakayama, S.; Ojida, A.; Hamachi, I. *Chem. Commun.* **2013,** *49,* 5022–5024. doi:10.1039/C3CC41979G
31. Lai, Y.-T.; Chang, Y.-Y.; Hu, L.; Yang, Y.; Chao, A.; Du, Z.-Y.; Tanner, J. A.; Chye, M.-L.; Qian, C.; Ng, K.-M.; Li, H.; Sun, H. *Proc. Natl. Acad. Sci. U. S. A.* **2015,** *112,* 2948–2953. doi:10.1073/pnas.1419598112
32. Sigal, G. B.; Bamdad, C.; Barberis, A.; Strominger, J.; Whitesides, G. M. *Anal. Chem.* **1996,** *68,* 490–497. doi:10.1021/ac9504023
33. You, C.; Piehler, J. *Anal. Bioanal. Chem.* **2014,** *406,* 3345–3357. doi:10.1007/s00216-014-7803-y
34. Poksinski, M.; Arwin, H. *Thin Solid Films* **2004,** *455–456,* 716–721. doi:10.1016/j.tsf.2004.01.037
35. Jung, L. S.; Campbell, C. T.; Chinowsky, T. M.; Mar, M. N.; Yee, S. S. *Langmuir* **1998,** *14,* 5636–5648. doi:10.1021/la971228b
36. Vanderah, D. J.; Vierling, R. J.; Walker, M. L. *Langmuir* **2009,** *25,* 5026–5030. doi:10.1021/la803896a
37. Klenkar, G.; Valiokas, R.; Lundström, I.; Tinazli, A.; Tampé, R.; Piehler, J.; Liedberg, B. *Anal. Chem.* **2006,** *78,* 3643–3650. doi:10.1021/ac060024+
38. Nabok, A.; Tsargorodskaya, A. *Thin Solid Films* **2008,** *516,* 8993–9001. doi:10.1016/j.tsf.2007.11.077
39. Rodenhausen, K. B.; Kasputis, T.; Pannier, A. K.; Gerasimov, J. Y.; Lai, R. Y.; Solinsky, M.; Tiwald, T. E.; Wang, H.; Sarkar, A.; Hofmann, T.; Ianno, N.; Schubert, M. *Rev. Sci. Instrum.* **2011,** *82,* 103111. doi:10.1063/1.3653880
40. Rauch, S.; Eichhorn, K.-J.; Kuckling, D.; Stamm, M.; Uhlmann, P. *Adv. Funct. Mater.* **2013,** *23,* 5675–5681. doi:10.1002/adfm.201300849
41. Azzam, R. M. A.; Bashara, N. M. *Ellipsometry and Polarized Light,* 3rd ed.; North-Holland: New York, 1977.
42. Fujiwara, H. *Spectroscopic Ellipsometry: Principles and Applications,* 1st ed.; Wiley: Chichester, United Kingdom, 2007.
43. Tompkins, H.; Irene, E., Eds. *Handbook of ellipsometry,* 1st ed.; Andrew: Norwich, 2005.
44. Shi, J.; Hong, B.; Parikh, A.; Collins, R.; Allara, D. *Chem. Phys. Lett.* **1995,** *246,* 90–94. doi:10.1016/0009-2614(95)01085-N
45. Bordi, F.; Prato, M.; Cavalleri, O.; Cametti, C.; Canepa, M.; Gliozzi, A. *J. Phys. Chem. B* **2004,** *108,* 20263–20272. doi:10.1021/jp047141y
46. Prato, M.; Moroni, R.; Bisio, F.; Rolandi, R.; Mattera, L.; Cavalleri, O.; Canepa, M. *J. Phys. Chem. C* **2008,** *112,* 3899–3906. doi:10.1021/jp711194s
47. Prato, M.; Alloisio, M.; Jadhav, S. A.; Chincarini, A.; Svaldo-Lanero, T.; Bisio, F.; Cavalleri, O.; Canepa, M. *J. Phys. Chem. C* **2009,** *113,* 20683–20688. doi:10.1021/jp906298m
48. Toccafondi, C.; Prato, M.; Maidecchi, G.; Penco, A.; Bisio, F.; Cavalleri, O.; Canepa, M. *J. Colloid Interface Sci.* **2011,** *364,* 125–132. doi:10.1016/j.jcis.2011.07.097
49. Solano, I.; Parisse, P.; Gramazio, F.; Cavalleri, O.; Bracco, G.; Castronovo, M.; Casalis, L.; Canepa, M. *Phys. Chem. Chem. Phys.* **2015,** *17,* 28774–28781. doi:10.1039/C5CP04028K
50. Toccafondi, C.; Cavalleri, O.; Bisio, F.; Canepa, M. *Thin Solid Films* **2013,** *543,* 78–82. doi:10.1016/j.tsf.2013.02.117
51. Kang, E.; Park, J.-W.; McClellan, S. J.; Kim, J.-M.; Holland, D. P.; Lee, G. U.; Franses, E. I.; Park, K.; Thompson, D. H. *Langmuir* **2007,** *23,* 6281–6288. doi:10.1021/la063719e
52. Canepa, M.; Maidecchi, G.; Toccafondi, C.; Cavalleri, O.; Prato, M.; Chaudhari, V.; Esaulov, V. A. *Phys. Chem. Chem. Phys.* **2013,** *15,* 11559–11565. doi:10.1039/C3CP51304A
53. Hamoudi, H.; Prato, M.; Dablemont, C.; Cavalleri, O.; Canepa, M.; Esaulov, V. A. *Langmuir* **2010,** *26,* 7242–7247. doi:10.1021/la904317b
54. Hamoudi, H.; Uosaki, K.; Ariga, K.; Esaulov, V. A. *RSC Adv.* **2014,** *4,* 39657–39666. doi:10.1039/C4RA05476H
55. Mårtensson, J.; Arwin, H. *Langmuir* **1995,** *11,* 963–968. doi:10.1021/la00003a045
56. Hamoudi, H.; Guo, Z.; Prato, M.; Dablemont, C.; Zheng, W. Q.; Bourguignon, B.; Canepa, M.; Esaulov, V. A. *Phys. Chem. Chem. Phys.* **2008,** *10,* 6836–6841. doi:10.1039/b809760g
57. Block, H.; Maertens, B.; Spriestersbach, A.; Brinker, N.; Kubicek, J.; Fabis, R.; Labahn, J.; Schaefer, F. Immobilized-Metal Affinity Chromatography (IMAC): A Review. In *Guide to Protein Purification,* 2nd ed.; Burgess, R. R.; Deutscher, M. P., Eds.; Methods in Enzymology, Vol. 463; Academic Press, 2009; pp 439–473.
58. Prato, M.; Gussoni, A.; Panizza, M.; Cavalleri, O.; Mattera, L.; Canepa, M. *Phys. Status Solidi C* **2008,** *5,* 1304–1307. doi:10.1002/pssc.200777882
59. Toccafondi, C.; Occhi, L.; Cavalleri, O.; Penco, A.; Castagna, R.; Bianco, A.; Bertarelli, C.; Comoretto, D.; Canepa, M. *J. Mater. Chem. C* **2014,** *2,* 4692–4698. doi:10.1039/C4TC00371C
60. Thompson, L. B.; Mack, N. H.; Nuzzo, R. G. *Phys. Chem. Chem. Phys.* **2010,** *12,* 4301–4308. doi:10.1039/B920713A
61. Vaish, A.; Silin, V.; Walker, M. L.; Steffens, K. L.; Krueger, S.; Yeliseev, A. A.; Gawrisch, K.; Vanderah, D. J. *Chem. Commun.* **2013,** *49,* 2685–2687. doi:10.1039/C3CC00077J
62. Gupta, P.; Loos, K.; Korniakov, A.; Spagnoli, C.; Cowman, M.; Ulman, A. *Angew. Chem., Int. Ed.* **2004,** *43,* 520–523. doi:10.1002/anie.200352249
63. Losurdo, M.; Bergmair, M.; Bruno, G.; Cattelan, D.; Cobet, C.; de Martino, A.; Fleischer, K.; Dohcevic-Mitrovic, Z.; Esser, N.; Galliet, M.; Gajic, R.; Hemzal, D.; Hingerl, K.; Humlicek, J.; Ossikovski, R.; Popovic, Z. V.; Saxl, O. *J. Nanopart. Res.* **2009,** *11,* 1521–1554. doi:10.1007/s11051-009-9662-6
64. Oates, T. W. H.; Wormeester, H.; Arwin, H. *Prog. Surf. Sci.* **2011,** *86,* 328–376. doi:10.1016/j.progsurf.2011.08.004
65. Sanavio, B.; Scaini, D.; Grunwald, C.; Legname, G.; Scoles, G.; Casalis, L. *ACS Nano* **2010,** *4,* 6607–6616. doi:10.1021/nn101872w
66. Scaini, D.; Castronovo, M.; Casalis, L.; Scoles, G. *ACS Nano* **2008,** *2,* 507–515. doi:10.1021/nn700342p